

AD-A111 638

SCIENCE APPLICATIONS INC MCLEAN VA
GEOPHYSICAL PLASMAS AND ATMOSPHERIC MODELING.(U)

F/G 4/1

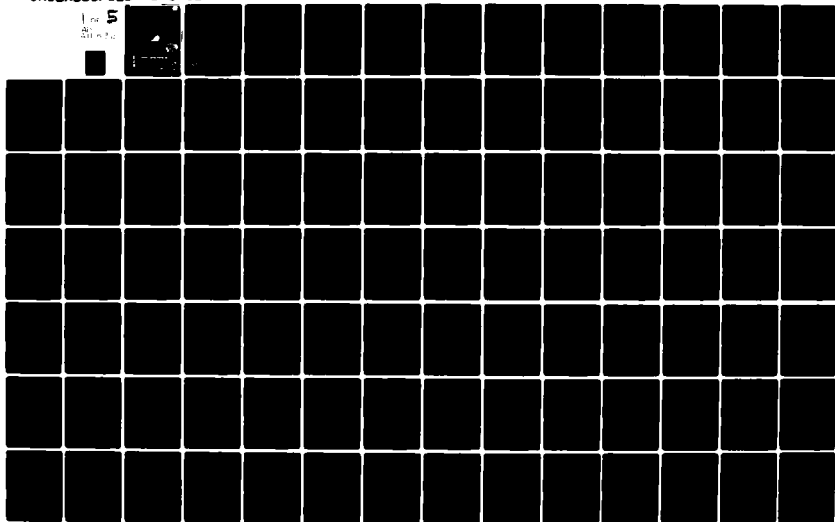
JAN 82 E HYMAN, J APRUZESE, S BRECHT, W CHAO N00014-81-C-2038

UNCLASSIFIED

SAI-88-676-WA

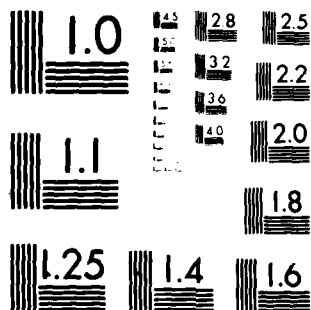
NL

1 of 5
20 x 10



UNC

11163



MICROCOPY RESOLUTION TEST CHART
NATIONAL BUREAU OF STANDARDS-1963-A

ADAI11632

12

GEOPHYSICAL PLASMAS
AND ATMOSPHERIC MODELING
FINAL REPORT
SAI-82-676-WA

January 1982

DTIC
ELECTE
MAR 3 1982
S D
H

DISTRIBUTION STATEMENT A
Approved for public release;
Distribution Unlimited



ATLANTA • ANN ARBOR • BOSTON • CHICAGO • CLEVELAND • DENVER • HUNTSVILLE • LA JOLLA
LITTLE ROCK • LOS ANGELES • SAN FRANCISCO • SANTA BARBARA • TUCSON • WASHINGTON

GEOPHYSICAL PLASMAS
AND ATMOSPHERIC MODELING

FINAL REPORT
SAI-82-676-WA

Submitted to:

Dr. Sidney Ossakow
Geophysical and Plasma Dynamics Branch
Plasma Physics Division
Naval Research Laboratory
Washington, D.C. 20375

Prepared Under:

Contract No. N00014-81-C-2058

Prepared by:

Ellis Hyman with

John Apruzese, Steve Brecht, Winston Chao, James Chen
Richard Chen, Jim Drake, Parves Guddar, Joseph Hu!
Richard Lindzen, John Lyon, Dennis Papadopoulos,
Rick Rood, Harvey Rowland, George Schmidt,
and Robert Smith

SCIENCE APPLICATIONS, INC.

1710 Goodridge Drive
P.O. Box 1503
McLean, Virginia 22102

(703) 754-5840



Accession For
NTIS GRA&I
DTIC TAB
Unannounced
Justification
By
Distribution/
Availability Codes
Special
A

TABLE OF CONTENTS

<u>Section</u>	<u>Page</u>
I TECHNICAL DISCUSSION	1
II REFERENCES	58
Appendix A - A SIMULATION STUDY OF EAST-WEST IMF EFFECTS ON THE MAGNETOSPHERE	A-1
Appendix B - A TIME-DEPENDENT THREE-DIMENSIONAL SIMULATION OF THE EARTH'S MAGNETO- SPHERE: RECONNECTION EVENTS	B-1
Appendix C - THE LOWER-HYBRID-DRIFT INSTABILITY IN NON-ANTIPARALLEL REVERSED FIELD PLASMA	C-1
Appendix D - PHYSICAL MECHANISM OF WAVE-PARTICLE RESONANCES IN A CURVED MAGNETIC FIELD	D-1
Appendix E - VLASOV SIMULATION OF PLASMA DOUBLE LAYERS	E-1
Appendix F - ONE-DIMENSIONAL DIRECT CURRENT RESIS- TIVITY DUE TO STRONG TURBULENCE	F-1
Appendix G - ANOMALOUS RESISTIVITY ON AURORAL FIELD LINES	G-1
Appendix H - WIRELESS GENERATION OF ELF/VLF RADIA- TION IN THE IONOSPHERE	H-1
Appendix I - ELF CURRENT GENERATION IN THE IONOSPHERE	I-1

TABLE OF CONTENTS (Continued)

<u>Section</u>	<u>Page</u>
Appendix J - STRUCTURING CAUSED BY RAYLEIGH-TAYLOR INSTABILITY	J-1
Appendix K - PRELIMINARY NUMERICAL SIMULATION OF IR STRUCTURE DEVELOPMENT IN A HYPOTHETICAL URANIUM RELEASE	K-1
Appendix L - THE PHARO CODE	L-1
Appendix M - INFLUENCE OF VELOCITY SHEAR ON THE RAYLEIGH-TAYLOR INSTABILITY	M-1
Appendix N - TWO-BUBBLE INTERACTIONS IN EQUATORIAL SPREAD-F	N-1
Appendix O - EVALUATIONS OF ATMOSPHERIC COOLING MODEL	O-1
Appendix P - OZONE TRANSPORT BY STATIONARY PLANETARY WAVES: AN INTERIM REPORT	P-1
Appendix Q - A NOTE ON THE LIMITS OF ROSSBY WAVE AMPLITUDES	Q-1
Appendix R - FORMULATION OF A MODAL-SPLIT-EXPLICIT TIME INTEGRATION METHOD FOR USE IN THE UCLA ATMOSPHERIC GENERAL CIRCULATION MODEL	R-1
Appendix S - DIOCOTRON INSTABILITY OF A RELATIVISTIC COAXIAL MULTI-RING HOLLOW ELECTRON BEAM	S-1

Section I
TECHNICAL DISCUSSION

↓
The work performed by Science Applications, Inc. (SAI) on this contract, "Geophysical Plasmas and Atmospheric Modeling," Contract Number N00014-81-C-2058, SAI Project Number 1-157-13-705-00, encompasses a wide range of topics in space plasma physics and atmospheric modeling in support of the programs of the Geophysical and Plasma Dynamics Branch of the Naval Research Laboratory (NRL). This report covers the period 1 December 1980 to 30 November 1981. In this section we will summarize the various subjects studied and the results obtained. Details will be included in Appendices which will document reports and publications resulting from our work.

Significant results were obtained in the following areas which will be discussed in succeeding sub-sections below: (A) solar wind-magnetospheric interaction using 2D and 3D MHD computer simulations, (B) investigations of the lower hybrid drift instability, (C) double layer modeling, (D) auroral electron acceleration, (E) ELF/VLF generation in the ionosphere, (F) high altitude nuclear effects, (G) evaluations of atmospheric cooling model, (H) ozone transport, (I) limitations on stratospheric dynamics, (J) general circulation model studies, and (K) collective particle acceleration.

A. SOLAR WIND-MAGNETOSPHERIC INTERACTION USING 2D
AND 3D MHD COMPUTER SIMULATIONS

During this contract year the 2D code was used to answer further questions about forced reconnection and the effects of various forms of resistivity on the behavior of the magnetotail. The latter problem was attacked by modifying the 2D global magnetosphere code to eliminate numerical reconnection in the tail. This was accomplished by enforcing a symmetry plane at $z = 0$. A number of new results were found:

- 1) For a reasonable model for the lower hybrid drift resistivity the size scale for the field reversed region must become $\approx 0.1 R_E$ before appreciable reconnection can occur.
- 2) When a resistivity $\propto J^2$ was used everywhere in the tail with a southward IMF, the x-point that formed was stable during the course of the run. This contrasts with our earlier work in which the x-point underwent relaxation oscillations. However, the position of x-point formation is the same in both cases. The import of the result is that the conditions in the solar wind may have even more of a controlling effect on substorms than we had found earlier.

5. When reconnection was forced to occur in the far tail, high velocity earthward motions were found in the plasma sheet, as expected. Surprisingly, however, very high tailward velocities were found just on the boundary of the plasma sheet. These tailward streams are similar to what is observed on the plasma sheet boundary.

The other problem studied was that of forced reconnection. Our approach was to vary the form of the resistivity in a series of calculations to see what effect upon the final result the form might have. We tried three types of resistivity: constant, current driven, and lower hybrid drift. The results can be summarized as follows:

- 1) Quantitatively the results are quite similar. There is a slow shock along the separatrix with outflow speeds on the order of the initial Alfvén speed.
- 2) No equilibrium is reached. At late times the system slowly evolves through a sequence of quasi-static states. In all cases the inflow boundary is discontinuous-further indicating the lack of an equilibrium.

- 5 The type of forced reconnection simulation done here and by others is probably not realistic and should be modified to something like a constant "pressure" inflow boundary.

The results do lend credence to the idea that the large scale features of forced reconnection do not depend on the specific resistivity mechanism. This was a crucial assumption--now supported--in our earlier 2D simulation of a geomagnetic substorm.

The two problems described above were reported at respectively the meeting of the American Geophysical Union (AGU), May 1981 and the American Physical Society (APS), Division of Plasma Physics, October 1981. The abstracts follow.

An MHD Simulation Study of the Factors Controlling Substorms*. J.G. LYON, S.H. BRECHI, Science Applications, Inc., J.A. FEDDER, Naval Research Laboratory--Our previous work has shown the possibility of modelling a substorm-like event using a global 2D MHD model of the magnetosphere. In this paper, we discuss the behavior of these simulated substorms with respect to variations in the incoming solar wind parameters and in the internal magnetospheric convection rate. We find little correlation of the x-point formation or behavior with the convection rate. The solar wind magnetic field does correlate with x-point position. (The stronger the southward IMF, the closer the x-point tends to form to the earth.) Short temporal scale phenomena also correlate with IMF strength. Finally, our MHD code has been modified to prevent almost totally spurious numerical reconnection. With this tool we are able to study the possible roles of microinstabilities and nonlinear tearing in substorm initiation.

* Work supported by NASA and ONR.

2D MHD Simulations of Forced Reconnection Processes with Anomalous Resistivity*. J.G. LYON, S.H. BRECHT, J.F. DRAKE, Science Applications, Inc., J.D. HUBA, Naval Research Laboratory--The study of forced reconnection processes in collisionless plasmas is of current interest to both the laboratory and space plasma communities. One of the key issues is understanding anomalous dissipation mechanisms and how they influence the macroscopic evolution of the plasma. To this end we present a series of 2D MHD simulations of forced reconnection processes for a variety of resistivity models. The calculations were performed with a 2D single fluid MHD code employing a 20th order spatial, leapfrog temporal flux corrected transport (FCT) scheme. The resistivity models considered are (1) no resistivity ($\eta_{an} = 0$); (2) constant resistivity ($\eta_{an} = \eta_0$); (3) current driven resistivity ($\eta_{an} \propto J^2$); and (4) resistivity based upon the non-local mode structure of the lower hybrid-drift instability in a reversed field plasma ($\eta_{an}(B=0) \ll \eta_{an}(B=B_0)$ where B_0 is the asymptotic value of B). We compare and contrast the results of these resistivity models, and our results with previous simulations.

* This work was supported by ONR and NASA.

During this contract year the development of the 3D MHD code to model the earth's magnetosphere has reached the point that actual research investigations into the earth's magnetosphere have begun. Two different simulations were performed. The first was to study the effect of rotating the solar wind interplanetary magnetic field (IMF) from a southerly direction to that of a southeasterly direction (-2° south, +5° east). The results showed a general change in the topological structure of the magnetotail. The added B_y in the IMF induced a B_y in the magnetotail and caused a general asymmetry in the lobe structure of the tail. These results had been suggested

from experimental work but had never been shown to be true analytically. This work has been published in Geophys. Res. Lett. entitled "A Simulation Study of East-West IMF Effects on the Magnetosphere" and appears in this report as Appendix A.

The second study performed concerned the effects on the magnetosphere produced by a steady southward IMF. In this simulation we created the magnetosphere and then allowed numerical reconnection to take place. The result was a series of magnetic islands being formed in the magnetotail and being convected tailward. In this simulation we studied the temporal behavior of the magnetic field and plasma parameters. These results were compared with magnetospheric observations and found to demonstrate almost all of the various features seen in the magnetotail during a substorm. The interesting result was that virtually all of the characterizations of magnetotail behavior generally attributed to magnetic substorms were seen in this simulation. The conclusion we draw from this is that differences of opinion as to magnetotail behavior may be attributed to variations in locations and timing rather than the uniqueness of any individual substorm. A report on this work has been submitted to J. Geophys. Res. entitled "A Time-Dependent Three-Dimensional Simulation of the Earth's Magnetosphere: Reconnection Events." It has also been published as NRL Memorandum Report 4690, 1981 and appears

in this report as Appendix B. This work was presented as an invited paper in December 1980 of the AGU meeting. The abstract of the paper follows.

MHD Simulations of Magnetospheres, S.H. BRECHI, J. LYON, Science Applications, Inc., J.A. FEDDER, K. HAIN, P.J. PALTAVOSSO, Naval Research Laboratory--Understanding the interaction of the solar wind with planetary magnetospheres continues to be one of the outstanding problems in space physics. The recent development of numerical MHD simulations of magnetospheres is now becoming an important tool in solving this problem. In this presentation we show the results of numerical simulations for the interaction of the solar wind with the earth's magnetosphere in both 2 and 3 dimensional models. The dynamic equilibrium which occurs in the simulations bears a strong resemblance to satellite experimental data and to empirical magnetospheric models. These results will be presented and discussed.

We will also show substorm-like magnetic reconnection events and plasma flows in the numerical magnetospheric model which result from changes in the solar wind parameters. These disturbances in the simulation magnetotail look remarkably like a particular existing substorm empirical model. Other interesting features of the simulations will also be presented and discussed.

Results of the above work were also presented at the May, 1981 Meeting of the AGU. The abstract follows.

Three Dimensional Calculations of Magnetospheric Structures*, S.H. BRECHI, J.G. LYON, Science Applications, Inc., J.A. FEDDER, Naval Research Laboratory--An understanding of the general structure of the magnetosphere is vitally important if further knowledge is to be gained about processes such as magnetospheric substorms. Using a 3 dimensional time dependent MHD code we have simulated the magnetosphere under varying IMF orientations. The purpose was to see what distinguishing factors exist when either no IMF, a southward IMF, a northward IMF or an east west IMF is present. We will present the results of these computations.

* Work supported by ONR and NASA.

More recently, at the APS, Division of Plasma Physics, Meeting in October 1981 an invited paper was presented on this work. The abstract for this paper, and for a second paper presented on this subject follow.

Abstract for an Invited Paper
for the Twenty Third Annual Meeting of the
Division of Plasma Physics

Oct 12-16, 1981

Numerical Simulations of Planetary Magnetospheres*.
J.A. FEDDER, Naval Research Laboratory, Washington,
D.C., S.H. BRECHT and J. LYON, Science Applications,
Inc., McLean, Virginia

The interaction of the solar wind with planetary magnetospheres presents many interesting problems to plasma physicists. These problems include collisionless shock physics, energy and momentum coupling processes, and generation of magnetospheric substorm phenomena. The recent development of numerical MHD simulations of magnetospheres is now becoming an important tool in solving these problems. At NRL we have recently completed numerical simulations of magnetospheres on a global scale. Results of these simulations will be shown. The dynamic equilibrium which occurs in the simulations bears a strong resemblance to satellite experimental data and to empirical magnetospheric models. Magnetospheric substorm-like magnetic reconnection events and plasma flows in the numerical model will be shown and discussed. These disturbances in the simulation look remarkably like the empirical "neutral line" substorm model. We will also discuss other effects of a changing interplanetary magnetic field on the simulation results. Finally, results of the solar wind interaction with comets will be presented. These results show the formation of a cometary magnetosphere in the absence of an intrinsic cometary magnetic field. Certain interesting features of cometary ion tails will be discussed.

* Work supported by the Office of Naval Research and by the National Aeronautics and Space Administration.

Three Dimensional Structures of the Earth's Magnetosphere, S.H. BRECHT, J.G. LYON, Science Applications, Inc., J.A. FEDDER, and K. HAIN, Naval Research Laboratory*--In this paper we present results of our research into the structure of the earth's magnetosphere and its dependence on and interaction with the solar wind. This research is carried out by performing a 3-D MHD simulation of the earth's magnetospheric structure. The code does not suffer from unwanted numerical reconnection. This enables us to study the effects of reconnection models on the structure of the magnetosphere. Results of this work will be displayed. Particular emphasis has been placed on the effects of bow resistivity and its interaction with the solar wind on the magnetotail.

* This work is sponsored by ONR and NASA.

During this contract year we have also undertaken simulation of cometary tails using the 3-D code. From this research we noted direct correlation of the shape of the tail with the IMF and its orientation. In addition we have resolved at least on the MHD scale the controversy as to the magnitude of the magnetic field in the tail. This work is now in preparation for publication. It has been presented at the AGU Meeting, May 1981 (see following abstract) and in the invited APS paper previously referred to.

Comet Magnetospheres, J.A. FEDDER, Naval Research Laboratory, S.H. BRECHT, J.G. LYON, Science Applications, Inc.--We have completed 3 dimensional, time dependent, MHD simulations of a cometary magnetosphere in the solar wind. This presentation will show results of the simulations including plasma densities, plasma pressures, and magnetic fields. Changes in cometary magnetospheres created by IMF variations or comet plasma production changes will also be presented and discussed.

B. INVESTIGATIONS OF THE LOWER HYBRID DRIFT INSTABILITY

The primary research topic investigated is the generation of microturbulence in reversed field plasmas. This is an important area since the anomalous transport properties associated with the turbulence can strongly affect the macroscopic evolution of the plasma (i.e., lead to reconnection processes which are believed to be crucial to the dynamics of the earth's magnetosphere). To this end we have conducted an extensive on-going study of the lower-hybrid-drift (LHD) instability in reversed field plasmas. Our recent work has focussed on the excitation of this instability in non-antiparallel reversed field plasmas, i.e., the magnetic fields on either side of the neutral line are not antiparallel. Such a magnetic field configuration contains magnetic shear which has a stabilizing influence on the lower-hybrid-drift instability. We find that magnetic shear has an inhibiting effect on the linear penetration of the mode toward the neutral line. This result suggests that the evolution of non-antiparallel reversed field plasma may be quite different than that of antiparallel reversed field plasmas. A report on this work is to be published in the J. Geophys. Res. It appears in this report as Appendix C, entitled "The Lower-Hybrid-Drift Instability in Non-antiparallel Reversed Field Plasmas."

Both linear stability properties and the nonlinear evolution and stabilization of the lower hybrid drift instability have been studied to understand plasma transport in inhomogeneous finite β plasmas. Completed work on linear stability includes the effect of shear and magnetic field curvature on the LHD mode. Magnetic shear has a strong stabilizing effect on the LHD instability. Analytic expressions for the critical magnetic shear necessary for stabilization of the instability have been obtained in finite β plasmas (see Appendix C). The implication of this work is that magnetic reconnection may be strongly inhibited when merging magnetic fluxes are not antiparallel. The physics of curvature-drift resonances in curved magnetic fields and the role of the drifts in the lower hybrid drift instability has been explored. When the radius of curvature of the magnetic field is comparable to the density scale length, strong damping of the lower hybrid drift instability can occur. For further details refer to Appendix D of this report which has also been published as NRL Memorandum Report 4668.

The nonlinear behavior of the lower hybrid drift instability has been studied in two dimensions (perpendicular to the magnetic field B) and several important results have been obtained. First, the nonlinear behavior of the lower hybrid drift can be described by the Hasegawa-Mima

equation which predicts that the LHD wave spectrum becomes two dimensional at rather low amplitude. A two dimensional spectrum implies first that ion trapping or quasilinear flattening can not saturate the lower hybrid drift instability and second that the formation of two dimensional vortices (ExB trapping) can cause irreversible electron transport. The saturation of the lower hybrid drift instability by coupling to high k modes which dissipate energy by heating electrons is currently under investigation. This work has been reported at the March, 1981 Sherwood Theory Meeting. The abstract follows.

Saturation and Transport by the Lower Hybrid Instability in Two Dimensions*, J.F. DRAKE, University of Maryland, J.D. HUBA, Science Applications, Inc.--The nonlinear saturation of the lower hybrid drift (LHD) instability and associated particle transport is studied for a two dimensional wave spectrum (perpendicular to B). In previous 1-D calculations, it has been demonstrated that LHD can not irreversibly transport electrons across B unless a rather large threshold $e\phi/T_i \sim (k_y \rho_{es})^{-2} \sim .25$ is exceeded.¹ In a two dimension wave spectrum, irreversible electron transport can take place when the $E \times B$ trapping threshold is exceeded, $e\phi/T_i > (k_y L_n)^{-1}$, x being the direction of inhomogeneity with scale length L_n . An unstable lower hybrid drift mode propagating along the diamagnetic drift direction y is found to decay into off angle modes with $k_x \sim k_y$ which saturate as they $E \times B$ trap the electrons. The original unstable mode saturates at an amplitude $e\phi/T_i \approx (m_e/m_i)^{1/2}$. The finite k_x decay modes therefore act as an intermediary which both transports electrons irreversibly and saturates the original instability.

* Work supported by the office of Naval Research.

¹ J. F. Drake and T. T. Lee, Phys. Fluids (June 1981).

² R. E. Aamondt, SAI Report #76-668-LI; S. P. Hirshmann, Phys. Fluids 23, 562 (1980).

C. DOUBLE LAYER MODELING

A 1-D time-dependent Vlasov code was developed to study the evolution of plasma double layers. The code includes provisions for boundary conditions suitable to the study of both laboratory and auroral plasmas. First results were reported at the December, 1980 AGU Meeting. A detailed simulation of double-layer formation was obtained in the Buneman flow regime, where the electron drift velocity U_e exceeds the electron thermal velocity V_e , and the ion drift velocity U_i exceeds the ion sound speed C_s , and where $T_e = T_i$. A run has been begun to extend the parameter regime into the ion-acoustic regime with $U_e < V_e$ and $T_e = 10 T_i$. This run has been interrupted at a stage where a double layer has formed but is not yet in steady state.

Development of a post-processing code has begun and is continuing, for detailed analysis of the particle and field dynamics. In addition, we have begun initial stages of an analytical model, motivated by the simulations, of the transition from the wave-instability-dominated initial phase to a longer-length-scale structure. This transition is effected through ion trapping, and we are attempting to develop an analytical description of the trapping process and the consequent phase-space dynamics. This effort is highly preliminary.

Talks on this subject, all with the title "Vlasov

Simulation of Plasma Double Layers", were presented at the following: the AGU Meeting, University of Iowa, and UCLA December 1980, IAGA, 4th Scientific Assembly, Edinburgh, Scotland, Chalmers University, Gothenburg, Sweden, and Royal Institute of Technology, Stockholm, Sweden, August, 1981. The following abstract is for the talk at the IAGA Meeting.

VLASOV SIMULATION OF PLASMA DOUBLE LAYERS*

Robert A. Smith (Science Applications, Inc., McLean, VA,
22102 U.S.A.)

We have developed a 1-D Vlasov code to study the temporal evolution of double layers, subject to initial and boundary conditions specifically appropriate to space plasmas. A primary object of this study is to determine whether double layers can actually develop under these conditions, viz:

(i) The double layer is simulated in a finite plasma column which forms a part of a complete circuit; the circuit also contains an ideal battery, a lumped resistance, and a lumped inductance. In the magnetospheric analogue, these latter elements represent the convection electric field, the ionosphere, and the magnetosphere, respectively;

(ii) The external potential is initially applied across the resistance alone, not across the plasma column.

The circuit equation depends on the time history of the double layer, and is solved simultaneously with the 1-D Vlasov and Poisson equations which describe the double-layer evolution. The current determined by the circuit equation provides the boundary condition for the simulation. Auxiliary plasma sources, representing the auroral flux tube upstream and downstream of the double layer, are necessary to inject supplementary current contributions to satisfy the boundary condition.

The way in which this injection is implemented is in effect a model of the local magnetospheric response to the double-layer evolution, and affects both the dynamics of the structure's evolution and its stability.

*Work supported by and performed at the Naval Research Laboratory, Washington, D.C., U.S.A.

A paper on this subject has been published as an SAI Report # SAI 81-344-WA, January 1981, and will appear in Physica Scripta. It appears in this report as Appendix E.

D. AURORAL ELECTRON ACCELERATION

During the past year we have made significant progress in understanding when anomalous resistivity can appear on auroral field lines and lead to the local acceleration of auroral electrons.

With P. J. Palmadesso and K. Papadopoulos we studied the effects of strong low frequency turbulence on electron acceleration. We showed that in a strong magnetic field ($\Omega_{ce} > \omega_{pe}$) such as exists on auroral field lines, finite amplitude ion cavities with $\delta n_i/n_0 > 0.2$ trap over half the electrons. When a parallel dc electric field is applied only the untrapped electrons are accelerated. This leads to the appearance of a field aligned runaway beam, streaming instabilities between the trapped and untrapped electrons and anomalous resistivity. This work was published in Phys. Fluids 24, 832 (1981) and appears in this report as Appendix F, under the title "One-dimensional direct current resistivity due to strong turbulence."

With P. J. Palmadesso and K. Papadopoulos we carried out a series of particle simulations which included the effects of finite ion cavities and pitch angle scattering at the anomalous Doppler resonance. With ion fluctuations, the electric field forms a strongly field aligned beam of energetic electrons. When these runaways are accelerated above a critical velocity [$v_c \approx 3(\Omega_{re}/\omega_{pe})v_{te}$],

where v_{te} is the electron thermal velocity, ω_{pe} is the plasma frequency, and Ω_{ce} is the cyclotron frequency, a plasma instability at the anomalous Doppler resonance pitch angle scatters the electrons. This breaks the adiabatic invariance of the electron's magnetic moment and leads to the appearance of very strong anomalous resistivity and isotropized energetic electron beams. Preliminary results of the simulations were presented as an invited talk at the 1980 APS Plasma Physics meeting. Further results with applications to the aurora were given at another invited paper at the spring meeting of the AGU (1981). The abstract for this paper follows.

Strong Turbulence and its Effects on D.C. Resistivity on Auroral Field Lines*, H.L. ROWLAND, K. PAPADOPOULOS, University of Maryland, P. PALIADESSO, Naval Research Laboratory--A classical problem in laboratory and space plasma physics is the existence of field aligned potential drops in strongly magnetized ($\omega_{pe} < \Omega_{ce}$) collisionless plasmas. Even in the presence of effects that would generate strong anomalous resistivity in an unmagnetized plasma, the invariance of the magnetic moment, μ , of the electrons will result in runaway. We demonstrate by theory and computer simulations that the adiabaticity of μ for electrons accelerated above a certain critical velocity breaks down due to the anomalous Doppler resonance instability. This along with some recent concepts of strong turbulence allows us to present a coherent theory of anomalous resistivity and electron acceleration, which fits the observed distribution of energetic electron fluxes. In the presence of ion density fluctuations with $\delta n/n_0 > 0.2$ such as observed in the auroras, the electron response to a field aligned potential occurs in three stages. The first stage is one dimensional and a long, flat tail forms on one side of the electron distribution as the electric field separates

* This work was supported by the NSF ATM-782524A01 and ONR.

untrapped electrons and electrons nonlinearly trapped by the ion fluctuations. When the electrons reach a critical velocity for the onset of the anomalous Doppler resonance instability, the current is clamped and the electrons are heated in the perpendicular direction. Until the tail electrons are heated such that $T_{\perp} = T_{\parallel}$, the current does not increase and one sees a strong resistivity. On longer time scales the behavior of the system depends upon the loss rate of the electrons with large perpendicular velocities.

A paper covering the preliminary results of this work has been accepted for publication by Geophys. Res. Lett. This paper, entitled "Anomalous Resistivity on Auroral Field Lines," appears in this report as Appendix G. A longer more detailed manuscript is in preparation. The hot isotropized electron distributions seen in our computer simulations are in excellent agreement with the observed electron distributions in the auroral zones. Most exciting are some new measurements based on AE-D data. With C. S. Lin, Southwest Research Institute (SRI), we have found several events where because of the high time resolution of the data (60 ms) we could see in detail the acceleration of the electrons. Based upon our model and simulations so long as the electron's velocity is below v_c we expect to see strongly field aligned beams. Above this velocity the beam should become isotropized. For example during one event seen by AE-D there was a downward beam of energetic electrons with a peak energy of ~ 1 keV. The ratio of particle flux at 10^0 to the magnetic field to that at

60° was 10:1. Within 0.3 sec the energy of the beam increased to 7 keV and at the same time the flux ratio dropped to one. This work was presented at the 1981 fall meeting of the AGU.

E. ELF/VLF GENERATION IN THE IONOSPHERE

Studies of RF heating of the ionosphere for the purpose of generating oscillating currents at low frequencies have been performed. It was found that maximum heating and associated changes of conductivity occurred on the x-mode for altitudes between 70-80 km. The results, which are relevant to wireless communications, have been applied to that subject in a paper entitled, "Wireless Generation of ELF/VLF Radiation in the Ionosphere" which appeared in the 1981 Symposium on the Effects of the Ionosphere on Radio Wave Systems. The paper is included in this report as Appendix H.

In addition, the direct excitation of ELF currents by transferring wave momentum to electrons or by cyclotron resonance enhancement of their magnetic moment was studied. Preliminary estimates indicate that significant currents can be achieved with antennas having a power of 100 MW. A paper describing this work in more detail appears in Appendix I, entitled "ELF Current Generation in the Ionosphere."

F. HIGH ALTITUDE NUCLEAR EFFECTS

Several efforts during this contract period which have direct relevance to the needs of the high altitude effects community have been completed. These include: (1) analysis of structuring observed in the STARFISH event and early time structure formation in the LWIR predicted for a standard event, (2) IR structure development in a hypothetical uranium release, (3) the effect of velocity shear on plasma instabilities, (4) two bubble interaction effects in the equatorial spread-F phenomenon, and (5) analysis of the plasma torus observed around the moon, Io, of the planet Jupiter. Each of these topics is described in the following sections.

(1) Structuring in Nuclear Bursts

The effort in the high altitude area was directed toward understanding some of the structured phenomena seen in the Starfish event and providing DNA with estimates of the structuring expected for early times during a Spartan event.

In the effort to understand the structuring seen in the Starfish event particular attention was paid to the high altitude streaks. It was found that our work in cross field jetting provided a consistent picture of the dynamics and structure seen in the Starfish event. This research

was published as an NRL Memorandum Report #4553, 1981. What follows is the unclassified abstract from the report, which is classified CONFIDENTIAL. The report is titled "Interpretation of High Altitude Streaks in Starfish (U)" and is authored by S. H. Brecht, C. Agritellis, and E. Hyman of SAI and P. J. Palmadesso of NRL.

In this report the high altitude streaks of radiating plasma seen in Starfish photographs are discussed. It is proposed that these streaks, as seen in photographs from the LASL aircraft, are in fact the result of solar illumination. The mechanism for transporting plasma to the altitude of these streaks is proposed to be Rayleigh-Taylor instabilities driven by centrifugal force and laminar acceleration of ions ahead of the expanding shock. This explanation is supported by the correlation between analysis of the photographs produced independently from this work and our calculations of the instability onset conditions along with the location of the earth's shadow line. It is felt that in light of this explanation further analysis of the photographic data may yield very useful information concerning the amount and type of plasma that is radiating and better estimates of long term trapped radiation at high L shells.

In response to a request from NRL to provide DNA with some estimates for early time structure for the LWIR problem, the SCORPIO code was coupled to a numerical module which describes the behavior of the Rayleigh-Taylor instability, as discussed by Brecht and Papadopoulos.⁽¹⁾ These calculations were completed and delivered to DNA. Entitled "Structuring Caused by the Rayleigh-Taylor Instability" by S. H. Brecht and E. Hyman of SAI and P. J. Palmadesso of NRL, it appears in this report as Appendix J.

(2) Structure Development in a Uranium Release

We developed a model and performed a 3D simulation of a daytime hypothetical uranium release at 200 km altitude, and calculated emission in the LWIR (11-14 μ) induced by sunlight and earthshine. Of the constituents in nuclear debris the uranium atom is of particular interest because it associatively ionizes in the upper atmosphere ($U+O \rightarrow UO^+ + e^-$). At altitudes above ~100 km this ion will be very long-lived and is potentially a strong emitter in the LWIR, resulting in a strongly emitting structured plasma in the atmosphere, potentially important for many defense systems.

Based on a model consisting of a one-level fluid and assuming an integrated Pedersen conductivity ratio (cloud to ambient) of 5, we followed the motion of the cloud as it diffuses in a direction parallel to the magnetic field. Gradient drift striations developed rapidly transverse to the magnetic field and across the direction of the relative velocity of neutrals to ions. We obtained contour plots of the radiance in the LWIR as a function of time, and as observed by sensors in various locations. Power spectra were calculated to quantify the development of spatial irregularities in the radiance. We found that, because of parallax large changes can occur in the structuring if we alter the distance from observer to cloud or change slightly the direction of observation. The significance of these

results to the defense community is still being evaluated. This work has been published as an NRL Memorandum Report #4659 (1981) entitled "Preliminary Numerical Simulation of IR Structure Development in a Hypothetical Uranium Release" and it appears here in Appendix K.

The description of the technique for obtaining radiance contour plots is given in Appendix L, "The PHARO Code" which has been published as NRL Memorandum Report #4667 (1981).

(3) The Effect of Velocity Shear on Plasma Instability Properties

We have undertaken the study of the effect of velocity shear on certain ionospheric phenomena.

(a) The Effect of Velocity Shear on the Rayleigh-Taylor Instability

Using the low frequency ordering for ions and electrons, a mode structure equation was derived for the Rayleigh-Taylor mode in the presence of velocity shear. The numerical solution of this equation shows that there is a preferential stabilization of the modes for which $k_y L_v > 1$, where k_y is the wave vector in the east-west direction and L_v is the scale length of the velocity shear. Hence the maximally growing modes occur for $k_y L_v < 1$ (i.e., long wavelength modes). This may explain the observation of long wavelength bottomside irregularities. For further details on this phenomenon refer to the paper "Influence

of Velocity Shear on the Rayleigh-Taylor Instability,"

P. N. Guzdar, P. Satyanarayana, J. D. Huba and S. L. Ossakow.

This work has been submitted for publication in Geophys.

Res. Lett. It also has appeared as NRL Memorandum Report #4701 (1981) and is reproduced in this report in Appendix M.

(b) The Effect of Velocity Shear on the $E \times B$ Instability

Using self consistent density and velocity profiles we have studied the Perkins and Doles equation for the $E \times B$ Instability. We find for $\vec{E} = E_{ox}(x) \sin\theta \hat{e}_x + E_{oy} \cos\theta \hat{e}_y$ the instability survives for $\theta \leq 80^\circ$ and moves toward longer wavelengths as we increase θ from 0 to $\pi/2$. This may be of relevance to some observations of high latitude irregularities as well as barium cloud experiments.

(4) Two-Bubble Interaction Effects in the Equatorial Spread-F Phenomenon

Considerable work has recently been done to understand the phenomenon of equatorial spread-F (ESF). In this regard, extensive theoretical, numerical and experimental efforts have been made to study the linear and nonlinear behavior of non-interacting single or an array of density depletions ("bubbles") under the influence of the $E \times B$ drift. For detailed recent reviews, see, for example, Ossakow (1981)(Appendix N) and references therein. In these previous models, the interaction between the depletions is not

included. In reality, however, such density depletions are not necessarily isolated from each other. We have recently completed an analysis to assess the quantitative effects of interactions between two neighboring depletions (Chen and Satyanarayana, 1981; manuscript in preparation).

The techniques developed in this analysis allow us to calculate to a high degree of accuracy the effects on the rise velocities of depletions, the forces (repulsive) between two depletions, the degree of distortion of the depletions and other effects of interest. The techniques can also be extended to treat an infinite array of depletions straightforwardly. The quantitative results gained from this analysis may be useful in understanding the more realistic behavior of equatorial spread-F irregularities.

A summary of the upcoming paper is given in Appendix N.

(5) Analysis of the Plasma Torus Observed Around the Moon, Io, of the Planet Jupiter

Another major effort this year has been the formulation of a theory of wave-particle interaction governing the thermodynamics of the Io plasma torus. This can be considered an additional means of testing our understanding of various plasma mechanisms by comparing with experimental measurements. Voyager satellite observations reveal the torus plasma to consist of S (sulfur) and O (oxygen) ions

in various charge states and with quasi-Maxwellian distributions at temperatures between 20 eV and 80 eV, and electrons at approximately 5 eV. The electrons must be maintained at 5 eV against energy losses in exciting the ions to radiate, at $\sim 10^{12}$ Watts, in the extreme ultra-violet (EUV). Moreover, the plasma is believed to be created with the ions at 300 eV - 600 eV and the electrons at ≤ 0.1 eV, indicating that the energy transfer is from the ions to the electrons. The lifetime of plasma in the torus is $\leq 10^6$ sec, too short for the energy balance to be effected by collisional processes alone.

We have developed a model incorporating the ion loss-cone (Post-Rosenbluth) instability, which is strong when there is a distinct nonthermal peak in the ion distribution $f(v_{\perp})$; such a peak exists at the creation velocity. We solve a steady-state quasi-linear equation for the ion distribution, including the effects of ion-ion and ion-electron collisions, quasi-linear velocity diffusion with a diffusion coefficient for the ion loss-cone instability, charge exchange, ionization sources, and macroscopic plasma loss. Detailed balance between wave growth and electron damping is assumed to exist, justifying the steady-state approach.

Armed with the ion distribution function, we can determine the effect of various processes in the energy

budget. Preliminary results are encouraging but not yet definitive. Using a simplified treatment of the quasi-linear diffusion coefficient, we have found the wave-particle transfer to be competitive with, but not dominating, collisional transfer. The ion distribution resulting from this treatment, however, is hotter than that observed, and so exaggerates the collisional transfer.

This work is still in progress; the next steps will include a refinement of the treatment of the quasi-linear diffusion coefficient (making a more accurate approximation which will enhance the diffusion) and the possibility of including a non-local source of colder ions.

During the contract period, this work has been discussed, under the title "Wave-particle energy transfer in the Io plasma torus," at the conference on "The Physics of the Jovian and Saturnian Magnetospheres" at JHU/APL (October, 1981), at the APS Plasma Physics Division meeting, October 1981 and at the AGU meeting, December 1981. The abstract for the latter talk follows.

Wave-Particle Energy Transfer in the Io Plasma Torus*, R.A. SMITH, Science Applications, Inc., P.J. PALMADESSO, D.F. STROBEL, Naval Research Laboratory--One of the more intriguing problems posed by the discovery of the Io plasma torus is the mechanism whereby the newly created and accelerated ions transfer their gyration energy to the cold electrons, which in turn collisionally excite ambient O and S ions to radiate 3×10^{12} W in the extreme ultraviolet (EUV). Coulomb collisions are insufficient

* This work supported by NASA.

to account for the observed temperatures and the EUV radiative power loss. We propose that wave-particle instabilities are the principal means of energy transfer, and construct a simple model based on the Post-Rosenbluth instability. We predict an ion velocity distribution function characterized by a thermal collision-dominated Maxwellian and a secondary peak at the pickup speed which is the signature of newly created ions accelerated to corotation and charge exchange. Approximately 0.3 of all ions are suprathermal, and the electrons are heated by wave absorption. The fraction of hot ions is diagnostic of the ion creation rate and/or residence time.

G. EVALUATIONS OF ATMOSPHERIC COOLING MODEL

During this contract period we have tested the adequacy of our model by calibrating calculated fluxes against satellite measurements. We, also, have evaluated the accuracy of using globally averaged approximations for obtaining infrared cooling rates. The model we have developed is important in enabling us to understand the balance between incoming solar radiation and outgoing IR emitted to space from the earth's surface, from clouds, and by the atmosphere. This balance will be critically affected by the concentrations of IR active constituents, particularly O_3 and CO_2 .

To validate our two-stream model we calibrated our predicted CO_2 and O_3 fluxes against published satellite observations⁽²⁾ of the specific intensity perpendicular to the earth's surface. The agreement, both for CO_2 and O_3 , is good. In addition to the above, we evaluated the effect on the global temperature of varying the O_3 concentration. We find the peak stratospheric temperature decreases by more than $20^{\circ}K$ while the equilibrium surface temperature increases by $0.6^{\circ}K$. We have also compared the validity of the single temperature profile against radiative equilibrium calculations on a multi-latitude grid. The single profile approximation is shown to be very good. This work is described in more detail in Appendix O of this report, which is in preparation for submission to the J. Geophys. Res.

H. OZONE TRANSPORT

Ozone transport has been studied using both steady state and time dependent models of planetary waves propagating into the winter stratosphere. A diabatic circulation is superimposed on the zonal mean flow forced by the planetary waves in the time dependent model.

The steady state results indicate increasing ozone in the polar regions and decreasing ozone in the tropical regions. This transport is confined largely to the region where there is a transition from photochemical to dynamic control of the ozone distribution. The rate of change of the zonal mean ozone field calculated with the steady state model indicates that the transport of ozone by steady dissipating planetary waves is insufficient to produce the observed spring ozone maximum. The results of the steady state model were presented at a seminar at Florida State University, Tallahassee, Fl., in March, 1981. A report documenting this work is included herein as Appendix P.

The time dependent model simulates stratospheric sudden warmings. When there is no diabatic circulation, it is found that the time of the warming is a time of large poleward and downward transport of ozone. The transport is correlated with the descent of zonal mean easterlies during the warming.

Inclusion of the diabatic circulation greatly increases the downward transport of ozone at all latitudes.

This transport produces an unrealistically high concentration of ozone in the lower stratosphere. This large buildup may indicate the omission of an important transport mechanism of smaller scale than planetary waves.

An abstract has been submitted to the Fifth International Symposium on Solar Terrestrial Physics to be held in Ottawa, Canada, in May 1982 where we will present the results of the time dependent model. The following is an abstract for this presentation.

The Effect of Stratospheric Warmings on the Zonal Mean Ozone Distribution, R.B. ROOD, Science Applications, Inc.--A plane planetary wave model capable of simulating stratospheric warmings is used to study the transport of ozone in the middle atmosphere. The model indicates that the ozone distribution is primarily controlled by the diabatic circulation and planetary wave transport during sudden warmings. The major effect of the warming is to enhance the northward transport of ozone; therefore, producing a larger spring maximum than associated with the diabatic circulation alone.

During a strong warming, ozone is decreased by more than 15% in the tropics and likewise increased in the polar regions. Much of this change is counteracted by the chemistry returning the distribution to its equilibrium values. After the warming event there is an increase of approximately 1 ppm in the polar lower stratosphere where ozone is chemically inert. The possibility of such enhancement of polar ozone concentration by stratospheric warmings is indicated by Zullig (1973).

Reports describing the results of both models are in preparation and will be submitted to the Journal of the Atmospheric Sciences.

I. LIMITATIONS ON STRATOSPHERIC DYNAMICS

We have performed an investigation of certain constraints imposed on the amplitude of internal Rossby waves by the conservation of potential vorticity and by the requirement of hydrodynamic stability. We find that these constraints restrict the amplitude of Rossby waves to be less than a certain prescribed maximum value. This maximum amplitude is close to what is observed in the lower stratosphere. For further details refer to Appendix Q, entitled "A Note on the Limits of Rossby Wave Amplitudes" which will be submitted to the Journal of the Atmospheric Sciences.

J. GENERAL CIRCULATION MODEL STUDIES

Comparison computer runs were performed with the UCLA General Circulation Model (GCM) both with and without inclusion of the modal-split-explicit (MSE) method. The results were compared as to stability, efficiency, and accuracy and the MSE method came out with high marks. These results have been published in the Proceedings of the Fifth Conference on Numerical Weather Prediction of the American Meteorological Society, November 1981, at which meeting they were presented. This work was also published as an NRL Memorandum Report #4572 entitled "Formulation of a Modal-Split-Explicit Time Integration Method for use in the UCLA Atmospheric General Circulation Model," 1981 and is included in this report as Appendix R.

K. COLLECTIVE PARTICLE ACCELERATION

There has been some resurgence of interest in the production of high-energy particle beams by collective acceleration processes in the last few years. A negative-energy wave train grown on the intense annular relativistic electron beam, propagating parallel to the applied magnetic field inside a conducting drift tube, can transfer energy to those trapped particles in the center of the tube. We have studied the stability of this multi-beam system using a fluid-Maxwell theory of the diocotron instability. A dispersion relation was derived for the special case of a strong magnetic field, a tenuous particle beam and a sharp boundary density profile. The stability analysis for the case of infinitely long beams indicates that the kink mode becomes unstable for most geometry and beam parameters used in the NRL collective accelerator experiment. Nevertheless, the finite geometry effects have a substantial influence on the behavior of a real device. The group velocity of transverse oscillation is very small compared to the beam particle speed so that the instability does not prevent acceleration of the beam head. Other methods, such as increasing the beam energy and applied magnetic field or chopping the solid beam, can reduce the instability substantially.

Another problem, that of choosing the parameters of an injection system with a spatially modulated magnetic field, was also considered for the collective particle accelerator. The energy threshold of the injected particle was calculated using a simple one dimensional model for different beam parameters and various phases of the accelerating wave. Any particle with insufficient injection energy will be rejected from propagating into the tube.

These results were presented at the APS, Division of Plasma Physics Meeting, October 1981. The following is an abstract of the paper delivered.

Injection and Propagation of Intense Coaxial Multiple Beams in the Collective Particle Accelerator, H.C. Chen, Science Applications, Inc., and P.J. PALMADESSO, Naval Research Laboratory*--A fluid-Maxwell theory of the diocotron instability has been extended¹ to study a system of multi-beams propagating parallel to an applied axial magnetic field in a conducting drift tube, including some effects of finite geometry. The stability analysis for the case of infinitely long beams gives results in agreement with those obtained by Uhm,² but finite geometry effects have a substantial influence on the behavior of a real device.

The problem of choosing the parameters of an injection system with a spatially modulated magnetic field is also considered for the collective particle accelerator at NRL. The energy injection threshold of the particle is calculated for different beam parameters and various phases of the accelerating wave.

* This work was supported by ONR.

¹ H.C. Chen and P.J. Palmadesso, Phys. Fluids 24 257 (1981)

² H. Uhm, private communication

A paper, published in Phys. Fluids entitled "Diocotron Instability of a relativistic coaxial multi-ring hollow electron beam" resulted from this work and is included in this report as Appendix S.

Section II

REFERENCES

1. Brecht, S. H. and K. Papadopoulos, "Cross-Field Jetting of Energetic Ions Produced by Rayleigh-Taylor Instability," NRL Memorandum Report 4068, 1979.
2. Kunde, V. G., B. J. Conrath, R. A. Hanel, W. C. Maguire, C. Probhakara, and V. V. Salomonson, J. Geophys. Res. 79, 777 (1974).

Appendix A

A SIMULATION STUDY OF EAST-WEST IMF EFFECTS
ON THE MAGNETOSPHERE

A SIMULATION STUDY OF EAST-WEST IMF EFFECTS ON THE MAGNETOSPHERE

S.H. Brecht and J. Lyon

Science Applications, Inc., McLean, Virginia 22102

J.A. Fedder and K. Hain

Naval Research Laboratory, Geophysical & Plasma Dynamics Branch
Washington, D.C. 20375

Abstract. The effect of adding a B_y magnetic component to a solar wind already carrying a B_z magnetic component is studied using 3-D MHD computer simulations. It is found that the tail structure and the B_x lobe fields are rotated and become asymmetric. In addition a B_y component is generated in the neutral sheet. These results are found to correlate with observational data.

Introduction

The need to study the earth's magnetosphere as a three-dimensional entity has been discussed by many authors, more recently by Akasofu et al., (1978), Lui et al., (1978), Fairfield (1979) and Coroniti et al., (1980). These authors, to mention a few, have presented considerable evidence that the two-dimensional models and pictures of the earth's magnetosphere are incomplete. This is in part due to the three-dimensional nature of the solar wind, particularly to the Interplanetary Magnetic Field (IMF) carried by it.

Time dependent numerical global modeling of the magnetosphere has been carried out for several years, but only in two-dimensions by LeBoeuf et al., (1978) and Lyon et al., (1980, 1981). LeBoeuf et al., (1978) used a fluid particle approach in their MHD modeling and were able to reproduce a Dungey (1961) type magnetosphere with a very resistive algorithm. Lyon et al., (1980), solving the standard MHD equations, addressed a very dynamical effect, shock focusing; they studied the effect of solar shocks on the magnetosphere. It was found that solar shocks interacted with the magnetosphere in such a way as to focus the shock in the tail region at -15 to -20 R_E . This focusing produced increased temperatures and pressures in this region. It was speculated in this paper, as well as in Brecht et al., (1980), that such effects might well trigger magnetic substorms. Substorm-like events triggered by southward directed IMF were modeled by Lyon et al., (1981). At present, three-dimensional global MHD simulations have been undertaken; Brecht et al., (1980a), Brecht et al., (1980b), LeBoeuf et al., (1980), and Wu et al., (1980).

In this letter we present the results of a three-dimensional simulation of the magnetosphere. In this simulation the three-dimensionality of the IMF plays an important role in the dynamics and structure of the magnetotail. What is shown is the dynamical effect of changing the IMF from $B_z = -2\gamma$ to $B_y = -2\gamma$ and $B_z = -5\gamma$. This change results in a B_x being introduced into the plasma sheet and leads to a

general rotation of the tail lobes of the magnetosphere.

The Simulation

A new 3-D MHD code was constructed to perform the calculations shown. The simulation region covered from 30 R_E to -100 R_E in the earth-sun direction and $\sim 30 R_E$ in the north, south, dawn, and dusk directions respectively. The exact MHD equations solved are as follows:

$$\frac{\partial \rho}{\partial t} = -\nabla \cdot \rho \vec{v} \quad (1)$$

$$\frac{\partial \vec{v}}{\partial t} = -\vec{v} \cdot \nabla \vec{v} - 1/\rho \nabla(P+Q) + \vec{B} \times \vec{J}/c \quad (2)$$

$$\frac{\partial P}{\partial t} = -\vec{v} \cdot \nabla P - (\gamma-1)(P+Q)\vec{v} \cdot \nabla \quad (3)$$

$$\frac{\partial \vec{B}}{\partial t} = -c \nabla \times \vec{E} \quad (4)$$

where $\vec{E} = -(\vec{v} \times \vec{B})/c$ and $J = c \nabla \times \vec{B}/4\pi - \frac{\partial \vec{E}}{\partial t}$.

The variables ρ , \vec{v} , P , B , and Q are the mass density, velocity, plasma pressure, magnetic field and artificial viscosity. Artificial viscosity is necessary to insure that the Rankine-Hugoniot relations are satisfied throughout the code. It provides dissipation known to exist in collisionless shocks. These equations are solved using the partial donor cell method (PDM), Hain (1978), with inflow boundary conditions on the +X boundary and outflow conditions on all other boundaries. The code uses 29x21x21 cells in the x,y and z directions with a stretched mesh.

The earth's dipolar field is formed by placing a current loop in one of the cells with appropriate current strength to replicate the earth's field. A solar wind is then introduced into the calculations from the +X boundary, which distorts the dipole field and creates the magnetosphere. This solar wind may carry an IMF of any strength and orientation. In the simulation discussed here the earth's magnetosphere has had a southward IMF ($B_z = -2\gamma$) interacting with it for about an hour in real time. A B_y component of -5γ is then added to the IMF. The results shown here are after this new IMF ($B_z = -2\gamma$, $B_y = -5\gamma$) has interacted with the earth and propagated tailward to about -70 R_E . The solar wind velocity is 400 km/sec and its density is 5/cc. For this simulation we chose to allow resistive reconnection on the bow, but to prevent it is the tail region.

The general features of the calculation are a bow shock at approximately 10 R_E with a density jump of about 3, and a magnetopause of appropriate form and shape. Before the IMF is

changed a plasma sheet exists from about $X = -15$ to $-20 R_E$ and is discernible to the end of the calculational grid, $X \sim -100 R_E$. Figure 1 displays the general orientation of the magnetic field in the noon-midnight (x,z) plane for this case. The magnetic field components (x,z) are normalized by the local total magnitude of B . The B_z component is not shown, but is essentially zero everywhere except in the near earth region. The B_x field in the equatorial region of the magnetotail is on order B_1 . In Figure 2 the magnitude of B is plotted in a $y-z$ plane $15 R_E$ tailward of the earth for the case where the IMF has only B_z component. One notes the symmetrical tail lobe and neutral sheet structure.

Results

The result of adding the B_y component to the IMF is a rotation in the orientation and an enhancement of the magnitude of the IMF. This rotated field then interacts with the previously formed magnetosphere. Merging occurs at the nose between the IMF and the magnetospheric field. This interaction results in the B_y component of magnetosphere being enhanced in some regions and reduced in others. This produces electric fields in the near earth region, which when applied in Faraday's law lead to a rotation of the magnetic field structure.

Figure 3 shows the magnitude of B in the same $y-z$ plane as Fig. 2 some time after the B_y component has been introduced into the IMF. The applied rotational discontinuity in the IMF has by this time propagated about $70 R_E$ beyond the earth for portions of the solar wind only slightly affected by interaction with the magnetosphere. Here one sees a significant modification to the tail structure previously seen in Figure 2. The tail lobes and the neutral sheet have been tilted with respect to the equatorial plane. In addition, note that the magnitude of B in the plasma sheet region has been enhanced. More features of this change can be seen in Figures 4 and 5. Here B_x vs. B_z and B_x vs. B_y vectors are plotted, they have been normalized

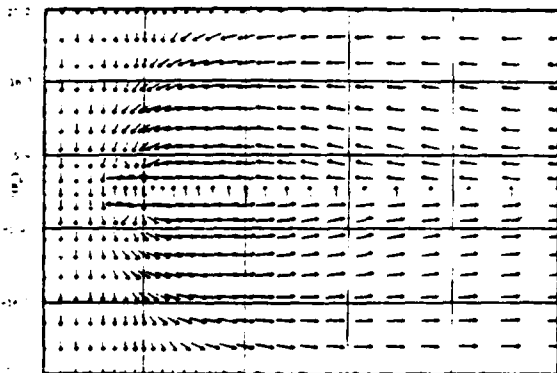


Figure 1. A normalized plot of B_x and B_z in the noon-midnight meridional plane. A south field $B_z = -2\gamma$ is being carried by the IMF.

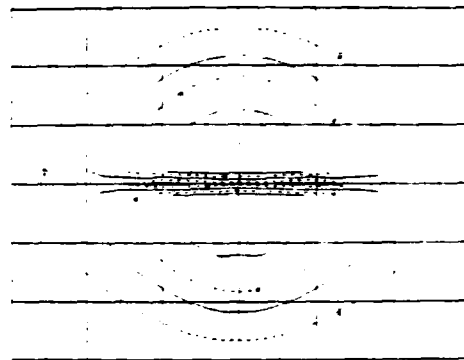


Figure 2. A contour plot of the magnitude of B in the $y-z$ plane at $X = -15 R_E$. In this case, only a southward IMF is interacting with the magnetosphere.

by the local magnitude of B . One sees that B_y is present in the neutral sheet region and that it has a wave-like structure in this region. This structure is propagating in a tailward direction and involves both the B_y and B_z components. The magnitude of B_y is approximately 5γ , which is the IMF value. A further demonstration of the rotation in the tail, due to the introduction of the eastward IMF, is seen by looking at the orientation of the B_x field in Figure 5 which is plotted in the equatorial plane. One sees the introduction of lobe B_x field in the equatorial plane. The appearance of the lobe fields is due to the general rotation of the magnetospheric tail. An additional feature of this rotation is the delay of the B_y field penetration into the central neutral sheet relative to locations closer to the magnetopause. The B_y component of the reconnected solar field propagates along the magnetopause at magneto-sheath velocities. It is introduced to

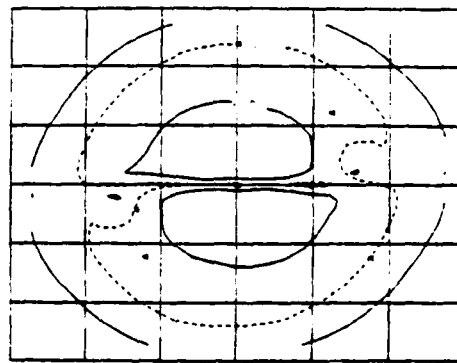


Figure 3. A contour plot of the magnitude of B in the $x-y$ plane at $X = -15 R_E$. In this case, both $B_z = -2\gamma$ and $B_y = -5\gamma$ are carried by the IMF. The asymmetry shown here becomes even more pronounced tailward of this region.

the neutral sheet by an MHD wave with a different speed, leading to the delay. This effect is exemplified by Figure 5, where the effect of adding B_y to the IMF can still be seen propagating tailward.

Discussion

Although many of the results from our simulation are still under study several aspects seem clear and appear to shed light on previously published work. The first is the direct correspondence between the existence of B_y in the IMF and the appearance of B_y in the magnetotail, i.e., the lobes and plasma sheet. This correspondence has been noted by Fairfield (1979) and Hardy et al., (1979) in studies correlating occurrence of B_y in the tail and the IMF. The appearance of B_y in the IMF leads to several dynamical features in the magnetotail. The most general is the rotation of the tail lobes, the results of which are seen in Figure 3. This rotation or generation of asymmetry in the lobes appears to be entirely consistent with results reported by Hardy et al., (1979) using experimental apparatus on the lunar surface to study tail lobe behavior. They reported that for a negative y component of the IMF the probability of encountering the lobe plasma is highest when the moon is on the duskside of the northern lobe and the dawnside of the southern lobe. The opposite relation is found if the y component is positive. Another feature of this rotation is the appearance of the B_x field in the equatorial plane, Figure 5. Such a scenario was reported by Lui et al., (1978). In this work the authors proposed that the observed reversals in B_y orientation in conjunction with the reversal of B_x might indicate a departure from plane geometry in the neutral sheet. While our calculations do not refute such an interpretation, they indicate that the plane may simply be rotated to produce the results reported. The final feature noted in this letter is the existence of B_y in the neutral sheet in the noon-midnight plane and its wave-like nature. It was

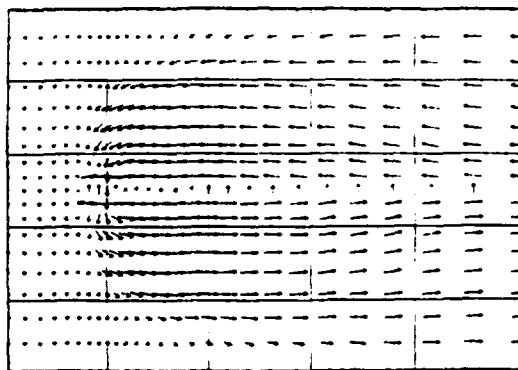


Figure 4. A normalized vector plot of B_x and B_z in the noon-midnight meridional plane. Here both B_z and B_y are carried in the IMF. The existence of B_y can be seen by noting diminished lengths of z vectors.

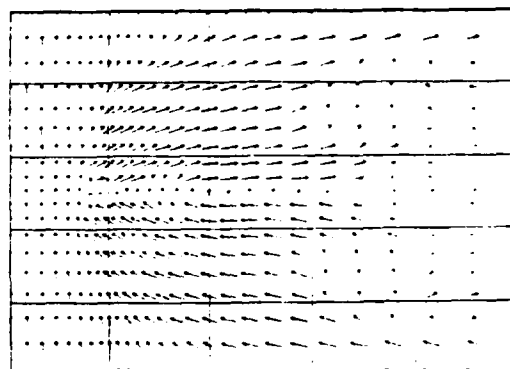


Figure 5. A normalized vector plot of B_x and B_y in the noon-midnight equatorial plane. Both B_z and B_y are carried in the IMF. Note regions in the neutral sheet where B_y dominates B_z and the appearance of B_y in this plane. The propagation of B_y to $\sim 70 R_E$ in the magnetopause region can be seen.

found that B_y dominated all components in some region of the tail, see Figures 4 and 5. Such phenomenon have been previously reported by Akasofu et al., (1978), Lui (1979), and Coroniti et al., (1980). It appears that the result of Akasofu et al., (1978) which states that B_z and B_y in the midplane often varied systematically is in agreement with our result that the B_y in the tail is directly related to the IMF and will attempt to vary as the IMF does.

In conclusion, we have used a 3-D MHD simulation to examine the effect of the IMF on the earth's magnetotail configuration for a very simple scenario. We have found that by adding a B_y of -5γ to solar wind already carrying a $B_z = -2\gamma$ that a rotation or asymmetry was produced in the magnetotail as well as enhancement of the total magnitude of the tail fields. These asymmetries correlate well with data. In addition, it was found that the neutral sheet was directly affected by this rotation and that a B_y component was induced in it. This later result indicates a direct connection between variability of the IMF and the variability of the field orientation in the magnetotail. Further work is underway to study other scenarios and to understand and quantify the rather complicated plasma behavior seen in the calculations, but not reported, as yet.

Acknowledgement

This work was supported in part by the Office of Naval Research, and in part by the National Aeronautics and Space Administration, under contract W-14365.

References

- Akasofu, S.-I., A.T.Y. Lui, C.I. Meng, and M. Haurwitz, Need for a Three-Dimensional Analysis of Magnetic Fields in the Magneto-

- tail During Substorms, Geophys. Res. Lett., 5, 283, 1978.
- Brecht, S.H., J.G. Lyon, K. Hain, J.A. Fedder, and P.J. Palmadesso, Three-Dimensional Simulations of the Earth's Magnetosphere, Bull. of the Am. Phys. Soc., 25, 915, 1980a.
- Brecht, S.H., J.G. Lyon, J.A. Fedder, K. Hain, and P.J. Palmadesso, MHD Simulations of Magnetospheres, EOS., Trans. Am. Geophys. Soc., 61, 1072, 1980b.
- Brecht, S.H., J.G. Lyon, J.A. Fedder, P.J. Palmadesso, Comments on Plasma Dynamics in the Earth's Magnetotail, Comments on Plasma Physics and Controlled Fusion, 6, 59, 1980.
- Coroniti, F.V., L.A. Frank, D.J. Williams, R.P. Lepping, F.L. Scarf, S.M. Krimigis, and G. Gloeckler, Variability of Plasma Sheet Dynamics, J. Geophys. Res., 85, 2957, 1980.
- Dungey, J.W., Interplanetary Magnetic Field and the Auroral Zones, Phys. Rev. Lett., 6, 47, 1961.
- Fairfield, D.H., On the Average Configuration of the Geomagnetic Tail, J. Geophys. Res., 84, 1950, 1979.
- Hain, K., The Partial Donor Cell Method, NRL Memorandum Report No. 3713, 1978.
- Hardy, D.A., H.K. Hills, and J.W. Freeman, Occurrences of the Lobe Plasma at Lunar Distance, J. Geophys. Res., 84, 72, 1979.
- LeBoeuf, J.N., T. Tajima, C.F. Kennel, and J.M. Dawson, Global Simulation of the Time-Dependent Magnetosphere, Geophys. Res. Lett., 5, 609, 1978.
- LeBoeuf, J.N., T. Tajima, C.F. Kennel, and J.M. Dawson, UCLA, Plasma Physics Group Rep. No. 450, 1980.
- Lui, A.T.Y., C.-I. Meng, and S.-I. Akasofu, Wave Nature of the Magnetotail Neutral Sheet, Geophys. Res. Lett., 5, 179, 1978.
- Lui, A.T.Y., Observations on Plasma Sheet Dynamics During Magnetospheric Substorm, Dynamics of the Magnetosphere, 565-597, Reidel Pub. Co., 1979.
- Lyon, J., S.H. Brecht, J.A. Fedder, and P.J. Palmadesso, The Effect on the Earth's Magnetotail from Shocks in the Solar Wind, Geophys. Res. Lett., 7, 711, 1980.
- Lyon, J., S.H. Brecht, J.D. Huba, and J.A. Fedder, Computer Simulation of a Geomagnetic Substorm, Phys. Rev. Lett., in press, 1981.
- Wu, C.C., R.J. Walker, and J.M. Dawson, A Three-Dimensional MHD Model of the Earth's Magnetosphere, UCLA Report, pp. G-528, Nov., 1980.

(Received January 27, 1981;
accepted March 12, 1981.)

Appendix B

A TIME-DEPENDENT THREE-DIMENSIONAL SIMULATION
OF THE EARTH'S MAGNETOSPHERE: RECONNECTION EVENTS

Stephen H. Brecht and John G. Lyon
Science Applications, Inc.
McLean, Virginia 22102

and

Joel A. Fedder and K. Hain
Geophysical and Plasma Dynamics Branch
Plasma Physics Division
Naval Research Laboratory
Washington, D. C. 20375

Abstract

This paper presents the results of 3-D simulation of the earth's magnetosphere. The simulation region is $-100 R_e < X < 30 R_e$, $|Y| < 40 R_e$ and $|Z| < 40 R_e$ with solar wind parameters $B_z = -2\gamma$, density of 5 cm^{-3} and velocity of 400 km sec^{-1} . The results show the existence of multiple x-points in the tail. Strong plasma flow is seen to exist in both earthward and tailward directions during formation of neutral lines. The exact magnetic field and plasma behavior is found to be very position dependent.

Introduction

Time dependent global simulations of the earth's magnetosphere have been performed for several years. The purpose of such a simulation has been and still is to obtain information concerning the general topological structure of the earth's magnetosphere and to address possible cause and effect relationships leading to dynamic phenomena such as magnetic substorms. These large scale calculations can also be used as boundary condition calculations for investigation into the relevant microphysics that produce small scale, but important effects. Finally it is hoped that, as an additional benefit, large scale time dependent simulations might provide further insight into magnetospheric dynamics, so that experimental data might be correlated with the calculation, and a better understanding of the earth's magnetosphere could be reached.

The global simulations to be discussed below all have one thing in common. They are time dependent solutions of the MHD equations. Other than boundary conditions, none of these calculations assumes a particular structure for the magnetosphere nor do they have any adjustable parameters to affect the structure. The number of ad hoc assumptions is held to those required for the validity of the MHD equations. Customarily in a model, macroscopic structure may be manipulated, e.g., the magnetopause boundary might be positioned at will. In these simulations, only the microscopic structure - the underlying physics - is determined. The macroscopic structure then either fits what it is being simulated, or it does not. While questions of accuracy of solution are always important, what the simulations test is whether the physics embodied in the equations solved is adequate to explain the simulated system.

Initially only two-dimensional simulations of the magnetosphere were performed; LeBoeuf et al. (1978), Lyon et al. (1980, 1981a). LeBoeuf et al. (1978) used a fluid particle approach in the MHD modeling and were able to reproduce a Dungey (1961) type magnetosphere using the very resistive Lax algorithm, Lax (1954). Lyon et al. (1980), solving the standard MHD equations using a combination of flux corrected transport (Boris and Book, 1973; Zalesak, (1979), and partial donor cell method, (PDM) Hain (1978), addressed the very dynamic problem of, shock focusing. In this work they studied the effect of solar shocks on the earth's magnetosphere. It was found that solar shocks interacted with the magnetosphere in such a way as to focus the shock in the tail region at -15 to $-20 R_e$. This focusing produced increased temperature and pressures in this region. It was speculated in this paper, as well as in Brecht et al., (1980), that such effects might well trigger magnetic substorms. In addition, Lyon et al. (1981a) studied the problem of substorm-like events triggered by southward directed IMF. For this problem a code was developed that used a leap-frog time-integration scheme and 20^{th} order finite-difference approximation to the spatial derivatives along with a flux-convected transport algorithm (Boris and Book, 1973, Zalesak, 1979) which provides the minimum possible numerical dissipation consistent with a solution showing no extraneous extrema. The results of these simulations produced behavior in the tail which tended to support the neutral-line model for magnetic substorms (Dungey, 1961; Hones, 1973, and McPherron et al, 1973). Research is continuing into the 2-D modeling, particularly with regard to resistive reconnection and how it might be affected by variations in the solar wind.

However, the earth's magnetosphere is a three-dimensional entity. The need to consider it as such has been discussed by many authors, most recently by Akasofu et al. (1978), Lui et al., (1978), Fairfield (1979), and Coroniti et al. (1980). These authors, to mention a few, have presented considerable evidence that two-dimensional models of the earth's magnetosphere are incomplete. This is in part due to the variability and three-dimensional nature of the solar wind, particularly the Interplanetary Magnetic Field (IMF) carried by the wind. Within the last year, three-dimensional codes have been constructed and the results of their initial work reported; (Leboeuf et al., 1981; Brecht et al., 1981, and Wu et al., 1981). These three simulations considered three somewhat different problems. The first calculation was by LeBoeuf et al. (1981). In this simulation a southward IMF interacted with a current loop. The calculation used periodic bounding conditions and a particle fluid approach with a Lax scheme to solve the MHD equations. The calculation was reported to reproduce a Dungey (1961) like magnetosphere. Unfortunately, the scheme was so diffusive that close inspection of the published magnetic field vector plots reveal no obvious northward field such as one expects to see near the earth's dipole field. The code also had limited spatial extent in the y, z direction causing the possibility of boundary effects to be of concern. The strong numerical diffusion in addition to causing eradication of some, if not all, of the dipole field also prevents the studying of any dynamics of reconnection regions in the tail.

Brecht et al. (1981) studied the effects of an east-west component of the IMF being added to a solar wind carrying a -2γ southward field. This calculation was fully three-dimensional with no planes of symmetry

used. This was necessary to allow for the rotation of the IMF. The code used in-flow boundary conditions on the $+x$ boundary and out-flow conditions on all other boundaries. The numerical scheme employed was a partial donor cell method (PDM), Hain (1978). PDM couples a low order numerical scheme to a high order scheme in a nonlinear fashion in order to prevent numerical oscillations while maintaining good accuracy and minimum numerical diffusion. The results showed that a rotation of the IMF toward an east-west direction rotated or skewed the entire magnetotail and produced an induced B_y in the plasma sheet of the size seen in the solar wind. These results were found to be consistent with experimental data; Hardy et al. (1979), Lui (1979), and in agreement with an analytic calculation by Cowley (1981).

The simulation by Wu et al. (1981) addressed the case where no IMF exists in the solar wind. They used a Rusanov numerical scheme to solve the MHD equations. The calculation was performed on a quadrant of the magnetosphere meaning that both the meridional and equatorial planes were planes of symmetry. Because of the symmetry planes no reconnection can occur due to numerical resistivity. The boundary conditions required out-flow at 45° from the x axis. The calculation reproduced, apart from the diffusion effects noted by the authors, many of the major features of the magnetosphere.

In this paper we present results of refined simulations where we consider the structure and dynamics of the magnetosphere in the presence of a -2γ IMF. The paper will discuss in detail the calculational set up and equations used in the simulation. In addition, we present time resolved results of island formation in the tail and attendant flows and densities. Finally, the conclusions derived from these simulations will be presented.

Calculation

As mentioned earlier in this paper, the code uses a PDM scheme for solving the MHD equations. This scheme allows resolution of shocks in 3 cells and therefore permits the use of fewer grid cells than is necessary for schemes where more numerical diffusion is present, for example, Lax or Rusanov. The MHD equations the code solves are

$$\frac{\partial \rho}{\partial t} = - \nabla \cdot \rho \mathbf{v}$$

$$\frac{\partial \mathbf{v}}{\partial t} = - \mathbf{v} \cdot \nabla \mathbf{v} - \frac{1}{\rho} [\nabla(P + Q) + \mathbf{J}/c \times \mathbf{B}]$$

$$\frac{\partial P}{\partial t} = - \nabla \cdot P \mathbf{v} - (\gamma - 1) (P + Q) \nabla \cdot \mathbf{v} - \eta \mathbf{J}^2$$

$$\frac{\partial \mathbf{B}}{\partial t} = - c \nabla \times \mathbf{E}$$

where $\mathbf{E} = - (\mathbf{v} \times \mathbf{B})/c - \eta \mathbf{J}$ and $\mathbf{J} = c \nabla \times \mathbf{B}/4\pi - \frac{\partial \mathbf{E}}{\partial t}$.

The variables $\rho, \mathbf{v}, P, \mathbf{B}, \eta$, and Q are mass density, velocity, plasma pressure, magnetic field, resistivity and artificial viscosity. Artificial viscosity is necessary to insure that the Rankine-Hugoniot relations are satisfied throughout the code. It is only activated in the region of the simulation where there is compressive flow, $\nabla \cdot \mathbf{v} < 0$. The PDM algorithm in conjunction with this set of equations guarantees that numerically $\mathbf{v} \cdot \mathbf{B} = 0$ everywhere in the code, a critical feature to the validity of the simulation not automatically obtained by all schemes. The effect of high Alfvén speeds in requiring unreasonably short time steps is controlled by the $\partial \mathbf{E} / \partial t$ term in Amperes' law. The inclusion of the displacement current effectively limits the propagation speed of the

Alfven waves to the speed of light, which can be arbitrarily set in the code. The boundary conditions for this simulation are the same as those used in our previous 3-D paper [Brecht et al., 1981]. The + X boundary has an inflow condition and all other boundaries have an outflow condition.

The simulation presented in this paper was performed on a grid using a stretched mesh of $29 \times 21 \times 21$ cells in the x,y and z directions of the solar-magnetospheric coordinate system. The spatial extent of the numerical grid is $-100 R_e < X < 30 R_e$, $-40 R_e < Y < 40 R_e$ and $-40 R_e < Z < 40 R_e$. The earth's dipole field is formed by placing a current loop at $X = Y = Z = 0$ with the appropriate current to replicate the earth's field. A solar wind is then introduced into the calculation from the + x boundary, which distorts the dipole field and creates the magnetosphere. The solar wind may carry an IMF of any strength and orientation. The solar wind introduced into the calculation presented here has a velocity of 400 km sec^{-1} , a density of 5 cm^{-3} and a $B_z = -2\gamma$. The grid was initially loaded with a plasma density of 1 cm^{-3} .

Results

The results presented here are a 3-D time evolution calculation of the magnetosphere as a southward (-2γ) IMF interacts with the earth's magnetic field. Reconnection was permitted to occur in this simulation. We had the option of no reconnection, using real resistivity in the equation, or permitting numerical reconnection. We chose the latter case for several reasons. Foremost among these is the fact we did not know where to put the resistivity and in what amount. Arbitrary prescriptions did not appeal to us. Numerical resistivity occurs mainly where opposed fields are being driven together in a compressive fashion causing the location of reconnection regions to be determined by the dynamics of the calculation not the predisposition of the author. At this juncture of our research we are actively testing various ways to model the microinstabilities, Lyon et al. (1981b), which are thought to provide the necessary resistivity for the reconnection process. However the present, the proper physics and its implementation is not well resolved. It should be noted that for steady state configurations such as those used in the research of Birn and Hones (1981) the PDM scheme will not numerically reconnect. The numerical reconnection shown here is purely a driven phenomenon. One disadvantage of using numerical reconnection is that with this code there is no resistive heating of the plasma. Therefore, only the magnetic field and pressure forces caused by the compressive flow will affect the plasma dynamics. As will be shown in this paper these terms alone provide rather impressive effects in the earth's magnetotail.

The calculation begins with the earth's dipole field being acted upon by a solar wind of the previously stated properties as well as

the -2γ southward IMF. A reconnection point forms in the near earth tail region approximately 4500 secs into the calculation. (In this paper all times quoted are real time and not computer simulation time). This reconnection point begins to move tailward. Eventually another reconnection point occurs and a magnetic island forms and begins to move in tailward direction. As this island moves tailward another island is formed. The general dynamics of the system is quite similar to the 2-D simulations reported by Lyon et al. (1981a) and the 3-D simulation by Birn and Hones (1981). One main difference in the results of the 2-D and 3-D simulations is that for the 3-D simulations strong earthward flows are observed whereas in 2-D this was not the case. It was speculated by Lyon et al. (1981a) that the lack of earthward flow could be due to the two-dimensionality of the calculation and this appears to be the case.

In figures 1 -5 the global temporal dynamics of the various plasma parameters are shown. Each set of figures begins at 7691 sec (0 min) into the calculation and run through 11351 secs (~ 65 min) and therefore cover slightly over one hour of real time. The beginning time was selected because most of the initial transients produced as the dipole field was transformed into a magnetospheric topology were out of the system. One remnant of such a transient is seen as a reversed field structure in the tail of the magnetosphere in Fig. 1 at about $55 R_e$. In addition we have chosen two locations in the magnetotail at $Y = 0$, $Z = 0$, and $X \sim -19 R_e$ and $-32 R_e$ to display plasma properties that a satellite would detect during this time frame (Figs. 6 - 10).

Fig. 1 is a time sequence of magnetic vector plots on the x - z meridional plane. The vectors are normalized to the local magnitude of B , so the size of the vector provides no indication as to the strength of

the magnetic field. In Fig. 1a one notes the existence of a reconnection point at about $-68 R_e$ in the tail as well as an o-point in the $-35 R_e$ to $-40 R_e$ region. In the following several snapshots one sees the interior island grow in the tailward direction and by 9766 secs is beginning to accelerate tailward. The last timestep shows the formation of a new island with the inner x-point located at approximately $-20 R_e$ in tail.

The velocities that correspond to the creation and motion of these sets of neutral lines or o-points can be seen in Fig. 2. Here we show the velocities in the equatorial, x-y plane. In these plots the arrow length indicates the magnitude of velocity. The unit vector is set to be 400 km sec^{-1} , the solar wind velocity. The general features of the magnetosphere can be seen in Fig. 2a. The stagnation point in the bow is located at about $X = 12 R_e$, and the magnetopause can be seen draped around to the sides. In the interior region of the magnetotail one notes a demarcation line of very low velocities at $X \sim -29 R_e$ corresponding to the location of the x-point seen in the magnetic field plots at the same time. Earthward of this point there is flow toward the earth. Tailward of this point the flow is predominately away from the earth. It should be noted that in the meridional plane one sees these flow patterns restricted primarily to $-2 R_e < Z < 2 R_e$. To a large extent the magnitude of the flow is determined by the mass loading of the magnetic field. The correspondence between high flow regions and low densities is quite high as can be seen in Fig. 2 and 4, which show the perspective plots of velocity and density in the equatorial plane.

As one scans through the various time steps shown in Fig. 2, one notes the velocities pulsate within a period of about 20-30 minutes. This is noticeable if one considers the $X \sim -22 R_e$ grid line shown in

Fig. 2. As time progresses one notes two obvious features. The first is that the speed of the flows increases with time as successive islands are formed. This feature was noted in the 2-D simulation by Lyon et al. (1981a). In both calculations each succeeding reconnection event reduces the amount of mass on the field lines and consequently the flow speed becomes larger. Fig. 2f also shows the second feature, an asymmetry in the flow pattern. This is a particularly interesting feature caused by the motion of the x-point at the bow of the magnetosphere. Because of the large number of timesteps in this calculation numerical noise permitted the reconnection point on the bow to shift slightly. Once this occurs the continued flow begins to develop an asymmetry on the bow which manifests itself as motion in the tail and produced the asymmetric flow, much as one might expect in the real magnetosphere. The density and pressure are noted to be asymmetric. In this simulation the asymmetry existed in only the dawn - dusk direction. The fact that the reconnection point has become slightly asymmetric may be more realistic than the usual perfectly symmetric simulation. It should also be noted that the region of very rapid flow is restricted mainly to the equatorial plane, but as can be seen does, in fact, cover a large spatial region in both the x and y directions. The flow speeds reach velocities as high as 650 km sec^{-1} in the earthward direction and 800 km sec^{-1} tailward.

Coincident with the cycling of the island formation one can see considerable effects on the density and pressure in the magnetotail. Looking at the density in the meridional plane (Fig. 3) one sees two important features. The first is that, as the successive neutral lines move tailward the plasma sheet thins tremendously, and second that the plasma sheet density is considerably reduced. In Fig. 4f the density in

the middle of the tail is quite low, but an enhancement of the density is occurring on the flanks of the tail. The asymmetry caused by the shifted reconnection point is only about 10% in density from the dawn side to the dusk side. Fig. 5 shows the pressure in the meridional plane where one sees the rather dramatic sheet thinning often associated with reconnection events, Hones and Schindler (1979), and Hones (1979). In Fig. 5a-f one notes the progressive thinning of the sheet as indicated by the pressure dropout and a general overall reduction in pressure along the plasma sheet, $Z = 0$. Also, one notes a slight recovery of the pressure occurring inside of about $X = -20 R_e$ and moving tailward.

In the next several paragraphs we discuss data taken from the code at two locations in the magnetotail. The time resolution of the data is approximately 5 min intervals. In a sense this is plasma and field data as a satellite would detect it during the hour we have displayed. The two locations are located at $Y = 0$, $Z = 0$, $X \sim -19 R_e$ and $-32 R_e$.

In Fig. 6 we show the x velocity as seen at the two locations mentioned above. The inner location sees an earthward flow which becomes progressively stronger with time. There is a slight oscillation in the velocity, but generally it is increasing. The maximum velocity is reached at about 55 min. At this time the magnetotail neutral line has moved to beyond the $X \sim -32 R_e$ location, Fig. 1e. Shortly after this time the tail reconnects and a x -point forms at about $X \sim -22 R_e$, as can be seen on the B_z field evolution in Fig. 1f. The creation of the inward neutral line corresponds to the rather precipitous drop in velocity seen at the inner point. The outer location experiences an oscillating velocity of about 100 km sec^{-1} . During the outward stretching phase at about 55 min the tailward flow drops to about 50 km sec^{-1} . Locations

slightly closer to the earth experience a complete flow cycle from negative to positive and back to negative flow. As soon as the x-point forms earthward of the observation point one sees the tailward velocity go from -50 km sec^{-1} to -650 km sec^{-1} in less than 5 min. Similar to the results of Lui (1979) and Hones and Schindler (1979), strong dawn-dusk velocities are detected at these two locations. The inner point displayed primarily a duskward flow until the neutral line appeared at $-22 R_e$. At this time the flow changed rapidly to -300 km sec^{-1} in the dawnward direction. The outer point in the meantime displayed a constantly increasing duskward flow which peaked at -160 km sec^{-1} . The location of the observation point with respect to the neutral line seems to determine which direction the dawn-dusk flows go, Fig. 7. The z velocity generally stayed under 10 km sec^{-1} for both locations and oscillated between the positive and negative direction.

The B_x field was quite variable with the inner point experiencing larger fields as expected. The B_y field in these simulations remained negligible throughout the simulation as detected at these locations. In Fig. 8, the time evolution plots of the z magnetic fields are displayed. Here one sees some very interesting behavior. The inner point experiences fairly large positive B_z components ranging from 5 to 8 gamma. However, at the time the neutral line is established at $\sim -22 R_e$ one sees a precipitous drop in the B_z component. This is caused by the close proximity of the neutral line. The outer point experiences more dynamic changes in B_z . Initially the neutral line is earthward of this point. One can correlate the expansion of the magnetic island seen in Fig. 1a-c with the general decrease of B_z from $\sim -1\gamma$ to $\sim -1.25\gamma$. The island then moves tailward and passes beyond the outer point as shown

by the change of B_z from $\sim -1.25\gamma$ to $\sim 1.5\gamma$. As discussed earlier and coincident with the rapid increase of plasma flow a neutral line is established earthward of this point and the B_z changes from $\sim 1.5\gamma$ to $\sim -2\gamma$ in about the same 5 minute interval.

The relationship between the pressure, density and B_z component of the magnetic field is somewhat confused. Figure 9 shows that the two locations in the tail experience approximately the same pressure variation with perhaps a slight time delay. However, the formation of the new x-point causes the pressure behavior to change at about 65 min. At this time both locations show quite similar pressure levels. The inner location shows a drop of a factor of approximately two and the outer point is enhanced by about the same factor. In the density plot, Fig. 10, a build up of density occurs at about 20 min. Subsequent to this a general decline in density occurs. The build up is associated with the recovery of the plasma sheet from the passage of the previous island now located far in the tail, Figs. 1c and d. The decline in density after the 20 min mark is associated with the movement tailward of the o-point located at $X \sim -35 R_e$, see Fig. 1d and e, and the associated stretching out of the tail. However, as can be seen the density plots do not display the variations seen in the pressure plots.

Comparing the pressure plots, Fig. 9, with magnetic field plots, Fig. 8, one notes that the outer location shows increases in pressure associated with decreases in the magnitude of B_z . This relationship holds until about the 60 min mark. By this time an x-point has passed by this location and a new one is about to form at $X \sim -22 R_e$. The pressure is found to increase by a factor of about two. The magnitude of the B_z field passes through zero and ends up larger than it has been

during this whole data sequence. The inner point exhibits different behavior. For the first 20 min the pressure and the magnitude of B_z follow one another. Then the pressure drops while B_z increases. During the final 30 min of data the two quantities then follow one another again. The correspondence of the density to either pressure or B_z is weak. Only the build up of density at 20 min appears to effect the variations seen in either the pressure or B_z .

These, then, are the basic results from the calculation. In the next section we discuss implications of these results and how they correlate with experimentally obtained data.

Discussion

While one encounters considerable difficulty in correlating in an exact fashion the published experimental results with those of a numerical simulation, the experimental results do provide a guideline to the kind of questions one ought to ask concerning the numerical results. There have been many articles published reporting satellite data from all areas of the magnetosphere during substorm events. However, for the purposes of this discussion we have restricted ourselves to the data reported from the IMP-6 satellite by Hones and Schindler (1979), and Lui (1979). It is not our intention, nor within our capability, to resolve differences between their respective analyses of the IMP-6 data. Our intention here is to compare the reported data with the calculation we have performed.

As discussed earlier we have selected and shown temporal data from various locations in the magnetosphere. The detailed data shown by Hones and Schindler (1979) are taken primarily in the $X \sim -30 R_e$ region, but varies somewhat in the y and z direction. Lui (1979) displays detailed data in the same region, but shows not only data at $X \sim -30 R_e$, but $X \sim -20 R_e$ as well. In their statistical analysis the respective authors included data from all positions in x, subject to the various criteria placed on the data to determine its applicability.

At the risk of over-simplification of these authors' results one can sum up the major results in the following way. As a general rule the measured flows appeared to be field aligned. There appeared coincident with these events a dawn-dusk flow favoring the duskward direction. Lui (1979), arguing in favor of the current interruption model which we cannot assess with this particular calculation, reported that

statistically speaking there was not a strong correlation between negative B_z and tailward flow. Hones and Schindler (1979) found that for "40 - 50 percent of the events, no substorm effect on the flow is seen: in another 40 - 50 percent there is tailward flow associated with the substorms; and in 10 - 15 percent there is earthward flow". In addition, to comparing AE index to plasma flows, both Lui and Hones and Schindler also correlated plasma flow and sheet thinning. The respective authors reached apparently opposite conclusions based on their IMP-6 data for the relation between plasma sheet thinning and flow direction during a substorm.

Our calculations do not resolve the differences of these authors. For one thing it is not clear that the solar wind conditions in our simulation accurately represent the solar wind conditions that were present during the events for which these authors show data. As we have found earlier, [Brecht, et al. (1981)], inclusion of effects such as B_y in the solar wind makes considerable modifications to the magnetotail, not to mention the possible effects on microinstabilities thought to provide resistivity for tearing. We can, however, from our simulation either add to the confusion or provide some clarification, depending on the reader's point of view.

It is heartening to note that the magnitude of the quantities displayed in Figs. 6-10 are similar to those found in the magnetotail. We see in Fig. 8 variations and magnitudes of B_z consistent with the data shown by Lui (1979), see Figs. 14 and 16, which correspond with our selected observation data points. The velocities seen in our calculation are also consistent with those seen during substorm events. The pressures also appear to be consistent with the data albeit somewhat

lower, possibly due to the lack of ohmic heating expected to occur because of resistivity. We do not, however, see dropouts of several orders of magnitude in the data at $Y = 0$, $Z = 0$. Factors of five seem to be the most we see directly in the magnetotail. However, consideration of Figs. 3-5 show that any displacement from the central part of the plasma sheet either in y or z can result in considerable drop in either pressure or density.

We have found in this simulation that the data one collects is extremely dependent on location. Consider Fig. 2 at a position of $Z = 0$, $Y \sim > 6 R_e$ and X between $-23 R_e$ and $-45 R_e$. One notes that if the satellite had been located here during the hour that several x -points existed in the tail virtually no flow modification would have been detected. This type of event was reported by Hones and Schindler (1979) at $Y = 10.6 R_e$. However, at $Y < -6 R_e$ during this same time one would have seen flows approaching 400 km sec^{-1} . At the point $X = -22.8 R_e$ the displacement in y also changes the characteristics of the flow because of curvature of the neutral line itself. An additional feature of this calculation is the dependence on Z seen in terms of earthward and tailward flows. All the flows shown here are on the equatorial plane, $-2 R_e < Z < 2 R_e$. If one moves above or below the $Z = 0$ plane one quite frequently finds flows of smaller magnitude. These flows occurred in x locations where strong flows existed at $Z = 0$.

Simultaneous data taken at the two locations in the sheet show the effects of the x -point motion. In Fig. 8 one sees that the point at $X \sim -19 R_e$ experiences variations in B_z , which remains positive although it drops in magnitude as the x -point forms close to it. The outer point sees a reversal in B_z as the x -point passes this location and then

returns to negative as the new x-point forms at $\sim 22 R_e$. Looking at Fig. 6 one sees that the inner point detects earthward flow most of the time, but the outer point sees only tailward flow, although the sign of B_z reversed. As the new x-point forms the tailward flow jumps to over -600 km sec^{-1} . Not shown in these figures is a point located at $X \sim -27 R_e$. Here an observer would not only experience reversal of B_z , but also reversal of the flow pattern from tailward to 100 km sec^{-1} earthward back to $> 700 \text{ km sec}^{-1}$ tailward. The point to be made is that during the passage of the x-point the dynamics of the new x-point formation caused the data to be extraordinarily sensitive to location. The existence of dusk-dawn flows were also found at our two data points. The flow was duskward for most of the simulation, but when the new x-point formed the outer location experienced a tremendous change. The flow went from 140 km sec^{-1} to -350 km sec^{-1} . The pressure shows the type of plasma sheet dropouts seen in the data. However, one interesting point should be noted. As the neutral line approached the inner point at 65 min., the plasma pressure dropped along with the plasma flow speed and the magnitude of B_z . At the outer point the opposite result occurred at this time.

Finally, as reported by Lui (1979), and Hones and Schindler (1979) we find that most of the energetic flows appear to be field aligned. These flows are found to originate at the neutral line. In fact, they cannot be generated elsewhere because $\eta = 0$ and only $\mathbf{J} \times \mathbf{B}$ and pressure forces are in effect. A comparison of Figs. 1 and 2 illustrates this point. While Fig. 1 does not display magnetic field lines, B_y is typically an order of magnitude smaller than the other components.

In short, within this one simulation we find conditions and plasma

behavior quite similar to the various statistical features reported by Hones and Schindler (1979), and Lui (1979). Whether or not they would be detected depended entirely on the observer's locations in the magnetotail at the time of the substorm like event.

Conclusions and Summary:

The 3-D time dependent simulations of the magnetosphere presented in this paper display many of the features commonly associated with substorms. It was found that motion of the x-point caused plasma dropout to occur in the magnetotail. The flows seen in this calculation appeared to be oriented in a field aligned direction. The speed of flow was inversely related to the plasma density on the field line. As the simulation progressed the density declined in the tail and the flow speeds increased. The magnitude of these flows and of other plasma and magnetic parameters appears consistent with satellite data during substorm periods. However, until the mass on the field lines is removed, the reconnection events do not produce behavior that corresponds to the usual picture of substorms. This fact is reasonable because the local Alfvén speed is a good estimate for the maximum velocities produced by reconnection. For plasma parameters typically found in the tail, $B \sim 20 \gamma$ and $n \sim 1 \text{ cm}^{-3}$ the Alfvén speed is 400 km/sec. In the neutral sheet the Alfvén speed drops to 40 km/sec. Therefore, in order to have large scale accelerations one needs plasma-dropout to achieve the $500 - 1000 \text{ km sec}^{-1}$ speeds reported for substorms. Thus, if the neutral line model for substorms is correct, our results indicate that reconnection is a necessary, but not sufficient condition for substorm formation.

The simulation exhibited the tendency for multiple x-points or neutral lines in the tail. This result is consistent with Lyon et. al., (1981). The inner x-point for the time segment shown here tended to remain at $X \sim -27 R_e$ in the tail until the o-point grew sufficiently. It then began to move tailward, stretching the tail. At this point in

time a new x-point was seen to form at $X \sim -20 R_e$. An interesting aspect of the simulation was the temporal behavior at various locations in the tail. Due to the multiple x-point formation and the asymmetric flow caused by the x-point shift on the bow, it was found that almost all of the various categories of events reported by Lui (1979), and Hones and Schindler (1979) could be observed in this one simulation. The location that remained earthward of x-points experienced no field reversal nor a flow reversal in v_x as the various x-points were formed and moved tailward. Points shifted in y from $Y = 0$ often displayed no modification to plasma flow during these events. Yet as the flow moved toward the dawn side due to the shift in the bow reconnection point one found that at $Y < -6.7 R_e$ flows were detected to coincide with the formation of the x-point while at $Y > 6.7 R_e$ no effects were detected. Observation points were found in the tail at $Y = 0$, $Z = 0$, $X = -27 R_e$ and $-32 R_e$ which showed field reversal from negative B_z to positive B_z and a return to negative as a neutral line passed these locations and a new one was formed closer to the earth. These points experienced different flow behavior with the reversal of B_z . The point located at $X = -27 R_e$ experienced reversals in the v_x direction consistent with the neutral point being either earthward or tailward of that point. The point at $X = -32 R_e$ did not experience reversal of v_x , but only saw a reduction of the tailward flow. This lack of the flow reversal can probably be attributed to the formation of the x-point at $X \sim -20 R_e$ within five minutes of the previous neutral line passage.

Finally, the various statistical categories used by Hones and Schindler (1979) and Lui (1979) to categorize plasma and magnetic behavior during the many substorm events experienced by IMP-6 appear to

be found in this one simulation. This leads one to the not so profound conclusion that, because of the complicated magnetotail behavior, spatial and temporal variations allow one to sample a full range of dynamic behavior determined primarily by the location of the observer.

Acknowledgement

This work was supported by the Office of Naval Research and NASA.

References

- Akasofu, S.-I., A.T.Y. Lui, C.I. Meng, and M. Haurwitz, "Need for a three-dimensional analysis of magnetic fields in the magnetotail during substorms, Geophys. Res. Lett., 5, 283, 1978.
- Birn, J., and E.W. Hones, "Three-dimensional computer modeling of dynamic reconnection in the geomagnetic tail", J. Geophys. Res., 86, 6802, 1981.
- Boris, J.P., and D.L. Book, "Flux-corrected transport I: SHASTA, a transport algorithm that works, J. Comp. Phys., 11, 38, 1973.
- Brecht, S.H., J.G. Lyon, J.A. Fedder, and P.J. Palmadesso, "Comments on plasma dynamics in the earth's magnetotail", Comments on Plasma Physics and Controlled Fusion, 6, 59, 1980.
- Brecht, S.H., J. Lyon, J.A. Fedder, and K. Hain, "A simulation study of east-west IMF effects on the magnetosphere", Geophys. Res. Lett., 8, 397, 1981.
- Coroniti, F.V., L.A. Frank, D.J. Williams, R.P. Lepping, .F.L. Scarf, S.M. Krimigis, and G. Gloeckler, "Variability of plasma sheet dynamics", J. Geophys. Res., 85, 2957, 1980.
- Cowley, S.W.H., "Magnetospheric asymmetries associated with the y-component of the IMF", Planet. Space Sci., 29, 79, 1981.
- Dungey, J.W., "Interplanetary magnetic field and the auroral zone", Phys. Rev. Lett., 6, 47, 1961.
- Fairfield, D.H., "On the average configuration of the geomagnetic tail, J. Geophys. Res., 84, 1950, 1979.

- Hain, K., "The partial donor cell method," NRL Memorandum Report, No. 3713, 1978.
- Hardy, D.A., H.K. Hills, and J.W. Freeman, "Occurrence of the lobe plasma at lunar distances", J. Geophys. Res., 84, 72, 1979.
- Hones, E.W., Jr. "Plasma flow in the plasma sheet and its relation to substorms", Radio Sci., 8, 979, 1973.
- Hones, E.W., Jr., and K. Schindler, "Magnetotail plasma flow during substorms: A survey with IMP6 and IMP8 satellites", J. Geophys. Res., 84, 7155, 1979.
- Hones, E.W., Jr., "Transient phenomena in the magnetotail and their relation to substorms", Space Sci. Rev., 23, 395, 1979.
- Lax, P.D., "Weak solution of nonlinear hyperbolic equations and their numerical computation", Communication on Pure and Applied Math., 17, 159, 1954.
- LeBoeuf, J.N., T. Tajima, C.F. Kennel, and J.M. Dawson, "Global simulations of the time-dependent magnetosphere, Geophys. Res. Lett., 5, 609, 1978.
- LeBoeuf, J.N., T. Tajima, C.F. Kennel, and J.M. Dawson, "Global simulations of the three-dimensional magnetosphere", Geophys. Res. Lett., 8, 257, 1981.
- Lui, A.T.Y., C.-I. Meng, and S.-I. Akasofu, "Wave nature of the magnetotail neutral sheet", Geophys. Res. Lett., 5, 279, 1978.
- Lui, A.T.Y., "Observations on plasma sheet dynamics during magnetospheric substorms", Dynamics of the Magnetosphere, 563-597, Reidel Pub. Co., 1979.
- Lyon, J., S.H. Brecht, J.A. Fedder, and P.J. Palmadesso, "The effect on the earth's magnetotail from shocks in the solar wind", Geophys. Res.

Lett., 7, 712, 1980.

Lyon, J., S.H. Brecht, J.D. Huba, J.A. Fedder, and P.J. Palmadesso,
"Computer simulation of a geomagnetic substorm", Phys. Rev. Lett.,
46, 1038, 1981(a).

Lyon, J.G., S.H. Brecht, and J.A. Fedder, "An MHD simulation study of the
factors controlling substorms", EOS, Tran. Am. Geophys. EOS., 62,
355, 1981(b).

McPherron, R.L., C.T. Russell, and M.P. Aubry, "Phenomenological model
for substorms", J. Geophys. Res., 78, 3131, 1973.

Wu, C.C., R.J. Walker, and J.M. Dawson, "A three-dimensional MHD model of
the earth's magnetosphere", Geophys. Res. Lett., 8, 525, 1981.

Zalesak, S.T., "Fully multidimensional flux-connected transport algorithms
for fluids", J. Comp. Phys., 31, 335, 1979.

Figure Captions

Figure 1 Time evolution of the B_x and B_z magnetic field components plotted in the meridional (noon-midnight) plane. For purposes of discussion 7698 sec and 11351 secs correspondes to 0 min. and ~ 65 min respectively. The length of the vector drawn provides no information about the magnitude of the fields. All distances are measured in earth radii.

Figure 2 Time evolution of V_x and V_y velocities in the equatorial plane. The unit vector is 400 km sec^{-1} which is the solar wind velocity.

Figure 3 Perspective plots of density in the meridional plane. Units for the density scale are in particles cm^{-3} . The rather jagged appearance of the bow shock is due to the perspective plotter, not data. This is true for all perspective plots shown.

Figure 4 Perspective plots of density in the equatorial plane.

Figure 5 Perspective plots of pressure in the meridional plane. Units for the pressure scale are ergs cm^{-3} .

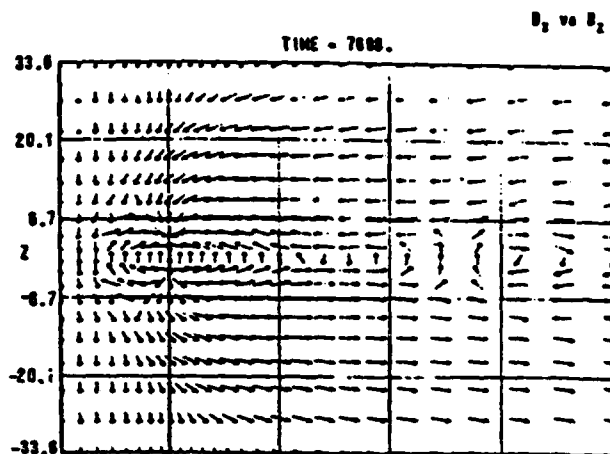
Figure 6 Temporal variations of V_x as seen at the locations $X = -19 R_e$, $Y = 0$, $Z = 0$ denoted by squares and $X = -32 R_e$, $Y = 0$, $Z = 0$ denoted by triangles.

Figure 7 Temporal variations of V_y as seen by the two tailward locations. Squares indicate $X = -19 R_e$ and triangles $X = -32 R_e$.

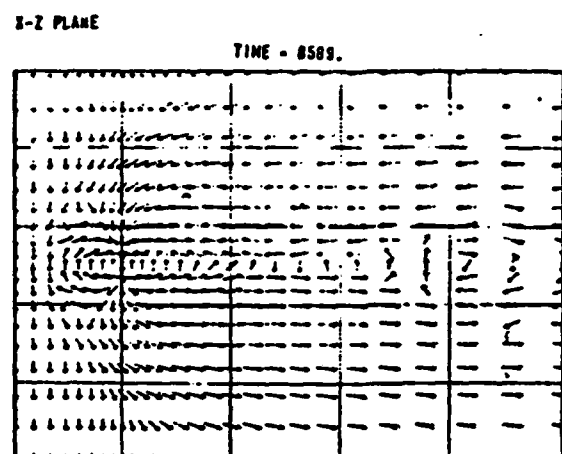
Figure 8 Temporal variations of B_z as seen by the two tailward location. Squares indicate $X = -32 R_e$ and triangles $X = -32 R_e$.

Figure 9 Pressure as a function of time for the location $X = -19 R_e$ (squares) and $X = -32 R_e$ (triangles).

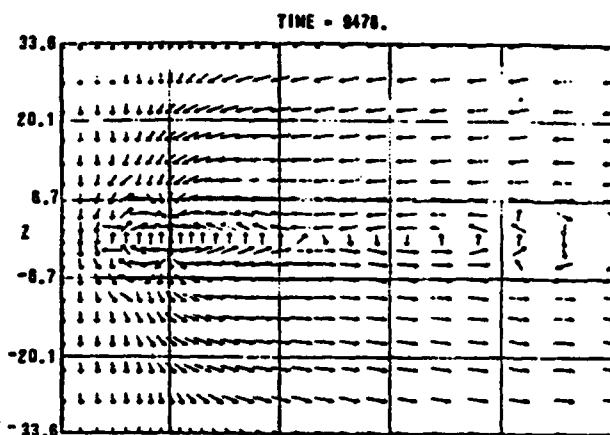
Figure 10 Density as a function of time for the locations $X = -19 R_e$ (squares) and $X = -32 R_e$ (triangles).



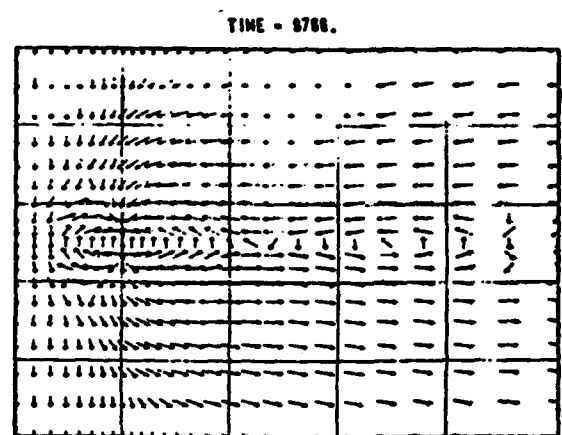
(a)



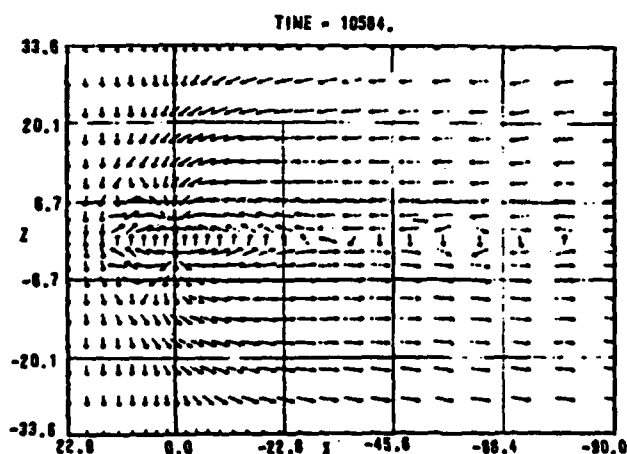
(b)



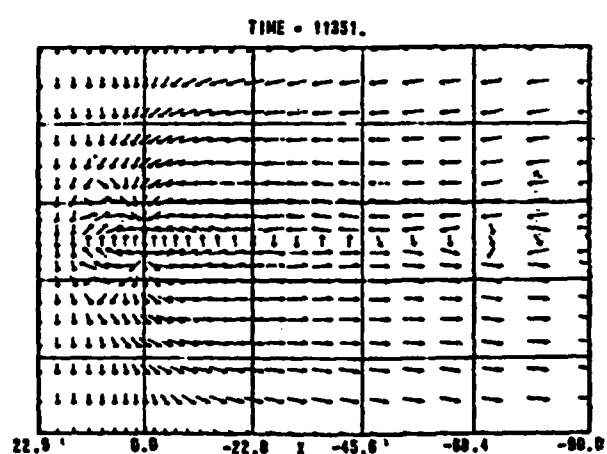
(c)



(d)

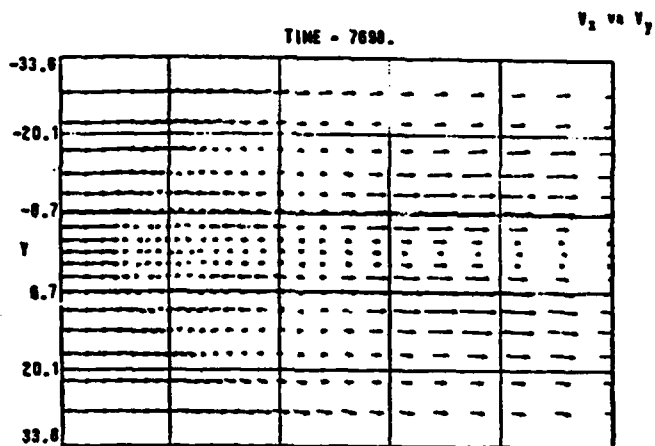


(e)

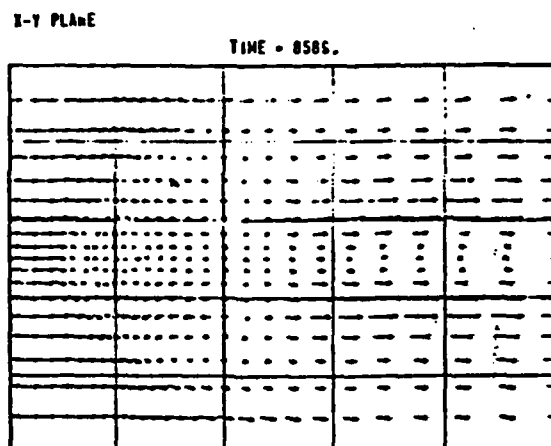


(f)

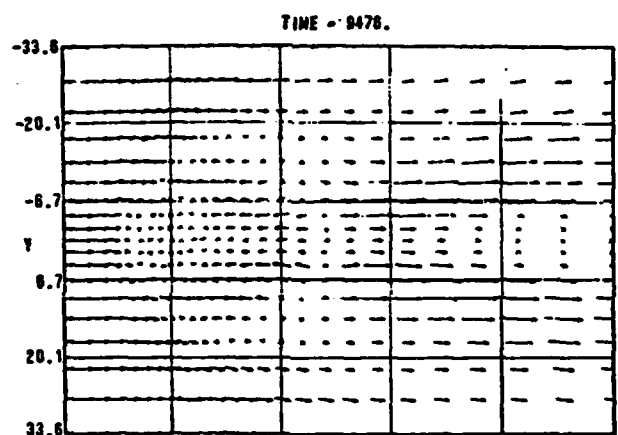
Figure 1



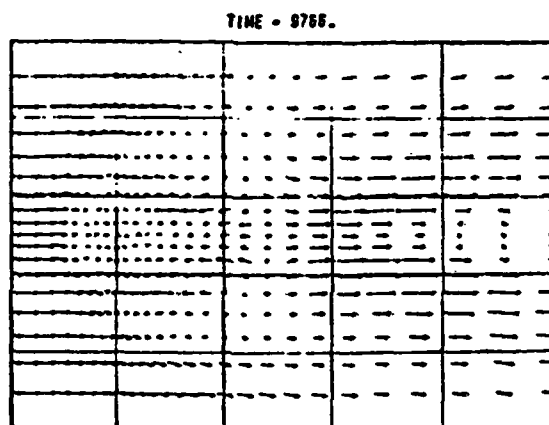
(a)



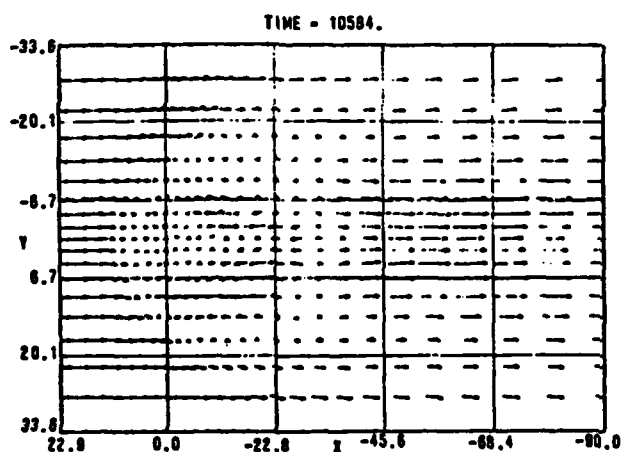
(b)



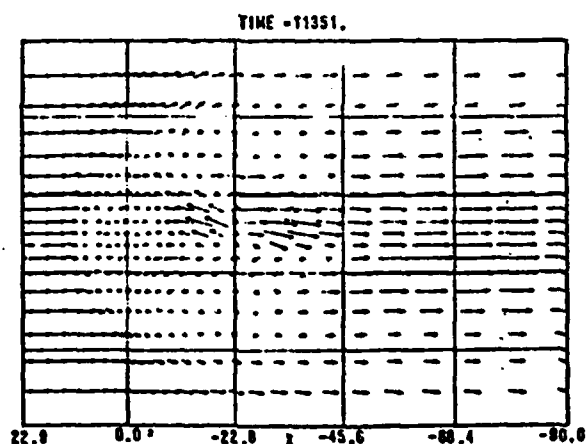
(c)



(d)

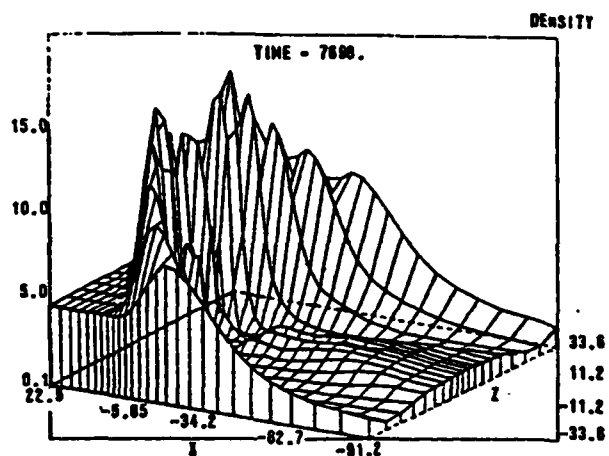


(e)

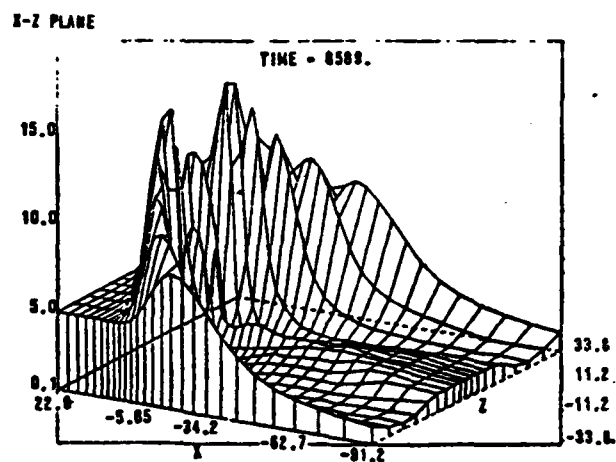


(f)

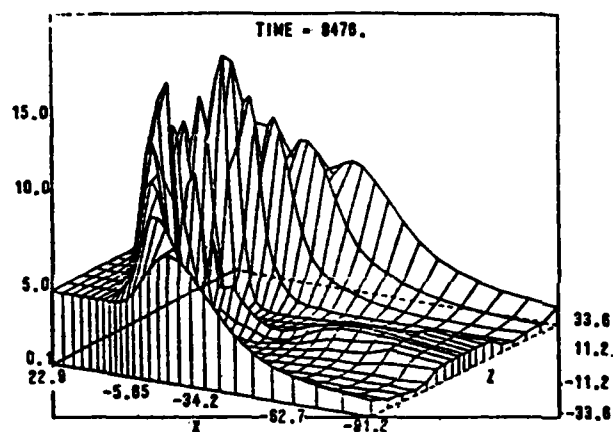
Figure 2



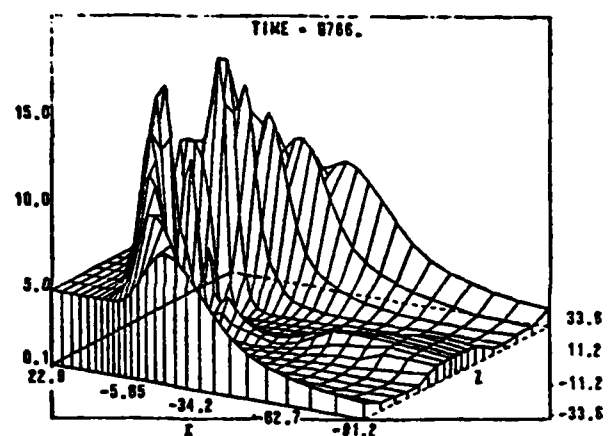
(a)



(b)



(c)



(d)

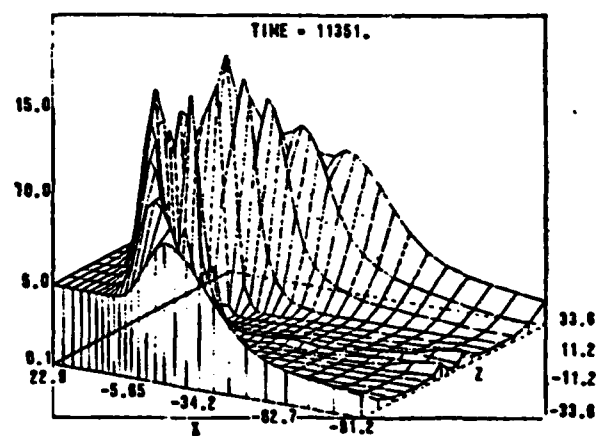
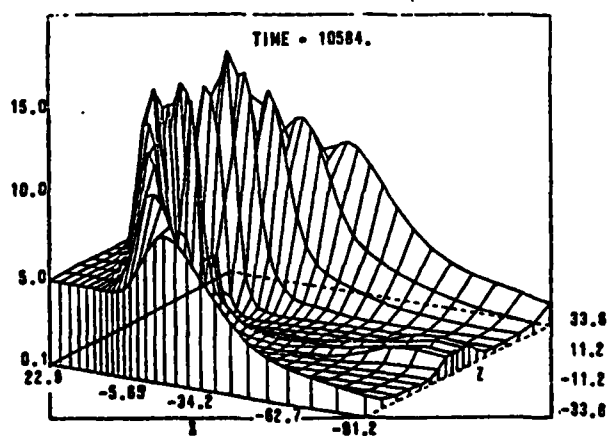


Figure 3

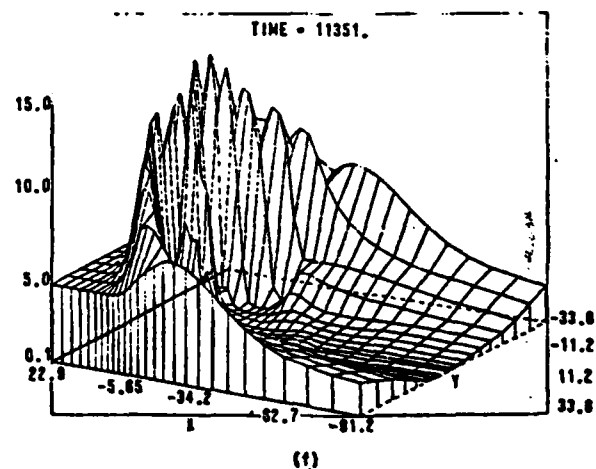
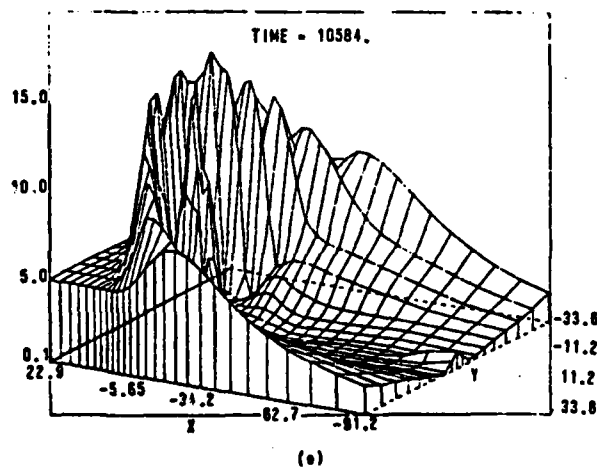
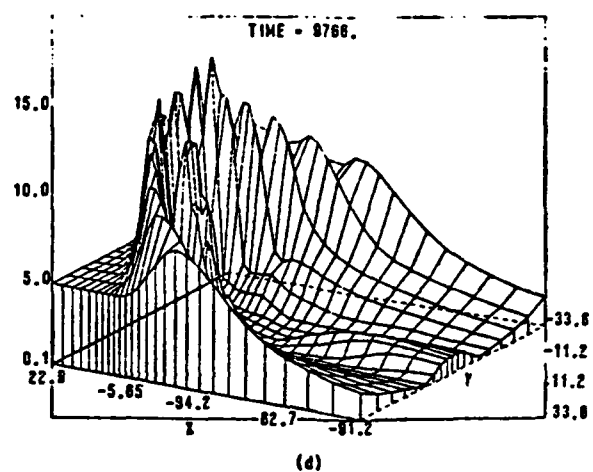
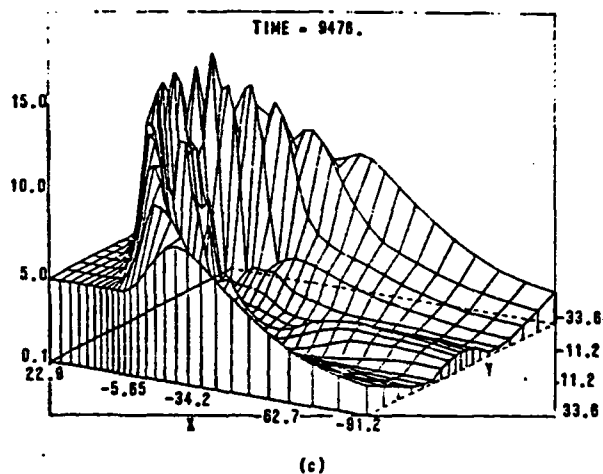
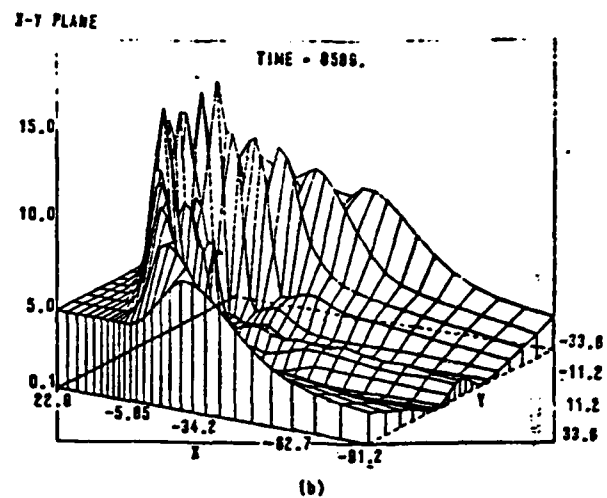
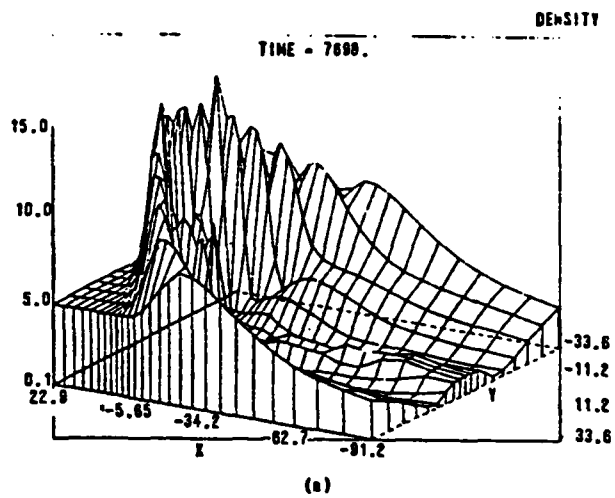


Figure 4

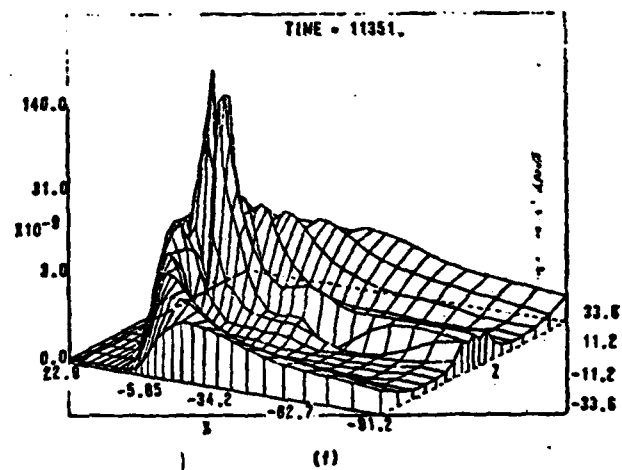
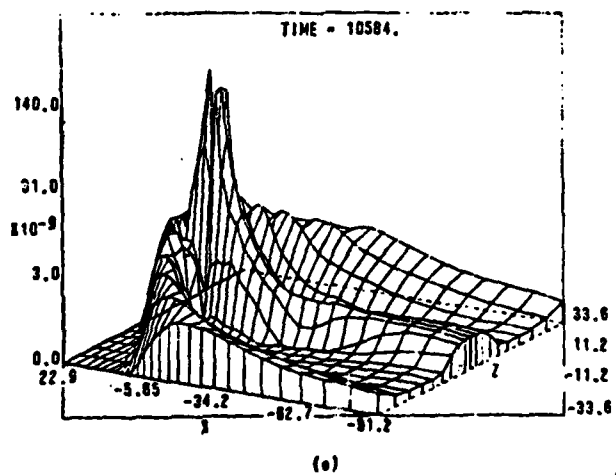
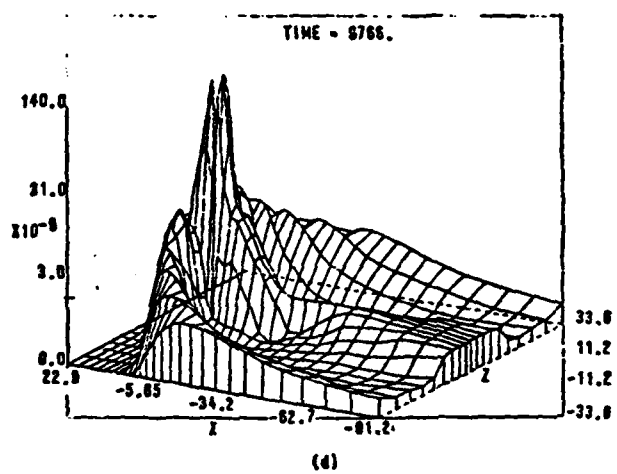
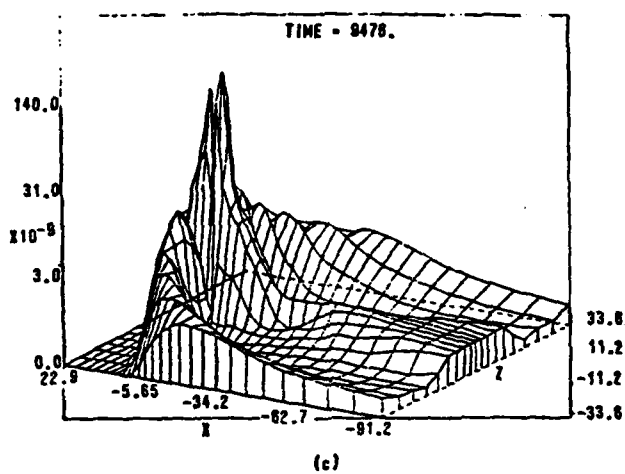
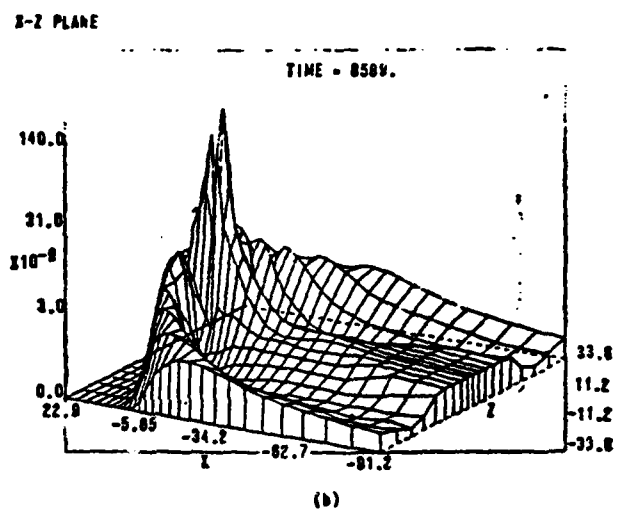
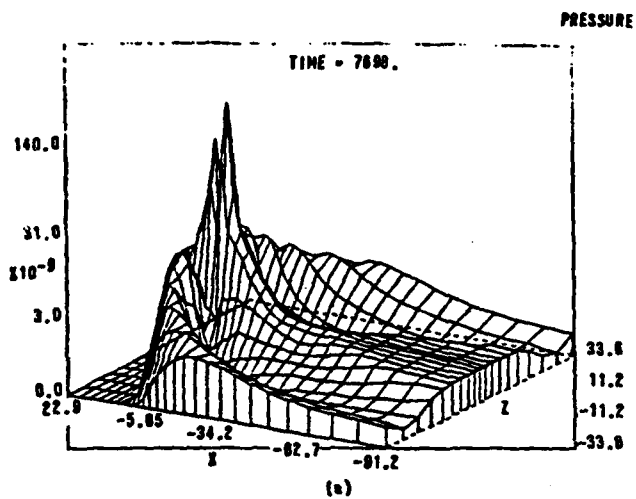


Figure 5

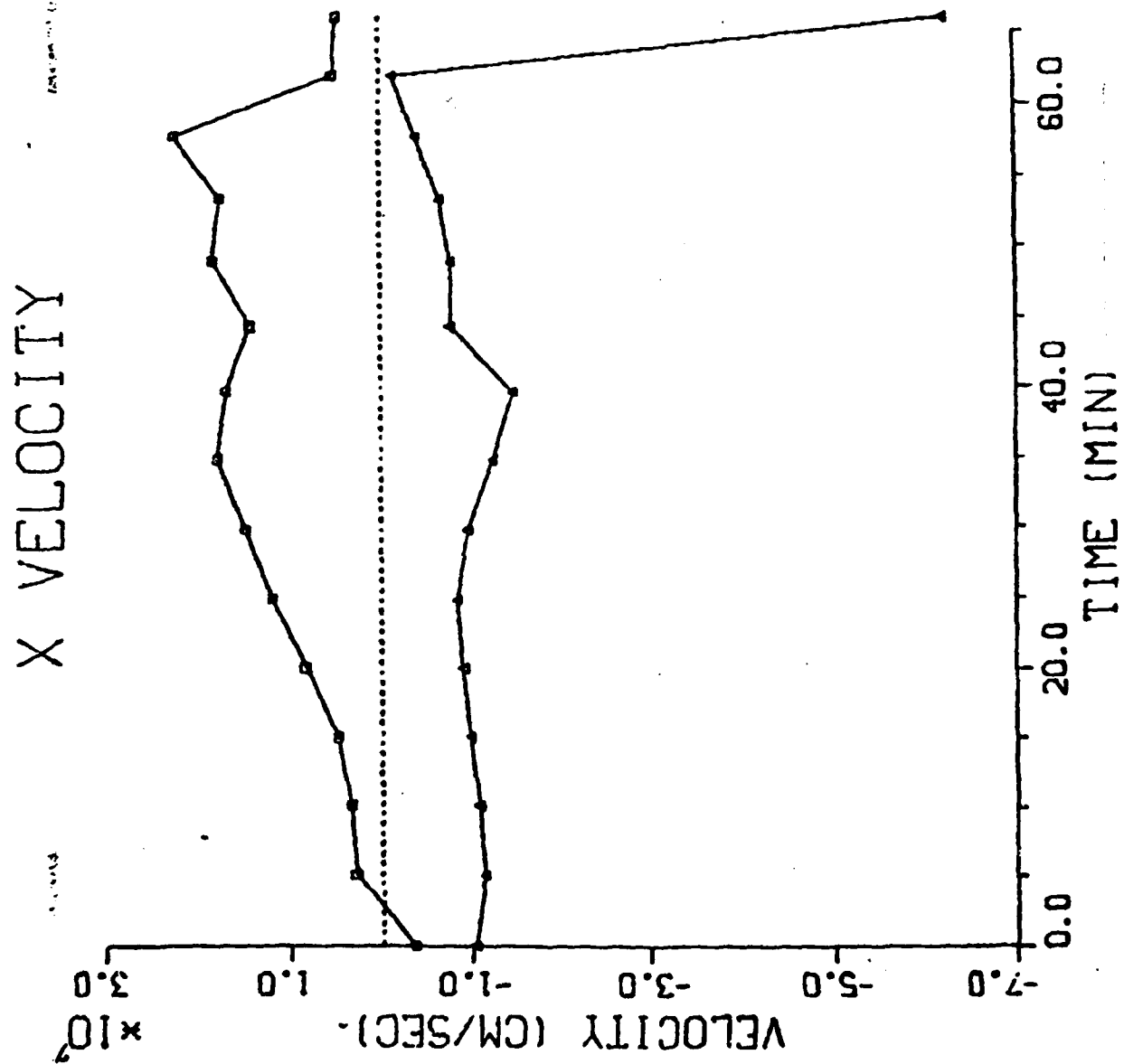


Figure 6

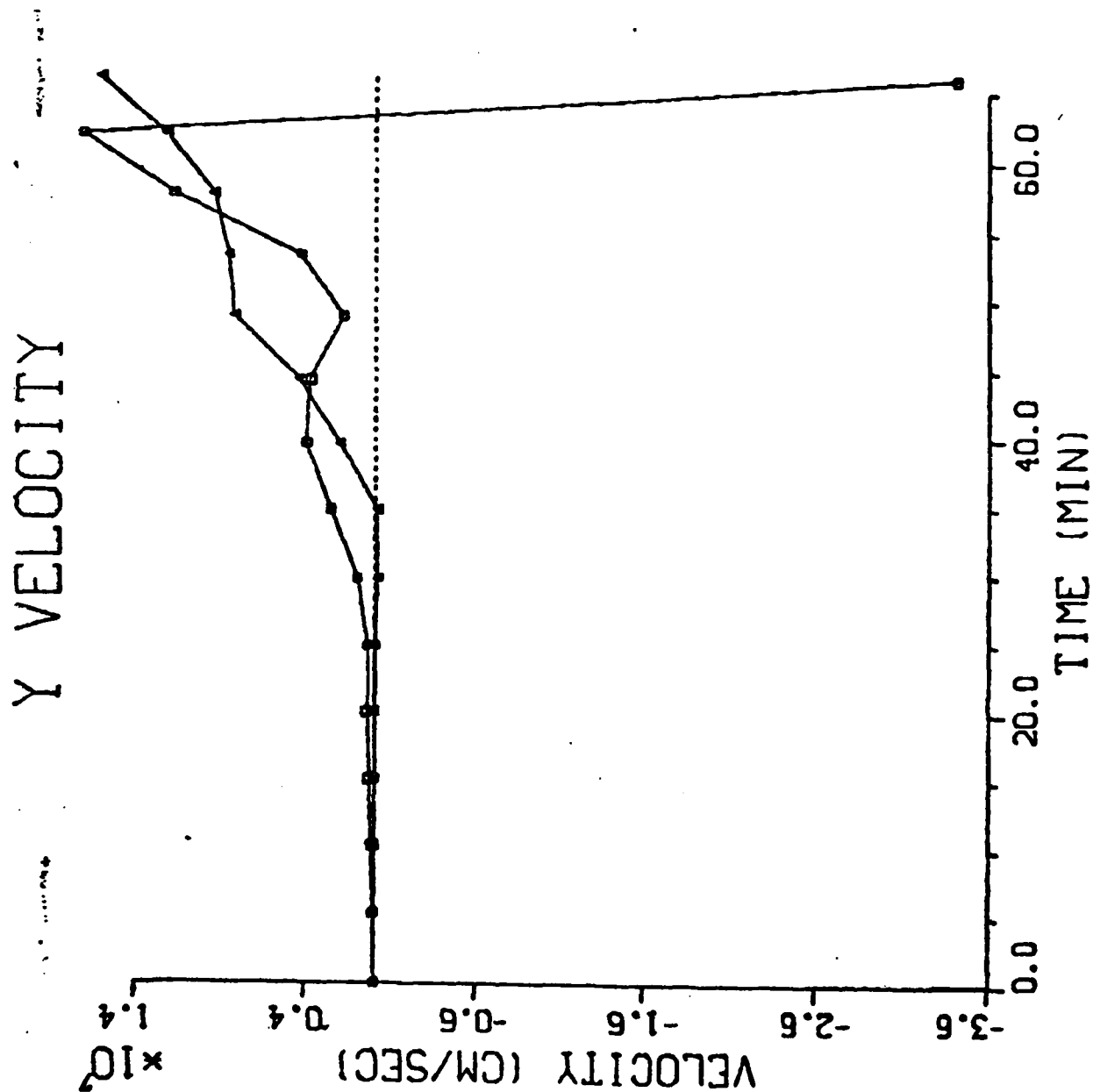


Figure 7

Z MAG FIELD

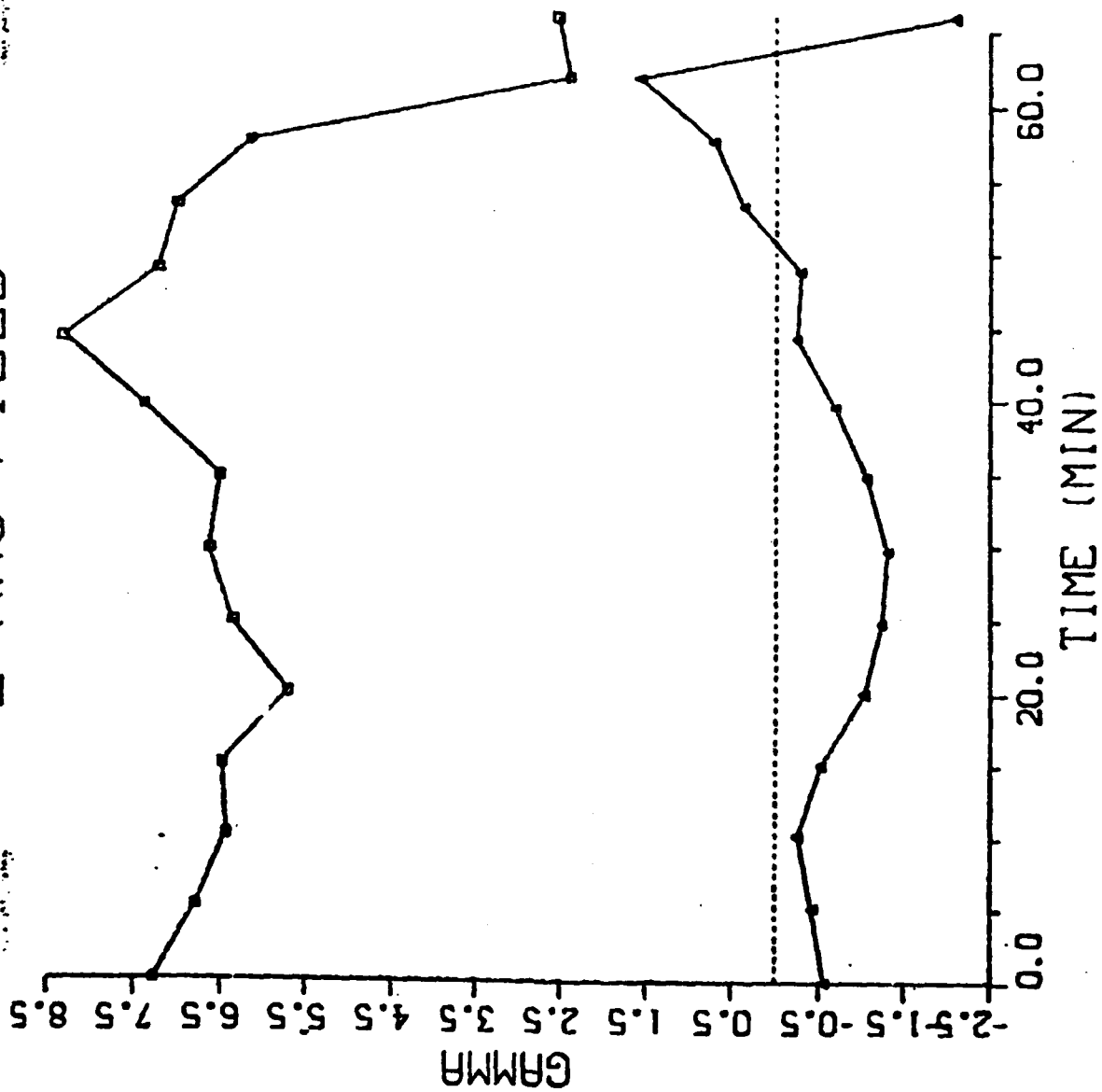


Figure 8

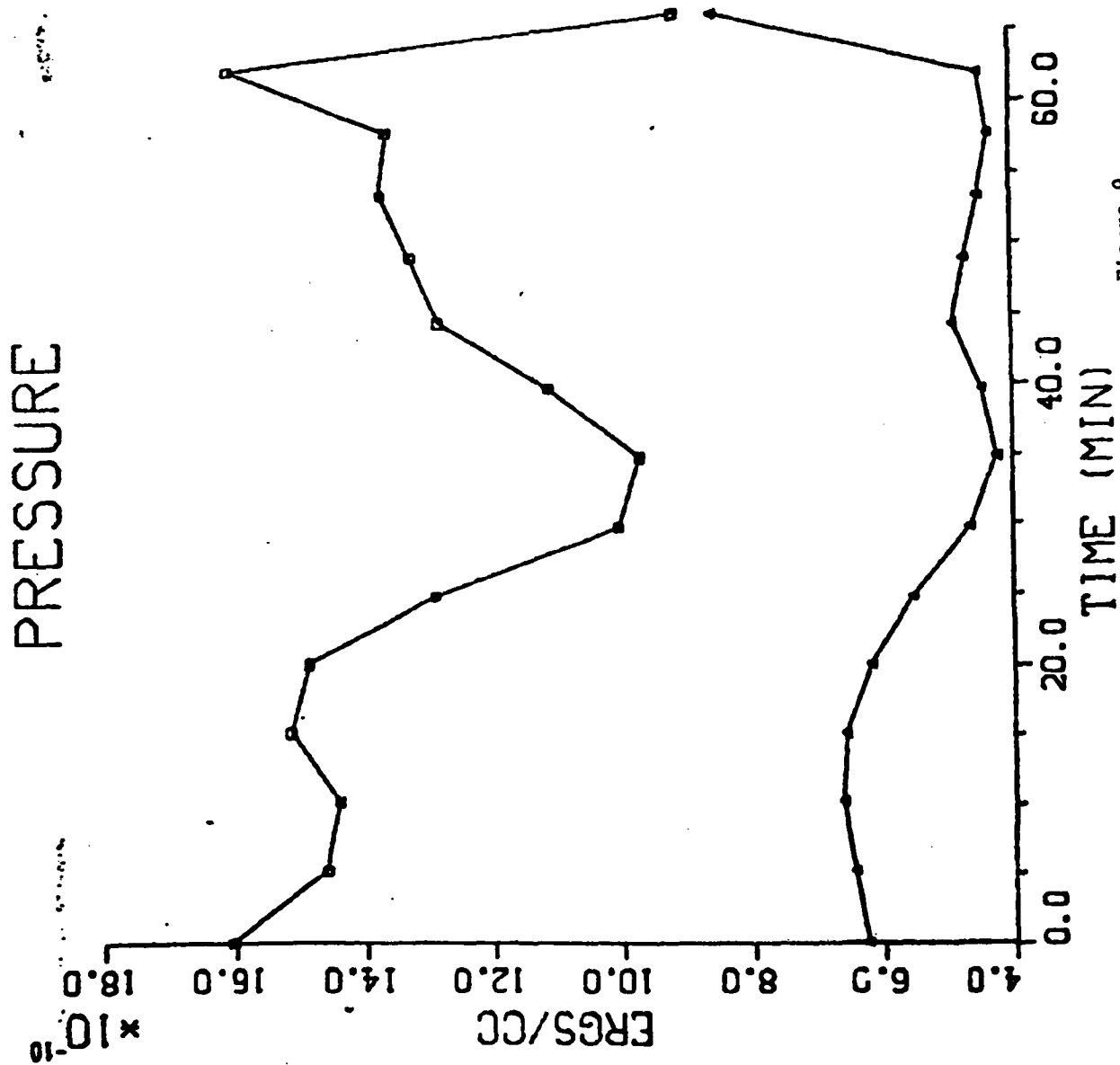


Figure 9

DENSITY

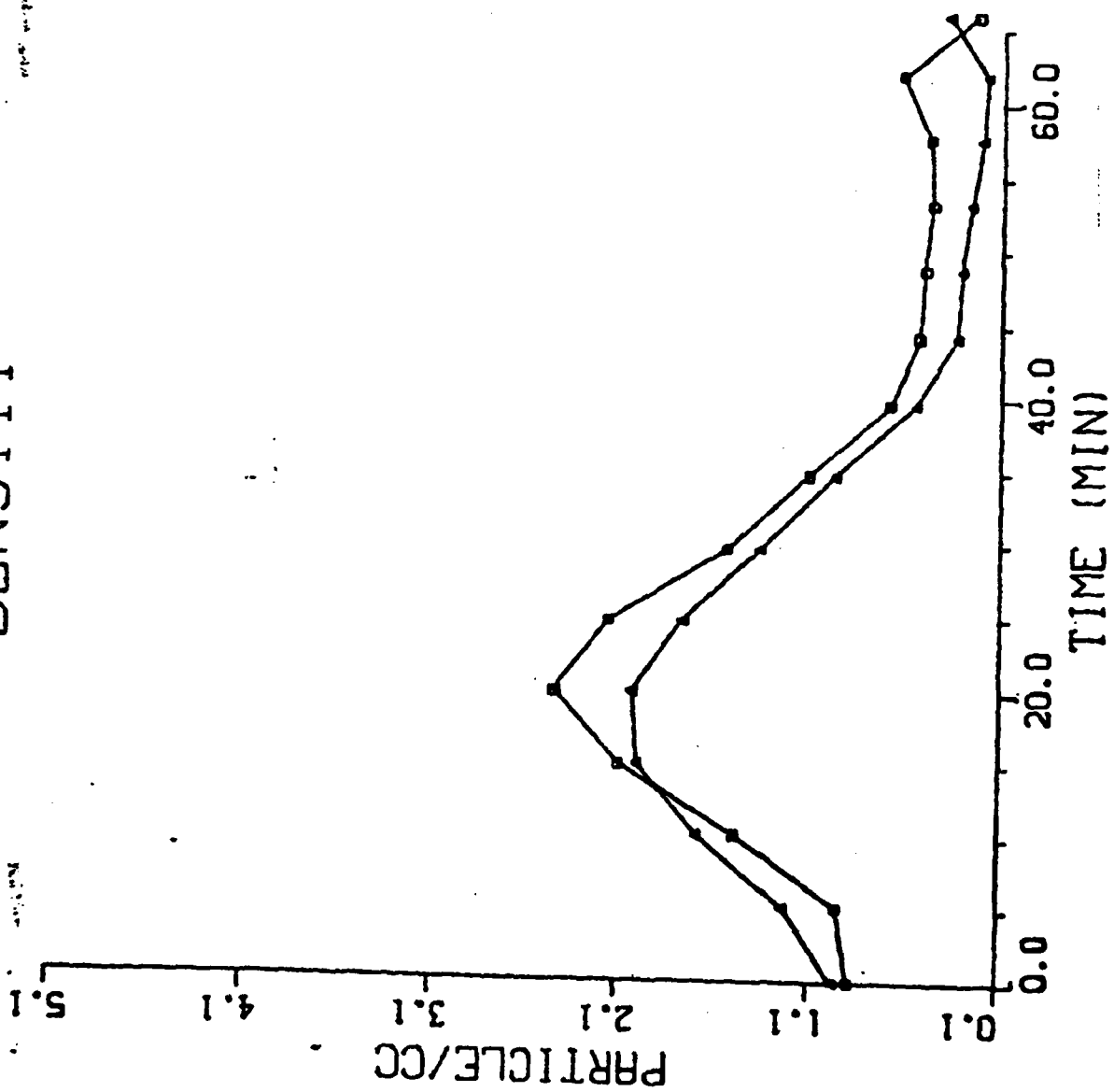


Figure 10

Appendix C

THE LOWER-HYBRID-DRIFT
INSTABILITY IN NON-ANTIPARALLEL
REVERSED FIELD PLASMAS

J.D. Huba¹ and J.F. Drake²
Science Applications, Inc.
McLean, VA 22102

and

N.T. Gladd³
Geophysical and Plasma Dynamics Branch
Plasma Physics Division
Naval Research Laboratory
Washington, D.C. 20375

¹Present address: Geophysical and Plasma Dynamics Branch
Plasma Physics Division
Naval Research Laboratory
Washington, D.C. 20375

²Permanent address: University of Maryland
College Park, MD 20742

³Present address: JAYCOR
San Diego, CA 92138

The Lower-Hybrid-Drift
Instability in Non-antiparallel
Reversed Field Plasmas

J.D. Ruba, N.T. Gladd¹ and J.F. Drake²
Geophysical and Plasma Dynamics Branch
Plasma Physics Division
Naval Research Laboratory
Washington, D.C. 20375

Abstract

The lower-hybrid-drift instability is investigated in non-antiparallel reversed field plasmas, i.e., the magnetic fields on either side of a neutral line are not anti-parallel. Such a magnetic field configuration contains magnetic shear which has a stabilizing influence on the lower-hybrid-drift instability. It is found that magnetic shear has an inhibiting effect on the linear penetration of the lower-hybrid-drift mode toward the neutral line. The implications of this result to reconnection processes in the magnetosphere (i.e., the nose and the magnetotail) are discussed.

¹ Present address: JAYCOR
San Diego, CA 92138

² Permanent address: University of Maryland
College Park, MD 20742

I. INTRODUCTION

An important set of problems in plasma physics consists of understanding the physical processes which can occur in reversed field plasmas. For example, how can magnetic field energy be rapidly converted into particle energy? How does the topology of the magnetic field change? Under what conditions can topological changes occur? An enormous amount of work has been devoted to these (and related) questions over the past 20 years. Generally speaking, this research has been focused on the investigation of magnetic field reconnection processes. Some particular topics of interest have been field line annihilation (e.g., 1D Sweet-Parker models); forced reconnection (e.g., 2D Petschek model); and tearing instabilities. In an astrophysical context, this research has been relevant to a variety of space phenomena such as solar flares, interplanetary D sheets and geomagnetic substorms.

One process which can be important in reconnection physics is plasma microturbulence. In general, plasma microinstabilities can often produce anomalous transport of particles, momentum and energy. This can be critical to a reconnection process, especially in the null region ($B = 0$), since it allows the plasma to "decouple" from the magnetic field. Moreover, anomalous transport effects can greatly enhance the rate of energy conversion from the magnetic field to the plasma. A variety of microinstabilities which can lead to fine scaled turbulence have been analyzed to determine their relevance to reconnection (see Papadopoulos (1979) for a review). However, a drawback of many of these analyses is the assumption of a one-dimensional magnetic field (i.e., $\underline{B} = B_z(x)\underline{e}_z$); an assumption not usually justified in space plasmas. Other components of the magnetic field lead to the following effects. First, a component of \underline{B} normal to the neutral line (i.e., $\underline{B} = B_x \hat{e}_x + B_z \hat{e}_z$) introduces field line curvature. This effect, which is generally incorporated in microinstability theories via an artificial gravity, leads to additional particle drifts and can be either a stabilizing or

destabilizing influence depending upon the plasma conditions. Secondly, a component of B parallel to the current (i.e., $\underline{B} = B_y \hat{e}_y + B_z \hat{e}_z$) introduces magnetic shear. Physically, this corresponds to the situation where the magnetic fields on either side of the neutral line are not anti-parallel. Magnetic shear leads to the coupling of cross-field modes to parallel propagating modes and to Landau resonances of particles and waves. Magnetic shear is generally a stabilizing influence on instabilities. Since the magnetic shear induced Landau resonances and parallel mode couplings are strongly dependent on spatial position, the analysis of this effect requires a nonlocal theory. In contrast, the magnetic curvature induced particle drifts are not strongly dependent on spatial position and can be accurately analyzed with a local theory.

In this paper we analyze the effect of magnetic shear on the lower-hybrid-drift instability and discuss some of the implications of magnetic shear as it regards the dynamics of reversed field plasmas in the magnetosphere. We choose the lower-hybrid-drift instability since it is the most likely instability to be excited in reversed field space plasmas of interest (i.e., the earth's magnetopause and magnetotail (Huba et al., 1978; Gary and Eastman, 1979)). Moreover, the anomalous transport properties associated with this instability can be important to reconnection processes (Huba et al., 1977; Drake et al., 1981; Huba et al., 1980). We focus here on the effect of magnetic shear on the lower-hybrid-drift instability since it has been shown to have a strong stabilizing effect on this mode (Krall, 1978). We will not consider the effect of field line curvature since it has a much weaker influence on the instability (Krall and McBride, 1977; Rajal and Gary, 1981).

The scheme of the paper is as follows. In Section II we present a general discussion of the lower-hybrid-drift instability and the effect of magnetic shear on it; showing the stabilizing influence of shear. We also apply these results to a particular sheared, reversed magnetic field configuration. In

Section III we discuss the implications of these results on reconnection processes in the earth's magnetosphere.

II. THEORY

A. Assumptions and Plasma Configuration

The plasma configuration and slab geometry we consider is described as follows. The ambient magnetic field is in the y-z plane ($\underline{B} = B_y \hat{e}_y + B_z \hat{e}_z$) and is only a function of x. The density is also a function of x but we take the ion temperature to be finite and constant. We take $T_e \ll T_i$ which is typical of the magnetopause and magnetotail. Equilibrium force balance on an ion fluid element in the x direction requires $V_{iy} = V_{di}$ where $V_{di} = (v_i^2/2\Omega_i) \partial \ln n / \partial x$ is the ion diamagnetic drift velocity. Here, $v_i = (2T_i/m_i)$ is the ion thermal velocity and $\Omega_i = eB_0/m_i c$ is the ion Larmor frequency. We can relate the ion diamagnetic velocity to the mean ion Larmor radius and scale length of the density gradient by $V_{di}/v_i = r_{Li}/2L_n$ where $r_{Li} = v_i/\Omega_i$ and $L_n = (\partial \ln n / \partial x)^{-1}$. The electrons are assumed to be magnetized, while the ions are treated as unmagnetized. This is reasonable since, in treating the lower-hybrid-drift instability, we are considering waves such that $\Omega_i \ll \omega \ll \Omega_e$ and $k^2 r_{Li}^2 \ll 1$. Also, we consider the coupling of electrostatic and electromagnetic oscillations which is important in finite β plasmas. We assume that the plasma is weakly inhomogeneous in the sense that $r_{Le}^2 (\partial \ln n / \partial x)^2 \ll 1$. Finally, we assume that the local equilibrium magnetic field is

$$\underline{B}(x) = B_0 \{ [1 + (x-x_0)/L_B] \hat{e}_z + (x-x_0)/L_S \hat{e}_y \} \quad (1)$$

in the vicinity of

$x = x_0$ (i.e., $(x-x_0)/L_S \ll 1$ and $(x-x_0)/L_B \ll 1$) where $L_S = (\partial \phi / \partial x)^{-1}$ and $\phi = \tan^{-1} (B_y/B_z)$. Thus, L_S and L_B are the scale lengths characterizing the magnetic shear and the magnetic field gradient, respectively. We note from Eq. (1) that an ambient parallel current, J_z , is needed to produce the variation of B_y in the x-direction (i.e., the magnetic shear). For the lower-hybrid-drift instability, a parallel current has a negligible effect on the mode unless $V_{di} > v_e$, where V_{di} is the

relative parallel velocity of ions and electrons, and v_e is the electron thermal velocity. Since this is not usually the case at the magnetopause (Lee and Kan, 1980) or the magnetotail (Frank et al., 1979) we can neglect J_z in the analysis.

If, for the moment, we consider $\underline{B} = B_0 \hat{e}_z$, then the plasma configuration just described is unstable to the kinetic lower-hybrid-drift instability when $1 > v_{di}/v_i > (m_e/m_i)^{1/4}$ (Davidson et al., 1977). The instability is driven by the cross-field current and is excited via an ion-wave resonance (i.e., inverse Landau damping). The waves are characterized at maximum growth by $\omega_r \sim k_y v_{di} < \omega_{ih}$, $\gamma < \omega_r$, $k_y \rho_{es} \approx 1$ and $-\underline{k} \cdot \underline{B} = 0$ where $\rho_{es} = (T_i/m_e) / \Omega_e$. For modes such that $\underline{k} \cdot \underline{B} \neq 0$ (i.e., $k_{\parallel} \neq 0$), parallel mode coupling or electron Landau damping reduces their growth rate or stabilizes them, depending on the magnitude of k_{\parallel} and T_e/T_i . We now let $\underline{B} = B_y(x) \hat{e}_y + B_z \hat{e}_z$ as in Eq. (1), which introduces magnetic shear as shown in Fig. 1. The magnetic field rotates in the y-z plane as a function of x so that k_{\parallel} is also a function of x. At $x = x_0$ we note that $k_{\parallel} = 0$ ($\underline{k} \cdot \underline{B} = 0$) but at $x = x_1$, ($k_{\parallel} \neq 0$). Thus the dispersive properties of the plasma are also a function of x (e.g., electron Landau damping and parallel mode coupling can occur at x_1 but not at x_0). Making use of Eq. (1), we use the prescription $k_z(x) = k_{z0} + k_y(x-x_0)/L_s$ to incorporate magnetic shear into the analysis where we choose $k_{z0} = k_z(x=x_0) = 0$.

R. Dispersion equation

Within the context of the assumptions outlined in the previous subsection, the equation which describes the lower-hybrid-drift instability in a sheared magnetic field is given by [Davidson et al., 1978]

$$A \frac{\partial^2 \phi}{\partial x^2} + [B - C(x-x_0)^2] \phi = 0 \quad (2)$$

where

$$A = - \frac{1}{k_y^2} \frac{2\omega_{pi}^2}{k^2 v_i^2} [k^2 \rho_{es}^2 - Z''(\zeta_i)] \quad (3)$$

$$B = \frac{2\omega_{pi}^2}{k^2 v_i^2} \left\{ 1 + k^2 \rho_{es}^2 \left(1 + \frac{\omega_{pe}^2}{c^2 k^2} \right) - \frac{k_y v_{di}}{\omega} \left(1 + \frac{\beta_i}{2} \right) \right. \quad (4)$$

$$\left. + \zeta_i Z(\zeta_i) + i\pi \frac{T_i}{T_e} s_e \exp(-s_e) \Lambda_0^2 \right\}$$

$$C = \frac{\omega_{pe}^2}{\omega^2} \frac{1}{L_s^2} \left(1 + \frac{\omega_{pe}^2}{c^2 k^2} \right)^{-1} \quad (5)$$

$$\Lambda_0 = J_0(\zeta_r) - \frac{\beta_i}{k \rho_{es}} \left(\frac{T_e}{2T_i} \right)^{1/2} s_e^{1/2} J_1(\zeta_r)$$

and $\omega_{pi}^2 = 4\pi n e^2 / m_i$, $v_i^2 = 2T_i / m_i$, $\rho_{es}^2 = T_i / m_i \Omega_e^2$, $v_{di} = (v_i^2 / 2\Omega_i) \partial \ln n / \partial x$, $\zeta_i = (\omega - k_y v_{di}) / k v_i$, $\beta_i = 8\pi n T_i / B^2$, $\zeta_r = k r_{Le} s_e$ and $s_e = (\omega / k_y v_{di}) (2/\beta_i) (T_i / T_e)$. In writing Eqs. (2)-(5) we have also assumed $2\omega_{pi}^2 / k^2 v_i^2 \gg 1$, $\omega_{pe}^2 \gg \Omega_e^2$, and $s_e \gg 1$, $\omega / k_y v_e \gg 1$ and $k^2 r_{Le}^2 \ll 1$.

The influence of magnetic shear retained in Eqs. (2)-(5) is the coupling of the perpendicular and parallel propagating modes. The influence of electron Landau damping has been neglected since the localization of the mode due to shear is such that $\omega / k_y v_e \gg 1$ or $\Delta x \ll L_s (\omega / k_y v_e)$ (to be shown a posteriori).

The finite β corrections included in Eq. (2) are as

AD-A111 638

SCIENCE APPLICATIONS INC MCLEAN VA
GEOPHYSICAL PLASMAS AND ATMOSPHERIC MODELING.(U)
JAN 82 E HYMAN, J APRUZESE, S BRECHT, W CHAO

F/O 4/1

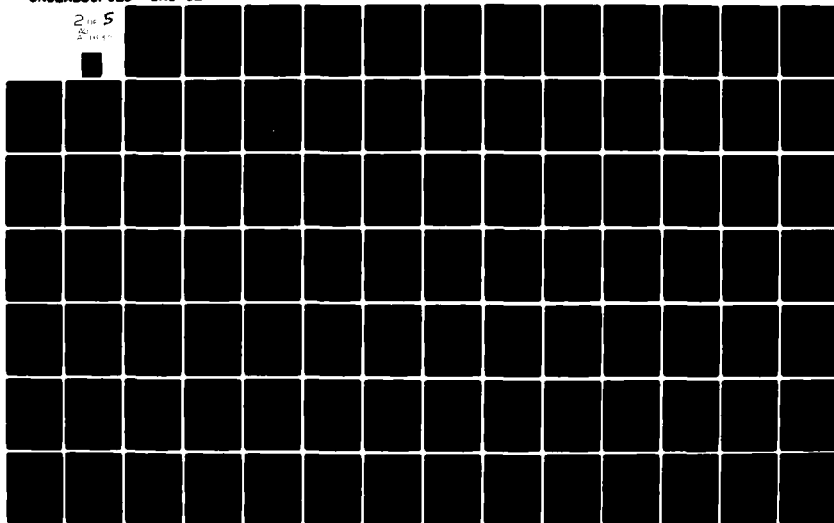
N00014-81-C-2038

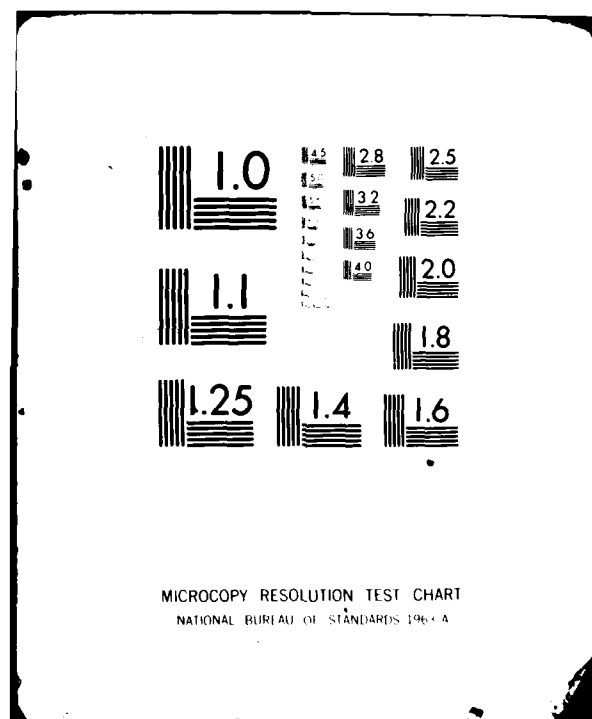
NL

UNCLASSIFIED

SAI-82-678-WA

2 OF 5
A 111 638





follows. First, the coupling of electromagnetic and electrostatic perturbations arises from terms proportional to ω_{pe}^2/c^2k^2 . The β dependence can be seen by noting that $k^2\rho_{es}^2(\omega_{pe}^2/c^2k^2) = \beta_i/2$ (albeit somewhat artificial). Second, nonresonant electron VB effects are contained in the term proportional to $\beta_i(k_y v_{di}/\omega)$. This is a fluid-like response of the electrons to the inhomogeneous magnetic field (i.e., L_B in Eq. (1)). Finally, resonant electron VB effects are contained in the final term in Eq. (4). The resonance is given by $s_e = \omega_r/k_y v_{Be}$ where $v_{Be} = (v_e^2/2\Omega_e)\partial \ln B/\partial x$ and $L_B = (\partial \ln B/\partial x)^{-1}$. Equations (3)-(5) are similar to those derived by Davidson et al. (1977) but, in addition, contain electron resonance terms (Huba and Wu, 1977; Davidson et al., (1978)).

Equation (2) is in the form of Weber's equation and the eigenfrequency is defined by

$$B = (2m + 1) (AC)^{1/2} \quad (6)$$

where m is the mode number (i.e., $m = 0, 1, 2, \dots$). The branch is chosen according to the outgoing energy prescription of Pearlstein and Berk (1969). The associated eigenfunction is

$$\phi = \phi_0 R_m(\alpha x) \exp[-\alpha^2 x^2/2] \quad (7)$$

where $\alpha = (C/A)^{1/4}$ and R_m is the Hermite polynomial of order m . In general, a numerical analysis is required to solve Eq. (6) (using Eqs. (3)-(5)). However, we first consider a limiting case to obtain an analytical solution to Eq. (6).

We consider the low β , weak drift limit (i.e., $v_{di} \ll v_i$, $\beta_i \ll 1$). The Z function can be approximated by $Z(\zeta_i) = i/\pi$. The dispersion equation (Eq. (6)) is then

$$D(\omega, k) = 1 + k^2 \hat{\rho}_{es}^2 - \frac{k_y v_{di}}{\omega} + i \left\{ \sqrt{\pi} \left(\frac{\omega - k_y v_{di}}{k v_i} \right) + \right. \quad (8)$$

$$\frac{kv_i}{\sqrt{2}\omega_{pi}} \frac{\omega_{pe}}{\omega} \frac{\rho_{es}}{L_s} (2m+1) + \pi \frac{T_i}{T_e} s_e \exp(-s_e) \Lambda_o^2 \}$$

where $\hat{\rho}_{es}^2 = \rho_{es}^2 / (1 + \beta_1/2)$. The first imaginary term is a destabilizing term due to inverse ion Landau damping. The second imaginary term is the stabilizing effect of magnetic shear. It's origin in the analysis is a term $\propto (k_\parallel/\omega)^2$ in the magnetized electron response. Physically, magnetic shear leads to stabilization since it allows wave energy to propagate away from the excitation region (i.e., where $k_\parallel = 0$). The final term is a damping term due to the electron VB drift-wave resonance.

The real frequency is given by

$$\omega_r = k_y V_{di} / (1 + k^2 \hat{\rho}_{es}^2) \quad (9)$$

where shear corrections to ω_r have been neglected. The mode is stabilized when $\text{Im}D(\omega, k) = 0$ or

$$\left(\frac{L_n}{L_s}\right)_{cr} = \frac{\sqrt{\pi}}{1 + k^2 \hat{\rho}_{es}^2} \left(1 + \frac{\beta_1}{4k^2 \rho_{es}^2}\right) \left[\frac{V_{di}}{V_i} \frac{k^2 \hat{\rho}_{es}^2}{1 + k^2 \hat{\rho}_{es}^2} + \sqrt{\pi} \frac{T_i}{T_e} s_e \exp(-s_e) \Lambda_o^2 \right]. \quad (10)$$

Here, we have taken $m = 0$ and the subscript refers to the critical value of L_n/L_s . The maximum value of the RHS of Eq. (10) occurs for $k^2 \hat{\rho}_{es}^2 = k^2 \rho_{es}^2 = 1$ so that all wavenumbers are stable when

$$\left(\frac{L_n}{L_s}\right)_{cr} = \frac{\sqrt{\pi}}{4} \left(1 + \frac{\beta_1}{4}\right) \left(\frac{V_{di}}{V_i} + 2\sqrt{\pi} \frac{T_i}{T_e} s_e \exp(-s_e) \Lambda_o^2 \right) \quad (11)$$

and $s_e = 1/\beta_e$.

Two interesting points concerning Eqs. (10) and (11) are the following. First, the finite β_1 dependence in the first term of Eqs. (10) and (11) arise from the electromagnetic correction due to δA_\parallel (i.e., the transverse magnetic field fluctuations). The influence of this correction is to increase the amount of shear

necessary to stabilize the mode (Davidson et al., 1978). That is, as β_1 increases then the shear length L_s necessary for stabilization decreases so that the mode is harder to stabilize. Physically, this occurs because the fluctuating electric field associated with δA_1 inhibits free streaming electron flow along the magnetic field which reduces the rate at which energy can be convected away from the localization region (Pearlstein and Berk, 1969). Secondly, the final term in Eq. (11) represents the resonant VB correction which is a damping effect. This term tends to decrease the amount of shear necessary to stabilize the mode. Thus, the finite β corrections have different influences on the shear stabilization criterion. Loosely speaking, electromagnetic effects are destabilizing (i.e., a stronger shear is needed to stabilize the mode from the $\beta = 0$ situation) while the resonant VB effects are stabilizing (i.e., a weaker shear is needed to stabilize the mode from the $\beta = 0$ situation).

We now relax the weak drift assumption and solve Eq. (6) numerically for the critical value of shear necessary to stabilize the instability as a function of drift velocity. The parameters chosen are $\omega_{pe}/\Omega_e = 10.0$, $T_e/T_i = 0.1$ and $m = 0$ for $\beta = 0.1$ and $\beta = 0.2$. The growth rate γ is maximized with respect to kp_{es} for each value of V_{di}/v_i and $(L_n/L_s)_{cr}$ is the value of shear for which $\gamma = 0$. For

$L_n/L_s > (L_n/L_s)_{cr}$ ($L_n/L_s < (L_n/L_s)_{cr}$) the mode is stable (unstable) as shown. The influence of finite β effects is illustrated by comparing the $\beta = 2.0$ curves to the $\beta = 0.1$ curve. First, note that $(L_n/L_s)_{cr}(\beta = 2.0) > (L_n/L_s)_{cr}(\beta = 0.1)$ so that a stronger amount of shear is necessary to stabilize the mode as β increases. This is caused by the finite β coupling to electromagnetic modes. Second, the dashed $\beta = 2.0$ curve corresponds to the situation where electron VB drift-wave resonances have been neglected (Eq. (6) with $\tau_e \rightarrow \infty$). Since this curve lies above the $\beta = 2.0$ solid curve, the damping effect of the electron resonances is apparent. For a sufficiently large β , the amount of shear to stabilize the

instability will be less than that needed to stabilize the mode
in a low β plasma.

C. Application to Reversed Field Plasmas

In order to apply these results to a reversed field plasma, we consider the following magnetic field profile

$$\mathbf{B} = B_0 \left(\sin \frac{\theta}{2} \hat{e}_y + \cos \frac{\theta}{2} \tanh \frac{x}{\lambda} \hat{e}_z \right) \quad (12)$$

Equation (12) describes reversed field plasma (i.e., the z-component reverses direction at $x = 0$) with the field undergoing a total directional change $\pi + \theta$ in the y-z plane. Thus, the standard one-dimensional Harris profile is recovered (i.e., anti-parallel field) with a discontinuous rotation at $x = 0$ if $\theta = 0$. On the other hand, for $\theta \neq 0$ the field continuously rotates in the y-z plane and remains finite everywhere. This profile (Eq. (12)) is a rough approximation to the magnetic field of the nose of the magnetosphere of the earth. It also approximates the distant geomagnetic tail when no normal field component is present.

We plot L_n/L_s vs. x/λ for several values of θ ($\theta = 50^\circ, 100^\circ, 150^\circ, 200^\circ, 250^\circ, 300^\circ, 450^\circ$) in Figure 3. We note that L_n/L_s varies 2-3 orders of magnitude over the range of x/λ as shown. Also, as θ increases so does L_n/L_s , as anticipated. In the region $x/\lambda < 0.25$, the shear is strong (i.e., $L_s > L_n$) and the theory discussed in this paper is not adequate. Thus, we restrict our attention to regions such that $L_n > L_s$. Also, β is plotted as a function of x/λ for $\theta = 0^\circ$ and 45° . This curve indicates the range in values of β as θ changes from 0° to 45° .

We combine the results of Figs. 2 and 3 in Fig. 4 which plots θ vs. x_p/λ for two values of V_{di}/v_i ($V_{di}/v_i = 0.25$ and 1.00 which correspond to $\lambda/r_{Li} = 4.0$ and 1.0 , respectively). Here x_p/λ represents the linear penetration distance of the lower-hybrid-drift instability. That is, we expect the modes to be linearly stable for $x < x_p$ because of shear stabilization. This figure is based on the assumption that the mode is sufficiently localized so that the x variation of the ambient

profiles can be neglected. Numerical solutions of Eq. (6) indicate that the mode is localized by shear within a region $\Delta x \approx 10 \rho_{es}$ which is substantially smaller than the localization due to the variation of n and B (Huba et al., 1980). The dashed portion of the curves correspond to regions where $kr_{Le} > 1$. Since our theory is restricted to the regime $k^2 r_{Le}^2 \ll 1$ these values of x_p/λ are estimates. Moreover, we have chosen $x_p/\lambda \approx 0.25$ as the minimum penetration distance based on previous work (Huba et al., 1980).

We find that (1) as the ion diamagnetic drift increases (i.e., the current sheet becomes thinner) the mode can penetrate closer to the "null" region (i.e., $x = 0$) and (2) as θ increases, which increases the magnetic shear, the penetration distance x_p/λ becomes larger. Nonlocal analysis of the lower-hybrid-drift instability in a field reversed plasma (Huba et al., 1980) has found that the dominant mode is localized at a position $x/\lambda \approx 1.25$ for $T_e = 0$. Thus, even for $\theta = 45^\circ$ the fastest growing mode is not stabilized due to shear. However, higher order modes, which penetrate closer to $x = 0$, are expected to be affected by shear. These results, however, are highly profile dependent. If the dominant shearing of the field occurred in the region where the LHD was localized, rather than in the null region (the situation implied by Eq. (12)), then the stabilizing effect of shear would be much more pronounced.

III. DISCUSSION

The purpose of this brief report has been to study the influence of magnetic shear on the lower-hybrid-drift instability in reversed field plasmas. As mentioned in the introduction, microturbulence associated with such modes can play an important role in the dynamic evolution of a reversed field plasma via its anomalous transport properties. The lower-hybrid-drift instability, although linearly stable in the field reversal region near the neutral line (Huba et al., 1980), does play a dramatic role in the evolution of an anti-parallel field reversed plasma (Drake et al., 1981; Winske, 1981; Tanaka and Sato, 1981). It has been shown both theoretically and by computer simulations that the mode causes magnetic flux to diffuse towards the neutral line which leads to an enhanced current density at the neutral line. Eventually microturbulence penetrates to the null region and permits field line reconnection/annihilation to occur, thereby dissipating magnetic energy. In the case where the reversed field is non-antiparallel (i.e., the field is sheared) we have found here that the lower-hybrid-drift instability will be linearly unstable further away from the neutral line than the case where the field is completely anti-parallel (Fig. 4). Thus, magnetic shear has an inhibiting effect on the penetration of the lower-hybrid-drift mode toward the neutral line. We anticipate that this means that the evolution of a non-antiparallel reversed field plasma will differ from that of an anti-parallel one. For example, if the shear is sufficiently strong the mode may take substantially longer to penetrate to the neutral line or may not penetrate at all. This conjecture, of course, is based on our linear analysis and must be substantiated by further (nonlinear) analysis.

Two regions of the magnetosphere in which the magnetic field can reverse direction (in one component) and is also sheared are the nose and magnetotail. In both these regions reconnection processes are believed to occur and can be important to the dynamic interaction of the solar wind and the magnetosphere. In

the case of the nose, the angle between the incoming IMF and the earth's geomagnetic field varies from 0 to π . A thin magnetopause boundary layer exists (whose width is roughly r_{Li}) over which the \underline{B} field undergoes a directional change. In the magnetotail it is known that a substantial crosstail magnetic field $B_y < 15\gamma$ can exist at times [Akasofu et al., 1978]. Such a magnetic field can introduce a strong shear, i.e., the magnetic field undergoes a rotation as one passes from the north to south lobe.

Crooker (1978) has suggested that the nose reconnection only occurs in regions where the IMF and geomagnetic field are anti-parallel (no shear). Classical reconnection theories predict reconnection even if the fields are nonantiparallel [Ugai, 1981] so that some "anomalous" process may be responsible for inhibiting reconnection in this instance. We suggest one possibility for such an effect is the influence of magnetic shear on the lower-hybrid-drift instability (or other instabilities) and its associated microturbulence. Finally, we suggest that experimentalists studying reconnection events at the nose should attempt to correlate these events with the relative direction of the IMF and the geomagnetic field.

ACKNOWLEDGMENTS

This research has been supported by ONR and NASA.

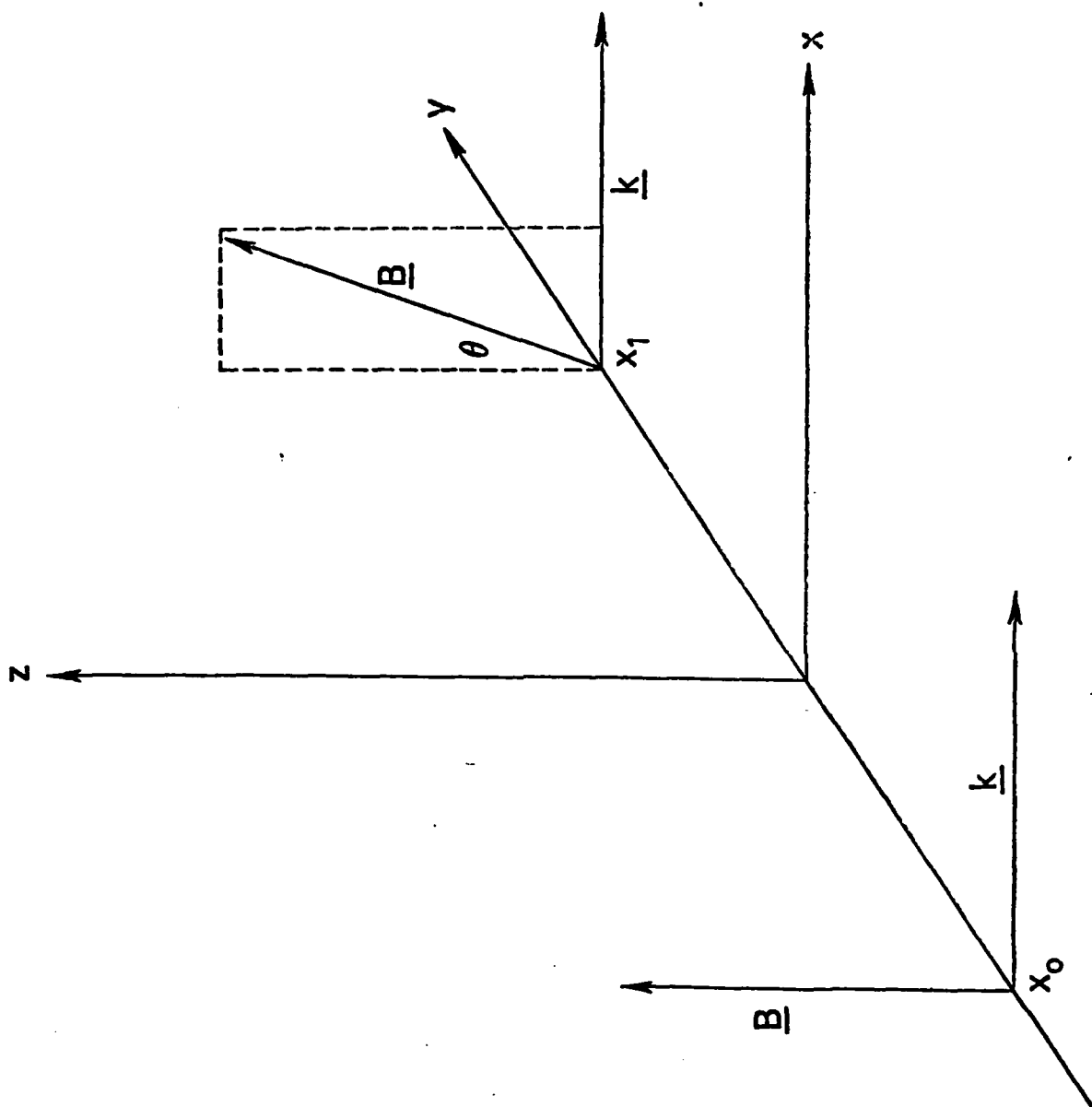
REFERENCES

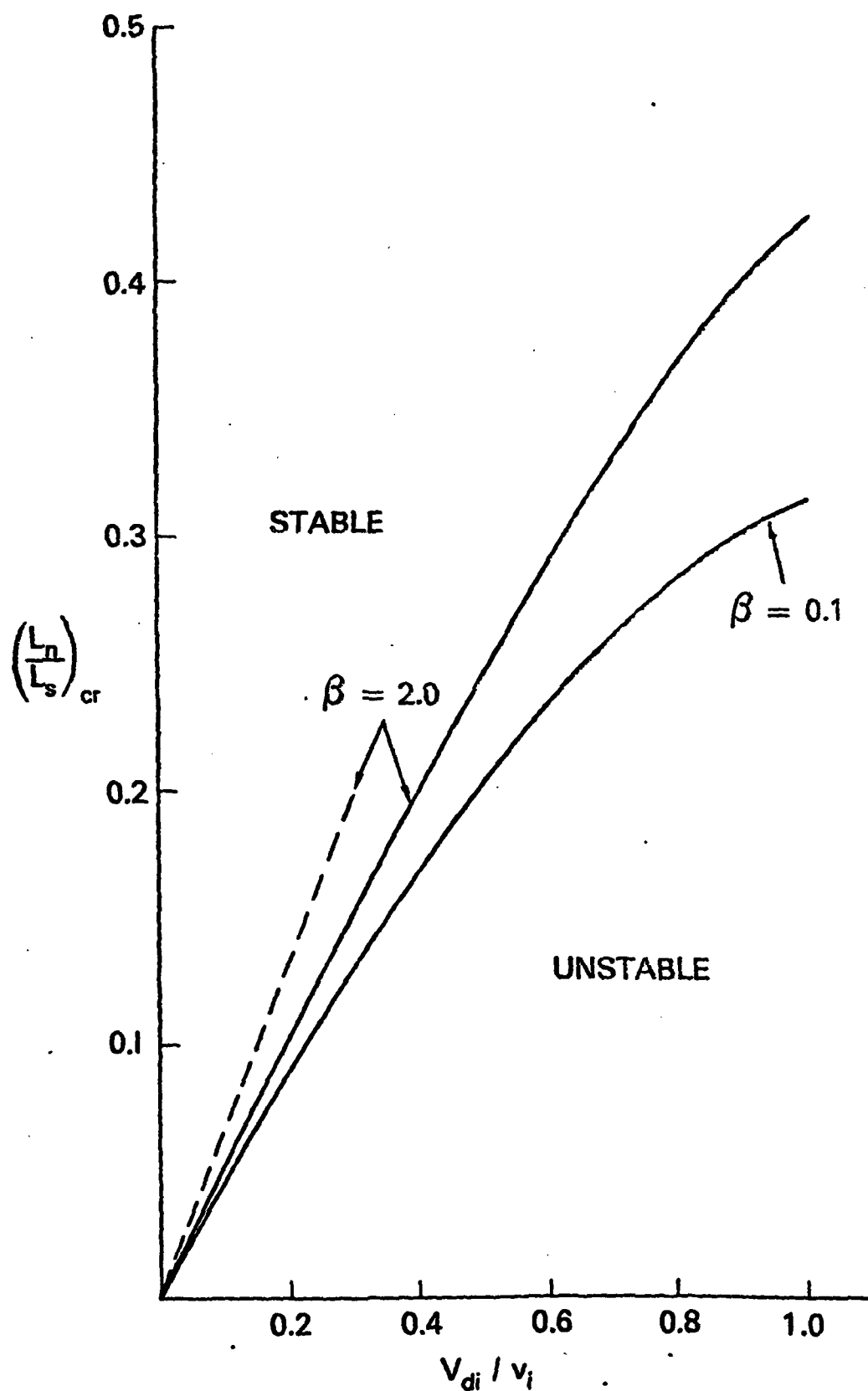
- Akasofu, S.-I., A.T.Y. Lui, C.I. Meng and M. Haurwitz, Need for a three-dimensional analysis of magnetic fields in the magnetotail during substorms, Geophys. Res. Lett. 5, 283, 1978.
- Crooker, N.U., The half-wave rectifier response of the magnetosphere and anti-parallel merging, J. Geophys. Res. 85, 575, 1980.
- Davidson, R.C., N.T. Gladd and Y. Goren, Influence of magnetic shear on the lower-hybrid-drift instability in toroidal reversed-field plasmas, Phys. Fluids 21, 992, 1978.
- Drake, J.F., N.T. Gladd and J.D. Huba, Magnetic field diffusion and dissipation in reversed field plasmas, Phys. Fluids 24, 78, 1981.
- Frank, L.A., R.J. DeCoster, B.G. Burek, K.L. Ackerson, R.L. McPherron, and C.T. Russell, "Measurements of field-aligned currents in the earth's magnetotail," EOS 60, 912, 1979.
- Gary, S.P. and T.E. Eastman, The lower-hybrid-drift instability at the magnetopause, J. Geophys. Res. 84, 7378, 1979.
- Huba, J.D. and C.S. Wu, Effects of a magnetic field gradient on the lower-hybrid-drift instability, Phys. Fluids 19, 988, 1976.
- Huba, J.D., N.T. Gladd and K. Papadopoulos, The lower-hybrid-drift instability as a source of anomalous resistivity for magnetic field line reconnection, Geophys. Res. Lett. 4, 125, 1977.
- Huba, J.D., N.T. Gladd and K. Papadopoulos, Lower-hybrid-drift wave turbulence in the distant magnetotail, J. Geophys. Res. 83, 5217, 1978.
- Huba, J.D., J.F. Drake and N.T. Gladd, Lower-hybrid-drift instability in field reversed plasmas, Phys. Fluids 23, 552, 1980.
- Huba, J.D. N.T. Gladd and J.F. Drake, On the role of the lower-hybrid-drift instability in substorm dynamics, to be published in J. Geophys. Res., 1981.

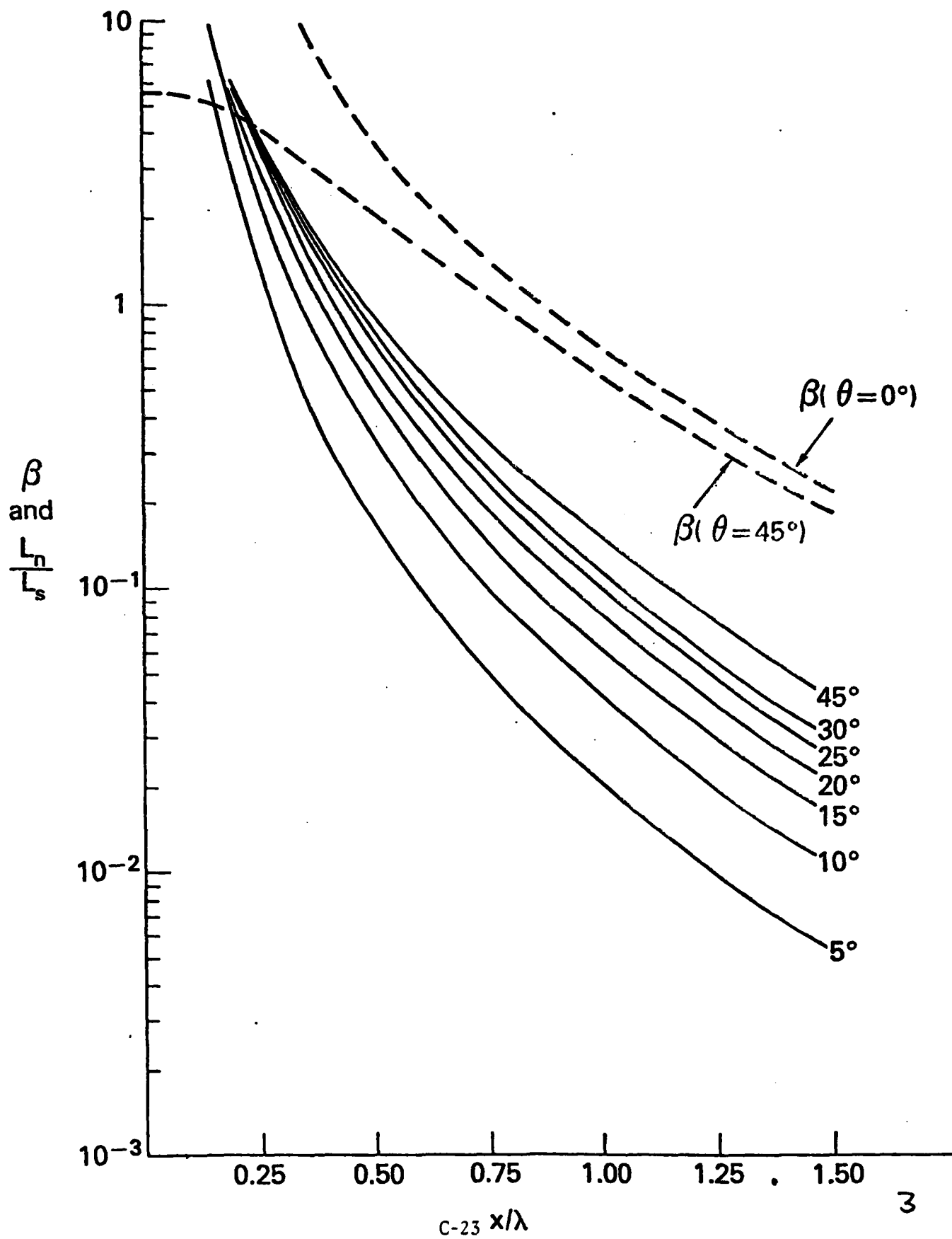
- Krall, N.A. and J.B. McBride, Magnetic curvature and ion distribution function effects on lower-hybrid-drift instabilities, Phys. Fluids 19, 1970, 1976.
- Krall, N.A., Shear stabilization of lower-hybrid-drift instabilities, Phys. Fluids 20, 311, 1977.
- Lee, L.C. and J. Kan, "Field-aligned currents in the magnetospheric boundary layer," J. Geophys. Res. 85, 37, 1980.
- Pearlstein, L.D. and H.L. Berk, Universal eigenmode in strongly sheared magnetic field, Phys. Rev. Lett. 23, 220, 1969.
- Rajal, L.J. and S.P. Gary, The lower-hybrid-drift density drift instability with magnetic curvature, submitted to Phys. Fluids, 1981.
- Tanaka, M. and T. Sato, Simulations in lower-hybrid-drift instability and anomalous resistivity in magnetic neutral sheet, to be published in J. Geophys. Res., 1981.
- Ugai, M., Magnetic field reconnection in a sheared field, J. Plasma Phys. 25, 89, 1981.
- Winske, D., Current-driven microinstabilities in a neutral sheet, Phys. Fluids, 1981.

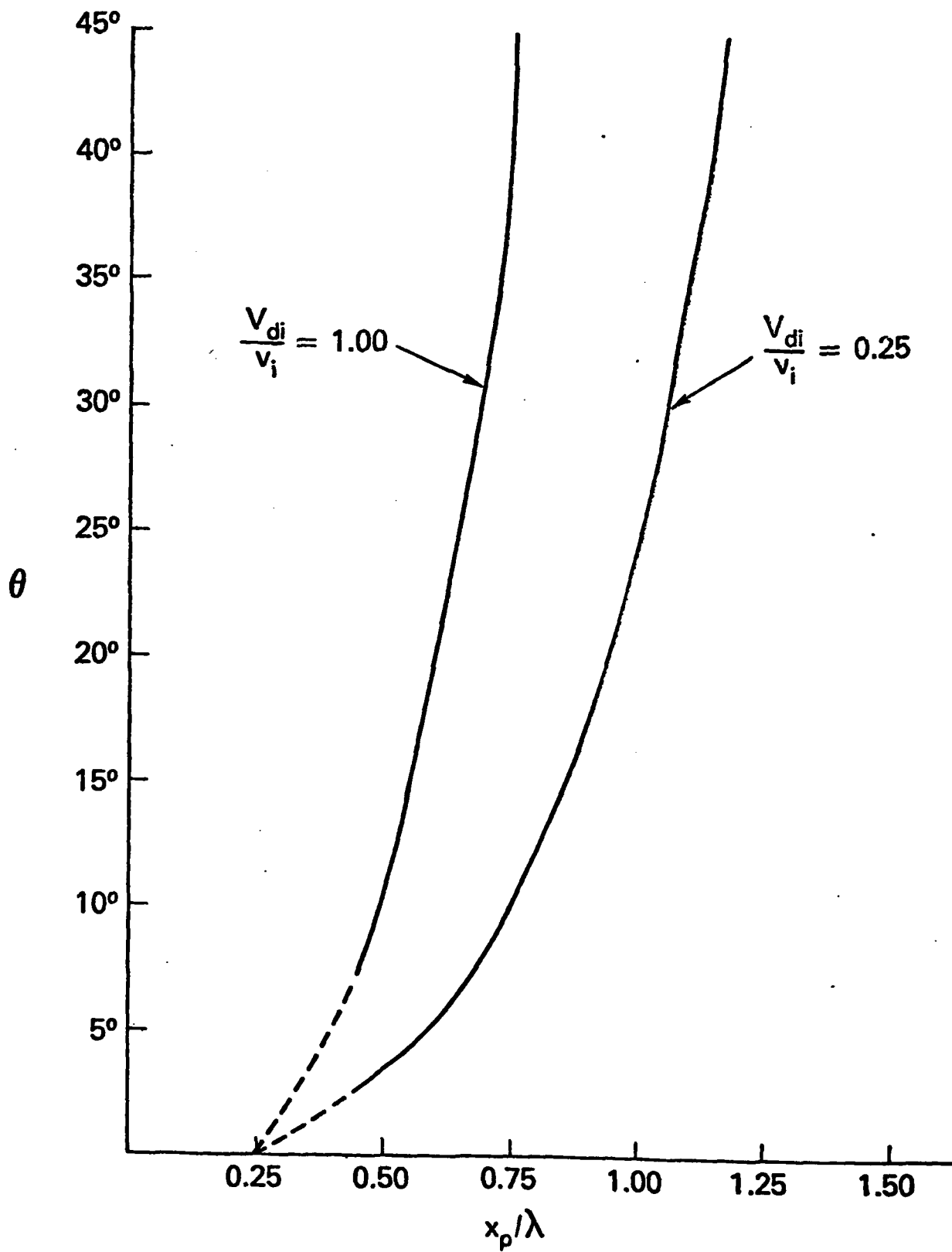
FIGURE CAPTIONS

1. Geometry of sheared magnetic field .
2. Plot of $(L_n/L_s)_{cr}$ vs. V_{di}/v_i for $\omega_{pe}/\Omega_e = 10.0$, $T_e/T_i = 0.1$, $m = 0$, $\beta = 0.1$ and $\beta = 2.0$. The lower-hybrid-drift instability is stable (unstable) for $L_n/L_s > (L_n/L_s)_{cr}$ ($L_n/L_s < (L_n/L_s)_{cr}$). The dashed curve for $\beta = 2.0$ considers the case where electron VB drift-wave resonances have been neglected.
3. Plot of L_n/L_s vs. x/λ for the magnetic field profile given by Eq. (12). Also, shown is θ vs. x/λ for $\theta = 0^0$.
4. Plot of θ vs. x_p/λ for $V_{di}/v_i = 0.25$ and 1.00 . Here, θ represents the strength of the magnetic shear in reversed field plasma (i.e., $\theta = 0$: no shear, fields anti-parallel; $\theta \neq 0$: shear, fields non-antiparallel) and x_p/λ is the linear penetration distance of the lower-hybrid-drift instability to the neutral line. The mode is linearly stable (unstable) in the region $x < x_p$ ($x > x_p$). As the amount of shear increases, i.e., θ becomes larger, the mode is stabilized further away from the neutral line ($x = 0$). The dashed portion of the curves are approximate since they are in the regime $kr_{Le} > 1$; the theory presented requires $kr_{Le} < 1$.









Appendix D

PHYSICAL MECHANISM OF WAVE-PARTICLE RESONANCES
IN A CURVED MAGNETIC FIELD

Physical Mechanism of Wave-Particle Resonances in a Curved Magnetic Field

J. D. HUBA

*Geophysical and Plasma Dynamics Branch
Plasma Physics Division*

J. F. DRAKE

*Science Applications, Inc.
McLean, VA 22102*

November 27, 1981

This research was supported by the Office of Naval Research.



NAVAL RESEARCH LABORATORY
Washington, D.C.

Approved for public release; distribution unlimited.

SECURITY CLASSIFICATION OF THIS PAGE (When Data Entered)

REPORT DOCUMENTATION PAGE		READ INSTRUCTIONS BEFORE COMPLETING FORM
1. REPORT NUMBER NRL Memorandum Report 4668	2. GOVT ACCESSION NO.	3. RECIPIENT'S CATALOG NUMBER
4. TITLE (and Subtitle) PHYSICAL MECHANISM OF WAVE-PARTICLE RESONANCES IN A CURVED MAGNETIC FIELD	5. TYPE OF REPORT & PERIOD COVERED Interim report on a continuing NRL problem.	
	6. PERFORMING ORG. REPORT NUMBER	
7. AUTHOR(s) J.D. Huba and F. Drake*	8. CONTRACT OR GRANT NUMBER(s)	
9. PERFORMING ORGANIZATION NAME AND ADDRESS Naval Research Laboratory Washington, DC 20375	10. PROGRAM ELEMENT, PROJECT, TASK AREA & WORK UNIT NUMBERS 61153N; RR03300244; 47-0884-01	
11. CONTROLLING OFFICE NAME AND ADDRESS	12. REPORT DATE November 27, 1981	
	13. NUMBER OF PAGES 23	
14. MONITORING AGENCY NAME & ADDRESS (if different from Controlling Office)	15. SECURITY CLASS. (of this report) UNCLASSIFIED	
	15a. DECLASSIFICATION/DOWNGRADING SCHEDULE	
16. DISTRIBUTION STATEMENT (of this Report) Approved for public release; distribution unlimited.		
17. DISTRIBUTION STATEMENT (of the abstract entered in Block 20, if different from Report)		
18. SUPPLEMENTARY NOTES *Science Applications, Inc., McLean, Virginia 22102 (Permanent address: University of Maryland, College Park, MD 20742). This research was supported by the Office of Naval Research.		
19. KEY WORDS (Continue on reverse side if necessary and identify by block number) Wave-particle resonances Inhomogeneous plasmas Drift waves		
20. ABSTRACT (Continue on reverse side if necessary and identify by block number) The physical mechanism of wave-particle resonances in a curved magnetic field is investigated. Specifically, the energy exchange process between a wave and resonant curvature drifting particles is discussed (i.e., $\omega \sim k \cdot V_c$ where $V_c = v^2/R_c\Omega$ is the curvature drift, R_c is the radius of curvature of the magnetic field and Ω is the cyclotron frequency). A general expression for the wave damping/growth rate is derived based upon physical arguments. The theory is applied to the lower-hybrid-drift instability and non-linear consequences are discussed.		

DD FORM 1473
1 JAN 73

EDITION OF 1 NOV 65 IS OBSOLETE
S/N 0102-014-6601

SECURITY CLASSIFICATION OF THIS PAGE (When Data Entered)

CONTENTS

I. INTRODUCTION	1
II. PHYSICAL DESCRIPTION OF THE WAVE-PARTICLE RESONANCE	4
III. PHYSICAL DERIVATION OF THE WAVE DAMPING/GROWTH RATE	9
IV. DISCUSSION	13
ACKNOWLEDGMENTS	15
REFERENCES	16

PHYSICAL MECHANISM OF WAVE-PARTICLE RESONANCES IN A CURVED MAGNETIC FIELD

I. INTRODUCTION

One of the most important phenomena in plasma physics is the wave-particle resonance.¹ These resonances allow collisionless plasmas to undergo irreversible processes such as energy and momentum exchange, and are crucial to such diverse phenomena as RF heating of laboratory plasmas,² isotope separation³ and anomalous transport of particles, momenta and energies across boundary layers.⁴ The classic work of Landau demonstrated that in an unmagnetized collisionless plasma, an electron plasma wave is damped by electrons that are in resonance with the wave; those particles which have a velocity such that $\omega \sim kv$.¹ In magnetized plasmas, Landau resonances can also occur when $k_{\parallel} = k \cdot \underline{B}/B$, the component of the wave vector parallel to the magnetic field B , is non-zero (for $\omega \sim n\Omega - k_{\parallel}v_{\parallel}$ with Ω the cyclotron frequency and n an integer). On the other hand, flute modes with $k_{\parallel} = 0$ are important in a number of physical phenomena, including plasma instabilities and radio frequency heating. If the confining magnetic field is inhomogeneous, a cross-field, wave-particle resonance can occur for particles undergoing a magnetic drift, i.e., $\omega \sim k \cdot \underline{V}_B$ where \underline{V}_B may be due to the spatial inhomogeneity of the magnetic field (∇B drift) and/or to the curvature of the magnetic field (curvature drift). These drifts are described as follows.

In an inhomogeneous magnetic field, the two important magnetic drifts that can exist⁵ are the ∇B drift

$$\underline{V}_{\nabla B} = \frac{v_{\perp}^2}{2\Omega} \frac{(\underline{B} \times \nabla)B}{B^2} \quad (1)$$

and the curvature drift

$$\underline{V}_c = \frac{v_{\parallel}^2}{\Omega} \frac{\underline{B} \times (\underline{B} \cdot \nabla)B}{B^3} \quad (2)$$

where $\Omega = eB/mc$ is the cyclotron frequency. If both types of

drifts exist and the magnetic field is produced by an external source (so that there are no plasma currents) then the total drift is given by

$$\underline{V}_B = (v_{\perp}^2/2 + v_{\parallel}^2) \frac{(\underline{B} \times \nabla)B}{\Omega B^2} \quad (3)$$

Two salient features of \underline{V}_B are the following. First, \underline{V}_B is a microscopic drift so that individual particles actually undergo a drift proportional to v_{\perp}^2 and/or v_{\parallel}^2 . It is this property that allows a wave-particle resonance to occur; unlike diamagnetic drifts (due to ∇n or ∇T) which are macroscopic drifts.

Second, \underline{V}_B is charge dependent so that electrons and ions drift in opposite directions. This implies that only one species of particles can be resonant with a given wave. Recently, we have investigated the physical processes underlying the wave-particle resonance due to a VB drift ($\omega \sim k \cdot \underline{V}_{VB}$).^{6,7} In this paper we complete our study of magnetic drift resonances by focussing on curvature drift resonances ($\omega \sim k \cdot \underline{V}_C$). Of course, both drifts exist in many plasmas of interest but we will ignore the VB drift for pedagogical purposes.

The curvature drift can be viewed as arising from the centrifugal force acting on the particle in its rest frame.⁸ This is shown in Fig. 1. Here, $\underline{B} = B_x(z) \hat{e}_x + B_z \hat{e}_z$, F_{cp} is the centripetal force acting on the particle as it follows the curved field line and $F_{cf} = -F_{cp}$ is the centrifugal force felt by the particle in its rest frame. We restrict our attention to the xy plane and take

$$\underline{F}_{cp} = \frac{mv_{\parallel}^2}{R_c} \hat{e}_x = -\underline{F}_{cf} \quad (4)$$

where R_c is the radius of curvature of the field at the origin. The curvature drift can then be written as

$$\underline{V}_C = \frac{1}{m\Omega} \frac{\underline{F}_{cf} \times \underline{B}}{B} = \frac{v_{\parallel}^2}{R_c \Omega} \hat{e}_y \quad (5)$$

so that ions (+e) drift in the +y-direction and electrons (-e) drift in the -y-direction as shown in Fig. 1. From Eq. (5) it is clear that a wave travelling in the +y-direction can be in phase with ions if $\omega \sim k_y v_{\parallel r}^2 / R_c \Omega$ where $v_{\parallel r}$ is the parallel velocity necessary for resonance. Also, since V_c depends upon v_{\parallel}^2 , both $+v_{\parallel r}$ and $-v_{\parallel r}$ particles can be in resonance.

We point out that in some previous treatments of the curvature drift, the centrifugal force F_{cf} is replaced by a gravitational force such that $\underline{g} = -2T/mR_c \hat{e}_x$ (again, we restrict our attention to the xy plane).^{9,10} The curvature drift then becomes $\underline{V}_c = \underline{g}/\Omega \hat{e}_y$. For this representation of V_c , wave-particle resonances cannot occur and only the non-resonant behavior of the particles due to V_c is considered. That is, all of the particles are drifting at V_c . Thus, by simply considering $\underline{V}_c = \underline{g}/\Omega \hat{e}_y$, potentially important wave-particle resonances are neglected.

The purpose of this paper is to discuss the physical mechanism of wave-particle resonances in a curved magnetic field. The scheme of the paper is as follows. In the next section we present a discussion of the energy exchange process that occurs in this type of resonance. In Section III we present a derivation of the damping/growth rate due to this resonance based upon the physical arguments set forth in Section II. In the final section we discuss an application of this work to the lower-hybrid-drift instability and nonlinear effects.

II. PHYSICAL DESCRIPTION OF THE WAVE-PARTICLE RESONANCE

To elucidate the energy exchange mechanism of wave-particle resonances in a curved magnetic field we consider the following simplified model. A slab geometry is used with

$\vec{B} = B_x(z) \hat{e}_x + B_z \hat{e}_z$ as shown in Fig. 1. The plasma is assumed to be homogeneous. An electrostatic wave is imposed on the system such that $\vec{E} = \delta E \sin(ky - \omega t) \hat{e}_y$ with $\omega \ll \Omega$ and $kr_L \ll 1$ where Ω is the cyclotron frequency and r_L is the mean particle Larmor radius. For this wave, which is propagating in the +y-direction (see Fig. 2), only the positively charged species can resonate with it so we limit our discussion to the ions. Resonant ions satisfy the phase matching condition

$$v_{ph} = \frac{\omega}{k} = v_c^r = \frac{v_{||}^2}{R_c \Omega} \quad (6)$$

where v_c^r is the curvature drift, $v_{||r}$ is the parallel velocity of the particle in resonance and R_c is the local radius of curvature of the field. Note that in Fig. 2 we have translated our coordinate system to the wave frame.

Resonant particles at $y = y_1$ see a constant electric field $\vec{E} = \delta E \hat{e}_y$ and $\vec{E} \times \vec{B}$ drift in the +x-direction with a velocity $\delta v_{\perp} = c\delta E/B$. Since these particles are moving in the same direction as the centripetal force, the centripetal force is doing work on the particles and therefore is increasing their parallel energy. Thus, these particles absorb energy from the wave and cause damping. Alternatively, the increase in the particle's parallel energy can be obtained from conservation of angular momentum, $L = v_{||}R = \text{const.}$ As the particles move in the +x-direction, the radius of rotation decreases so that $v_{||}$ increases to conserve L .

On the other hand, resonant particles at $y = y_2$ see a constant electric field $\vec{E} = -\delta E \hat{e}_y$ and $\vec{E} \times \vec{B}$ drift in the -x-direction with a velocity $\delta v_{\perp} = c\delta E/B$. Since these particles are moving opposite to the centripetal force, they must expend energy to overcome this force and hence, decrease their parallel

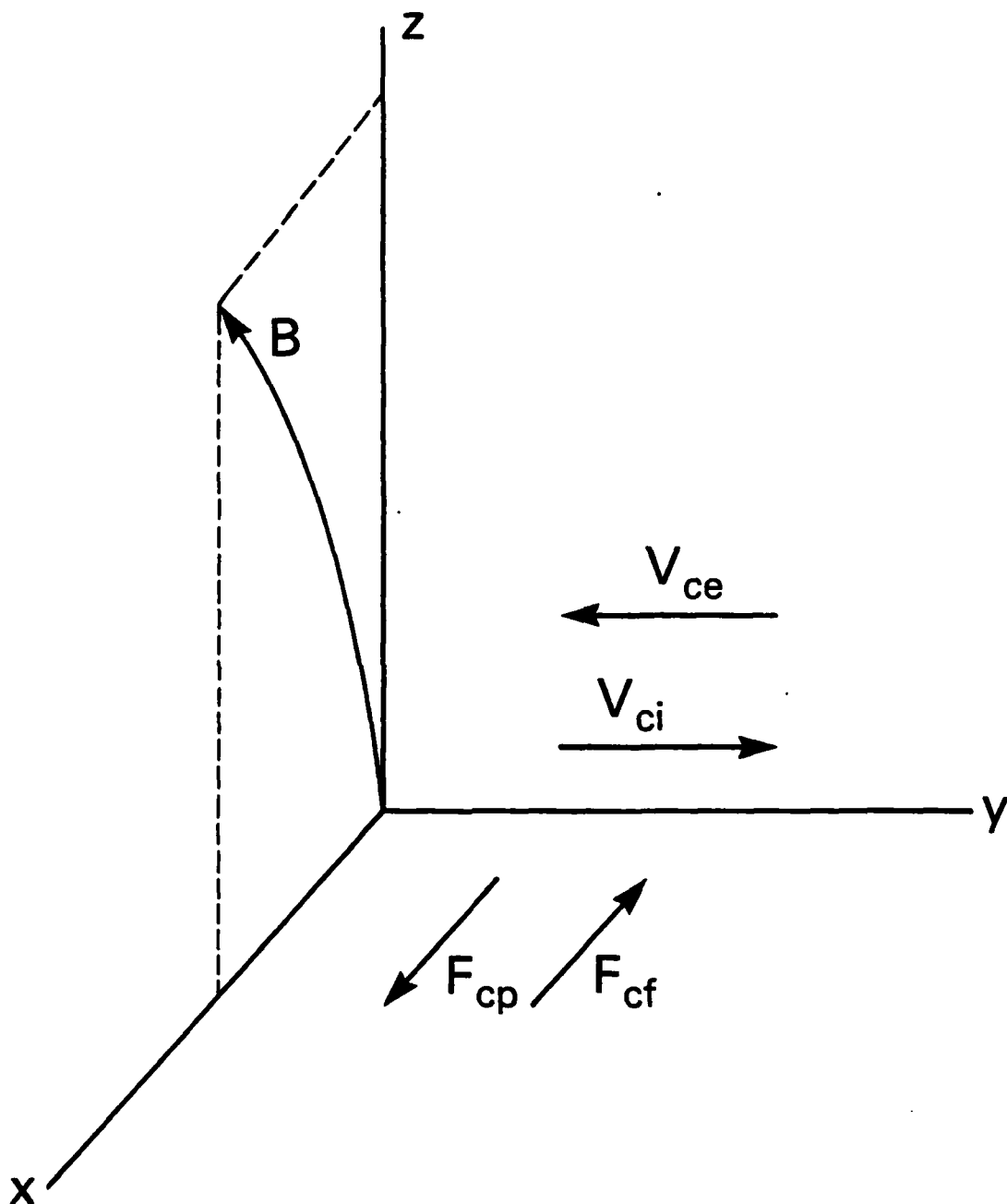


Fig. 1 — Slab geometry used in the analysis with $\underline{B} = B_x \hat{e}_x + B_z \hat{e}_z$. Here, F_{cp} is the centripetal force, F_{cf} is the centrifugal force and $V_{c\alpha}$ is the curvature drift of species α .

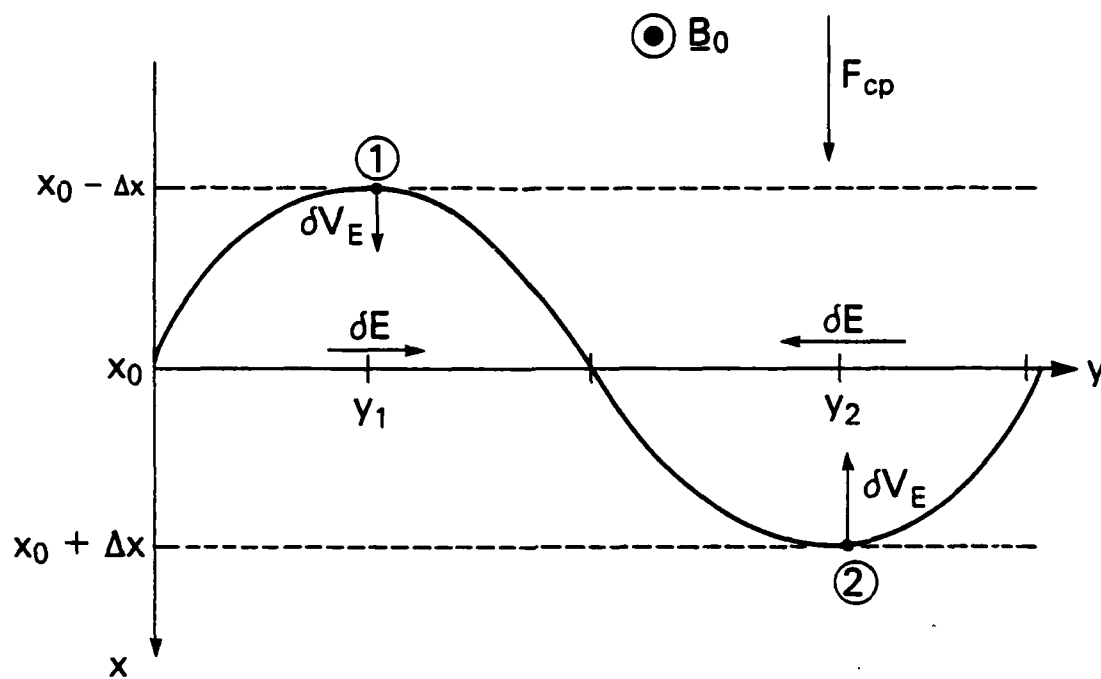


Fig. 2 — Electrostatic wave in a plasma containing a curved magnetic field (wave frame)

energy. Thus, these particles lose energy to the wave and cause wave growth. Again, this can be seen from conservation of L . As particles move in the $-x$ -direction, the radius of rotation increases so that v_{\parallel} decreases to conserve L .

Clearly, if there are an equal number of particles at position (1) and (2), then there is no net energy exchange between the wave and the resonant particles. However, this is not the situation in general as we now show. The key point is that the number of resonant particles is locally proportional to $f(v_{\parallel}, x)$, the particle distribution function. As in the case of Landau damping, unequal numbers of particles participate in energy gain/loss transfer to the wave if $\partial f / \partial v_{\parallel} \neq 0$ (or, in this case also $\partial f / \partial x \neq 0$). We now expand upon this point.

We consider resonant particles ($v_{\parallel} = v_{\parallel r}$) at $x = x_0$ and at some time $t_0 + \Delta t$, i.e., $f(x_0, v_{\parallel r}, t_0 + \Delta t)$. We ask the question, where were these particles at an earlier time $t = t_0$? A portion of these particles were at position (1) ($x = x_0 - \Delta x$, $y = y_1$) with a velocity $v_{\parallel} = v_{\parallel r} - \Delta v_{\parallel}$. In a time Δt , these particles move a distance Δx and increase their velocity by Δv_{\parallel} to arrive at $x = x_0$ and $v_{\parallel} = v_{\parallel r}$. Thus, these particles are described by $f(x_0 - \Delta x, v_{\parallel r} - \Delta v_{\parallel}, t_0)$ and absorb energy from the wave, i.e., lead to damping. The rest of the particles were at position (2) ($x = x_0 + \Delta x$, $y = y_2$) with a velocity $v_{\parallel} = v_{\parallel r} + \Delta v_{\parallel}$. In a time Δt these particles also move a distance Δx but decrease their velocity by Δv_{\parallel} to arrive at $x = x_0$ and $v_{\parallel} = v_{\parallel r}$. Thus, these particles are described by $f(x_0 + \Delta x, v_{\parallel r} + \Delta v_{\parallel}, t_0)$ and give energy to the wave, i.e., lead to growth. Thus, if

$f(x_0 - \Delta x, v_{\parallel r} - \Delta v_{\parallel}, t_0) > f(x_0 + \Delta x, v_{\parallel r} + \Delta v_{\parallel}, t_0)$ then more particles absorb energy from the wave than give energy to the wave and wave damping results. Neglecting any spatial dependence on f , i.e., no density or temperature gradients, this means that $\partial f / \partial v_{\parallel} < 0$ for wave damping, as in the Landau resonance. Alternatively, if $\partial f / \partial v_{\parallel} > 0$ then wave growth can result. Finally, we note that resonance particles exist at both $v_{\parallel} = v_{\parallel r}$ and $v_{\parallel} = -v_{\parallel r}$ since $v_c^r = v_{\parallel}^2$. For symmetric particle

distribution functions in v_{\parallel} this introduces a factor of 2 in the damping/growth rate (see Fig. 3).

Thus, energy transfer can occur in wave-particle resonances due to magnetic field curvature drifts because the wave electric field cause particles to $E \times B$ drift in the same direction or opposite to the centripetal force acting on the particle as it moves along the curved field line. Alternatively, the energy transfer mechanism can be viewed as conservation of angular momentum, $L = v_{\parallel} R$. We now derive a specific expression for the damping/growth rate due to a magnetic curvature drift-wave resonance based on this physical picture.

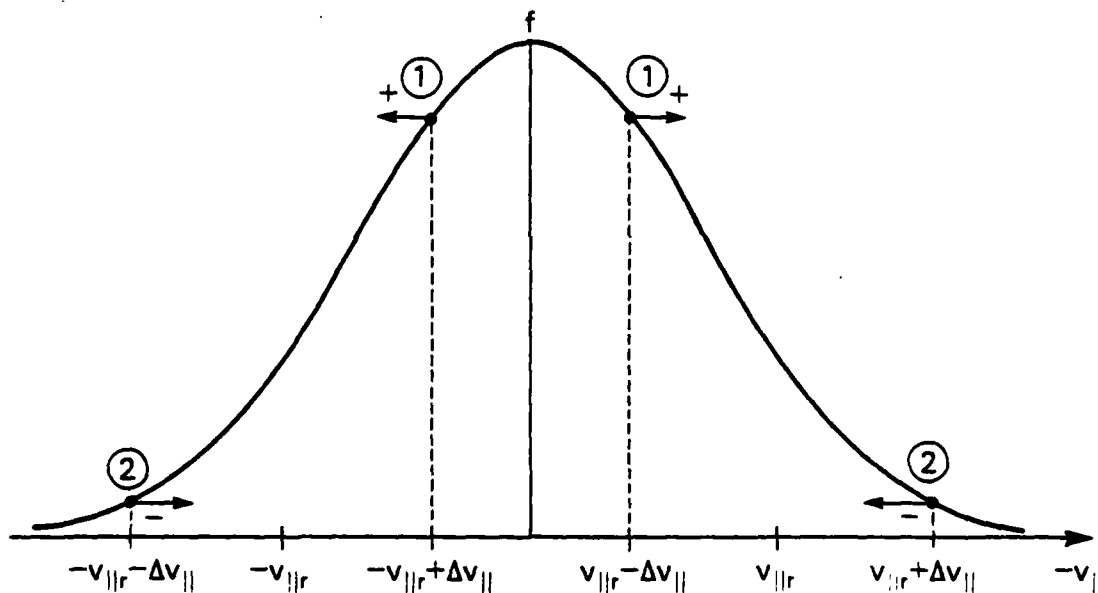


Fig. 3 — Particle distribution function indicating resonant parallel velocities. Here, $v_{\parallel} = v_{\parallel r} - \Delta v_{\parallel}$ and $v_{\parallel} = -v_{\parallel r} + \Delta v_{\parallel}$ are the resonant velocities at position (1), and $v_{\parallel} = v_{\parallel r} + \Delta v_{\parallel}$ and $v_{\parallel} = -v_{\parallel r} - \Delta v_{\parallel}$ are the resonant velocities at position (2). The + signs indicate that particles at position (1) gain energy, while the - signs at position (2) indicate that the particles lose energy.

III. PHYSICAL DERIVATION OF THE WAVE DAMPING/GROWTH RATE

We calculate the damping/growth of the wave due to the particle curvature drift resonance using energy conservation. Total energy conservation can be expressed as

$$\dot{\Sigma}_p + \dot{\Sigma}_w = 0 \quad (7)$$

where Σ_p and Σ_w are the particle and wave energy density, respectively, and the dot indicates a time differentiation. The wave energy density contains both the electrostatic field energy and the sloshing energy of the particles. Our method is similar to that of Meade,¹¹ who calculated the growth rate of the universal drift instability.

The wave energy density of an electrostatic wave in a lossless medium is given by

$$\Sigma_w = \frac{|\delta E|^2}{8\pi} [\omega \partial D / \partial \omega] \quad (8)$$

where D is the dielectric function. Assuming that the perturbed field varies as $\exp(i\omega t)$ where $\omega = \omega_r + i\gamma$ we obtain

$$\dot{\Sigma}_w = \gamma \frac{|\delta E|^2}{4\pi} [\omega \partial D / \partial \omega] \quad (9)$$

The change in energy of a single particle is given by

$$\Delta W_p = \vec{F} \cdot \Delta \vec{x} = F_x \Delta x \quad (10)$$

where $F_x = mv_{\parallel r}^2 / R_c$ is the centripetal force acting on the particle locally at $(x, z) = (0, 0)$. We then obtain

$$\Delta W_p = \frac{mv_{\parallel r}^2}{R_c} \Delta x \quad (11)$$

Since the particle velocity is $\delta \vec{v}_E = c\delta E / B \hat{e}_x$ we find that

$$\Delta W_p = \frac{mv_{\parallel}^2}{R_c} \frac{c\delta E}{B} \Delta t \quad (12)$$

or

$$\dot{W}_p = \frac{mv_{\parallel r}^2}{R_c} \frac{c\delta E}{R} \quad (13)$$

Noting that $v_c^r = v_{\parallel r}^2 / R_c \Omega$, we rewrite Eq. (13) as

$$\dot{W}_p = e \delta E v_c^r \quad (= j \cdot E / n) \quad (14)$$

so that the time rate of change of a single particle's energy is related to its Joule heating since $j = enV_c$ for the curvature drift particles. From Eq. (14) we point out that for $\delta E > 0$ the particle gains energy while for $\delta E < 0$ it loses energy.

The time rate of change of the total particle energy density $\dot{\bar{E}}_p$ is found by calculating the change of energy of all the resonant particles in a time Δt . We integrate the equilibrium distribution function over the range $v_{\parallel r} - \Delta v_{\parallel r}$ to $v_{\parallel r} + \Delta v_{\parallel r}$ where $\Delta v_{\parallel r}$ is the spread in v_{\parallel} for a particle to remain in resonance with the wave. Making use of Eq. (14) we find that

$$\begin{aligned} \dot{\bar{E}}_p = \frac{1}{2} e \delta E v_c^r \left([f(v_{\parallel r} - \Delta v_{\parallel r}, x_0 - \Delta x) - f(v_{\parallel r} + \Delta v_{\parallel r}, x_0 + \Delta x)] \right. \\ \left. + [f(-v_{\parallel r} + \Delta v_{\parallel r}, x_0 - \Delta x) - f(-v_{\parallel r} - \Delta v_{\parallel r}, x_0 + \Delta x)] \right) \Delta v_{\parallel r} \quad (15) \end{aligned}$$

where Δv_{\parallel} and Δx represent the change in parallel velocity and position in a time Δt , respectively, and the ϕ and v_{\perp} integrations have been performed. In Eq. (15) we only consider a density inhomogeneity since a temperature inhomogeneity is usually only important for flute modes when $kr_L = 1$ and we are assuming $k^2 r_L^2 \ll 1$.⁹

From Eq. (15) we note that the resonant particles in the first bracket occur at $v_{\parallel} = +v_{\parallel r}$ while those in the second bracket occur at $v_{\parallel} = -v_{\parallel r}$ (see Fig. 3). Moreover, the particles at $(x_0 - \Delta x, v_{\parallel r} - \Delta v_{\parallel})$ and $(x_0 - \Delta x, -v_{\parallel r} + \Delta v_{\parallel})$ increase their

energy (+ sign in Eq. (15)) and particles at $(x_0 + \Delta x, v_{||r} + \Delta v_{||})$ and $(x_0 + \Delta x, -v_{||r} - \Delta v_{||})$ decrease their energy (- sign in Eq. (15)). We can rewrite Eq. (15) as

$$\begin{aligned} \dot{\epsilon}_p = e\delta E V_c^r & \left(\left[-(\Delta v_{||} \frac{\partial f}{\partial v_{||}} + \Delta x \frac{\partial f}{\partial x}) v_{||r, x_0} \right. \right. \\ & \left. \left. + (\Delta v_{||} \frac{\partial f}{\partial v_{||}} - \Delta x \frac{\partial f}{\partial x}) -v_{||r, x_0} \right] \Delta v_{||r} \right) \end{aligned} \quad (16)$$

Assuming f is symmetric in $v_{||}$, i.e.,

$$(\partial f / \partial v_{||})_{v_{||r}} = -(\partial f / \partial v_{||})_{-v_{||r}} \quad (17)$$

we finally obtain

$$\dot{\epsilon}_p = -2e\delta E V_c^r \left[\Delta v_{||} \frac{\partial f}{\partial v_{||}} + \Delta x \frac{\partial f}{\partial x} \right] v_{||r, x_0} \Delta v_{||r} \quad (18)$$

so that the dependence of $\dot{\epsilon}_p$ on the slope of the distribution function is evident.

We now compute Δx , $\Delta v_{||}$ and $\Delta v_{||r}$ as follows. The distance a particle moves in a time Δt is simply $\Delta x = \delta V_p \Delta t = (c\delta E/B)\Delta t$. The change in a particle's parallel energy is found from Eq. (12) and the definition $\Delta W_p = \Delta(mv_{||}^2/2)$. We find that

$$\Delta v_{||} = \frac{v_{||r}}{R_c} \frac{c\delta E}{B} \Delta t. \quad (19)$$

This can also be obtained from the conservation of angular momentum, i.e., $L = v_{||}R = \text{constant}$ and using $\partial R / \partial t = -\delta V_p$. Finally, $\Delta v_{||r}$ is determined by noting that for a particle to remain in resonance with a wave, we require

$$\Delta V_c^r < \frac{\pi}{k\Delta t} \quad (20)$$

That is, particles will only be in resonance ($\omega \sim kv_c^r$) as long as

they do not move more than a half-wavelength in a time Δt . Making use of the definition of v_{cr}^r (Eq. (6)) we find that

$$\Delta v_{cr} = \frac{\pi}{2} \frac{\Omega R_c}{v_{cr} k \Delta t} \quad (21)$$

Substituting Δx , Δv_{cr} and Δv_{cr}^r into Eq. (18), we arrive at

$$\dot{f}_p = - \frac{\pi e^2 \omega^2}{m k^2} \left[\frac{\partial f}{\partial v_{cr}} + \frac{R_c}{v_{cr}} \frac{\partial f}{\partial x} \right] v_{cr} x_0 |\delta E|^2 \quad (22)$$

The damping/growth rate due to the curvature drift resonance is now found from Eqs. (7), (6) and (22). We find that

$$\frac{\gamma_c}{\omega} = \pi \frac{\omega_p^2}{k^2} \left[\frac{\partial f}{\partial v_{cr}} + \frac{R_c}{v_{cr}} \frac{\partial f}{\partial x} \right] v_{cr} x_0 \left[\omega \frac{\partial D}{\partial \omega} \right]^{-1} \quad (23)$$

where $\omega_p^2 = 4\pi n e^2 / m$, $\Omega = eB/mc$ and we have normalized f to $n_0 = n(x=x_0)$. Thus, Eq. (23) is a general expression for the damping/growth rate, γ_c , of an electrostatic wave propagating across a magnetic field due to a wave-particle resonance arising from magnetic field curvature drifting particles. Interestingly, for $\partial f / \partial x = 0$, Eq. (23) is the same as for the Landau resonance except for an additional factor of 2 due to the two resonances at $\pm v_{cr}$.^{13,14}

IV. DISCUSSION

A substantial amount of literature exists on the physics of Landau wave-particle resonances (i.e., $\omega \sim k_{\parallel} v_{\parallel}$),^{12,13} yet there is little discussion of cross-field, wave-particle resonances due to magnetic drifts. The two important cross-field magnetic drifts are the ∇B drift and the magnetic curvature drift. Recently, we have investigated the physics of the wave-particle resonance for ∇B drifting particles.^{6,7} In this paper we focus our attention on the energy exchange between waves and resonant curvature drifting particles ($\omega \sim k_{\parallel} \tilde{v}_c$). The curvature drift can be viewed as arising from the centrifugal force acting on the particle in the particle's rest frame. That is, $\tilde{v}_c = \tilde{F}_{cf} \times \tilde{B}$ where $F_{cf} = -mv_{\parallel}^2/R_c$ and R_c is the radius of curvature of the field line. Curvature drifting particles, resonant with a wave, see a constant electric field which causes them to $E \times B$ drift in the same direction or opposite to the centripetal force acting on them, depending on the phase of the wave. The particle's energy then changes by an amount $\Delta W_p = \Delta(mv_{\parallel}^2/2) = F_{cp} \Delta x$ where $F_{cp} = mv_{\parallel}^2/R_c$ is the centripetal force and $\Delta x = (c\delta E/B)\Delta t$. Depending on the relative number of particles absorbing energy from or giving energy to the wave, which is a function of the slope of the particle distribution function in v_{\parallel} and x space, wave damping or growth can occur. Alternatively, the energy exchange process can be viewed in terms of conservation of angular momentum, $L = v_{\parallel} R = \text{const.}$ The $E \times B$ drift of the resonant particles causes the particles to move to smaller or larger radii of rotation (R) depending on the phase of the wave. Thus, v_{\parallel} increases or decreases accordingly in order to conserve L . A general equation for the damping/growth rate has been derived based upon these physical arguments, Eq.(23). As an application of this theory we now consider the lower-hybrid-drift wave instability.

The dielectric function for the lower-hybrid-drift mode is given by⁴

$$D = \frac{\omega_{pe}^2}{\Omega_e^2} + \frac{2\omega_{pi}^2}{k^2 v_i^2} (1 - kv_{di}/\omega) \quad (24)$$

where $v_{di} = (v_i^2/2\Omega_i) \partial \ln n / \partial x$ and we have assumed $T_e \ll T_i$, $v_{di} \ll v_i$ and $\omega_{pe}^2 \gg \Omega_e^2$ for simplicity. This mode propagates in the direction of the ion diamagnetic drift. In writing Eq. (24) we have ignored the ion Landau resonance to highlight the curvature resonance. Since this instability requires $\gamma > \Omega_i$, the ions behave as unmagnetized particles and cannot participate in the type of resonance discussed in this paper. On the other hand, field line curvature does effect the ion equilibrium drift.¹⁴ We choose the field line curvature to be such that an electron-wave resonance can occur. The electron distribution function is chosen to be

$$f_e = \frac{n(X)}{n_0} (1/\pi v_e^2)^{1/2} \exp(-v_{\parallel}^2/v_e^2) \quad (25)$$

where $v_e^2 = 2T_e/m_e$ and $X = x - v_y/\Omega_e$ is a constant of the motion. Expanding X about x_0 we obtain

$$\frac{\partial f}{\partial v_{\parallel}} = -\frac{2v_{\parallel}}{v_e^2} f \quad ; \quad \frac{\partial f}{\partial x} = \epsilon_n f \quad (26)$$

where $\epsilon_n = \partial \ln n / \partial x$. Using Eqs. (23) and (26), we find that

$$\frac{\gamma_c}{\omega} = -\sqrt{\pi} \frac{T_i}{T_e} (1 - \epsilon_n R_c / 2\zeta^2) \zeta \exp(-\zeta^2) \quad (27)$$

where $\zeta = v_{\parallel r}/v_e = (\omega/kv_{ce})$ and $v_{ce} = v_e^2/R_c \Omega_e$. If we define $R_c = 1/\epsilon_n$ then Eq. (27) is consistent with the results of Rahal and Gary.¹⁵ For the curvature damping to be significant one requires that $\zeta^2 \sim 1$ which places the following condition on R_c . We take $\omega/k \sim v_{di}$ so that we require $v_{di} \sim v_{ce}$ which leads to $R_c \sim 2L_n(T_e/T_i)$ where $L_n = (\partial \ln n / \partial x)^{-1} = 1/\epsilon_n$. Thus, the radius of curvature of the magnetic field lines has to be comparable to the scale length of the density gradient for the electron curvature drift-wave resonance to be a significant damping mechanism for the lower-hybrid-drift wave instability. It should be noted that this electron-wave resonance always leads

to damping. For the geometry shown in Fig. 1, we require $\epsilon_n < 0$ for an electron-wave resonance to occur because $\tilde{v}_{di} = -v_{di} e_y$; from Eq. (27) it is clear that $\epsilon_n < 0$ leads to damping. On the other hand, if $\epsilon_n > 0$, (which could conceivably lead to $\gamma_c > 0$), no resonance can occur because then the wave and drifting electrons are not moving in the same direction. In fact, this is the situation considered by Rahal and Gary¹⁵ so that they did not find any resonance damping.

Finally, we note that this resonance may lead to spatial trapping of particles as in the case of the VB drift-wave resonance. That is, as particles drift in the x-direction they eventually lose resonance with the wave; they either drift faster or slower than the wave. This can arise because $v_{||}$ changes, or because R_c and Ω are functions of x . The particles then "circle around" and become resonant with the wave in its opposite phase. Thus, they drift in the opposite direction and become trapped. However, it is unclear that such a process can occur since it requires $\tau_{tr} \ll \tau_b$, where τ_{tr} is the spatial trapping period and τ_b is the bounce period in a curved field (e.g., mirroring period), which is probably difficult to satisfy in most plasmas of interest.

ACKNOWLEDGMENTS

We thank an anonymous referee from a previous paper for calling our attention to the curvature drift resonance. One of us (JDH) thanks S.P. Gary and K.R. Chu for some helpful discussions. This research has been supported by the Office of Naval Research.

REFERENCES

1. L.D. Landau, J. Phys. U.S.S.R. 10, 25 (1946).
2. T.H. Stix, Phys. Rev. Lett. 15, 878 (1965).
3. J.M. Dawson, H.C. Kim, D. Arnush, B.D. Fried, R.W. Gould, L.O. Hellinger, C.F. Kennel, P.E. Romesser, R.C. Stenzel, A.Y. Wong and R.F. Wuerker, Phys. Rev. Lett. 37, 1547 (1976)
4. R.C. Davidson and N.A. Krall, Nucl. Fusion 17, 1313 (1977).
5. N. Krall and A. Trivelpiece, Principles of Plasma Physics (McGraw-Hill, New York, 1973) p. 624.
6. J.D. Huba and J.F. Drake, in press, Phys. Fluids (1981).
7. J.F. Drake and J.D. Huba, submitted to Phys. Fluids (1981).
8. L. Spitzer, Physics of Fully Ionized Gases (Interscience, New York, 1967) p. 7.
9. N.A. Krall, in Advances in Plasma Physics, edited by A. Simon and W.B. Thompson (John Wiley, New York, 1968) Vol. 1, p. 153.
10. A.B. Mikhailovskii, in Reviews of Plasma Physics; Vol. 3 (Consultants Bureau, New York, 1969) p.159.
11. D.M. Meade, Phys. Fluids 12, 947 (1969).
12. D. Montgomery and D. Tidman, Plasma Kinetic Theory (McGraw-Hill, New York, 1964) p. 265.
13. T.H. Stix, The Theory of Plasma Waves, (McGraw-Hill, New York, 1962) p. 48.
14. N.A. Krall and J.B. McBride, Phys. Fluids 19, 1970 (1976).
15. L.J. Rahal and S.P. Gary, Phys. Fluids 24, 1588 (1981).

Append. E

VLASOV SIMULATION OF PLASMA DOUBLE LAYERS

Robert A. Smith
Science Applications, Inc.
1710 Goodridge Drive
McLean, Virginia 22102

ABSTRACT

Evolution of electrostatic plasma double layers is simulated in a 1-D Vlasov model with novel boundary conditions, in which the double layer forms part of an RL circuit. The double layer develops from the nonlinear stage of a convective, current-driven instability. Its evolution is characterized by strong trapping of both ions and electrons; ion heating appears to play a prominent role in the intermediate stages of development. Results are discussed for two cases: (i) $L \rightarrow \infty$ (constant-current); and (ii) L/R = the ion transit time.

Electrostatic double layers are of interest both in laboratory¹⁻³ and space⁴⁻⁶ plasmas. The steady-state double layer has been studied in fluid^{5,7} and BGK⁸ analyses, and its formation investigated in numerical simulations.^{9-11,15} In this Letter we present preliminary results of a new type of simulation. A fuller description and analysis will be published elsewhere.

The simulation described here is unique in that it treats the double layer as a nonlinear element in a self-consistent model circuit,¹⁶ shown in Fig. 1. The simulation region is a 1-D plasma column $0 \leq x \leq l$ of arbitrary cross-section A. The column is connected in series by imagined grids at $x = 0, l$ to a potential source Φ , a resistance R, and an inductance L. We denote the potential and current density in the column by $\phi(x,t)$ and $J(x,t)$, respectively; by convention $\phi(0,t) = 0$, and we denote $\phi_{DL}(t) = \phi(l,t)$. Assuming the circuit to have been closed at $t \rightarrow -\infty$, the circuit current $I_0(t)$ is given by

$$I_0(\tau) = R^{-1} \left[-\Phi + \int_0^\theta d\theta' \phi_{DL}(\theta') \exp(\theta' - \theta) \right], \quad (1)$$

where $\theta \equiv t/\tau$, $\tau \equiv L/R$, $\Phi > 0$, and $\phi_{DL}(t \leq 0) = 0$.

Simultaneously with Eq. (1), the plasma column is described by

$$\left(\frac{\partial}{\partial t} + v \frac{\partial}{\partial x} + \frac{q_j}{m_j} E \frac{\partial}{\partial v} \right) f_j(x, v, t) = 0, \quad (2)$$

$$\partial E(x, t) / \partial x = 4\pi \sum_j q_j \int_{-\infty}^{\infty} f_j dv,$$

where $E = -\partial\phi/\partial x$. Equation (2) is solved with a flux-corrected transport algorithm¹² originally employed by Rowland¹³ and modified here to allow for open boundaries.

The boundary condition

$$J(0, t) = J(\ell, t) = J_0(t), \quad (3)$$

where $J_0 \equiv I_0/A$, ensures that the plasma column remains neutral overall, so that $E(0, t) = E(\ell, t) = 0$. To satisfy Eq. (3), the current density at the boundaries must in general contain a component δJ injected from external "source" plasmas. Thus

$$J(0, t) = J_{<}(0, t) + \delta J_{>}(0, t), \quad (4)$$

$$J(\ell, t) = J_{>}(\ell, t) + \delta J_{<}(\ell, t),$$

where subscripts ">", "<" indicate moments over $v > 0$ and $v < 0$, respectively. Equations (4) are implemented by defining source distributions

$$f_j^s(v) = (2\pi v_j^2)^{-1/2} \exp \left[-(v - U_j)^2 / 2v_j^2 \right]. \quad (5)$$

The components $J_<(0,t)$ and $J_>(\ell,t)$ are assumed to contribute totally to the boundary current $J_0(t)$, and the distributions composing $J_<, J_>$ are assumed not to affect the source distributions. Then at each time step, $\delta J_<$ and $\delta J_>$ are injected by transporting across each boundary distributions

$$f_j^{\text{inj}}(0,t) = \alpha(0,t) f_j^S(v), \quad f_j^{\text{inj}}(\ell,t) = \alpha(\ell,t) f_j^S(v),$$

where the α 's are chosen such that Eq. (4) is satisfied. This implementation is not unique until a prescription is given for the U_j in Eq. (5). In the simulations discussed in this Letter, $U_{e,i}$ are held fixed at their initial values.

In what follows, time and length scales are respectively normalized to the electron plasma period ω_{e0}^{-1} and Debye lengths λ_{e0} in the initial plasma: $t \rightarrow \omega_{e0} t$, $x \rightarrow x/\lambda_{e0}$. Potentials are in terms of T_e/e , and $R \rightarrow R A e^2 / m_e v_e$.

We shall describe two cases, differing essentially in the inductance time constant τ . For both cases, we have $m_i = 16 m_e$, $T_i = T_e$, $U_e = 2V_e$, and $U_i = -2V_i = -0.5V_e$; $U_{e,i}$ are chosen to satisfy the Langmuir criterion⁵ $U_i/U_e = (m_e/m_i)^{1/2}$ and the Bohm criteria^{5,11}

$$U_e \gtrsim (3 + T_i/T_e)^{1/2} V_e, \quad U_i \gtrsim (3V_i^2 + T_e/m_i)^{1/2}. \quad (6)$$

The applied potential $\phi = 20$, and $J_0(0) = -0.5$. Parameters differing between the two cases are:

	Case I	Case II
Spatial resolution $\Delta x/\lambda_{eo}$	0.68	0.90
Temporal resolution $\omega_{eo}\Delta$	0.02	0.05
System length ℓ/λ_{eo}	21	57
Induction time $\omega_{eo}\tau$	10^5	90

Case I, for which τ is much longer than the evolution time of the double layer, corresponds to a constant-current boundary condition. In Case II, τ is the time for an ion to traverse the system at speed U_i .

We now describe briefly the salient features of the double-layer evolution. A fuller description, including supporting spectral data and extensive phase-space histories, will be published elsewhere.

We earlier proposed⁶ that, compatibly with the Bohm criterion (6), double layers would evolve in the presence of a current-driven instability. We trigger such instability by superimposing neutral, random-phase, white-noise density fluctuations on the initial plasma and in the injected current. The two-stream instability develops for a set of wave modes near the wavenumber for peak growth in linear theory [14], with dispersion in the finite system modified by the condition $E(0,t) \neq E(\ell,t) = 0$. The waves appear aperiodic or nearly so, with their envelope growing spatially in the direction of electron drift.

Initially, there are four to five principle wavelengths in the system. After the convective growth of the envelope is completed, the potential wells begin to coalesce, apparently due to nonlinear trapping effects (electrons being trapped first). The spatially oscillating wave potential becomes rectified by a DC electric field component, which grows to dominate the k-spectrum as the potential wells coalesce and the potential profile develops a scale length longer than the linearly unstable wavelengths. The electron trapping causes local current interruption; this leaves increased ion concentration at the high-potential end, which is accentuated by rarefaction of accelerated electrons. Eventually the ions too become trapped at the potential crest(s); the evolution of the double layer is dominated by the strong heating of trapped ions (see the discussion below).

Energy balance for the entire circuit is described by the dimensional equation

$$\begin{aligned} \frac{\partial}{\partial t} \left(A W_E + A \int_0^L dx \sum_j \frac{m_j}{2} \int dv v^2 f_j + \frac{1}{2} L I_0^2 \right) = \\ = |I_0| \phi - I_0^2 R - A P_J + \sum_j \frac{m_j}{2} \oint ds \int dv v^3 f_j, \end{aligned} \quad (7)$$

where $W_E \equiv \int_0^L dx E^2/4\pi$ and $P_J \equiv \int_0^L dx E(J-J_0)$. The simulations conserve total energy according to Eq. (7) to within one part in 10^4 , an advantage of the self-consistent circuit formulation.

Analysis shows $\partial W_E / \partial t \sim -P_J$; note that P_J is the dissipation of the interrupted current, $J-J_0$. We note here an intriguing result; P_J tracks in detail the evolution of ϕ_{DL} itself. In Figures 2 and 3, we plot $\phi_{DL}(t)$ and $W_J(t) = \int_{t-\Delta T}^t P_J dt$, where ΔT is the interval between the plotted points. Fluctuations in W_J are reflected in detail (with a slight time lag) in the slope of $\phi_{DL}(t)$.

In Case I (Fig. 2), ϕ_{DL} rises rapidly and monotonically to a final value of 43.4. Because the external potential source ϕ and the essentially infinite inductance L combine to produce (on the evolutionary time scale) a current source, this value of ϕ_{DL} is related not to ϕ but is instead determined by the scaling law (8) given below.

In Case II (Fig. 3), the evolution is marked by inductive overshoots and recoveries, finally stabilizing at $\phi_{DL} = 19.2 < \phi$. In Fig. 3b, we see rapid relaxation oscillations in W_J accompanying the overshoots; note that these occur not on the time scale τ but over only a few ion plasma periods. In Fig. 4, we show the field profiles and phase spaces at $t = 85, 100$, and 125 , which are labelled a, b, and c in Fig. 3b. At $t = 85$ (Fig. 4a) we see two distinct vortices in the ion phase space beginning to mix strongly, accompanied by large gradients in the electric field. At $t = 100$ (Fig. 4b) the vortex interaction is nearly complete; the electric field profile is smoothed somewhat and one of its reversals in Fig. 4a has nearly vanished. At $t = 125$, we

see a jet of energetic ions accelerated to the right, forming a beam on the tail of the ion distribution. Such ion heating and acceleration during a double-layer disruption (similar to the undershoot seen here) has been reported experimentally.³

As the turbulently mixed ions are accelerated out of the system, the double layers approach an asymptotic state characterized by laminar distributions. This state is stable in the sense that no further evolution is seen to occur, over a time scale comparable to that of significant development in the transient evolution. In both Cases I and II, the saturated potential ϕ_{DL} and length scale $\ell_* \equiv \phi_{DL}/\max|E|$ are related by a scaling law

$$\phi_{DL} = 0.165 \ell_*^2 / \lambda_{e*}^2, \quad (8)$$

where λ_{e*} is the upstream Debye length. The form of this scaling is easily found by dimensional analysis. The coefficient is not well understood; other authors find 0.17 (Ref. 9) and 0.04 (Ref. 11).

In a future publication, we shall discuss these and other results in fuller detail. Points currently being investigated include an expanded range of initial drift conditions and different implementation of the boundary

conditions, as well as detailed analysis of the oscillation spectrum. In addition, we hope to develop a model of the double layer as a nonlinear plasma capacitor.

I am grateful to S.L. Ossakow and P.J. Palmadesso for numerous discussions and for their continued interest in this work. I have also benefitted from conversations with C. K. Goertz, G. R. Joyce, J. A. Fedder, A. T. Drobot, N. Hershkowitz, and C. L. Grabbe. I owe many thanks to S. J. Marsh, S. T. Zalesak, W. B. Miner, and H. L. Rowland for dicussions on numerics. This work was supported by and performed at the Naval Research Laboratory, under Contract N00174-81-C-2038.

REFERENCES

1. S. Torvén, in Wave Instabilities in Space Plasmas (P.J. Palmadesso and K. Papadopoulos, eds), Reidel, 109 (1979); F.W. Crawford, J.S. Levine, and D. B. Ilić ibid. 129; B.H. Quon and A.Y. Wong, Phys. Rev. Lett. 37, 1393 (1976); P. Leung, A.Y. Wong, and B.H. Quon, Phys. Fluids 23, 992 (1980); K.D. Baker, L.P. Block, R. Kist, W. Kampa, N. Singh, and H. Thiemann, to be published.
2. P. Coakley and N. Hershkowitz, Phys. Fluids 22, 1171 (1978).
3. K. Saeki, S. Iizuka, and N. Sato, Phys. Rev. Lett. 45, 1853 (1980).
4. H. Alfvén, J. Physique 40, C7-1 (1979); P. Carlqvist, Solar Phys. 7, 377 (1969).
5. L. P. Block, Cosmic Electrodyn. 3, 349 (1972).
6. R. A. Smith and C. K. Goertz, J. Geophys. Res. 83, 2617 (1978).
7. J. S. Levine and F. W. Crawford, J. Plasma Phys. 23, 223 (1980).
8. G. Knorr and C. K. Goertz, Astrophys. Space Sci. 31, 209 (1974); D. W. Swift, J. Geophys. Res. 81, 3935 (1976); D. W. Swift, J. Geophys. Res. 84, 6427 (1979).
9. C. K. Goertz and G. Joyce, Astrophys. Space Sci. 32, 165 (1975).

10. G. Joyce and R. F. Hubbard, J. Plasma Phys. 20, 391, (1978); J. S. deGroot, C. Barnes, A. E. Walstead, and O. Buneman, Phys. Rev. Lett. 38, 1283 (1977).
11. N. Singh, Plasma Phys. 22, 1 (1980).
12. J. P. Boris and D. L. Book, Methods of Computational Physics 16, 85 (1976).
13. H. L. Rowland, Phys. Fluids 23, 508 (1980).
14. O. Buneman, Phys. Rev. 115, 503 (1959).
15. T. Sato and H. Okuda, Phys. Rev. Lett. 44, 740 (1980).
16. Reference 15 also employs the idea of an external circuit, but does not include inductive effects. Moreover, Ref. 15 employs periodic boundary conditions for current continuity, which is inconsistent with the circuit itself.

FIGURE LEGENDS

- Fig. 1 Schematic of the circuit model.
- Fig. 2 Time histories of (a) double-layer potential and (b) dissipation of interrupted current, for Case I. $J_0 = -0.5 = \text{constant}$.
- Fig. 3 Same as Fig. 2, for Case II. Also shown in (a) is $J_0(t)$. Details of system at A, B, C are shown in Fig. 4.
- Fig. 4 Field profiles and x-v phase spaces for Case II at (a) $t = 85$, (b) $t = 100$, (c) $t = 125$, showing an inductive overshoot. Contours are of the logarithm of $f_j(x,v)$.

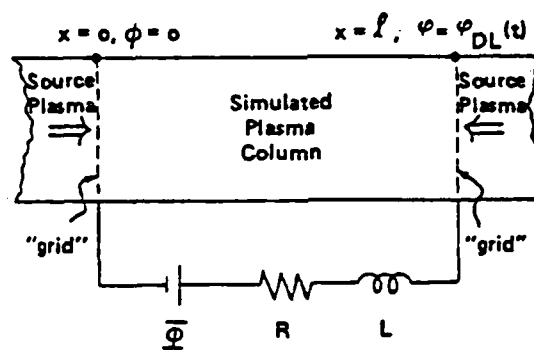


Figure 1

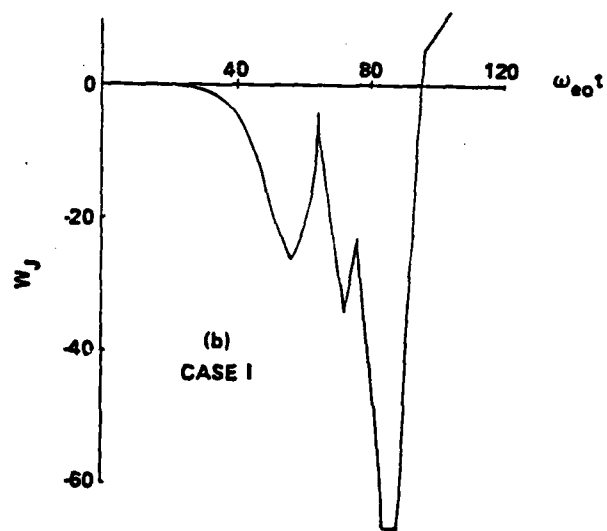
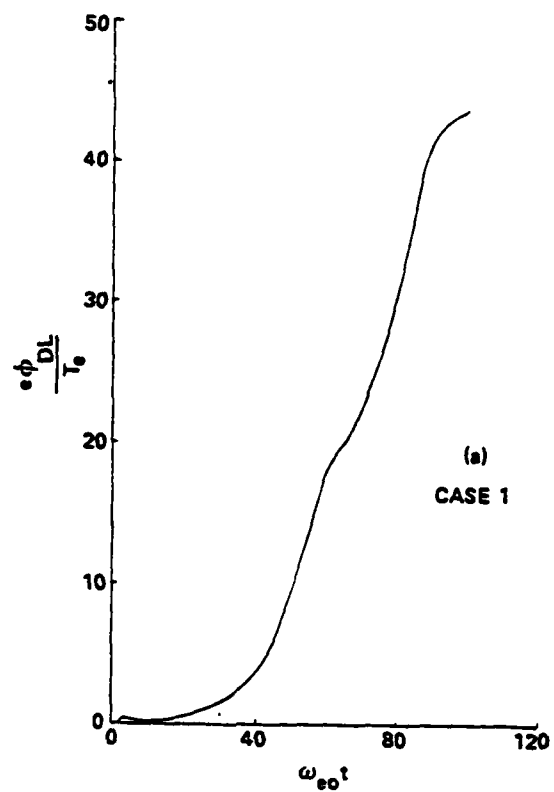


Figure 2

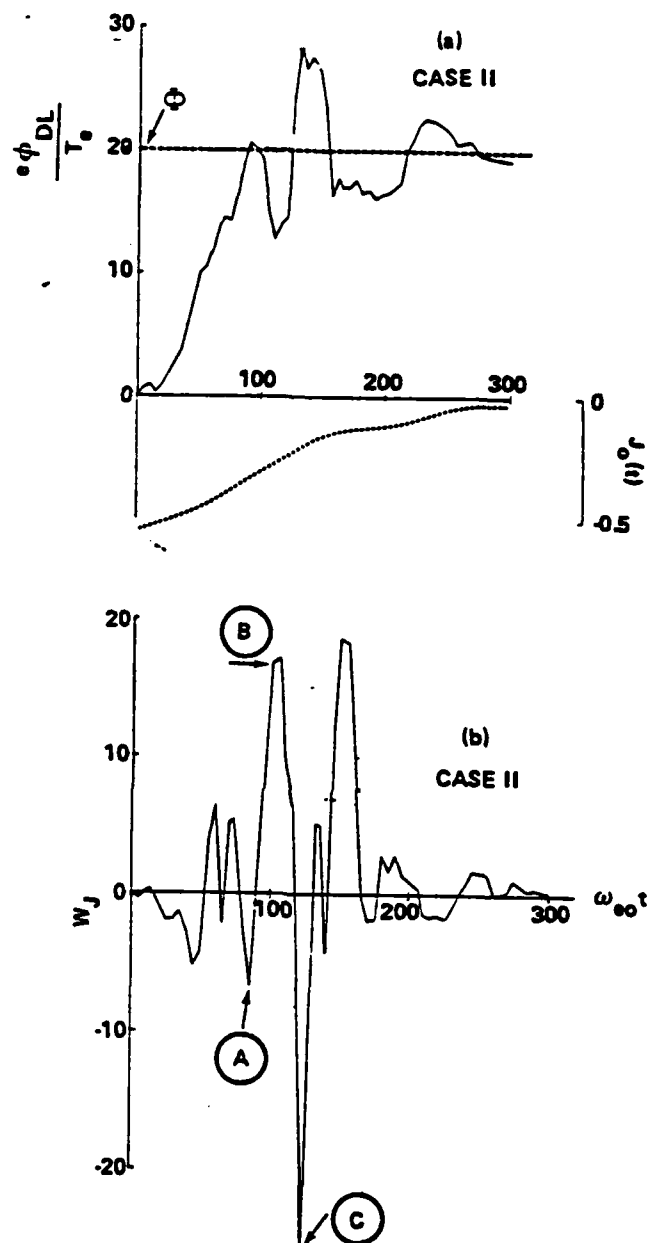


Figure 3

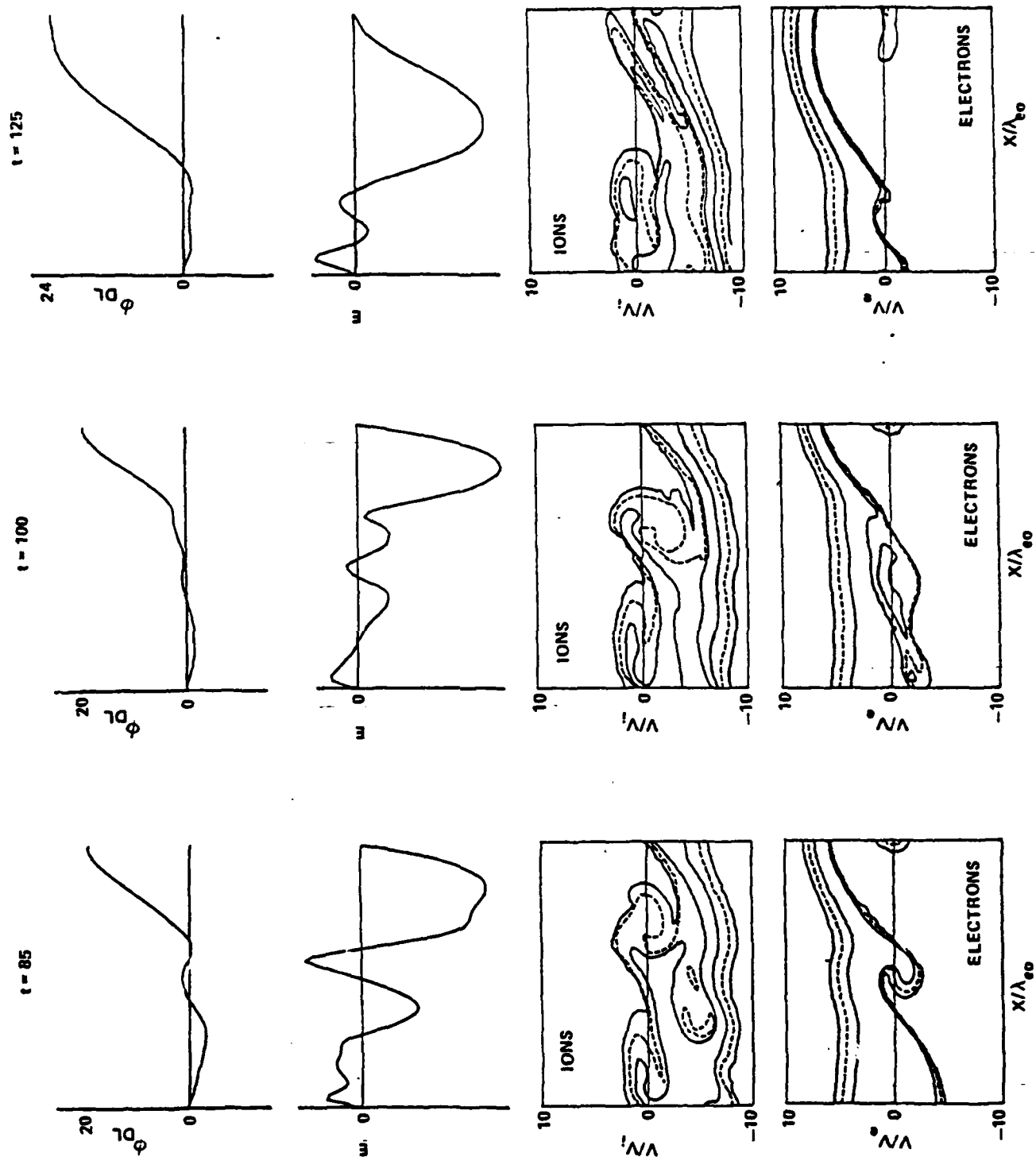


Figure 4

Appendix F

ONE-DIMENSIONAL DIRECT CURRENT RESISTIVITY
DUE TO STRONG TURBULENCE

One-dimensional direct current resistivity due to strong turbulence

H. L. Rowland, P. J. Palmadesso, and K. Papadopoulos

Naval Research Laboratory, Washington, D.C. 20375 and Department of Physics and Astronomy, University of Maryland, College Park, Maryland 20740

(Received 11 August 1980; accepted 29 January 1981)

Strong Langmuir turbulence acts to generate localized spiky fields and ion cavities. It is shown that these cavities generate potential barriers that can trap a significant fraction of the electrons. For example, a 20% cavity traps 50% of the electrons. This can seriously change the direct current properties of a collisionless plasma and lead to the appearance of anomalous dc resistivity.

I. INTRODUCTION

The problem of anomalous plasma dc resistivity in one dimension is one of the oldest basic plasma physics questions. Its resolution has eluded the plasma community despite intensive theoretical and experimental efforts.^{1,2} Besides its fundamental nature, the question of anomalous resistivity is of utmost practical importance for laboratory plasma heating and for energy dissipation and particle acceleration in space plasmas.³ In weak turbulence models, the presence of a field aligned electron current in the plasma with a drift velocity v_d , higher than a threshold, excites density fluctuations which then scatter the electrons with a collision frequency ν^* larger than the small angle Coulomb frequency ν , thereby producing a higher dissipation rate. This provides a consistent and experimentally satisfactory picture if $\nu^* > \Omega_e$, where Ω_e is the electron cyclotron frequency. However, when $\nu^* < \Omega_e$, the electron magnetic moment is conserved and the electrons should be treated as one dimensional. In this case, as clearly shown by Petviashvili,⁴ the formation of a plateau in the electron distribution function precludes any resistivity enhancement beyond a few percent of the classical value. It is the purpose of this paper to demonstrate that inclusion of strong turbulence effects can remove most of the fundamental difficulties encountered in one-dimensional anomalous resistivity and produce a consistent and satisfactory picture. The basic idea is that density cavities in the ion background cause the existence of low frequency potential barriers. When a dc electric field is applied, these barriers can prevent the free streaming acceleration of a significant fraction of the electrons.

An important step forward in understanding when anomalous dc resistivity can appear, was the observation of Papadopoulos and Coffey⁵ that the low frequency density fluctuations could be generated by means other than current-driven instabilities. This removes the threshold requirement on v_d of the ambient plasma. In their paper the low frequency fluctuations appeared due to the presence of suprathermal electron beams. Such situations exist both in relativistic beam plasma heating and in auroras due to the presence of the energetic precipitating electrons. It was noted^{4,5} that the presence of the beams creates electron plasma

oscillations whose ponderomotive force, acting on the plasma, drives low frequency density fluctuations. In going into the one-dimensional situation and within the framework of weak turbulence theory the same difficulties reappear as in the current-driven case. However, under strong turbulence conditions [i.e., $W/nT > (\lambda_D)^2$, where W is the field energy in the beam resonant waves and k is their wavenumber], the density fluctuations have been shown to form large localized density cavities (cavitons) in which the high frequency field is trapped (solitons).⁶⁻⁹ Figure 1 shows a typical structure as seen in a computer simulation of such cavities produced by the high frequency (ω_{pe}) waves due to the existence of a beam (see also Figs. 13 and 16 of Ref. 8).

While our original work centered on such beam-generated cavities which occur in many situations of current physical interest, the basic physical effects noted here will appear whenever finite amplitude ion cavities exist in the ambient plasma. A description of the interaction of the background electrons with the cavities requires a local theory going beyond the limit of weak turbulence quasi-linear wave-particle interaction. In view of the analytical complexity of the subject we present below a phenomenological theory supplemented by computer simulations.

II. THEORY

Assume that there is a density cavity in the ion background with a depth $\delta n_i/n_0$, where n_0 is the average ion density. In order to maintain charge neutrality at low frequency, there must exist a low frequency potential internal to the plasma, $\delta\phi$, large enough to exclude a

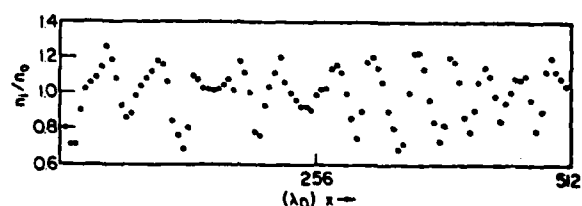


FIG. 1. Typical ion density fluctuations generated by the presence of a high velocity electron beam as seen in a particle simulation.

fraction of the electrons equal to δn_i . This means that inside the cavity

$$\left(1 - \frac{\delta n_i}{n_0}\right) n_0 = \int_{-\infty}^{\infty} f_{e, \text{int}}(v) dv. \quad (1)$$

From the Vlasov equation, since f is constant along lines of constant energy we can determine $f_{e, \text{int}}$ in terms of $f_{e, \text{ext}}$. If $f_{e, \text{ext}}$ is a nondrifting Maxwellian then $(1 - \delta n_i/n_0) = \exp(-\delta\phi/2)$, where $\delta\phi$ is normalized to the electron thermal energy and $v_{te} = 1$. Defining a trapping velocity $v_{tr}^2 = \delta\phi$, the fraction of trapped electrons is

$$\frac{\delta n_{e, \text{tr}}}{n_0} = \left(\frac{2}{\pi}\right)^{1/2} \int_0^{v_{tr}} \exp(-\frac{1}{2}v^2) dv.$$

This is plotted in Fig. 2 as a function of cavity depth. As can be seen in Fig. 2, the fraction of trapped electrons is greater than the cavity depth. For example, a cavity with $\delta n_i/n_0 = 0.2$ generates a low frequency potential that traps or blocks half of the electrons. One might assume that in order to maintain quasi-neutrality the plasma would generate a potential just large enough so that $\delta n_{e, \text{tr}} = \delta n_i$. However, as noted earlier, a collisionless plasma will conserve flux along a constant energy surface. As particles pass over the potential barrier they slow down and bunch, increasing the local density. In order to maintain charge neutrality, the plasma must raise the height of the potential barrier so that $\delta n_{e, \text{tr}} > \delta n_i$.

On the basis of this picture we can compute the electron response to an external dc field. In the absence of any cavities, the electrons will free stream with an average velocity $v_{fs}(t) = (q/m)Et$ when an external dc field is applied. The presence of the density cavities divides the electrons into two classes (Fig. 3). The central part of the distribution with $|v| < v_{tr}$ does not accelerate, since it is reflected by the potential barriers. The tail with initial velocities parallel to v_{fs} being untrapped is displaced by v_{fs} ; untrapped particles that have an initial velocity opposite to v_{fs} can only slow down to a velocity $|v_{min}| \approx (\delta\phi)^{1/2}$. At that point they are scattered for 180° by the potential. This

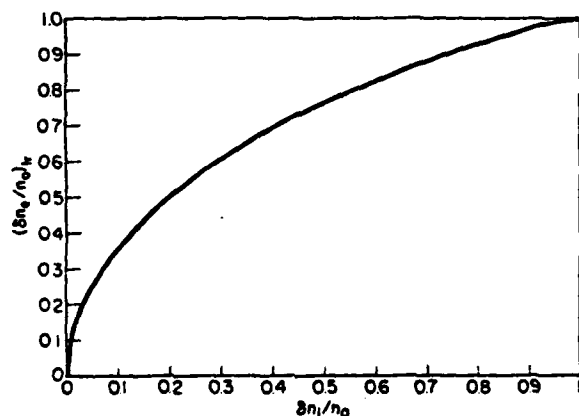


FIG. 2. The fraction of the electron population trapped by an ion cavity of depth δn_i . Note that a cavity of depth of 0.2 traps approximately half of the electrons.

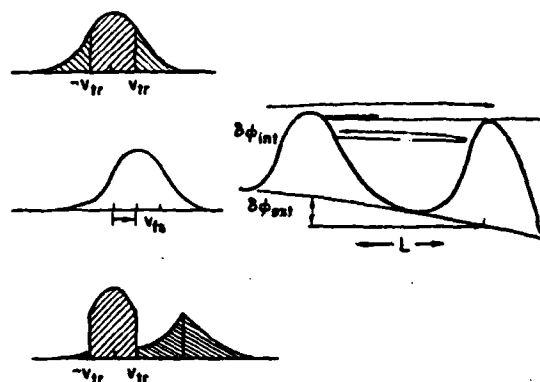


FIG. 3. The presence of a finite amplitude ion cavity causes a collocated low frequency potential, $\delta\phi_{\text{int}}$. When an external potential is applied, $\delta\phi_{\text{ext}}$, a fraction of the electrons are trapped and prevented from accelerating. If we ignore streaming instabilities, the electron velocity distribution will form the shape shown on the left.

means that the electrons in the left-hand tail have undergone a sudden increase in velocity equal to $2v_{min}$. Therefore, the average electron drift velocity is

$$v_d = \left(1 - \frac{\delta n_{e, \text{tr}}}{n_0}\right) v_{fs} + 2v_{min} \int_{v_{min}}^{v_{tr}} \left(\frac{dv}{(2\pi)^{1/2}} \exp\left(-\frac{v^2}{2}\right)\right). \quad (2)$$

The maximum contribution from the integral is $(1 - \delta n_{e, \text{tr}}/n_0)v_{min}$. Therefore, on long time scales

$$\dot{v}_d = (1 - \delta n_{e, \text{tr}}/n_0) \dot{v}_{fs}.$$

III. SIMULATION RESULTS

Here, we present a series of one-dimensional computer simulations showing the effect of ion density cavities on the ability of a collisionless plasma to carry a dc current.

A particle-fluid hybrid code⁷ and a Vlasov simulation code^{8,9} were used. First, we looked at the acceleration of the plasma by a constant dc electric field (Eq. (2)). To study this case we carried out two groups of runs. We first imposed a fixed ion density fluctuation on the plasma. This allowed us to easily vary $\delta n_i/n_0$ and the shape of the fluctuations. In the next simulations, the ion fluctuations were generated self-consistently by the ponderomotive force of a high frequency long wavelength pump, such as expected in the presence of weak electron beams or a laser. We next looked at the effect of ion cavities on an existing dc current. In these simulations the ion cavities were generated by the collapse of a long wavelength Langmuir wave.

Figure 4 shows the results of the first set of runs. The straight line is the free streaming velocity of the plasma and occurs when $\delta n_i = 0$. The curves lines are calculated from Eq. (2) assuming $v_{min} = v_{tr}$. Three of the simulations plotted used the particle fluid hybrid code. The electrons were particles. The ions were a fixed fluid background. The small differences in the simulations from the theoretical curves can be at-

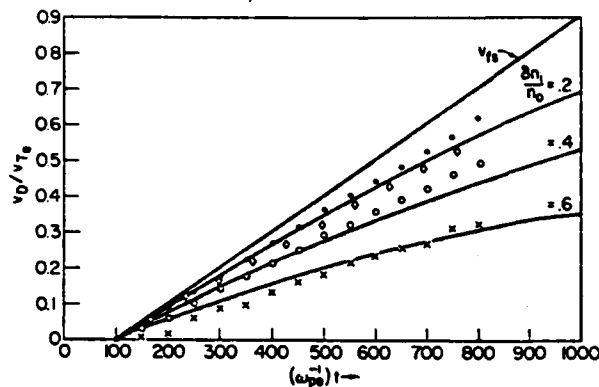


FIG. 4. The electron drift velocity due to a constant dc field. The top line is the free streaming response of the electrons. The three lower lines are the theoretical predictions for different cavity depths as marked, \bullet , \circ , \times are particle-fluid simulations with $\delta n_1/n_0 = 0.2, 0.4$, and 0.6 . \circ is a Vlasov simulation with $\delta n_1/n_0 = 0.2$.

tributed to the electron noise due to the finite number of particles. In the first simulations we ran with what we considered to be a reasonable number of particles per Debye length ($n_0 = 10-20$); we did not see the enhancement of $\delta n_{e,\text{tr}}$ over δn_i . As we increased the number of particles per cell the simulation results were in better and better agreement with theory. For the simulations shown in Fig. 4 the number of particles per cell was 400. The appearance of the enhancement is due to the conservation of flux along constant energy surfaces. If the plasma is collisional, this condition is not true. The numerical collision frequency, ν , can be estimated as $(\alpha n_0)^{-1}$, where α depends upon the spatial filtering applied in the code. Based upon test runs with this code, $\alpha \approx 7$. For these particle simulations the width of the cavities is approximately $30\lambda_D$, for $\delta n_1/n_0 = 0.2$, $n_{e,\text{tr}} \approx 0.5v_{Te}$; particles with $v \approx v_{Te}$ are most slowed by the barrier and contribute most to the enhancement of $\delta n_{e,\text{tr}}$ over δn_i . From this we can make a rough estimate of the time required for such a particle to pass over the barrier, t , and thus we see that $v_{Te}t \approx 1$ for $n_0 = 10$. This, of course, is really a lower limit on $v_{Te}t$ since the barrier will slow such particles down therefore increasing t . As can be seen in Fig. 4 this was actually confirmed by using the noise-free Vlasov code. This code due to its noise free property allowed us to clearly distinguish between trapped and untrapped electrons. Figure 5 shows the electron distribution at $t=0$ and $\omega_{pe}t=750$. With $\delta n_1/n_0 = 0.2$, 50% of the particles were trapped in agreement with the theory. Whitfield and Skarsgard¹¹ observed this splitting of the electron distribution function in particle simulations in which they modeled the effect of a bumpy magnetic field with a fixed sinusoidal density variation.

In order to determine the effects of the cavity width and spacing on the interactions, we initialized the ions in the Vlasov simulations four different ways as shown in Fig. 6. It was found that the interaction was independent of both the width and the spacing and dependent

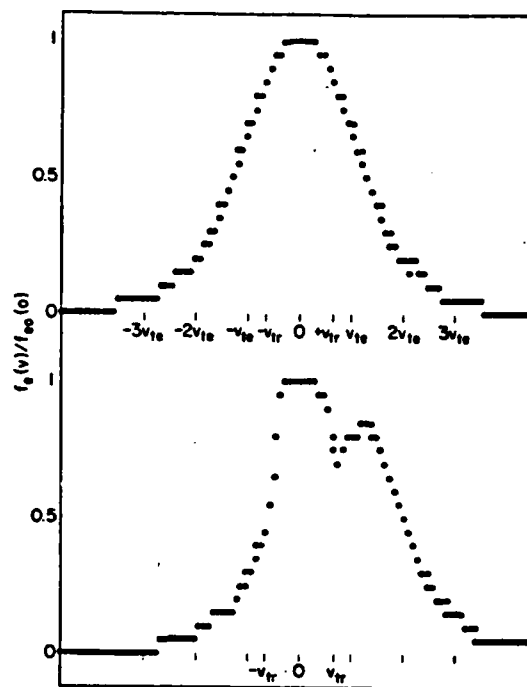


FIG. 5. The electron velocity distribution from the Vlasov simulation shown in Fig. 4, $\delta n_1/n_0 = 0.2$. The top figure shows the initial distribution; the bottom figure shows the distribution at $750\omega_{pe}^{-1}$. The theoretically predicted v_{Tr} is marked.

only on the value of the density minimum. These results are consistent with the simplified theory presented here.

We next examined three situations where the ion cavities are self consistently generated due to strong turbulence.

Figure 7 shows the results of a hybrid simulation with $m_i = 128m_e$, where a kinetic beam plasma instability with growth rate $\gamma = 0.006\omega_{pe}$ and phase velocity $v_{ph} = 81v_{Te}$ was driven. The mode was nonlinearly stabilized¹²⁻¹⁴ by creating a set of 10 density cavities (see Fig. 1). The rms value of the density fluctuations was 15%, while the localized cavity depth was 0.2-0.3. An electric field was turned-on at $\omega_{pe}t = 700$. It can be seen that the value of the acceleration was substantially smaller than free streaming.

In another run the Vlasov code was used with a constant dipole pump of energy $E_0^2/8\pi n_e T_{e0} = 0.1$. Such a run simulates the possibility of a microwave or laser pump

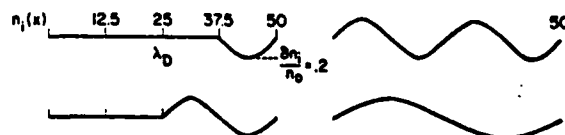


FIG. 6. The different ion densities for the Vlasov simulation shown on Fig. 4. $\delta n_1/n_0 = 0.2$. All four simulations gave the same response.

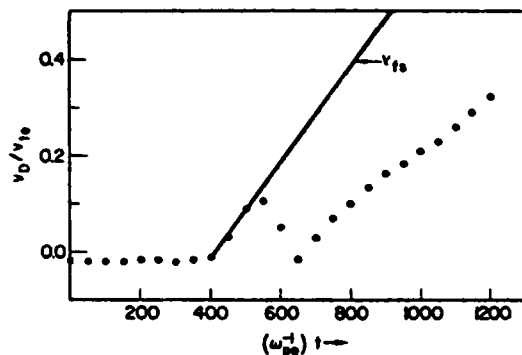


FIG. 7. The response of the electrons to a dc electric field with an electron beam present. The electric field was turned on at $400\omega_{pe}^{-1}$. The ion density at $400\omega_{pe}^{-1}$ is shown in Fig. 1. Note that the ion cavities in this simulation are generated self-consistently.

at ω_{pe} across the current carrying system. A large single cavity was formed in this case. The plasma response was again consistent with the simple theoretical picture.

Next, we considered the effects of ion cavities on an existing dc current. Figure 8 shows the results from a Vlasov simulation where the electrons have an initial drift, v_d , equal to $-0.5v_{te}$; $T_e = T_i$ and, hence, the current is stable. Between 0 and $200\omega_{pe}$, a long wavelength Langmuir wave is brought up in the plasma with $E_0^2/8\pi T_{e0} = 1$ and $\omega_{pe}/k_0 = 20v_{te}$ (k_0 is the wavenumber of the Langmuir wave). The system length is $128\lambda_D$ and the ion-electron mass ratio is 100. Since $E_0^2/8\pi n T_{e0} \gg \frac{1}{2}(k_0\lambda_D)^2$, this wave is nonlinearly unstable and we see the transfer of the field energy to localized spikey fields where it can be resonantly absorbed by the electrons. Simultaneously, this leads to the formation of ion cavities inside of which the spikey fields are trapped [Fig. 8(a)]. A series of such simulations without a dc are reported in Ref. 8. In particular, Figs. 12, 13, and 14 of Ref. 8 provide a dynamical picture of the formation of the spiky turbulence and ion cavities. In Fig. 8(b) we show the electron and ion momentum normalized to $m_e v_{te}$. Initially, the electrons drift freely through the stationary ions. As the strong turbulence begins to drive up the ion cavities the electrons and ions start to couple. At the time the ion cavities reach this maximum depth ($\delta n_i/n_0 = 0.28$), we see the strong coupling of the electrons and ions. The electrons lose 30% of their initial momentum to the ions. Figure 9 shows the electron distribution at $t=0$ and $2000\omega_{pe}^{-1}$. One can clearly see that the low energy electrons have been blocked and shifted to smaller velocities.

As can be seen in Figs. 4 and 9, the presence of the ion cavities can lead to the formation of a double peaked electron velocity distribution. If a dc electric field is continuously applied to the plasma, one would see the formation of a runaway beam of electrons. The behavior of the plasma on these longer time scales depends upon how these beams are thermalized. One

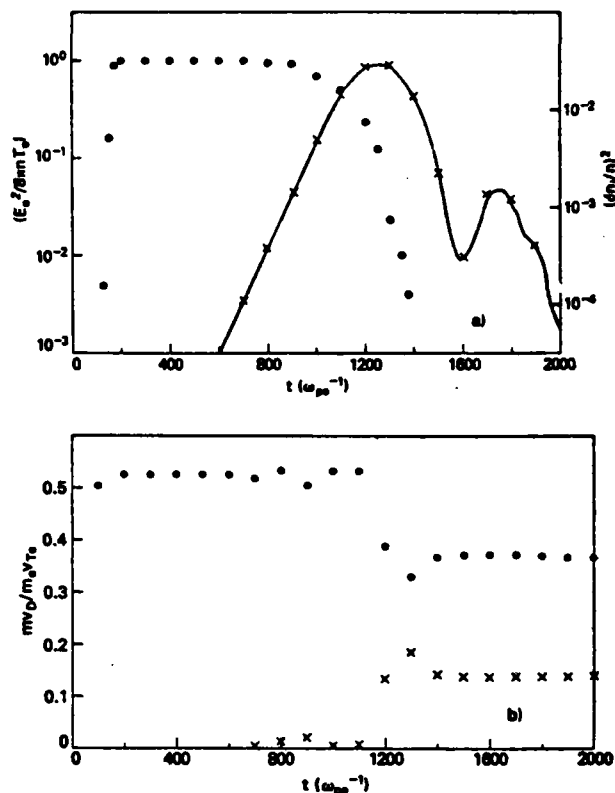


FIG. 8. The effect of strong turbulence collapse on a electron current. (a) This shows the time evolution of the total field energy (\bullet) and $(\delta n_i/n_0)^2$ (\times). For this simulation a long wavelength Langmuir wave with a phase velocity equal to $20v_{te}$ is brought up in the system between 0 and $200\omega_{pe}^{-1}$. At $200\omega_{pe}^{-1}$ all of the field energy was in the long wavelength mode. Strong turbulence acts to transfer the energy to shorter wavelength modes which can resonantly interact with the electrons, damping the high frequency fields. At the same time the strong turbulence drives up ion cavities. (b) This shows the time history of the electron (\bullet) and ion (\times) momentum. Initially, the electrons have a drift of $0.5v_{te}$ and the ions are stationary. $T_e = T_i$ and therefore the drift is stable. As the ion cavities are driven up, the ions and the electrons are coupled. The electrons are slowed down with the momentum being gained by the ions.

possibility is a two stream interaction between the trapped and untrapped electrons. How this process evolves depends upon the ratio of trapped to untrapped electrons and the spacing between the ion cavities. Also, on these longer time scales, the evolution of the ion cavities becomes important and this depends upon how the ion cavities are generated. As discussed in Ref. 8, if the cavities are generated via strong turbulence due to the beam plasma instability, one can see different behavior depending upon the strength of the beam and the electron ion temperature ratio. For example, when $W/nT_e > 0.1$ and $T_e \approx T_i$, the ion cavities will begin to damp on longer time scales following the initial stabilization of the beam. Figure 1 of Ref. 8 shows this behavior as seen with the hybrid code and with the

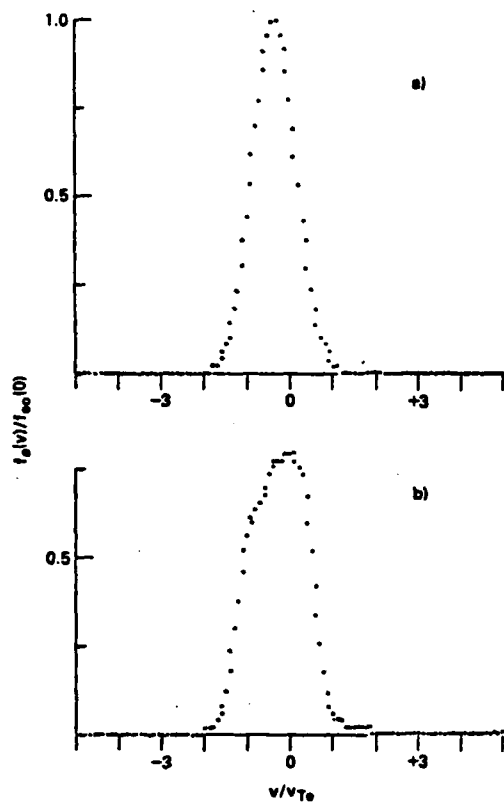


FIG. 9. The electron distribution for the simulation shown in Fig. 8(a), $t=0$. (b) $t=2000\omega_{pe}^{-1}$. The low velocity electrons have been trapped by the finite ion cavities.

Vlasov code. Except for the fact that there was no external dc field applied in those simulations, they are the same as the simulation shown in Fig. 7. As the ion cavities are damped away by Landau damping on the ions, fewer particles are trapped and the bulk acceleration starts to increase. This is what we begin to see at the end of the simulation shown in Fig. 7. However, as the level of ion turbulence drops, the beam-plasma instability starts to grow again. This acts to drive the ion cavities back up. This long term behavior can be seen in Fig. 4 of Ref. 8. Also note that the damping of the ion cavities as seen in the simulations takes place on a faster time scale because of the artificial mass ratio. This periodic reappearance of the beam-plasma instability and strong turbulence could lead to periodic quenching of the current. However, in other parameter regimes the ion cavities are much more stable in time. Because of this large number of parameters, the following simulation should be viewed as only an example of how these runaway beams could be thermalized. It is most interesting however because of its connection with some earlier work on runaway electrons.¹² To study this interaction we ran a simulation similar to the one shown in Fig. 8 where the ion cavities were created by the strong turbulence collapse of a high phase velocity Langmuir wave. The simulation parameters are the same as those of the simulation shown in Fig. 8 except

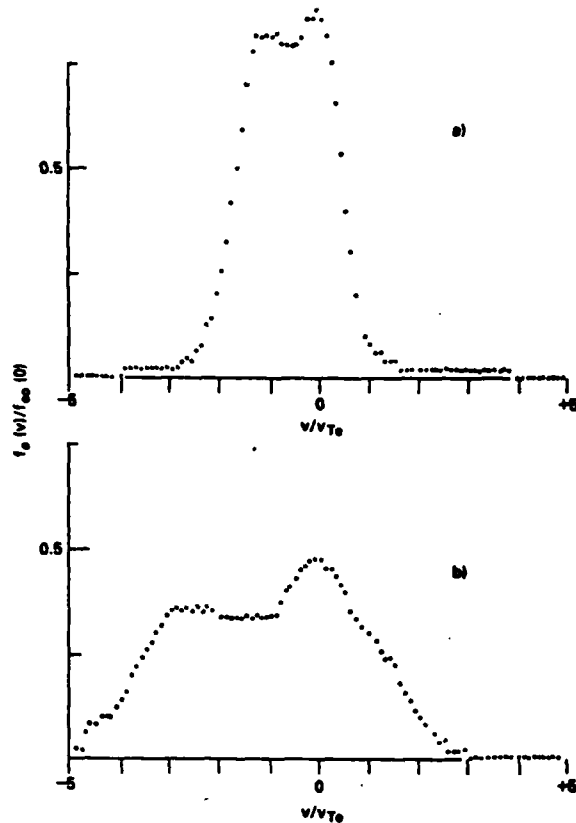


FIG. 10. On longer time scales the acceleration of the untrapped electrons can lead to the appearance of the two-stream instability. The ion cavities were generated by the collapse of a long wavelength Langmuir wave and then, in order to study only the electron dynamics, they were fixed. The maximum $\delta n_i/n_0$ was 0.21. A constant dc field was then applied to the electrons. (a) This shows the initial splitting of the trapped and untrapped electrons. (b) The distribution $1600\omega_{pe}^{-1}$ later. When the separation between the peaks of the two distributions became greater than $1.5 v_{Te}$, a two-stream instability was triggered. This led to the growth of electrostatic waves with phase velocities midway between the two peaks and a flattening of the runaway distribution.

that there was no initial electron drift. As before, the collapse of the wave led to the formation of ion cavities with most of the high frequency field energy going into the production of superthermal electron tails. At this point we applied a dc electric field and in order to look at just the electron thermalization, we froze the ions. The ions had three large cavities and two smaller ones. The maximum depth was $\delta n_i/n_0 \approx 0.21$. We again saw the initial splitting of the electron distribution [Fig. 10(a)]. As we continued to accelerate the electrons, the velocity difference between the trapped and untrapped particles increased and the relative minimum in the distribution function between the two peaks increased. When the separation between the peaks became greater than approximately 1.5 to 2 times the electron thermal velocity, we began to see the growth of electrostatic waves and a filling in of the valley between the two peaks. Since $\delta n_i = 0.21 n_0$, the

rapped and untrapped electron distributions have close to the same density. This threshold for instability is in good agreement with the Penrose stability criterion for two equal density, warm beams. Figure 10(b) shows the electron distribution $1600 \omega_{pe}^{-1}$ later. For the constant electric field used the electron should have increased their velocity by $1.28 v_{te}$. The leading edge of the untrapped electrons has been accelerated to the free streaming velocity. However, the low velocity part of the distribution is still trapped by the ion cavities and the free electrons have formed a long flat runaway distribution. This distribution [Fig. 10(b)] should be compared with the distribution shown in Fig. 1 of Ref. 12. It was shown in this paper that an electron distribution with such a long flat tail can be driven unstable by the resonant transfer of tail particle energy to $\omega_e \cos \theta$ waves. This leads to the formation of a positive slope on the tail distribution which is unstable. The overall effect is a large pitch angle diffusion of the tail particles and a reduction in the velocity of the leading edge of the runaway distribution. As discussed here the effect of the ion cavities is to split the electron distribution into two parts. The part trapped by the ion cavities cannot respond to the dc electric field. The untrapped part gets pulled out to higher velocities and can form a long flat runaway tail. While the response of the plasma electrons to the dc field has been greatly reduced, the leading edge of the distribution can still run away. If we now include the pitch angle diffusion of the leading edge of the beam as shown in Ref. 11, it may be possible to prevent the untrapped electrons from running away. We are presently carrying out simulations to study, simultaneously, the effects of finite ion cavities and pitch angle scattering.

Preliminary results from simulations with fixed ion cavities and the same parameters as those in Ref. 11 show that the pitch angle scattering does strongly limit the acceleration of the runaways while the ion cavities prevent the acceleration of the main body of the electron distribution.

The simulation results reported here are all one dimensional. Recent simulation results¹³ of the study of the turbulent collapse of Langmuir waves in two dimensions in a magnetic field indicate that, for an initial spectrum of waves parallel to the magnetic field with a small transverse spread such as would be generated by a warm electron beam, the ion cavities that form are much wider across the field than in the parallel direction. Most importantly for our work, the transverse scale is much greater than the electron gyroradius so that the low velocity electrons will see a one-dimensional barrier due to the cavities.

IV. SUMMARY AND CONCLUSIONS

The results reported here should be considered as a preliminary but major step in understanding and modeling the long time anomalous resistivity in one dimension. Referring first to our self-consistent results we demonstrated that:

(a) In agreement with previous studies the presence of electron beams^{5-9,14} or externally imposed high fre-

quency (ω_{pe}) electromagnetic fields,¹⁵ large local density cavities ($b\pi/n_e \approx 0.2-0.6$) can be formed.

(b) The potentials associated with these cavities are large enough to trap a significant fraction of the thermal electrons, so that the entire current will be carried by a small fraction of untrapped electrons. This effect will appear experimentally as an enhanced resistance and the appearance of localized runaway beams. The long time scale behavior of the system will depend on how these beams are thermalized. A possible mechanism is further two-stream interaction of the runaways with the trapped electrons. This process will depend critically on the spacing among cavities and is presently under study. The preliminary simulation results indicate that this can lead to the formation of a flat runaway distribution. This type of distribution has been shown to be unstable to pitch angle scattering in a strong magnetic field.¹² This acts to reduce the velocity of the high velocity edge of the runaway beam. By combining these two effects, it may be possible to produce a quasi-steady current in the presence of a constant dc electric field.

Furthermore, the results of the first simulations demonstrated that similar resistivity will appear any time an instability can create finite amplitude density fluctuations. The ion cyclotron instability seems to be a good candidate and is currently under study.

In concluding we mention that these concepts can help in understanding return current heating in beam-plasma interactions and extend the Papadopoulos-Coffey anomalous resistivity in the auroral zones to regions where $\omega_{pe}/\Omega_e \approx 1$. The results of the constant pump runs suggest the possibility that a laser created corona with large cavities can produce short electron beam deposition lengths for *e*-beam-pellet fusion.

ACKNOWLEDGMENTS

We would like to thank Dr. David Book for his valuable help and guidance with the Vlasov simulation code.

This work was supported in part by the Office of Naval Research (ONR N00014 79 C0665) and in part by the National Aeronautics and Space Administration under contract W-14365. Partial support was provided by the National Science Foundation ATM-782524A01 (H. L. R.).

¹S. M. Hamberger and J. Jancarik, *Phys. Fluids* **15**, 825 (1972).

²K. Papadopoulos, *Rev. Geophys. Space Phys.* **15**, 113 (1977).

³V. I. Petviashvili, *Zh. Eksp. Teor. Fiz.* **45**, 1467 (1963) [*Sov. Phys. JETP* **18**, 1014 (1964)].

⁴K. Papadopoulos and T. Coffey, *J. Geophys. Res.* **79**, 1558 (1974b).

⁵K. Papadopoulos, *Phys. Fluids* **18**, 1769 (1975).

⁶P. J. Palmadesso, T. P. Coffey, I. Haber, and K. Papadopoulos, *Bull. Am. Phys. Soc.* **20**, 1277 (1975).

⁷H. L. Rowland and K. Papadopoulos, *Phys. Rev. Lett.* **39**, 1276 (1977).

⁸H. L. Rowland, *Phys. Fluids* **23**, 508 (1980).

⁹H. P. Freund, I. Haber, P. Palmadesso, and K. Papadopoulos,

Phys. Fluids 23, 518 (1980).

¹⁰J. P. Boris and D. L. Book, in *Methods in Computational Physics*, edited by John Killen (Academic, New York, 1976), Vol. 16, p. 85; H. L. Rowland and D. L. Book, in *Proceedings of the Eighth Conference on Numerical Simulations of Plasma* (Lawrence Livermore Laboratory, Livermore California, 1978), PE-7.

¹¹D. W. A. Whitfield and H. M. Skaragard, Phys. Fluids 17, 2255 (1974).

¹²I. Haber, J. D. Huba, P. Palmadesso, and K. Papadopoulos,

Phys. Fluids 21, 1013 (1978).

¹³H. L. Rowland, J. Lyon, and K. Papadopoulos, Phys. Rev. Lett. 46, 346 (1981).

¹⁴S. Kainer, J. Dawson, and T. Coffey, Phys. Fluids 15, 2419 (1972); L. E. Thode and R. N. Sudan, *ibid.* 18, 1552 (1975).

¹⁵W. L. Kruer, in *Advances in Plasma Physics*, edited by A. Simon and W. B. Thompson (Wiley, New York, 1976), Vol. 6, p. 237; E. Valeo and W. Kruer, Phys. Rev. Lett. 33, 750 (1974); N. R. Pereira, R. N. Sudan, and J. Denavit, Phys. Fluids 20, 271 (1977).

Appendix G

ANOMALOUS RESISTIVITY ON AURORAL FIELD LINES

H. L. Rowland¹
Science Applications, Inc.
McLean, VA 22102

P. J. Palmadesso
Naval Research Laboratory
Washington, D.C. 20375

K. Papadopoulos
Laboratory for Plasma and Fusion Energy Studies
University of Maryland
College Park, MD 20742

¹Permanent address: Laboratory for Plasma and Fusion Energy Branch
University of Maryland
College Park, Maryland 20742

ANOMALOUS RESISTIVITY ON AURORAL FIELD LINES

H. L. Rowland,¹ P. J. Palmadesso² and K. Papadopoulos¹

¹Laboratory for Plasma and Fusion Energy Studies
University of Maryland
College Park, Maryland 20742

²Naval Research Laboratory
Washington, D.C. 20375

Abstract

Conditions that exist along auroral field lines ($\delta n_1/n_0 > .25$, $\Omega_e/\omega_e > 1$) act to break the adiabatic invariance of the electron magnetic moment, cause strong anomalous dc resistivity and generate electron distributions in good agreement with observations.

I. INTRODUCTION

The understanding of acceleration processes in the auroral zones, due to parallel electric fields (E_{\parallel}), is closely connected with the problem of one dimensional anomalous resistivity and the breakdown of runaway acceleration. The one dimensional aspect of the problem comes from the fact that in the auroral regions of interest (i.e. $h > 1000$ km), $\Omega_e / \omega_e > 1$ (where ω_e, Ω_e are the plasma and cyclotron frequencies). In this case, the Larmor radius of the electrons is less than the Debye length, so that even in the case of ion acoustic turbulence of Debye length scales, the magnetic moment of the electrons ($\mu = mv_{\perp}^2 / 2B$) is an adiabatic invariant. The weak magnetic field case ($\omega_e \gg \Omega_e$) results related to anomalous resistivity are not directly applicable. This is obvious since the physical process by which anomalous resistivity results when $\omega_e \gg \Omega_e$, is the interaction of electrons with low frequency fluctuations which has the form of elastic scattering. The rapid scattering of the electrons then converts the directed velocity into heating and the appearance of anomalous resistivity. For $\Omega_e > \omega_e$, the elastic scattering is not allowed since μ is constant and the electrons can only slow down by parallel diffusion. However, as noted by Petviashvili (1963), the parallel diffusion is accompanied by the formation of a quasilinear plateau, which reduces the anomalous friction and produces trivial resistivity changes, independently of the amplitude of the low frequency waves. A corollary puzzle is what, if anything, inhibits the electrons in the plateau region as well as the negative slope region from freely accelerating [Dupree (1970); Papadopoulos

(1977)]. If distributed parallel electric fields are to exist in the auroral regions, the above questions should be answered.

It is the purpose of the present letter to demonstrate that under conditions prevailing in the aurora, the conservation of the first adiabatic invariance is violated for electrons above a certain threshold velocity. This effect combined with trapping of a major portion of the electron distribution function, by large amplitude ion cyclotron waves such as observed by S3-3 (Kintner et al, 1978) and in laboratory experiments (Bohmer and Fornaca, 1979), is sufficient to answer the major questions posed above and reproduce most of the observed features of the auroral energetic electron fluxes.

II. PHYSICAL MODEL

Consider a plasma in a uniform magnetic field \underline{B}_0 with $\Omega_e > \omega_e$, and an electric field \underline{E}_0 , parallel to \underline{B}_0 , which causes the electrons to acquire a drift velocity v_d such that for a $T_e/T_i \approx 1$ plasma drives an ion cyclotron wave. There are two basic questions to be answered. First, what ultimately limits the growth? Second, what, if anything, inhibits the electrons from freely accelerating?

Several processes have been discussed in the literature for limiting the growth (Dum and Dupree, 1970; Palmadesso et al., 1974). In view of the recent experimental evidence for large amplitude ($\delta n/n \approx 1/2$) coherent ion cyclotron waves in the aurora (Kintner et al. 1978) we consider here trapping as the basic stabilization mechanism. The effect of large amplitude low frequency density fluctuations on the plasma resistivity has been recently examined by Rowland et al. (1981). It was shown, that by including the quasineutrality effect, most of the electrons can be trapped for $\delta n/n > 1/4$. The electron distribution function is composed of a central part carrying little or no current, and a runaway tail of density n_r due to the untrapped electrons, which carry the current. Therefore $J(t) = n_r e v_r(t)$ where the ratio n_r/n is controlled by the level of $\delta n_i/n_i$; as shown in Rowland et al. (1981), while in the absence of a mechanism that can break the adiabatic invariance of the energetic electrons, $v_r = (eE_0/m)t$. From the above we see that the existence of a steady or quasisteady state reduces to the answer to the second question, i.e. the mechanism that can inhibit the free acceleration of runaways.

To answer this question, we examine the stability of distributions which are composed of a cold core with a runaway tail. The linear stability was studied by Kadomtsev and Pogutse (1967), who showed that low frequency oscillations $\omega_k = \omega_e k_{\parallel} / k \ll \Omega_e$, where k_{\parallel} is the wave vector along the magnetic field, are unstable even for flat distributions. These modes are principally driven by the first cyclotron resonance at velocities $(\omega_k + \Omega_e) / k_{\parallel}$. The instability has a growth rate $\gamma_k = n_r / n (\omega_e / \Omega_e)^2 \omega_k$. The nonlinear theory of the instability has been studied extensively (Papadopoulos et al. 1977, Liu et al. 1977, Haber et al. 1978). It was shown there that it results in a fast isotropization for particles with velocities $v_{\parallel} > v_c \approx 3(\Omega_e / \omega_e) v_{te}$ (v_{te} is the electron thermal velocity). A consequence of this is the breakdown of the adiabatic invariance for electrons with $v_{\parallel} > v_c$. An additional slowing down process was discussed first in Papadopoulos et al. (1977) and confirmed by particle simulations by Haber et al. (1978). Since only particles with $v_{\parallel} > v_c$ participate in the resonant scattering and have their v_{\parallel} reduced, electrons will tend to pile up at v_c leading to the formation of a beam. This distribution function can suffer friction in the parallel direction due to wave emission not only by the cyclotron resonance but also by Cerenkov type beam plasma instability at the lower or upper hybrid branch. Moreover in the presence of a constant dc electric field this piling up can be enhanced by particles being accelerated up from lower velocities. This reappearance of an electron beam and the slowing down of the electrons in the parallel direction will further isotropize the electron distribution function.

Another interesting effect that is seen in the simulations is the acceleration of particles in the opposite direction to the electric field. The electrostatic waves that are generated in the parallel direction can be backscattered by the ion fluctuations and create superthermal tails by Landau damping. These particles can also interact via the normal Doppler resonance $[v = (\omega_k - \Omega_e)/k_{\parallel}]$ with the waves that are pitch angle scattering the runaways and isotropize the counter streaming particles.

III. Simulations

We report next the results from a series of particle simulations that combine the effects of finite ion cavities and pitch angle scattering at the anomalous Doppler resonance (ADR). The parameters for the simulations are the same as those used by Haber et al. (1978). However, instead of starting with a runaway distribution, we start with a Maxwellian distribution and a fixed ion cavity with an effective depth of 0.3. We will apply a constant dc field to show the formation of the runaway distribution such as was seen in the earlier strictly one dimensional simulations of Rowland et al. (1981). We will then continue to drive the electrons to determine the effect of the pitch angle scattering on the further acceleration of the electrons.

Fig. 1a shows the initial electron distribution. The magnetic field is at 55° to the x axis and $\Omega_e = 2\omega_e$. The electric field is parallel to B and has a magnitude of $0.01(m/e)v_{te0}\omega_e$ [where $m(e)$ is the electron mass (charge) and v_{te0} is initial electron thermal velocity and ω_e is the plasma frequency]. Fig. 2b shows the electron velocity distribution at $2000\omega_e^{-1}$. The ion cavity has prevented the bulk of electrons from being accelerated and one can see the cold dense core of electrons at zero velocity. The untrapped electrons accelerated along the magnetic field forming a flat runaway tail. One can see that the temperature of the electrons transverse to the field did not increase and up to this point the acceleration was 1D parallel to the magnetic field. However, the high velocity edge of the distribution has become greater than v_c and these particles started to pitch angle scatter as

seen by the spreading of the upper edge of the distribution.

At this point in time, that 2D effects started taking place, the simulation was stopped. This state was used as an initial state for a series simulations using different values for the external dc electric field. Our earlier theoretical and computational work [Rowland et al. (1981)] demonstrated that during the initial 1D stage, changing the strength of the dc electric field did not effect the formation of the runaway distribution beyond changes in the timescale; namely with a stronger electric field the runaway distribution formed faster. The simulation presented in detail here had an electric field starting from $2000 \omega_e^{-1}$ of magnitude $2 \cdot 10^{-3} (m_e/q) v_{teo} \omega_e$. As the pitch angle scattering continues, the formation of a beam in the parallel direction similar to the one seen by Haber et al. (1978) is observed. The region of positive slope is unstable to Cherenkov interactions with both lower and upper hybrid waves. This acts to reduce the parallel current and to further symmetrize the distribution. Fig. 2a shows the distribution at $3800 \omega_e^{-1}$. No further parallel acceleration of the electrons is observed. Electrons with $v_{\parallel} > v_c$ which could be pitch angle scattered to large v_{\perp} were slowed down by the beam instability. Thus one sees electrons with $v_{\parallel} < v_c$ but with $v_{\perp} \gg v_{teo}$. This isotropization continues. Fig. 2b shows the electron distribution function at $8800 \omega_e^{-1}$. It is composed of a cold dense core of electrons surrounded by a hot, isotropic cloud.

Fig. 3 shows the parallel electron distribution at 2400, 3200, 4800, $8800 \omega_e^{-1}$ (a,b,c,d). The high velocity beam seen at $2400 \omega_e^{-1}$ is due to the pitch angle scattering. By $3200 \omega_e^{-1}$ beam instabilities have

flattened the runaway distribution. It is clearly seen that the instability at the anomalous Doppler resonance prevents electron runaway. If the high velocity electrons had continued to freely accelerate the upper edge of the distribution would have been at the right edge of Fig. 4d.

Fig. 4 shows the growth of the parallel drift velocity normalized to the initial electron thermal velocity. Note that the time axis between 0 and $2000 \omega_e^{-1}$ is stretched by a factor of five to compensate for E_0 being five times larger during that time. Thus the time axis is linear in terms of the effective acceleration time, $E_0 t$. Between 0 and $150 \omega_e^{-1}$ the ion cavity was adiabatically formed in the plasma. At $150 \omega_e^{-1}$ the dc electric field was turned on. The solid line shows for comparison the rate of acceleration of the electrons in the absence of the cavity. Between 150 and $2000 \omega_e^{-1}$ we have essentially a 1D system parallel to the magnetic field. The cavities prevent the acceleration of the bulk of the plasma and the current is carried by a small fraction of high velocity electrons streaming along the field lines. At approximately $2000 \omega_e^{-1}$ the velocity of the fastest particles $> v_c$ and pitch angle scattering begins; the high velocity electrons are heated in the transverse direction with v_\perp becoming $> v_{te0}$ and the adiabatic invariance is broken. The current continues to increase until approximately $2300 \omega_e^{-1}$ when the instability at the ADR has grown to such a level that it removes energy from the parallel motion slowing the electrons down faster than E_0 accelerates them. The current is clamped and strong transverse heating is observed. Finally, at much longer times ($> 7000 \omega_e^{-1}$) the current begins to increase again but at a slower

rate than during the 1D stage. For $v_{\parallel} > v_c$ the instability heated the plasma so that $\partial f / \partial v_{\parallel} = \partial f / \partial v_{\perp}$ (or $T_{\parallel} = T_{\perp}$). The electric field can begin to increase v_{\parallel} for these particles but the rate of increase is slowed due to pitch angle scattering which acts to keep $T_{\parallel} = T_{\perp}$. The increase in the current can be seen in Fig. 3. The cutoff at v_c is still being maintained but a few particles are accelerated to higher velocities.

Fig. 6 shows the log of the electron distribution at $t = 8800 \omega_e^{-1}$. A cold dense core of trapped electrons surrounded by the hot isotropic accelerated electrons is seen. This distribution has marked similarity to the auroral electron distributions measured by Kaufmann, et al [1978].

IV. Conclusions

The acceleration in the auroral zones is, of course, a spatial problem. While temporal simulations such as reported here are very important for understanding the basic microphysics that takes place in the auroral environment, large scale macrophysics simulations are needed. The present results are a necessary input before a complete understanding of the total system dynamics can be gained. Development of such a capability is presently underway. We present below a qualitative picture of the macrostructure expected on the basis of our simulations. The first point is that for the pitch angle scattering to be effective requires $\Omega_e/\omega_e \gtrsim 1$. Thus one would expect to see strong dc resistivity and parallel electric fields between 2000 to 12000 km. The critical value of the current at which strong resistivity appears, increases with Ω_e/ω_e . Thus, there exists a maximum critical current that can be carried along the field line. Below this level the ion cavities prevent the bulk of the electrons from being accelerated and tails of field aligned electrons are formed. However, when this critical current is exceeded one expects the emission of both upper and lower hybrid waves, large parallel electric fields, and a hot isotropized electron distribution with a cold dense core. The strongest resistivity and hence the largest electric fields will appear in the region where the current is clamped. One can make a rough estimate of the initial extent of this region by assuming $\Delta r = v\tau$ where v is the speed of the high velocity particles and τ is the time over which the current is clamped. For the simulation shown $\tau = 4.10^3 \omega_e^{-1}$.

Assuming $n_p \approx 100 \text{ cm}^{-3}$ and a velocity of a keV electron this leads to a distance of 200 km. This is of course only a rough order of magnitude estimate but the main point is that the resistivity and the parallel electric fields should extend at least initially over a large region in comparison to the Debye length ($\approx 3\text{m}$). This is in agreement with a recent analysis of satellite data of potential drops along auroral field lines [Mozer (1981)]. The dynamic spatial behavior is a subject for further study but this region could shrink. For the simulation shown in detail the dc electric field $E_o = 2.7 \cdot 10^{-4} T_e^{1/2} n_p^{1/2}$ (where T_e is in eV, n_p is plasma density in cm^{-3} and E_o is in V/m) for $t > 2000 \omega_e^{-1}$. For $T_e = 20\text{eV}$ and $n_p = 100$, $E_o \approx 10^{-2} \text{V/m}$ and $\Delta\phi = E_o \cdot \Delta r = 2\text{keV}$. Based upon our series of simulation $\tau \propto E_o^{-1}$. For constant $\Delta\phi$ reduction of Δr would lead to a larger E_o . This, in turn, would lead to a shorter τ and further reduction of Δr . On the other hand, if the system responds by raising ϕ in order to drive a $j > j_{cr}$, an increased E_o and a shorter Δr will result. Such questions can only be studied with a large scale transport code. Another spatial effect presently under study is the anomalous transport of the hot electrons across the magnetic field and out of the acceleration region. If this takes place at a fast enough rate such that T_{\perp} remains less than T_{\parallel} the current will remain clamped. In this case τ will be determined by the timescale for this perpendicular transport.

ACKNOWLEDGEMENTS

It is a pleasure to acknowledge many useful discussions with Drs. J. A. Fedder, I. Haber and C. S. Liu. This work was supported in part by ONR and NASA W-14365 and by NSF ATM-782524A01.

REFERENCES

1. Böhmer, H., and S. Fornaca, "Experiments on nonlinear effects of strong ion cyclotron wave turbulence," J. Geophys. Res. 84, 5234, 1979.
2. Dum, C. T. and T. H. Dupree, "Non-linear stabilization of high frequency instabilities in a magnetic field," Phys. Fluids 13, 2064, 1970.
3. Dupree, T. H., "Theory of resistivity in collisionless plasma," Phys. Rev. Lett. 25, 789, 1970.
4. Haber, I., J. D. Huba, P. Palmadesso, and K. Papadopoulos, "Slope reversal of a monotonically decreasing electron tail in a strong magnetic field," Phys. Fluids 21, 1013, 1978.
5. Kadomtsev, B. B. and O. P. Pogutse, "Electric conductivity of a plasma in a strong magnetic field," Zh. Exp. Teor. Fiz. 53, 2025 (1967) [Sov. Phys. - JETP 26, 1146 (1968)].
6. Kaufmann, R. L., P. B. Dusenbery, B. J. Thomas, and R. L. Arnoldy, "Auroral electron distribution function, J. Geophys. Res. 83, 586, 1978.
7. Liu, C. S., Y. C. Mok, K. Papadopoulos, F. Engelmann, and M. Bornatici, "Nonlinear dynamics of runaway electrons and their interaction with tokamak liners," Phys. Rev. Lett., 39, 701, 1977.
8. Mozer, F. S., "Large electric field structures on auroral zone magnetic field lines," EOS 62, 362, 1981.
9. Palmadesso, P. J., T. P. Coffey, S. L. Ossakow and K. Papadopoulos, "Topside ionosphere heating due to electrostatic ion cyclotron turbulence," Geo. Res. Lett. 1, 105, 1974.

10. Papadopoulos, K. "A review of anomalous resistivity for the ionosphere," Rev. of Geophys. and Space Phys. 1, 113, 1977.
11. Papadopoulos, K., B. Hui, and N. Windsor, "Formation of a positive slope in electron runaways in tokamaks," Nucl. Fus. 17, 1067, 1977.
12. Petviashvili, V. I., "Non-linear oscillations and some effects due to a longitudinal current in a plasma," Zh. Eksp. Teor, Fiz. 45, 1467, 1963 [Sov. Phys. - JETP 18, 1014, 1964].
13. Rowland, H. L., P. J. Palmadesso, and K. Papadopoulos, "One-dimensional direct current resistivity due to strong turbulence," Phys. Fluids, 24, 833, 1981.

FIGURE CAPTIONS

- Fig. 1 The initial 1D acceleration of the electrons parallel to the magnetic field B and E_0 is at 55° to the axis. a) initial distribution, b) distribution at $2000 \omega_e^{-1}$. The ion cavities prevent the acceleration of the bulk of the electrons.
- Fig. 2 As the electrons continue to accelerate $v > v_c$, the pitch angle scattering breaks the invariance of 0 and strong transverse heating sets in. a) $t = 3800 \omega_e^{-1}$ b) $t = 8800 \omega_e^{-1}$.
- Fig. 3 The parallel electrons distribution. The pitch angle scattering prevents the free streaming acceleration of the electrons $t = 2400, 3200, 4800, 8800 \omega_e^{-1}$ (a,b,c,d).
- Fig. 4 The average electron drift velocity. When $v > v_c$, the pitch angle scattering clamps the current.
- Fig. 5 A 3D plot of the log of the electron distribution seen in Fig. 2b. Note the cold central core and the hot isotropized electrons.

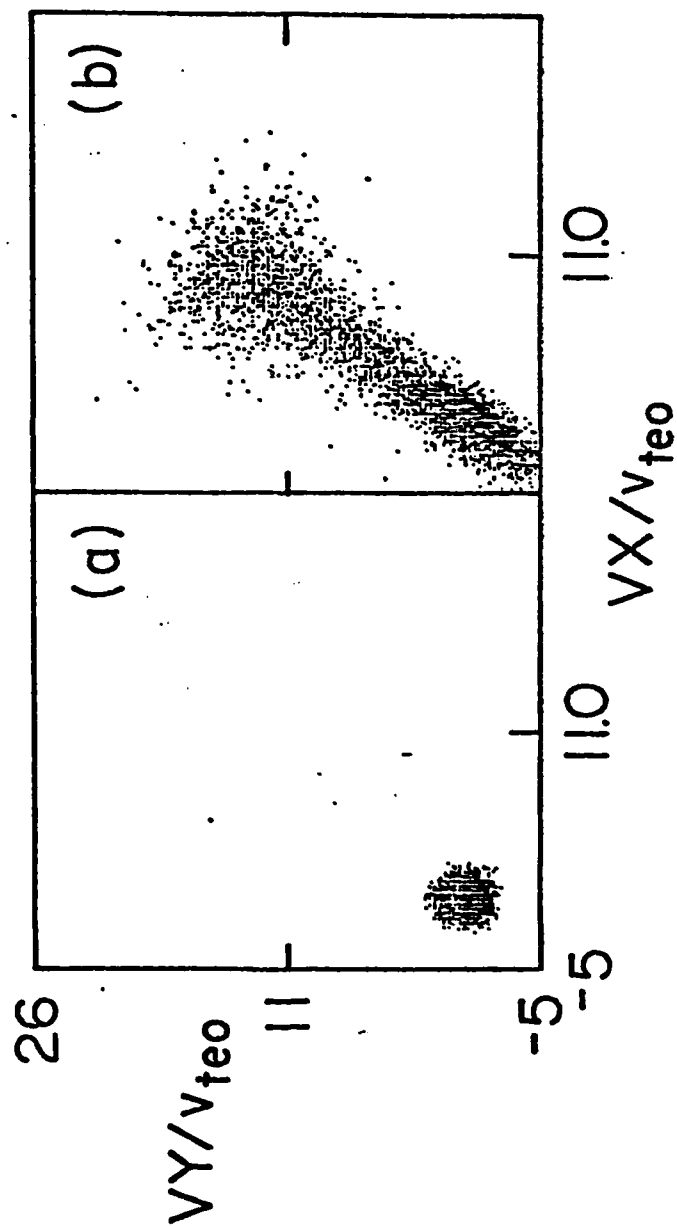


Figure 1

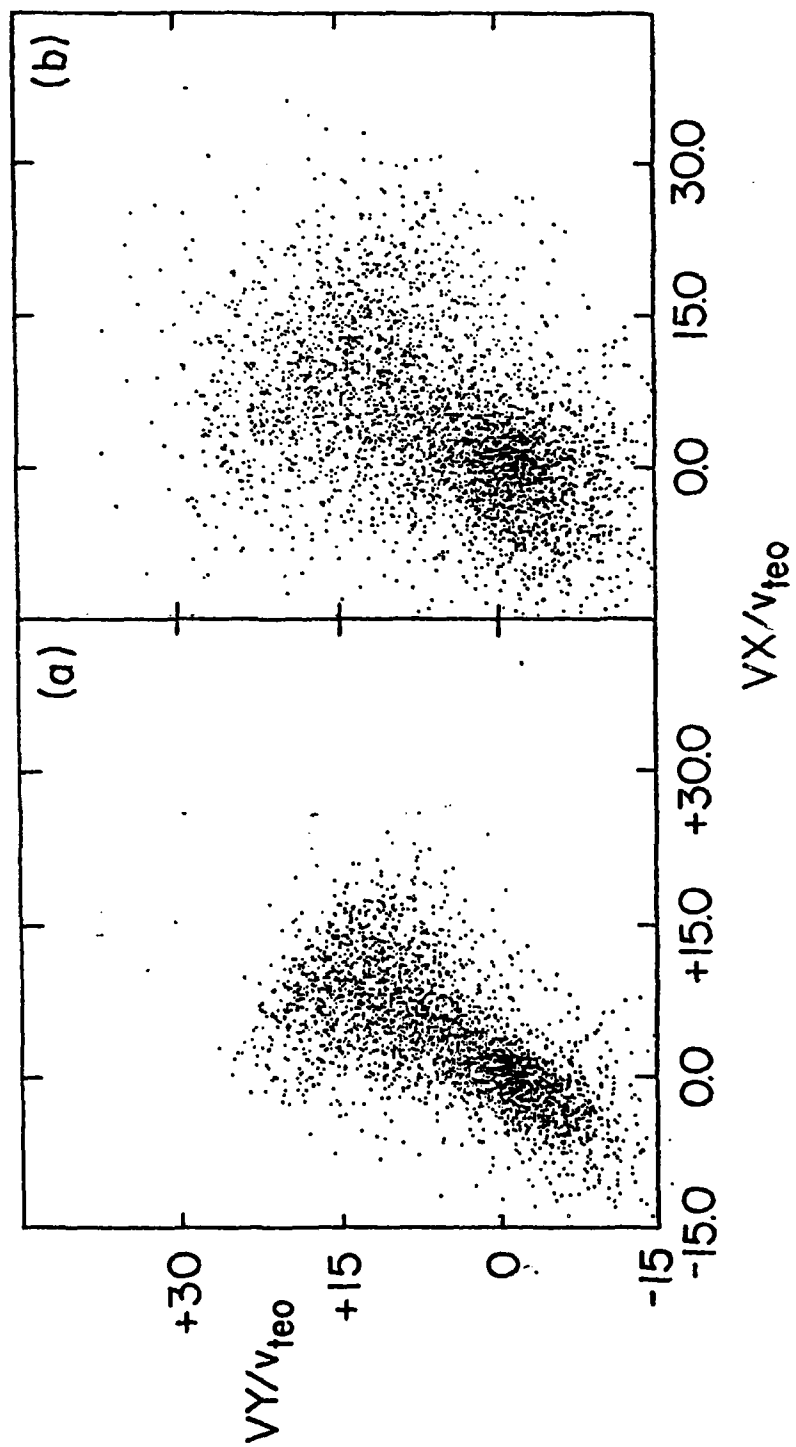


Figure 2

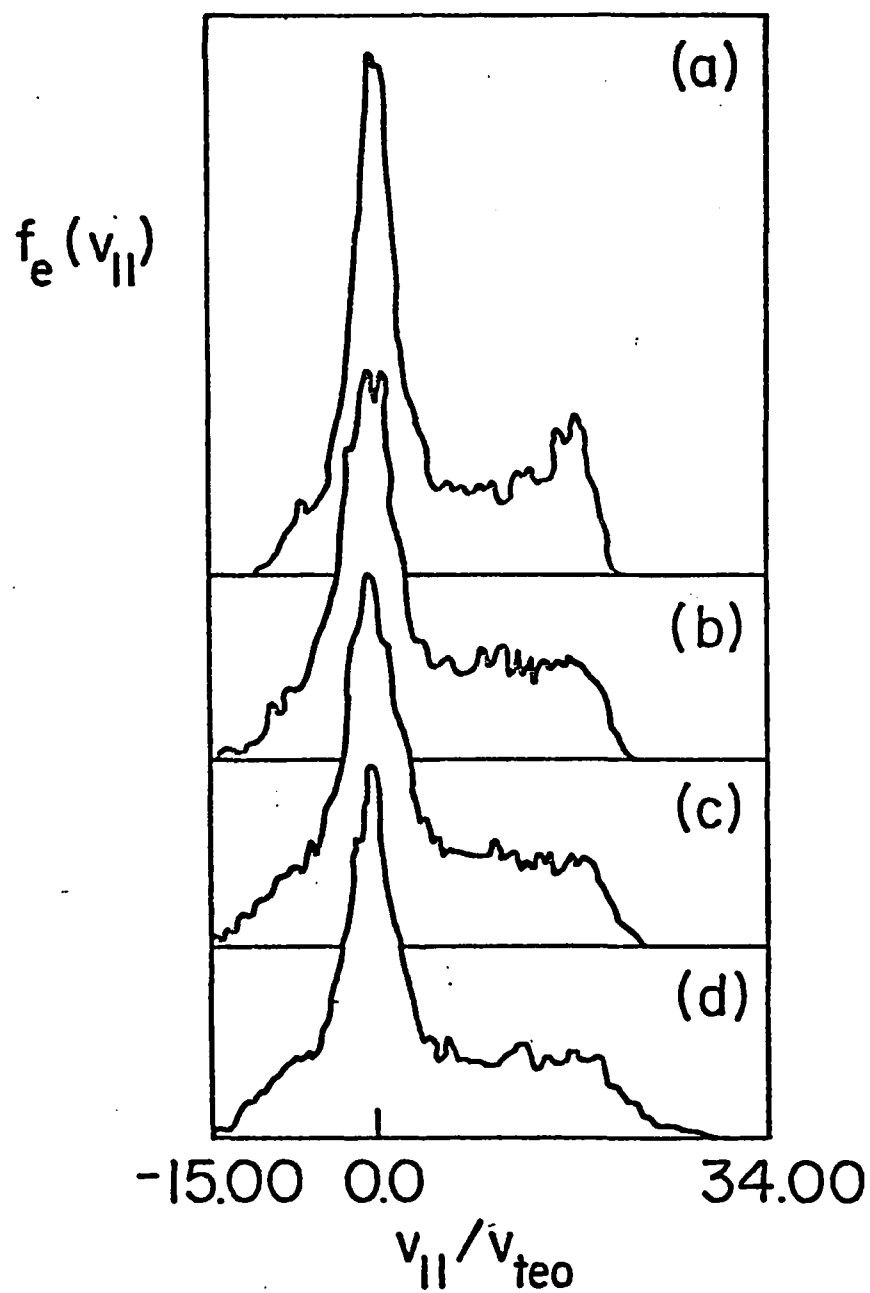
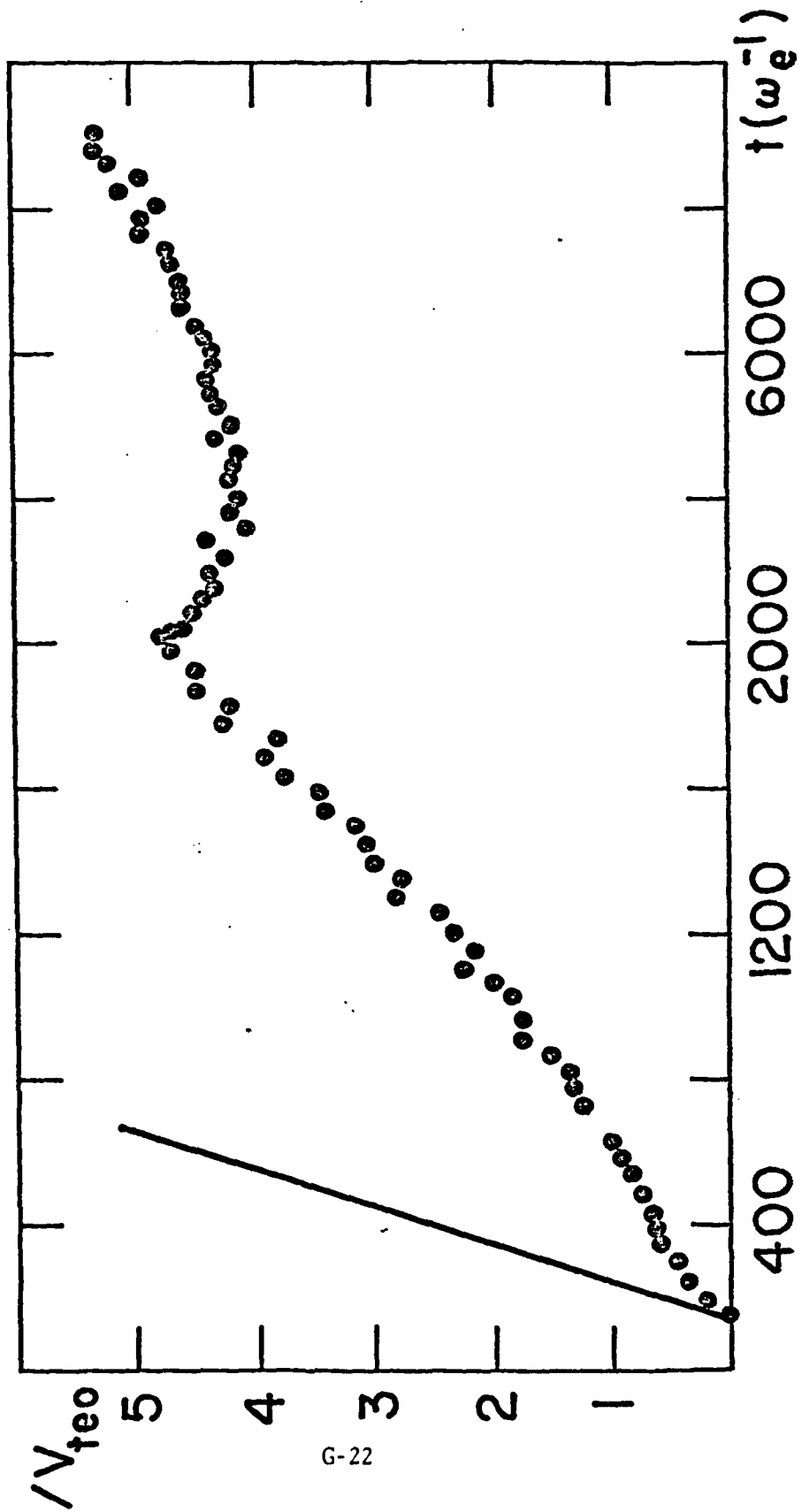


Figure 3
G-21



G-22

Figure 4

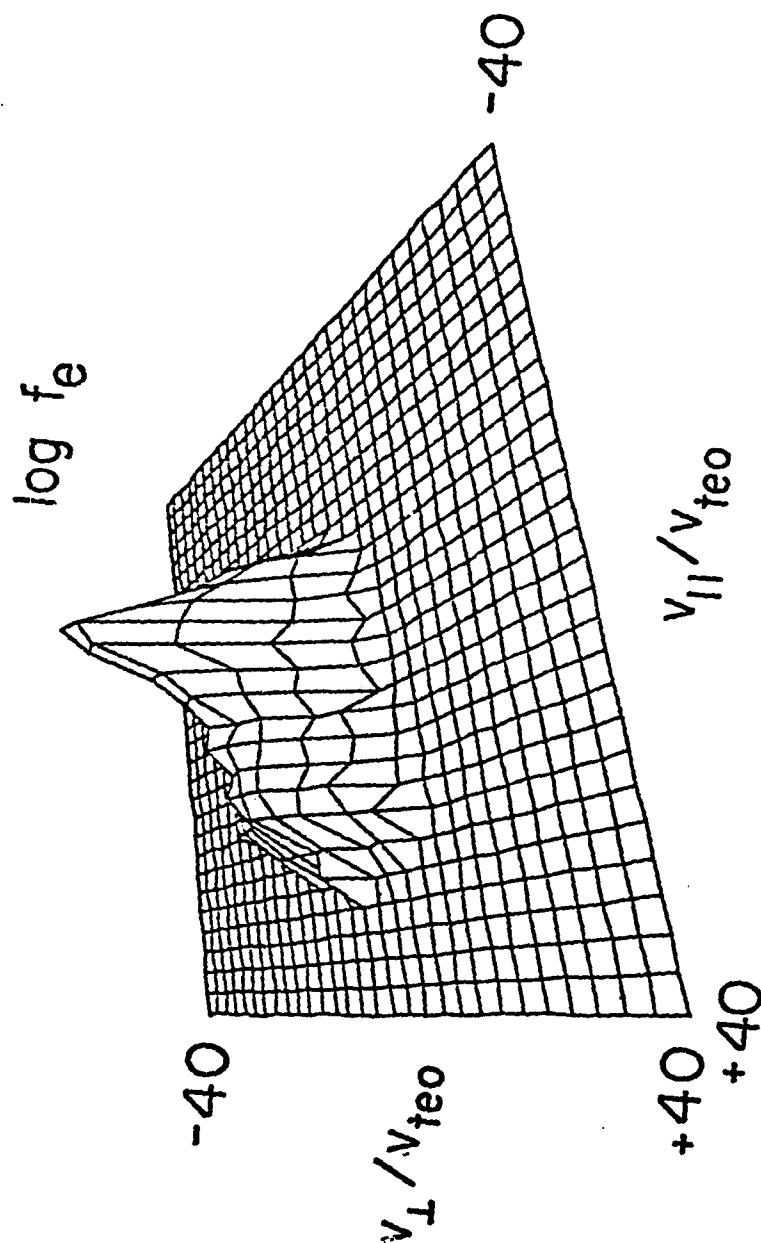


Figure 5

FRAME 1

Appendix H

WIRELESS GENERATION OF ELF/VLF RADIATION
IN THE IONOSPHERE

Wireless Generation of ELF/VLF Radiation in the Ionosphere

C. L. Chang,* V. Tripathi,*⁺ K. Papadopoulos,*⁺
J. Fedder,⁺⁺ P. J. Palmadesso,⁺⁺ and S. L. Ossakow⁺⁺

*Science Applications, Inc., McLean, VA 22102

⁺Permanent Address: University of Maryland,
College Park, MD 20742

⁺⁺Geophysical & Plasma Dynamics Branch, Plasma Physics Division
Naval Research Laboratory, Washington, D.C. 20375

ABSTRACT

The ionospheric plasma may be used as a nonlinear active medium for the generation of radio waves in the ELF/VLF frequency range. A number of different concepts have been proposed which seek to avoid difficulties associated with large and inefficient ground or satellite based antennas by creating a "virtual" antenna in the ionospheric plasma. There are two major approaches to the problem of creating a radiating current pattern in the ionospheric plasma without the use of solid conductors. The first approach involves the use of ground based pulsed r.f. transmitters or "heaters" to generate a periodic variation in the ionospheric conductivity in regions where strong natural current systems exist. The result is an A.C. component of current which radiates at the desired frequency. Modulation of the parallel conductivity in the auroral electrojet, for example, leads to the formation of a closed circular Hall current pattern which acts like a vertical magnetic dipole antenna. Modulation of the Pedersen or Hall conductivities in this region produces a double vortex current pattern with a strong linear component in the center, which acts like a horizontal electric dipole radiator. Studies are now being conducted to determine the optimum altitude for modulation, power requirements, etc. Preliminary results suggest that systems of this type should be feasible. The second approach to the creation of a virtual antenna involves the generation and mode coupling of two higher frequency waves to produce the ELF/VLF signal. In simplest form, this method involves the transfer of energy from two waves (ω, k) and (ω_1, k_1) to a low frequency third wave (ω, k) which satisfies the condition $\omega = \omega_1 \pm \omega_2$, ω_1 and $k = k_1 \pm k_2$ in some region of the ionosphere. Thus one can use efficient high frequency transmitters radiating either from the earth or from satellites to produce low frequency radiation. Many variations of this scheme are possible, depending on the choice of high frequency modes, excitation geometry, etc. Again, results of preliminary studies of systems of this type are promising. While some of these ideas have been suggested previously, considerable additional research is needed in order to establish an adequate theoretical base for experiment design and for assessment of the feasibility of these concepts for communications.

INTRODUCTION

A key Navy communications channel, especially for submarine communications, utilizes VLF and ELF frequencies. The technical and political problems associated with direct generation of ELF waves by ground based large antenna arrays¹ (i.e., Sanguine and Seafarer projects) have been recently reviewed by Starkey.² However, recent progress in theoretical and computational plasma physics,³ allows us to look confidently to the possibility of ELF generation and coupling in the earth ionosphere waveguide, by utilizing the ionospheric plasma as an active medium.⁴ The basic idea involves the formation of a virtual ELF antenna in the ionospheric plasma, using modulated HF ionospheric heaters.⁴ The resulting interactions are mainly nonlinear and go much beyond the usual Luxemburg effect type ideas. Conceptually, a variety of possible schemes could arise, depending on the use of particular nonlinear interactions and HF heaters based on the ground or space. In this paper we present preliminary results, with respect to two potential schemes. The first one relies on modulating pre-existing ionospheric currents, such as the auroral or equatorial electrojet, at ELF frequency, by modulating the conductivity of the ionospheric plasma through which they flow. The second relies on modified stimulated forward Brillouin scattering, of two HF modes off a low frequency compressible Alfvén mode.^{4,5} The excited Alfvén ionospheric eigenmode, couples in the

earth ionosphere waveguide and the horizontal part of its electric field penetrates into the water. It should be stressed that a major advantage of exciting the waveguide from the ionosphere rather than the ground is the fact that the relevant wavelengths in the dielectric are 10^3 smaller than in free space due to the high refractive index. We proceed below to discuss the two concepts separately.

CURRENT MODULATION

The first approach involves using a powerful ground antenna to modulate the ambient electron temperature T_e at a low frequency. The T_e variation changes the electron-neutral collision rate ν and indirectly modulates the ambient plasma conductivities through their ν dependence, i.e.,

$$\begin{bmatrix} \sigma_{Pe} \\ \sigma_{He} \\ \sigma_{||e} \end{bmatrix} = \frac{N_e e^2}{\pi} \begin{bmatrix} \nu / (\Omega^2 + \nu^2) \\ \Omega / (\Omega^2 + \nu^2) \\ 1/\nu \end{bmatrix} \quad (1)$$

where Ω is the electron gyrofrequency and σ_{Pe} , σ_{He} , $\sigma_{||e}$ are the Pedersen, Hall and parallel conductivities of the electrons, respectively. Any ionospheric current, therefore, oscillates in the modified region at the specified frequency. The current perturbation serves as a "virtual" antenna to radiate electromagnetic waves. In estimating the ELF efficiency of the concept, the following computations should be performed: (a) Determination of the ionospheric region where T_e relaxes to its ambient value at a rate τ^{-1} much faster than the ELF radiation frequency ω (i.e., $\omega\tau \ll 1$); (b) the energy deposition altitude profiles of the HF power, and the resulting modifications in the T_e and the electron conductivity profiles; (c) the modulated current patterns self consistently created by the conductivity modulation; and (d) the resulting antenna strength as a function of the frequency and the HF radiated power. We have developed a series of coupled numerical schemes to achieve the above tasks. We present below some very preliminary results, for a typical situation of an HF antenna with ERP (ERP = power x antenna gain) 100 MW, modulated at 100 Hz, for auroral electrojet parameters. We again caution the reader that the results are very preliminary and should be used with caution.

The answer to the first question can be found by the following considerations. The large heat capacity of the neutrals does not allow any significant ion temperature change. This restricts the interesting altitudes to regions where the electron conductivity dominates. According to Fig. 1, which plots the ambient conductivity profiles versus the altitude, this region lies below 100 km in altitude. Another important factor in determining the optimal heating region arises from the relaxation process of electron energy. Specifically, in order to modulate the electron temperature at ELF, T_e must relax to its ambient value in a time scale shorter than the modulation period. Therefore, we are restricted to conduct the experiment in a region where $\delta\nu > f$, with δ the average fraction of energy lost in each collision ($\delta \sim 10^{-3}$) and f the modulation frequency. This additional requirement further limits the interesting region to under 90 km in altitude.

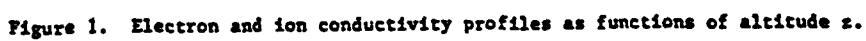
In computing the conductivity modifications the electron temperature $T_e(\tau)$ is given by

$$\frac{dT_e}{d\tau} = \left(\frac{2}{3N_e} \right) \frac{Q_0 K(z)}{4\pi z^2} \exp \left[-2 \int_0^z K(z') dz' \right] - \delta\nu_e (T_e - T_{e0}) \quad (2)$$

where Q_0 is the effective radiation power (ERP). The absorption coefficient $K(z)$ corresponds to the inverse of the local wave attenuation length and, for the case of parallel field propagation, can be expressed as

$$K(z) \approx \frac{\omega_e^2}{2c} \frac{\nu}{[\nu^2 + (\omega_b \pm \Omega)^2]} \quad (3)$$

where the + and - signs correspond to the polarization of the ordinary (O) and extra-ordinary (X) mode, and ω_e is the plasma frequency. We note that at lower ionospheric heights the electron heat conduction is negligible and the electron density variations are due to changes in the recombination rate which are also negligible. Equations (2) and (3) constitute the basic heating equations and can be solved by numerical integration. Heating curves are presented in Fig. 2 for the typical case; we plot the electron temperature T_e as a function of altitude after 1 msec of X and O mode heating. Most efficient absorption is ensured by selecting the frequency at $\omega_b \sim \Omega$ which maximizes the absorption coefficient in (3). One important feature of this figure is that the wave energy of the X mode gets absorbed rapidly at 70 km with little heating observed above 78 km. This can be understood as follows. At $\omega_b = \Omega$, the absorption coefficient has the simple relation $K(z) = N_e(z)/\nu(z)$. A sharp decrease in ν from 60 to 70 km leads to a marked increase in $K(z)$ and suppresses dissipation by reducing the background neutral collisions. This creates profound peaks in the temperature profile. At a higher heating frequency $\omega_b \gg \Omega$, as shown in the same figure, the absorption coefficient $K(z) = N_e(z)\nu(z)/\omega_b^2$ decreases gradually with height and the heated T_e profile exhibits no peak. This suggests that the heating characteristics are sensitive to both wave frequency and



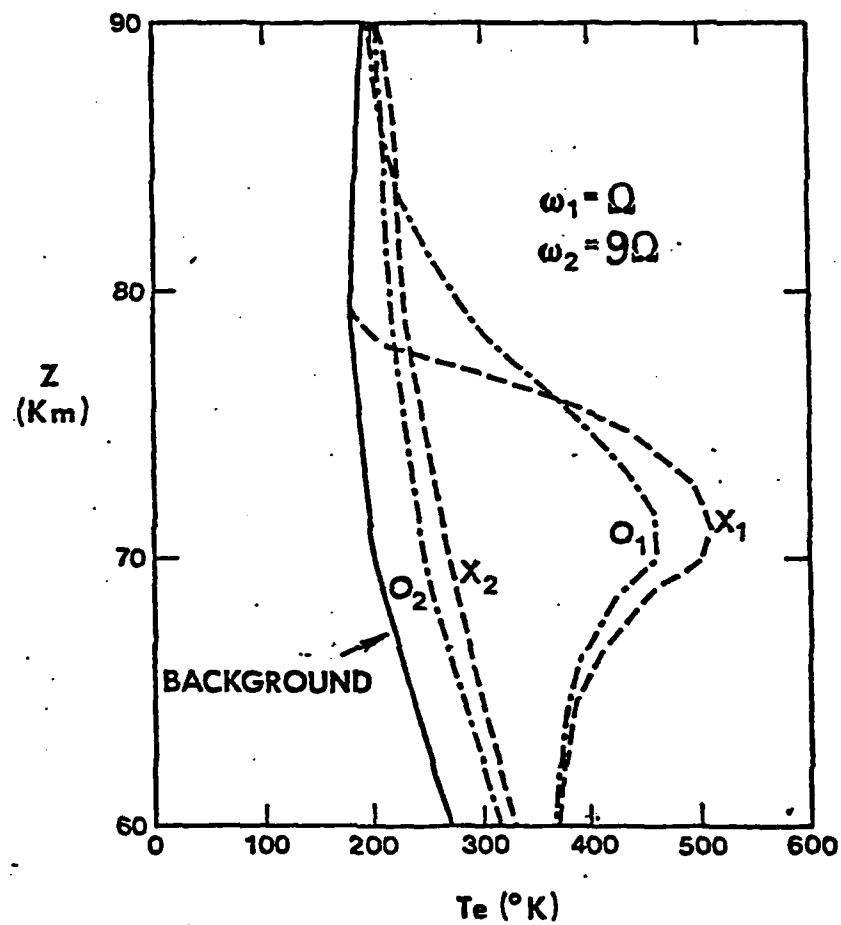


Figure 2. Modified electron temperature profiles $T_e(z)$ after 1 msec of heating at two different wave frequencies. X and O represent the extraordinary and ordinary modes of propagation.

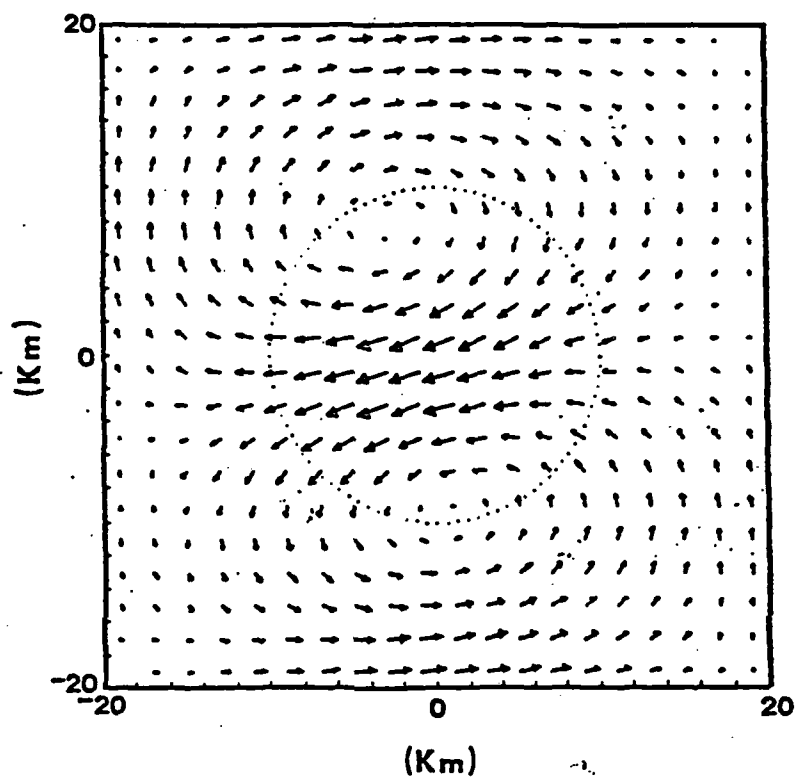


Figure 3. Illustration of the perturbed current pattern. The modified region is specified by the dotted circle with a radius of 10 km. The ambient electric field in this case is taken to be $E_0 = 25$ mV/m in the x direction and the magnetic field points into the paper.

background neutral and electron concentrations. In Fig. 2, the percentage changes of total conductivities at the temperature peak (for the X mode) are estimated to be -35% for σ_p and -70% for σ_H .

To simplify the description of the ionospheric current modulation, we reduce the problem to two dimensions by introducing the height-integrated conductivities Σ_p and Σ_H . The height-integrated current density is then

$$\underline{J} = \underline{\Sigma} \cdot \underline{E}$$

where

$$\underline{\Sigma}(x,y) = \begin{bmatrix} \Sigma_p & \Sigma_H \\ -\Sigma_H & \Sigma_p \end{bmatrix} \quad (4)$$

is the conductivity tensor. The total electric field \underline{E} is the sum of an ambient field \underline{E}_0 and a perturbation $\underline{E}_1 = -\nabla\phi$, with \underline{E}_0 pointing in the x direction. From the current continuity equation $\nabla \cdot \underline{J} = 0$, we obtain

$$\frac{\partial}{\partial x} \left(\Sigma_p \frac{\partial \phi}{\partial x} \right) + \frac{\partial}{\partial y} \left(\Sigma_p \frac{\partial \phi}{\partial y} \right) + \left(\frac{\partial \Sigma_H}{\partial x} \right) \left(\frac{\partial \phi}{\partial y} \right) - \left(\frac{\partial \Sigma_H}{\partial y} \right) \left(\frac{\partial \phi}{\partial x} \right) = \epsilon_0 \frac{\partial \Sigma_p}{\partial x} - \epsilon_0 \frac{\partial \Sigma_H}{\partial y} \quad (5)$$

This equation is solved numerically for $\phi(x,y)$ with a given set of Σ_p and Σ_H profiles. Knowing ϕ , one can calculate the current perturbation \underline{J}_1 from the expression

$$\underline{J}_1 = -\underline{\Sigma} \cdot \nabla \phi \quad (6)$$

An illustration of this current pattern is presented in Fig. 3.

From this figure we can see that the current perturbations form a double vortex flow pattern with a strong linear component in the center. This component is in the opposite direction of the ambient Pedersen current and is located inside the main lobe of the conductivity profile. As seen from Fig. 3 the flow pattern corresponds to an equivalent horizontal electric dipole radiation source. The strength of the dipole can be determined, by numerically integrating over the distribution $\underline{J}_1(x,y)$. The resulting dipole moment for ionospheric electric fields of the order $E = 25$ mV/m, is on the order of 10^4 Am. Using Wait's formula,⁶ we can estimate the ELF field on the ground as $E \approx 10^{-6}$ V/m and $H \approx 10^{-7}$ A/m indicative of interesting signal to noise ratios.

PARAMETRIC EXCITATION

The parametric excitation of ELF, does not rely on the presence of ionospheric currents, providing us with greater freedom in site selection and relative independence from the ionospheric state. The particular nonlinear mechanism considered is the parametric decay of an HF pump radio-wave (ω_0, k_0), where $\omega_0 \gg \omega_e$, into a low frequency (ω, k) compressional Alfvén wave and a high frequency sideband $\omega_1 = \omega_0 - \omega, k_1 = k_0 - k$, which is also directly driven from the ground. The double resonance excitation is advantageous over the single parametric excitation for ELF communications, because it tunes the desired ELF frequency and reduces the instability threshold. Since for ELF frequencies $\omega \ll \omega_0, |k| \ll k_0$, the process is analogous to forward stimulated scattering off Alfvén waves. In order to determine the coupling efficiency and the instability threshold, we compute first the ponderomotive force due to the waves (ω_0, k_0) and (ω_1, k_1) and from this the growth rate γ_0 for a homogeneous plasma. Following the derivation of Papadopoulos et al.,⁵ we find

$$\gamma_0 = \frac{k_x^2 V_0^2 \omega_1}{16 \omega \omega_0} \quad (7)$$

where k_x is the wave-vector in the direction perpendicular to both \underline{E}_0 and the ambient magnetic field, ω_1 is the ion plasma frequency and $V_0^2 = e^2 E_0^2 / m_e^2 \omega_0^2$. As an order of magnitude result $\gamma_0 \approx 10^2 \text{ sec}^{-1}$, for a 10 MW, 5 MHz transmitter with a $G = 10^3$ at ionospheric altitudes of 120 km.

Due to the existence of the vertical density profile and the finite region of the interaction, the wave resonance conditions are satisfied only locally. We should therefore examine the boundary value inhomogeneous problem. Using the Rosenbluth techniques,⁷ and taking the x axis as the vertical (parallel to ∇n) and z as the horizontal, we find that in the WKB approximation the mode coupled equations read⁵

$$\frac{\partial c}{\partial t} + \frac{V_z}{2} \cdot \frac{\partial c}{\partial z} = \gamma_0(z) c_1 \exp \left(-\frac{1}{2} \frac{k^2 x^2}{2} \right) \quad (8)$$

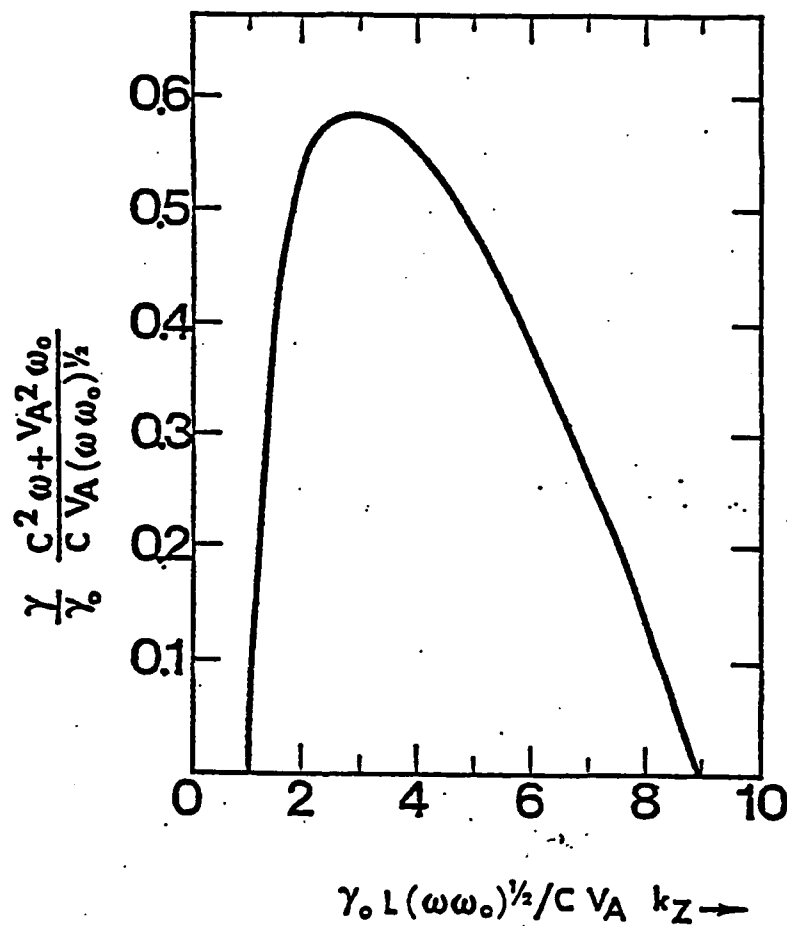


Figure 4. Growth rate of the fastest growing Alfvén wave for a gaussian pump in an inhomogeneous plasma. The parameters are: rf power density $\sim 0.5 \text{ W/m}^2$, $\omega_0 \sim 5 \text{ MHz}$, $\omega \sim 10^2$, $\Omega \sim 2 \times 10^2 \text{ rad. sec}^{-1}$, $c/V_A \sim 10^3$, $L \sim 3 \text{ km}$.

$$\frac{\partial c_1}{\partial t} + \frac{v_{g1}}{v_{g1}} \cdot \frac{\partial c_1}{\partial x} = \gamma_0(z) c \exp\left(\frac{ik'x^2}{2}\right) \quad (9)$$

where $c_1 = E_1 V_A / c$, $c = E_2 (w_0/w)^{1/2}$, $v_{g1} = V_A^2 k/w$, $v_{g2} = c^2 (k-k_0/w)$, and V_A is the local Alfvén speed. Details of the numerical solution of the above Eqs. can be found in Papadopoulos et al.⁵ We restrict ourselves here to some of the key points. For a gaussian pump profile e^{-x^2/L^2} , the growth rate as a function of the extent of the pump is shown in Fig. 4. This was computed for the particular case where the parameter

$$\lambda = \frac{v_{g0}^2}{v_{g1} v_{g2}} \left(\frac{dk}{dx}\right)^{-1} \quad (10)$$

was $\lambda = 2$ (it corresponds to HF power density $.5 \text{ W/m}^2$ at 5 MHz, for $w = 10^2$ at 120 km altitude). It is obvious from Fig. 4 that the instability is absolute for values of $\gamma_0 L (w/w_0)^{1/2} / k_z c V_A$ between 1 and 9. The growth rate maximizes at

$$\gamma_{\max} = 0.2\gamma_0 \quad (11)$$

This condition can be achieved by a 20 MW transmitter having a large gain $G \approx 10^4$ (i.e., $L \approx 3 \text{ km}$). For more details on this scheme we refer the interested reader to Papadopoulos et al.⁵ A determination of the amplitude of the excited waves requires a nonlinear theory and is presently under consideration. The theoretical upper limit will be given by the Manley-Rowe relations, which will give power levels in the source region of the order of $(w/w_0) \text{ ERP} \approx 10^3$ watts. We are therefore aiming at only a few percent of the theoretical limit.

SUMMARY AND CONCLUSIONS

We have presented here some preliminary results indicating that with present day technology ELF waves at powers of interest for submarine communications, could be generated. In the current analysis only the simplest approach has been examined. Effects such as the three dimensionality of the currents, the role of the ponderomotive force on local density profile modifications, anomalous HF absorption and many others are presently under study and will be reported in time.

At this point we should comment on the experimental stage of the ideas. A number of results have appeared in the literature, following the initial suggestion by Papadopoulos⁴ of their potential interest for Navy communications. The most extensive work has been done in the USSR; however, very few results appeared in the literature. The most interesting result was reported by Kapustin et al.,⁸ which showed 2 kHz generation from 5 MHz modulated pumps. The opening of the Tromsø, Norway, heating facility last year by the Max Planck Institute, offers the possibility of testing some of these ideas.⁹ Actually, Kopka and Stubbe (private communication, 1980) have observed, on the ground near the antenna site, low frequency waves (500 Hz - 2 kHz) when modulating auroral electrojet currents at the appropriate frequency. They also detected micropulsations. Finally, we should mention an ongoing effort at the Pennsylvania State University, which is still at a very preliminary stage.¹⁰ In summary, the experimental results are very rare, not well documented and not properly guided by theoretical planning to produce conclusive evidence of the particular interactions occurring and their potential optimization. The preliminary evidence is, however, positive.

In concluding we should mention that a well coordinated experimental and theoretical effort is urgently needed in this area. The design and optimization aspects require extensive theoretic nonlinear plasma physics input, and cannot be achieved by random experimentation. From the other side, idle theorizing without experimental guidance is apt to be an equally futile exercise, as far as practical systems are concerned.

ACKNOWLEDGEMENT

One of the authors (K.P.) greatly appreciates many discussions with Drs. T. Coffey, P. Stubbe, N. Kopka, A. Drobot, R. Sharma, and P. Sprangle. This work was supported at SAI by NRL Contract No. N00173-80-C-0194 and at NRL by ONR and NAVELEX.

REFERENCES

1. S. L. Bernstein, M. L. Burrows, J. E. Evans, A. S. Griffiths, D. A. McNeill, C. W. Niessen, I. Richer, D. P. White, D. K. Willim, "Long Range Communications at ELF," M.I.T. Lincoln Laboratory Report, 1973.
2. R. Starkey, Military Electronics/Countermeasures, p. 26, Jan. 1981.
3. C. S. Liu, "Parametric Instabilities in Inhomogeneous Unmagnetized Plasmas," Advances in Plasma Physics, Volume 6, pg. 83, 1976.
4. K. Papadopoulos, "Nonlinear Production of ELF Waves by Two High Frequency Waves," March 1975 (NRL Plasma Physics Division, internal report).
5. K. Papadopoulos, R. R. Sharma, and V. K. Tripathi, SAI Report 81-343-WA (1981). (Phys. Rev. Lett., communicated).
6. J. Wait, Electromagnetic Waves in Stratified Media, Pergamon Press, 1962.
7. M. Rosenbluth, Phys. Rev. Lett., 29, 565, 1972.
8. I. N. Kapustin, et al., JETP Lett., 24, 228, 1977.
9. P. Stubbe and H. Kopka, J. Geophys. Res., 82, 2319, 1977.
10. A. J. Ferraro and H. S. Lee, Penn. State University Report PSU-IRL-FR-79/1 (1979).

Appendix I

ELF CURRENT GENERATION IN THE IONOSPHERE

ELF CURRENT GENERATION IN THE IONOSPHERE

by:
George Schmidt

Abstract

Two mechanisms for current generation in the ionosphere are investigated. In the first, momentum of waves generated by a land based antenna are absorbed by electrons. In the second the magnetic moment of electrons is enhanced by cyclotron resonance in the polar region, giving rise to currents due to magnetic mirror effects. The two effects are additive with the first one dominating in the highly collisional ionosphere. Order of magnitude estimates indicate that with a land based antenna of 100MW power, significant currents can be generated.

INTRODUCTION

In order to produce ELF electromagnetic waves for communication, the use of an ionospheric antenna has been suggested. Various mechanisms for low frequency current generation in the ionosphere have been proposed, in particular parametric excitation of such waves from a land based antenna structure,¹ and electrojet current modulation.² Here we wish to point out two other possible avenues to reach the same goal.

1. A land based antenna radiating into the ionosphere produces waves that can easily be absorbed by ionospheric plasma electron. Regardless of the absorption mechanism, the momentum of photons is converted into the momentum of electrons giving rise to a current.³ If the wave is pulsed this gives rise to current pulses, that can be used as an antenna. If the wave is reflected rather than absorbed a factor of two is gained in the current.
2. The earth's magnetic field forms a magnetic mirror. If the energy of the electromagnetic wave in the polar region is absorbed by electrons via cyclotron resonance, the magnetic moment of these electrons is

increased, resulting in increased acceleration of these particles along the magnetic field toward the equatorial plane. Now the background magnetic field provides the source of momentum to produce the desired current.

MOMENTUM ABSORPTION

Consider electromagnetic waves propagating along the earth's magnetic field carrying energy E , momentum $p = E^k/w$. For simplicity we take $w/k = c$, so $p = \epsilon/c$. This momentum is absorbed by a cylindrical volume of plasmas, cross sectional area A , length L . If the free electron density is n , the current generated is

$$I = enA\delta v \quad (1)$$

where δv is the velocity increment of the electrons due to photon absorption. From momentum conservation

$$\epsilon/c = ALnm\delta v \quad (2)$$

Substituting δv from (2) into (1) results in

$$IL = -\frac{e\epsilon}{mc} = 586\epsilon \quad (3)$$

Note that (3) does not depend on the size of the absorption volume, electron density, or any other details of the

AD-A111 638

SCIENCE APPLICATIONS INC MCLEAN VA
GEOPHYSICAL PLASMAS AND ATMOSPHERIC MODELING.(U)

F/O 4/1

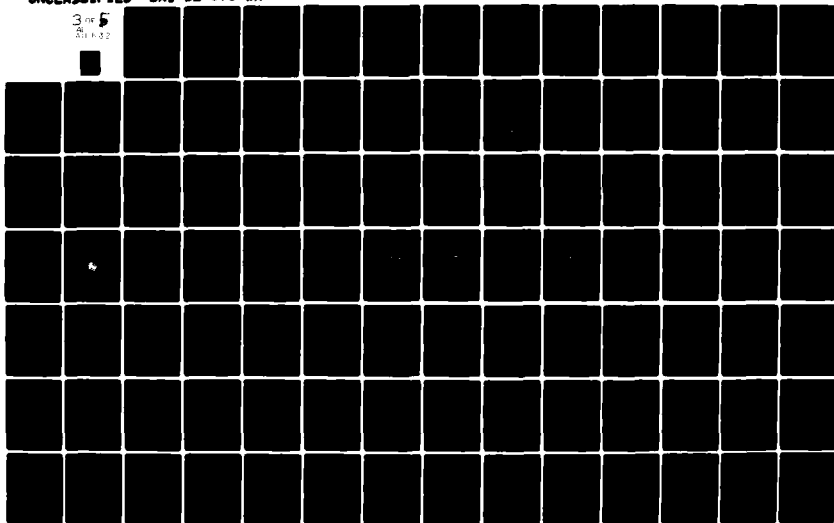
JAN 82 E HYMAN, J APRUZESE, S BRECHT, W CHAO
SAI-82-676-WA

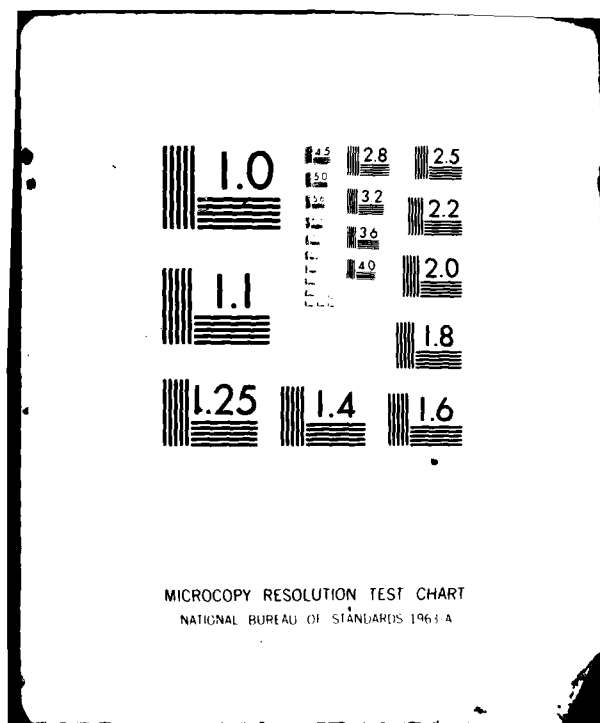
N00014-81-C-2038

NL

UNCLASSIFIED

3 of 5
SAI 1-32





absorber. A more elaborate calculation, integrating over a nonuniform plasma yields the same result. If the wave, instead of being absorbed, is reflected, the electrons take up twice the wave momentum $p = 2\epsilon/c$, and one has

$$IL = -1172\epsilon \quad (4)$$

So far we have not considered the interaction of the electrons with the environment. The effect of electron-neutral, electron-ion collisions is easy to account for. If the collision frequency is ν , the effective acceleration time is ν^{-1} , so in (3) and (4) $\epsilon = P\nu^{-1}$, where P is the radiated power. Since ν is sensitively dependent on light over the ground, this results in a strong dependence on the number of Amp meters generated. Good results can be obtained above an altitude of 100 kms, where $\nu < 10^4 \text{ sec}^{-1}$. With a power of 100 MW, $\nu = 10^4 \text{ sec}^{-1}$, one obtains from (3) $IL = -5, 86.10^6 \text{ Am}$, which is quite respectable. The drawback is the higher altitude than the one used in the electrojet generation scheme.

The electromagnetic interaction with the background magnetoplasma is more difficult to calculate. The push on the electrons due to photon absorption is equivalent to an electromotive force, driving the current. One expects that this current will close outside the absorption region, creating a dipole type current configuration. So the

problem boils down to the investigation of the following model.

An electromotive force is generated in a closed region. Calculate the current pattern in a tensor dielectric with $\Delta \cdot \vec{J} = 0$ (\vec{J} is the current density). This calls for a numerical calculation, similar to the one by Chang and Papadopoulos² for the electrojet modulation problem.

The equivalent electric field E_0 , due to power absorption is easily estimated

$$E_0 \approx \frac{P}{cV_{eh}} \quad (5)$$

where P is the power absorbed in volume V .

MIRROR ACCELERATION

Consider now the situation where an electron in the polar region picks up the energy δW_{\perp} , perpendicular to the magnetic field B by cyclotron acceleration. This results in an increase of its magnetic moment $\delta \mu_m = \delta W_{\perp} B^{-1}$. In consequence there will be an incremental acceleration along the B field $\delta \dot{V}_{\parallel} = -1/m \delta \mu_m dB/dx$, where B is the coordinate along the magnetic field. The particle (without interaction with others) arrives at the equatorial plane with the incremental velocity

$$v_{\parallel} = \frac{W_{\perp}}{m} \int \frac{1}{B} \frac{dB}{dx} \frac{J}{v_{\parallel}} dx \quad (6)$$

For an order of magnitude estimate we replace v_{\parallel} with some average $\langle v_{\parallel} \rangle$, and integrate to obtain

$$\delta v_{\parallel} = \frac{\delta W_{\perp}}{m \langle v_{\parallel} \rangle} \ell n \frac{B_1}{B_0} \quad (7)$$

where B_1 is the magnetic field at the polar, B_0 at the equatorial region.

For n electrons per unit volume, this leads to the current in the equatorial plane, using (1) and (7)

$$I \approx - en A \frac{\delta W}{m \langle v_{\parallel} \rangle} \ell n \frac{B_1}{B_0} \quad (8)$$

The energy absorbed by all electrons is $\epsilon = LAn\delta W$, to yield

$$IL \approx \frac{e\epsilon}{m \langle v_{\parallel} \rangle} \ell n \frac{B_1}{B_0} \quad (9)$$

Since $\ell n \frac{B_1}{B_0}$ is of order unity, it seems that the current generated is $c/\langle v_{\parallel} \rangle$ times larger than the one obtained by momentum absorption, an enormous increment.

The fly in the ointment is our neglect of collisions. In reality electrons collide many times in their passage from the polar to the equatorial region.

A more realistic approach is the calculation of the equivalent electric field from $-eE_1 = -\delta\mu_m dB/dx$, or

$$E_1 = \frac{\delta W_{\perp}}{B_e} \frac{dB}{dx} \quad (10)$$

This is to be compared to the equivalent electric field from momentum absorption. Since $P/v_{\parallel} \approx \delta W/\tau$, where τ is the mean collision time, from (5)

$$E_0 \approx \frac{\delta W}{c\tau e} \quad (11)$$

So finally

$$\frac{E_0}{E_1} \approx \frac{L}{c\tau} \approx 7, 1.10^{-3} v \quad (12)$$

where L is the characteristic scale length of the earth's magnetic field. This ratio is typically larger than one so the first process is more effective.

It should however be emphasized that these two mechanisms are not competing but cooperating. As energy is being absorbed by the electrons to increase their magnetic moment, momentum is simultaneously absorbed.

The next task is a numerical study on collective effects in an anisotropic lossy dielectric to determine the current pattern.

REFERENCES

1. K. Papadopoulos, "Nonlinear Production of ELF Waves by Two High Frequency Waves," March 1975 (NRL, Internal Report).
2. C. L. Chang, K. Papadopoulos, "ELF Communication by Electroject Current Modulation," July 1981 (SAI Internal Report).
3. G. Schmidt, Phys. Letters, 74A, 222 (1979).

Appendix J

STRUCTURING CAUSED BY RAYLEIGH-TAYLOR INSTABILITY

STRUCTURING CAUSED BY RAYLEIGH-TAYLOR INSTABILITY

Stephen Brecht

Ellis Hyman

Science Applications, Inc.

McLean, Virginia 22102

Peter J. Palmadesso

Geophysical and Plasma Dynamics Branch

Plasma Physics Division,

Naval Research Laboratory

Washington, D.C. 20375

In addressing the question of the wavelengths of structures that LWIR sensors might encounter in an atmosphere disturbed by a high altitude nuclear event we have made use of some calculations and models developed for DNA to address the early time jetting of plasma across magnetic field lines and field aligned acceleration of plasma. These calculations and models make use of the detailed work on the collisionless coupling between expanding debris and ambient air. It is our opinion that structure created at early times, i.e., < 10 sec will greatly affect systems for hundreds of seconds after the burst. In addition to effects on the system produced by stimulated plasma emission from high electron densities, we feel that radiation from or scatter by metallic ions or their oxides resulting from chemistry during the mixing of high densities of metallic ions and oxygen could present a major problem to LWIR systems. This latter effect could be particularly important in regions either horizontal to or above the burst point where electron densities are not expected to be extremely large.

The calculation of the minimum and maximum wavelengths for the structure is based on studies of the Rayleigh-Taylor instability. The Rayleigh-Taylor instability has been discussed for many years as a candidate for causing early time structure particularly in situations where the plasma is collisional, such as low altitude bursts or perhaps the bottom side of a standard Spartan. One of the earliest references is probably Zinn et al., 1965. The Rayleigh-Taylor instability that will be discussed here is driven by terms that result from small scale kinetic instabilities which provide the interaction between rapidly expanding debris and air in a collisionless plasma (Lampe et al., 1975, and Clark and Papadopoulos, 1976). It is found that this interchange instability is operative during a high altitude nuclear detonation (Brecht and

Papadopoulos, 1979). Comparison between Starfish data and the predictions of phenomena resulting from this instability appear to agree and explain the existence of very high altitude debris in times less than 30 sec (Brecht et al., 1981).

A very brief summary of the expected dynamics of the plasma is as follows. As the ionized debris expands outward from the burst point it interacts with the ambient air. At lower altitudes (≤ 150 km) this interaction is collisional. For high altitude bursts and especially for the portion of the burst going upward, classical collisions are rare. In this latter case plasma instabilities are excited which couple the expanding debris and the air to form a shock. The very thin region which interfaces the bulk of the expanding debris and the cold air is called the coupling shell. Within this region resides the metallic debris and the air ions that are picked up and mixed. The dynamics here is extremely complicated but suffice it to say that it provides the mechanism for the Rayleigh-Taylor instability described by Brecht and Papadopoulos. This instability occurs with very definite upper and lower limits on participating wavelengths. These limits depend on local plasma parameters such as temperature, density, magnetic field, and gradient scale lengths. Once the instability is operative it can reach the nonlinear regime where the perturbations to the expanding shell can actually detach themselves from the shell and $E \times B$ drift across the magnetic field lines. This kind of jetting was observed in Starfish and has certain characteristics that allow comparison between data and this theory (Brecht et al., 1981). The result of all this is that not only is the expanding shell expected to be structured, but one could also reasonably expect discrete blobs of plasma to break off.

The data displayed here is the result of merging the Rayleigh-Taylor calculations with a code which models the temporal evolution of the basic plasma parameters in the coupling shell. This code is called SCORPIO and is basically described in a report by Clark and Papadopoulos (1976). It is not a hydrocode, but a code developed to model the evolution of the coupling shell in terms of thickness, temperature, plasma density, and field aligned acceleration. It maintains an energy budget and depletes the coupling shell of material and energy in a time dependent fashion consistent with our best knowledge of the microphysics active in this region. For general hydro it relies on a snowplow model. Therefore the global features such as radius are not as accurate as the high resolution codes from which it is derived.

The result of uniting the Rayleigh-Taylor theory with the SCORPIO code are shown in the accompanying figures. The first set of graphs show the maximum and minimum wavelength for the instability as a function of time for several angles relative to the ambient field direction. The data here is displayed as a function of angle where zero is along the field line in a downward direction. One finds that the instability for a standard Spartan begins to grow one second after the detonation. Note that the squares represent the maximum wavelengths and the triangles the minimum. The wavelengths range from about 1 km to 20 km for the various angles. The size of the actual striation will of course be $1/2$ the wavelength. Therefore this instability induces structures ranging in size from $\sim .5$ km to ~ 10 km at times of 5 sec or less. The next set of figures shows the growth rates associated with the instability at the maximum and minimum wavelengths. The convention for the boxes and triangles carries over to these plots. The boxes represent the growth rate for the maximum

wavelength and so forth. One notes here that the maximum wavelengths have the highest growth rates. It is expected that the long wavelength modes would go unstable first and, having reached saturation, the shorter wavelength modes would develop.

The figure shows ion density in the coupling shell as a function of time. It is expected that the ion density in the coupling shell will be representative of the density in the structures at the time of instability onset. The line denoted by the squares represents the total ion density in the shell including both debris and picked up air. The calculation continuously accounts for the loss of ions down the field lines due both to thermal effects and to field aligned acceleration. The second line (triangles) is our best estimate of debris density. It has been assumed that the nominal mass of the ion is 27. It is this second line that we feel provides cause for concern. At times of 2 seconds one finds debris density of 10^6 cm^{-3} or so. We have not done the chemistry here, but oxidation processes occurring on the time scales of interest (100 sec), would provide large amounts of radiation in the LWIR. The next set of graphs shows the ion temperature as a function of time and angle. One notes that in the direction upward the temperature remains high. The ions will, in fact continue to cool at later times, but by this time pieces of the plasma may be well removed from the original disturbed region.

The last plot gives the radius of burst as a function of time and angle as computed by the code. It is here to provide general information regarding the calculation.

These then are the data resulting from merging the analytic treatment of the Rayleigh-Taylor instability with the large scale numerical results. The data has been limited to times of 5 secs and earlier and

angles of 72° or higher. The latter limitation is due to the increasing classical collisionality in the downward direction for bursts of this altitude. For very high altitude bursts these restrictions on the output can be relaxed. As mentioned earlier the theory did not include classical collisions and therefore any numbers, no matter how reasonable, are suspect in regions where classical collisions are dominant.

The results of this work indicate several features that must be considered in assessing the LWIR problem. First, there will be structuring and transport of ionic material across magnetic field lines. Second, the material will consist of metallic debris in significant concentration, as well as oxygen that is picked up by the expanding debris. If the Starfish data is any indication some of this material will be found at large distances from the burst point. Finally, the size of the structured material will range from .5 km to ~ 10 km. The instability favors longer wavelengths, but the shorter ones can grow on the large scale perturbations. The initial structure is expected to form in less than 5 sec after detonation and remain for hundreds of seconds.

References

- S. H. Brecht, C. Agridellis, E. Hyman, and P. J. Palmadesso (1981),
see authors for reference.
- S. H. Brecht, and K. Papadopoulos, "Cross-Field Jetting of Energetic
Ions Produced by Rayleigh-Taylor Instability," NRL Memo Report 4068,
1979.
- R. W. Clark and K. Papadopoulos (1976) see authors for reference.
- J. Finn, H. Hoerlin, and A. Petschek, "The Motion of Bomb Debris
Following the Starfish Test," Radiation Trapped in the Earth's
Magnetic Field (Proceedings of the NATO Advisory Study Institute),
(Norway), 1965.
- M. Lampe, W. M. Manheimer, and K. Papadopoulos, "Anomalous Transport
Coefficients for HANE Application Due to Plasma Micro-Instabilities,"
NRL Memo Report 3076 (1975).

Figure Captions

Figure 1. Maximum and minimum wavelength as a function of time. The angles shown on each plot with respect to the local magnetic field line with zero being directed downward.

Figure 2. Growth rates for the maximum and minimum wavelength. The squares refer to the maximum wavelength and the triangles refer to the minimum wavelength.

Figure 3. Ion density as a function of time for various angles. Squares represent total ion density. The triangles represent debris ion density, assumed mass 27.

Figure 4. Ion temperature as a function of time for various angles with respect to the magnetic field lines.

Figure 5. Radius of coupling shell for relevant angles and times.

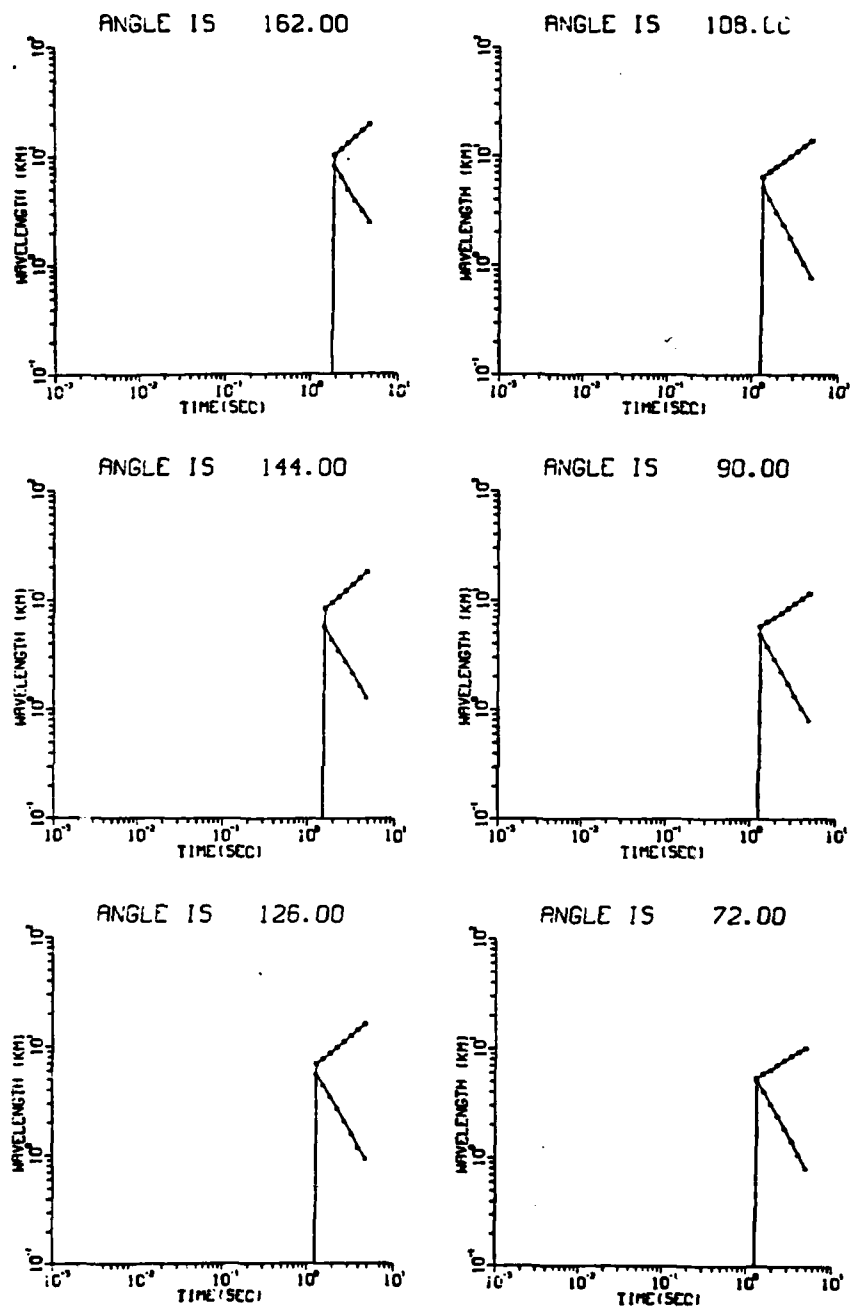


Figure 1.

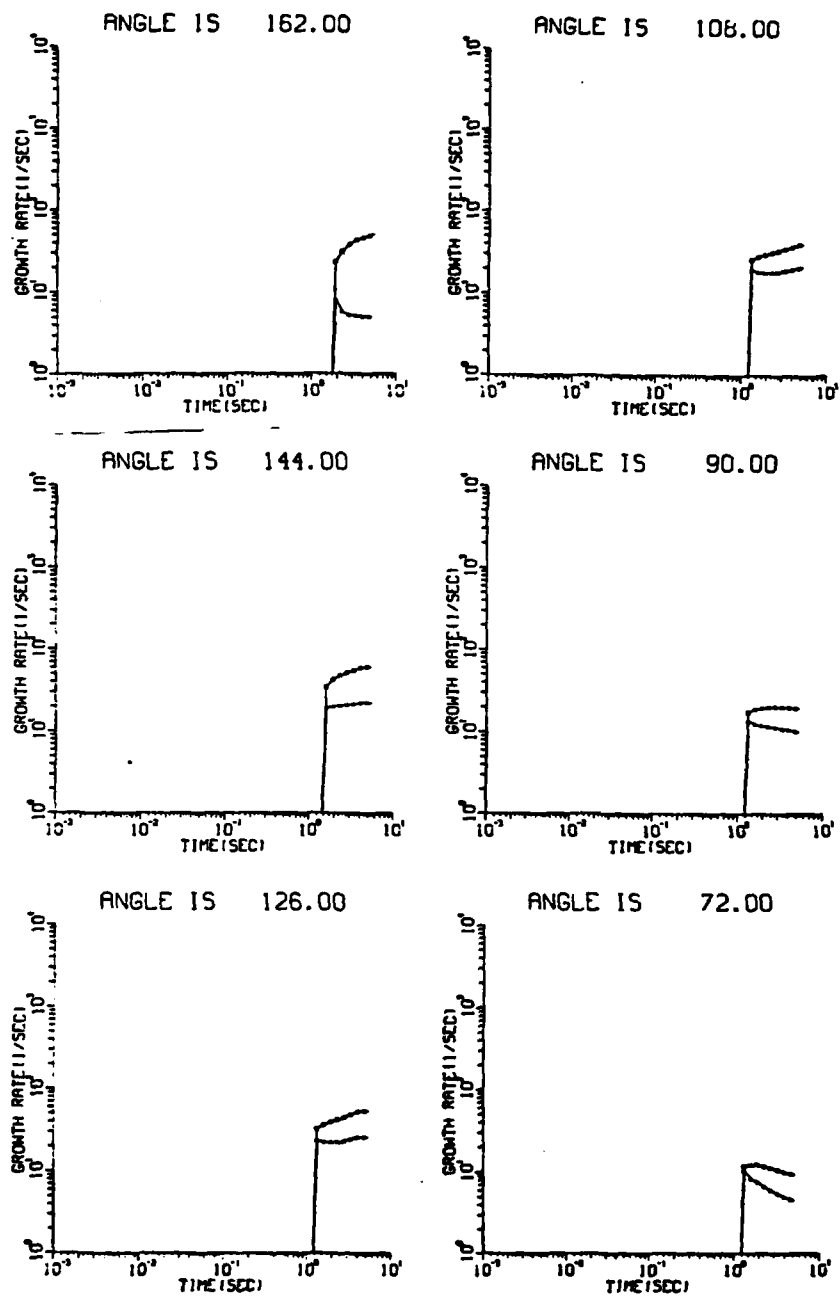


Figure 2.

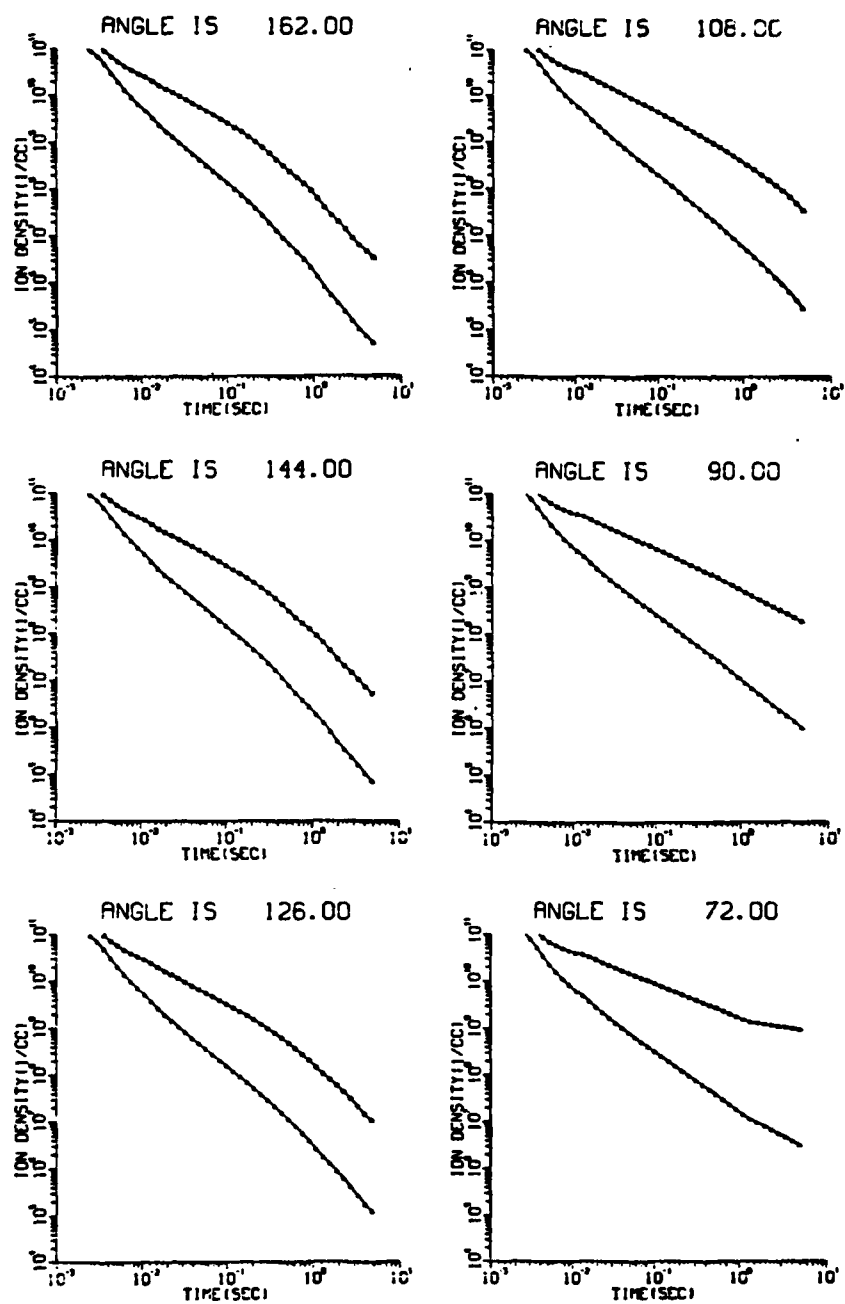


Figure 3.

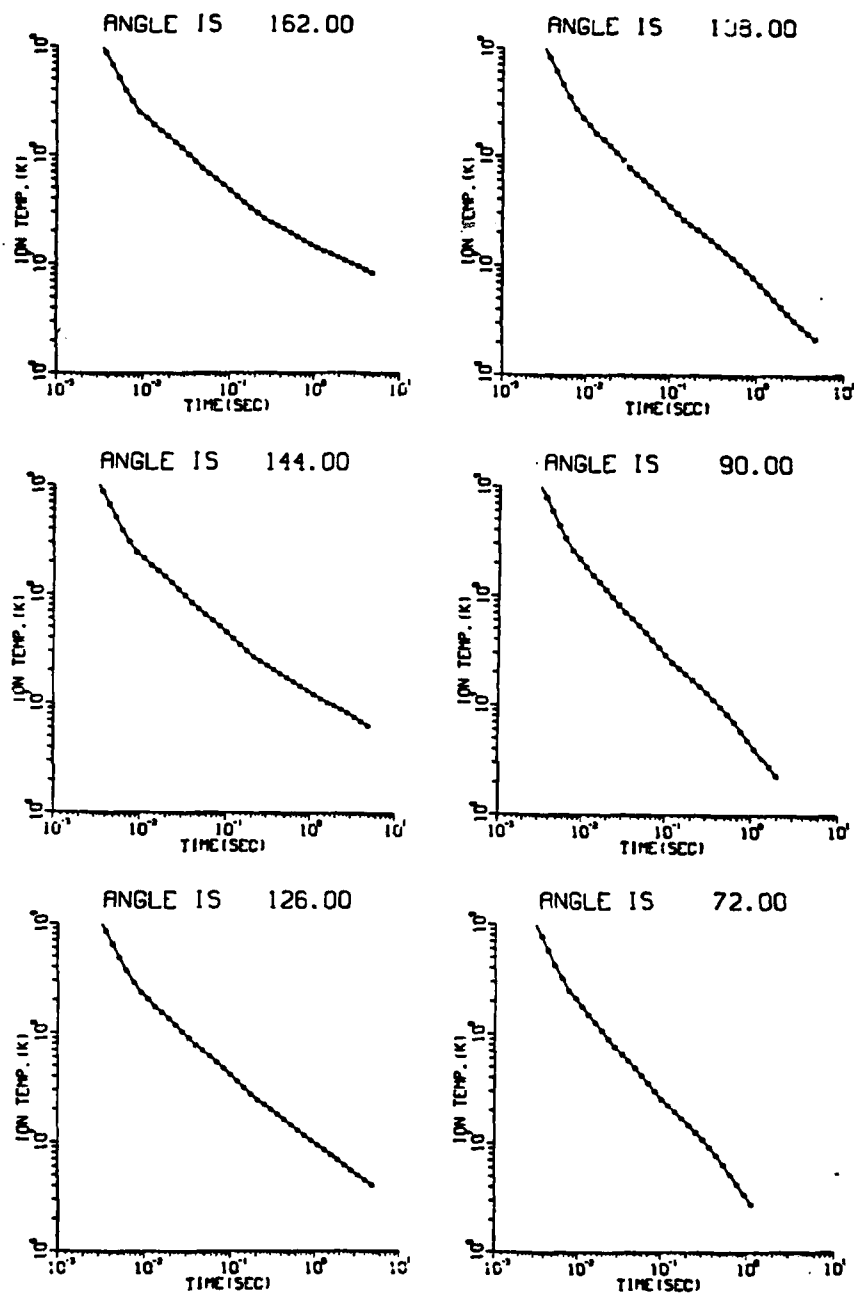


Figure 4.

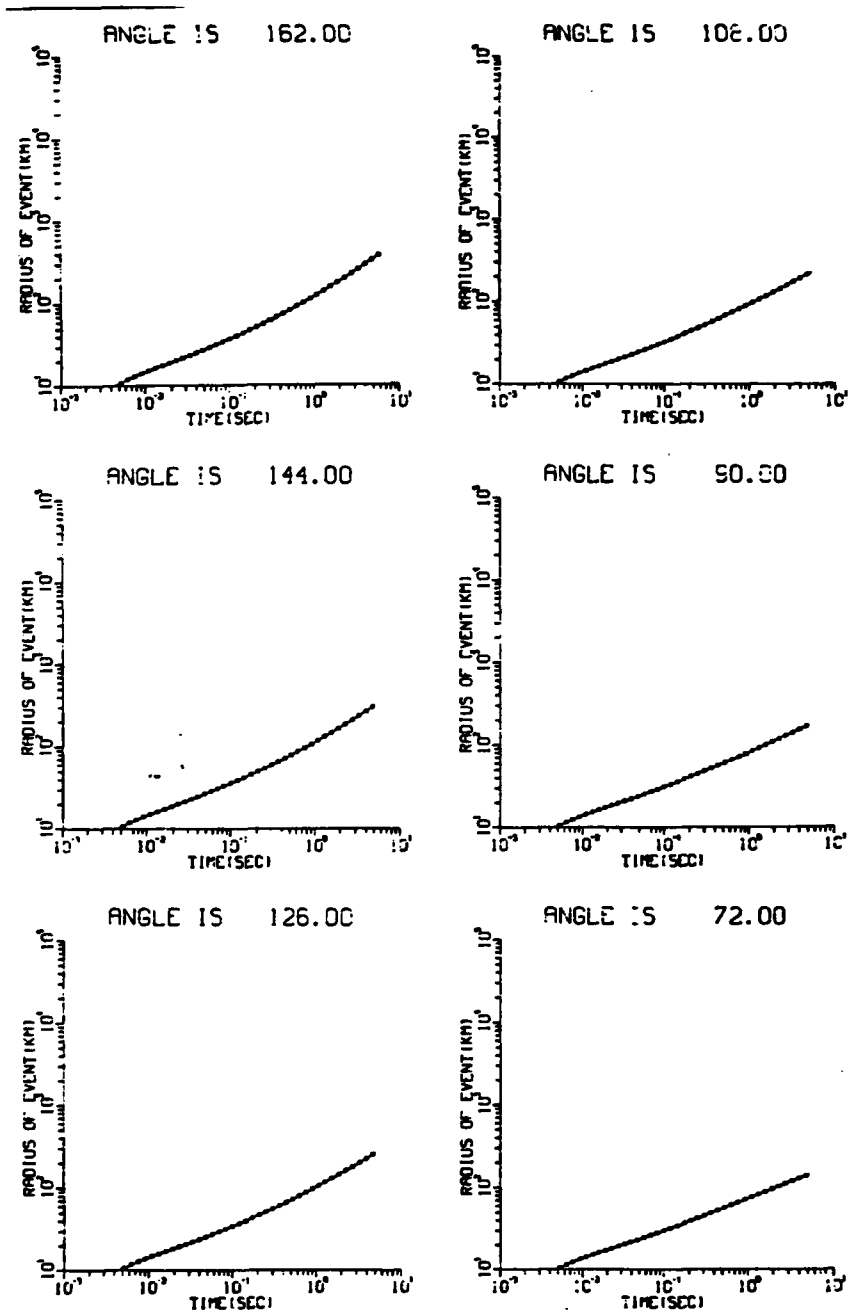


Figure 5.

Appendix K

PRELIMINARY NUMERICAL SIMULATION OF IR STRUCTURE
DEVELOPMENT IN A HYPOTHETICAL URANIUM RELEASE

Preliminary Numerical Simulation of IR Structure Development in a Hypothetical Uranium Release

E. HYMAN

*Science Applications, Inc.
McLean, VA 22102*

M. MULBRANDON AND S. L. ~~ORLANDO~~

*Geophysical and Plasma Dynamics Research
Plasma Physics Division*

B. E. McDONALD

*Naval Oceanographic Research and Development Activity
Bay St. Louis, MS 39520*

November 16, 1981

This research was sponsored by the Defense Nuclear Agency under Subtask S99QAXHI,
work unit 00001, and work unit title, "IR Structure."



**NAVAL RESEARCH LABORATORY
Washington, D.C.**

Approved for public release; distribution unlimited.

SECURITY CLASSIFICATION OF THIS PAGE (When Data Entered)

REPORT DOCUMENTATION PAGE		READ INSTRUCTIONS BEFORE COMPLETING FORM								
1. REPORT NUMBER NRL Memorandum Report 4659	2. GOVT ACCESSION NO.	3. RECIPIENT'S CATALOG NUMBER								
4. TITLE (and Subtitle) PRELIMINARY NUMERICAL SIMULATION OF IR STRUCTURE DEVELOPMENT IN A HYPOTHETICAL URANIUM RELEASE		5. TYPE OF REPORT & PERIOD COVERED Interim report on a continuing NRL problem.								
7. AUTHOR(s) E. Hyman*, M. Mulbrandon, S. L. Ossakow, and B. E. McDonald**		6. PERFORMING ORG. REPORT NUMBER								
9. PERFORMING ORGANIZATION NAME AND ADDRESS Naval Research Laboratory Washington, DC 20375		8. CONTRACT OR GRANT NUMBER(s)								
11. CONTROLLING OFFICE NAME AND ADDRESS Defense Nuclear Agency Washington, DC 20305		10. PROGRAM ELEMENT, PROJECT, TASK AREA & WORK UNIT NUMBERS 62074H; 47-0917-0-1								
14. MONITORING AGENCY NAME & ADDRESS (if different from Controlling Office)		12. REPORT DATE November 16, 1981								
		13. NUMBER OF PAGES 51								
		15. SECURITY CLASS. (of this report) UNCLASSIFIED								
		15a. DECLASSIFICATION/DOWNGRADING SCHEDULE								
16. DISTRIBUTION STATEMENT (of this Report) Approved for public release; distribution unlimited.										
17. DISTRIBUTION STATEMENT (of the abstract entered in Block 20, if different from Report)										
18. SUPPLEMENTARY NOTES *Present address: Science Applications, Inc., McLean, VA 22102 **Present address: Naval Oceanographic Research and Development Activity, Bay St. Louis, MS 39520 This research was sponsored by the Defense Nuclear Agency under Subtask S99QAXHI, work unit 00001, and work unit title, "IR Structure."										
19. KEY WORDS (Continue on reverse side if necessary and identify by block number) <table border="0"> <tr> <td>IR Structure</td> <td>Power spectrum</td> </tr> <tr> <td>Uranium release</td> <td>Parallax effects</td> </tr> <tr> <td>Numerical simulation</td> <td>PHARO code</td> </tr> <tr> <td>Isophots</td> <td>LWIR</td> </tr> </table>			IR Structure	Power spectrum	Uranium release	Parallax effects	Numerical simulation	PHARO code	Isophots	LWIR
IR Structure	Power spectrum									
Uranium release	Parallax effects									
Numerical simulation	PHARO code									
Isophots	LWIR									
20. ABSTRACT (Continue on reverse side if necessary and identify by block number) <p>We present a three-dimensional (3D) simulation of a daytime hypothetical uranium release at 200 km altitude. Of interest is the LWIR emission from uranium oxide ions, induced by sunlight and earthshine. Assuming a one-level fluid and integrated Pedersen conductivity ratio (cloud to ambient) of 5, the cloud diffuses along the magnetic field in time and rapidly develops gradient drift striations transverse to the magnetic field and across the direction of the relative velocity of neutrals to ions. Using the PHARO code, we produce contour plots of radiance in the 11-14 μ region to simulate observations from various</p> <p style="text-align: right;">(Continues)</p>										

DD FORM 1473

1 JAN 73

EDITION OF 1 NOV 65 IS OBSOLETE
S/N 0102-014-6601

SECURITY CLASSIFICATION OF THIS PAGE (When Data Entered)

20. ABSTRACT (Continued)

locations both along and transverse to the magnetic field. Contours of radiance vary in intensity and character from different vantage points. Power spectra are calculated to quantify the development of spatial irregularities in the radiance. We find parallax to be an important effect which alters both the appearance of the radiance contours and the spectral characteristics. This inherently 3D effect could not be observed in previous 2D simulations. Altering the distance from observer to cloud or changing slightly the direction of observation can produce drastic changes in the observations.

CONTENTS

I. INTRODUCTION	1
II. A HYPOTHETICAL EXPERIMENT	2
III. THE SIMULATION	4
IV. RESULTS	8
a. PHARO Plots	8
b. Power Spectra	11
c. Parallax Effects	14
V. SUMMARY	16
ACKNOWLEDGMENT	17
REFERENCES	45

PRELIMINARY NUMERICAL SIMULATION OF IR STRUCTURE DEVELOPMENT IN A HYPOTHETICAL URANIUM RELEASE

I. INTRODUCTION

The significance to U.S. defense systems of long wave infrared (LWIR) emissions from metallic oxides in the debris from a high altitude nuclear explosion (HANE) is an important unanswered question. Of most concern are structured or striating media since they degrade optical systems at intensities many orders of magnitude lower than smooth media. Those debris species which result in long lived ions are of most interest because they are the ones most likely to structure. For this reason uranium deserves careful scrutiny. Because of the low ionization potential of UO, uranium reacts with atomic oxygen via an associative ionization process to form UO^+ . Thus, this molecular ion is stable to dissociative recombination, and deionization requires a three body reaction. Uranium deposited in the high altitude atmosphere (>100 km) in a nuclear burst will, therefore, induce very long lived ionization. The emission characteristics of UO^+ have not been measured, although on general theoretical grounds a very large line density is expected in the $11\text{-}14\mu$ region. A laboratory experiment to measure the UO^+ spectrum (wavelengths and band strengths) in this region of the LWIR has been described by Bien.⁽¹⁾ It has not yet been carried out.

Because of the potential importance of uranium debris from HANE events in the performance of defense optical systems,

the RAAE Division of the Defense Nuclear Agency has suggested that numerical simulations be performed to model high altitude uranium releases. Based on reasonable estimates of oscillator strengths for transitions in the LWIR, these simulations will predict structuring characteristics of the hypothetical plasma cloud released in the ionosphere. In this paper we will present results of a three dimensional simulation of a uranium release. Using the PHARO code we will show plots of radiance (watts/cm² ster) in the 11-14 μ region as a function of time, (assuming the emission to be optically thin), viewing both along and transverse to the magnetic field. These plots will show the development of structure in time. In addition, we will show the power spectra for the structure, giving the distribution of spatial wavelengths in the emitting band. Parallax effects will also be described.

II. HYPOTHETICAL EXPERIMENT

We will simulate a hypothetical release based on the parameters presented at the DNA Infrared Program Meeting at the Naval Research Laboratory in January 1980 by W. Reidy;⁽²⁾ A release at 200 km altitude in daylight with an atomic uranium content of 2 kgm ($\sim 5 \times 10^{24}$ atoms) is modeled. Initially the uranium vapor will expand radially with a thermal velocity somewhat less than 1 km/sec. The expanding uranium vapor would be slowed when it has interacted with an equal mass of the atmosphere (~ 1.2 km). However, before this occurs it will interact with an equal number of atomic oxygen atoms ($\sim .75$ km). Assuming an oxygen density $\sim 3 \times 10^9$ cm⁻³ and a reaction rate coefficient

of $4 \times 10^{-10} \text{ cm}^3/\text{sec}$,⁽³⁾ the ionization will occur with an e-folding time of ~ 0.8 sec. This will restrict further growth of the cloud transverse to the magnetic field, and the cloud will initially develop a sausage-like shape with a radial dimension transverse to the magnetic field ~ 0.75 km. However, $\vec{E} \times \vec{B}$ convection will elongate the cloud in the direction of the relative velocity of the neutral atmosphere to the ion cloud, and will narrow it in the other direction transverse to the magnetic field.⁽⁴⁾

Because of the presence in the normal atmosphere at 200 km of a substantial amount of molecular oxygen, which may not be present in the nuclear disturbed atmosphere, a further reaction will occur: UO^+ will react with O_2 to form UO_2^+ . Assuming a reaction coefficient of $2 \times 10^{-9} \text{ cm}^3/\text{sec}$ ⁽⁵⁾ and an O_2 density of $\sim 4 \times 10^8 \text{ cm}^{-3}$ the e-folding time for conversion of UO^+ to UO_2^+ is just 1.2 sec. Thus, after the first several seconds the predominant ion will be UO_2^+ . This will have little effect on the dynamics and structuring of the ion cloud but the LWIR spectrum will be different, of course. Because in the nuclear case the O_2 molecules may be dissociated, the transition from UO^+ to UO_2^+ may take much longer. On the other hand, even in a high altitude burst much of the debris will typically be deposited at lower altitudes (~ 100 km) where there will be large amounts of O_2 .

Metal oxides are excited from the ground state to higher electronic levels by visible radiation from sunlight. These

excited levels rapidly decay, in general, to excited vibrational levels of the ground electronic state which radiate in the LWIR. In addition, there is direct excitation of vibrational levels caused by earthshine at LWIR wavelengths, leading to LWIR emission as these levels decay. Typical emission rates for metal oxides in the LWIR are $\sim 10^{-2}$ photons/molecule/sec due to earthshine, and $\sim 10^{-1}$ photons/molecule/sec due to sunlight.⁽⁶⁾ There has been some speculation that the emission rates for UO^+ and UO_2^+ may be substantially higher than these values⁽⁷⁾ because of the presence of low-lying electronic levels, but that has not been established. In the case of aluminum oxide the rate is $\sim .2$ photons/molecule/sec both for sunlight and for earthshine. LWIR emission is expected to be in the 11-14 μ region but the results in this paper do not depend on this specific wavelength interval.

III. THE SIMULATION

The model assumes a one ionic species, one-level fluid and follows the analysis used for the Avefria barium cloud releases.⁽⁸⁾ The conductivity ratio (UO^+ plasma cloud to background ionosphere Pedersen conductivity ratio), as defined in Reference 8, is taken to be 5 which is based on an assumption of 30% efficiency of vaporization of the uranium. Briefly, the conductivity ratio 5 was obtained as follows. The 5×10^{24} atoms of U was assumed to be 30% vaporized and the resulting UO^+ was gaussianly distributed over a sphere, with a gaussian radius of 0.75 km. Using a UO^+ ion-neutral collision-frequency (ν_{in}) of 0.2 s^{-1} and a gyro-frequency (Ω_i) of 18.8 s^{-1} , the integrated Pedersen conductivity of the UO^+ cloud was found to be 30 mhos. For the daytime high

latitude ionosphere, a value of 6 mhos for the integrated Pedersen conductivity was taken.

The altitudes and sizes of the ionized clouds are similar in the two releases as are the striation formation mechanisms and lead to the rapid development of gradient drift striations. Whereas, in the Avefria simulation, however, the F region ionospheric plasma cloud was reduced to two dimensions (transverse to the magnetic field) by performing field-line-integrations over the Pedersen conductivity, here in the model this is not done and the cloud also diffuses in time along the magnetic field, providing a three dimensional simulation. This enables one to view the cloud, using the PHARO code,⁽⁹⁾ from an arbitrary direction and to automatically incorporate any effects of parallax due to the three-dimensionality of the cloud. A PHARO plot is obtained by summing the volume emission rates along an array of rays originating at the camera location. A 2D array of radiance values is determined, from which a contour plot of the radiance is constructed.

Thus, the cloud is spherical for the first few seconds until it becomes ionized. From then on, after this time t_i , diffusion transverse to the magnetic field can be neglected. Along the magnetic field, we assume an initial density distribution $n(t_i) \sim \exp(-z^2/L^2)$, where z is the coordinate along the magnetic field (\underline{B}) direction and $L \sim .75$ km. With a parallel to

B diffusion constant $K_{\parallel} = c_s^2 / v_{in}$, where $c_s \sim .3$ km/sec and $v_{in}(UO^+) \sim .2$ sec⁻¹, we have $K_{\parallel} \sim 4.15 \times 10^{-1}$ km²/sec. The density diffuses in time according to

$$\frac{\partial n}{\partial t} = K \frac{\partial^2 n}{\partial z^2} \quad (1)$$

At time t then, we will have

$$n(t, z) \propto \left[\frac{1}{1 + b(t-t_i)} \right]^{1/2} \exp \left(- \frac{z^2}{L^2} \left[\frac{1}{1 + b(t-t_i)} \right] \right) \quad (2)$$

with $b = 4K / L^2 \sim 3.2$ sec⁻¹.

The above analysis is strictly correct only for a uniform atmosphere. For a release in equatorial regions the z direction is horizontal and there is no problem. At high latitudes, where the magnetic field is nearly vertical, diffusion will be significantly faster in the upward direction than in the downward direction. Now, the diffusion scale size grows like the square root of the time and at 200 km is ~ 13.4 km at 100 sec. Therefore, at times of the

order of 100 sec this effect is not major (atmospheric scale size at 200 km \sim 43 km). We have, for this reason, not corrected for this effect in our simulation.

The above analysis is performed while simultaneously following the perpendicular motion and structuring of the UO^+ plasma cloud according to the one-level set of equations⁽⁸⁾

$$\frac{\partial \Sigma}{\partial t} = - \nabla_{\perp} \cdot (\Sigma \underline{V}) + \nabla_{\perp} \cdot (K_{\perp} \nabla_{\perp} \Sigma) \quad (3)$$

$$\underline{V} = - \frac{c}{B} \nabla_{\perp} \phi \times \hat{z} \quad (4)$$

$$\nabla_{\perp} \cdot (\Sigma \nabla_{\perp} \phi) = \underline{E}_0 \cdot \nabla_{\perp} \Sigma \quad (5)$$

where Σ , \underline{V} , K_{\perp} , ϕ , B and \underline{E}_0 are the integrated plasma cloud (UO^+) Pedersen conductivity ($\Sigma = \int \sigma_p(x, y, z) dz$, where σ_p is the Pedersen conductivity) and is a function of x , y (coordinates perpendicular to \underline{B}), perpendicular plasma velocity, relative to the ambient perpendicular plasma drift, the cross-field ($\perp \underline{B}$) diffusion coefficient, the cloud-induced potential, magnetic field strength, and ambient perpendicular electric field in the rest frame of the uniform neutral flow, respectively and the electrostatic approximation ($\underline{E} = \underline{E}_0 - \nabla_{\perp} \phi$) has been made. In addition⁽⁸⁾ $K_{\perp} = (2kT/m_i)(\nu_{en} + \nu_{ei}/\Omega_e \Omega_i)$ where k , T , m_i , ν_{en} , ν_{ei} , Ω_e and Ω_i are Boltzmann's constant, the plasma temperature, ion mass, electron-neutral collision frequency, electron-ion collision frequency, electron gyrofrequency and ion gyrofrequency,

respectively. Values of $E_0 = 5\text{mV/m}$, $B = 0.5$ gauss (and resulting in a cE_0/B velocity of 100 m/s), and $K_{\perp} \sim 1\text{ m}^2/\text{sec}$ were chosen for the simulations. The computational mesh consisted of 162×82 grid points in the x and y directions (see Figure 1). The plasma density distribution $n(x,y)$ at each time was unfolded from (3) - (5) by distributing the density along z according to the gaussian (with a time dependent gaussian length) given by (1) and (2), using $v_{in}(UO^+)$ and $\Omega_i(UO^+)$, integrating over z and setting the resultant integral equal to $\Sigma(x,y)$.

In Figure 1 we indicate the coordinate system fixed in the ionized cloud, and illustrate the formation of striations transverse to the magnetic field, B , and across the direction of the relative velocity of the neutral atmosphere, v_n , to the ionized plasma. (In this system $\underline{E}_0 \times \underline{B}$ would be in the $-x$ direction). The calculational mesh follows the striating edge and has an outflow boundary condition on the negative x boundary. Thus, in time more and more ions are lost from the calculation out of the "tail". Figure 1 also exhibits the locations of 3 potential observation directions for infrared detectors (cameras). In the next section we will show plots of ir emission contours as observed from each of the camera locations. The emission rate is assumed to be $0.11\text{ photons/ion/sec}$ in the $11\text{-}14\mu$ band.

IV. RESULTS

a. PHARO Plots

Figures 2-8 show the contours of radiance in $\text{watts/cm}^2/\text{ster}$

at several times as observed from camera 1, placed a distance away of 200 km. Camera 1 looks along the magnetic field. Figure 2 shows a PHARO plot of the radiance 60 sec after the release. The abscissa and ordinate are in degrees and are respectively along the x and y directions in the coordinate system of Figure 1. An 82 x 82 mesh has been used in the PHARO part of the calculation in the camera plane of view. The contour values, defined in the headings of the plot, potentially range from 1.125×10^{-7} watts/cm² ster, (the "9" contour) to 0.0 (the "0" contour) in steps of 1.25×10^{-8} watts/cm² ster. The largest contour appearing in Figure 2 is the "8" contour which represents a radiance of 1.00×10^{-7} watts/cm² ster. A key at the bottom of the plot gives the value of some of the contours in watts/cm² ster. At 60 sec there is no sign of the fingering behavior which becomes so evident at later times. In Figure 3, 80 sec, the striating behavior has clearly begun developing. The structuring intensifies at 100, 120, 140, 160 and 180 sec shown in Figures 4, 5, 6, 7 and 8 respectively. The overall radiance has not diminished with time.

Camera 2 looks along the relative velocity vector of the neutral atmosphere and the ion cloud from a distance of 200 km. In Figure 9 we exhibit the PHARO plot at 140 sec as observed from camera 2 with a sufficiently large field of view that the entire cloud is in view. While this plot is useful to exhibit the entire cloud, there is not enough resolution to distinguish the contours.

For this, we return to the high resolution in Figure 10, which is at 60 sec. Only a portion of the cloud is in view here, of course. The magnetic field in Figure 10 is along the ordinate, and the abscissa is the y coordinate of Figure 1. Here the maximum contour value observed is 1.0×10^{-8} watts/cm² ster. The values of radiance determined from camera 2 are substantially lower than those from camera 1 since from this vantage point lines of sight do not pass through as much of the cloud as in the end view observed by camera 1. Furthermore, from camera 2 we are looking up the "tail", along the x-direction, and, as we pointed out, some of the ions have left the calculational mesh. This means that not only are the radiance levels too small as observed from this direction, but any nonuniformity in the "tail" has been lost. On the other hand, there is no fine structure lost, as this is all in the leading edge. Our calculations indicate that approximately 1/3 of the ions have left the mesh by 140 sec.

Note the near perfect symmetry at 60 sec, corresponding to the symmetry observed from camera 1 at this time. In Figures 11-14 we observe the changes in time from the camera 2 vantage point. At 100 sec, Figure 11, we see the maximum contour begin to shift to the left, corresponding to the maximum in Figure 4 shifting downward. A relative minimum forms just to the right of the central vertical axis corresponding to the depression in Figure 4 just above the central horizontal axis. These effects become more pronounced at succeeding times. Particularly interesting from

this direction is the alternation in intensities as we scan horizontally across the field of view (Figures 12-14). There is a gradual reduction with time in the radiance, also, as more of the cloud diffuses along the magnetic field out of the field of view, and, also, out of the calculational mesh (negative x boundary). The former is a real physical effect, the latter an artifact of the calculation.

Camera 3 looks in the direction transverse to the magnetic field and to the drift direction from a distance of 200 km. Again, in these views (Figures 15-19) not all of the cloud is included. The ordinate is along the magnetic field (z) and the abscissa is along the relative velocity (x). The steep gradients at the left of Figure 15 correspond to those on the right in Figure 2. As from camera 2, the radiance decreases with time as the cloud diffuses out of the field of view but there is no loss from missing ions, as the "tail" is not in the field of view of camera 3. Here the structuring leads to an appearance significantly distinct from either of the other two views.

b. Power Spectra

Spatial irregularity power spectra have been produced for each camera view. For example, consider the radiance as viewed from camera 1 at a distance of 200 km at 140 sec (Figure 6). Using a mesh dimension of 82×82 we construct a two dimensional (2D) power spectrum. This is converted to two one dimensional spectra: the x power spectrum is a result of integrating over the y components of the wavenumber (k_y) of the 2D power spectrum; the

y power spectrum comes from integrating over the x components (k_x). Typical results are shown in Figures 20 and 21. The power scale on the ordinate is in units of the logarithm of the square of the radiance. The abscissa has two scales: (1) the logarithm of the spatial wavelength in km, and (2) the logarithm of the mode number, k/k_1 , where $k_1 = 2\pi/D$. In the y direction D is the system size = 2.7km. By the system size we mean the distance across the field of view based on the distance between the camera and the cloud, and neglecting the dimensions of the cloud. In the x direction D is twice the system size, because of the Neumann boundary condition in x.

A typical power spectrum plot can be conveniently divided into two segments. The low mode number region at the left contains most of the power and characterizes the gross structure. The positions of peaks in this region are a measure of the size of the structure, e.g. in Figure 21 there is a clear peak at a wavelength just under 0.5 km. This characterizes the typical widths of the fingers in Figure 6. The second region is the asymptotic regime, which begins, roughly speaking at a wavelength corresponding to the smallest scale size of the gross structure. This region can be fit approximately by a straight line (in the log of the power vs. the log of the mode number). The slope of that fit, N, is the asymptotic slope of the power spectrum. The value of the slope is determined by the steepest gradient in the field of view. A value of -2 corresponds to a square wave; steeper slopes to more gradual gradients. We have discarded the highest 15% of the modes

from this calculation since the highest modes are subject to severe 'aliasing' effects and to computational errors.⁽¹⁰⁾ The resolution we used (82 x 82) was dictated by the cost of the PHARO calculations and should be considered only marginally adequate. Thus, the values of N should be considered illustrative but not definitive. Figures 20 and 21 do indicate steeper gradients in the x direction than in the y direction.

We find that the steep gradients are established fairly early, certainly by 100 sec. However, as time proceeds the number of steep gradients increases. This shows up as an increase in the power level of this part of the spectrum, but with no change in slope. Since, as we have said, very little of the power is in the asymptotic part of the spectrum there need be very little change in the power spectrum at the lower modes to accommodate this increase.

From camera 2 we view along the x axis. Thus, the only power spectrum that is meaningful is the y power spectrum, in which the z components have been integrated over. The ion distribution in the z direction is strictly gaussian, and, thus, uninteresting. Figure 22 shows the y power spectrum from camera 2 at 140 sec at a distance of 200 km. Refer to Figure 15. While there is clearly mode structure here in the asymptotic region the value of N is not too different from that in Figure 21.

From camera 3 we view along the y axis. Only the x power spectrum, in which the z components have been integrated over, is of interest. Figure 23 shows the x power spectrum from camera 3

at 140 sec at a distance of 200 km. Refer to Figure 18. Again, there is a great deal of structure in the asymptotic region but the general falloff, characterized by the N value, is not too different from that in Figure 20.

c. Parallax Effects

Previous simulations⁽⁸⁾ have been two dimensional so that parallax effects were unobservable. We find that including the third dimension has a profound effect both on the radiance contours and on the irregularity spectral characteristics. We will illustrate this in two ways, by showing: (1) how these properties vary with distance and (2) how they vary with change in pointing direction.

Consider again camera 1 at 140 sec at a distance of 200 km, Figure 6, and compare with Figures 24 and 25, which are views from camera 1 at 140 sec at respectively 50 km and 600 km from the cloud. Clearly, at 50 km parallax has spread the contours greatly and substantially reduced the gradients. At 600 km the reverse has occurred and the gradients are larger. This is borne out by the power spectral results. Figures 26 and 27 are the x power spectra from, respectively, 50 km and 600 km and should be compared with Figure 20 for 200 km. The spectral index, N , at 50 km is -3.44, at 200 km is -2.90, and at 600 km is -2.39 documenting the clear sharpening of the steepest gradients as we recede from the cloud. Figures 28 and 29 are the y power spectra from, respectively, 50 km and 600 km which should be compared with

Figure 21 for 200 km. The y spectral index, N , is the same at 50 km and 200 km, within the accuracy of the fitting technique, but has decreased by $\approx 10\%$ at 600 km. This is because in the y direction there are steep gradients near the center of the field of view, where parallax effects are small, so that the steep gradients have been somewhat preserved. However, if we compare the power levels in the asymptotic regime at 50 km and 600 km, at some intermediate fixed wavenumber, we find the power down by about half a decade both in the x and y spectra (compare Figures 26 and 27 and Figures 28 and 29) at 50 km relative to 600 km. This is the best measure of the effect of parallax on the measured gradients.

Suppose now we imagine that camera 1, at 140 sec and a distance of 200 km, is rotated about the x axis by just 1° , toward camera 3. How does this affect the radiance contours? Figure 30 shows the resulting contours, which have been greatly spread out. Although the maximum radiance values have been reduced, compared to Figure 6, the irradiance at the camera is unchanged. As is obvious in Figure 30, the greatest change has occurred with the gradients in the y direction. The spectral index of the y power spectrum has increased from ~ -4 to ~ -7 .

Figure 31 shows the effect of rotating camera 1, about the y axis by 1° , toward the x axis. Here the changes from Figure 6 are moderate. However, the x power spectrum index does change from ~ -2.9 to ~ -5.5 and the y index increases by about 20%.

Thus, when we rotate toward the y direction we lose the y gradients and when we rotate toward the x direction we lose the x gradients.

V. SUMMARY

The severe degradation of radio signals due to structuring of electron densities in the atmosphere, following a HANE event, has been known for some years now. A great deal of analysis has been performed at the Naval Research Laboratory (NRL) to understand the plasma instability mechanisms that underlie this phenomenon, as well as related phenomena in the natural ionosphere, such as spread F. It is clear that these mechanisms also will result in structuring in the emission of LWIR radiation and consequently is potentially of serious concern to the U.S. defense community. Ultimately we want to use our theoretical understanding of striation phenomena along with our capabilities to simulate HANE phenomena using 3D magnetohydrodynamic computer models, to permit predictions of structuring following these events.

At present there is at issue the question of what, if any, sources of LWIR emission are likely to be most important in HANE events. The most likely candidates at present are (1) atomic oxygen and/or nitrogen recombination radiation and (2) LWIR emission from metallic oxides, such as uranium. To shed light on some of the unknowns in the second category DNA requires a reliable model of a hypothetical uranium release at high altitudes to clarify the emission wavelengths, intensities, and structuring. In this paper we have reported on the results of a numerical simulation of a uranium release at 200 km in daylight, making reasonable assumptions about

the values for some of the unknown parameters. We have presented contour plots of radiance in the 11-14 μ region of the LWIR as it would be observed from detectors placed at various locations along and transverse to the magnetic field and at various distances from the cloud.

This enables us to observe the development in time of the radiance from the cloud as it would appear from any vantage point of interest. We see clearly the steepening of the cloud, the development of fingering, and how this is related to the power spectral characteristics that are observed. Most importantly, we have shown that the three dimensional nature of the cloud has a profound effect on the radiance contours and on the observed spectral characteristics. Being stationed closer or observing slightly off axis can greatly reduce the gradients in the radiance of the cloud and change the power spectral characteristics accordingly. The results of our simulation should provide a theoretical understanding of a hypothetical experimental release. It should also be recognized that the simulations we have presented are a first cut, i.e., of a preliminary nature. Clearly, improvements in the numerical simulations presented here will be made. Nevertheless, these simulations provide some interesting results on structuring in the LWIR regime.

ACKNOWLEDGMENT

This work was supported by the Defense Nuclear Agency. We would like to thank Professor N. J. Labusky for useful discussions on obtaining the power spectra from the PHARO plots.

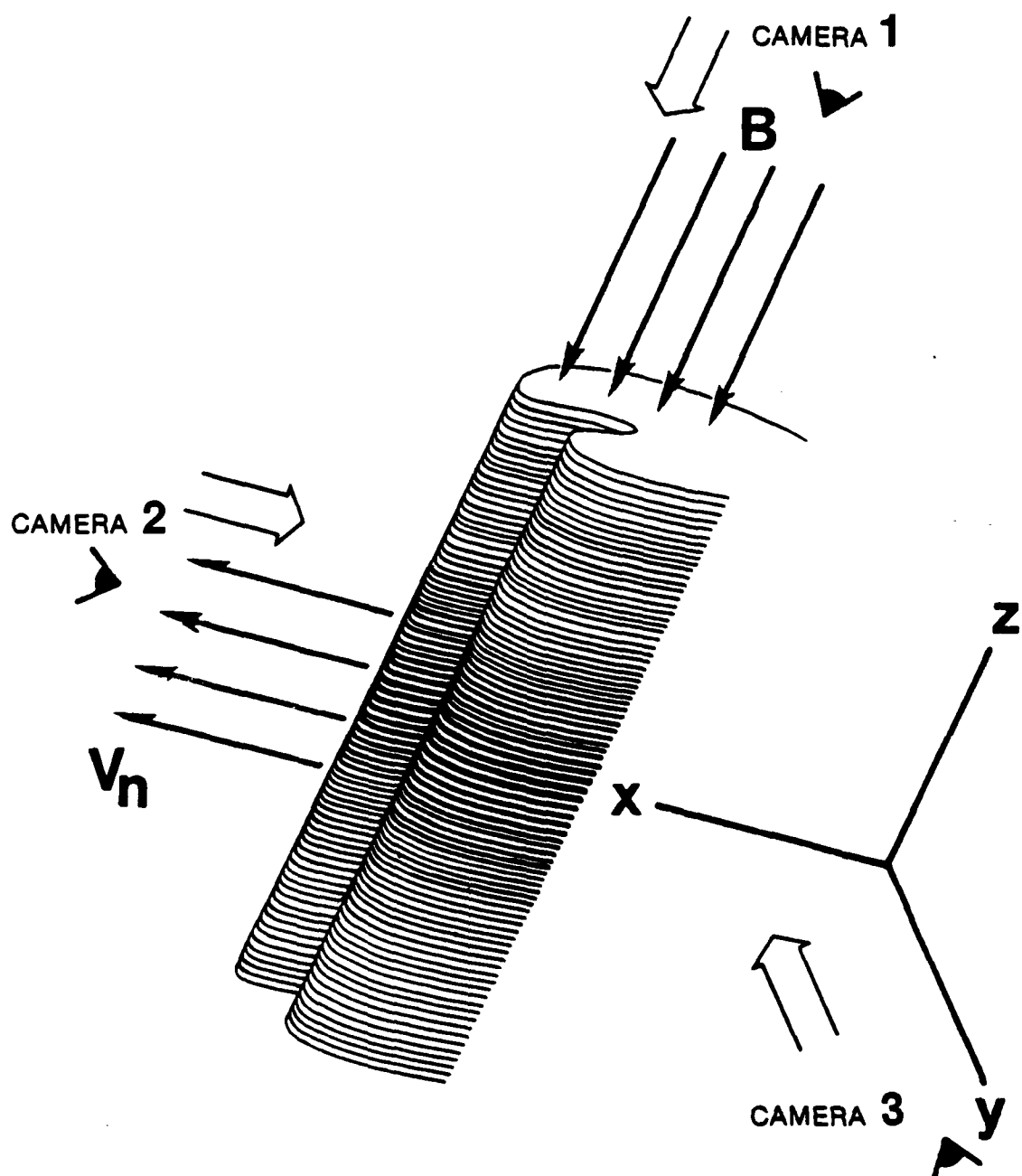


Fig. 1 - Schematic view of the uranium cloud and the coordinate system, showing diffusion along the magnetic field, and striation formation across the direction of the neutral-ion relative velocity direction v_n . Locations of the cameras discussed in the text are indicated.

CAMERA 1 T(SEC) 6.0110E 01
 0.39 CONTOURS 0.00E 00 1.12E-07 1.25E-08

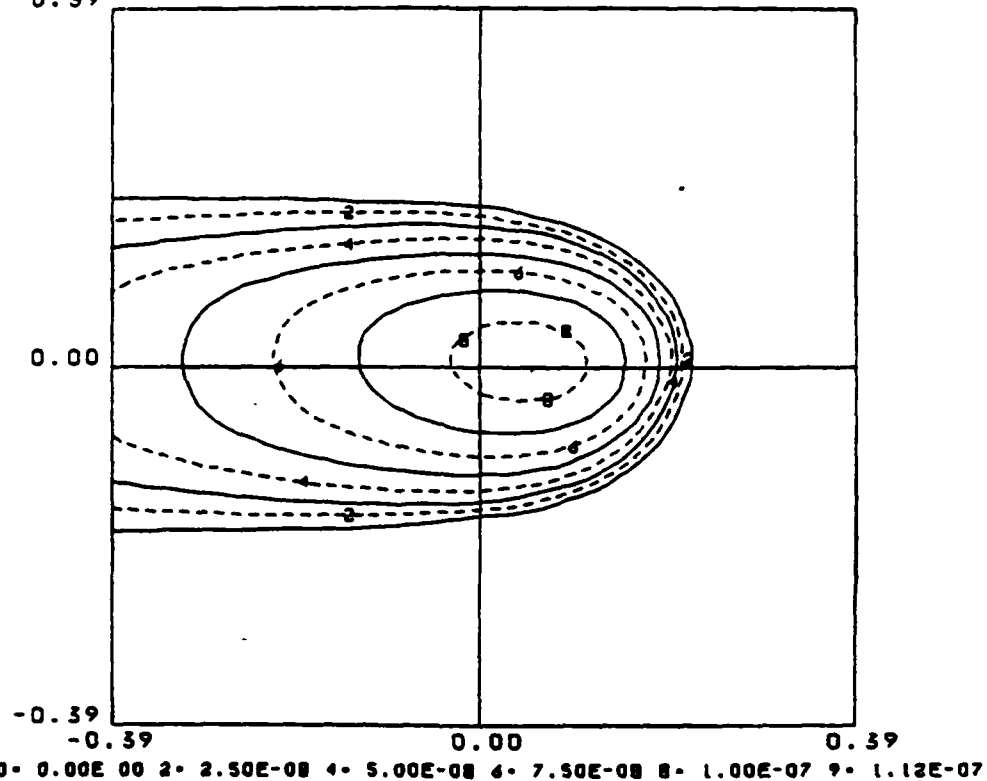


Fig. 2 - Camera 1 radiance contours (watts/cm² ster) 200 km from the cloud origin, 60 sec after release. Abscissa and ordinate are in degrees. Refer to text for contour label values or to key at bottom.

CAMERA 1 T(SEC) 8.0114E 01
 0.39 CONTOURS 0.00E 00 1.12E-07 1.25E-08

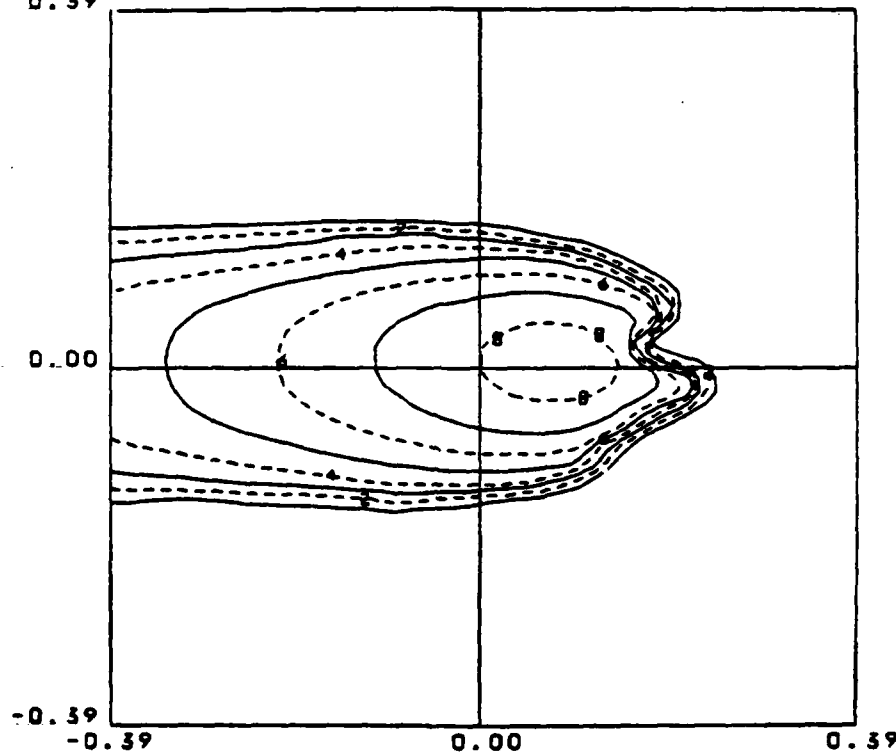


Fig. 3 - Camera 1 radiance contours (watts/cm² ster) 200 km from the cloud origin, 80 sec after release. Abscissa and ordinate are in degrees. Refer to text for contour label values or to key at bottom.

CAMERA 1 T(SEC) 1.0007E 02
 0.39 CONTOURS 0.00E 00 1.12E-07 1.25E-08

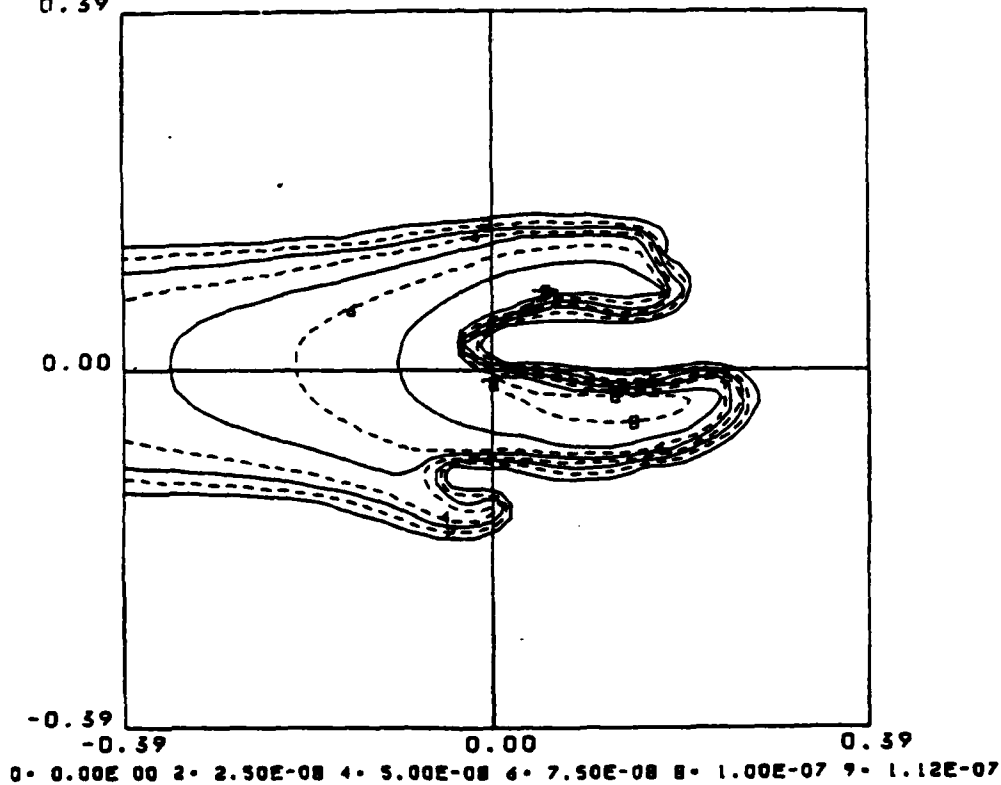


Fig. 4 - Camera 1 radiance contours (watts/cm² ster) 200 km from the cloud origin, 100 sec after release. Abscissa and ordinate are in degrees. Refer to text for contour label values or to key at bottom.

CAMERA 1 T(SEC) 1.2007E 02
 0.39 CONTOURS 0.00E 00 1.12E-07 1.25E-08

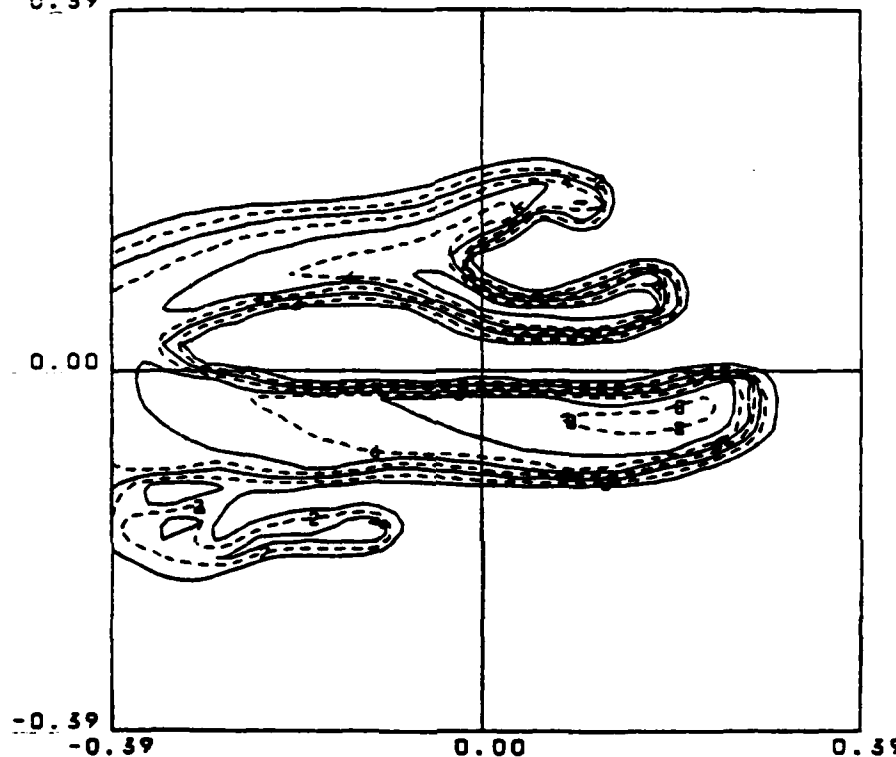


Fig. 5 - Camera 1 radiance contours ($\text{watts/cm}^2 \text{ster}$) 200 km from the cloud origin, 120 sec after release. Abscissa and ordinate are in degrees. Refer to text for contour label values or to key at bottom.

CAMERA 1 T(SEC) 1.4005E 02
 0.39 CONTOURS 0.00E 00 1.12E-07 1.25E-08

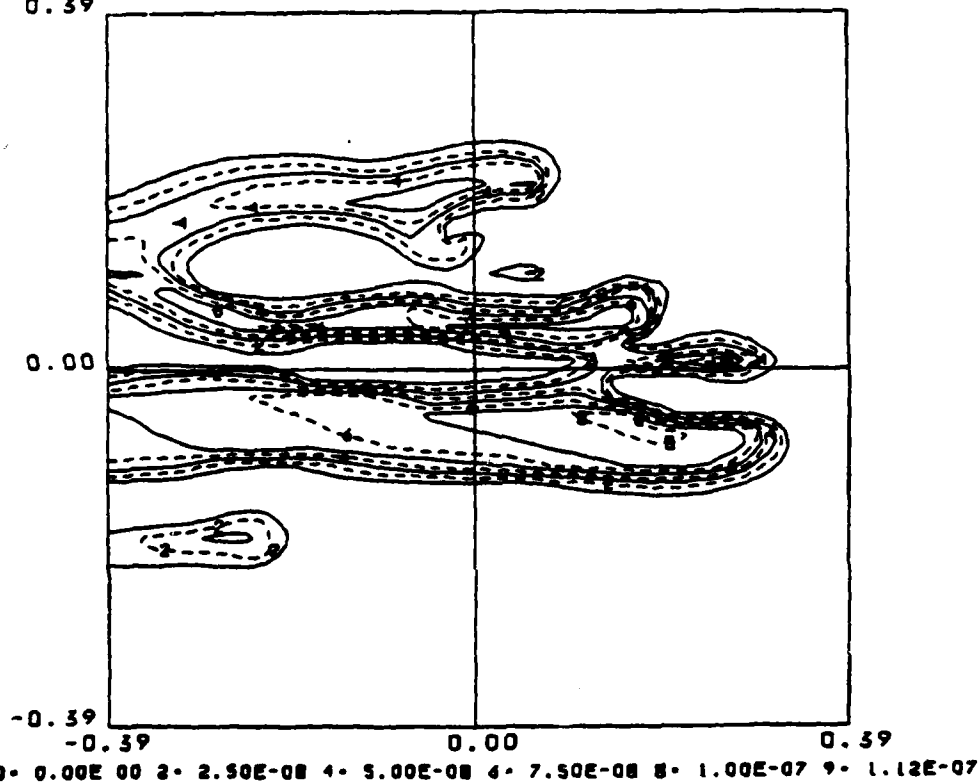


Fig. 6 - Camera 1 radiance contours ($\text{watts/cm}^2 \text{ster}$) 200 km from the cloud origin, 140 sec after release. Abscissa and ordinate are in degrees. Refer to text for contour label values or to key at bottom.

CAMERA 1 T(SEC) 1.6007E 02
 0.39 CONTOURS 0.00E 00 1.12E-07 1.25E-08

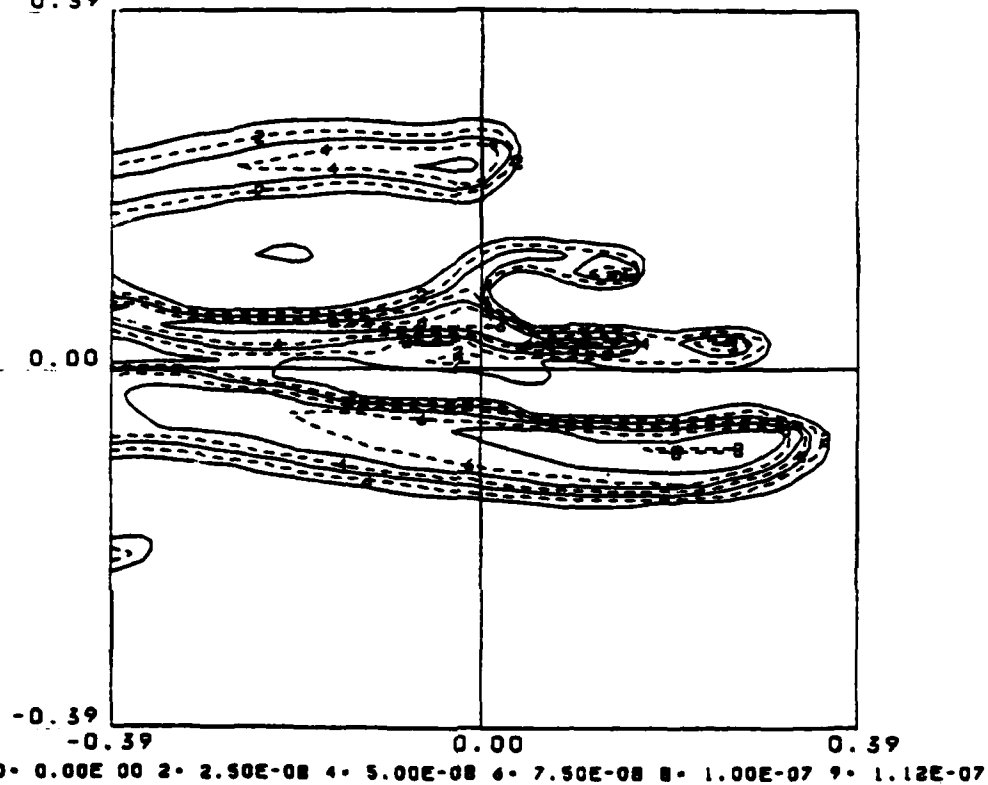


Fig. 7 - Camera 1 radiance contours (watts/cm² ster) 200 km from the cloud origin, 160 sec after release. Abscissa and ordinate are in degrees. Refer to text for contour label values or to key at bottom.

CAMERA 1 T(SEC) 1.8002E 02
 0.39 CONTOURS 0.00E 00 1.12E-07 1.25E-08

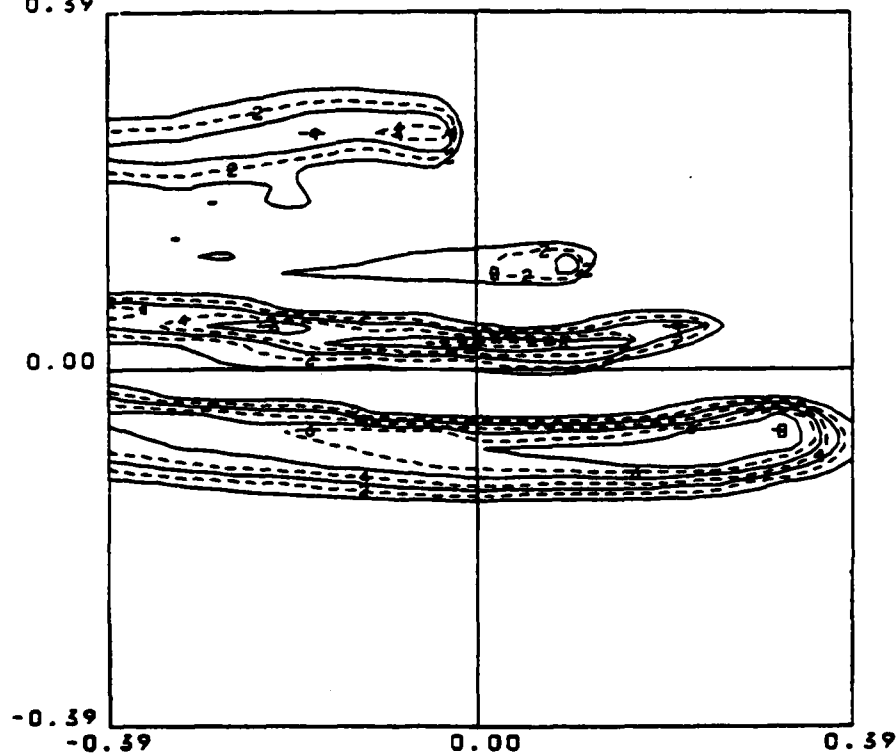


Fig. 8 - Camera 1 radiance contours (watts/cm² ster) 200 km from the cloud origin, 180 sec after release. Abscissa and ordinate are in degrees. Refer to text for contour label values or to key at bottom.

CAMERA 2 T(SEC) 1.4005E 02
 7.93 CONTOURS 0.00E 00 3.60E-09 4.00E-10

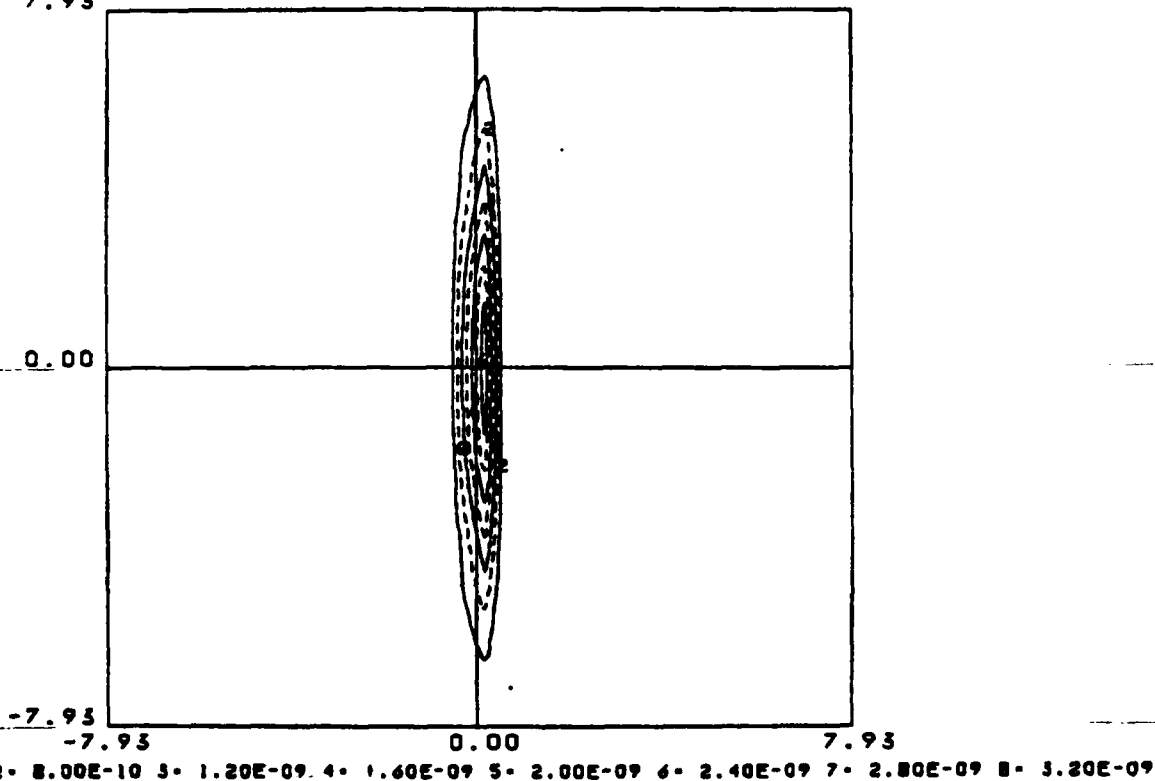


Fig. 9 - Camera 2 radiance contours (watts/cm² ster) 200 km from the cloud origin, 140 sec after release. Abscissa and ordinate are in degrees. This camera view has a large field of view so that the entire extent of the cloud is evident. Refer to text for contour label values or to key at bottom.

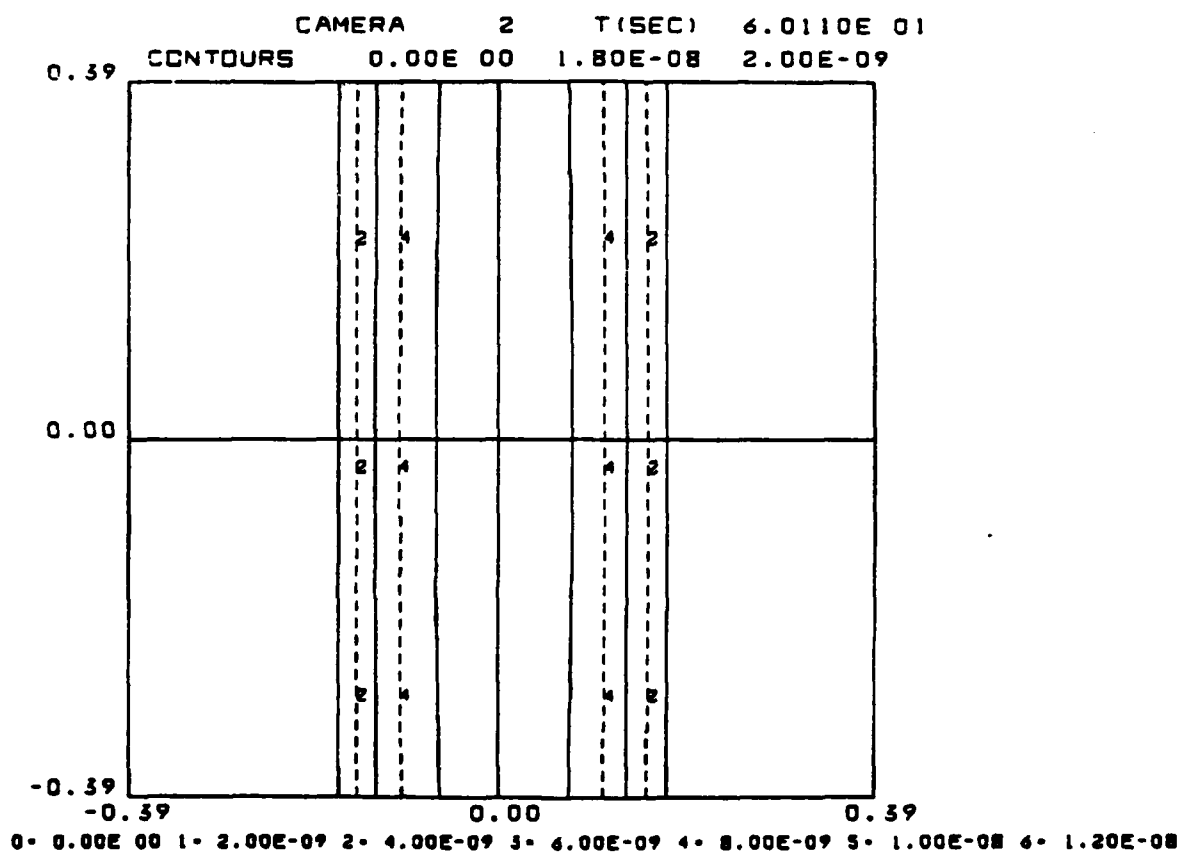


Fig. 10 - Camera 2 radiance contours (watts/cm²ster) 200 km from the cloud origin, 60 sec after release. Abscissa and ordinate are in degrees. Refer to contour label values in text or to key at bottom.

CAMERA 2 T(SEC) 1.0007E 02
 0.39 CONTOURS 0.00E 00 1.12E-08 1.25E-09

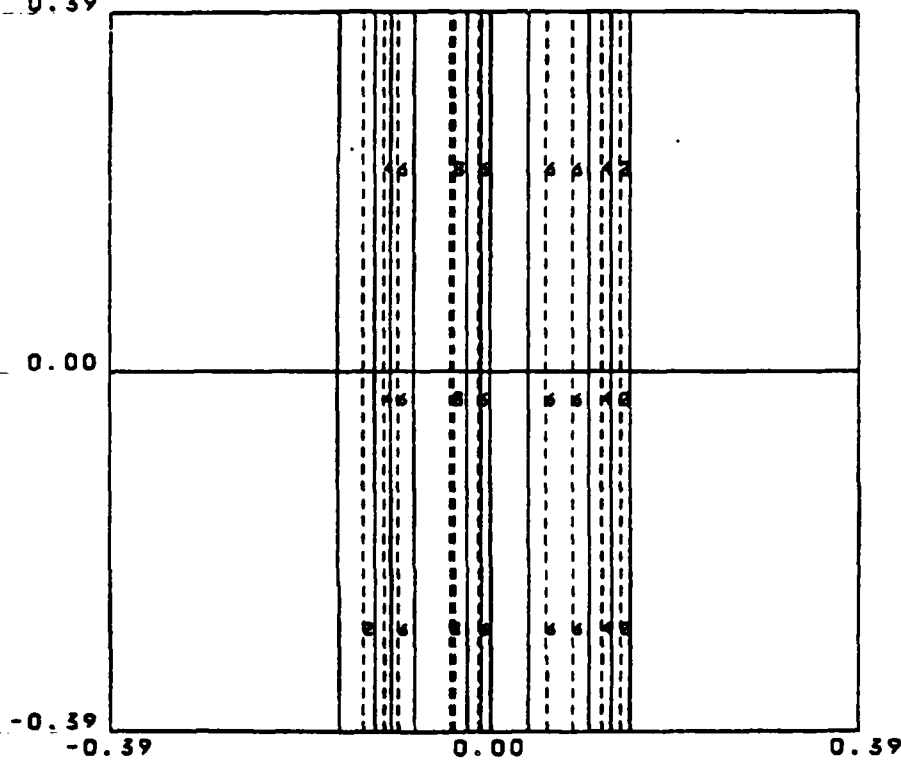


Fig. 11 - Camera 2 radiance contours ($\text{watts/cm}^2 \text{ster}$) 200 km from the cloud origin, 100 sec after release. Abscissa and ordinate are in degrees. Refer to contour label values in text or to key at bottom.

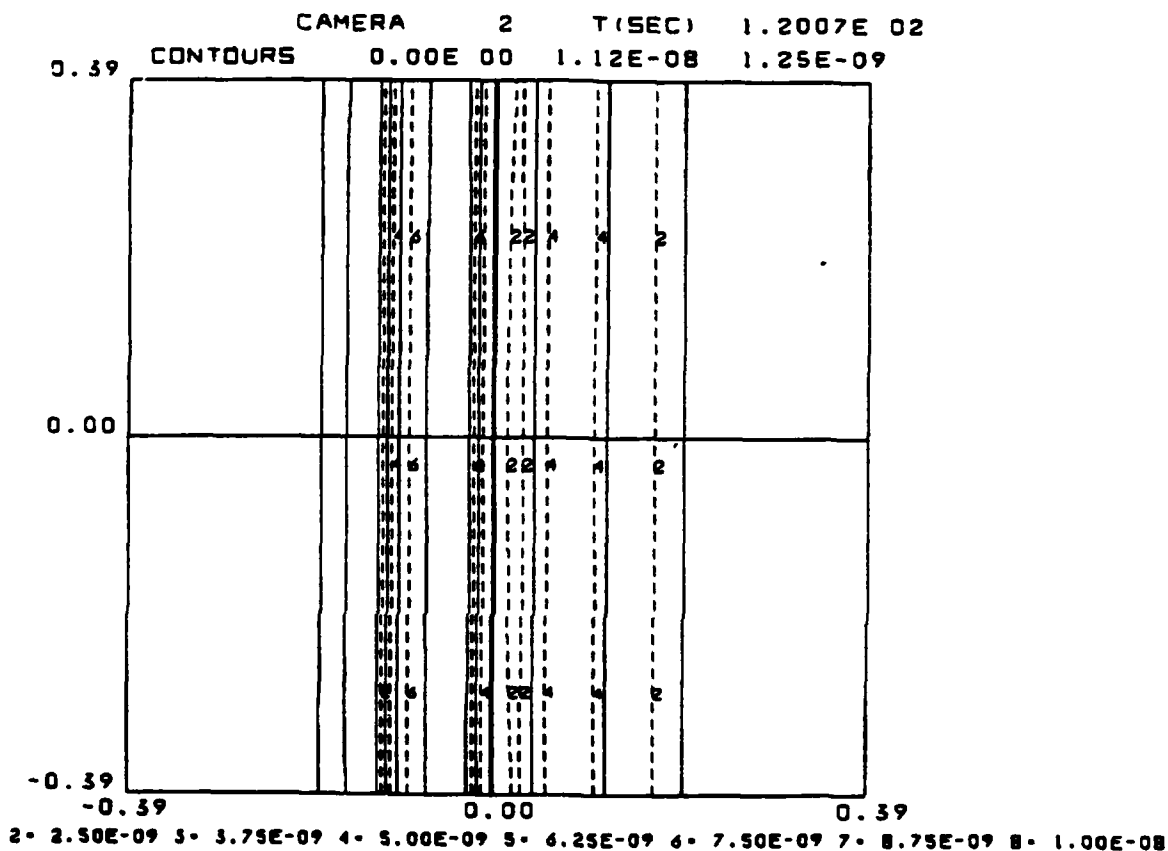


Fig. 12 - Camera 2 radiance contours (watts/cm² ster) 200 km from the cloud origin, 120 sec after release. Abscissa and ordinate are in degrees. Refer to contour label values in text or to key at bottom.

CAMERA 2 T(SEC) 1.4005E 02
 0.39 CONTOURS 0.00E 00 9.00E-09 1.00E-09

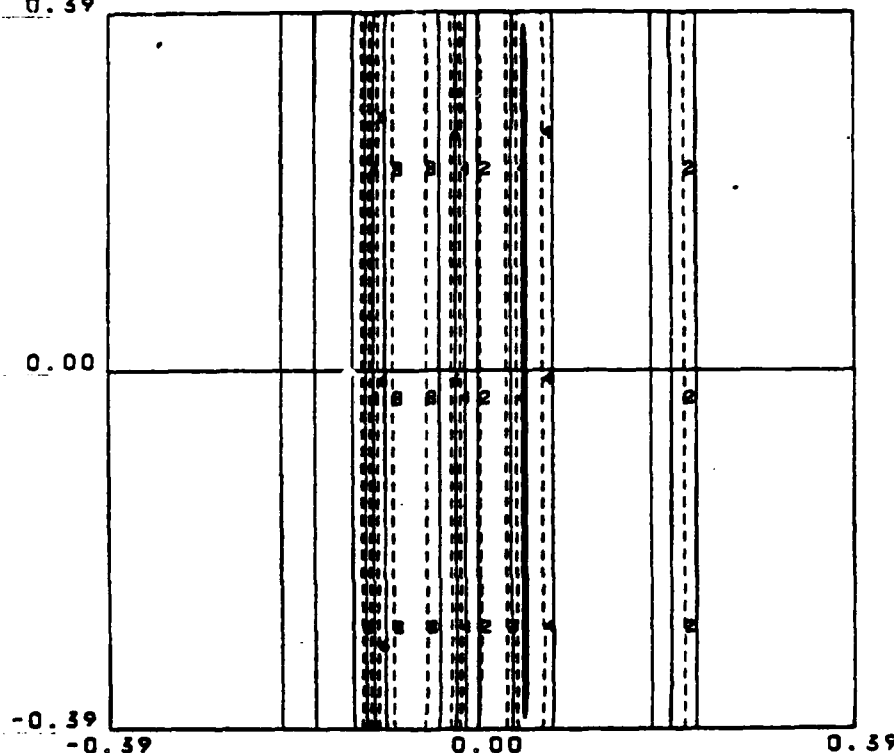


Fig. 13 - Camera 2 radiance contours (watts/cm²ster) 200 km from the cloud origin, 140 sec after release. Abscissa and ordinate are in degrees. Refer to contour label values in text or to key at bottom.

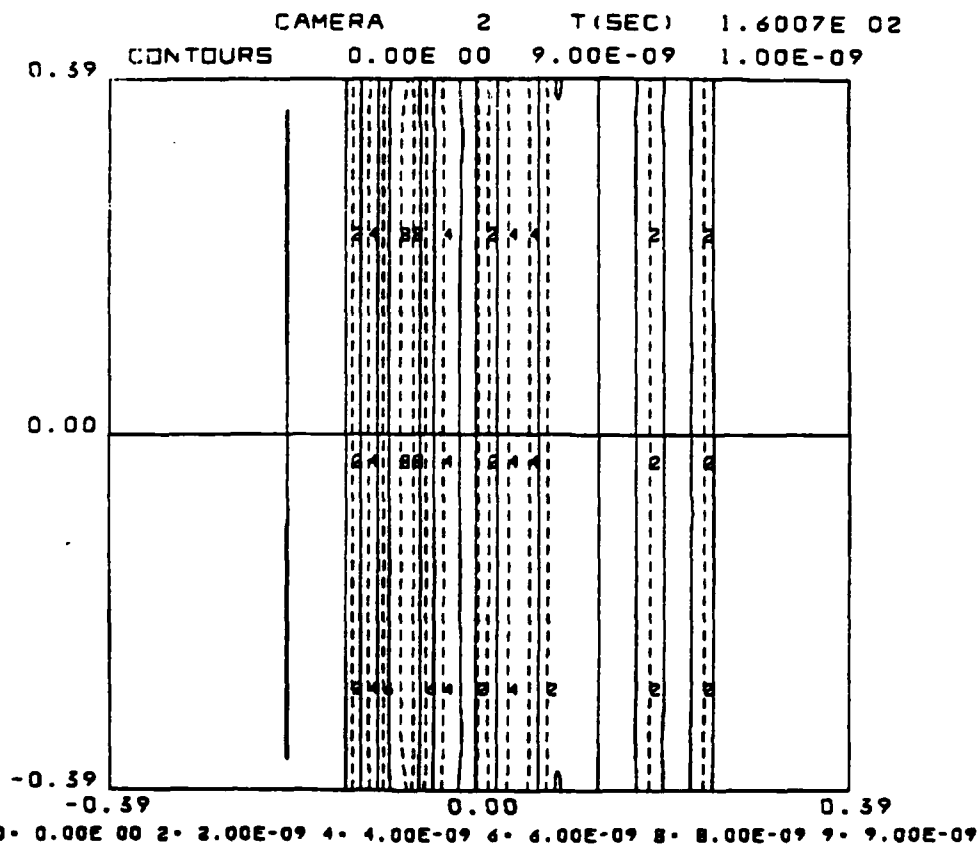


Fig. 14 - Camera 2 radiance contours (watts/cm² ster) 200 km from the cloud origin, 160 sec after release. Abscissa and ordinate are in degrees. Refer to contour label values in text or to key at bottom.

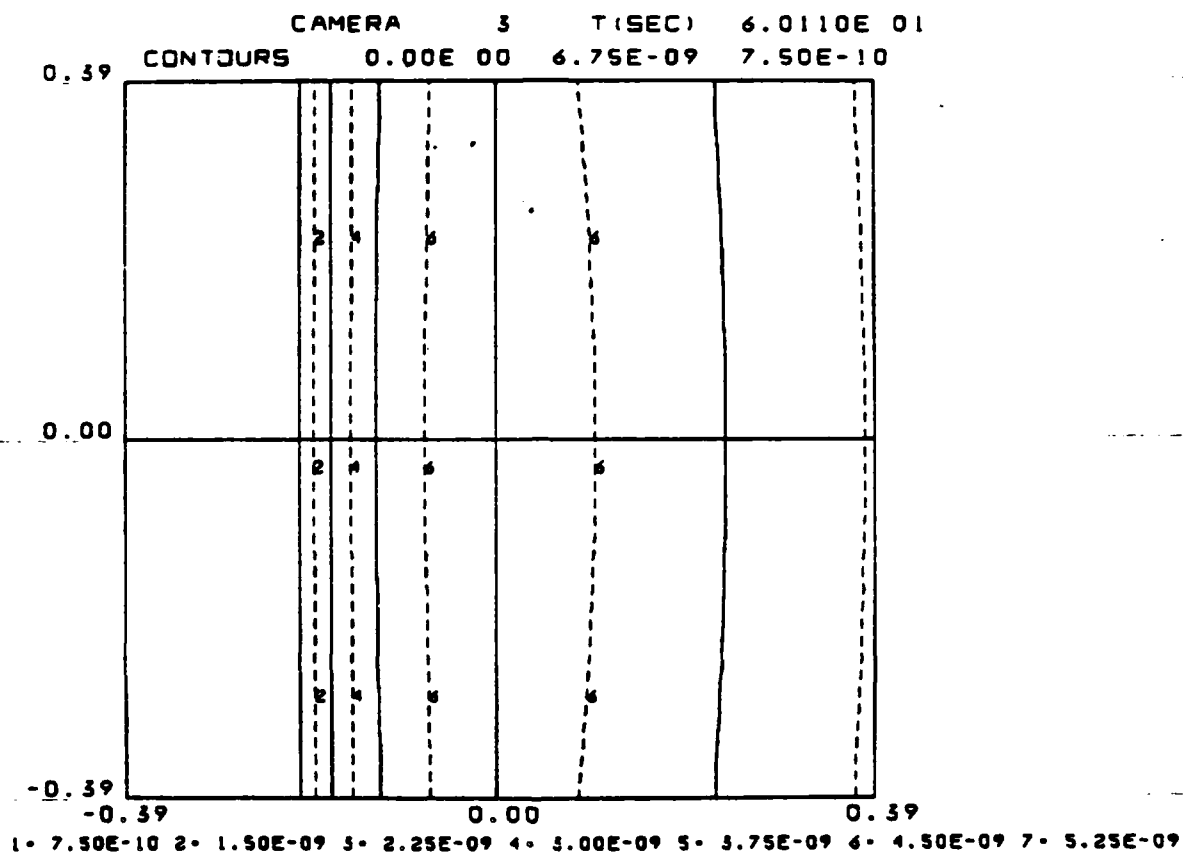


Fig. 15 - Camera 3 radiance contours (watts/cm²ster) 200 km from the cloud origin, 60 sec after release. Abscissa and ordinate are in degrees. Refer to contour label values in text or to key at bottom.

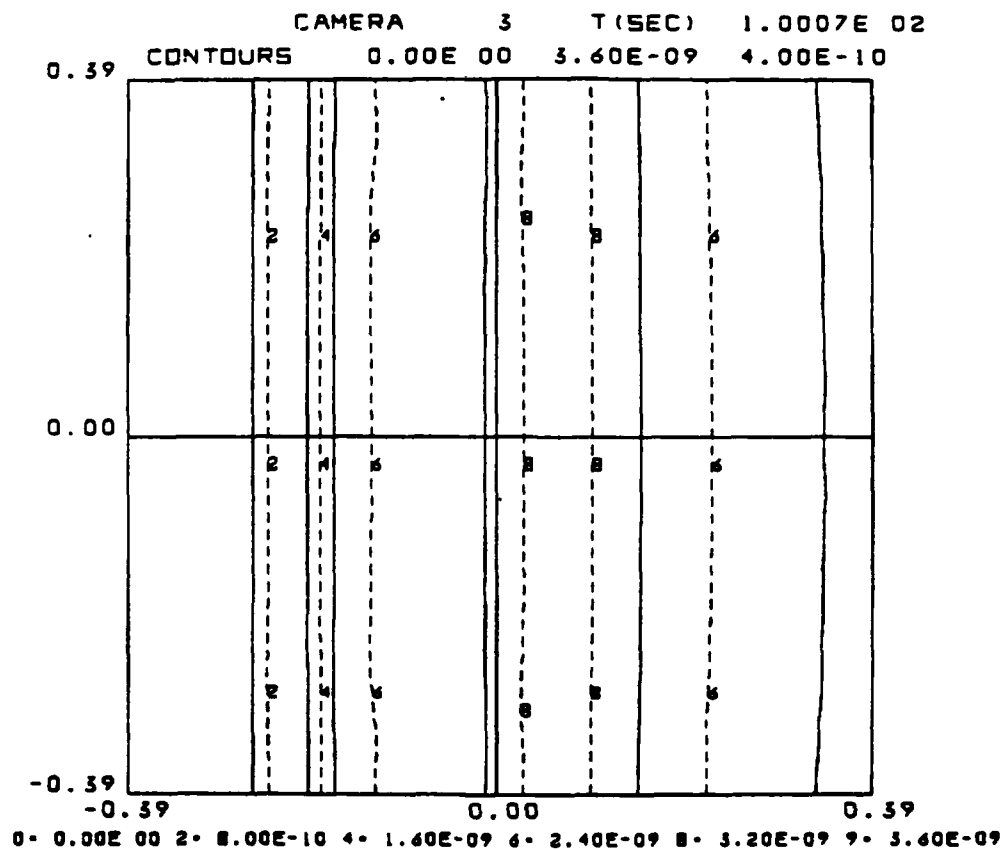


Fig. 16 - Camera 3 radiance contours (watts/cm² ster) 200 km from the cloud origin, 100 sec after release. Abscissa and ordinate are in degrees. Refer to contour label values in text or to key at bottom.

CAMERA 3 T(SEC) 1.2007E 02
 0.39 CONTOURS 0.00E 00 2.70E-09 3.00E-10

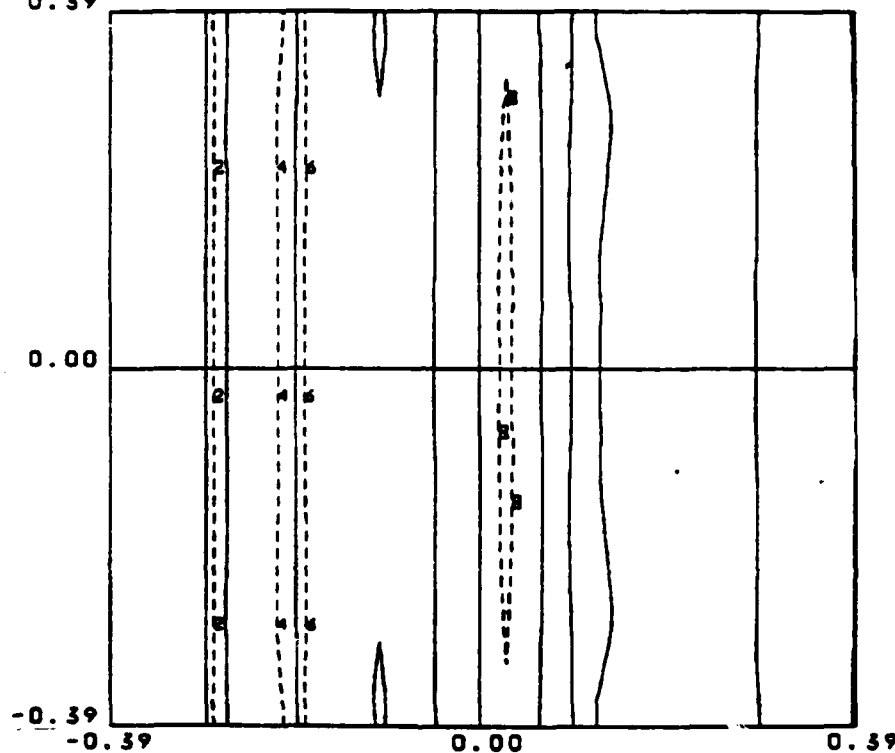


Fig. 17 - Camera 3 radiance contours (watts/cm² ster) 200 km from the cloud origin, 120 sec after release. Abscissa and ordinate are in degrees. Refer to contour label values in text or to key at bottom.

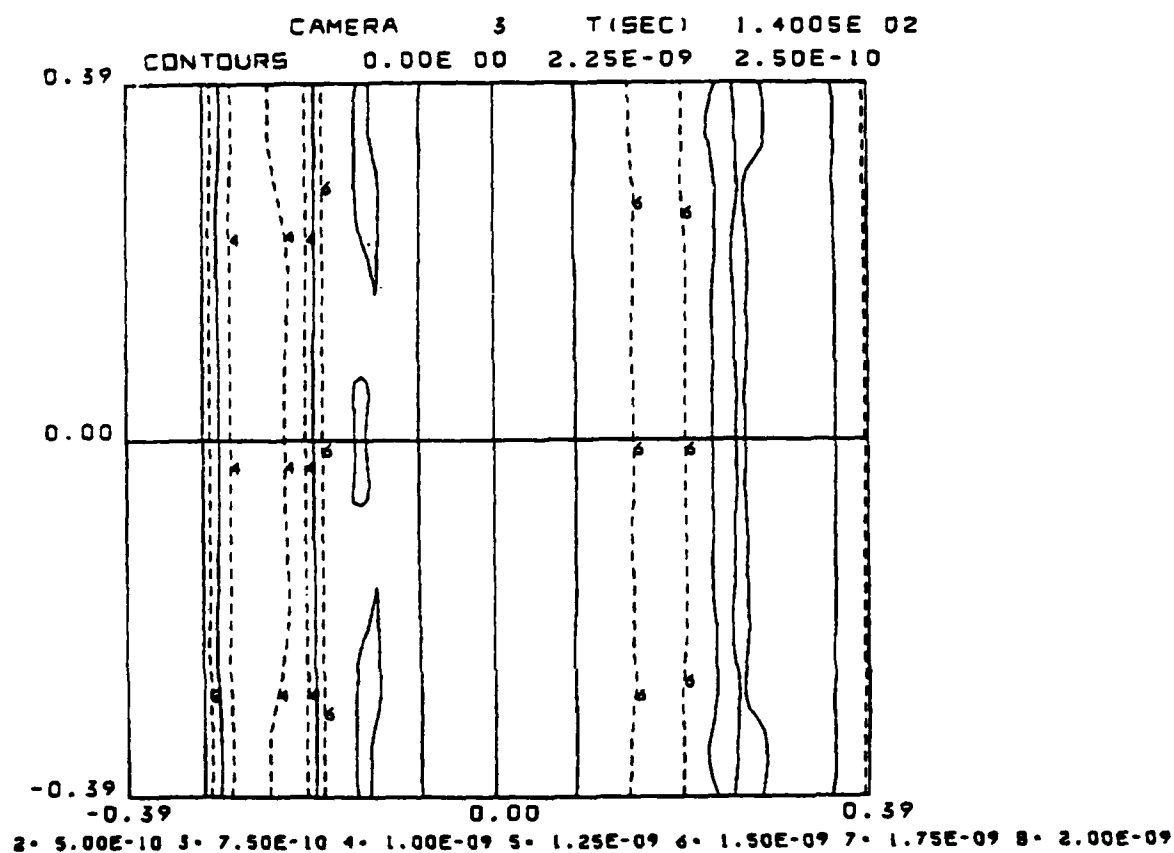


Fig. 18 - Camera 3 radiance contours ($\text{watts/cm}^2 \text{ster}$) 200 km from the cloud origin, 140 sec after release. Abscissa and ordinate are in degrees. Refer to contour label values in text or to key at bottom.

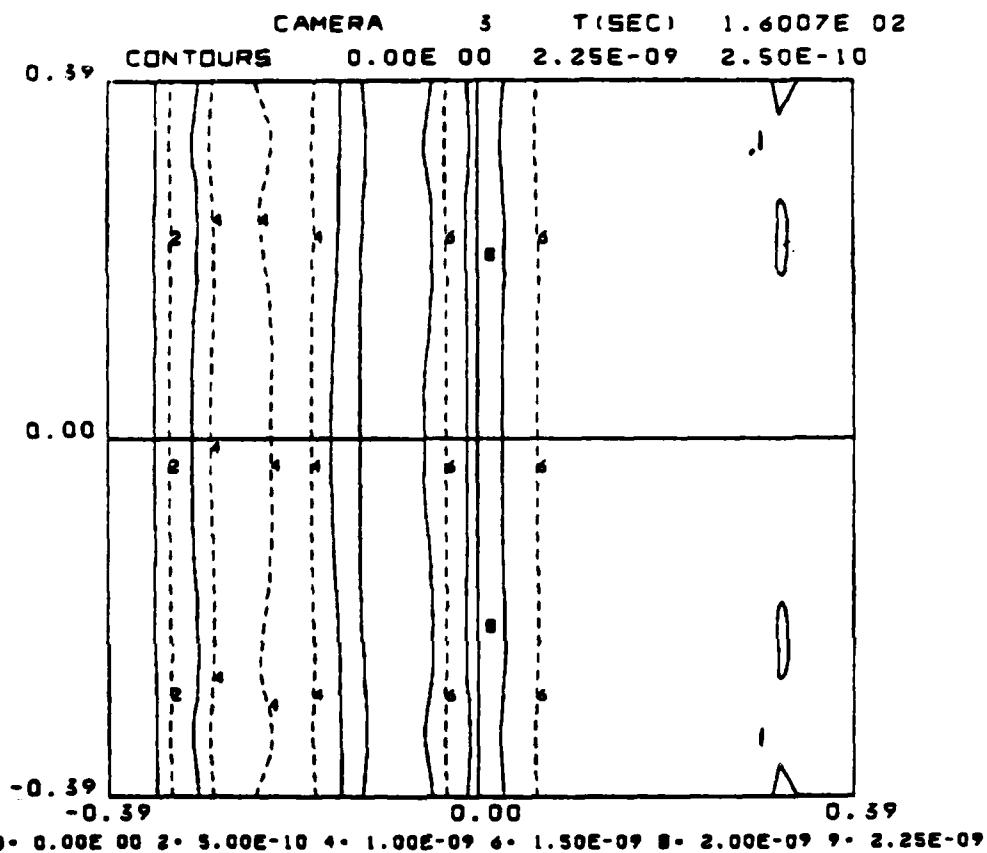


Fig. 19 - Camera 3 radiance contours (watts/cm²ster) 200 km from the cloud origin, 160 sec after release. Abscissa and ordinate are in degrees. Refer to contour label values in text or to key at bottom.

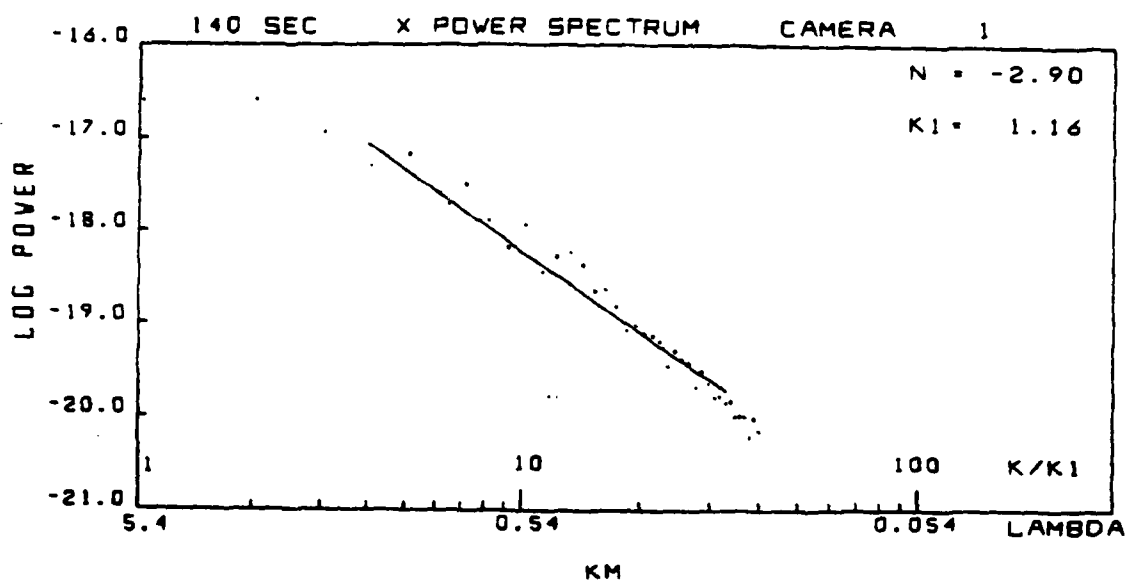


Fig. 20 - x Power spectrum from camera 1 (Figure 6 field of view).
Refer to text for explanation of scales.

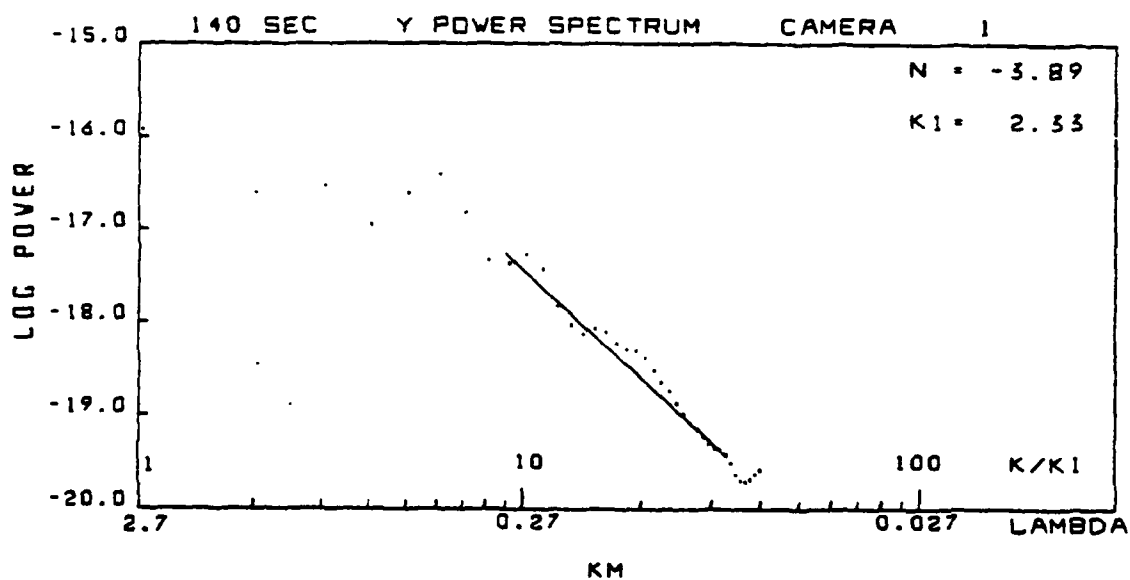


Fig. 21 - y Power spectrum from camera 1 (Figure 6 field of view).
Refer to text for explanation of scales.

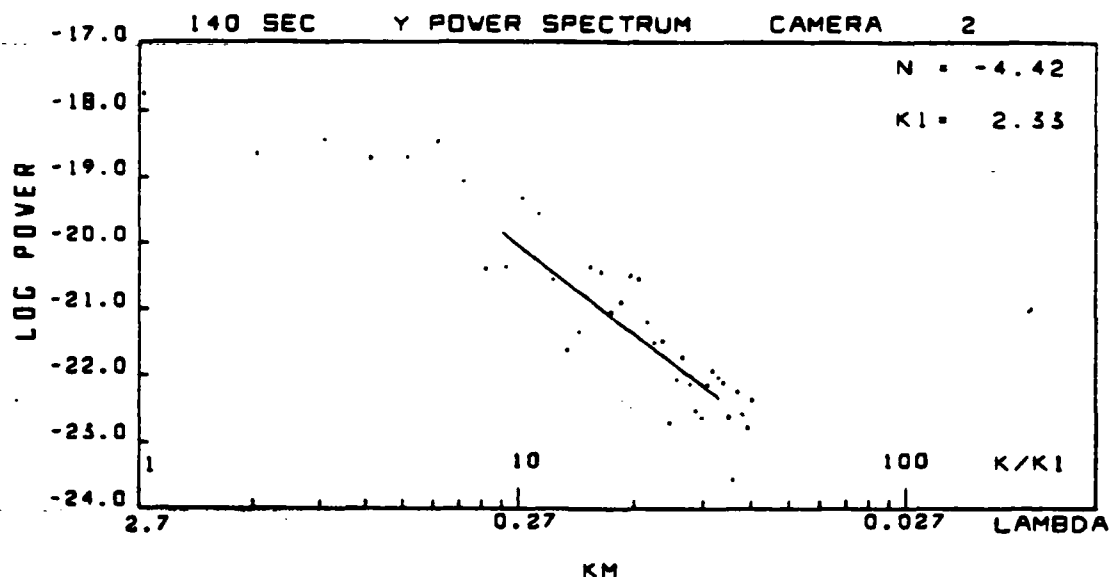


Fig. 22 - y Power spectrum from camera 2 (Figure 13 field of view).
Refer to text for explanation of scales.

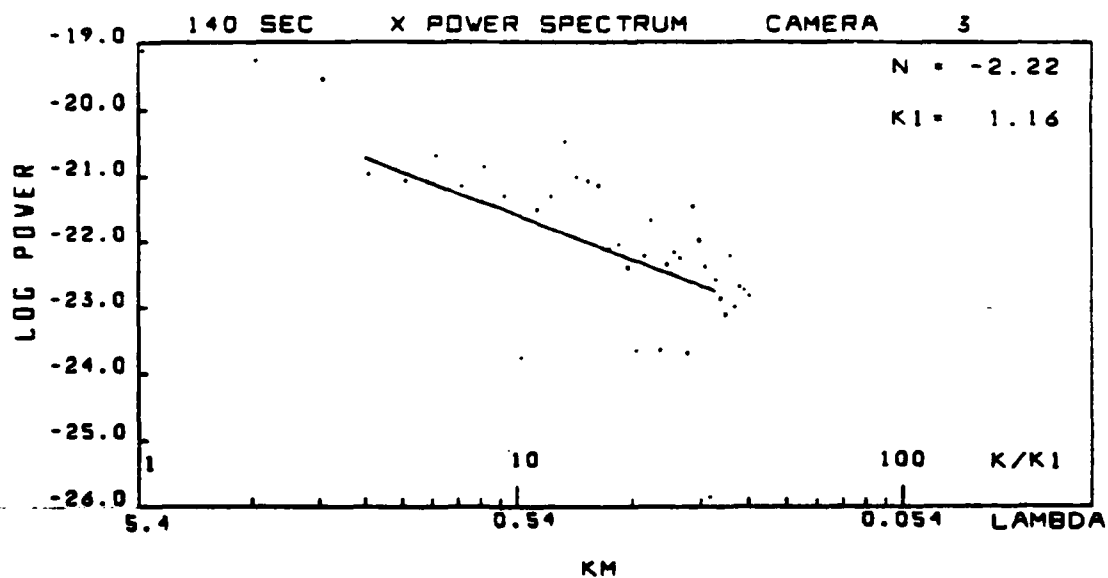


Fig. 23 - x Power spectrum from camera 3 (Figure 18 field of view).
Refer to text for explanation of scales.

CAMERA 1 (50 km) T(SEC) 1.4005E 02
 1.57 CONTOURS 0.00E 00 1.12E-07 1.25E-08

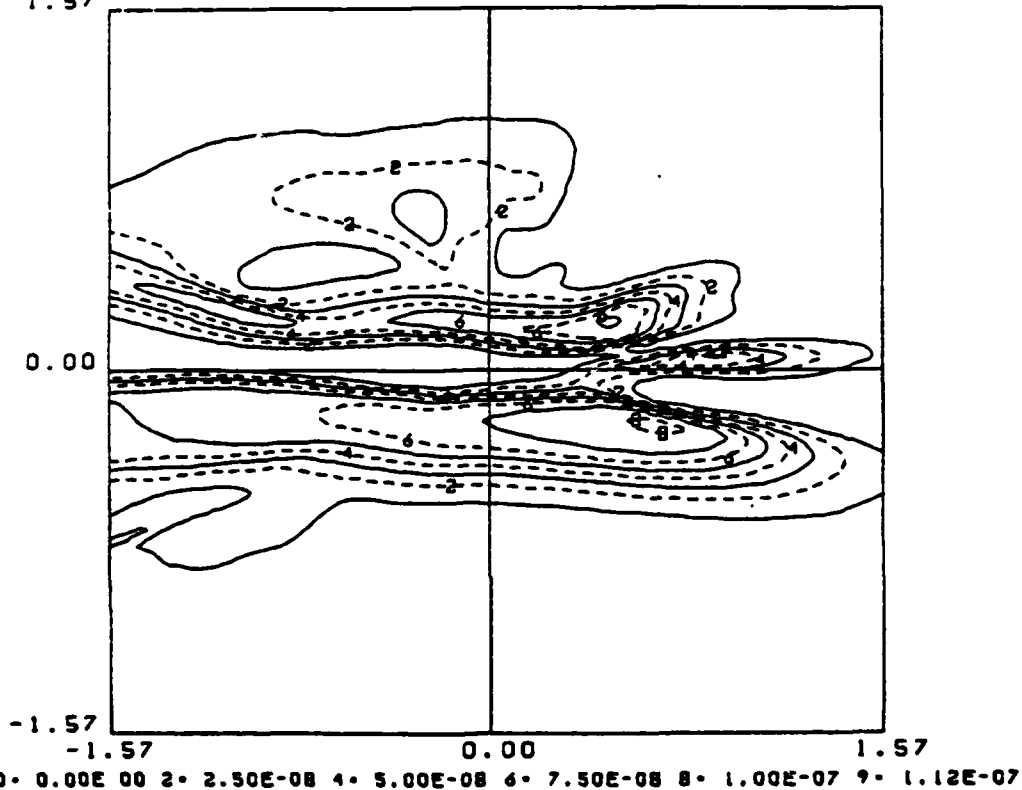


Fig. 24 - Camera 1 radiance contours ($\text{watts/cm}^2 \text{ster}$) 50 km from the cloud origin, 140 sec after release. Abscissa and ordinate are in degrees. Refer to text for contour label values or to key at bottom.

CAMERA 1 (600 km) T(SEC) 1.4005E 02
 0.13 CONTOURS 0.00E 00 1.12E-07 1.25E-08

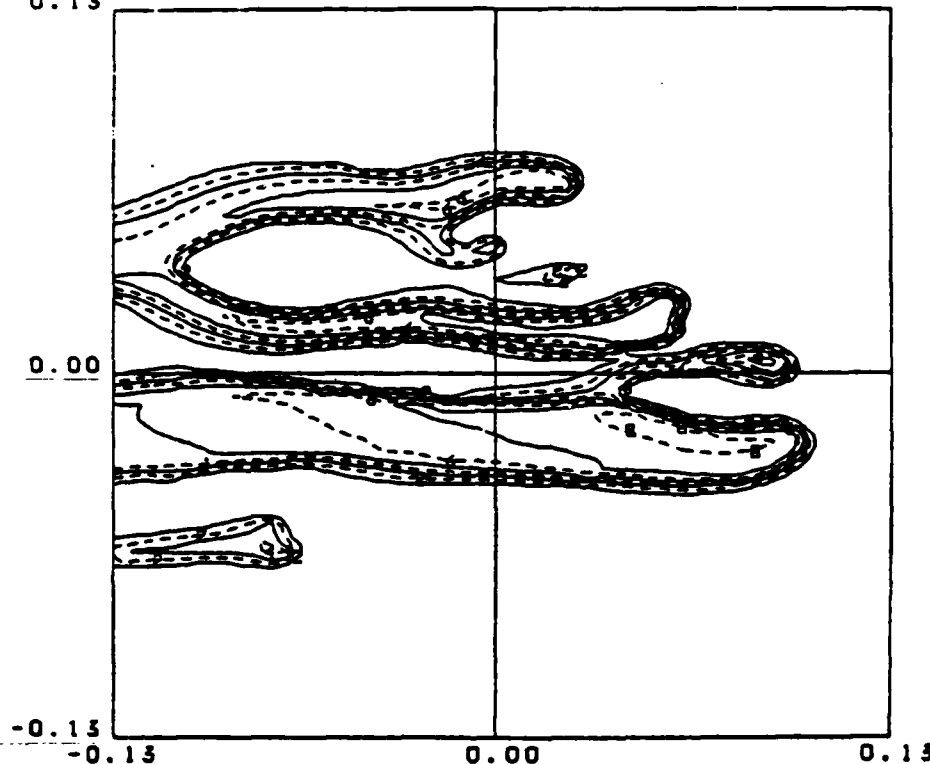


Fig. 25 - Camera 1 radiance contours (watts/cm²ster) 600 km from the cloud origin, 140 sec after release. Abscissa and ordinate are in degrees. Refer to text for contour label values or to key at bottom.

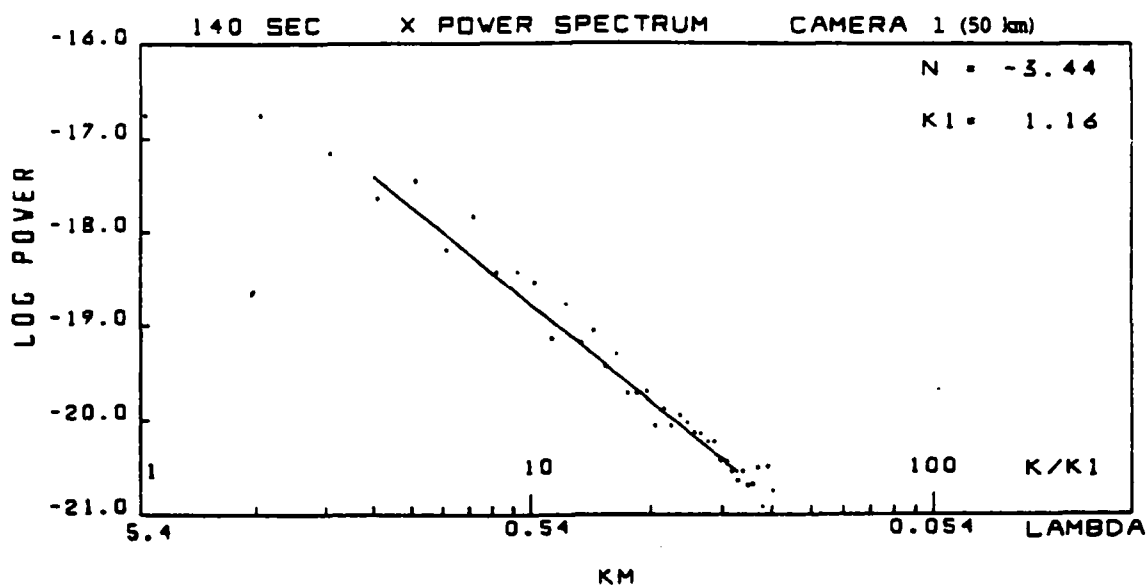


Fig. 26 - x Power spectrum from camera 1 (Figure 24 field of view).
Refer to text for explanation of scales.

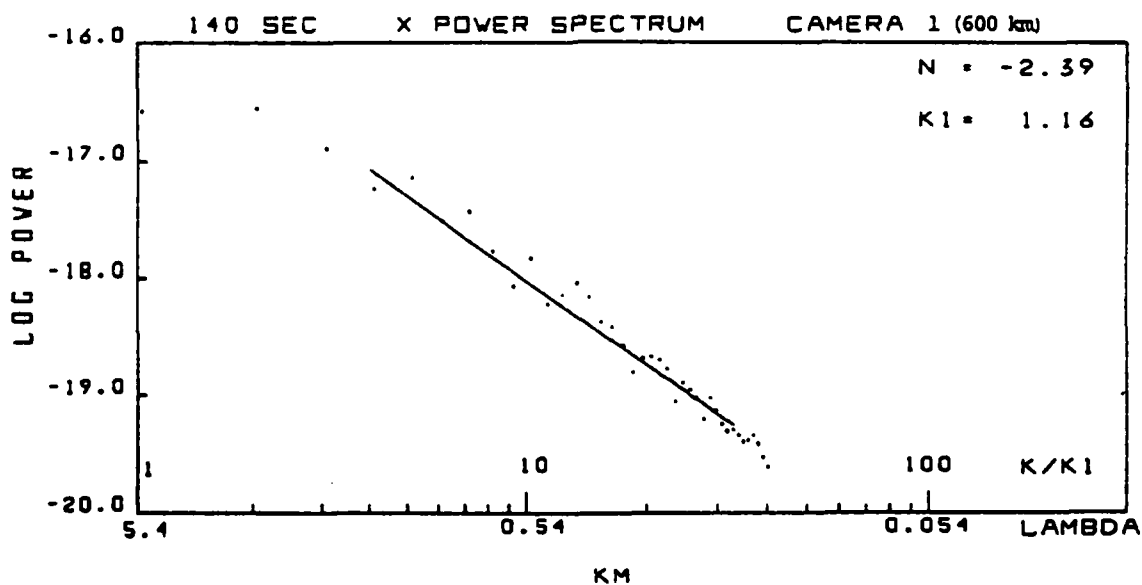


Fig. 27 - x Power spectrum from camera 1 (Figure 25 field of view).
Refer to text for explanation of scales.

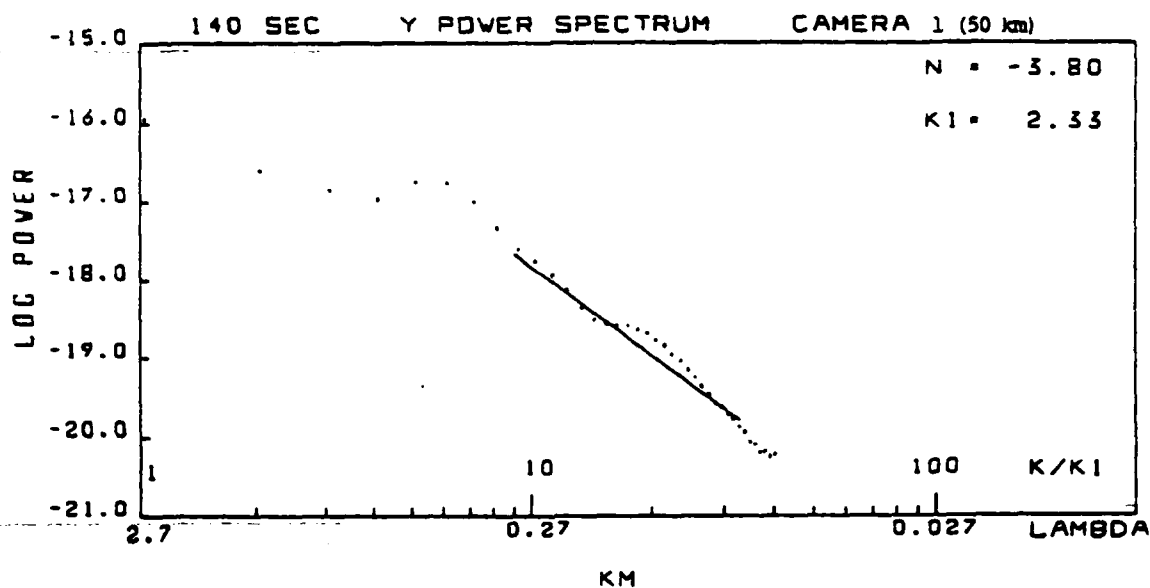


Fig. 28 - y Power spectrum from camera 1 (Figure 24 field of view).
Refer to text for explanation of scales.

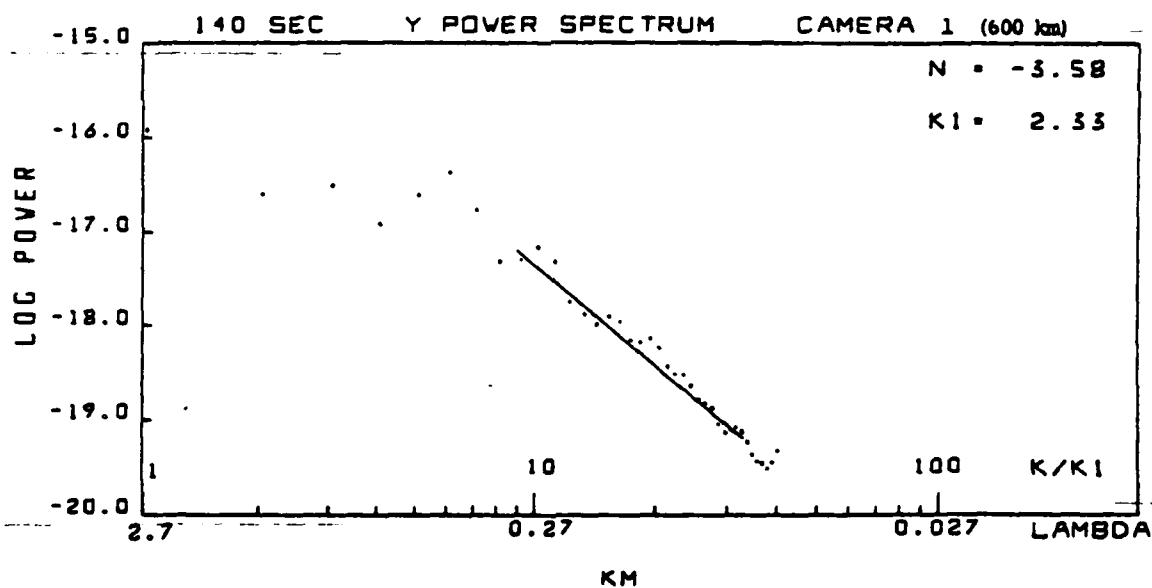


Fig. 29 - y Power spectrum from camera 1 (Figure 25 field of view).
Refer to text for explanation of scales.

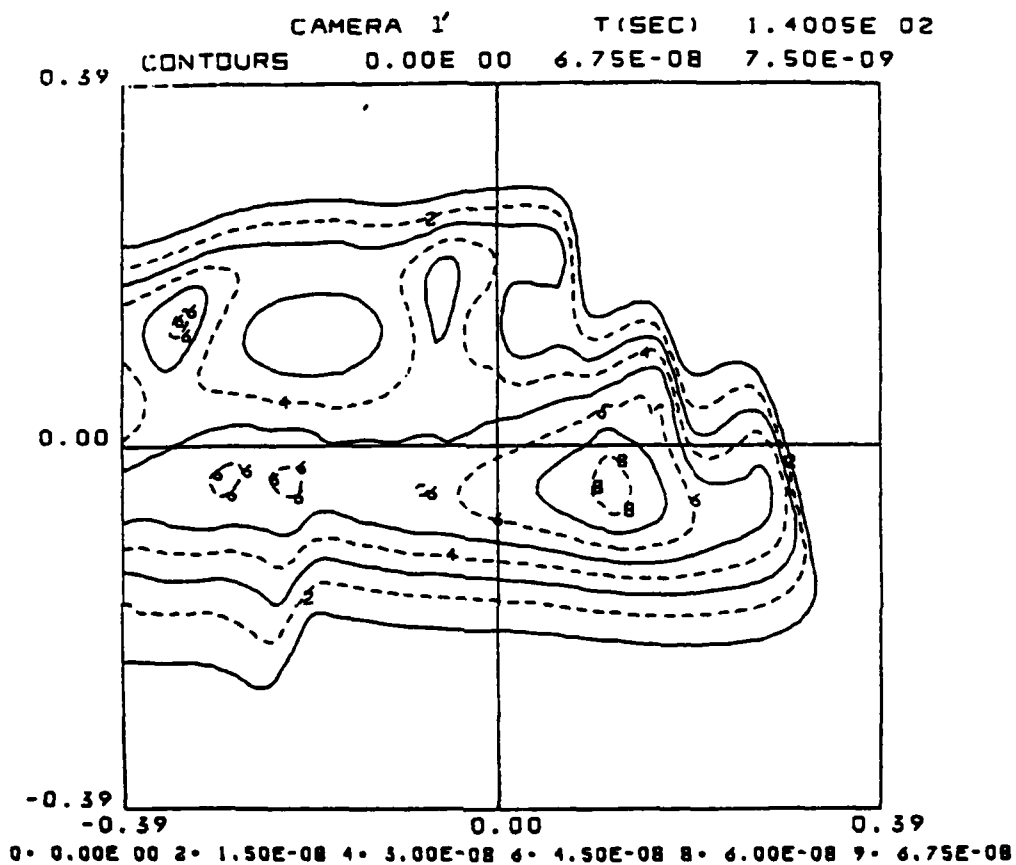


Fig. 30 - Camera 1, rotated 1° about x axis toward camera 3, radiance contours (watts/cm²ster) 200 km from the cloud origin, 140 sec after release. Abscissa and ordinate are in degrees. Refer to text for contour label values or to key at bottom.

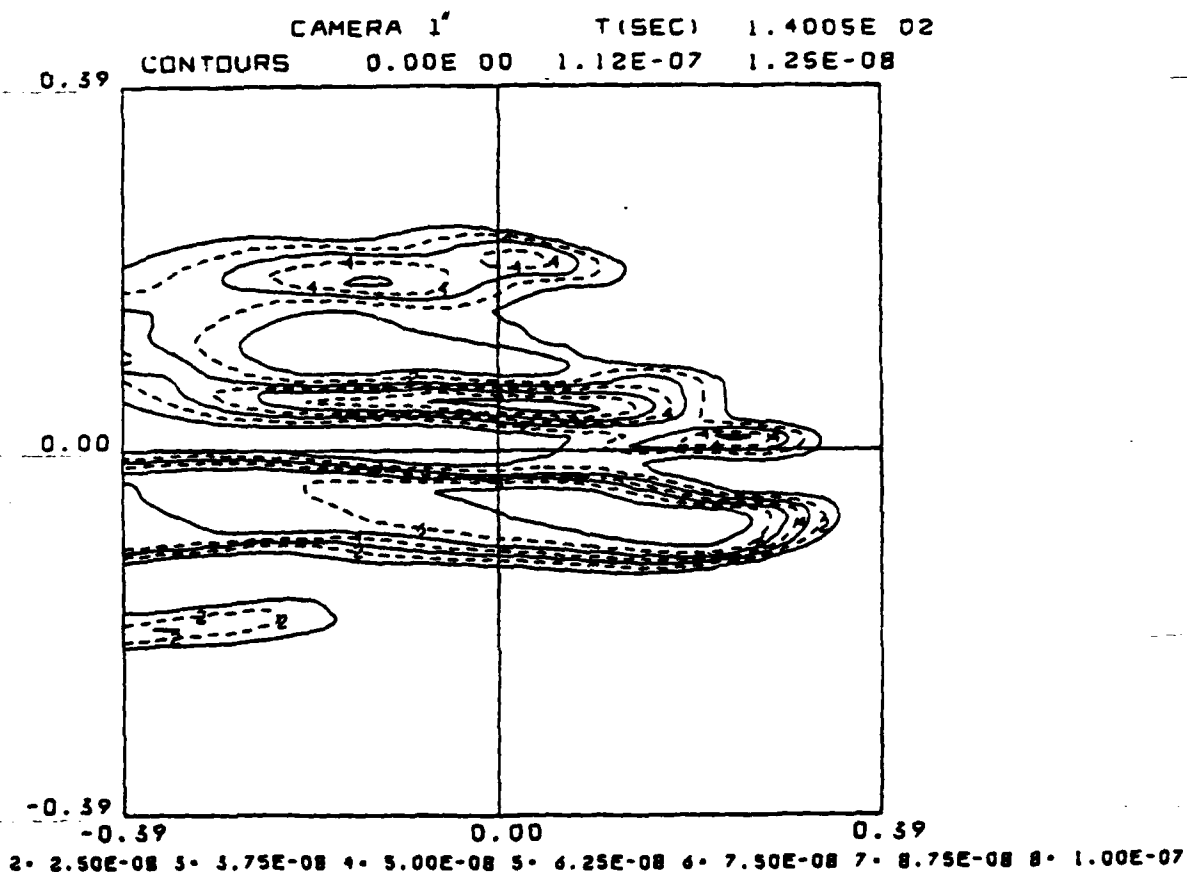


Fig. 31 - Camera 1, rotated 1° about y axis toward camera 2, radiance contours (watts/cm²ster) 200 km from the cloud origin, 140 sec after release. Abscissa and ordinate are in degrees. Refer to text for contour label values or key at bottom.

REFERENCES

1. Bien, F., "Nitric Oxide and Uranium Oxide Ion Studies", AFGL-TR-79-0164, June 1979.
2. Reidy, W.P., "LWIR/Structured Release Characteristics", Proceedings of the DNA Infrared Program Meeting, 23-24 January 1980.
3. Fite, W.L., T.A. Patterson, and M.W. Siegel, "Cross-Sections for Thermal Reactions Between Uranium Atoms and Atmospheric Species", AFGL TR77-0029, (1977).
4. Ossakow, S.L. and P.K. Chaturvedi, "Morphological Studies of Rising Equatorial Spread F Bubbles", J. Geophys. Res. 83, 2085 (1978).
5. Fite, W.L. and H.H. Lo, "Reactions of UO^+ with Atmospheric Gases", AFGL TR77-0029 (1977).
6. Gilmore, F., "Metal Oxides", Proceedings of the DNA Infrared Program Meeting, 23-24 January 1980.
7. Reidy, W.P., private communication.
8. McDonald, B.E., M.J. Keskinen, S.L. Ossakow, and S.T. Zalesak, "Computer Simulation of Gradient Drift Instability Processes in Operation Avefria", J. Geophys. Res. 85, 2143 (1980).
9. Hyman, E., M. Mul Brandon, and S. Ossakow, "The PHARO Code", NRL Memorandum Report 4667 (1981).
10. Zabusky, N.J. and J. Block, "Estimating the Spectrum of Electron Density Fluctuations from Simulations of Ionospheric Plasma Clouds", NRL Memorandum Report 3586, July 1978.

Appendix L
THE PHARO CODE

The PHARO Code

E. HYMAN

*Science Applications, Inc.
McLean, Virginia 22102*

M. MULBRANDON AND S. L. OSSAKOW

*Geophysical and Plasma Dynamics Branch
Plasma Physics Division*

November 24, 1981

This research was sponsored by the Defense Nuclear Agency under Subtask S990AXHC, work unit 00011, and work unit title, "Phoenix."



NAVAL RESEARCH LABORATORY
Washington, D.C.

Approved for public release; distribution unlimited.

SECURITY CLASSIFICATION OF THIS PAGE (When Data Entered)

REPORT DOCUMENTATION PAGE		READ INSTRUCTIONS BEFORE COMPLETING FORM
1. REPORT NUMBER NRL Memorandum Report 4667	2. GOVT ACCESSION NO.	3. RECIPIENT'S CATALOG NUMBER
4. TITLE (and Subtitle) THE PHARO CODE	5. TYPE OF REPORT & PERIOD COVERED Interim report on a continuing NRL problem.	
	6. PERFORMING ORG. REPORT NUMBER	
7. AUTHOR(s) E. Hyman*, M. Mulbrandon, and S. L. Ossakow	8. CONTRACT OR GRANT NUMBER(s)	
9. PERFORMING ORGANIZATION NAME AND ADDRESS Naval Research Laboratory Washington, DC 20375	10. PROGRAM ELEMENT, PROJECT, TASK AREA & WORK UNIT NUMBERS 62704H; 47-0890-0-1	
11. CONTROLLING OFFICE NAME AND ADDRESS Defense Nuclear Agency Washington, DC 20305	12. REPORT DATE November 24, 1981	
	13. NUMBER OF PAGES 29	
14. MONITORING AGENCY NAME & ADDRESS (if different from Controlling Office)	15. SECURITY CLASS. (of this report) UNCLASSIFIED	
	15a. DECLASSIFICATION/DOWNGRADING SCHEDULE	
16. DISTRIBUTION STATEMENT (of this Report) Approved for public release; distribution unlimited.		
17. DISTRIBUTION STATEMENT (of the abstract entered in Block 20, if different from Report)		
18. SUPPLEMENTARY NOTES Present address: Science Applications, Inc., McLean, Virginia 22102 This research was sponsored by the Defense Nuclear Agency under Subtask S99QAXHC, work unit 00011, and work unit title, "Phoenix."		
19. KEY WORDS (Continue on reverse side if necessary and identify by block number) Visible radiation Sensors Infrared radiation Line and band transitions Isophots High altitude nuclear data comparisons Cameras		
20. ABSTRACT (Continue on reverse side if necessary and identify by block number) The PHARO code predicts the visible and infrared radiative output of high altitude nuclear bursts. Using the results of the large scale NRL hydrocodes, both the spatial and temporal variation of the radiation (watts/cm ² sr) in arbitrary wavelength intervals is determined. The results are a series of "isophot" plots for arbitrarily placed cameras or sensors which can be directly compared with experiment. In addition to monitoring the important line and band transitions the bound-bound, free-bound, and free-free radiation is calculated for a recombining oxygen plasma. In particular, the bound-bound (Continues)		

DD FORM 1473
1 JAN 73EDITION OF 1 NOV 68 IS OBSOLETE
S/N 0102-014-6601

SECURITY CLASSIFICATION OF THIS PAGE (When Data Entered)

SECURITY CLASSIFICATION OF THIS PAGE (When Data Entered)

20. ABSTRACT (Continued)

radiation does not assume a Saha population of excited levels but calculates this radiation as a function of electron temperature and density and ground state oxygen density. Comparisons with representative high altitude data are exhibited.

SECURITY CLASSIFICATION OF THIS PAGE (When Data Entered)

CONTENTS

I. INTRODUCTION	1
II. HANE RADIATIVE EMISSION CALCULATIONS	2
III. PHARO GEOMETRY	5
IV. RESULTS AND DISCUSSIONS	6
ACKNOWLEDGMENT	8
REFERENCES	18

THE PHARO CODE

SECTION I

INTRODUCTION

PHARO, an acronym for "Phenomenology and Radiation Output," is a computer code developed to calculate the visible and infrared (IR) emission from a disturbed atmosphere. As part of NRL's high altitude nuclear effects (HANE) program, it utilizes the results of NRL's high altitude phenomenology calculations, specifically the MRHYDE (and its successor, PHOENIX) computer code. It is currently being used, also, to study LWIR emission from plasma cloud releases, using codes which model the development of spatial irregularities in the high altitude atmosphere. PHARO calculates emission in the visible and IR from all sources of radiation including:

- (1) bound-bound transitions in the decaying atomic plasma and transitions from the low lying metastable states of atoms and atomic ions,
 - (2) band emission from molecules due to electron impact excitation or heavy particle reactions, which leave a product species in an excited electronic or vibrational state (e.g., chemiluminescence),
 - (3) free-bound and free-free continuum transitions.
- A detailed description of these lines and bands is given in Section II.

The output of the PHARO code consists of contour plots of radiative intensity ($\text{watts/cm}^2\text{ster}$) or "isophot" plots for arbitrarily placed sensors. These will be described in more detail in Section III. A series of these plots give both a spatial and

Manuscript submitted August 25, 1981.

temporal picture of the radiation, which is directly comparable with experiments. In Section IV we present a comparison between PHARO results and some measured values, and a discussion of further potential comparisons.

Briefly, PHARO works as follows: the calculation of the radiation starts with the results of a computer code such as MRHYDE, a three-dimensional, two fluid MHD reactive flow code which describes both the hydrodynamics and chemistry of the high altitude burst. MRHYDE begins its calculations on the order of one second after burst, using as initial conditions the atmosphere after prompt x-ray emissions and deposition of uv energy, debris energy, and inclusion of a blast wave.

The PHARO code reads from tape the MRHYDE results at prespecified times and at a large number of mesh points. For the results we will present in this report, there were of order 10^4 mesh points (due to reflection symmetry about a vertical plane through the magnetic field there are effectively twice this number).

This report will describe PHARO II which differs from PHARO I⁽¹⁾ primarily in the treatment of the bound-bound radiation. In PHARO I the calculations assumed a hydrogenic recombining plasma with Saha populations of the excited states. In PHARO II an oxygen plasma is assumed and actual population densities of the excited states are calculated.⁽²⁾

SECTION II

HANE RADIATIVE EMISSION CALCULATIONS

The species carried in the MRHYDE code are given in Figure 1. The temperatures listed are the electron temperature, T_e , the

vibrational temperature of N_2 , T_v , and the heavy particle kinetic temperature, T_a . Some of the HANE codes currently carry separately the ion temperature, T_i , and the neutral temperature, T_n . N_2^+ is not carried in MRHYDE since it is generally a minor ion by the time the MRHYDE calculations are initiated. It is carried in the uv deposition code which provides initial conditions for MRHYDE, however. In Figure 2 we exhibit the major line emissions from metastable states and molecular bands that the PHARO code monitors. It is apparent that not all of the excited state species that we require for PHARO are carried in MRHYDE. Those not carried we assume to be in quasi-steady state equilibrium and calculate their populations. The species for which this assumption is used are $N(^2P)$, $O(^1S)$, $N^+(^1S)$, $O^+(^2D)$, $O^+(^2P)$, $O_2(a^1\Delta)$, and $O_2(b^1\Sigma)$.

To calculate the NO chemiluminescence in the fundamental at 5.3μ and the overtone at 2.7μ the following assumptions were used. The vibrationally excited NO, formed via the reaction $N + O_2 \rightarrow NO + O$, is sufficiently exothermic to populate NO up to the 6th vibrational state. In addition, $N(^2D) + O_2 \rightarrow NO + O$ can excite up to the 18th vibrational level of NO. We assume half the exothermicity is available to vibrational states. A straight-forward steady state calculation then gives the number of photons of the fundamental and overtone for these reactions. Since quenching has not been included, this will give an upper limit to the emitted radiation. Also, we include the translation-vibration reaction between NO and hot O atoms which is frequently a critically important source of 5.3μ and 2.7μ radiation. In some applications more sophisticated models have been used for determining the number of photons/reaction.

In a similar way the NO^+ radiation from vibrational transitions at 4.3μ and 2.15μ are calculated⁽³⁾ assuming formation of vibrationally excited NO^+ via $\text{N}^+ + \text{NO} \rightarrow \text{N} + \text{NO}^+$, $\text{N} + \text{O}_2^+ \rightarrow \text{NO}^+ + \text{O}$, $\text{N}_2 + \text{O}^+ \rightarrow \text{NO}^+ + \text{N}$, $\text{N}^+ + \text{O}_2 \rightarrow \text{NO}^+ + \text{O}$. In addition, the N_2^+ Meinel Bands are assumed to arise⁽³⁾ via $\text{N}_2 + \text{O}^+(^2\text{D}) \rightarrow \text{N}_2^+(\text{A}^2\pi, v = 1) + \text{O}$ and the second negative of O_2^+ in the visible is assumed⁽³⁾ to result from $\text{O}^+(^2\text{D}) + \text{O}_2 \rightarrow \text{O}_2^+(\text{A}^2\pi) + \text{O}$. Finally, a model for the 4.3μ and 10.6μ radiation from CO_2 is included.

To calculate the late-time atomic bound-bound line radiation PHARO II assumes the late-time disturbed atmosphere to be a decaying oxygen plasma. Calculation of the radiation requires a knowledge of the population of the excited states of oxygen as a function of electron density and temperature and, for sufficiently high temperature, the ground state population, $\text{O}(^3\text{P})$. To accomplish this a model⁽²⁾ has been developed which determines the population densities of all triplet and quintet oxygen levels up to $n = 18$ as a function of these parameters. These calculations have been performed for 11 electron temperatures ranging between .03 and 2.0 eV, 7 electron densities between 10^6 and 10^{12}cm^{-3} , and, in the case of electron temperatures equal to or greater than .5 eV, the same range of oxygen ground state densities.

The results of the above calculations, the population of 338 excited levels for each of the above set of parameters, are stored on disk. Once wavelength intervals are specified a separate code reads the disk and determines the radiation emitted in each wavelength interval for each set of parameters. These results are, in turn, stored on a disk which is read by the PHARO code for

interpolation to the actual temperature and densities at a given point.

Finally, the continuum radiation, oxygen free-bound and free-free emission, are based on the calculations of Davis and Lewis.⁽⁴⁾

SECTION III

PHARO GEOMETRY

In Figure 3 we display the geometry used in the PHARO code to produce the "isophot" plots. B represents the initial burst position. The X-axis is in the direction of the horizontal component of the earth's magnetic field. The proposed position of the camera or sensor is specified by its distance from the burst point, s , a polar angle relative to the upward vertical direction at the burst, Θ , and an azimuthal angle, Φ , measured relative to the horizontal magnetic field direction. A camera at this position may have an arbitrary orientation relative to the burst point. Two angles specify the direction of the line of sight of the sensor: a polar angle, θ , relative to the burst-sensor line and an azimuth angle, ϕ , (not shown in Figure 3) measured relative to the plane defined by the burst point, the sensor position, and the center of the earth.

Having specified the sensor position and orientation a set of rays is constructed. The first ray is along the line of sight of the sensor (as indicated in Figure 3) and the others are arrayed on a set of equally spaced cones with common apex at the sensor point and common axis along the sensor line of sight. On each cone the rays are equally spaced around the cone. Next, a set of equally spaced points is chosen along each ray, from the sensor to

the far side of the MRHYDE mesh. By interpolation between the MRHYDE mesh points and these points the total emission at each point along the rays is determined for each wavelength interval of interest, using an appropriate volume as illustrated in Figure 3. Finally, a summation is performed along each ray and the total radiation ($\text{watts/cm}^2\text{ster}$) from each ray direction determined. In the present version of the code, PHARO II, the emission is assumed to be optically thin. Furthermore, the code permits attenuation of the radiation as it travels from its source through the ambient atmosphere to the sensor. An atmospheric model has been developed and incorporated into PHARO based on the models of McClatchey at AFGL.

The set of ray directions relative to the sensor line of sight form a two-dimensional polar grid of intensities from which the contour plots are constructed. In some applications of the PHARO code, the rays are arrayed on a rectangular grid and the contour plots are constructed from a two-dimensional rectangular grid. With a PHARO sensor placed where measurements were taken it is possible to construct plots that can be directly compared with experimental isophot plots.

SECTION IV

RESULTS AND DISCUSSION

In Figures 4-8 we exhibit typical PHARO plots predicting the radiance ($\text{watts/cm}^2\text{ster}$) in the 8-14 μ band from a high altitude nuclear burst at successive times following initiation of the MRHYDE calculation (times 0.0, 20.0, 60.0, 100.0, and 140.0 seconds). The camera is a distance of 500 km from the burst with its optic

axis passing through the burst point. The ordinate and abscissa give the angle in degrees from the camera axis. Alternate contours are solid lines or dots, with the latter, only, labeled. The numbers at the top of the plot label the radiance values. Reading from left to right, the leftmost value corresponds to contour number 1 which is the smallest radiance value that can be plotted, the middle number to contour number 10, and the rightmost number the inverse of the number of contours per logarithmic decade. Thus, in Figure 4, contour 8 represents a radiance of 1×10^{-5} watts/cm²ster and contour 2 is 1×10^{-8} watts/cm²ster. The Figures 4-8 exhibit clearly the temporal effects: the effect of the hydrodynamics in heating the atmosphere and diffusing the plasma, and the chemistry in reducing the emission.

In Figure 9 we see a measured isophot plot of visible radiation from a high altitude burst (on the right) and the corresponding PHARO prediction. Additional predictions and comparisons with data have been documented in the literature.

We view the PHARO code as a very versatile code particularly useful in providing predictions that are easily compared directly with measurements. Specifically, the high altitude bursts that can be modeled by a MRHYDE (PHOENIX) 3D 2-fluid magnetohydrodynamic code provide a set of measurements that can provide direct tests of our understanding of disturbed atmosphere phenomenology. In the past several years there have been important improvements in our understanding of a variety of these atmospheric phenomena that directly bear on measurements that were made, and that have not been tested by comparison with these results.

Consider the Starfish event. There are a set of isophot plots of visible radiation that have been published for times out to 33.9 seconds of the northern conjugate region from an aircraft. There are similar data from other locations that has not been analyzed. This kind of data is in an ideal form for comparison with PHARO predictions.

In addition, there were IR measurements made with a variety of detectors on each of two aircraft. In many cases data above background were obtained for 10^3 seconds. The measurements include the 1.1 - 3.0 μ band (spatial radiometer), 4.8 - 5.5 μ band and 2.6 - 2.7 μ band (filter photometer), a variety of bands between 1.5 and 2.8 μ (filter wheel radiometer), 1.55 - 1.62 μ (PbS radiometer), 5.0 - 5.5 μ (IR Spectrometer). There are, in addition, a variety of uv, visible, and near infrared measurements made both from aircraft and ground stations. The reliability, extent, and state of analysis of this large quantity and variety of data require evaluation. But, in principle, PHARO predictions make these measurements directly accessible to analysis.

ACKNOWLEDGMENT

This work was supported by the Defense Nuclear Agency.

N_2, O_2, NO

O_2^+, NO^+

$N, N(^2D), N^+$

$O, O(^1D), O^+$

T_e, T_v, T_a

Fig. 1 — Chemical species and temperatures carried in MRHYDE
(and PHOENIX) 3D hydrocode

PHARO II

PHENOMENOLOGY AND RADIATION OUTPUT CODE

OPTICAL AND IR TRANSITIONS

O	6300Å, 5577Å
N	5200Å, 1.04μ
N ⁺	6527Å, 5754Å
O ⁺	7320Å
N ₂ ⁺	3914Å, 9212Å, 1.5μ
O ₂	7619Å, 1.26μ
NO	2.7μ, 5.4μ
NO ⁺	2.15μ, 4.3μ

Fig. 2 — Important visible and infrared transitions monitored in PHARO

PHARO GEOMETRY

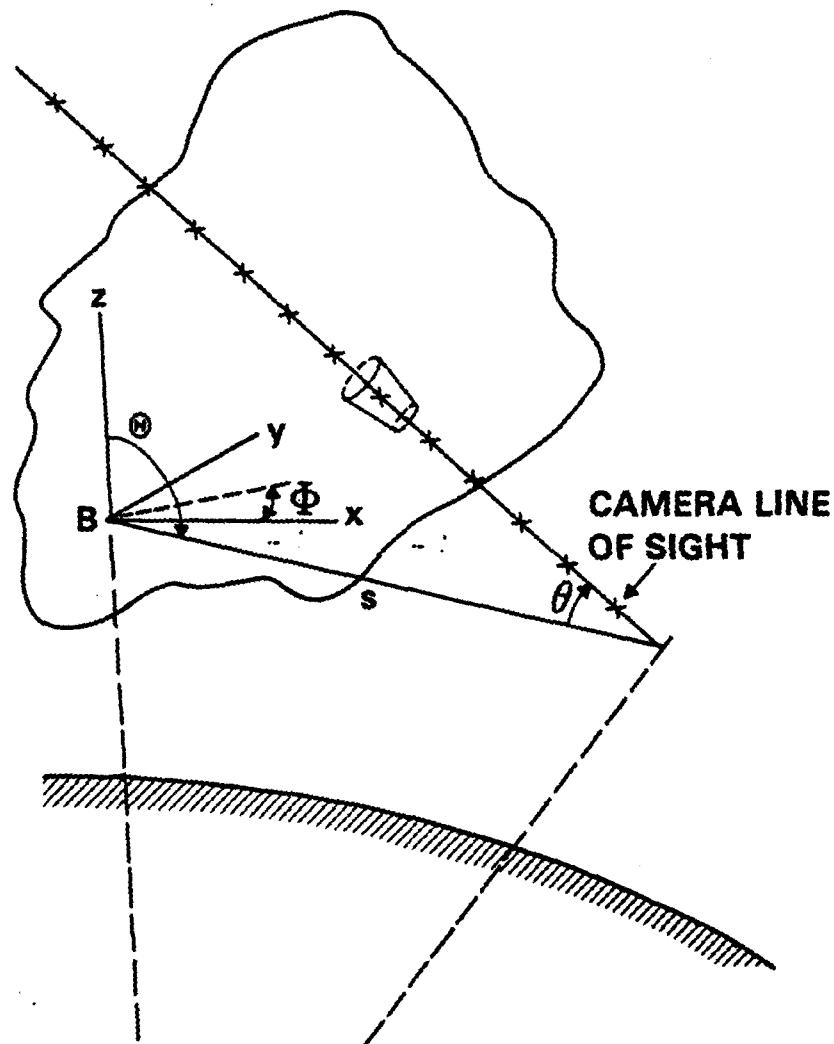


Fig. 3 — Line integration of volume emission from conical segments at a particular wavelength, along a ray, to obtain radiance. s is the distance between camera and burst point, B . Θ and Φ define the direction from burst to camera. θ and ϕ (not shown) define the direction of the camera line of sight relative to the burst point.

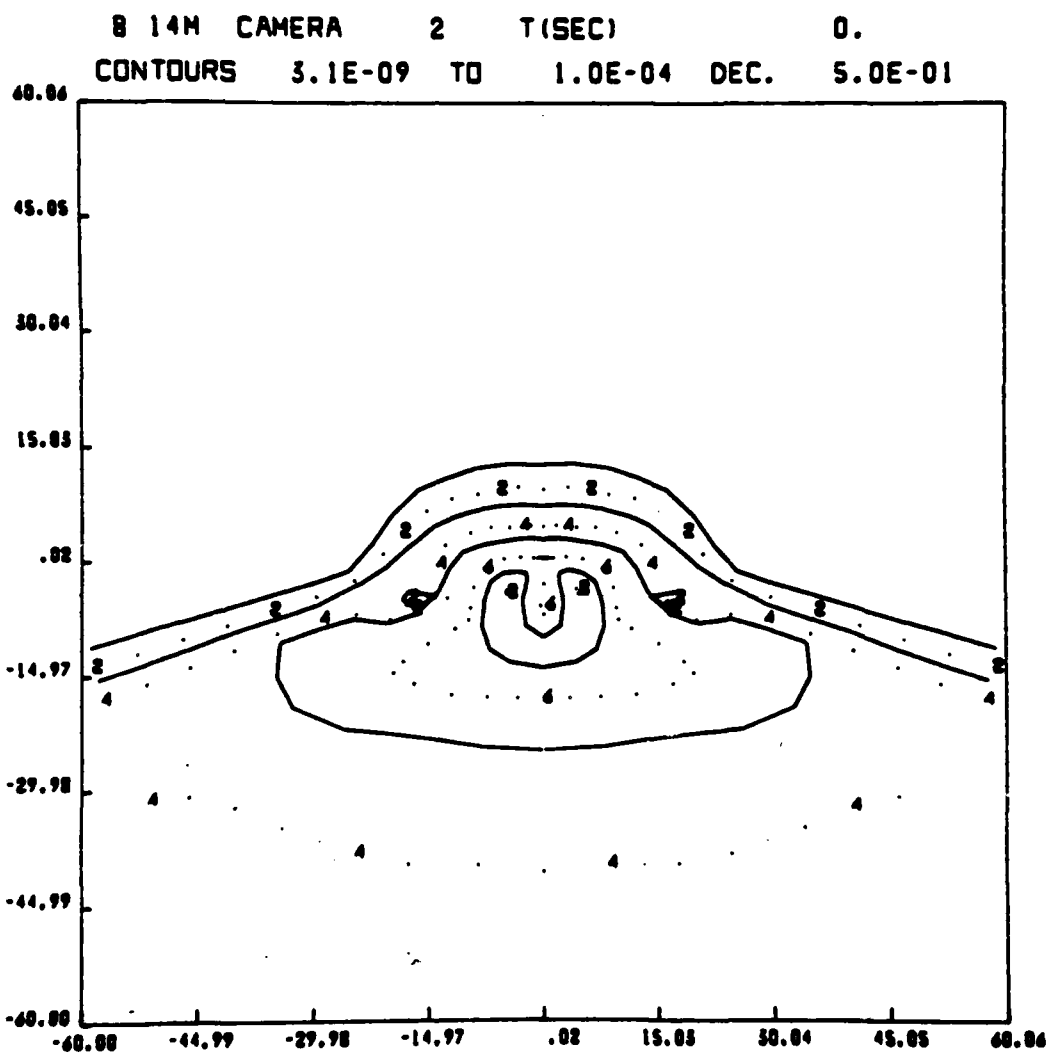


Fig. 4 — Radiance in the 8-14 μ band (watts/cm²ster) from a high altitude burst \sim 1. sec after burst. Abscissa and ordinate in degrees.

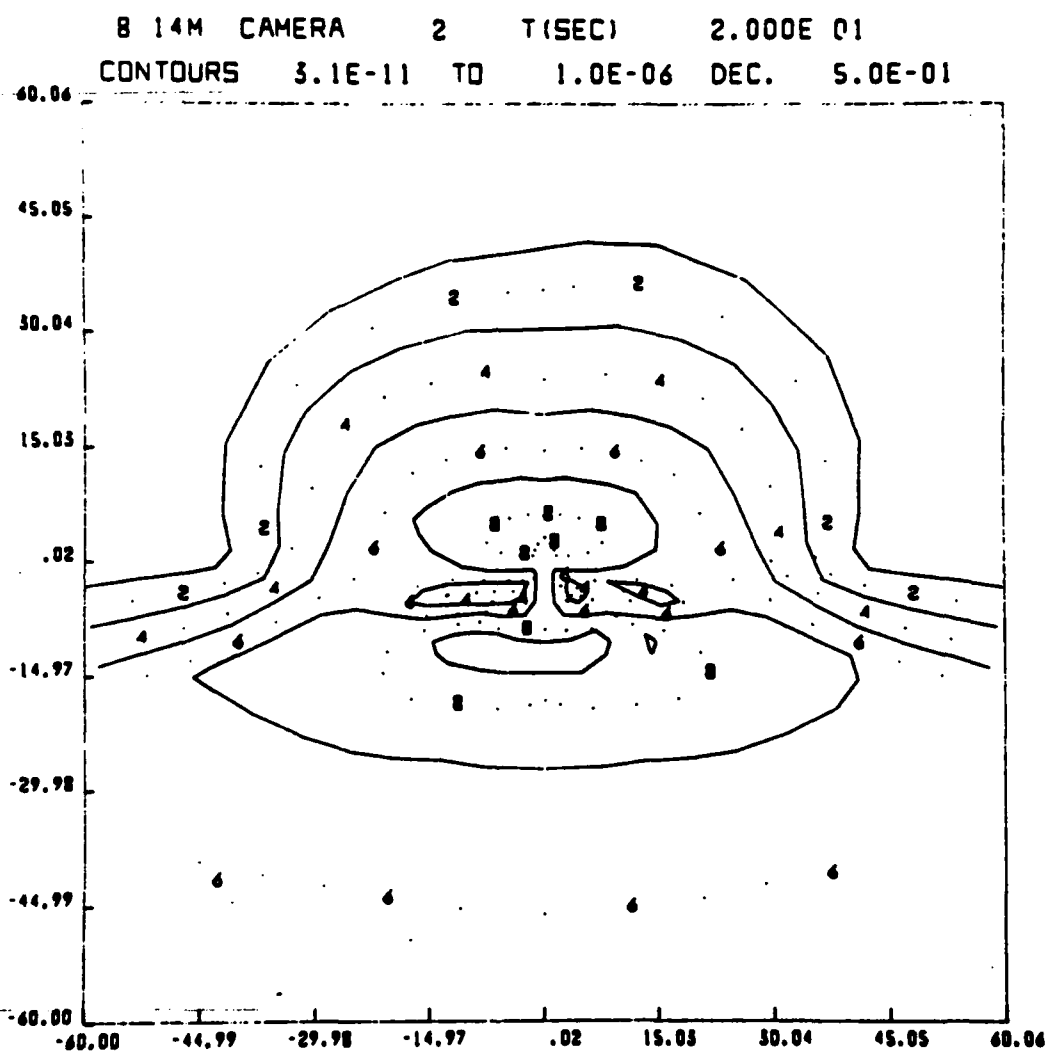


Fig. 5 — Radiance in the 8-14 μ band (watts/cm²ster) from a high altitude burst \sim 20. sec after burst. Abscissa and ordinate in degrees.

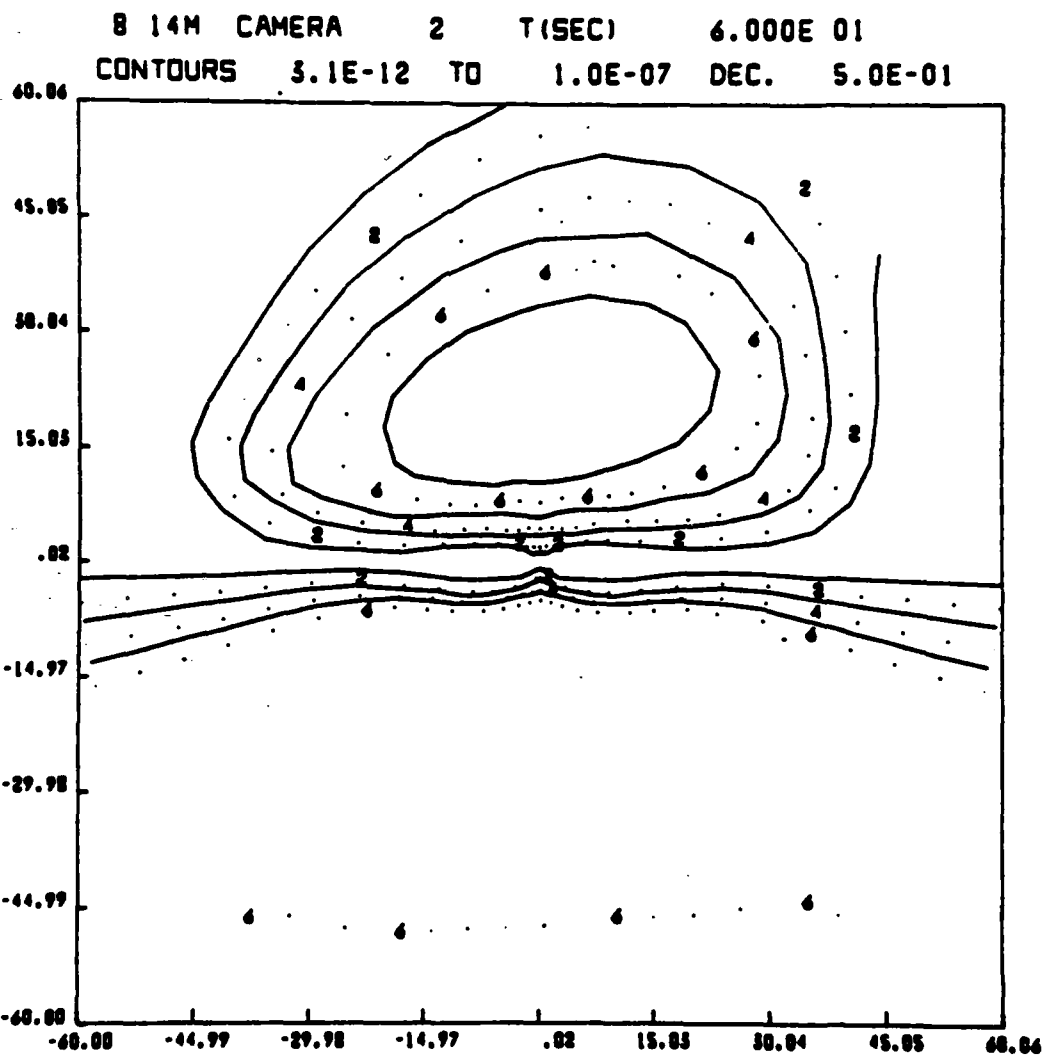


Fig. 6 — Radiance in the 8-14 μ band (watts/cm²ster) from a high altitude burst \sim 60. sec after burst. Abscissa and ordinate in degrees.

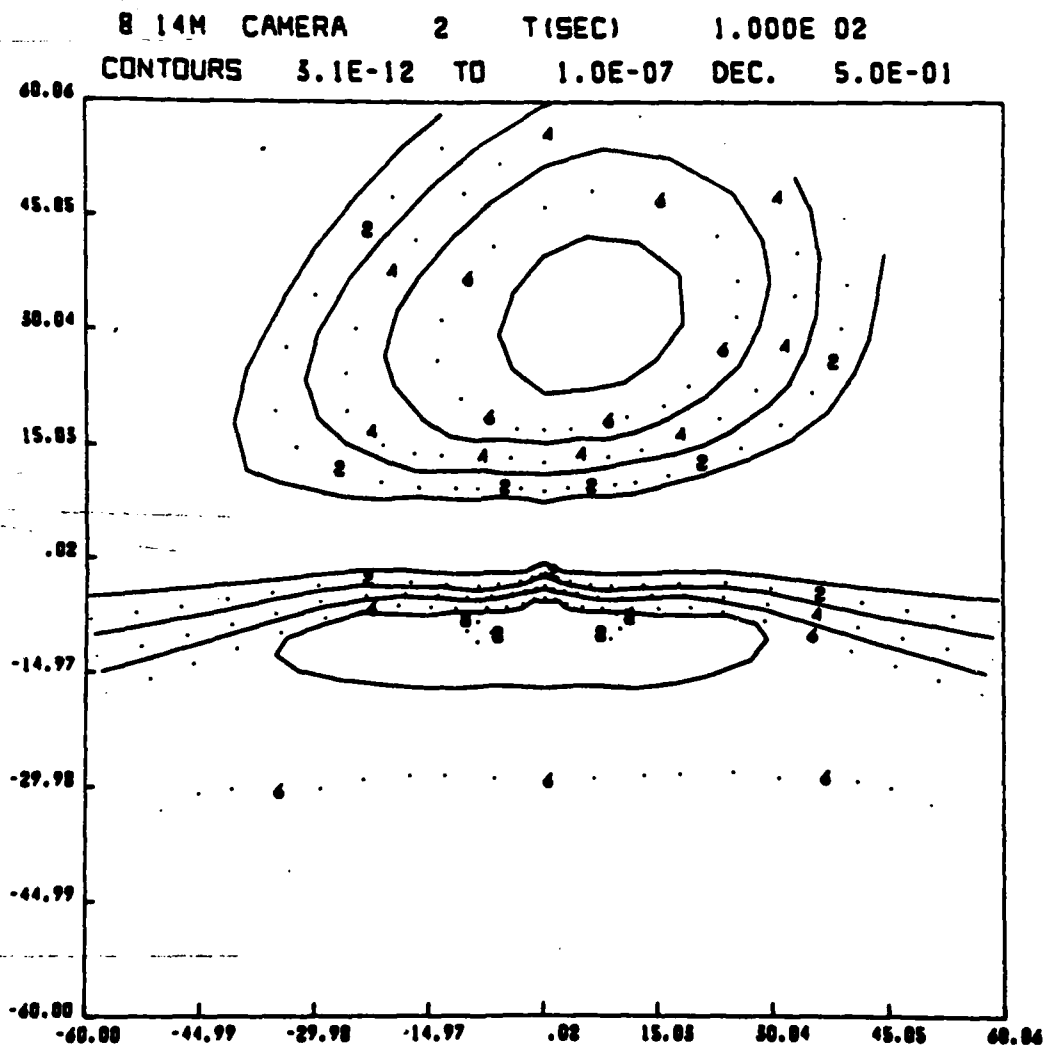


Fig. 7 — Radiance in the 8-14 μ band (watts/cm²ster) from a high altitude burst \sim 100. sec after burst. Abscissa and ordinate in degrees.

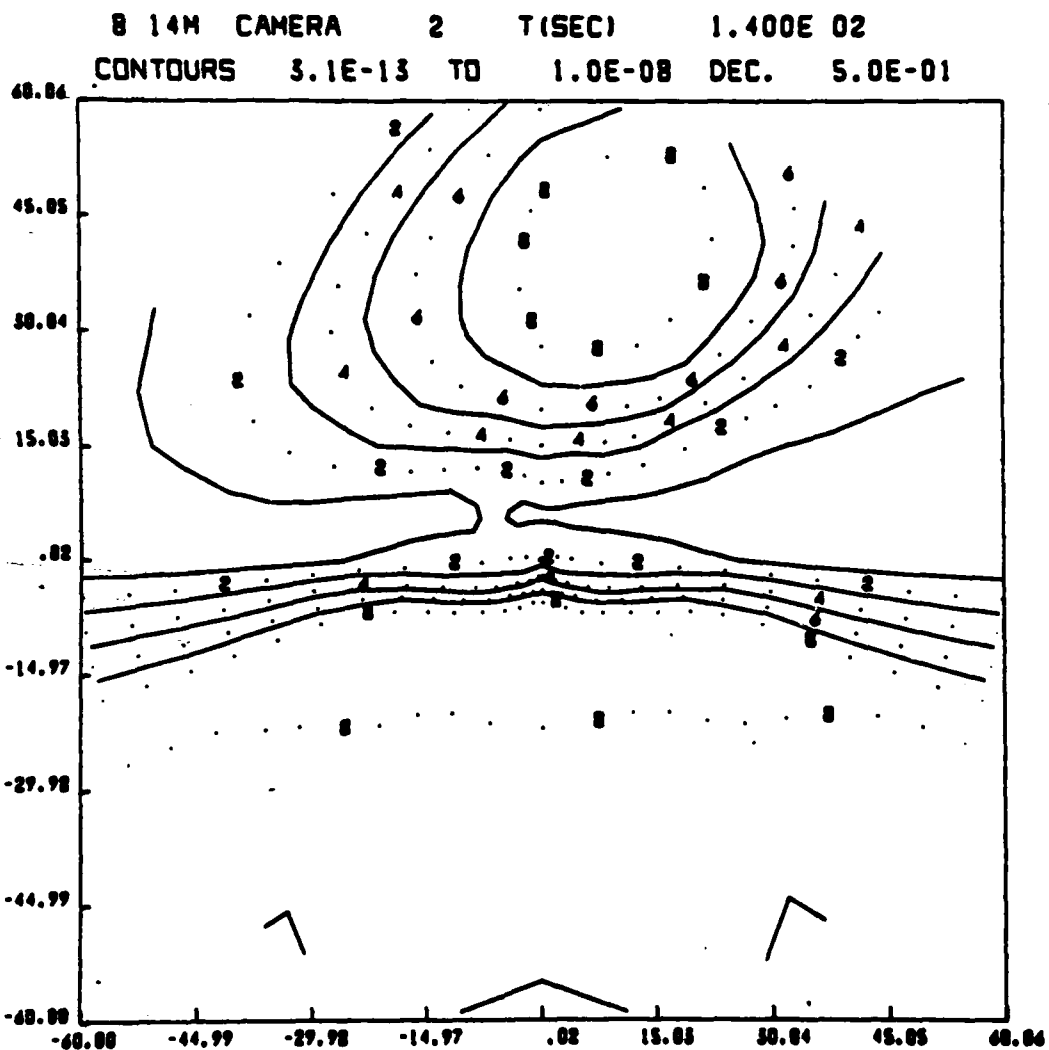
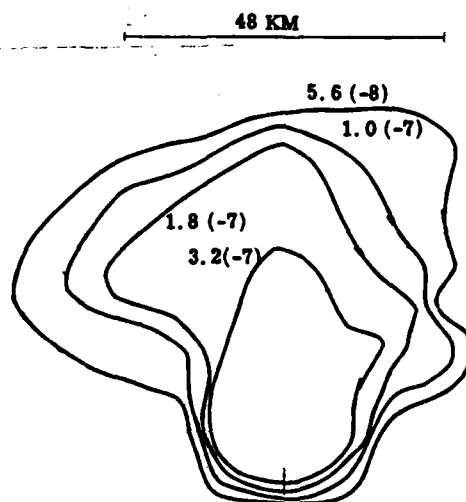
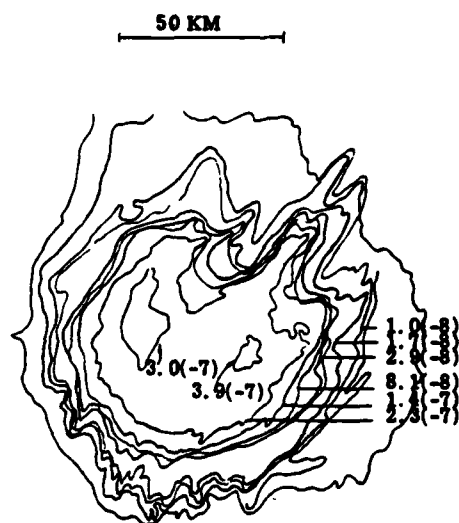


Fig. 8 — Radiance in the 8-14 μ band (watts/cm²ster) from a high altitude burst ~ 140. sec after burst. Abscissa and ordinate in degrees.



STATION KI
60 SECONDS
WATTS/CM² SR (3800 - 6800 Å)



STATION KI
57-58 SECONDS
WATTS/CM² SR (3800 - 6500 Å)

Fig. 9 — PHARO radiance contour predictions compared with measured contours for a high altitude burst in the visible spectrum at ~ 60. sec.

REFERENCES

1. Hyman, E., A.W. Ali and T.P. Coffey, "PHARO I - Phenomenology and Radiation Output Code," DNA Second Conference of Applications of Chemistry to Nuclear Weapons Effects, IDA, Arlington, September, 1972.
2. Hyman, E., P. Julienne and J. Davis, "Departure from LTE in an Oxygen Plasma, II. Collisional Model," DNA Atmospheric Effects Symposium, San Diego, April, 1973 and NRL Memorandum Report 2740, March 1974.
3. Ali, A.W., "Optical and Infrared Emission from Disturbed E and F Layers, Part 1: Theoretical Considerations," NRL Memorandum Report 2404, April, 1972.
4. Davis, J. and J. Lewis, "Photoionization Cross Sections and Recombination Coefficients for Oxygen and Nitrogen Plasmas," NRL Memorandum Report 2558, December, 1972.

Appendix M

INFLUENCE OF VELOCITY SHEAR ON THE
RAYLEIGH-TAYLOR INSTABILITY

Influence of Velocity Shear on the Rayleigh-Taylor Instability

P. N. GUZDAR

*Science Applications, Inc.
McLean, Virginia 22102*

P. SATYANARAYANA

*Berkeley Scholars, Inc.
Springfield, Virginia 22150*

J. D. HUBA AND S. L. OSSAKOW

*Geophysical and Plasma Dynamics Branch
Plasma Physics Division*

December 16, 1981

This research was sponsored partially by the Defense Nuclear Agency under Subtask S99QAXHC, work unit 00032, and work unit title, "Plasma Structure Evolution," and partially by the Office of Naval Research.



**NAVAL RESEARCH LABORATORY
Washington, D.C.**

Approved for public release; distribution unlimited.

REPORT DOCUMENTATION PAGE		READ INSTRUCTIONS BEFORE COMPLETING FORM
1. REPORT NUMBER NRL Memorandum Report 4701	2. GOVT ACCESSION NO.	3. RECIPIENT'S CATALOG NUMBER
4. TITLE (and Subtitle) INFLUENCE OF VELOCITY SHEAR ON THE RAYLEIGH-TAYLOR INSTABILITY		5. TYPE OF REPORT & PERIOD COVERED Interim report on a continuing NRL problem.
		6. PERFORMING ORG. REPORT NUMBER
7. AUTHOR(s) P.N. Guzdar*, P. Satyanarayana†, J.D. Huba, and S.L. Ossakow		8. CONTRACT OR GRANT NUMBER(s)
9. PERFORMING ORGANIZATION NAME AND ADDRESS Naval Research Laboratory Washington, DC 20375		10. PROGRAM ELEMENT, PROJECT, TASK AREA & WORK UNIT NUMBERS 61153N; RR0330244; 47-0883- 02 & 62715H; 47-0889-02
11. CONTROLLING OFFICE NAME AND ADDRESS Defense Nuclear Agency Office of Naval Research Washington, DC 20305 Arlington, VA 22217		12. REPORT DATE December 16, 1981
		13. NUMBER OF PAGES 27
14. MONITORING AGENCY NAME & ADDRESS (if different from Controlling Office)		15. SECURITY CLASS. (of this report) UNCLASSIFIED
		15a. DECLASSIFICATION/DOWNGRADING SCHEDULE
16. DISTRIBUTION STATEMENT (of this Report) Approved for public release; distribution unlimited.		
17. DISTRIBUTION STATEMENT (of the abstract entered in Block 20, if different from Report)		
18. SUPPLEMENTARY NOTES This research was sponsored partially by the Defense Nuclear Agency under Subtask S99QAXHC, work unit 00032, and work unit title, "Plasma Structure Evolution," and partially by the Office of Naval Research. (Continues)		
19. KEY WORDS (Continue on reverse side if necessary and identify by block number) Velocity shear Prompt barium cloud striations Rayleigh-Taylor instability Long wavelength selectivity Bottomside equatorial spread F		
20. ABSTRACT (Continue on reverse side if necessary and identify by block number) The influence of a transverse velocity shear on the Rayleigh-Taylor instability is investigated. It is found that a sheared velocity flow can substantially reduce the growth rate of the Rayleigh-Taylor instability in the short wavelength regime (i.e., $kL > 1$ where L is the scale length of the density inhomogeneity), and causes the growth rate to maxi- mize at $kL < 1.0$. Applications of this result to ionospheric phenomena [equatorial spread F (ESF) and ionospheric plasma clouds] are discussed. In particular, the effect (Continues)		

SECURITY CLASSIFICATION OF THIS PAGE (When Data Entered)

18. Supplementary Notes (Continued)

*Present address: Science Applications, Inc., McLean, VA 22102; permanent address: University of Maryland, College Park, MD 20742.

†Present address: Berkeley Scholars, Inc., Springfield, VA 22150.

20. Abstract (Continued)

of shear could account for, at times, the 100's of km modulation observed on the bottomside of the ESF ionosphere and the km scale size wavelengths observed in barium cloud prompt striation phenomena.

AD-A111 632

SCIENCE APPLICATIONS INC MCLEAN VA
GEOPHYSICAL PLASMAS AND ATMOSPHERIC MODELING. (U)
JAN 82 E HYMAN, J APRUZESE, S BRECHT, W CHAO

F/8 4/1

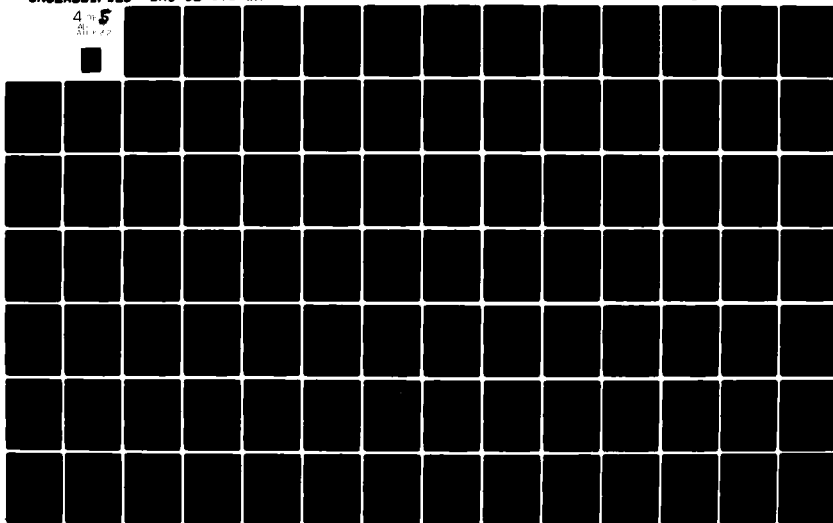
N00018-81-C-2038

UNCLASSIFIED

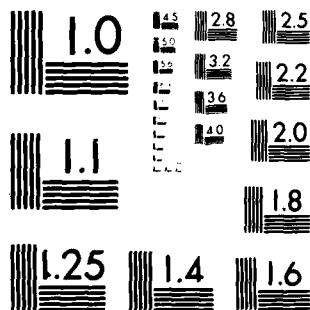
SAI-82-676-VA

ML

4 of 5
311 x 22



11163



MICROCOPY RESOLUTION TEST CHART
NATIONAL BUREAU OF STANDARDS 1963-A

CONTENTS

I. INTRODUCTION	1
II. THEORY	2
III. RESULTS	4
A. Rayleigh-Taylor Instability	4
B. Kelvin-Helmholtz Instability	5
C. Generalized Rayleigh-Taylor Instability	5
IV. DISCUSSION	8
ACKNOWLEDGMENTS	11
REFERENCES	12

INFLUENCE OF VELOCITY SHEAR ON THE RAYLEIGH-TAYLOR INSTABILITY

I. Introduction

An important instability in a variety of geophysical phenomena is the Rayleigh-Taylor instability. The instability is an interchange instability and is driven primarily by an opposing density gradient and gravitational force (e.g., a heavy fluid supported by a light fluid). In a magnetized plasma, the mode exists in both the collisionless and collisional regimes. However, in many regions of interest, such as the ionosphere, the plasma can also contain inhomogeneous velocity flows transverse to the magnetic field. In fact, in the absence of other effects (such as gravity, density gradients and collisions), this sheared flow can give rise to a transverse Kelvin-Helmholtz instability (Mikhailovskii, 1974). The purpose of this letter is to investigate the influence of velocity shear on the Rayleigh-Taylor instability (Drazin, 1958; Chandrasekhar, 1961).

We find that velocity shear can have a dramatic effect on the Rayleigh-Taylor instability. Namely, for a sufficiently strong velocity shear, the growth rates of the most unstable modes (i.e., those such that $kL > 1$ where L is the scale length of the inhomogeneity) are substantially reduced; leading to maximum growth in the regime $kL < 1$. Thus, velocity shear has the effect of preferentially exciting a long wavelength mode of the Rayleigh-Taylor instability which is in sharp contrast to the behavior of the mode in the absence of velocity shear. This result may explain the long wavelength oscillations (i.e., several hundred kms) of the bottomside F layer during equatorial spread F (Tsunoda, 1981a; Tsunoda and White, 1981; Kelley et al., 1981) and the early time structuring of injected barium clouds in the ionosphere (Simons et al., 1980; Wescott et al., 1980).

The scheme of this letter is as follows. In the next section we present the basic equation which describes the influence of velocity shear on the Rayleigh-Taylor instability. In Section III, the various instabilities are discussed (i.e., Rayleigh-Taylor, Kelvin-Helmholtz and the generalized Rayleigh-Taylor). Finally, in the last section, we discuss the application of our results to ionospheric phenomena, i.e., equatorial spread F and plasma cloud striations.

Manuscript submitted October 28, 1981.

II. Theory

The geometry of the plasma and field configuration used in the analysis are as follows. We consider $\vec{B} = B_0 \hat{e}_z$, $\vec{g} = g \hat{e}_x$, $n = n_0(x)$ and $\vec{V} = -V_0(x) \hat{e}_y$. We also include ion-neutral collisions ($\nu = \nu_{in}$) in the theory so that both collisionless and collisional instabilities are considered.

The basic assumptions used in the analysis are as follows. We assume perturbed quantities vary as $\delta p \sim \delta p(x) \exp(iky - i\omega t)$ with $\omega \ll \Omega_i$ and $kr_{Li} \ll 1$ where Ω_i is the ion gyrofrequency and r_{Li} is the mean ion Larmor radius. We neglect perturbations along the magnetic field ($k_z = 0$) so that only two dimensional mode structure in the xy plane is obtained. We assume $\nu_{in} \ll \Omega_i$ which is consistent with ionospheric F region conditions. Ion inertial effects are retained in the analysis, but electron inertial effects are neglected. We assume quasi-neutrality so that $n_e = n_i = n$.

A key feature of our analysis is that a nonlocal theory is developed. That is, the mode structure of the potential in the x-direction is determined by a differential equation rather than an algebraic equation obtained by Fourier analysis. This technique allows one to study modes which have wavelengths larger than the scale size of the inhomogeneities (i.e., $kL < 1$ where L represents the scale length of the boundary layer). In fact, this is crucial to describing the Kelvin-Helmholtz instability produced by a transverse velocity shear (Mikhailovskii, 1974).

Based upon the assumptions discussed above, the fundamental equations used in the analysis are

$$\partial n_\alpha / \partial t + \nabla \cdot (n_\alpha \vec{V}_\alpha) = 0 \quad (1)$$

$$0 = \vec{E} + \frac{\vec{V}_e \times \vec{B}}{c} \quad (2)$$

$$m_i (\partial / \partial t + \vec{V}_i \cdot \nabla) \vec{V}_i = e \vec{E} + \frac{e \vec{V}_i \times \vec{B}}{c} - m_i \nu_{in} \vec{V}_i + m_i \vec{g} \quad (3)$$

where α denotes species (e, i: electron, ion). We substitute $\vec{E} = -\nabla \phi$,

$\underline{V} = \underline{V}_0(x) + \delta \underline{V}$ and $n = n_0(x) + \delta n$ into Eqs. (1)-(3). Here, ϕ is the perturbed potential. We find the perturbed velocities to be

$$\delta \underline{V}_e = (c/R) [-ik\phi \hat{e}_x + (\partial\phi/\partial x) \hat{e}_y] \quad (4)$$

and

$$\begin{aligned} \delta \underline{V}_i = (c/R) & \left[-i \left(1 + \frac{1}{\Omega} \frac{\partial V_0}{\partial x} \right)^{-1} k\phi + \frac{\tilde{\omega} + i v_{in}}{\Omega} \frac{\partial \phi}{\partial x} \right] \hat{e}_x \\ & + (c/R) \left[\frac{\partial \phi}{\partial x} - \frac{\tilde{\omega} + i v_{in}}{\Omega} k\phi \right] \hat{e}_y \end{aligned} \quad (5)$$

where $\Omega = \Omega_i = eB/m_i c$ and $\tilde{\omega} = \omega - kV_0$. Substituting Eqs. (4) and (5) into Eq. (1), we arrive at the following equation

$$\frac{\partial^2 \phi}{\partial x^2} + p \frac{\partial \phi}{\partial x} + q \phi = 0 \quad (6)$$

where

$$p = \frac{\partial \ln n_0}{\partial x} \left(1 - \frac{i v_{in}}{\tilde{\omega} + i v_{in}} \frac{k V_0}{\tilde{\omega}} \right) \quad (7)$$

$$\begin{aligned} q = -k^2 + \frac{k V_0}{\tilde{\omega} + i v_{in}} & \left[\frac{1}{V_0} \frac{\partial^2 V_0}{\partial x^2} + \frac{gk}{\tilde{\omega} V_0} \frac{\partial \ln n_0}{\partial x} + \frac{\partial \ln V_0}{\partial x} \frac{\partial \ln n_0}{\partial x} \right. \\ & \left. - \frac{i v_{in}}{\tilde{\omega}} \left(\frac{1}{n_0} \frac{\partial^2 n_0}{\partial x^2} + \frac{\omega}{\tilde{\omega}} \frac{\partial \ln n_0}{\partial x} \frac{\partial \ln V_0}{\partial x} \right) \right] \end{aligned} \quad (8)$$

In obtaining Eq. (6) we have made use of the quasi-neutrality condition, assumed $\partial V_0/\partial x \ll \Omega_i$ and have retained ion inertial terms to order v_{in}/Ω_i .

III. Results

To highlight the influence of velocity shear on the Rayleigh-Taylor instability we first consider two limiting cases: (1) the Rayleigh-Taylor instability with no velocity shear and (2) the Kelvin-Helmholtz instability with no collisions, gravity or density gradient. Following this we discuss a general solution of Eq. (6).

A. Rayleigh-Taylor instability

We take $V_0 = 0$ so that Eq. (6) becomes

$$\frac{\partial^2 \phi}{\partial x^2} + \frac{\partial \ln n_0}{\partial x} \frac{\partial \phi}{\partial x} - k^2 \left[1 - \frac{g}{\omega + i v_{in}} \frac{1}{\omega} \frac{\partial \ln n_0}{\partial x} \right] \phi = 0 \quad (9)$$

Equation (9) can be easily solved in the local approximation (i.e., $k^2 L^2 \gg k_x^2 L^2 \gg 1$ where $L = (\partial \ln n_0 / \partial x)^{-1}_{x=x_0}$ and we have assumed $\phi(x) = \exp(ik_x x)$). We obtain the dispersion equation

$$\omega^2 + i v_{in} \omega - g/L = 0 \quad (10)$$

which has the solution (Hudson and Kennel, 1975; Haerendel, 1974)

$$\omega = -\frac{i v_{in}}{2} [1 \pm (1 - 4g/L v_{in}^2)^{1/2}] \quad (11)$$

Instability can occur when $g/L < 0$ (i.e., g and L are oppositely directed). The collisionless and collisional solutions are

$$\omega = \pm (g/L)^{1/2} \quad v_{in} \ll (4g/L)^{1/2} \quad (12)$$

$$\omega = -1 (g/L) v_{in}^{-1} \quad v_{in} \gg (4g/L)^{1/2} \quad (13)$$

We now solve Eq. (9) numerically for a density profile $n = n_0 \exp(-x^2/2L^2) + \Delta n$. The results are shown in Fig. 1 (curve A) which is a plot of $\gamma/(g/L)^{1/2}$ vs. kL for $\Delta n/n_0 = 0.01$ and $v_{in}/(g/L)^{1/2} = 0.5$. As expected, the growth rate maximizes in the regime $kL \gg 1$. However, note that the maximum growth rate ($\gamma/(g/L)^{1/2} = 1.1$) is slightly larger than that predicted from local

theory ($\gamma/(g/L)^{1/2} = 1.0$ from Eq. (11)). This is due to the Gaussian-like density profile chosen for the numerical example.

B. Kelvin-Helmholtz instability

We assume $V_0(x) \neq 0$ but take $v_{in} = 0$, $g = 0$ and $n_0 = \text{const.}$ Equation (6) becomes

$$\frac{\partial^2 \phi}{\partial x^2} - [k^2 - \frac{k \partial^2 V_0 / \partial x^2}{\omega - k V_0}] \phi = 0 \quad (14)$$

which is well-known (Mikhailovskii, 1974). Note that in the local approximation

$$\omega = k V_0 + k^{-1} (\partial^2 V_0 / \partial x^2)_{x=x_0} \quad (15)$$

so that the mode is stable. In general, an instability can occur only when $(\partial^2 V_0 / \partial x^2)_{x=x_0} = 0$ where $x_1 < x_0 < x_2$, and x_1 and x_2 are the boundaries (Rayleigh's theorem). As an example, we assume an equilibrium velocity profile $\underline{V}_0 = V_0 \tanh(x/L) \hat{e}_y$. The solution to Eq. (14) is shown in curve B of Fig 1 where $\gamma/(V_0/L)$ vs. kL is plotted. The instability is purely growing (i.e., $\omega_r = 0$) and only occurs in the regime $0 < kL < 1$. Maximum growth occurs at $kL = 0.5$ with $\gamma = 0.18 (V_0/L)$ (Michalke, 1964).

C. Generalized Rayleigh-Taylor instability

We now consider the general case where both the standard Rayleigh-Taylor and the Kelvin-Helmholtz instabilities coexist (Drazin, 1958). Since the wavelength regimes of these two instabilities are distinct from one another (i.e., Rayleigh-Taylor favors $kL > 1$ while Kelvin-Helmholtz favors $kL < 1$), one might think that these "modes" do not affect one another in the linear regime. However, this is not the case as is shown by curve C of Fig. 1. Here, we solve Eq. (6) for the following profiles: $n = n_0 \exp(-x^2/2L^2) + \Delta n$ and $\underline{V}_0 = V_0 \tanh[(x-x_0)/L] \hat{e}_y$ with $v_{in}/(g/L)^{1/2} = 0.5$, $V_0/(g/L)^{1/2} = 1.0$, $\Delta n/n_0 = 0.01$ and $x_0/L = -2.0$. Note that the scale lengths of the density and velocity gradients are assumed equal. The position of the sheared velocity flow is chosen to coincide with the

localization region of the Rayleigh-Taylor instability. As in curve A, we plot $\gamma/(g/L)^{1/2}$ vs. kL and it is found that the growth rate maximizes at $\gamma \approx 0.4 (g/L)^{1/2}$ for $kL \approx 0.7$ over the range considered ($0 < kL < 10$). The most dramatic feature of including velocity shear in the analysis is the strong reduction in the growth rate of modes in the short wavelength regime (i.e., $kL > 1$). Thus, the main influence of velocity shear on the Rayleigh-Taylor instability is to suppress the most unstable waves, those with $kL > 1$, and to maximize growth in the long wavelength regime ($kL < 1$).

This effect of velocity shear on the Rayleigh-Taylor instability can be easily seen from local theory. For simplicity, we consider Eq. (6) in the limit $k^2 L^2 \gg k_x^2 L^2 \gg 1$ and $v_{in} = 0$. The dispersion equation becomes

$$\tilde{\omega}^2 - k^{-1} \left(\frac{\partial^2 v_0}{\partial x^2} + \frac{\partial \ln n_0}{\partial x} \frac{\partial v_0}{\partial x} \right) \tilde{\omega} - g \frac{\partial \ln n_0}{\partial x} = 0 \quad (16)$$

where $\partial^2 v_0 / \partial x^2$, $\partial v_0 / \partial x$ and $\partial \ln n_0 / \partial x$ are defined locally at some point $x = x_0$. Writing $\partial^2 v_0 / \partial x^2 = v_0''$, $\partial v_0 / \partial x = v_0'$ and $\partial \ln n_0 / \partial x = 1/L$, the solution to Eq. (16) is

$$\tilde{\omega} = \frac{1}{2k} (v_0'' + v_0'/L) \pm \frac{1}{2} [(v_0''/k + v_0'/kL)^2 + 4g/L]^{1/2} \quad (17)$$

In the limit $v_0'' \rightarrow 0$ and $v_0' \rightarrow 0$, Eq. (11) is recovered. However for v_0'' , $v_0' \neq 0$ the velocity shear term is clearly stabilizing. Moreover, the stabilizing influence is k dependent and we expect that as k increases the influence of velocity shear becomes weaker. Qualitatively this result is shown in Fig. 1 (curve C); the most strongly suppressed modes have $kL \approx 1$ and growth increases as kL increases, albeit small. However, owing to the crude approximation made in obtaining Eq. (17), good quantitative agreement cannot be expected.

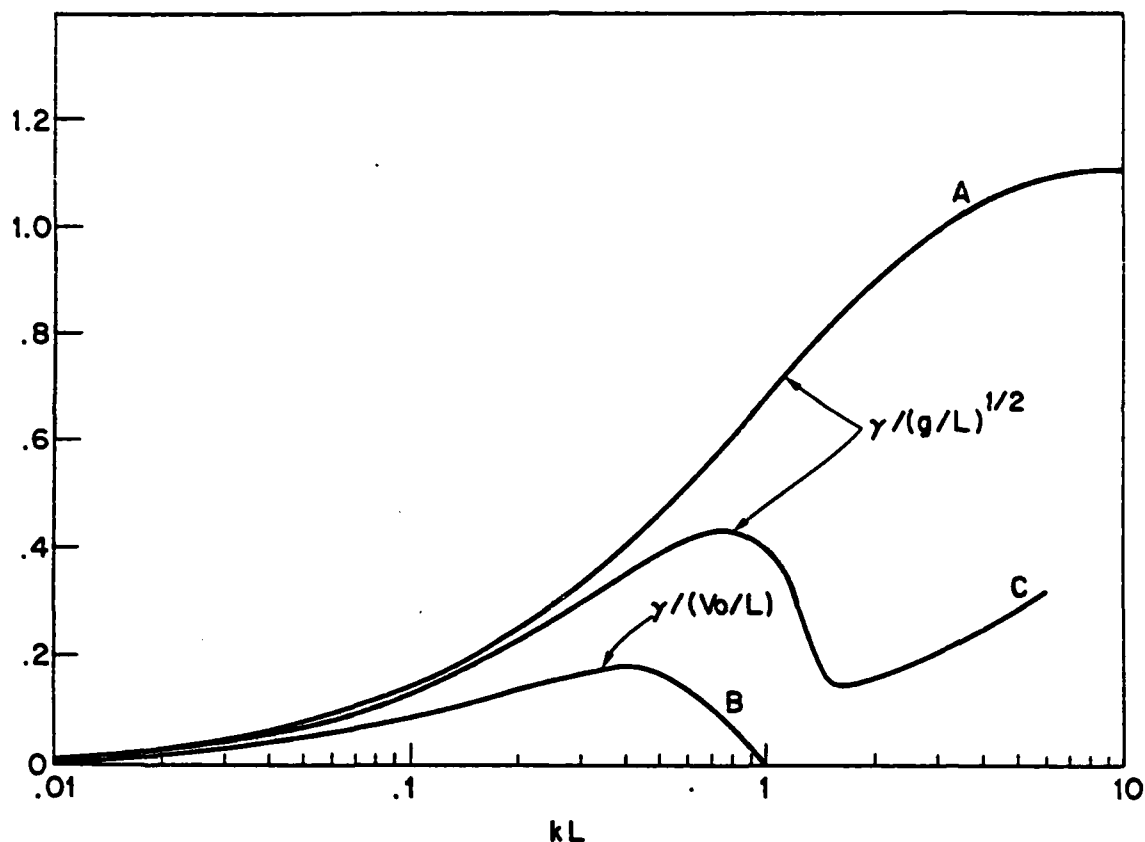


Figure 1

Plots of the growth rate (γ) vs. kL under various conditions. The profiles used are: $n = n_0 \exp(-x^2/2L^2) + \Delta n$ and $V = V_0 \tanh[(x - x_0)/L]$. (A) Rayleigh-Taylor instability with no velocity shear. Here, $\gamma/(g/L)^{1/2}$ vs. kL is plotted and we have assumed $v_{in}/(g/L)^{1/2} = 0.5$ and $\Delta n/n_0 = 0.01$. (B) Kelvin-Helmholtz instability with no density gradient, collisions and gravity. Here, $\gamma/(V_0/L)$ vs. kL is plotted. (C) Generalized Rayleigh-Taylor instability including velocity shear. Here $\gamma/(g/L)^{1/2}$ vs. kL is plotted. We have assumed $v_{in}/(g/L)^{1/2} = 0.5$, $V_0/(g/L)^{1/2} = 1.0$, $\Delta n/n_0 = 0.01$ and $x_0/L = -2.0$.

IV. Discussion

We have investigated the influence of velocity shear on the Rayleigh-Taylor instability. Our analysis includes gravity, density and velocity inhomogeneities and ion-neutral collisions. In general, the Rayleigh-Taylor instability is most unstable in the regime $kL > 1$ where L characterizes the inhomogeneity scale length. On the other hand, the Kelvin-Helmholtz instability, driven by a sheared transverse velocity flow, is unstable for $kL < 1$. In the presence of a sufficiently strong velocity shear, the short wavelength spectrum ($kL > 1$) of the Rayleigh-Taylor instability is strongly suppressed and a maximum in growth occurs for $kL < 1$. Thus, velocity shear may cause a long wavelength mode to be preferentially excited; whereas in the absence of velocity shear the dominant wave mode usually has a shorter wavelength determined by initial conditions or nonlinear processes. We now discuss two possible applications of this theory to ionospheric phenomena: equatorial spread F and ionospheric plasma cloud striations.

It is believed that the Rayleigh-Taylor instability can play a major role in the onset of equatorial spread F (see for example Ossakow, 1979; Fejer and Kelley, 1980). After sunset, the density gradient on the bottomside of the F layer steepens which initiates the Rayleigh-Taylor instability. However, there are also observations of (1) velocity shears existing in the F region during spread F (Kudeki et al., 1981; Tsunoda et al., 1981) and (2) long wavelength (i.e., several hundred kms) oscillations on the bottomside of the F layer (Tsunoda and White, 1981; Kelley et al., 1981). From our theory we expect velocity shear to preferentially excite the Rayleigh-Taylor instability at

$kL \approx 0.7$. If we take $L = 25$ km for the bottomside of the F layer then the most unstable wavelength occurs at $\lambda \sim 250$ km which is comparable with observations ($\lambda_{\text{obs}} \sim 600$ km Kelley et al., 1981; $\lambda_{\text{obs}} \sim 400$ km Tsunoda and White, 1981; $\lambda_{\text{obs}} \sim$ tens to a few hundred kms, Tsunoda, 1981b). Also, the magnitude of the velocity shear necessary for this is $V_0/L = 2 \times 10^{-2}$ Hz which is somewhat larger than, although comparable with, observational values (Kudeki et al., 1981) which are $V_0/L \sim 2 \times 10^{-3}$ Hz. Thus, the influence of velocity shear on the Rayleigh-Taylor instability may explain the long wavelength

oscillations of the bottomside of the F layer. We mention that gravity waves have also been proposed as a mechanism to generate these oscillations (Kelley et al., 1981).

Several aspects of the theory need further comment concerning this application to equatorial spread F. First, the velocity shear profile used in the calculation is based on observational data and not on a self-consistent equilibrium model. An equilibrium which provides the observed shear flows is beyond the scope of this paper. One possible mechanism to generate the velocity shear is via a neutral wind in the equatorial F region when the F layer is electrically coupled to a background E layer away from the equatorial region (Zalesak et al., 1981). It is interesting to note that when such a coupling occurs, the plume structures are tilted away from the vertical (Zalesak et al., 1981). Thus, the tilt of the plumes can be regarded as a measure of the coupling between the E and F regions, and therefore, as a measure of sheared velocity flows in the F region. Observationally, the largest amplitude, long wavelength oscillations occur when the plumes are strongly tilted (Kelley et al., 1981). This suggests that sheared velocity flows may play a role in their development. Second, the relative positions of the density and velocity profiles play a crucial part in the "interaction" of the velocity shear and the Rayleigh-Taylor instability. The strongest effect of shear occurs when the velocity shear is a maximum in the localization region of the Rayleigh-Taylor mode. Finally, collisions can destroy the local maximization of the growth rate in the long wavelength regime if they are sufficiently strong. This indicates that velocity shear will be more important at high altitudes (> 400 km) in affecting the Rayleigh-Taylor instability.

Artificial plasma clouds (e.g., barium releases) in the ionosphere are subject to a complex and dynamic evolution. One of the more notable characteristics is the striating of the clouds, i.e., "fingers" forming on one side of the cloud (Rosenberg, 1971; Davis et al., 1974). In many cases these striations can be explained by the $E \times B$ gradient drift instability (Linson and Workman, 1970; Zabusky et al., 1973; Scannapieco et al., 1976). However, recent shaped charge releases develop striations very rapidly (Simons et al., 1980; Wescott et al., 1980) and these

initial striations cannot be explained by the $\underline{E} \times \underline{B}$ drift instability because of its relatively slow growth rate. Simons et al. (1980) have proposed a kinetic instability driven by an ion ring distribution to explain the prompt striations in the Buaro release. However, it is unclear that a kinetic instability can produce the large density perturbations necessary to explain the structuring of the cloud. An alternative mechanism has been proposed by Pillip (1971) and Fedder (1980) which is based upon an interchange instability; this instability is similar to the Rayleigh-Taylor instability, but relies upon the deceleration of the cloud (Scholer, 1970) rather than gravitational acceleration. An inhomogeneous electric field can exist at the edges of the cloud due to polarization charges which produce a sheared transverse velocity flow (Sydora et al., 1981). Thus, our theory can be applied to the structuring of barium releases which are injected across the magnetic field. If the boundary layer is several hundred meters thick ($L \sim 100 - 300$ m) then from $kL \approx 0.7$ we obtain wavelengths $\lambda \sim 1 - 3$ km which are consistent with observations. Moreover such a layer thickness yields substantial growth rates according to Fedder's model ($\gamma \sim 10 \text{ sec}^{-1}$). This final example is largely suggestive at this time, yet is sufficiently encouraging that further investigation is warranted.

In conclusion, we have shown that a sheared transverse velocity flow can have a pronounced effect on the Rayleigh-Taylor instability. For a sufficiently strong velocity shear, the short wavelength spectrum of the instability is suppressed and growth maximizes at $kL < 1.0$ where L is the scale length of the inhomogeneity. This result may explain the long wavelength oscillations of the bottomside of the F layer during equatorial spread F and the prompt structuring of injected barium clouds. We emphasize that this is a preliminary report and that a more detailed analysis (i.e., parameteric variations) will be presented in a future paper.

Acknowledgments

We thank P. Chaturvedi for helpful discussions during the initial phase of this research and M. Schoeberl for pointing out the work of Drazin to us. This research has been supported by the Defense Nuclear Agency and the Office of Naval Research.

References

- Chandrasekhar, S., Hydrodynamic and Hydromagnetic Stability (Int. Ser. Monographs on Physics, Clarendon Press, Oxford, 1961) p. 494.
- Davis, T.N., G.J. Romick, E.M. Wescott, R.A. Jeffries, D.M. Kerr, and K.M. Peek, Observations of the development of striations in large barium clouds, Planet. Space Sci., 22, 67, 1974.
- Drazin, P.G., The stability of a shear layer in an unbounded heterogeneous inviscid fluid, J. Fluid Mech., 4, 214, 1958.
- Fedder, J.A., Structuring of collisionless, high velocity ion clouds, Memo Rept. 4307, Nav. Res. Lab., Washington, D.C., September, 1980.
- Fejer, B.G., and M.C. Kelley, Ionospheric irregularities, Rev. Geophys. Space Phys., 18, 401, 1980.
- Haerendel, G. Theory of equatorial spread F, Preprint, Max-Planck Institute for Physik und Astrophysik, Garching, West Germany, 1974.
- Hudson, M.K., and C.F. Kennel, Linear theory of equatorial spread F, J. Geophys. Res., 80, 4581, 1975.
- Kelley, M.C., M.F. Larsen, C. La Hoz, and J.P. McClure, Gravity wave initiation of equatorial spread F: A case study, J. Geophys. Res. (in press 1981).
- Kudeki, E., B.G. Fejer, D.R. Farley, and H.M. Ierick, Interferometer studies of equatorial F region irregularities and drifts, Geophys. Res. Lett., 8, 377, 1981.
- Linson, L.M., and J.B. Workman, Formation of striations in ionospheric plasma clouds, J. Geophys. Res., 75, 3211, 1970.
- Michalke, A., On the inviscid instability of the hyperbolic-tangent velocity profile, J. Fluid Mech., 19, 543, 1964.
- Mikhailovskii, A.B., Theory of Plasma Instabilities: Vol. II, Consultants Bureau, New York, 1974, p. 141.
- Ossakow, S.L. Ionospheric irregularities, Rev. Geophys. Space Phys., 17, 521, 1979.
- Pillip, W., Expansion of an ion cloud in the earth's magnetic field, Planet. Space Sci., 19, 1095, 1971.
- Rosenberg, N.W., Observations of striation formation in a barium ion cloud, J. Geophys. Res., 76, 6856, 1971.

- Scannapieco, A.J., S.L. Ossakow, S.R. Goldman, and J.M. Pierre, Plasma cloud late time striation spectra, J. Geophys. Res., 81, 6037, 1976.
- Scholer, M., On the motion of artificial ion clouds in the magnetosphere, Planet. Space Sci., 18, 977, 1970.
- Simons, D.J., M.B. Pongratz, and S.P. Gary, Prompt striations in ionospheric barium clouds due to a velocity space instability, J. Geophys. Res., 85, 671, 1980.
- Sydora, R., J.S. Wagner, L.C. Lee, E.M. Wescott and T. Tajima, Electrostatic Kelvin-Helmholtz instability in a radially injected barium cloud, to be published in Phys. Fluids, 1981.
- Tsunoda, R.T., Time evolution and dynamics of equatorial backscatter plumes, 1. Growth phase, J. Geophys. Res., 86, 139, 1981a.
- Tsunoda, R.T., ALTAIR radar study of equatorial spread F, SRI International Final Report, DNA 5689F, February, 1981b.
- Tsunoda, R.T., R.C. Livingston, and C.L. Rino, Evidence of a velocity shear in bulk plasma motion associated with the post-sunset rise of the equatorial F-layer, Geophys. Res. Lett., 8, 807, 1981.
- Tsunoda, R.T., and B.R. White, On the generation and growth of equatorial backscatter plumes-1. Wave structure in the bottomside F layer, J. Geophys. Res., 86, 3610, 1981.
- Wescott, E.M., H.C. Stenback-Nielsen, T.J. Hallinan, C.S. Deehr, G.J. Romick, J.V. Olsen, J.G. Roederer, and R. Sydora, A high-altitude barium radial injection experiment, Geophys. Res. Lett., 7, 1037, 1980.
- Zabusky, N.J., J.H. Doles III, and F.W. Perkins, Deformation and striation of plasma clouds in the ionosphere, 2. Numerical simulation of a non-linear two-dimensional model, J. Geophys. Res., 78, 711, 1973.
- Zalesak, S.T., S.L. Ossakow, and P.K. Chaturvedi, Nonlinear equatorial spread F: The effect of neutral winds and background Pedersen conductivity, J. Geophys. Res. (accepted for publication, 1981).

Appendix N

TWO-BUBBLE INTERACTIONS IN EQUATORIAL SPREAD-F

James Chen
Science Applications, Inc.
McLean, Virginia 22102

and

P. Satyanarayana
Berkeley Scholars, Inc.
Springfield, Virginia 22150

TWO-BUBBLE INTERACTIONS IN EQUATORIAL SPREAD-F

It has been shown (Ossakow and Chaturvedi, 1978) that the E x B rise velocities of isolated plasma density depletions ("bubbles") can be analyzed using the electrostatic analogy in which a cylindrical depletion can be thought of as a dielectric cylinder imbedded in a dielectric background and immersed in a uniform electric field. In these previous works (for a more comprehensive review, see, for example, Ossakow, 1981), the emphasis has been placed on understanding the linear and non-linear behavior of isolated bubbles with no interaction between them. In reality, however, such bubbles are not isolated. Thus, it is of interest to calculate the influence of the mutual interaction between these density depletions. In this report, we summarize the significant results of our analysis.

Just as in the one-bubble case, the two-bubble problem can be analyzed using the electrostatic analogy. In particular, the equation describing the electric field can be written as

$$\nabla \cdot (nE) = 0 \quad (1)$$

where

$$\underline{E} = - \nu_{in} \underline{\nabla} \psi + \frac{m_i}{e} \nu_{in} \underline{g} + \frac{B}{c} \underline{g} \times \underline{b} \quad (2)$$

with ν_{in} = ion-neutral collision frequency,
 ψ = electrostatic potential,
 \underline{g} = gravitational acceleration of the earth,
 $\underline{b} = \underline{B}/B$ = unit vector along the earth magnetic field in the equatorial F region,
 n = ion density,
 m_i = ion mass.

Equation (1) is equivalent to $\underline{\nabla} \cdot \underline{J}$ where \underline{J} is defined in terms of the drift velocities \underline{V}_i and \underline{V}_e by $\underline{J} = en(\underline{V}_i - \underline{V}_e)$.

It is useful to note that Eq. (1) can be thought of as the Poisson equation describing an uncharged dielectric material imbedded in another dielectric with a uniform applied electric field, \underline{E}_0 . In particular, the solution of this equation for the one-bubble case, corresponding to one dielectric cylinder, is well-known (Smythe; Jackson; Ossakow and Chaturvedi). However, no known analytic solution exists for the two-cylinder case.

Figure 1 shows schematically the two-bubble configuration to be considered. Two cylindrical depletions of radius a are separated by a distance $d = 2 X_0$. The gravitational acceleration is $\underline{g} = -g \hat{y}$ ($g > 0$) and the earth's magnetic field $\underline{B} = B \hat{z}$ is out of the paper. Using the electrostatic analogy, the uniform field \underline{E}_0 is in the x-direction.

In the absence of mutual interactions, the field outside the cylinders due to the presence of two cylinders separated by $d = 2 x_0$ can be given by

$$E_x^{(0)} = E_0 - E_0 \left(\frac{1-K}{1+K} \right) \left[\frac{a^2}{(x+x_0)^2 + y^2} \frac{(x+x_0)^2 - y^2}{(x+x_0)^2 + y^2} + \frac{a^2}{(x-x_0)^2 + y^2} \frac{(x-x_0)^2 - y^2}{(x-x_0)^2 + y^2} \right], \quad (3)$$

$$E_y^{(0)} = -2E_0 \left(\frac{1-K}{1+K} \right) \left[\frac{(x+x_0) y}{(x+x_0)^2 + y^2} \frac{a^2}{(x+x_0)^2 + y^2} + \frac{(x-x_0) y}{(x-x_0)^2 + y^2} \frac{a^2}{(x-x_0)^2 + y^2} \right] \quad (4)$$

where

$$K = \frac{n_{in}}{n_{out}} < 1. \quad (5)$$

In the interior of either cylinder, the field is

$$E_x^{(0)} = \frac{2 E_0}{1+K},$$

$$E_y^{(0)} = 0.$$

Since $K < 1$,

$$E_x^{(0)}(\text{out}) > E_o$$

on the boundary of the cylinder. The superscript (0) on the components of the field denotes the non-interacting fields. In the above equations, the quantity K is defined as

$$K = \frac{n_o - \delta n}{n_o} \quad (6)$$

where $(n_o - \delta n)$ is the ion or the electron density inside the bubble. Thus, for depletions, $K < 1$. In the electrostatic analogy, the cylinders have a dielectric constant smaller than that of the background dielectric.

We now calculate the lowest order interaction between the two cylinders. In the present analysis, we do not attempt a full self-consistent solution. Rather, we seek to account for the mutual interaction to a high degree of accuracy. In this regard, we note that each cylinder is subject to the self-field of the other cylinder in addition to the uniform field E_o . A useful approximation is to replace this self-field by the field of a line charge. It can be shown that a line charge density

$$\lambda_* = E_0 \left(\frac{1-K}{1+K} \right) \frac{a^2}{4d} \quad (7)$$

placed at the origin ($x=0, y=0$) can approximate the diverging field acting on the cylinder C1. (Figure 1). The errors incurred by this approximation will be discussed below. For C2, a line charge density of $-\lambda_*$ placed at the origin has the same effect. This procedure allows us to gain insight into the nature of the mutual interaction. The response of a dielectric cylinder to a parallel line charge is well-known (Smythe). The field outside the affected cylinder can be obtained by two image line charges inside the cylinder. That is, the response of one cylinder (say C1) can be approximately modeled by a pair of line charges λ'_* and $-\lambda'_*$ inside C1 such that

$$\lambda'_* = \frac{1-K}{1+K} \lambda_* \quad (8)$$

with $-\lambda'_*$ and λ'_* at $x = -x_0$ and $x = -x_0 + a^2/x_0$, respectively. Inside the cylinder C1, the field is that due to a line charge λ''_* placed at $x = 0$ where

$$\lambda''_* = \frac{2}{1+K} \lambda_* \quad (9)$$

Thus, we arrive at the following expressions for the components of the field. The field outside the cylinders is

$$\begin{aligned}
E_x = E_o - E_o \left(\frac{1-K}{1+K} \right) & \left[\frac{a^2}{(x+x_o)^2 + y^2} \frac{(x+x_o)^2 - y^2}{(x+x_o)^2 + y^2} \right. \\
& + \left. \frac{a^2}{(x-x_o)^2 + y^2} \frac{(x-x_o)^2 - y^2}{(x-x_o)^2 + y^2} \right] \\
- 2E_o \left(\frac{1-K}{1+K} \right)^2 \frac{a^2}{8x_o} & \left[\frac{x+x_o}{(x+x_o)^2 + y^2} - \frac{x+x_o - \frac{a^2}{x_o}}{\left(x+x_o - \frac{a^2}{x_o}\right)^2 + y^2} \right. \\
& - \left. \frac{x-x_o}{(x-x_o)^2 + y^2} + \frac{x-x_o + \frac{a^2}{x_o}}{\left(x-x_o + \frac{a^2}{x_o}\right)^2 + y^2} \right]
\end{aligned} \tag{10}$$

$$\begin{aligned}
E_y = -2E_o \left(\frac{1-K}{1+K} \right) & \left[\frac{(x+x_o) y}{(x+x_o)^2 + y^2} \frac{a^2}{(x-x_o)^2 + y^2} \right. \\
& + \left. \frac{(x-x_o) y}{(x-x_o)^2 + y^2} \frac{a^2}{(x-x_o)^2 + y^2} \right] \\
- 2E_o \left(\frac{1-K}{1+K} \right)^2 \frac{a^2}{8x_o} y & \left[\frac{1}{(x+x_o)^2 + y^2} - \frac{1}{\left(x+x_o - \frac{a^2}{x_o}\right)^2 + y^2} \right. \\
& - \left. \frac{1}{(x-x_o)^2 + y^2} + \frac{1}{\left(x-x_o + \frac{a^2}{x_o}\right)^2 + y^2} \right]
\end{aligned} \tag{11}$$

The field inside the cylinders (i.e., depletions) is given by

$$\begin{cases} E_x = \frac{2E_o}{1+K} \pm 4E_o \frac{1-K}{(1+K)^2} \frac{a^2}{8x_o} \frac{x}{x^2 + y^2} \\ E_y = \pm 4E_o \frac{1-K}{(1+K)^2} \frac{a^2}{8x_o} \frac{y}{x^2 + y^2} \end{cases} \quad (12)$$

where the upper (lower) sign corresponds to cylinder C1(C2) defined by $-x_o - a < x < -x_o + a$ and $-a < y < a$ ($x_o - a < x < x_o + a$ and $-a < y < a$).

Equations (10), (11) and (12) give, in principle, the necessary information with which to calculate the behavior of the depletions and the plasma in the surrounding regions. To assess the corrections due to the approximations used in our analysis, we note that, by simulating the effects of the divergence in the self-field by placing line charges at the origin, we have incurred corrections of the order of a/d in the field just outside each cylinder and corrections of the order of a^2/d^2 in the field near the other cylinder. Thus, the approximations affect the mutual interaction through terms of order a^2/d^2 .

Another important conclusion can be drawn from the above consideration. Because each cylinder is immersed in a diverging field, there is now a force acting on each

one. This should be contrasted with the fact that a dipole in a uniform field experiences zero net force. From a simple consideration using the electrostatic analogy, it is easy to see that $n_{in} < n_{out}$ implies that two depletions repel each other. A more quantitative calculation will be presented in a manuscript by Chen and Satyanarayana in preparation.

In summary, we have developed a method to calculate the mutual interactions between two ionospheric depletions (in F region). We have identified the dominant interaction, i.e., the effective dipole interaction, and including the interactions to the lowest order in a/d due to the divergent self-field of one cylinder which the other cylinder experiences. The components of the field including the interaction are explicitly given and summarized [Eqs. (10), (11), and (12)]. Moreover, our analysis leads to the important conclusion that depletions repel each other. This tendency may have a significant impact on the linear and non-linear behavior of a group of depletions (bubbles).

REFERENCES

- Chen, J. and P. Satyanarayana, manuscript in preparation, 1981.
- Jackson, J. D., Classical Electrodynamics, John Wiley and Sons, Inc., NY, 1962.
- Ossakow, S. L., J. Atmos. Terr. Phys. 43, 437, 1981.
- Ossakow, S. L. and Chaturvedi, P. K., J. Geophys. Res. 83, 2085, 1978.
- Smythe, W. R., Static and Dynamic Electricity, McGraw-Hill, New York, 1950.

FIGURE CAPTION

Fig. 1 Two interacting cylindrical depletions. The radius is a . The cylinder C1 is centered at $x = -x_0$ and the cylinder C2 is centered at $x = x_0$. The external field \underline{E}_0 is in the x -direction. The gravitational acceleration \underline{g} is in the negative y -direction. The earth's magnetic field is in the z -direction, pointing out of the paper.

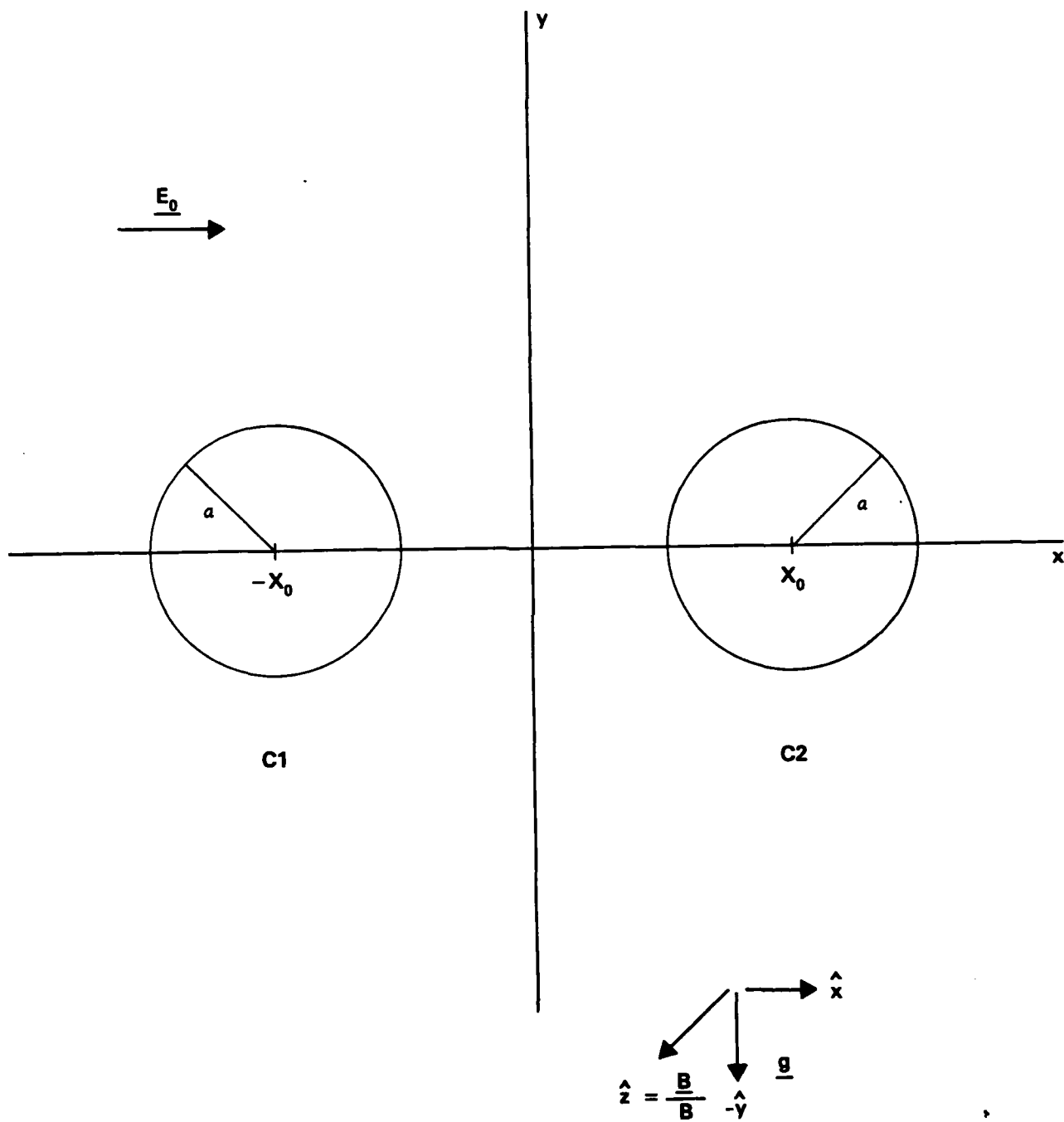


Figure 1

Appendix O

EVALUATIONS OF ATMOSPHERIC COOLING MODEL

John Apruzese
Science Applications, Inc.
McLean, VA 22102

EVALUATIONS OF ATMOSPHERIC COOLING MODEL

The mean annual temperature of the earth's surface and atmosphere is determined by the balance between incoming shortwave solar radiation and outgoing IR flux emitted to space by the surface, clouds, and atmosphere. This balance may be significantly altered if the atmospheric concentrations--hence the opacity--of the IR-active constituents vary. The possibility of changes in concentrations of two of the most important IR active constituents-- O_3 and CO_2 --has been extensively investigated by the atmospheric sciences community. SAI's two stream IR cooling model, developed for NRL on a previous contract has been utilized in performance of the present contract to investigate the interaction of the CO_2 and O_3 fluxes emitted to space and their potential effects on terrestrial climatology.

To validate the usefulness of the two-stream model for this type of study we have first calibrated the predicted CO_2 and O_3 fluxes against published satellite observations.⁽¹⁾ Unfortunately the only available observations are not direct measurements of the flux but of the specific intensity perpendicular to the earth's surface, (1). The relationship between the flux F emitted to space and I is

$$F = 2\pi \int_0^1 I(\mu) \mu d\mu \quad (1)$$

where μ is the cosine of the zenith angle of flow of the radiation. For isotropic radiation $I(\mu) = I_0$, $F = \pi I_0$. For a (severe) limb-darkening law of the form $I = I_0 \mu$ we obtain $F = 2.09 I_0$. Therefore, the "conversion factor" between specific intensity and flux would generally vary between 2.09 for severe limb-darkening and 3.14 for isotropy. Since the "true" angular distribution was not measured only an approximate comparison is therefore obtainable. This is still obviously worthwhile as a method of judging the realism of the model's predictions.

Since the ozone profile adopted for the two stream model reflects observations of mid-latitude concentrations, we compare our model predictions with the Wallops Island Nimbus 4 observations of June, 1970 as detailed in reference 1. The radiation measured in the 15μ CO_2 and 9.6μ O_3 spectral regions unavoidably includes radiation emitted by the earth itself as well as the atmosphere. Spectrally integrating the CO_2 observations between 550 and 775 cm^{-1} (where virtually all of the CO_2 opacity resides) yields a specific intensity (or radiance) of $17.3 \text{ w}/(\text{m}^2\text{-ster})$. The contribution from the earth is essentially negligible. Due to the high opacity and

overlapping lines of CO_2 the flux "formation" region is well above the ground. The CO_2 flux predicted by the model using the actual measured temperature profile above Wallops Island is 53.1 w/m^2 . This agrees exactly with the radiance of $17.3 \text{ w/(m}^2\text{-ster)}$ for a limb-darkening coefficient of $53.1/17.3 = 3.07$ (slight limb-darkening). Even if the actual limb darkening is severe the disagreement is at most 20%. Given this fundamental uncertainty, the prediction of flux is certainly reasonable. For O_3 the opacity resides between 1000 and 1100 cm^{-1} . Similar integration of the Nimbus 4 observations between these wave numbers yields a radiance of $5.2 \text{ w/(m}^2\text{-ster)}$. The model predicts a flux due purely to O_3 of 4.4 w/m^2 in this region. However, the mean transmission to space from the ground is predicted as 0.36 between 1000 and 1100 cm^{-1} . The Planckian emission from the ground, $\pi B_\nu(T_{\text{ground}}, \nu_0)$ (0.36) (110 cm^{-1}) amounts to 9.8 w/m^2 , giving a total predicted flux of 14.2 w/m^2 . This agrees exactly with the observed radiance for a limb-darkening coefficient of 2.73 . Again, given the unknown angular distribution, the agreement is quite reasonable.

The interaction of CO_2 and O_3 IR fluxes is illustrated most strikingly by the results presented in Table 1. In the table are presented the atmospheric temperatures obtained by requiring radiative equilibrium

on a globally averaged basis for two cases--present O_3 and 50% of present O_3 . Also presented are the CO_2 and O_3 fluxes emitted to space predicted by the model when these two assumptions are invoked. The result of halving O_3 is to decrease the peak stratospheric temperature by more than $20^{\circ}K$ --a direct consequence of the reduced UV solar heating of O_3 in this region. However, the equilibrium surface temperature rises by $0.6^{\circ}K$ as a result of the decreased O_3 . Inspection of the fluxes emitted by O_3 and CO_2 provides a ready explanation of this seeming anomaly. Due to the much colder stratosphere, the fluxes emitted to space by CO_2 and O_3 decrease by 1.3 and 1.4 w/m^2 , respectively. To maintain an IR flux equal to the constant solar input, the troposphere warms by $0.6^{\circ}K$, allowing increased flux from the ground to make up the CO_2 and O_3 deficits. In these calculations we have maintained the albedo of the earth at a constant 0.3.

The previous calculation made use of an assumption which has been adopted by many workers in atmospheric science--namely, that a reliable globally averaged temperature distribution may be obtained by solving for the temperature profile needed to balance, at each altitude, the globally averaged solar heating with IR cooling. However, due to nonlinearities in the Planck function and in the radiative transfer equation, it is far from obvious

that the globally averaged cooling (obtained accurately from multilatitude modeling) can be obtained from any single temperature profile. To test this assumption, we have run a series of radiative equilibrium calculations on a multilatitude grid at solstice. The observed tropospheric temperatures are adopted as a lower boundary condition, but the temperatures of the stratosphere and mesosphere are allowed to float until radiative equilibrium is achieved. The two-dimensional temperature profile is given in Figure 1. In Table 2 we present the heating (= cooling) rates and temperatures at several fiducial pressure points for both the single globally averaged run and the global average of the multilatitude grid runs. The results are a clear "victory" for the single profile approximation. The maximum deviation is a mere 6° at the stratopause, precisely where nonlinear effects would be expected due to the temperature gradient reversal. Elsewhere the approximation is excellent. Further details of this work will be presented in a paper now being prepared jointly with the NRL staff for submission to the Journal of Geophysical Research.

REFERENCES

1. V. G. Kunde, B. J. Conrath, R. A. Hanel, W. C. Maguire, C. Prabhakara, and V. V. Salomonson, J. Geophys. Res. 79, 777 (1974).

Table 1

z (km)	T ⁽¹⁾ (°K)	T ⁽²⁾ (°K)		O ₃	CO ₂
0	289.0	289.6	FLUX ⁽¹⁾	6.1	45.1
15	210.1	201.2	FLUX ⁽²⁾	4.7	43.8
30	224.5	216.3	(w/m ²)		
50	273.2	249.4			
60	243.3	212.9			
70	209.6	187.8			

(1) Radiative Equilibrium Run with Normal O₃.

(2) Radiative Equilibrium Run with O₃ Halved.

FLUX REFERS TO FLUX EMITTED TO SPACE.

Table 2

P (mb)	Q ⁽¹⁾	Q ⁽²⁾	T ⁽¹⁾	T ⁽²⁾
100	0.19	0.19	210	208
10	2.43	2.34	226	221
1	10.1	10.5	273	267
0.1	4.56	4.22	227	222
0.01	2.35	2.23	191	189

Q is IR cooling rate.

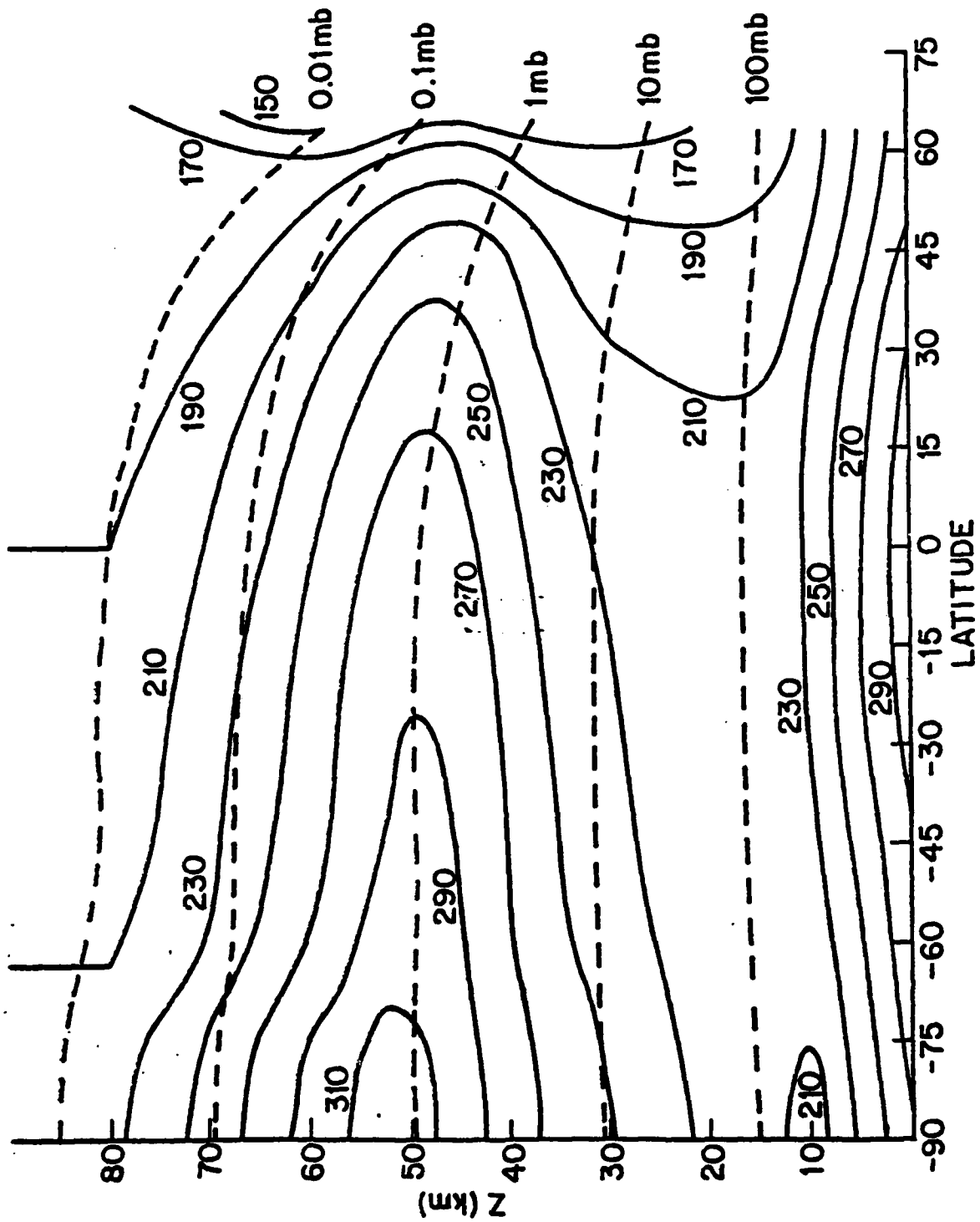
T is atmospheric temperature in °K.

(1) Refers to a single run using the globally averaged heating and cooling rates.

(2) Refers to the numerical global average of a series of runs on a multilatitude grid at solstice.

FIGURE CAPTION

Radiative equilibrium temperatures at solstice calculated with the two stream IR cooling model are presented, for summer in the southern hemisphere. Tropospheric temperatures are fixed at their observed values, and above 80 km radiative equilibrium is not enforced, but the 1962 U.S. Standard Atmosphere temperature gradient is preserved.



Appendix P

OZONE TRANSPORT BY STATIONARY
PLANETARY WAVES: AN INTERIM REPORT

OZONE TRANSPORT BY STATIONARY
PLANETARY WAVES: AN INTERIM REPORT

March 1981

by:

Richard B. Rood
Science Applications, Inc.
McLean, VA 22102

SCIENCE APPLICATIONS, INC.

P.O. Box 1303
1710 Goodridge Drive
McLean, Virginia 22102
(703) 734-5840

TABLE OF CONTENTS

	<u>Page</u>
INTRODUCTION	1
THE LAGRANGIAN-MEAN FORMULATION	4
THE DYNAMICAL MODEL	10
THE CHEMICAL MODEL	13
DIFFUSION MODELS	14
RESULTS	17
DISCUSSION AND EXTENSIONS	23
 Appendix A - NOMENCLATURE	 A-1
Appendix B - DERIVATION OF EQUATION (17) THE DIFFUSION MODEL	 B-1

REFERENCES

INTRODUCTION

Interest in stratospheric ozone intensified in the early 1970's when it was projected that a large fleet of supersonic transports would be in daily operation by 1985 (Johnston, 1971). It was predicted that such a fleet of airplanes operating in the stratosphere might cause a significant reduction of stratospheric ozone. The primary concern of such a depletion was the effect of increased ultraviolet radiation on the biosphere. Among other problems raised by the prospect of ozone depletion were the effects on the atmospheric radiation budget and subsequently the effects on the earth's climate (Ciap, 1975).

The consideration of supersonic transports and their interaction with the ozone budget was a major influence in the revision of ozone photochemistry. For many years ozone had been modeled with four reactions involving only molecular and atomic oxygen (Craig, 1965). However, a remeasurement of ozone reaction rates demonstrated that this simple chemistry was not adequate to describe the observed ozone profiles. Throughout the 1960's and 1970's catalytic destruction cycles involving hydrogen oxides, nitrogen oxides, and halogen oxides were identified as being important in ozone photochemistry. At this point in time there are well over 100 chemical reactions that relate

to the ozone problem (McConnell and McElroy, 1973; Molina and Rowland, 1974; Crutzen, 1974; Johnston and Podolske, 1978;

With such a large number of chemical reactions full scale chemical calculations are very time consuming and expensive. Full scale chemical studies coincident with realistic dynamical modeling are virtually impossible to perform even on the largest available computers. Therefore, it has been necessary for chemists to parameterize dynamical transport, and likewise dynamic modelers have had to extensively simplify the chemistry (Cunnold, et al., 1975). The simplest dynamic parameterization used by chemists is a vertical diffusion which is designed to transport ozone from regions where it is produced to lower altitudes where it is more nearly conserved (McConnell and McElroy, 1973). In an attempt to represent the dynamics more realistically two dimensional diffusion models have been developed. These two dimensional diffusion models use a symmetric diffusion tensor with diffusion coefficients derived from quasi-conservative tracers such as methane and radioactive fallout (Reed and German, 1965). The same diffusion coefficients are used for each chemical constituent. By virtue of all these assumptions the chemistry is independent and uncoupled from the dynamics (Harwood and Pyle, 1977; Mahlmann, 1975; and Tuck, 1979).

The ozone distribution has not been properly simulated by 2-D chemical models without significant tuning. Diffusion coefficients are derived so that they explain the distribution of a certain tracer. Then these coefficients are inserted into the chemical model, then the diffusion coefficients are recalculated in order to yield a reasonable profile. The final diffusion coefficients are highly unrealistic. For instance the Reed and German (1965) coefficients allow only for down gradient transport. However, up-gradient transport is often observed in the stratosphere. Despite these problems, a diffusion like model would be a very valuable aid to the chemists. Therefore the possibility of deriving more appropriate diffusion models should be investigated (NASA, 1979).

Since planetary waves dominate the eddy structure of the winter stratosphere a planetary wave model is used to model the winter stratosphere. Simplified photochemistry is incorporated into the dynamic models and ozone transport is studied. The ozone continuity equation is formulated in both the normal Eulerian zonal mean formulation and in the Lagrangian-mean formulation.* The goal of the project is

* Eulerian is an adjective generally used to refer to field like descriptions of a fluid flow. Lagrangian refers to particle descriptions of the fluid flow. In this paper Eulerian will refer to field like descriptions that have been decomposed into zonal mean and deviations from the zonal mean. Lagrangian-mean will refer to a field-like description decomposed into a mean based on particle displacements from a disturbance free state, and deviations from such a mean.

to find what mechanisms are important in the transport of ozone. With such information it may well be possible to limit the dynamics in chemical studies to only those mechanisms most responsible for ozone transport.

THE LAGRANGIAN-MEAN FORMULATION

Consider the ozone continuity equation where Q is a source term and u is the mixing ratio of ozone.

$$\frac{Du}{Dt} = Q. \quad (1)$$

By decomposing the fields into zonal averages and deviations from the averages the following mean field and perturbation equations are obtained:

$$\frac{\partial \bar{u}}{\partial t} + \bar{u}_i \frac{\partial \bar{u}}{\partial x_i} + \overline{u'_i \frac{\partial u}{\partial x_i}} = \bar{Q} \quad (2)$$

$$\frac{\partial u'}{\partial t} + u'_i \frac{\partial \bar{u}}{\partial x_i} + \bar{u}_i \frac{\partial u'}{\partial x_i} = Q' \quad (3)$$

Nomenclature is in Appendix A. The perturbation Eq. (3) has been linearized. Equations (2) and (3) are the equations that are referred to as the Eulerian formulation. It is pertinent to note that the zonal mean equation contains eddy flux terms: terms which can be thought of as wave forcing of the mean field. According to theory, for linear, steady, nondissipative waves in the absence of critical lines; the wave induced changes in the mean field are exactly counter-balanced by the eddy fluxes (Boyd, 1976). Therefore, when these criteria are met, the time rate of change of the mean field is zero. The atmosphere does not meet the

stipulations of the noninteraction theorem exactly, but the tendency of noninteraction is observed both in atmospheric data and in general circulation models (Mahlman and Moxim, 1978, and the references therein).

By transforming the constituent continuity equation to the Lagrangian-mean system it is possible to derive different diagnostic quantities which may help to clarify the important transport mechanisms. The Lagrangian-mean system is a hybrid Eulerian-Lagrangian system in which particle displacements are calculated as field variables. The formulation does not attempt to trace individual particle trajectories; it deals only with particle displacement fields. The concept of such a system has been in the literature for well over a century. Andrews and McIntyre (1978) present one of the most complete expositions on the Lagrangian-mean system.

The Lagrangian-mean coordinate system is obtained by transforming the reference coordinate system from \bar{x} to $\bar{x} + \bar{\xi}(\bar{x}, t)$. $\bar{\xi}(\bar{x}, t)$ is a disturbance associated displacement field; that is, when $\bar{\xi}(\bar{x}, t) = 0$ there exists a disturbance free basic state. Since the definition of disturbance is relative to some sort of mean, $\bar{\xi}(\bar{x}, t)$ must be constrained in some way in order to assure a unique transform. The constraint imposed by Andrews and McIntyre is

$$\overline{\xi}(\bar{x}, t) = 0. \quad (4)$$

With this definition $\overline{\xi}(\bar{x}, t)$ is said to represent a "true disturbance quantity."

The Lagrangian-mean for some quantity ϕ is defined as

$$\phi^L(\bar{x}, t) \equiv \overline{\phi(\bar{x} + \overline{\xi}(\bar{x}, t), t)}. \quad (5)$$

A conceptual diagram comparing the Eulerian to the Lagrangian-mean is given in Figure 1. The Eulerian zonal mean is a mean based on the geometry of the coordinate system. The Lagrangian-mean is based on the geometry of the fluid flow. The geometry of the fluid flow is based on the original coordinate system. Hence, the Lagrangian-mean system is dependent on the prescription of some other mean system, in this instance the Eulerian system.

The Lagrangian-mean material derivative is defined such that

$$\begin{aligned} D^L(\bar{x} + \overline{\xi}(\bar{x}, t)) &= \left(\frac{\partial}{\partial t} + u_i^L \frac{\partial}{\partial x_i} \right) (\bar{x} + \overline{\xi}(\bar{x}, t)) \\ &= \vec{u}(\bar{x} + \overline{\xi}(\bar{x}, t), t). \end{aligned} \quad (6)$$

$\vec{u}(\bar{x} + \overline{\xi}(\bar{x}, t), t)$ is the actual fluid velocity of a particle at its displaced position. If the Lagrangian-mean operator is applied to the material derivative the following is obtained:

$$\left(\frac{D}{Dt}\right)^L = D^L : L .$$

There are some important features of the Lagrangian-mean system that should be explicitly noted:

- (1) There are no wave forcing terms in the mean equation, (7).
- (2) For the premises of the noninteraction theorem the Lagrangian-mean velocity, \bar{u}^L , is zero.
- (3) The Lagrangian-mean velocity is the velocity of the center of mass of a particular ensemble of fluid particles.

The definition of the Lagrangian-mean coordinate system is so dependent on the flow field that its practical use is severely limited. It is in fact very similar to the natural coordinate system used in synoptic analysis. Due to the fact that the Lagrangian-mean coordinate system changes with the flow field, Lagrangian-mean quantities are often defined in terms of the more familiar Eulerian quantities.

By definition the difference between the Lagrangian-mean and the Eulerian mean is the Stokes correction, $:\bar{S}$. That is

$$\begin{aligned} \bar{c}^S &= \bar{c}^L - \bar{c} \\ \text{or} \\ \bar{c}^L &= \bar{c} + \bar{c}^S \end{aligned} \quad (8)$$

In order to determine the value of the Stokes correction it is possible to expand the value of c at the perturbed position in relation to the value of c at the unperturbed position.

$$c(\bar{x} + \bar{\xi}(\bar{x}, t), t) = c(\bar{x}, t) + \xi_i \frac{\partial c}{\partial x_i} + \frac{1}{2} \xi_i \xi_j \frac{\partial^2 c}{\partial x_i \partial x_j} + \text{higher order terms.}$$

where $\bar{\xi} = (\xi_1, \xi_2, \xi_3)$ is the displacement vector. First decomposing c into its zonal mean and deviation, and then taking the zonal average of the resulting series the Lagrangian-mean is found to be

$$\begin{aligned} \bar{c}^L &\equiv \overline{c(\bar{x} + \bar{\xi}(\bar{x}, t), t)} \\ &= \bar{c} + \overline{\xi_i \frac{\partial c}{\partial x_i}} + \frac{1}{2} \overline{\xi_i \xi_j \frac{\partial^2 c}{\partial x_i \partial x_j}}. \end{aligned} \quad (9)$$

The Stokes correction is seen from (8) and (9) to be

$$\bar{c}^S = \overline{\xi_i \frac{\partial c}{\partial x_i}} + \frac{1}{2} \overline{\xi_i \xi_j \frac{\partial^2 c}{\partial x_i \partial x_j}}. \quad (10)$$

It is assumed in the quasi-geostrophic dynamics used here that \bar{v} and \bar{w} may be neglected in the perturbation equations. This assumption is manifest to saying that any significant \bar{v} and \bar{w} fields are forced by the waves. Therefore, the mean fields are second order in wave amplitude. As a result the second term on the right hand side of (10) is fourth order in wave amplitude. With this assumption the Stokes correction becomes

$$i^S = \overline{\zeta_i \frac{\partial \zeta}{\partial x_i}} \quad (11)$$

Figure 2 provides a comparison of the Lagrangian-mean description to the Eulerian description of the general circulation. In the Eulerian view there is a three cell structure in the troposphere: the thermally direct Hadley cell, the thermally indirect Ferrel cell, and another thermally direct cell over the polar regions. In the stratosphere and the mesosphere there is a thermally direct cell from the summer pole to the winter pole. The Lagrangian-mean view is more in line with the intuitive circulation expected from simple consideration of the radiational energy sources and sinks. The stratosphere and the mesosphere still show the same basic structure. The troposphere, however, shows a much different structure. The mid-latitude Ferrel cell is not present, and there is a general circulation from the warm

equatorial regions to the cooler polar regions. The Ferrel cell does not appear because it is primarily produced by wave processes and these waves are incorporated into the definition of the Lagrangian-mean coordinate. Therefore, only the total effect of both wave and mean motions is seen in the Lagrangian-mean picture.

THE DYNAMICAL MODEL

The dynamical model used is meant to describe the gross features of the winter stratosphere. The linear, steady state, quasi-geostrophic perturbation potential vorticity equation is solved on a beta plane for a wave number one disturbance. The beta channel is 5000 km in north-south extension and is 128 km deep. The grid is 36 horizontal points by 63 vertical points. Waves are forced at the bottom boundary in a way analogous to steady zonal flow over a mountain. The mean flow is then calculated using the waves as forcing. The mean and perturbation equations are given below.

$$\frac{a}{f} \frac{\partial^2 \bar{\phi}}{\partial y^2} + \frac{f}{N^2} \frac{\partial}{\partial z} a \frac{\partial \bar{\phi}}{\partial z} - \frac{fa}{N^2 H} \frac{\partial \bar{\phi}}{\partial z} =$$

$$\frac{\partial^2}{\partial y^2} \overline{u'v'} - \frac{f}{N^2} \frac{\partial^2}{\partial z \partial y} \overline{v'c_z'} + \frac{f}{N^2 H} \frac{\partial}{\partial y} \overline{v'c_z'} \quad (12)$$

$$\left(a + \bar{u} \frac{\partial}{\partial x} \right) \left(-2\bar{c}_z' + \frac{f^2}{N^2} \frac{\partial^2}{\partial z^2} \bar{c}_z' - \frac{f^2}{N^2 H} \frac{\partial \bar{c}_z'}{\partial z} \right)$$

$$+ \bar{q}_y \frac{\partial \bar{c}_z'}{\partial x} = 0 \quad (13)$$

Damping is modeled by Newtonian cooling and Rayleigh friction. The coefficients of cooling and friction are assumed to be equal. In the upper regions of the model the damping increases exponentially to provide a sponge layer and thereby reduce reflections from the upper boundary. The

sponge layer is sufficiently above the prescribed ozone field to assure that the transport field is not obscured by reflections from the sponge layer. The wind field in this study is assumed to be a symmetric westerly jet with maximum winds of about 60 m/sec. There are no critical lines in this study. The velocities \bar{v} and \bar{w} are forced by the waves.

THE CHEMICAL MODEL

The chemistry is parameterized by

$$Q' = -Q_0' + \epsilon T' \quad (14)$$

ϵ is a parameter which represents the temperature dependence of the ozone reaction rates. The inverse of ϵ is the photochemical relaxation time. The numerical values of λ and ϵ are derived from the oxygen only chemistry and are taken directly from Hartmann and Garcia (1979). Since transport mechanisms, and not quantitative ozone transport, are being studied, this chemical scheme is considered adequate.

Figure 3 shows, schematically, the atmosphere divided into three regions based on the ratio of the dynamic to the photochemical time scale, $\lambda/\bar{u}k$. In the lower, conservative region, λ is so small that the ozone is essentially a conservative tracer. In the upper, photochemical region, λ is so large that the ozone will return to chemical equilibrium before it is transported anywhere. In the middle region λ and $\bar{u}k$ are of about the same size. This middle region is called the transition region. In the transition region both dynamic and photochemical effects are expected to be important.

DIFFUSION MODELS

Dynamic simplification by use of diffusion models often uses a climatological zonal mean state and a diffusion scheme to represent the effects of the waves (Harwood and Pyle, 1977). The diffusion coefficients are often assumed to be symmetric and identical for all chemical species.

For the dynamics used here the mean field and perturbation constituent continuity equations, Eqs. (2) and (3), can be written as

$$\frac{\partial \bar{u}}{\partial t} = - \bar{u}_1 \frac{\partial \bar{u}}{\partial x_1} - \frac{1}{\rho} \frac{\partial}{\partial x_1} \overline{u u_1} + \bar{Q} \quad (15)$$

and

$$\bar{u} \frac{\partial u'}{\partial x} = - v' \frac{\partial \bar{u}}{\partial y} - w' \frac{\partial \bar{u}}{\partial z} + Q' . \quad (16)$$

The eddy terms in Eq. (2) have been written in flux form in Eq. (15) by use of the mass continuity equation.

Using (16) to solve for the eddy flux terms Eq. (15) can be rewritten as

$$\frac{\partial \bar{u}}{\partial t} = - \bar{u}_1 \frac{\partial \bar{u}}{\partial x_1} - \frac{1}{\rho} \frac{\partial}{\partial x_1} D_{ij} \frac{\partial \bar{u}}{\partial x_j} . \quad (17)$$

This derivation is shown in Appendix B. In the derivation of (17) it has been assumed that \bar{Q} and Q' are zero. Therefore, Eq. (17) represents the transport for a conservative tracer. D_{ij} the diffusion tensor, is

$$D_{ij} = \begin{pmatrix} 0 & \frac{\overline{w'w'}}{\overline{u}} \\ -\frac{\overline{w'w'}}{\overline{u}} & 0 \end{pmatrix} \quad (18)$$

Three immediate observations can be made from (18). First the diffusion tensor is antisymmetric, not symmetric as is assumed by Reed and German (1965) and in chemical models (NASA, 1979). Second, the diffusion tensor elements are related to the vertical flux of energy and will vary strongly with time. Third, in the vicinity of a critical line ($\overline{u}=0$) the diffusion coefficients may obtain great size, and this region may be a region of aberrant transport.

In the formulation of the diffusion model the eddy terms in Eq. (2) have been written in terms of a diffusion tensor. Following the more general derivation of Dunkerton (1980) the eddy term in (2) can be written as

$$\overline{u_i' \frac{\partial \overline{c}}{\partial x_i}} = u_i^s \frac{\partial \overline{c}}{\partial x_i} + D_{ij}^L \frac{\partial^2 \overline{c}}{\partial x_i \partial x_j} - Q^s \quad (19)$$

Eq. (19) shows that the eddy flux terms depend on the chemical source; therefore, if a diffusion model is to be accurate the diffusion tensor must vary from constituent to constituent. Furthermore since only source terms that can be written as functions of the gradients of the mean

fields lend themselves to diffusion formulations all source terms such as temperature must be small if models of the form of (17) are to be valid.

Using (19) and (15) it is found that

$$\frac{\partial \bar{\rho}}{\partial t} = -\bar{u}_1 \frac{\partial \bar{\rho}}{\partial x_1} - u_1^S \frac{\partial \bar{\rho}}{\partial x_1} - D^L \bar{\rho} + Q^S + \bar{Q} \quad (20)$$

This is the continuity equation in the Lagrangian-mean system namely:

$$D^L L = \left(\frac{\partial}{\partial t} + u_1^L \frac{\partial}{\partial x_1} \right) \rho^L = Q^L; \quad (21)$$

For steady waves $\frac{\partial \bar{\rho}}{\partial t} = 0$. For small amplitude, quasi-geostrophic flow $u_1^L \frac{\partial \bar{\rho}}{\partial x_1}$ is fourth order in wave amplitude and can be neglected. Eq. (20) can then be written to second order in wave amplitude as

$$\frac{\partial \bar{\rho}}{\partial t} = -u_1^L \frac{\partial \bar{\rho}}{\partial x_1} + Q^S + \bar{Q} \quad (22)$$

Equations (15), (16), and (22) are the forms of the continuity equations that will be used in this study. \bar{Q} is neglected in both (15) and (22); not because it is small, but because it would have the same effect in both formulations and might obscure some eddy transport mechanism.

RESULTS

Figure 4 shows the mean ozone distribution used in this study. It is based on the data given by Dütsch (1969) and Krueger and Minzner (1976). Due to a lack of data the ozone field above 74 km is an arbitrary function of height and latitude. This arbitrariness is of little consequence as the photochemical time scale is so short that there is no dynamical effect on the ozone distribution.

Figures 5 and 6 show the mean dynamics of the model. In the Eulerian description the vertical velocity field is characterized by rising motion in the polar regions and sinking motion in the tropical regions. The meridional velocity is southward with its magnitude increasing with height. The Eulerian flow shows a meridional cell driven by the northward eddy heat flux of the planetary waves.

Figures 5b and 6b show the Stokes drifts as calculated with (11). The Stokes drifts are directed in the opposite sense of the Eulerian mean fields. Since the Stokes drifts represent mean wave effects, the opposition of the Stokes drifts to the Eulerian mean flow demonstrates the tendency towards nonacceleration of the mean zonal flow by the waves.

The Lagrangian-mean velocity, $v^L = \bar{v} + v^S$, is seen to be the sum of two quantities directed in an opposite sense. The Lagrangian-mean velocity is effectively the

small difference between two large numbers. It has proven difficult to calculate Lagrangian-mean velocities with a high degree of confidence.

In order to analyze the details of the calculation of the Lagrangian-mean velocity field an analytic model similar to the previously described numerical model was used. It was found that the assumption that the second term in Eq. (10) could be ignored was incorrect. The Lagrangian-mean velocity is of the same order as this term and both terms in (10) should be retained in the calculation of the Stokes correction.

It was also found that the calculation of the eddy meridional velocity, v' , should include damping and isalobaric corrections. The geostrophic approximation, $v' = 1/f \partial \phi' / \partial x$, used in this study, approximates the magnitude of v' quite closely; however, the phase is inaccurate enough that it affects the calculation of the Lagrangian-mean velocity.

Neither of these corrections have been incorporated into the results presented here. The Stokes corrections are calculated according to (11) and the geostrophic approximation has been used for v' . As the problem is being extended these inadequacies are being corrected.

Figures 7, 8 and 9 show the mean field ozone calculations for the Eulerian system. The vertical flux

shown in Figure 8 reflects the Eulerian mean vertical velocity field and is upward in the polar region and downward in the tropical region. The horizontal flux field shown in Figure 7 shows more structure. In the conservative region there are two centers of transport. There is a low level northward cell which is dominated by the meridional eddy flux. This northward flux is dependent on the vertical gradient of the mean ozone field (Clark and Rogers, 1978). Above this northward cell there is a southward cell where the flux is dominated by the Eulerian mean meridional velocity.

In the transition region there is a region of weak northward flux. If the constituent were conservative then both the mean flux and eddy flux would be southward in this region. Therefore, the northward cell in the transition region must be caused by dynamical-photochemical interaction.

Both the horizontal and vertical flux fields decrease rapidly with height in the photochemical region. Also both fields have their greatest magnitude in the conservative region. When the time rate of change of the mean ozone field (Figure 9) is calculated there is an almost complete cancellation of the horizontal and vertical fluxes in the conservative region. The change in mean ozone is concentrated in the transition region with increasing ozone in the polar region and decreasing ozone in the tropical region.

For the Lagrangian-mean calculation the continuity equation is written as

$$\frac{d\bar{q}}{dt} = - \bar{u}_1^L \frac{\partial \bar{q}}{\partial x_1} + \overline{u_1^L \frac{\partial q}{\partial x_1}} \quad (23)$$

The first term on the right hand side of (23) is the advection of the mean field by the Lagrangian-mean velocity and is labeled the advective term. The second term is labeled the stirring term and is discussed below.

Figure 11 shows the advective term. Its maximum magnitude is in the transition region. Since this term is independent of the photochemistry it is not yet understood why the maximum of the advective term is in the transition region. Because the Lagrangian-mean velocity calculations still contain some inaccuracies interpretation of this term is left for extensions of this report.

The time rate of change of the mean ozone field as calculated by the Lagrangian-mean system is shown in Figure 12. This tendency field is equivalent to the same field shown in Figure 9 for the Eulerian calculation. Examination of the stirring term shown in Figure 10 shows that the stirring term dominates the mean field changes

The stirring term is a factor of 5 or more greater than the advective term over most of the domain above 40 km. When the transport is conservative ($\lambda = 0$, $\epsilon = 0$) then the

stirring term is identically zero. The stirring term represents the displacement of particles from their equilibrium position and their subsequent stirring in a region of differential photochemistry.

Figure 13 shows the projection of a Lagrangian-mean displacement field on the latitude-height plane. The planetary wave displaces a particle from its equilibrium position, E, in the center of Figure 13. The particle encircles the globe in a helical trajectory about its equilibrium position. The number of complete revolutions about its equilibrium position per circumnavigation is equal to the integer wave number of the wave. The projection of this trajectory on the latitude-height plane is an ellipse. For the linear, steady state waves of this model the height of the ellipse is on the order of kilometers while the length is on the order of hundreds of kilometers.

With the ellipse situated in the particular position shown in Figure 13 the nature of the stirring term becomes clear. As a parcel moves from A to B in the transition region it does not reside at any particular point long enough to reach photochemical equilibrium. The ozone concentration of the parcel does however change as it moves from A to B and it arrives at B with a different ozone concentration than it had initially. Then as the parcel moves from B back to A the amount of ozone remains constant.

Therefore the parcel returns to A with a net change in ozone concentration. It is the effect of the planetary wave to stir the particle in a region of differential chemistry and thereby produce ozone field changes.

DISCUSSION AND EXTENSIONS

Both calculations of the mean ozone tendency demonstrate the importance of the photochemistry in determining the ozone field. In fact in the Lagrangian-mean formulation the stirring mechanism is so dominate that it obscures inaccuracies in the Lagrangian-mean velocity calculation.

It might then be concluded that it is not necessary to accurately calculate the Lagrangian-mean velocity. This however would be a spurious conclusion since the mean chemistry has been neglected. The mean chemistry will act counter to changes in the mean fields and may balance the changes to the extent that the Lagrangian-mean velocity is a significant factor in the mean tendency calculation. Furthermore, the Lagrangian-mean velocity in the vicinity of a critical line has been shown to be large (Matsuno and Nakamura, 1979) and critical lines have not been considered in this model. The effects of wave transience and other chemical active constituents might also significantly change the results of this study.

The major extension of this work is to repeat the calculations with a time dependent model that simulates stratospheric warmings. Hartmann and Garcia (1979) have shown that transient waves can also be responsible for transport in the transition region but their model did

not simulate stratospheric warmings. Transport during stratospheric warmings may be responsible for the spring ozone maximum at polar latitudes.

Using the time dependent model, diffusion parameters will be derived. These parameters can be compared with those in actual use in chemistry models. Conversely, the derivation of dynamical parameterizations from models designed to study ozone transport may allow for the construction of more realistic parameterizations.

Appendix A
NOMENCLATURE

a	damping: Newtonian cooling and Rayleigh friction, a function of height only
D_{ij}	diffusion tensor
f	coriolis parameter $(1.0 \times 10^{-4} \text{ sec}^{-1})$
H	scale height (7.0 km)
k	wave number $(2 \times 10^{-4} \text{ km}^{-1})$
N^2	Brünt-Väisälä frequency $(4.0 \times 10^{-4} \text{ sec}^{-1})$
P	pressure
P_0	reference pressure
Q	photochemical source function
\bar{q}_y	north south gradient of zonal mean potential vorticity
T	temperature
t	time
\vec{u}	velocity vector: $= (u, v, w) = (u_1, u_2, u_3)$
\vec{x}	position vector: $= (x, y, z) = (x_1, x_2, x_3)$ $= (\text{longitude, north-south beta}$ $\text{plane coordinate, height}$ $(-H \ln P/P_0))$
θ	photochemical temperature parameter
τ	photochemical time parameter
χ	ozone mixing ratio
ρ	density $= \rho_0 e^{-z/H}$

ϕ geopotential

\vec{r} displacement vector = $(\xi, \eta, \zeta) = (\xi_1, \xi_2, \xi_3)$

= (longitudinal, north-south,
height)

Averaging operators: for any f

\bar{f} Eulerian zonal average

$f' = f - \bar{f}$ deviation from Eulerian zonal average

\bar{f}^L Lagrangian-mean average

$f^S = \bar{f}^L - \bar{f}$ Stokes correction

Appendix B

DERIVATION OF EQUATION (17) THE DIFFUSION MODEL

ASSUMPTIONS

1. Steady perturbations $\frac{\partial \bar{u}'}{\partial t} = 0$ (B-1)

2. Linear perturbations (B-2)

3. The mean velocities, \bar{v} and \bar{w} can be ignored in the perturbation equations. (B-3)

4. Geostrophic v' $\left(v' = \frac{1}{f} \frac{\partial \phi'}{\partial x} \right)$ (B-4)

5. Q , the source term is zero (B-5)

Invoking (B-1), (B-2), and (B-3) the eddy constituent continuity equation can be written as

$$\bar{u} \frac{\partial \bar{u}'}{\partial x} = -v' \frac{\partial \bar{u}}{\partial y} - w' \frac{\partial \bar{u}}{\partial z} + Q' \quad (B-6)$$

multiplying (B-6) by u' and taking the zonal average of the result yields

$$\overline{v' u' \frac{\partial \bar{u}}{\partial y}} = - \overline{w' u' \frac{\partial \bar{u}}{\partial z}} + \overline{u' Q'} \quad (B-7)$$

The multiplying (B-6) by z' and zonally averaging and using (B-4) yields

$$-f\bar{u} \overline{v'w'} = -\overline{v'w'} \frac{\partial \bar{u}}{\partial z} - \overline{v'Q'} \quad (\text{B-8})$$

Using (B-5) allows for the following solution of $\overline{v'w'}$

$$\overline{v'w'} = \frac{\overline{v'w'}}{f\bar{u}} \frac{\partial \bar{u}}{\partial z} \quad (\text{B-9})$$

The using (B-9) to solve for $\overline{w'u'}$ in (B-7) yields

$$\overline{w'u'} = -\frac{\overline{v'w'}}{f\bar{u}} \frac{\partial \bar{u}}{\partial y} \quad (\text{B-10})$$

For $\bar{Q} = 0$ (15) can be written as

$$\frac{\partial \bar{u}}{\partial t} = -\bar{u}_i \frac{\partial \bar{u}}{\partial x_i} - \frac{1}{f} \frac{\partial}{\partial y} \overline{v'u'} - \frac{1}{f} \frac{\partial}{\partial z} \overline{w'u'} \quad (\text{B-11})$$

Then using (B-10) and (B-9) for the eddy fluxes in (B-11) yields

$$\frac{\partial \bar{u}}{\partial t} = -\bar{u}_i \frac{\partial \bar{u}}{\partial x_i} - \frac{1}{f} \frac{\partial}{\partial x_i} D_{ij} \frac{\partial \bar{u}}{\partial x_j}$$

where D_{ij} is given in (18).

REFERENCES

- Andrews, D.G. and M.E. McIntyre, 1978: An exact theory of nonlinear waves on a Lagrangian-mean flow. J. Fluid Mech. 89, part 4, 609-646.
- Boyd, J.P., 1976: The noninteraction of waves with the zonally averaged flow on a spherical earth and the interrelationships of eddy fluxes of energy, heat, and momentum. J. Atmos. Sci. 33, 2285-2291.
- CIAP, 1975: The Stratosphere Perturbed by Propulsion Effluents and other related reports from The Climatic Impact Assessment Program of the U.S. Dept. of Transportation. Report #DOT-TST-75-53.
- Clark, J.H.E. and T.G. Rogers. 1978: The transport of conservative trace gases by planetary waves. J. Atmos. Sci. 35, 2232-2235.
- Craig, R.A., 1965: The Upper Atmosphere: Meteorology and Physics. New York, Academic Press, p. 509.
- Crutzen, P.J., 1974: Estimates of possible variations in total ozone due to natural causes and human activities. Ambio 3, 201-210.
- Cunnold, D., F. Alyea, N. Phillips, and R. Prinn, 1975: A three-dimensional dynamical-chemical model of atmospheric ozone. J. Atmos. Sci. 32, 170-194.

- Dunkerton, T., 1980: A Lagrangian mean theory of wave, mean-flow interaction with applications to non-acceleration and its breakdown. Rev. Geophys. Space Phys. 18, 387-400.
- Dütsch, H.U., 1969: Atmospheric ozone and ultraviolet radiation. World Survey of Climatology, Vol. 4, D.F. Rex, Ed., Elsevier, 383-432.
- Hartmann, D.L. and R. Garcia, 1979: A mechanistic model of ozone transport by planetary waves in the stratosphere. J. Atmos Sci. 36, 350-364.
- Harwood, R.S. and J.A. Pyle, 1977: Studies of the ozone budget using a zonal mean circulation model and linearized photochemistry. Quart. J. Royal Met. Soc. 103, 319-343.
- Johnston, H., 1971: Reduction of stratospheric ozone by nitrogen oxide catalysts from supersonic transport exhaust. Science 173, 517-522.
- Johnston, H.S. and J. Podolske, 1978: Interpretations of stratospheric photochemistry. Rev. Geophys. Space Phys. 16, 491-520.
- Krueger, A.J. and R.A. Minzner, 1976: A mid-latitude ozone model for the 1975 U.S. Standard Atmosphere, J. Geophys. Res. 81, 4477-4481.

- Mahlman, J.D., 1975: Some fundamental limitations of simplified transport models as implied by results from a three-dimensional general-circulation/tracer model. Proceedings of the Fourth CIAP Conference, U.S. Dept. of Transportation, DOT-TSC-OST-75-38, 132-146.
- Mahlman, J.D. and W.J. Moxim, 1978: Tracer simulation using a global general circulation model: Results from a mid-latitude instantaneous source experiment. J. Atmos. Sci. 35, 1340-1374.
- Matsuno, T. and K. Nakamura, 1979: The Eulerian- and Lagrangian-mean meridional circulation in the stratosphere at the time of a sudden warming. J. Atmos. Sci. 36, 640-654.
- Molina, M.J. and F.S. Rowland, 1974: Stratospheric sink for chlorofluoromethanes: Chlorine atom catalyzed destruction of ozone. Nature 249, 810-812.
- McConnell, J.C. and M.B. McElroy, 1973: Odd nitrogen in the atmosphere. J. Atmos. Sci. 30, 1465-1477.
- NASA, 1979: The Stratosphere: Present and Future, NASA Reference Publication 1049.
- Reed, R.J. and K.E. German, 1965: A contribution to the problem of stratospheric diffusion by large-scale mixing. Mon. Wea. Rev. 93, 313-321.

Tuck, A.F., 1979: A comparison of one-, two- and three-dimensional model representations of stratospheric gases. Phil. Trans. R. Soc. Lond. A290, 477-494.

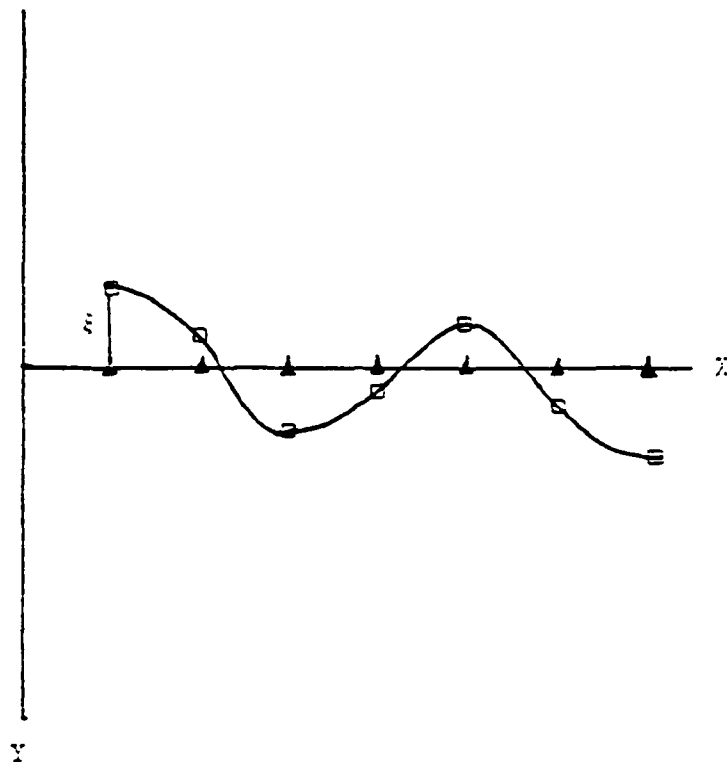
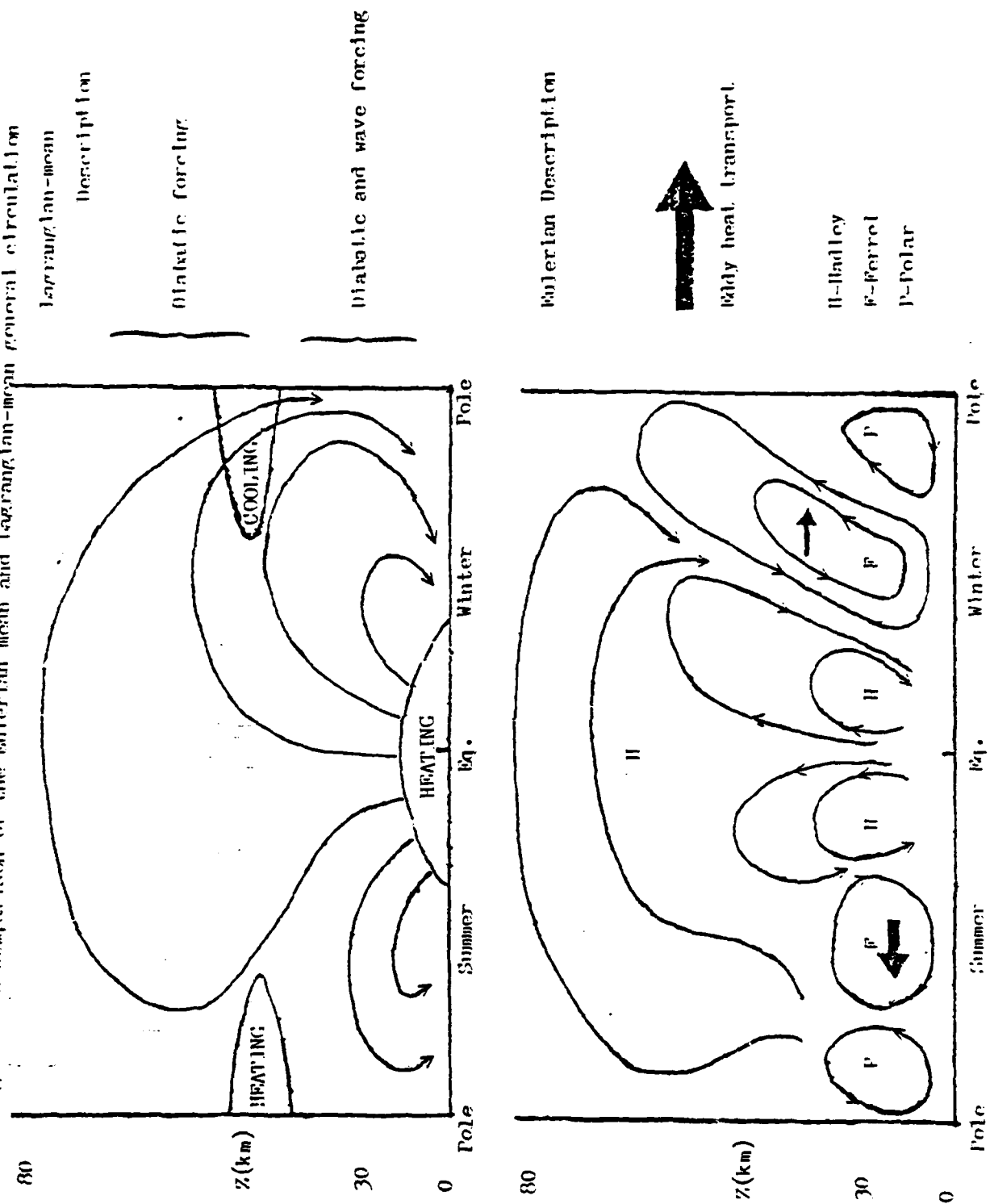


Figure 1

The Eulerian average is defined as the average using the particles labeled by the \blacktriangle 's on the X axis. The Lagrangian-mean average involves the particles labeled by the \square 's. If $\xi(X,Y,t)$ is zero, the disturbance free basic state, then the two averages would be equivalent. It is seen that the Lagrangian-mean depends on the structure of the disturbance field and on the definition of the Eulerian mean.

Figure 2 A comparison of the Eulerian mean and Lagrangian-mean general circulation



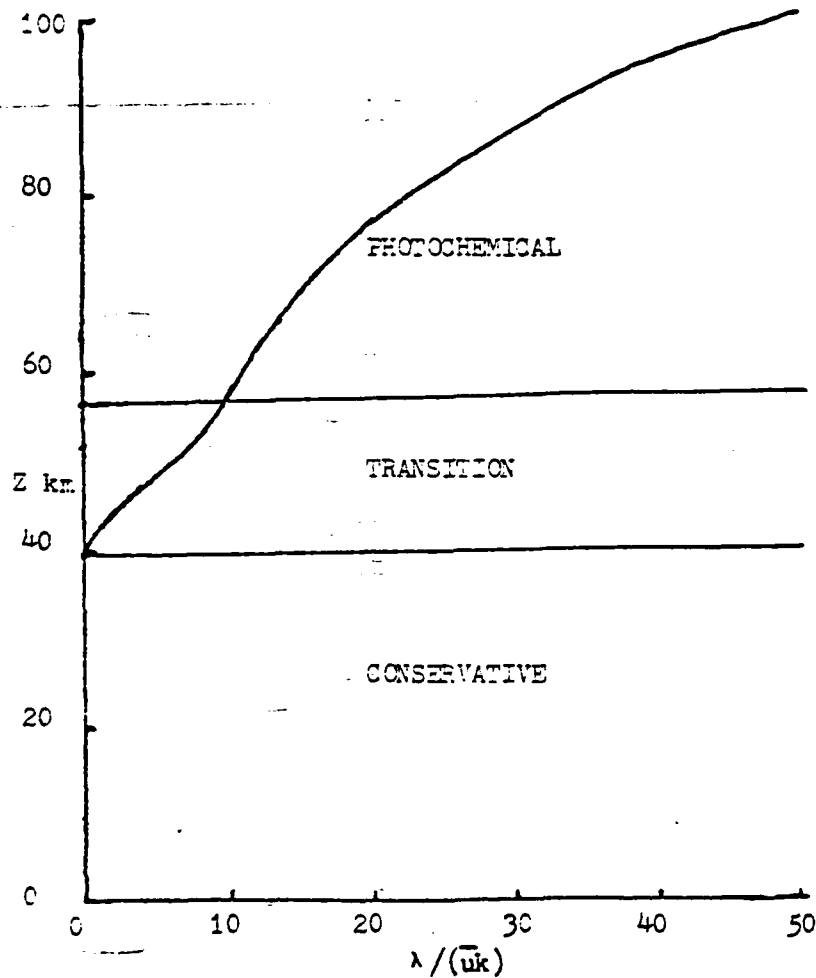


Figure 3

Ratio of the dynamic to the photochemical time scales

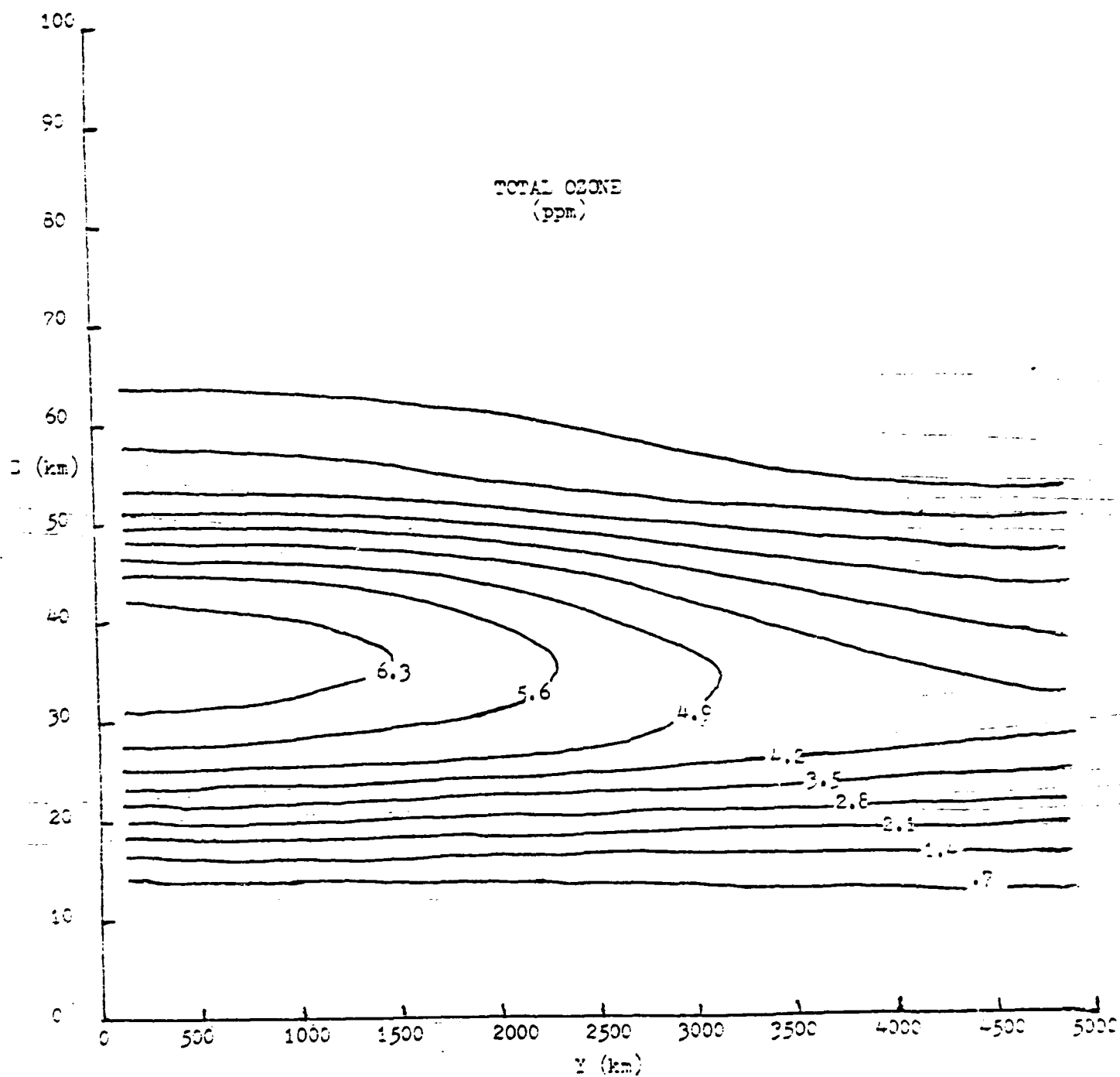


Figure 4

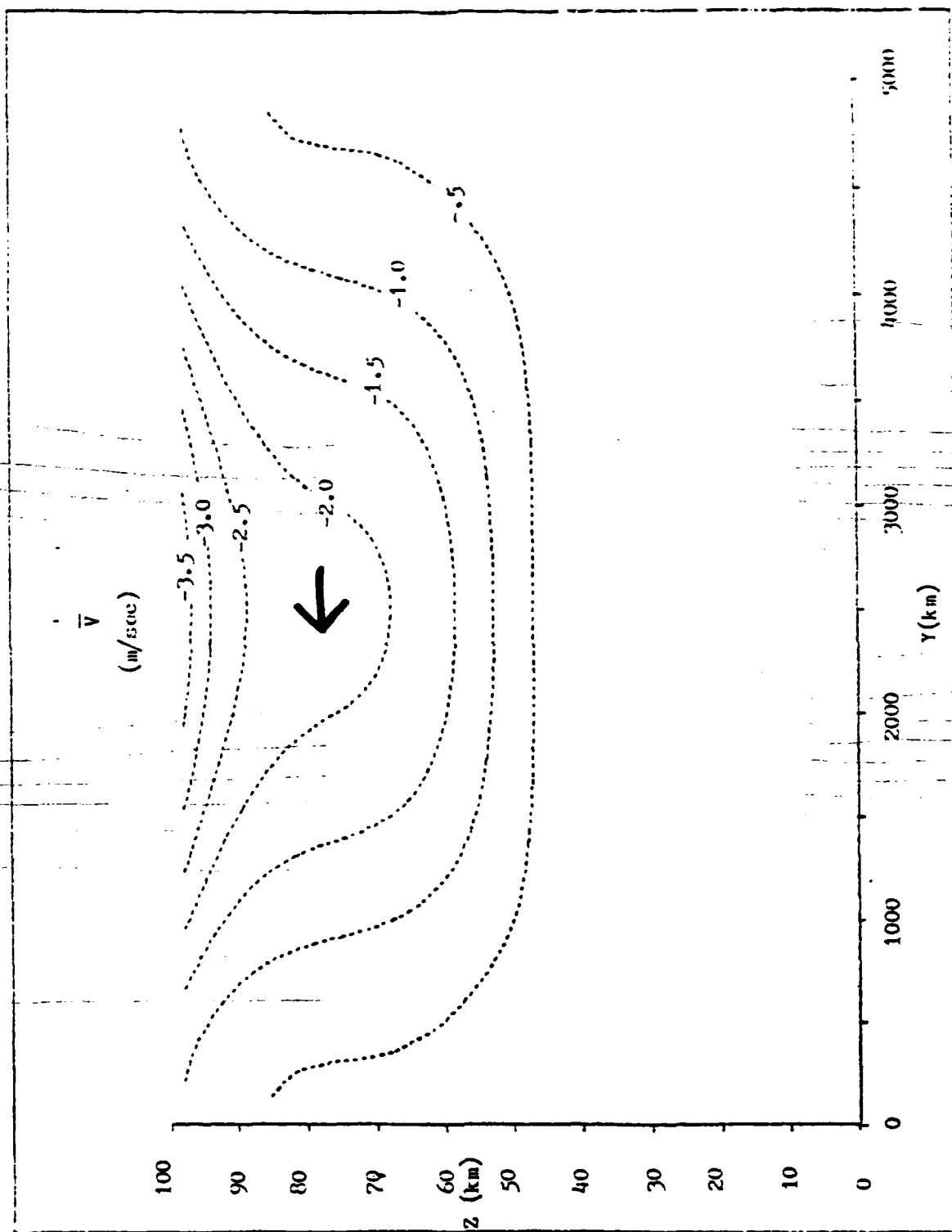


Figure 5a: \bar{V} , the Eulerian mean meridional velocity

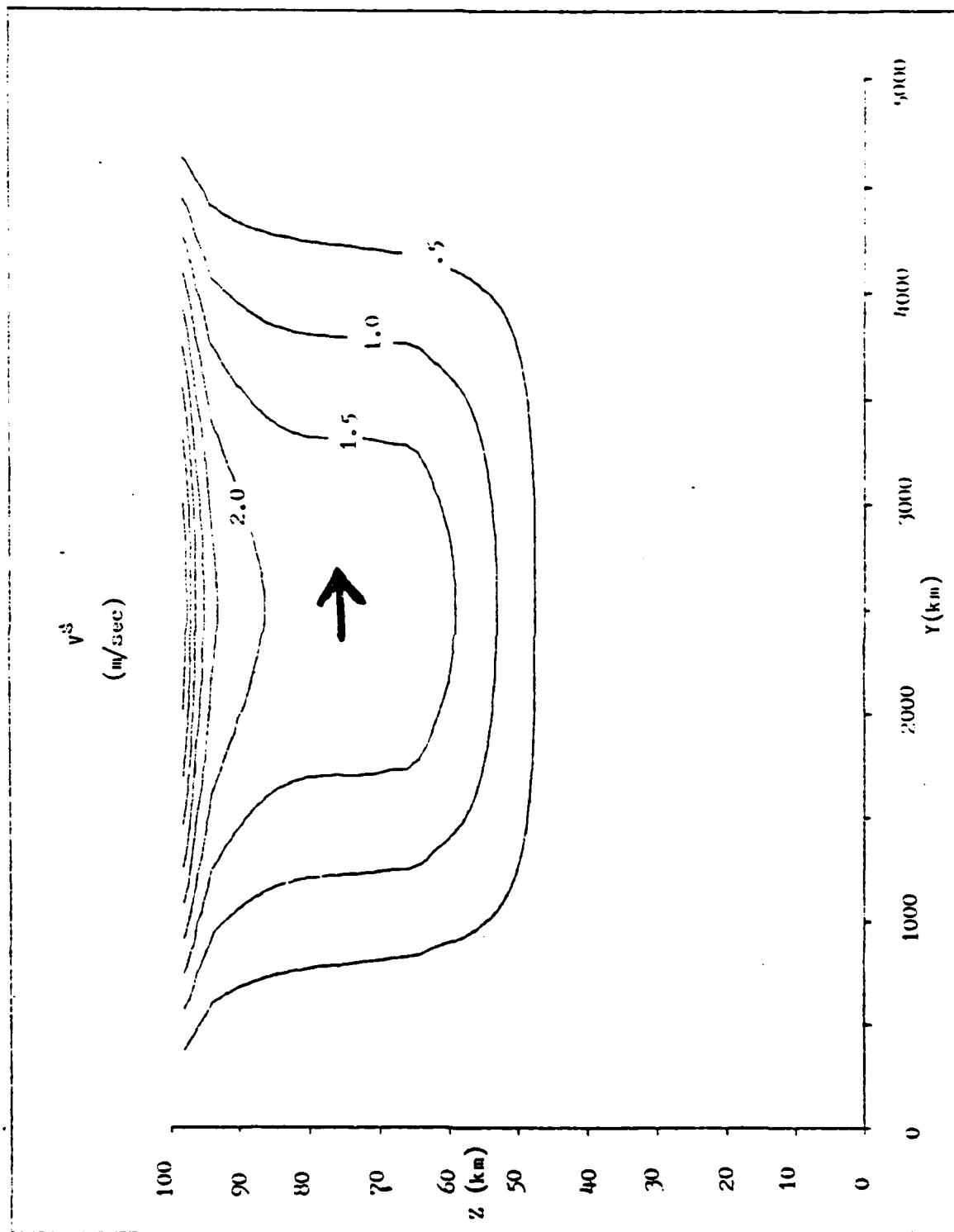


Figure 5b: v^S , the meridional Stokes drift.

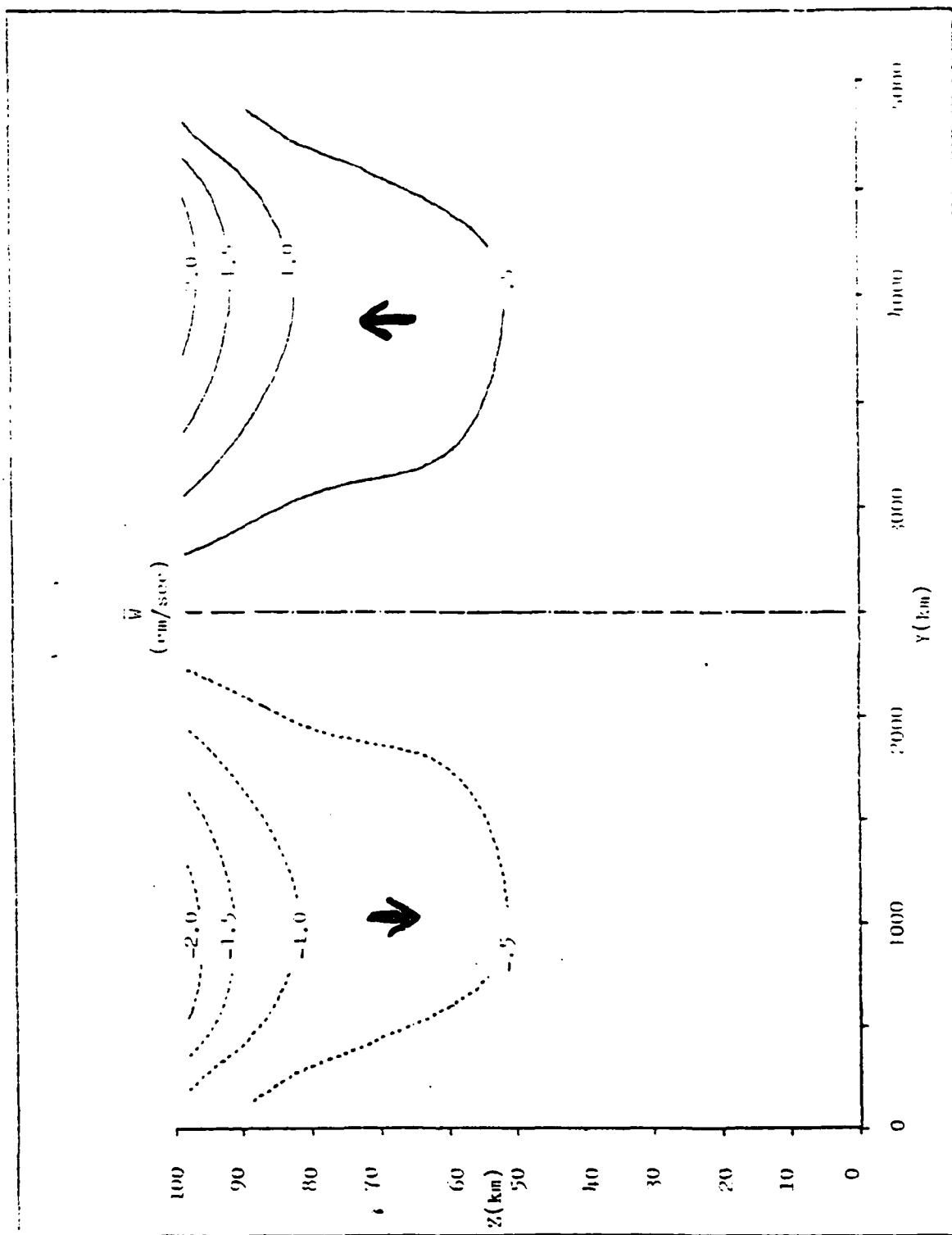


Figure 6a: \bar{W} , the Eulerian mean vertical velocity

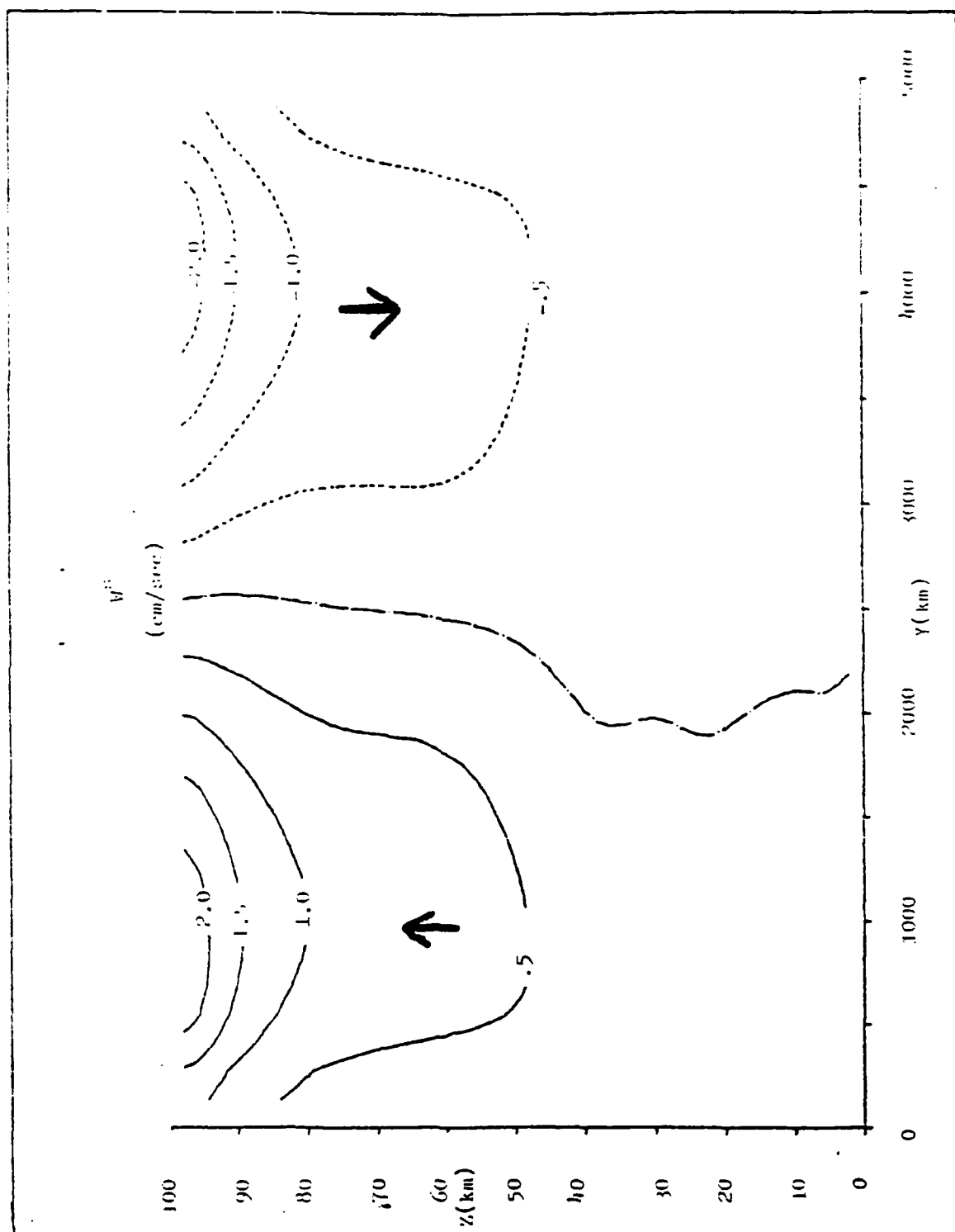


Figure 6b: W^v , the vertical Stokes velocity

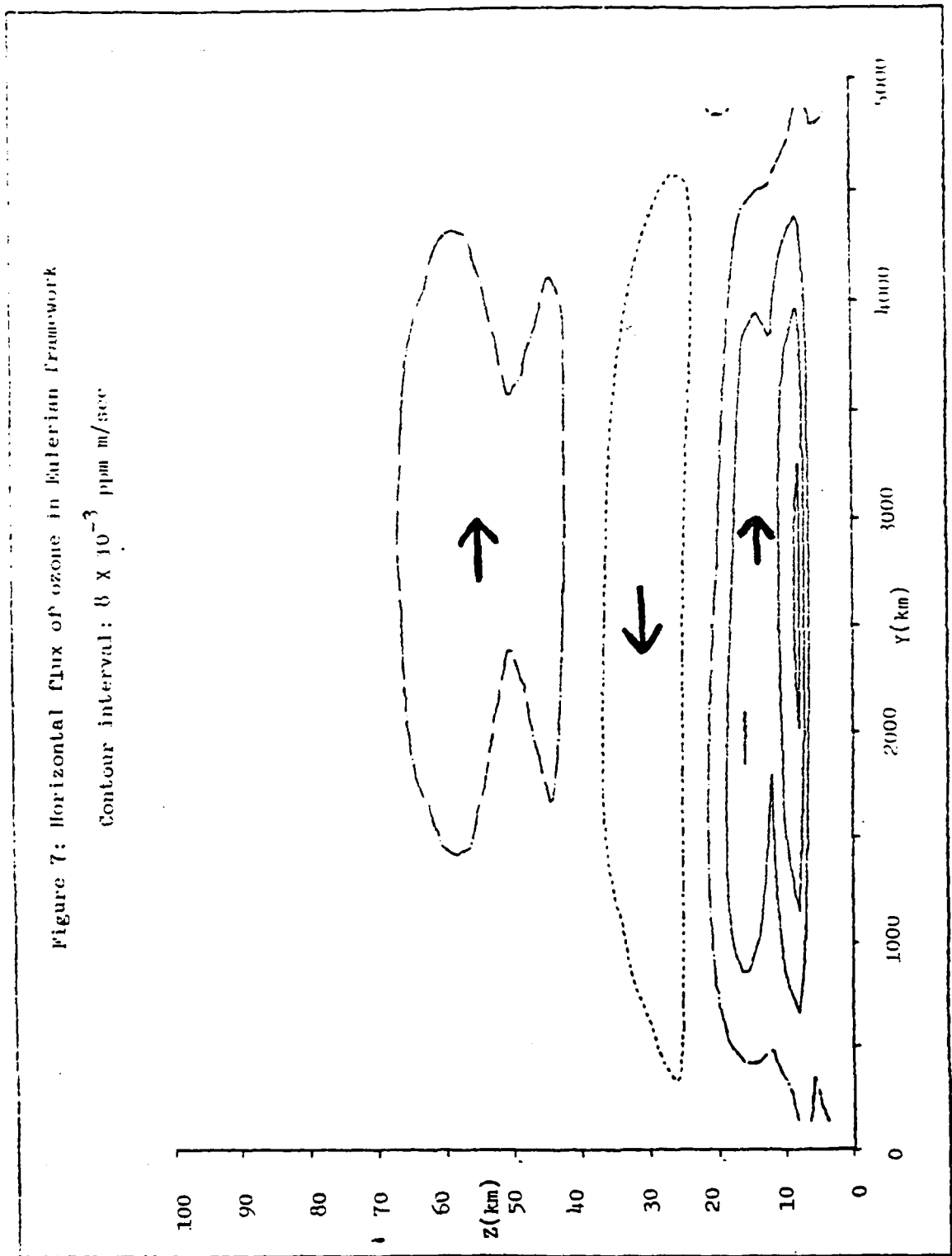
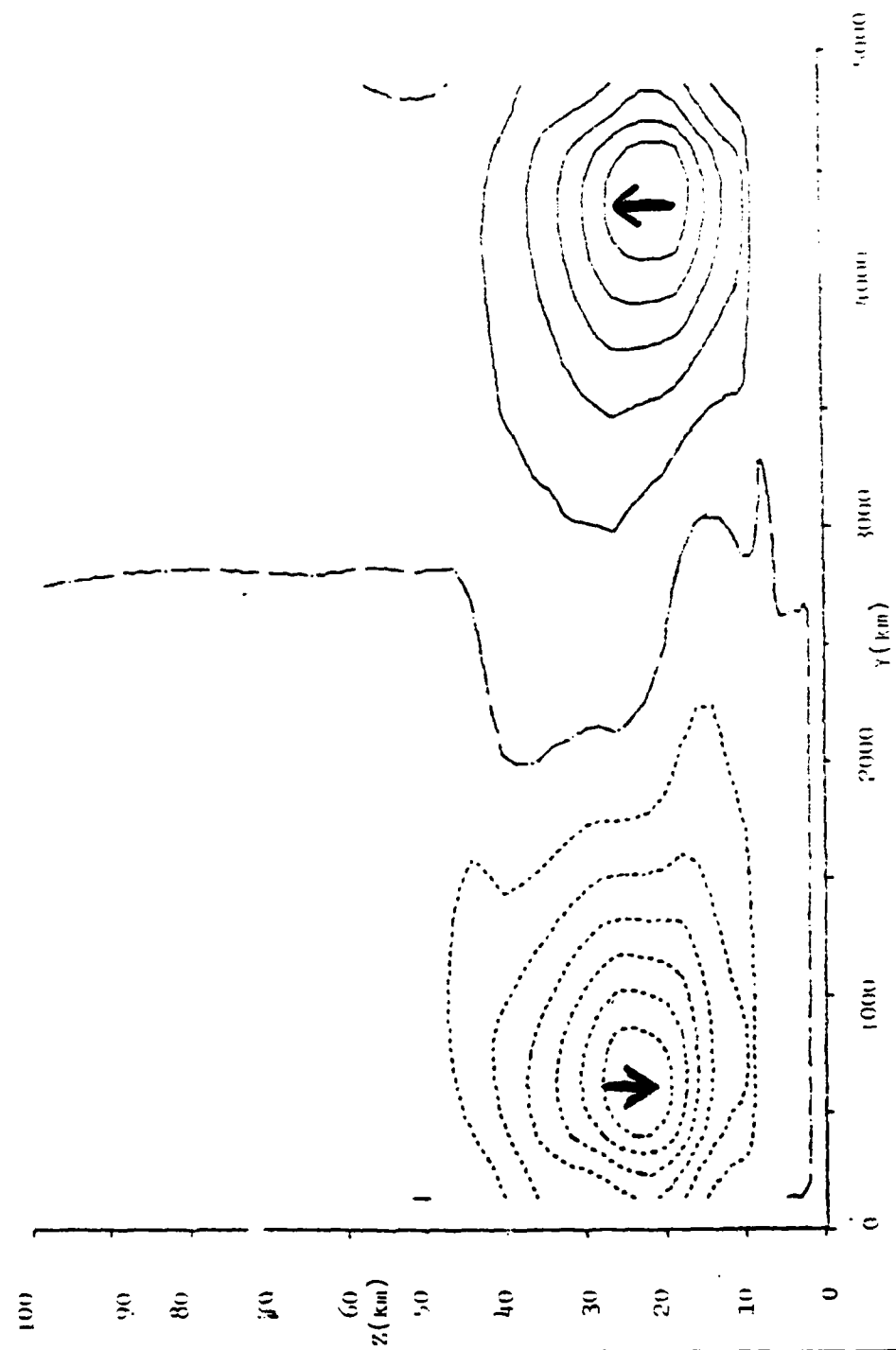
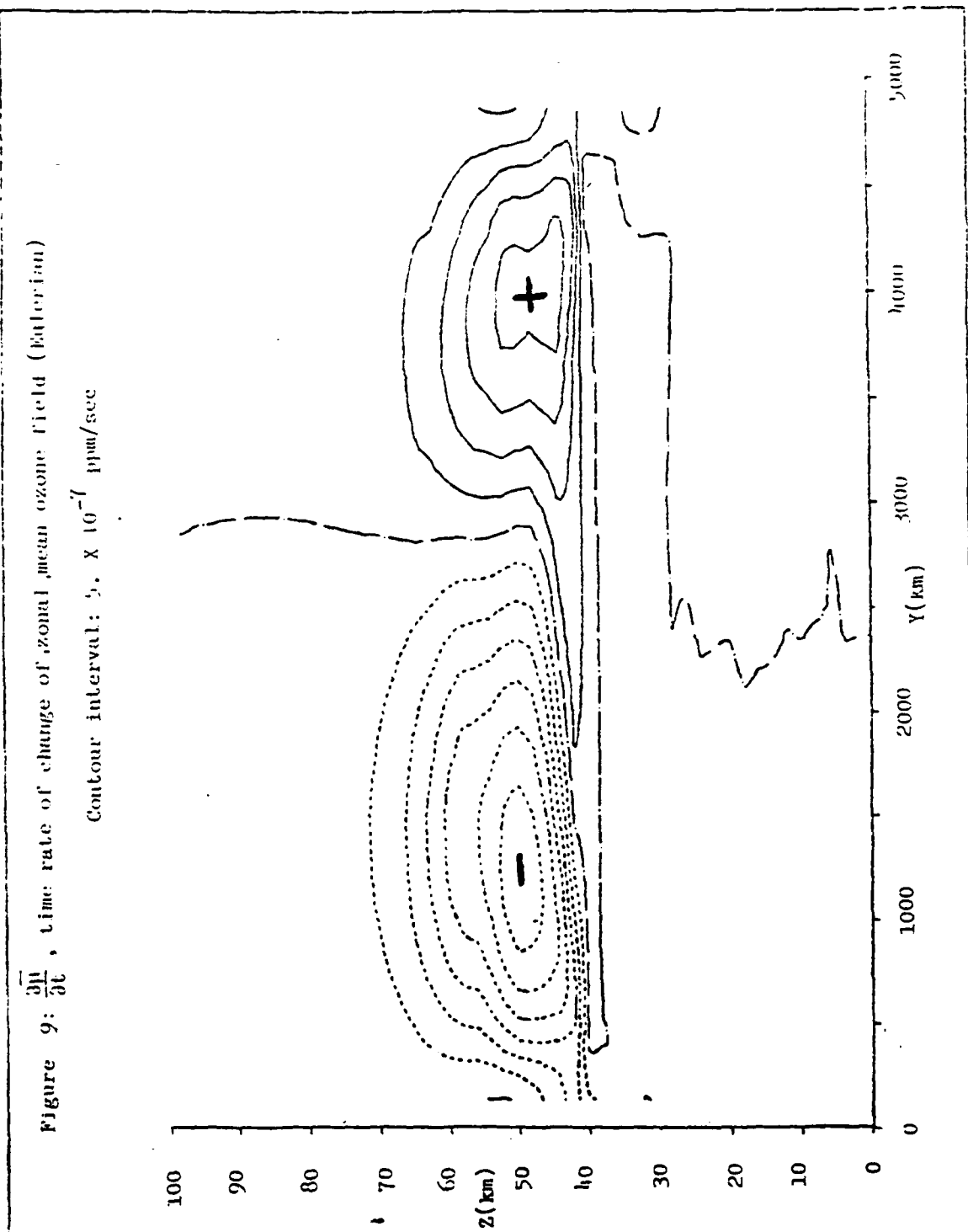
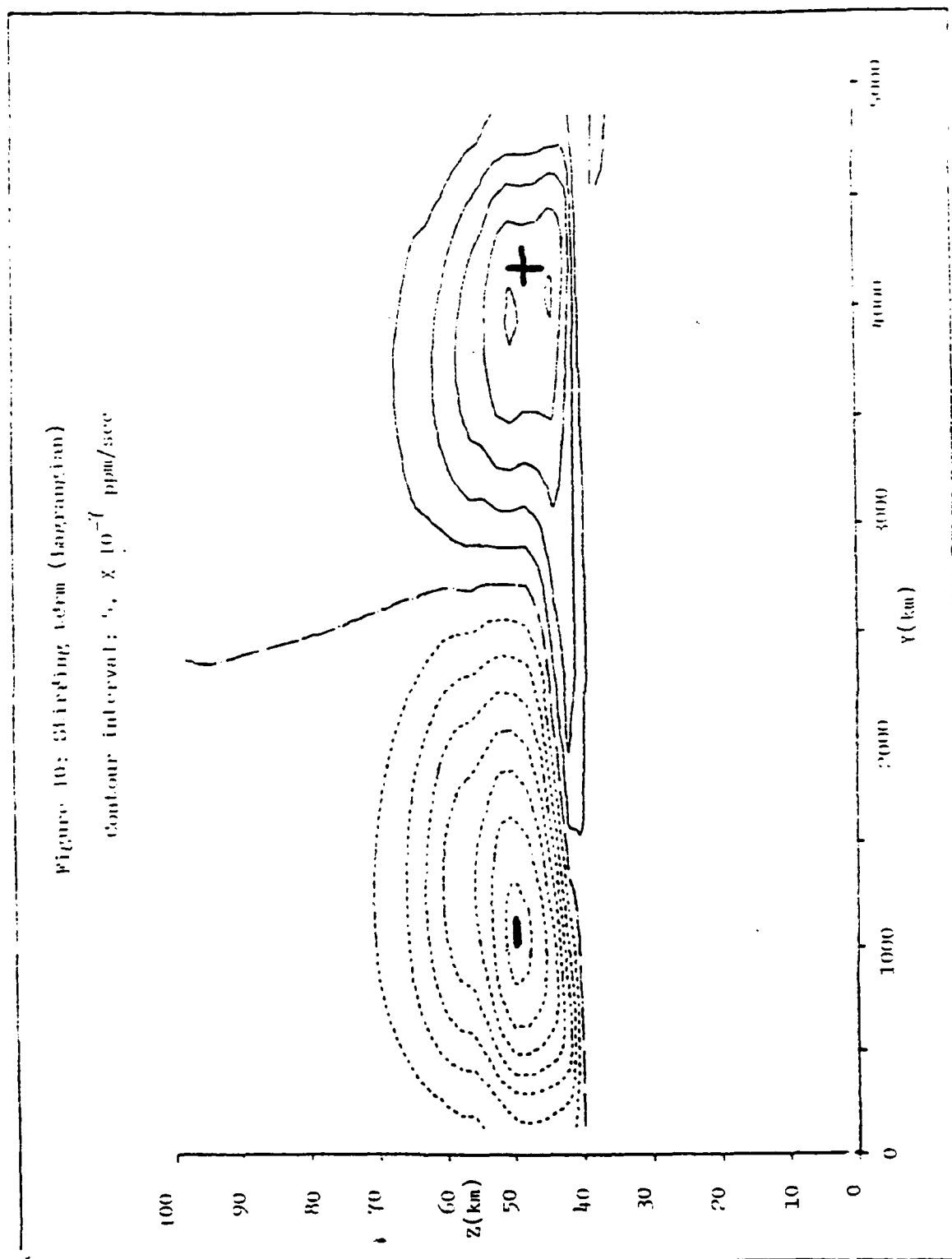


Figure 8: Vertical Flux of ozone in Eulerian Framework

Contour interval: 2×10^{-5} ppm m/sec







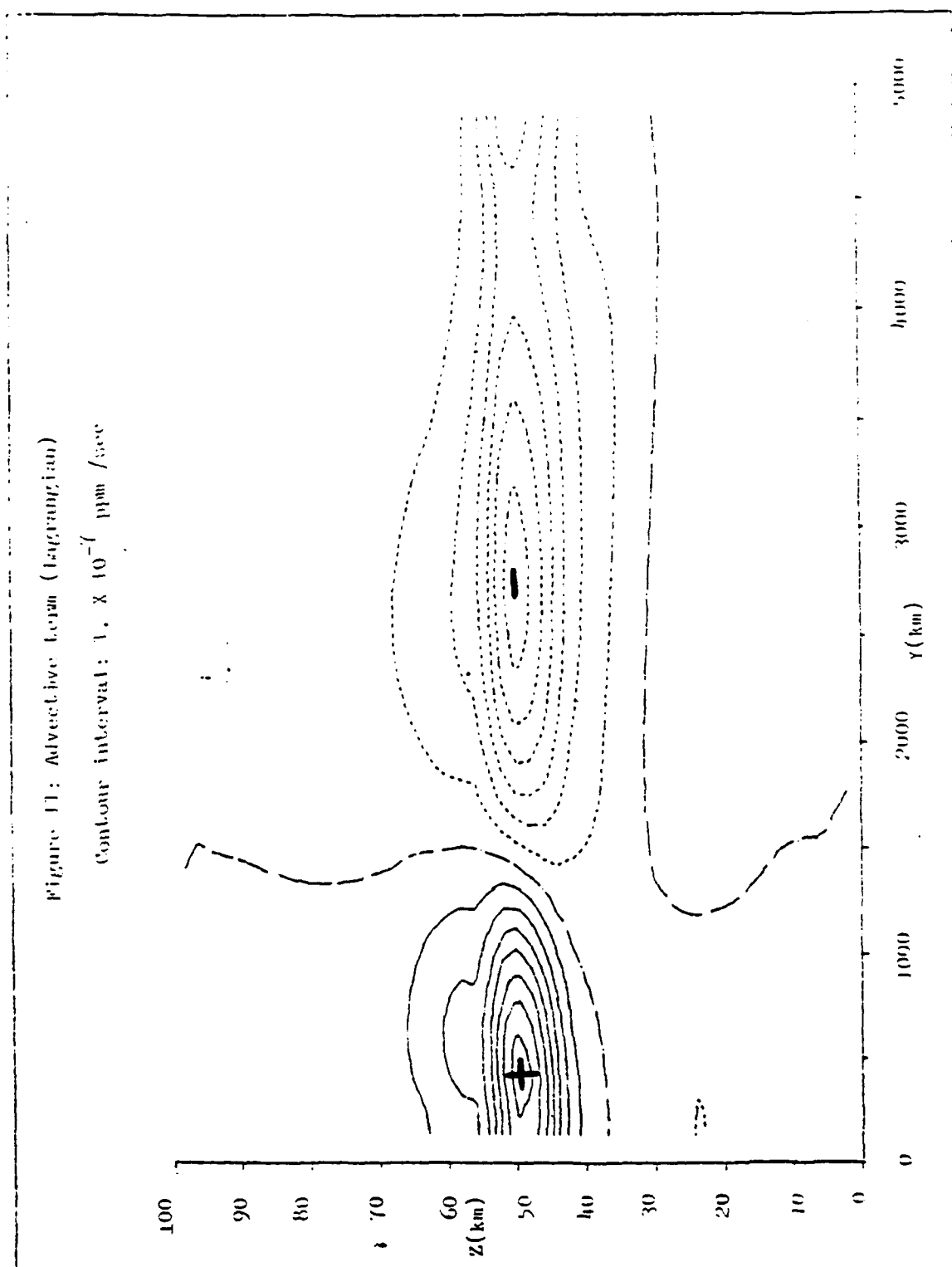
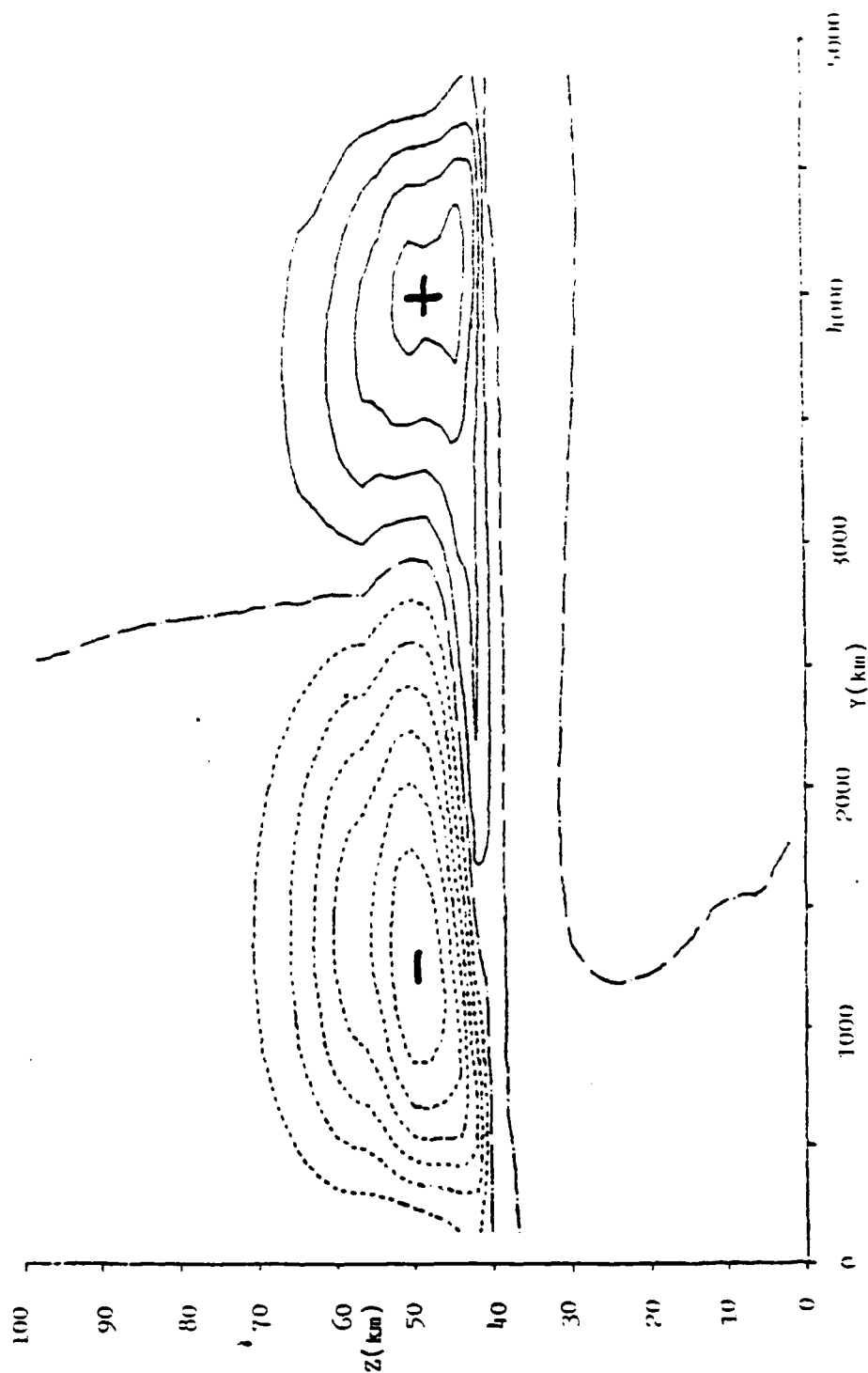


Figure 12: $\frac{\partial \bar{\mu}}{\partial t}$, time rate of change of zonal mean ozone field (lagrangian)

Contour interval: 5×10^{-7} ppm/sec



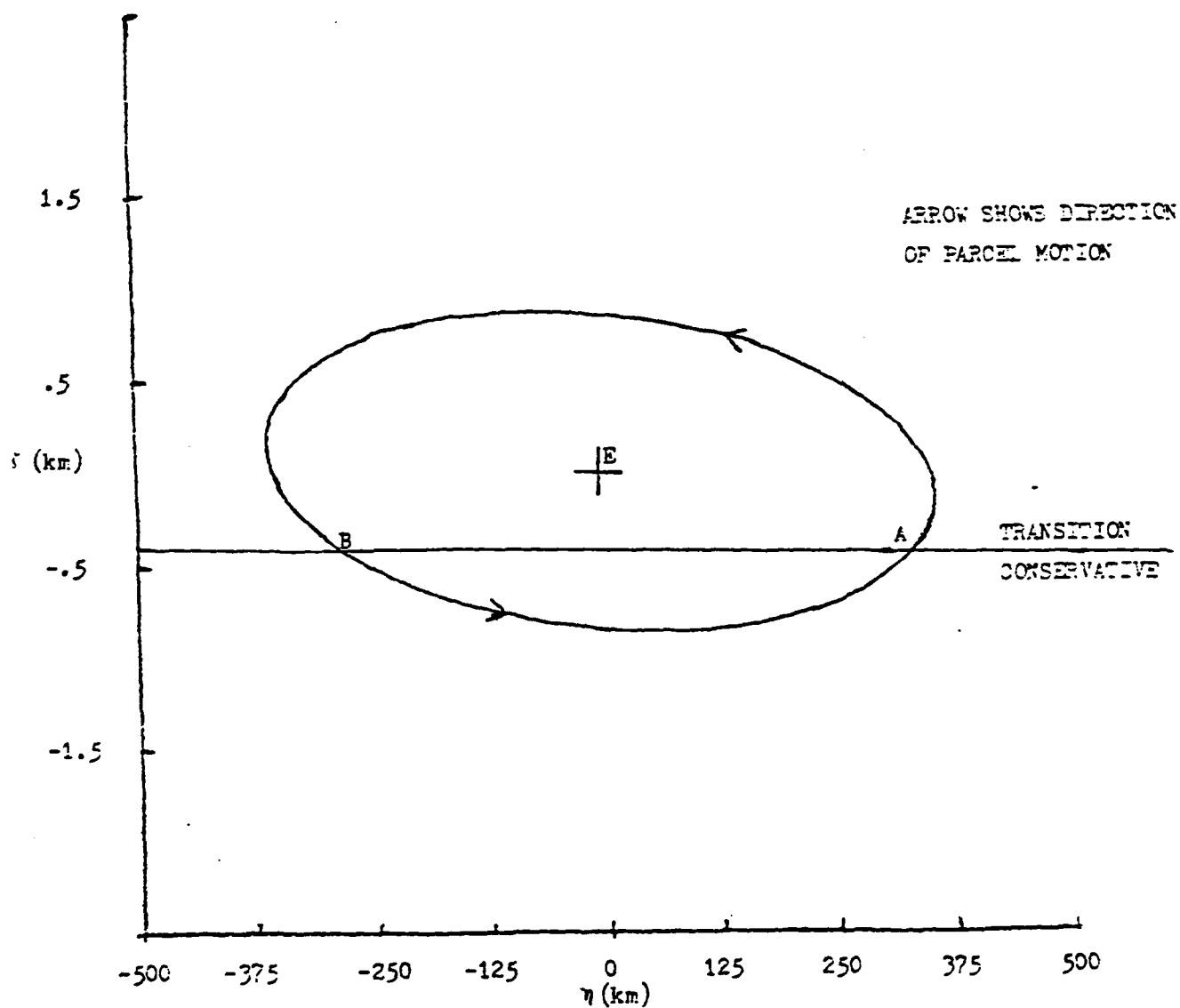


Figure 13: Latitude-height projection of
Lagrangian displacement field

Appendix Q

A NOTE ON THE LIMITS OF ROSSBY WAVE AMPLITUDES

A Note On the Limits of Rossby Wave Amplitudes

**Richard S. Lindzen
Science Applications Inc.
McLean, Va. 22102**

and

**Center for Earth and Planetary Physics,
Harvard University,
Cambridge, MA 02139**

and

**Mark R. Schoeberl
Naval Research Laboratory
Washington, D. C. 20375**

Abstract

The constraints imposed by conservation of potential vorticity and hydrodynamic stability on the amplitude of Rossby waves are investigated. Amplitudes of stationary waves in the stratosphere appear to be close to the theoretical limit.

1. Introduction

Quasi-geostrophic dynamics, as usually formulated, centers on the conservation of pseudo potential vorticity (hereafter simply potential vorticity or p. v.) on isobaric surfaces (Charney, 1973 ; Bretherton, 1966). The potential vorticity on a β - plane is given by

$$q = \hat{\nabla}^2 \psi + f \quad (1)$$

where $f = f_0 + \beta y$ and $\hat{\nabla}^2 = \frac{\partial^2}{\partial x^2} + \frac{\partial^2}{\partial y^2} + \frac{1}{\rho N^2} f_0^2 \frac{\partial \rho}{\partial z} \frac{\partial}{\partial z}$

ψ is the quasigeostrophic stream function and x , y , and z are eastward, northward and upward coordinates, respectively. z is $H \ln(p_0/p)$ where H is a scale height and p_0 is a reference pressure. ρ is the density, $\rho = \rho_0 \exp(-z/H)$; N is the buoyancy frequency assumed here to be constant.

The spherical approximation for the potential vorticity is

$$q = 2\Omega \sin \theta - \frac{1}{\cos \theta} \frac{\partial(\omega \cos^2 \theta)}{\partial \theta} + \frac{2\Omega \sin \theta R}{\rho H N^2} \frac{\partial(\rho T)}{\partial z} + \frac{1}{a \cos \theta} \frac{\partial v}{\partial \lambda} \quad (2)$$

(Matsuno, 1970). ω is $u/a \cos \theta$, the relative angular rotation rate of the earth's atmosphere; Ω is the angular rotation rate of the earth's surface and R is the dry air gas constant. T is the deviation of the zonal mean temperature from the global average temperature. The zonal coordinate is λ (longitude), and v is the meridional (northward) wind.

ω and T can both be obtained from the geopotential, ϕ , through the

hydrostatic and zonal momentum equations

$$\partial\phi/\partial z = RT/H$$

$$\omega = \frac{-1}{2\Omega a^2 \sin \theta \cos \theta} \partial\phi/\partial \theta$$

For (1), $\psi = \phi/f_0$ so equations (1) and (2) are held to be valid where the thermal wind relation holds. We will also use the standard notation that $(\bar{})$ indicates zonal average and $()'$ represents a deviation from the zonal average.

The purpose of this note is to investigate some simple constraints that conservation of p. v. imposes on internal Rossby waves. The conservation of p. v. can be written as

$$\frac{dq}{dt} = \frac{\partial q}{\partial t} + \vec{v}_g \cdot \nabla q = S \quad (3)$$

where S is the source or sink of p. v. For the β -plane \vec{v}_g is simply the geostrophic wind. However for a spherical atmosphere \vec{v}_g must include the isallobaric component, $\frac{u}{f} \frac{\partial u}{\partial x}$, for energetic consistency (Matsuno, 1970).

In this note we will examine some of the limitations that conservation of potential vorticity imposes on the dynamics of the stratosphere. We will also investigate some constraints imposed by hydrodynamic stability. The quantitative limitations these constraints put on the amplitudes of internal Rossby waves is assessed and found to be close to what is actually observed in the lower stratosphere.

Incidentally, we show that a question posed by Charney in 1960 (Charney

and Drazin, 1961) as to why the earth lacks a corona can be answered without reference to the dispersion properties or dissipation mechanisms of Rossby waves:

2. Constraints on the amplitude of internal Rossby waves for stable or unstable basic flows

The study of internal Rossby waves (and other perturbations including baroclinic instabilities) is almost always based on the linearized version of (3) solved for perturbations about a basic zonal flow $\bar{u}(y,z)$. The nature of these waves is discussed at length by Charney and Drazin (1961), Dickinson (1968), Matsuno (1970), Simmons (1974), Schoeberl et al. (1979) and others. If vertical propagation of the Rossby wave is possible then the amplitude of the geopotential height increases with altitude approximately as $e^{z/2H}$. This behavior stems from the implication in linear theory that the basic state can provide an infinite source of potential vorticity and that maximum amplitude the wave can achieve is only limited by energy conservation. For waves where the perturbation p. v. is small no difficulty arises.

For finite amplitude waves, (3) permits us to set some bounds on the amplitude of wave perturbations. These bounds are dictated by the fact that if there is no source of p. v. on a given isobaric surface then the p. v. of a wave cannot exceed the p. v. available from the basic state on the same surface. This result is obvious from the Lagrangian equation (3) and leads to several calculable conditions.

[1] The perturbation p. v., q' , at any point cannot be greater than the maximum or be smaller than the minimum p. v. found in the basic state on the isobaric surface passing through that point unless a source of p. v. is present. Since the development of a wave on an isobaric surface according to (3) can be viewed simply as the rearrangement of the isopleths of p. v. on that surface, this condition follows directly.

A special case of [1] arises when the basic state p.v., \bar{q} , is everywhere positive. This is generally the case; indeed if \bar{q} changes sign, the basic state is inertially unstable. If $q > 0$ everywhere on the isobaric surface then the amplitude of the perturbation at any point, $|q'|$, cannot exceed \bar{q} at the same point. If it did, the total p.v. at that point would turn negative during the wave's negative phase. It is this special case that we will employ in Section 3.

[2] The integrated perturbation enstrophy (q'^2) cannot exceed the integrated enstrophy of the basic state on an isobaric surface unless a source of p. v. is present. This condition follows directly from (3) after multiplying by q and integrating over the isobaric surface. Upper limit arguments for Rossby waves in the stratosphere using this condition are given by Schoeberl (1982) and will not be repeated here.

There is a third condition, which is intuitive rather than rigorous, and is not directly based on Eq. (3). Namely: [3] The meridional gradient of q' , q'_y should not exceed \bar{q}_y .

Several rationales can be offered for [3]. First, the restoring force for quasigeostrophic waves arises from the meridional variation of \bar{q} , i. e. \bar{q}_y . Intuitively, one expects that the existence of a wave would be compromised when the wave field is large enough to eliminate this restoring force. Second, if $|q'_y| > |\bar{q}_y|$, then there will be regions where q_y changes sign, and this is generally associated with either baroclinic or barotropic instability (Charney, 1973; Lindzen and Tung, 1979). Our experience with such instabilities on a basic state formed by a wave itself is at present limited; however, the work of Orr (1907) suggests that unstable growth can occur even when there are no unstable modes. Presumably such unstable growth will limit the

AD-A111 638

SCIENCE APPLICATIONS INC MCLEAN VA
GEOPHYSICAL PLASMAS AND ATMOSPHERIC MODELING.(U)

F/G 4/1

JAN 82 E HYMAN, J APRUZESE, S BRECHT, W CHAO

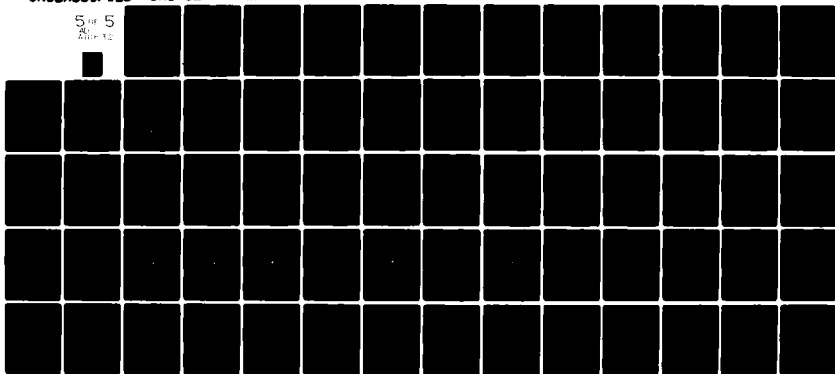
N00014-81-C-2038

UNCLASSIFIED

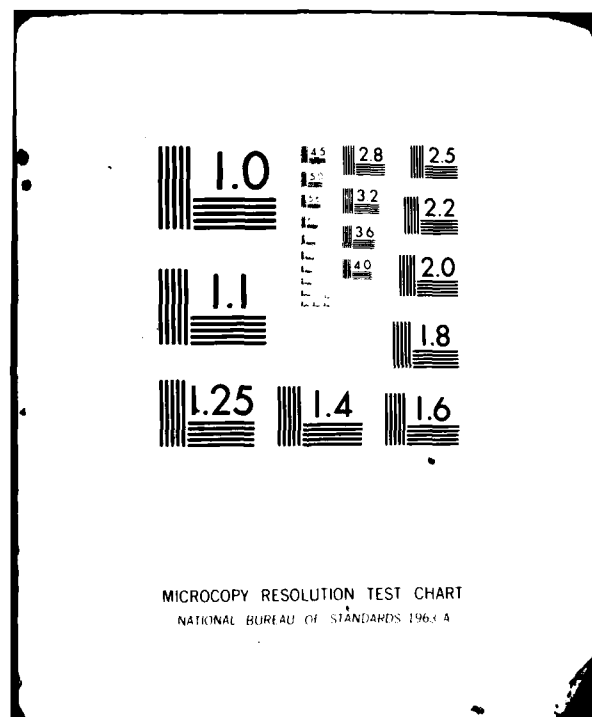
SAI-82-676-WA

NL

5 of 5
AD-A111 638



END
DATE
FILMED
6-82
DTIC



amplitude, $|\hat{q}_y|$.

While the condition [3] is not yet rigorously justified, it forms the strictest constraint on the wave amplitude. The reason for this is that the meridional scale of variation for \bar{q} is usually "a" (the earth's radius) while the meridional scale of variation of q' is much shorter as we shall show in Section 3. Thus the satisfaction of condition [3] generally guarantees the satisfaction of [1] and [2].

3. Quantitative Estimates for the Winter Stratosphere

The purpose of this section is to assess the amplitudes of planetary waves permitted in the stratosphere using conditions [1] and [3] discussed in the previous section. We have evaluated \bar{q} and \bar{q}_y for the zonal wind and temperature profiles given in Lindzen and Hong (1974). These profiles which are shown in Figures 1 and 2 suggest that $\bar{q} = f = 2\Omega \sin \theta$ and $\bar{q}_y = \beta = (2\Omega \cos \theta)/a$ in the extratropical stratosphere. Figure 3 shows the amplitude and phase of the climatological planetary zonal harmonic one ($s=1$) from van Loon et al. (1973). Although $s=1$ already suggests a large zonal scale, Figure 3 shows that the meridional scales are shorter, $O(1600 \text{ km})$, and dominate the zonal variations in the height field. The contributions of the vertical variations to (1) also seem relatively small in the lower stratosphere.

For present illustrative purposes a rough evaluation of conditions [1] and [3] should suffice. Thus, for $q' = \bar{v}^2 \psi'$ we will take

$$q' = \frac{g Z'}{f L^2} \quad (4)$$

where $g = 9.8 \text{ ms}^{-2}$, Z' = the amplitude of the height perturbation, L = the characteristic meridional scale (1600 km). Similarly for q'_y we will take

$$q'_y = \frac{g Z'}{f L^2} \quad (5)$$

We may now invoke condition [1] using the criterion that the stratosphere is inertially stable. We require that

$$Z' < f^2 L^2 / g = \frac{4 \Omega^2 L^2}{g} \sin^2 \theta = 5525 \text{ m} \sin^2 \theta \quad (6)$$

Condition [3] becomes

$$Z' \leq f \beta L^3 / g = \frac{4 \Omega^2 L^3 \sin \theta \cos \theta}{g a} = 691 \text{ m} \sin 2\theta \quad (7)$$

Clearly, the results in Fig. 3 satisfy, (6) by a large amount; however, (7) is marginally violated. Note in Fig. 4 that a maximum Z' of 600 m is found at $\theta = 65^\circ$ sin where $2\theta = .766$ and (7) implies

$$Z' \leq 529 \text{ m}$$

The simplicity of our procedure (as well as observational uncertainties) preclude taking such differences seriously. However, these results here and enstrophy arguments used by Schoeberl (1982) suggest that the maximum amplitudes shown in Fig. 3 may be as large as is possible. Thus, we may expect that $\exp(z/2H)$ growth will cease at about 30 - 40 km altitude. Above this height we may anticipate that nonlinearity and/or instability will play major roles unless damping reduces magnitudes to values satisfying condition [3].

4. Remark on the impossibility of a terrestrial corona forced by dissipating Rossby waves

The motivation of the seminal paper by Charney and Drazin (1961) on the vertical propagation of stationary Rossby waves was to explain why the earth's atmosphere lacks a corona. Since it was known that Rossby waves could propagate vertically they would grow in amplitude as $e^{z/(2H)}$ so as to conserve energy density. Thus waves which would be thermodynamically inconsequential in the upper troposphere could become overwhelming in the thermosphere where the enhanced molecular viscosity and thermal conductivity of the thermosphere would lead to the deposition of Rossby wave energy.

Charney and Drazin (1961) used linear theory to examine the dispersive properties of these waves including those properties which would prevent vertical propagation. Their study has been amplified by subsequent authors and the results have explained many of the salient features of stationary waves observed in the stratosphere. Nevertheless, numerical calculations using linear models generally show that wave number one could penetrate to the thermosphere during winter (Schoeberl et al., 1979).

Ironically, the answer to the original question posed by Charney and Drazin (1961) can be provided without reference to the propagation properties of Rossby waves. Our present results and those of Schoeberl (1982) establish a maximum amplitude for Rossby waves which appears to be reached in the lower stratosphere. Above that level there should be no further amplitude growth. Hence, instead of being conserved, the wave energy density will decrease proportional to the mean density. If the wave energy density is thermodynamically unimportant in the lower

stratosphere (as it may well be) then it will be no more important in the thermosphere.

6. Concluding remarks

This note describes some simple constraints on the amplitudes of Rossby waves. The constraints may seem inconsistent with the fact that Rossby waves are, under some conditions, exact nonlinear solutions regardless of amplitude. The point, however, is that Rossby waves of arbitrary amplitude cannot be set up without an external source of vorticity. Similarly, our constraint on q_y is also consistent insofar as an exact nonlinear solution can still be unstable.

The tests presented here provide a useful check on the validity of linear calculations and, perhaps, on observational analyses as well.

Acknowledgments

This work was partially supported by the National Science Foundation through grant # ATM 7823330 , by the National Aeronautics and Space Administration through grants NGL 22007228, and by the Office of Naval Research.

References

- Bretherton, F.P., 1966: Critical layer instability in baroclinic flows, Quart. J. P. Met. Soc., 92, 325-334.
- Charney, J. G. and P. G. Drazin 1961: Propagation of planetary-scale waves from the lower atmosphere into the upper atmosphere, J. Geophys. Res., 66, 83-109.
- Charney, J.G., 1973: Planetary fluid of dynamics. Dynamic Meteorology, P. Morel, Ed., D. Reidel, 97-351.
- Dickinson, R.E., 1969: Vertical propagation of planetary Rossby waves through an atmosphere with Newtonian cooling, J. Geophys. Res., 74, 929-938
- Lindzen, R.S., and S. Hong, 1974: Effects of mean winds and horizontal temperature gradients on solar and lunar semi-diurnal tides in the atmosphere, J. Atmos. Sci., 32, 1421-1446.
- Lindzen, R.S., and K.K. Tung, 1978: Wave over reflection and shear instability, J. Atmos. Sci., 35, 1626-1632.
- Matsuno, T., 1970: Vertical propagation of stationary planetary waves in the winter northern hemisphere, J. Atmos. Sci., 27, 871-883.
- Orr, W. McF., 1907: The stability or instability of the steady motions of a perfect liquid and of a viscous liquid. Part I. A perfect liquid. Proc. Roy. Irish Acad., A28, pp 9-138.
- Schoeberl, M.R., M.A. Celler, and S.R. Avery, 1979: The structure of stationary planetary waves in winter: A correction, J. Atmos. Sci., 36, 365-369.
- Schoeberl, M. R., 1982: Wave-mean flow statistics. Submitted to J. Atmos. Sci.

Simmons, A.J., 1974: Planetary scale disturbances in the polar winter stratosphere, Quart. J. R. Met. Soc., 100, 76 - 108.

Van Loon, H., R.L. Jenne, K. Labitzke, 1973: Zonal harmonic standing waves, J. Geophys. Res., 78, 4463 - 4471.

Figure Legends

Figure 1 The zonally averaged potential vorticity computed from the wind profiles given by Lindzen and Hong (1974). Units: 10^{-4} sec^{-1} .

Figure 2 The meridional gradient of the potential vorticity, $\partial \bar{q} / \partial \theta$, , for the potential vorticity shown in Figure 1. Units: 10^{-4} sec^{-1} .

Figure 3 The climatological amplitude and phase of planetary wave one (zonal harmonic one) in January from van Loon et al. (1973).

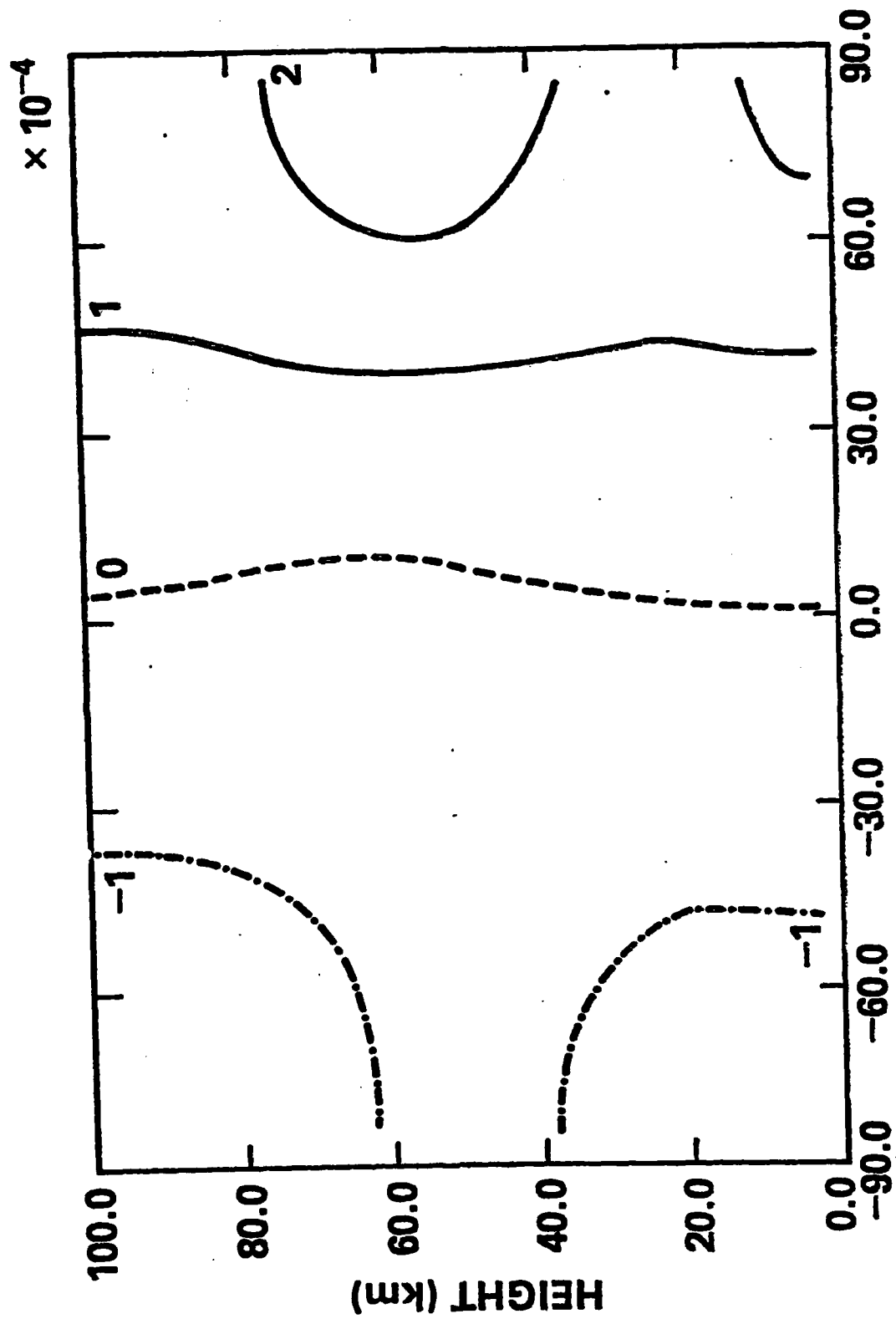


Figure 1

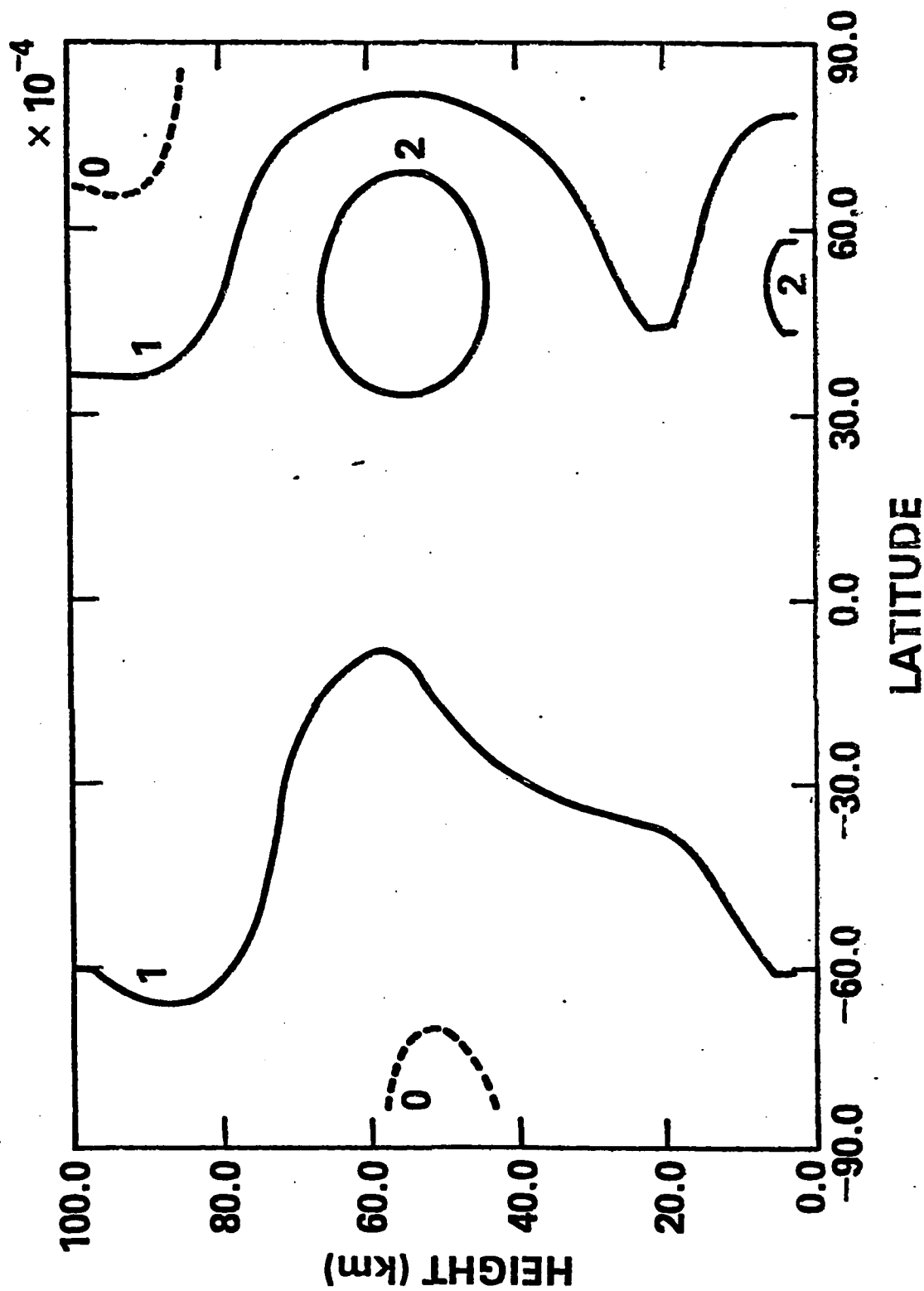


Figure 2

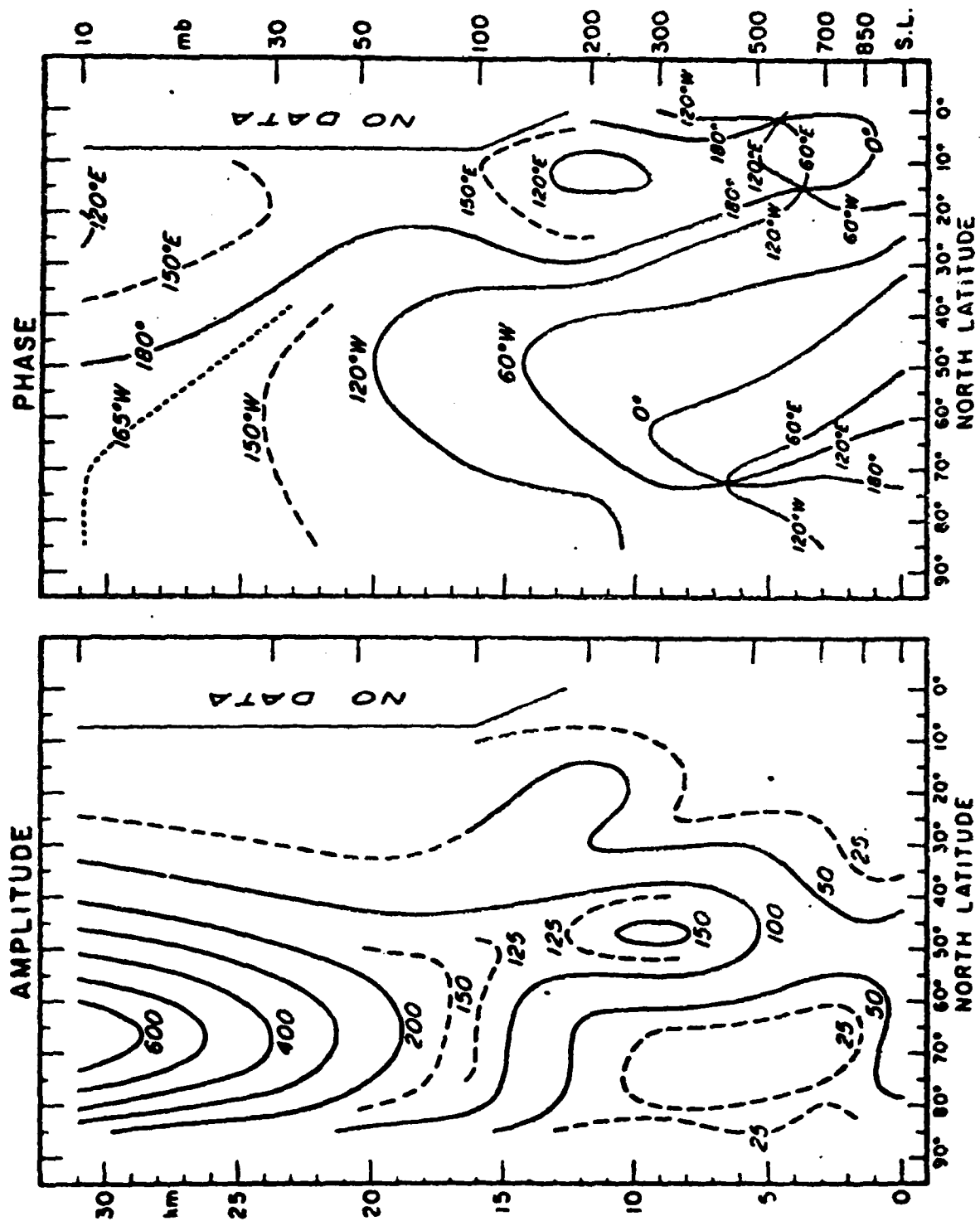


Figure 3

Appendix R

FORMULATION OF A MODAL-SPLIT-EXPLICIT
TIME INTEGRATION METHOD FOR USE IN
THE UCLA ATMOSPHERIC GENERAL
CIRCULATION MODEL

**Formulation of a Modal-Split-Explicit
Time Integration Method for use in
the UCLA Atmospheric General
Circulation Model**

W. C. CHAO

*Science Applications, Inc.
McLean, Virginia 22102*

R. V. MADALA

*Geophysical and Plasma Dynamics Branch
Plasma Physics Division*

July 24, 1981

This work was sponsored by the Naval Environmental Prediction Research Facility,
Program Element 62759N, Project WR59-551, "Atmospheric Environmental Support."



NAVAL RESEARCH LABORATORY
Washington, D.C.

Approved for public release; distribution unlimited.

SECURITY CLASSIFICATION OF THIS PAGE (When Data Entered)

REPORT DOCUMENTATION PAGE		READ INSTRUCTIONS BEFORE COMPLETING FORM
1. REPORT NUMBER NRL Memorandum Report 4572	2. GOVT ACCESSION NO.	3. RECIPIENT'S CATALOG NUMBER
4. TITLE (and Subtitle) FORMULATION OF A MODAL-SPLIT-EXPLICIT TIME INTEGRATION METHOD FOR USE IN THE UCLA ATMOSPHERIC GENERAL CIRCULATION MODEL		5. TYPE OF REPORT & PERIOD COVERED Interim report on a continuing NRL problem.
		6. PERFORMING ORG. REPORT NUMBER
7. AUTHOR(s) W.C. Chao* and R.V. Madala		8. CONTRACT OR GRANT NUMBER(s)
9. PERFORMING ORGANIZATION NAME AND ADDRESS Naval Research Laboratory Washington, D.C. 20375		10. PROGRAM ELEMENT, PROJECT, TASK AREA & WORK UNIT NUMBERS 62759N; WR59-551; 47-0885-01
11. CONTROLLING OFFICE NAME AND ADDRESS Naval Environmental Prediction Research Facility Monterey, California 93940		12. REPORT DATE July 24, 1981
		13. NUMBER OF PAGES 49
14. MONITORING AGENCY NAME & ADDRESS (if different from Controlling Office)		15. SECURITY CLASS. (of this report) UNCLASSIFIED
		15a. DECLASSIFICATION/DOWNGRADING SCHEDULE
16. DISTRIBUTION STATEMENT (of this Report) Approved for public release; distribution unlimited.		
17. DISTRIBUTION STATEMENT (of the abstract entered in Block 20, if different from Report)		
18. SUPPLEMENTARY NOTES *Current address: Science Applications, Inc., McLean, Virginia 22102. This work was sponsored by the Naval Environmental Prediction Research Facility, Program Element 62759N, Project WR59-551, "Atmospheric Environmental Support."		
19. KEY WORDS (Continue on reverse side if necessary and identify by block number) General circulation model Numerical methods Weather prediction		
20. ABSTRACT (Continue on reverse side if necessary and identify by block number) With appropriate modifications, a recently proposed modal-split-explicit time integration scheme (MSES) is incorporated into the UCLA atmospheric general circulation model. In this scheme, the terms in the governing equations that generate the linear gravity waves are split into different vertical modes. Each mode is integrated with an optimal time step, and at periodic intervals these modes are recombined. The other terms are integrated with a time step dictated by the CFL condition for low frequency waves. This large time step requires a special modification of the advective terms in the polar region to maintain stability. Seventy-two hour test runs show that MSES is a viable, efficient, and accurate scheme for global weather prediction purposes.		

DD FORM 1 JAN 73 1473

EDITION OF 1 NOV 65 IS OBSOLETE
S/N 0102-014-6601

SECURITY CLASSIFICATION OF THIS PAGE (When Data Entered)

CONTENTS

1.0 INTRODUCTION	1
2.0 FORMULATION	3
2.1 Basic Equations	3
2.2 The Modal-Split-Explicit Method	6
2.3 Modification of the Advective Terms Near the Poles	13
2.4 The Time Differencing Method	15
2.5 Addition of the Pressure Averaging Method	15
3.0 RESULTS AND DISCUSSION	16
3.1 Stability	16
3.2 Efficiency	17
3.3 Accuracy	17
ACKNOWLEDGMENTS	20
APPENDIX	38
REFERENCES	43

FORMULATION OF A MODAL-SPLIT-EXPLICIT TIME INTEGRATION METHOD
FOR USE IN THE UCLA ATMOSPHERIC GENERAL CIRCULATION MODEL

1.0 INTRODUCTION

In the explicit time integration of primitive equations, the time step is limited by the Courant-Friedrichs-Lewy (CFL) condition (Courant et al., 1928), based on the fastest phase speed of waves allowed in the model, which is the speed of the external gravity wave; thus the integration is rather slow. Since the meteorologically significant waves have speeds much slower than that of the external gravity wave and possess practically all of the energy of the atmospheric motion, the use of the explicit scheme is rather uneconomical. Two major approaches have been taken to circumvent this difficulty. First, since the gravity waves are quasi-linear, the portion of the primitive equations that govern the linear gravity waves can be integrated implicitly, and the rest of the equations can be integrated explicitly with a time step dictated by the CFL condition for slow moving waves. Known as the semi-implicit method, it has been used both in grid point models (Kwizak and Robert, 1971) and in spectral models (Robert, 1969) with significant savings in computing time and acceptable accuracy (Robert, et al., 1972). However, since the speed of the gravity waves is reduced in the implicit integration, its accuracy is questionable in the regions of gravity waves excitation (Messinger and Arakawa, 1977). The semi-implicit method can be modified; the terms governing the linear gravity waves can be separated into different vertical modes. Only modes with phase speeds greater than those of the meteorological waves--usually the external gravity wave and the

Manuscript submitted May 26, 1981.

first two or three internal gravity waves--need to be integrated implicitly (Burridge, 1978).

The second approach to expedite the integration involves separating the terms related to the gravity waves from the rest of the equations. One group of terms is integrated first with an optimal time step, either explicitly or implicitly, and the result of this step is used at the beginning of the marching for the other group, employing a different optimal time step. This is called the splitting method (Marchuk, 1974; Gadd, 1978). When explicit schemes are used, the splitting method does not have the adverse effect of retarding the gravity waves. However, since the different dynamic processes are calculated one at a time, the truncation errors of all steps are multiplied rather than added.

In a logical progression Madala (1980)* proposed a modal-split-explicit scheme (MSES), which combines the advantages of the aforementioned methods, yet avoids their shortcomings. In this method terms in the primitive equations governing linear gravity waves are decomposed into different vertical modes. Modes with phase speeds greater than the meteorological waves are integrated explicitly, with time steps allowed by the respective CFL conditions and are recombined at periodic intervals. The other modes and the rest of the equations are integrated explicitly with a time step determined by the speed of the slow moving waves, which is usually five times as large as the time step allowed for the fastest moving waves. This constitutes great savings in computing time. In addition since all waves

*Madala (1981) used the name "split-explicit;" the first author added the word "modal" to distinguish it from the split-explicit schemes used by other authors.

are integrated explicitly, no adverse effect on gravity wave speed occurs. Moreover, since all dynamic terms are integrated (or marched) simultaneously, the multiplicative truncation error characteristic of the splitting methods is avoided.

Thus far, MSES has been successfully applied to a tropical cyclone model (Madala, 1981). The speed of integration was increased by a factor of three over that using the explicit method; this factor, however, is an increasing function of horizontal resolution. The results also showed good accuracy. The present paper presents a further investigation of MSES in order to ascertain whether it is also a viable method in a global model, in which more complexities exist, such as high terrain and the diminishing zonal grid size toward the poles. The model chosen for this effort is the 1977 version of the UCLA model (Arakawa and Lamb, 1977; hereafter referred to as AL; Arakawa and Mintz, 1974).

This investigation shows that modifications are necessary (Section 2.2); that additional features should be added (Section 2.3); and that the pressure averaging technique can be used to improve the efficiency of MSES (Section 2.5). In addition, the results of a 72-hour test run showed that MSES is viable, efficient, and accurate for global weather prediction purposes.

2.0 FORMULATION

2.1 Basic Equations

Since MSES treats the terms governing linear gravity waves in the equations of motion differently from the rest, these terms must first be identified. The vertical coordinates

in the UCLA GCM is

$$\sigma = \frac{P - P_T}{\pi}, \quad (1)$$

where P is pressure; P_T is a constant pressure at the model top (currently $P_T = 50$ mb); $\pi = P_s - P_T$; and P_s is the pressure at the surface. Because there is only one layer in the stratosphere, the original definition of σ in the stratosphere (AL, p. 207) is not used for reasons of simplicity. All notations follow those of AL unless otherwise indicated.

The zonal momentum equation in the flux form is

$$\begin{aligned} \frac{\partial}{\partial t} (\pi u) + \frac{\partial}{\partial x} (\pi u^2) + \frac{1}{\cos^2 \phi} \frac{\partial}{\partial y} (\pi u v \cos^2 \phi) \\ + \frac{\partial}{\partial \sigma} (\pi u \dot{\sigma}) - \pi f v = -\pi \left(\frac{\partial \phi}{\partial x} \right)_{\sigma} \\ - (\pi \sigma \alpha) \left(\frac{\partial \pi}{\partial x} \right)_{\sigma} + \pi F_x, \end{aligned} \quad (2)$$

where u is zonal velocity, v , meridional velocity; ϕ , geopotential; α , specific volume; f , Coriolis parameter; ϕ , latitude, λ , longitude; a , earth's radius; F_x , zonal frictional force; $\dot{\sigma} = d\sigma/dt$; $\partial x = a \cos \phi \partial \lambda$; and $\partial y = a \partial \phi$.

Since $\phi = \phi_s + \phi_a$, where ϕ_s is the surface geopotential and ϕ_a is the ϕ measured from surface, the pressure gradient force terms in Eq. (2) can be written as

$$-\frac{\partial}{\partial x} (\pi \phi_a) + \left[\overline{(\phi_a - \sigma \pi \alpha)} + (\phi_a - \sigma \pi \alpha)' \right] \frac{\partial}{\partial x} \pi - \pi \frac{\partial}{\partial x} \phi_s,$$

where the double bar denotes global average on a σ -surface, and the prime denotes the deviation from it. If $\bar{\phi} = \pi\phi_a - \overline{(\phi_a - \sigma\pi\alpha)}\pi$, Eq. (2) becomes

$$\frac{\partial}{\partial t} (\pi u) + \frac{\partial}{\partial x} \overline{\overline{\phi}} = R_u, \quad (3)$$

where R_u denotes remaining terms, which vary slowly in time compared to the terms on the left side of Equation (3). The additional operator, denoted by the dash bar, suppresses the amplitude of the short waves to overcome the problem associated with the diminishing zonal grid size. This operator is fully described in AL, p. 248, and should be applied to the zonal pressure gradient term and to the zonal mass flux term. In a similar manner, the equation governing meridional momentum can be written as:

$$\frac{\partial}{\partial t} (\pi v) + \frac{\partial}{\partial y} \overline{\overline{\phi}} = R_v. \quad (4)$$

The surface pressure tendency equation is,

$$\frac{\partial}{\partial t} \pi + \langle N_2 \rangle^T \langle D \rangle = 0, \quad (5)$$

where $D \equiv \nabla \cdot (\pi v) = \frac{\partial}{\partial x} (\overline{\overline{\pi u}}) + \frac{1}{\cos \phi} \frac{\partial}{\partial y} (\pi v \cos \phi)$ (AL, Eq. (166)). The row vector $\langle N_2 \rangle^T$ is given in the appendix.

The thermodynamic equation (AL, Eq. (209)) is

$$\begin{aligned} \frac{\partial}{\partial t} (\pi T_k) + \nabla \cdot (\pi v_k T_k) + \frac{1}{\Delta \sigma_k} \left[(\pi \dot{\sigma})_{k+\frac{1}{2}} p_k \hat{\theta}_{k+\frac{1}{2}} \right. \\ \left. - (\pi \dot{\sigma})_{k-\frac{1}{2}} p_k \hat{\theta}_{k-\frac{1}{2}} \right] = \frac{1}{C_p} (\sigma \pi \alpha)_k \left(\frac{\partial}{\partial t} + v_k \cdot \nabla \right) \pi + \frac{\pi}{C_p} Q_k, \end{aligned} \quad (6)$$

where the subscripts are level indices; θ , potential temperature; $p = T/\theta = (P/1000)^K$; and C_p , specific heat at constant pressure. Integration of the continuity equation gives $\langle \pi \dot{\sigma} \rangle = [N_1] \langle D \rangle$. Thus, Eq. (6) can be written as:

$$\frac{\partial}{\partial t} (\pi T_k) + \overline{T_k} D_k + \frac{1}{C_p} (\sigma \pi \alpha)_k \langle N_2 \rangle^T \langle D \rangle + ([M_4] \langle D \rangle)_k = \langle R_{T_k} \rangle ,$$

or as:

$$\frac{\partial}{\partial t} (\pi \langle T \rangle) + [M_2] \langle D \rangle = \langle R_T \rangle , \quad (7)$$

where $[M_4] \langle D \rangle$ denotes the linear part of the last two terms on the left side of Equation (6), and R_T denotes all the remaining terms. The matrices $[M_2]$ and $[M_4]$ are given in the appendix. Instead of π , $\bar{\pi}$ is used in computing $[M_4]$.

Equations (3), (4), (5), (6) and the hydrostatic equation form the complete set of governing equations in the model. When $R_u = R_v = R_T = 0$, these equations govern the linear gravity waves in an atmosphere with no basic motion.

2.2 The Modal-Split-Explicit Method

In the UCLA GCM, ϕ_a is related to the temperature nonlinearly (AL, Eqs. (207)-(208)), and this will be denoted by a subscript N, thus $(\phi_a)_N$. However, one important requirement in the present scheme is that ϕ_a must be linearly related to temperature. This requirement is met by a previous definition of ϕ_a in the UCLA model (Arakawa, 1972; and Appendix), and this will be denoted by a subscript L, thus $(\phi_a)_L$. Accordingly, the

hydrostatic equation has the form: $\langle \phi_a \rangle_L = [M_1] \langle T \rangle$, where $[M_1]$ is given in the appendix. The matrix $[M_1]$ is a function of π , when P_T in Eq. (1) is not equal to zero; therefore, it is a function of the horizontal coordinates. As part of the simplification, $[M_1]$ computed with $\bar{\pi}$ will be used for all locations. In this way, the definition of $\langle \phi_a \rangle_L$ is modified.

Following the incorporation of the foregoing arguments Equation (3) should be rewritten as:

$$\frac{\partial}{\partial t} (\pi u) + \frac{\partial}{\partial x} \bar{\bar{\bar{\phi}}}_N = R_u. \quad (8)$$

When using leapfrog scheme in time, the finite difference form of (3) over a $2\Delta\tau$ interval can be written as,

$$\begin{aligned} (\pi u)^{t-\Delta t+(n+1)\Delta\tau} - (\pi u)^{t-\Delta t+(n-1)\Delta\tau} + 2\Delta\tau \frac{\partial}{\partial x} \bar{\bar{\bar{\phi}}}_N^{t-\Delta t+n\Delta\tau} \\ = 2\Delta\tau R_u^{t-\Delta t+n\Delta\tau}, \end{aligned} \quad (9)$$

where $\Delta\tau$ is a time interval allowed by the CFL condition based on the speed of fastest waves, and Δt is that based on the meteorological waves. The subscript N indicates that it is computed using nonlinear form of hydrostatic equation. Marching Eq. (9) with $2\Delta\tau$ intervals between $t-\Delta t$ and $t+\Delta t$ and averaging these equations in time given,

$$\begin{aligned} (\pi u)^{t+\Delta t} - (\pi u)^{t-\Delta t} + 2\Delta t \frac{\partial}{\partial x} \left(\bar{\bar{\bar{\phi}}} \right)_N^{t-2\Delta t} \\ = 2\Delta t \bar{R}_u^{2\Delta t} \doteq 2\Delta t R_u^t, \end{aligned} \quad (10)$$

where $(-)^{2\Delta t}$ is the discrete averaging over the $2\Delta t$ interval. With regard to the stability of the scheme, the approximation of $\tilde{R}_u^{2\Delta t}$ by R_u^t is allowed, since R_u does not create a high frequency variation in πu , and since it is a slow varying term. This approximation introduces a truncation error, which is, however, bearable. When the term $2\Delta t \frac{\partial}{\partial x} \left(\frac{\bar{\bar{\phi}}_L^{2\Delta t} - \bar{\bar{\phi}}_N^{2\Delta t} + \bar{\bar{\phi}}_L^t}{2} \right)$ is added to both sides, Eq. (10) becomes

$$\begin{aligned} (\pi u)^{t+\Delta t} - (\pi u)^{t-\Delta t} + 2\Delta t \frac{\partial}{\partial x} \left(\frac{\bar{\bar{\phi}}_L^{2\Delta t} - \bar{\bar{\phi}}_L^t}{2} \right) \\ = 2\Delta t R_u^t + 2\Delta t \frac{\partial}{\partial x} \left(\frac{\bar{\bar{\phi}}_L^{2\Delta t} - \bar{\bar{\phi}}_N^{2\Delta t} - \bar{\bar{\phi}}_L^t}{2} \right) \\ = 2\Delta t R_u^t + 2\Delta t \frac{\partial}{\partial x} \left(\frac{\bar{\bar{\phi}}_L^t - \bar{\bar{\phi}}_N^t - \bar{\bar{\phi}}_L^t}{2} \right) \\ = 2\Delta t R_u^t - 2\Delta t \frac{\partial}{\partial x} \bar{\bar{\phi}}_N^t \end{aligned} \quad (11)$$

The right side of Eq. (11) gives the change of πu over the $2\Delta t$ interval in one leapfrog step. Therefore, Eq. (11) becomes:

$$\begin{aligned} (\pi u)^{t+\Delta t} - (\pi u)^{t-\Delta t} + 2\Delta t \frac{\partial}{\partial x} \left(\frac{\bar{\bar{\phi}}_L^{2\Delta t} - \bar{\bar{\phi}}_L^t}{2} \right) \\ = (\pi u)_E^{t+\Delta t} - (\pi u)^{t-\Delta t} \end{aligned} \quad (12)$$

where the subscript E denotes the results from marching once with the $2\Delta t$ interval without the help of the MSES scheme. Thus, $(\pi u)^{t+\Delta t}$ can be found by marching Eq. (8) over $2\Delta t$ only once, if $\bar{\bar{\phi}}_L^{2\Delta t}$ is known.

Similarly, the other governing equations are:

$$\begin{aligned}
 (\pi v)^{t+\Delta t} - (\pi v)^{t-\Delta t} + 2\Delta t \frac{\partial}{\partial y} (\tilde{\phi}_L^{2\Delta t} - \bar{\phi}_L^t) \\
 = (\pi v)_E^{t+\Delta t} - (\pi v)^{t-\Delta t} ,
 \end{aligned} \tag{13}$$

$$\begin{aligned}
 \langle \pi T \rangle^{t+\Delta t} - \langle \pi T \rangle^{t-\Delta t} + 2\Delta t [M_2] \langle \tilde{D}^{2\Delta t} - D^t \rangle \\
 = \langle \pi T \rangle_E^{t+\Delta t} - \langle \pi T \rangle^{t-\Delta t} ,
 \end{aligned} \tag{14}$$

and

$$\begin{aligned}
 \pi^{t+\Delta t} - \pi^{t-\Delta t} + 2\Delta t \langle N_2 \rangle^T \langle \tilde{D}^{2\Delta t} - D^t \rangle \\
 = \pi_E^{t+\Delta t} - \pi^{t-\Delta t} .
 \end{aligned} \tag{15}$$

Since the aim now is to obtain the two sets of unknowns, $\langle \tilde{\phi} \rangle^{2\Delta t}$ and $\langle \tilde{D} \rangle^{2\Delta t}$, the four sets of equations can be reduced to two sets. Forming $[M_1](14) + \langle \overline{\sigma\pi\alpha - \phi_L} \rangle (15)$ gives:

$$\begin{aligned}
 \langle \bar{\phi}_L \rangle^{t+\Delta t} - \langle \bar{\phi}_L \rangle^{t-\Delta t} + 2\Delta t [M_3] \langle \tilde{D}^{2\Delta t} - D^t \rangle \\
 = \langle \bar{\phi}_L \rangle_E^{t+\Delta t} - \langle \bar{\phi}_L \rangle^{t-\Delta t} ,
 \end{aligned} \tag{16}$$

where $[M_3] = [M_1] [M_2] + \overline{\langle \sigma \pi \alpha - \phi_L \rangle} \langle N_2 \rangle^T$. The grid scheme C (AL, p. 182) used in the UCLA model is not changed.

In order to form the divergence equation from Eqs. (12) and (13) it is convenient to define π at the $u(v)$ points as the average of the two neighboring π 's in the zonal (meridional) direction. However, it should be emphasized that the original definition of π at the u and v points (AL, p. 242) are still used in computing $u_E^{t+\Delta t}$ and $v_E^{t+\Delta t}$.

Equations (12) and (13) give the divergence equation

$$\begin{aligned} \langle D \rangle^{t+\Delta t} - \langle D \rangle^{t-\Delta t} + 2\Delta t \nabla^2 \langle \overline{\overline{\phi_L}}^{2\Delta t} - \overline{\phi_L}^t \rangle \\ = \langle D \rangle_E^{t-\Delta t} - \langle D \rangle^{t-\Delta t}, \end{aligned} \quad (17)$$

where $\nabla^2 = \frac{\partial^2}{\partial x^2} + \frac{1}{\cos \phi} \frac{\partial}{\partial y} \left(\cos \phi \frac{\partial}{\partial y} \right)$. Note that the dash bar operator is used twice. Spectral equations governing the amplitudes of the natural gravity modes of the numerical model can be obtained by premultiplying equations (16) and (17) by $[E]^{-1}$, where $[E]$ is a matrix whose columns are the eigenvectors of $[M_3]$.

The spectral equations are,

$$\begin{aligned}
 & \left(\langle \bar{\phi}_L^E \rangle^{t+\Delta t} - \langle \bar{\phi}_L^E \rangle^t \right) - \left(\langle \bar{\phi}_L^E \rangle^{t-\Delta t} - \langle \bar{\phi}_L^E \rangle^t \right) \\
 & + 2\Delta t [\lambda] \langle D^E \rangle^{2\Delta t} - D^E{}^t > \\
 & = [E]^{-1} \left(\langle \bar{\phi}_L^E \rangle^{t+\Delta t} - \langle \bar{\phi}_L^E \rangle^{t-\Delta t} \right) , \quad (18)
 \end{aligned}$$

and

$$\begin{aligned}
 & \left(\langle D^E \rangle^{t+\Delta t} - \langle D^E \rangle^t \right) - \left(\langle D^E \rangle^{t-\Delta t} - \langle D^E \rangle^t \right) \\
 & + 2\Delta t \nabla^2 \langle \bar{\phi}_L^E \rangle^{2\Delta t} - \bar{\phi}_L^E{}^t > \\
 & = [E]^{-1} \left(\langle D^E \rangle^{t+\Delta t} - \langle D^E \rangle^{t-\Delta t} \right) , \quad (19)
 \end{aligned}$$

where $[\lambda]$ is equal to $[E]^{-1}[M_3][E]$, a diagonal matrix whose diagonal elements are the eigenvalues of $[M_3]$ and $\langle x \rangle^E \equiv [E]^{-1} \langle x \rangle$. Equations (18) and (19) can be used in a $\Delta\tau$ interval, and thus are written as:

$$\begin{aligned}
 & \left(\langle \bar{\phi}_L^E \rangle^{\tau+\Delta\tau} - \langle \bar{\phi}_L^E \rangle^\tau \right) - \left(\langle \bar{\phi}_L^E \rangle^{\tau-\Delta\tau} - \langle \bar{\phi}_L^E \rangle^\tau \right) \\
 & + 2\Delta\tau [\lambda] \langle D^E \rangle^{\tau} - D^E{}^\tau > \\
 & = \left(\Delta\tau / \Delta t \right) [E]^{-1} \left(\langle \bar{\phi}_L^E \rangle^{t+\Delta t} - \langle \bar{\phi}_L^E \rangle^{t-\Delta t} \right) \quad (20)
 \end{aligned}$$

and

$$\begin{aligned}
 & (\langle D^E \rangle_{t+\Delta t} - \langle D^E \rangle_t) - (\langle D^E \rangle_{t-\Delta t} - \langle D^E \rangle_t) \\
 & + 2\Delta t \nabla^2 \langle \bar{\phi}_L^E - \bar{\phi}_L^t \rangle \\
 & = (\Delta t / \Delta t) [E]^{-1} (\langle D \rangle_E^{t+\Delta t} - \langle D \rangle^{t-\Delta t}) , \quad (21)
 \end{aligned}$$

where the right sides of these equations are not changed (except for the $\Delta t / \Delta t$ factor), since they vary rather slowly over a $2\Delta t$ period.

Equations (20) and (21) are marched in the $2\Delta t$ interval with different Δt for each mode as determined by the CFL condition based on the phase speed of that mode. The right sides of Eqs. (19) and (20) are, of course, held constant in this marching. The quantities $(D^E - D^t)$ and $(\bar{\phi}_L^E - \bar{\phi}_L^t)$ are obtained from averaging the results of this marching. Only modes with phase speeds greater than the maximum speed of the meteorological waves have to be marched in this manner. Finally E is multiplied with $(D^E - D^t)$ and $(\bar{\phi}_L^E - \bar{\phi}_L^t)$ to obtain $(D^{2\Delta t} - D^t)$ and $(\bar{\phi}_L^{2\Delta t} - \bar{\phi}_L^t)$ respectively.

In summary, the procedure of the MSES method is:

- (1) Calculate the matrices, and the eigenvalues and eigenvectors of $[M_3]$, using the predetermined global mean quantities. This step is done only once,

- (2) Compute $\left(\overline{\phi}_L^E\right)^{t-\Delta t} - \left(\overline{\phi}_L^E\right)^t$ and $\left(\overline{D}^E\right)^{t-\Delta t} - \left(\overline{D}^E\right)^t$.
- (3) Use the larger time interval Δt , march forward one step and compute the right hand sides of Eqs. (20) and (21).
- (4) March Eqs. (20) and (21) with different Δt for different modes. For the six-level UCLA model (AL, p. 176), only the first three modes need to be integrated with $\Delta t = (1/5, 1/3, 1/2)\Delta t$.
- (5) Average the result from step (4) to obtain $\left(\overline{\phi}_L^E\right)^{2\Delta t} - \left(\overline{\phi}_L^E\right)^t$ and $\left(\overline{D}^E\right)^{2\Delta t} - \left(\overline{D}^E\right)^t$ which then allow the calculation of the predicted quantities at $t+\Delta t$ in Eqs. (12) through (15).

Although the above descriptions are based on the leapfrog scheme, the changes are minor when using the Matsuno scheme, which is periodically used in the UCLA GCM, (AL, p. 260). In the first part of the Matsuno scheme, the superscripts $t+\Delta t$, $t-\Delta t$ and $2\Delta t$ in the above equations are changed to t^* , t and Δt , respectively. Then, in the second part of the Matsuno scheme, the superscripts $t-\Delta t$ and $2\Delta t$ are changed to t^* and Δt , respectively. In both parts, of course, the factor $2\Delta t$ is changed to Δt .

2.3 Modification of the Advective Terms Near the Poles

Even when Δt is increased by a factor of five, the dash bar operator, described in subsection 2.2, is sufficient to circumvent the problem of linear instability related to the gravity wave terms, due to the diminishing zonal grid

toward the poles. However, the advective terms $\partial/\partial x [(\overline{\pi u})q]$ --where q denotes u , v and T --can create linear instability near the poles when Δt is enlarged. The time increment allowed for the advective terms, Δt , is limited by $\Delta t < \epsilon \Delta x / (u + c_m)$, where c_m is the speed of the meteorological waves, u is that of the basic flow, and ϵ has a magnitude of the order of 1, with its exact value depending on the time differencing scheme used. When u is large in the polar region, where Δx is small, Δt cannot be increased by a factor of five. One obvious, yet undesirable, solution is to use a smaller Δt . The solution used here is to apply the dash bar operator to q in the terms $\partial/\partial x [(\overline{\pi u})q]$ in Eqs. (272) and (299) of AL. Thus, in step 2 of the MSES procedure in subsection 2.2, the second term in Eq. (299) is changed to (with notation of AL):

$$\delta_{\xi} [\overline{F(\overline{T})}]^{\xi}.$$

Also, the changes in Eq. (272) are to substitute Eq. (275) into Eq. (272) and then to apply the dash bar operator on u in those terms containing $\overline{F^*}$. Similar changes are made for the v component equation. Short-term tests (72 hrs.) show this method is successful in controlling linear instability; however, since the quadratic conservation properties no longer hold, there can be some side effects in this approach, as will be shown in the result section.

2.4 The Time Differencing Method

As shown in Figure 1, the time differencing method used to calculate the dynamic terms consists of a series of the leapfrog schemes, with a periodic insertion of the Matsuno scheme. The source and sink terms, and the vertical flux convergence term of the moisture equation, are calculated as an instantaneous adjustment. For $\Delta t = 30$ min., these calculations are done after each leapfrog or Matsuno step. Thus, the time differencing method for the physical processes is not changed.

2.5 Addition of the Pressure Averaging Method

The pressure averaging method (Shuman et al., 1972) can be applied to the integration of Eqs. (19) and (20) to reduce the overhead in using the MSES scheme. Briefly, when this method is used on the 2-D linear gravity wave equations,

$$\phi_t + gH u_x = 0 ,$$

and

$$u_t + \phi_x = 0 ,$$

where u is the perturbed wind in the x -direction, ϕ the perturbed geopotential of the free surface, and H the basic state surface height. The time differencing scheme has the form:

$$(\phi^{\tau+1} - \phi^{\tau-1})/2\Delta t + gH u_x = 0 ,$$

and

$$(u^{\tau-1} - u^{\tau-1})/2\Delta t + \hat{\phi}_x^{\tau} = 0 ,$$

where

$$(\hat{\phi})^{\tau} = \alpha [(\phi)^{\tau+1} + (\phi)^{\tau-1}] + (1-2\alpha) (\phi)^{\tau} .$$

with this method, Δt can be almost twice as large as that allowed by the CFL condition. Thus, when this method is applied to Eqs. (20) and (21) the term $\bar{\phi}^E$ is changed to $\hat{\phi}^E$. In the present investigation, $\alpha = 0.24$ is used. Thus, Eqs. (20) and (21) can be integrated with $\Delta\tau = (1/3, 1/2, 1/1.5)\Delta t$ for the first three modes. A detailed analysis of this method was performed by Brown and Campana (1978).

3.0 RESULTS AND DISCUSSION

The performance of the present MSES formulation is of course judged by its stability, efficiency, and accuracy. The following discussions are directed toward these characteristics.

3.1 Stability

Two 12-hr. and one 72-hr. runs starting from different initial conditions showed that the present MSES formulation is capable of avoiding linear instability. Since the linear stability criterion depends not only on

the wave speeds but also on the wind speed, present formulation should be tested with large wind speed, especially in the polar region where zonal grid size is small. In one preliminary 12-hr. test run the wind speed near the northpole reached more than 50m/s and no linear instability occurred.

3.2 Efficiency

Tests show that when the UCLA GCM with $\Delta\phi = 4^\circ$, $\Delta\lambda = 5^\circ$ and $\Delta t = 30$ min. (five times of the original Δt) was run on a CDC 175 without physical processes, the reduction in integration CPU time by MSES is 48% of which 4% is due to the addition of the pressure averaging methods. The efficiency can be greater if the resolution increases. The net reduction in CPU time for the full model depends on the amount of the CPU time used for the physical processes, which of course get no improvement from MSES. The reduction is 24% for the full UCLA GCM with the aforementioned grid size. Only when a large portion of CPU time is allocated to dynamic processes does it pay to adopt the MSES.

3.3 Accuracy

Two 72-hr. runs with and without MSES were made starting from the same well-balanced initial conditions, which is the end of another 72-hr. run. The initial conditions and the results at hour 72 are shown in Figures 2 and 3 for sea level pressure and 500 mb geopotential height, respectively. The difference between the two runs is very small when compared with the changes over 72 hrs. The RMS differences in surface pressure, in 500 mb geopotential height, and in 500 mb zonal wind

between the two runs are given in Table 1. The RMS difference in 500 mb geopotential height at hour 72 is 16 meters, which is very small, when compared with a typical forecast error of 75 meters. Also the RMS difference in 500 mb zonal wind at hour 72 is 2.4 m/s compared with the typical 48 hr. forecast error of 8.5 m/s. Although there was concern whether computing the matrices using a globally averaged π was appropriate for high terrain areas, no adverse effect over these regions was detected. One obvious discrepancy between the two runs is that after 72 hrs., a strong high centered at 35° E, 80° S, appeared in the run using MSES, whereas only a weak high occupied this region in the other run. A separate 72-hr. run using MSES, and starting from the same initial conditions but without the physical processes, also has this intense high (Figure 4). Thus, it is reasonable to consider this discrepancy a side effect of the modification described in Section 2.3.

Table 1. RMS Differences

	RMS Difference		
	Surface Pressure (mb)	500 mb Geopotential Height (m)	500 mb Zonal Wind (m/s)
24 hr.	1.09	8.93	1.03
48 hr.	1.54	12.40	1.79
72 hr.	1.97	15.78	2.40

Overall, the results are remarkably good outside the regions very close to the poles. The poor performance near the poles, however, is not a direct consequence of applying MSES, but it is related to the horizontal differencing scheme, and to the diminishing zonal grid size near the poles. Whether this problem precludes long-term integration was not answered in this study, due to the limitations on computing resources.

Thus far the discussion on accuracy is based on the runs starting from a well-balanced initial condition. Whether the good accuracy can still be maintained in runs starting from an initial condition that is generated from an initialization program is again not answered due to the limitations on computing resources. Nevertheless, since a reasonably good initialization program should generate a fairly balanced initial condition, this problem may not be a justified concern. (However, incompatibility between the initial thermodynamic fields and the cumulus parameterization scheme can generate initial imbalance.) Besides, should this problem be serious, the use of MSES can be delayed for a while (say, 12 hrs.), after the initial imbalance has died down.

ACKNOWLEDGMENTS

This work was funded by the Naval Environmental Prediction Research Facility Program Element 62759N, Project WR59-551, "Atmospheric Environmental Support". Dr. Thomas E. Rosmond of Naval Environmental Prediction Research Facility provided the initial conditions for the test runs. His help in making the computing facility at Naval Fleet Numerical Oceanography Center accessible is greatly appreciated. Thanks are also extended to Drs. Simon W. Chang, Kay E. Cheney, and Darrell Strobel for reading the manuscript.

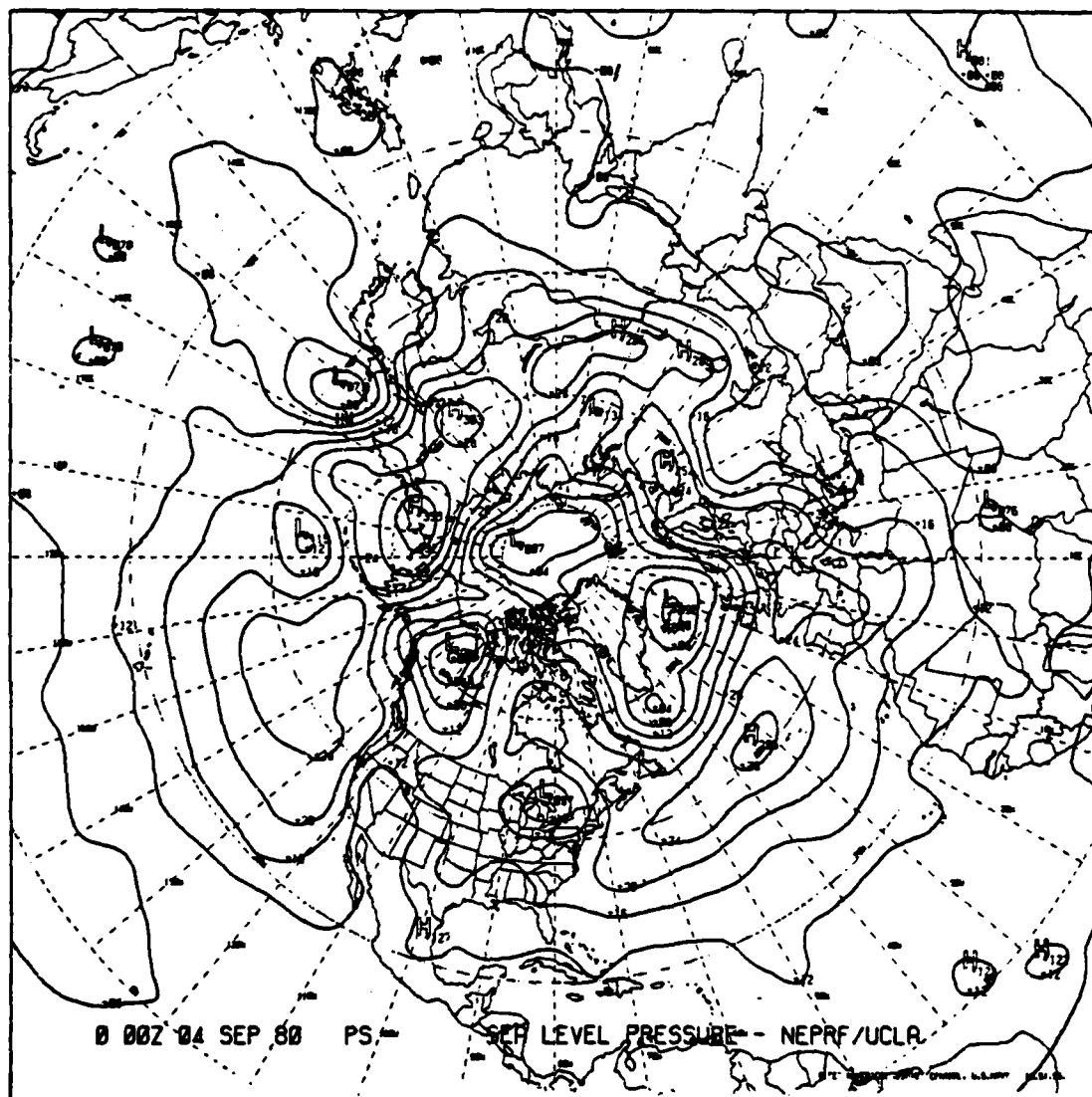


Fig. 2a — Initial sea level pressure (mb), Northern Hemisphere

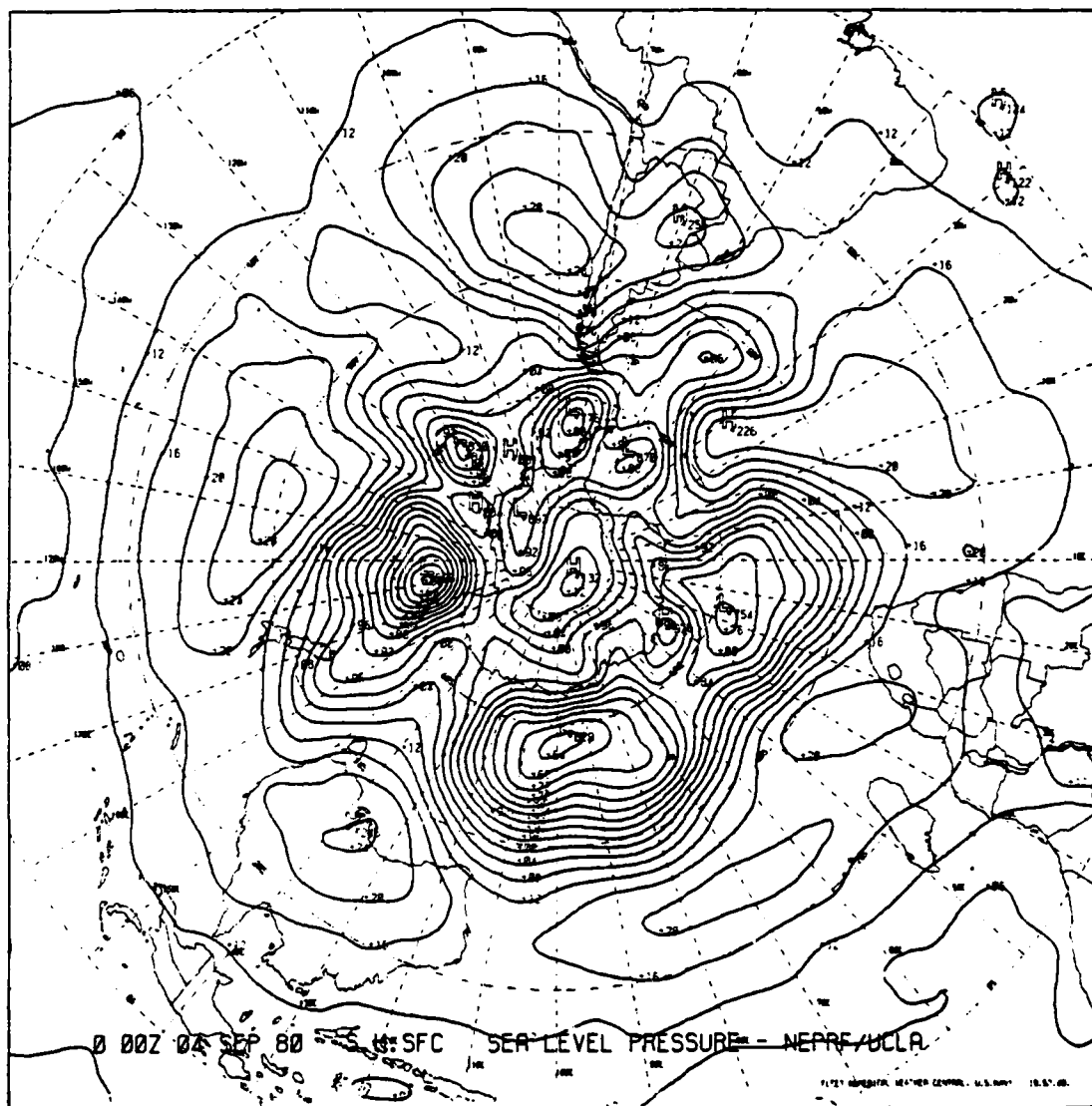


Fig. 2b — Initial sea level pressure (mb), Southern Hemisphere

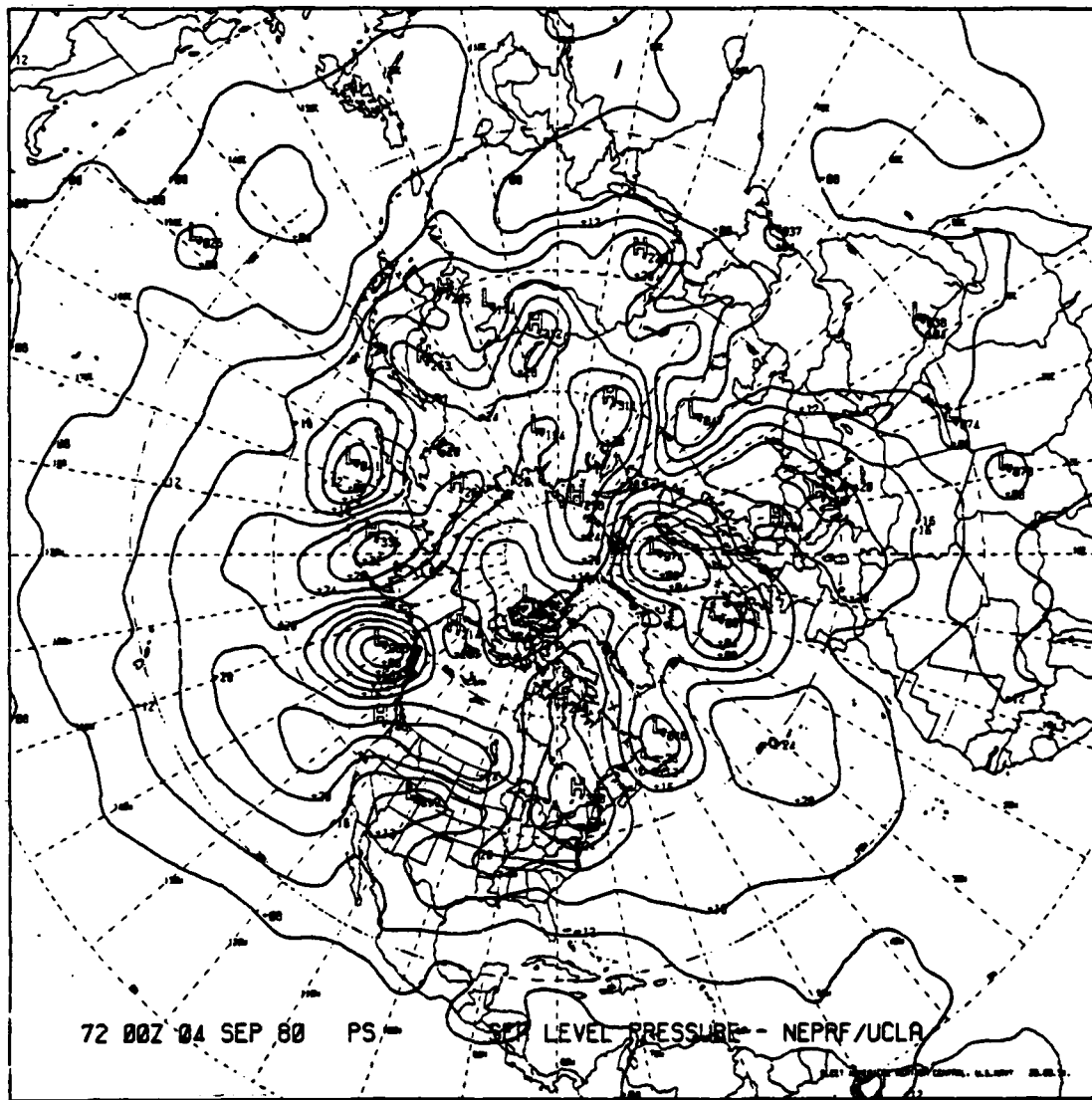


Fig. 2c — 72 hr. sea level pressure (mb), Northern Hemisphere, no MSES

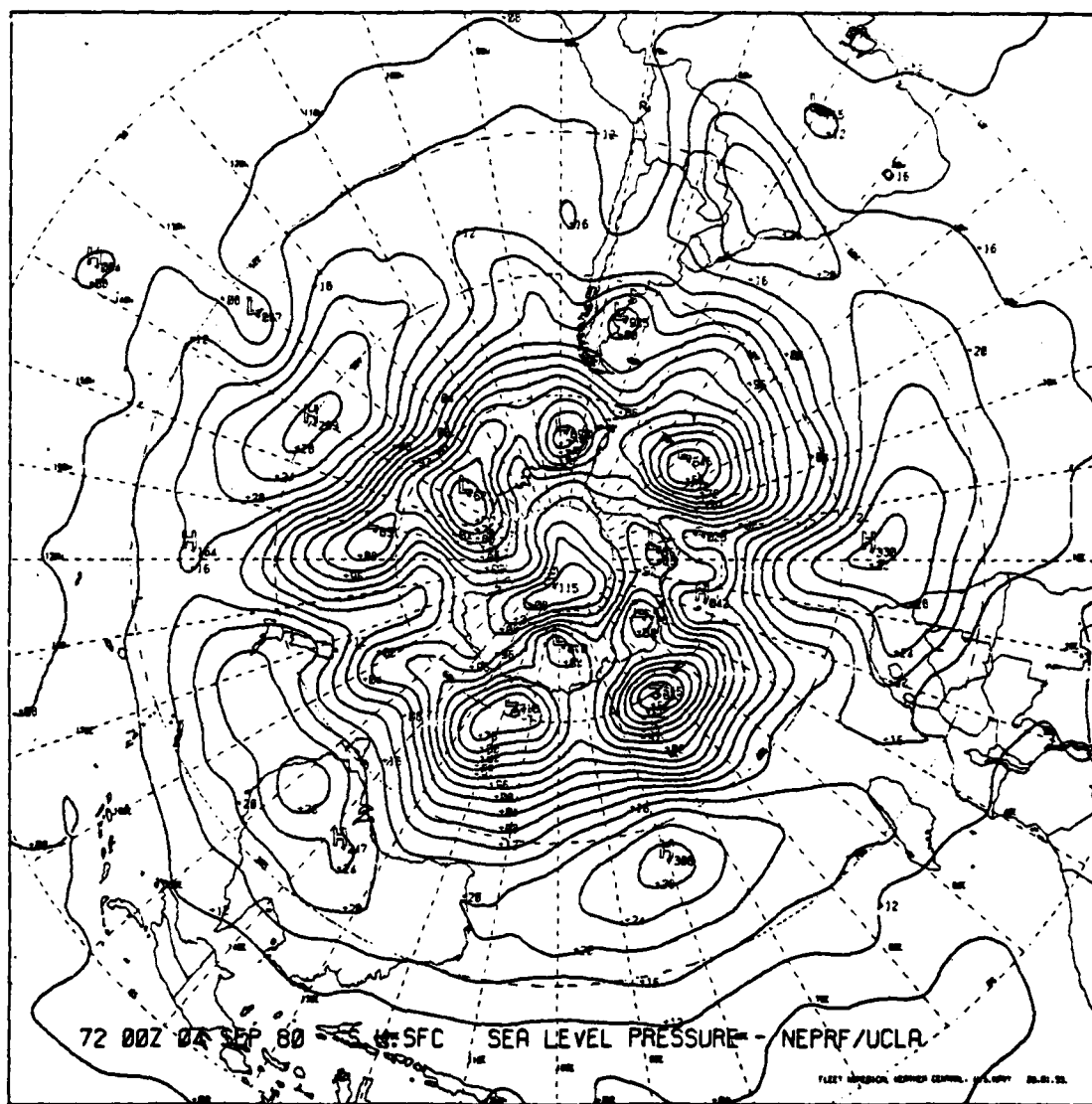


Fig. 2d — 72 hr. sea level pressure (mb), Southern Hemisphere, no MSES

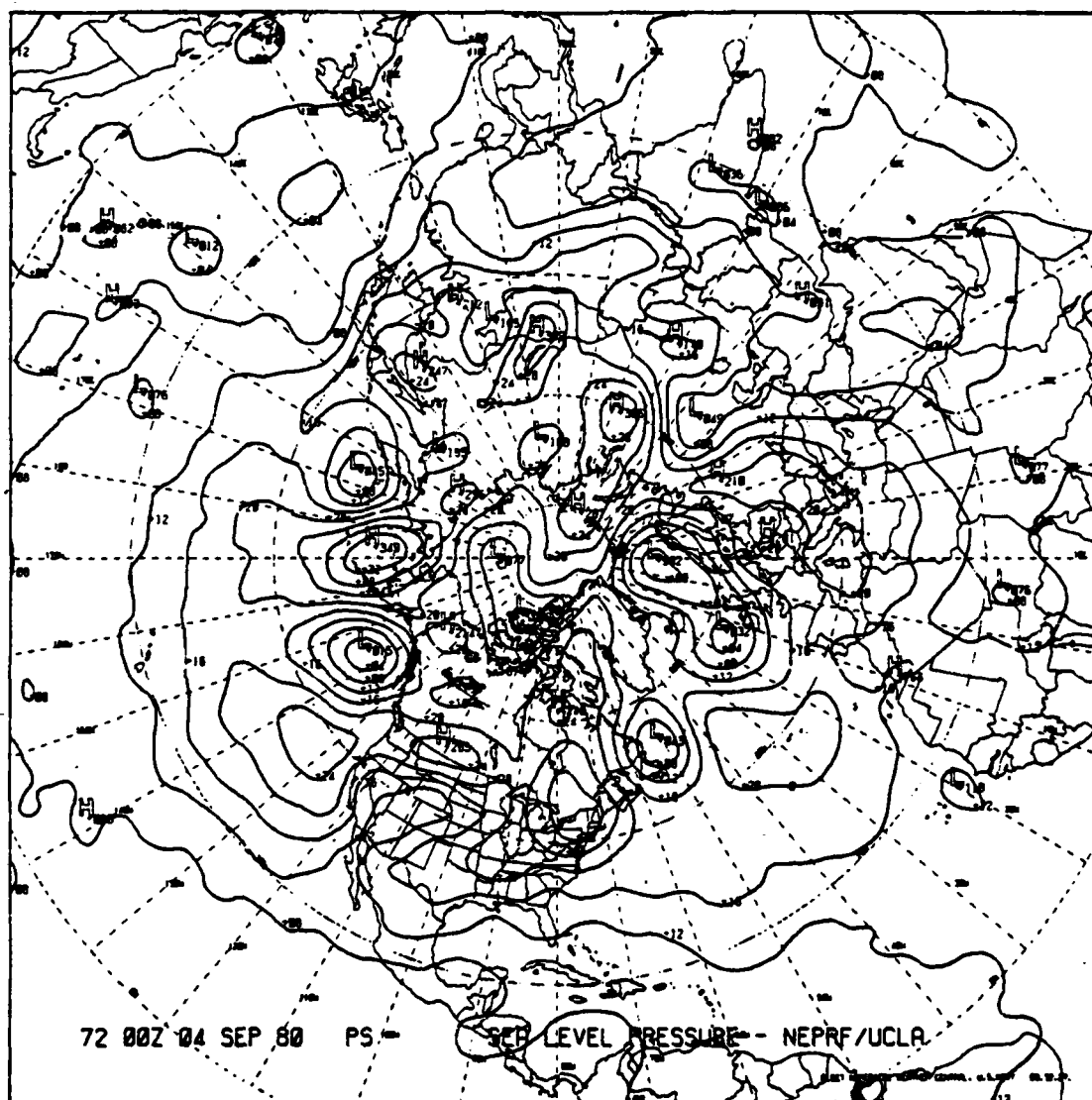


Fig. 2e - 72 hr. sea level pressure (mb), Northern Hemisphere, with MSES

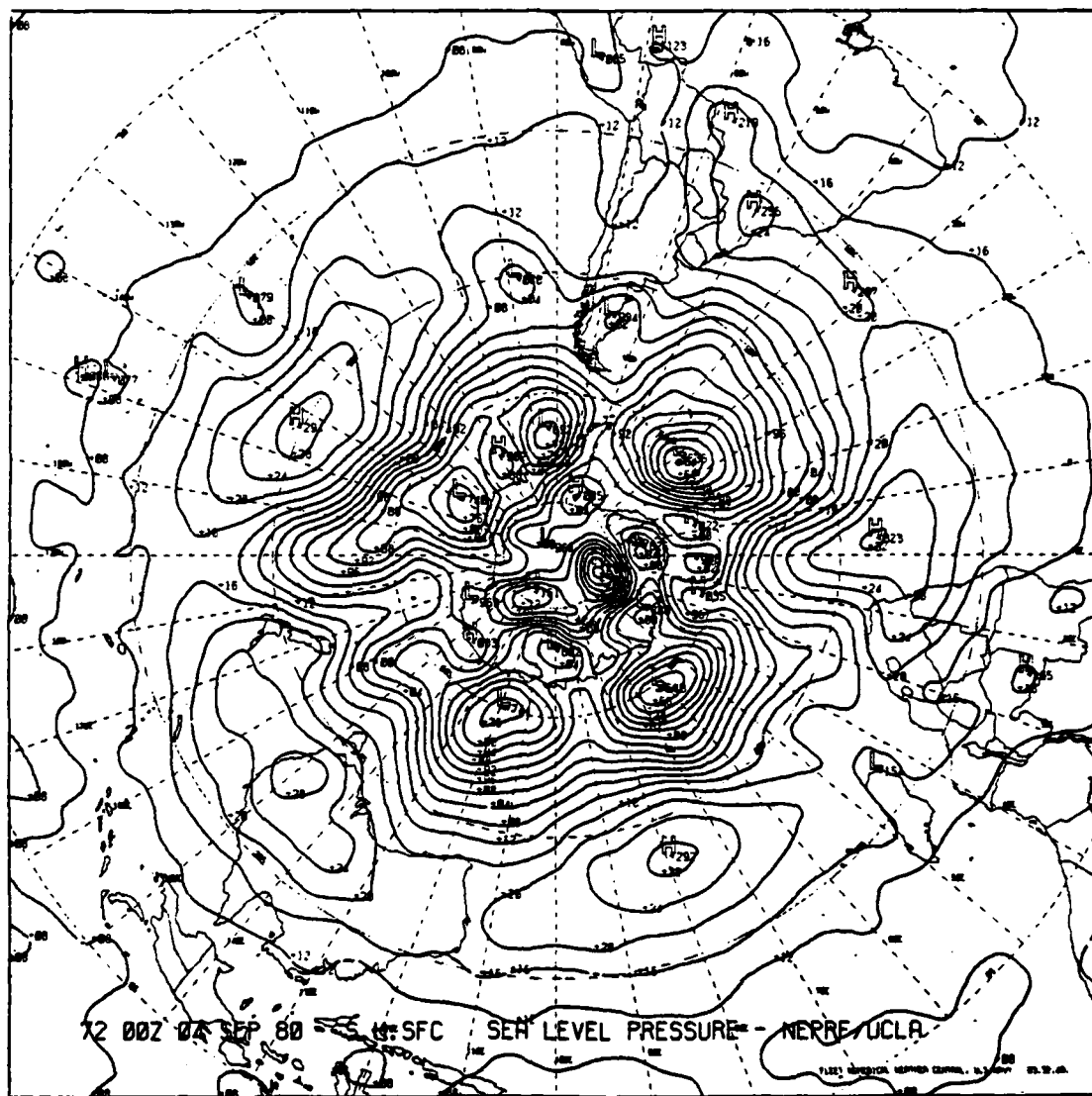


Fig. 2f - 72 hr. sea level pressure (mb), Southern Hemisphere, with MSES

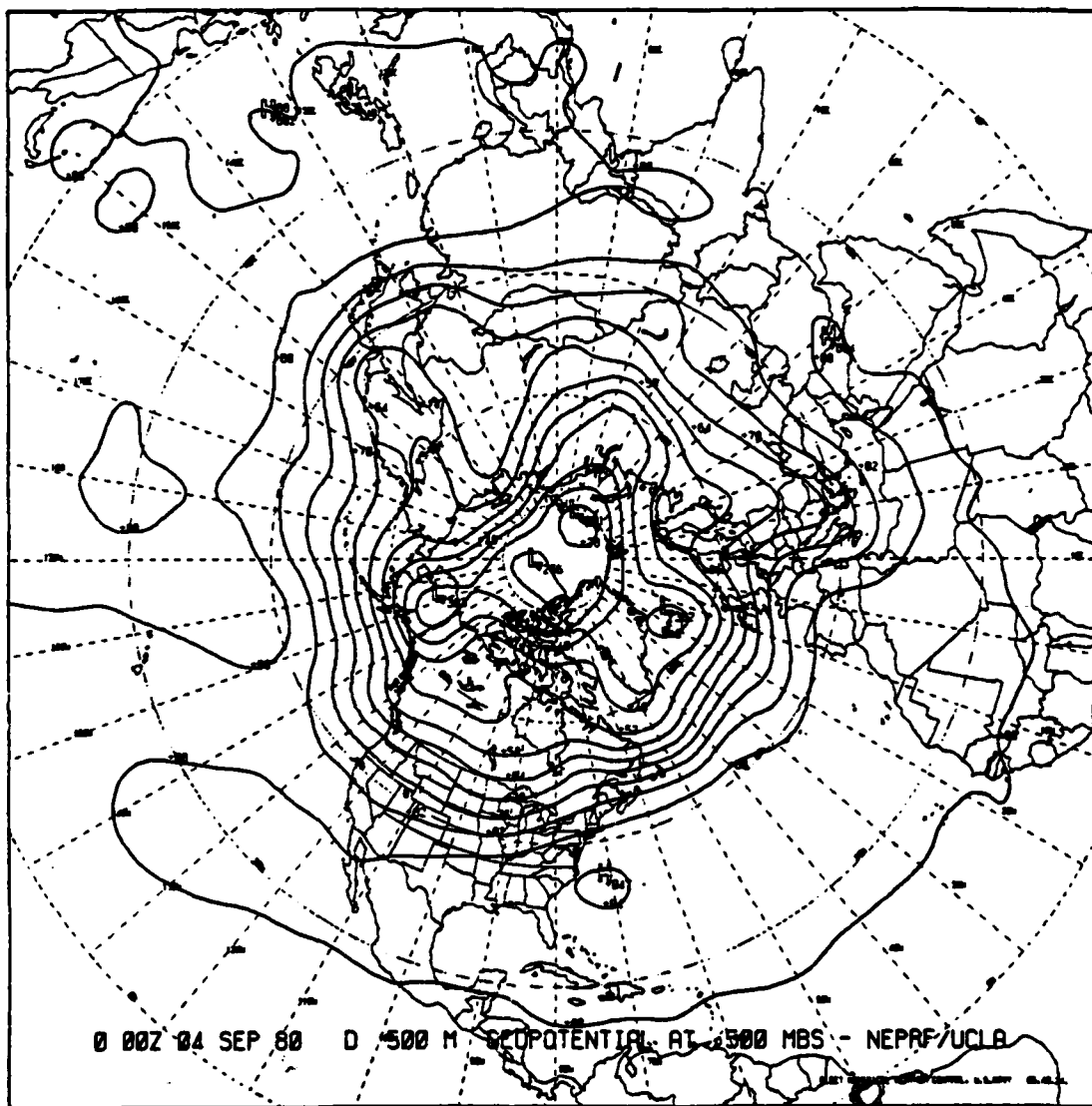


Fig. 3a — Initial 500 mb geopotential (60 meter interval), Northern Hemisphere

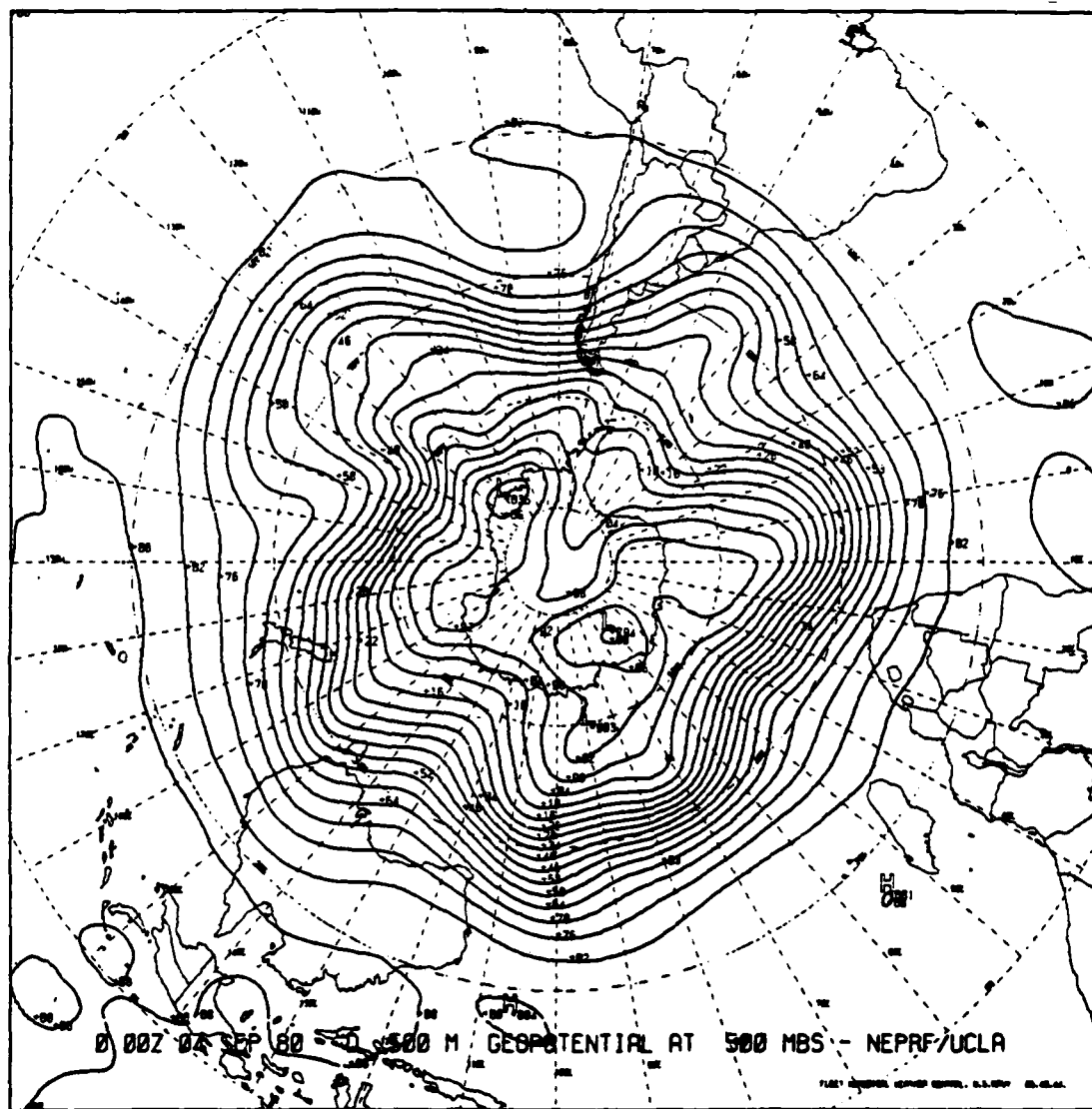


Fig. 3b — Initial 500 mb geopotential (60 meter interval), Southern Hemisphere

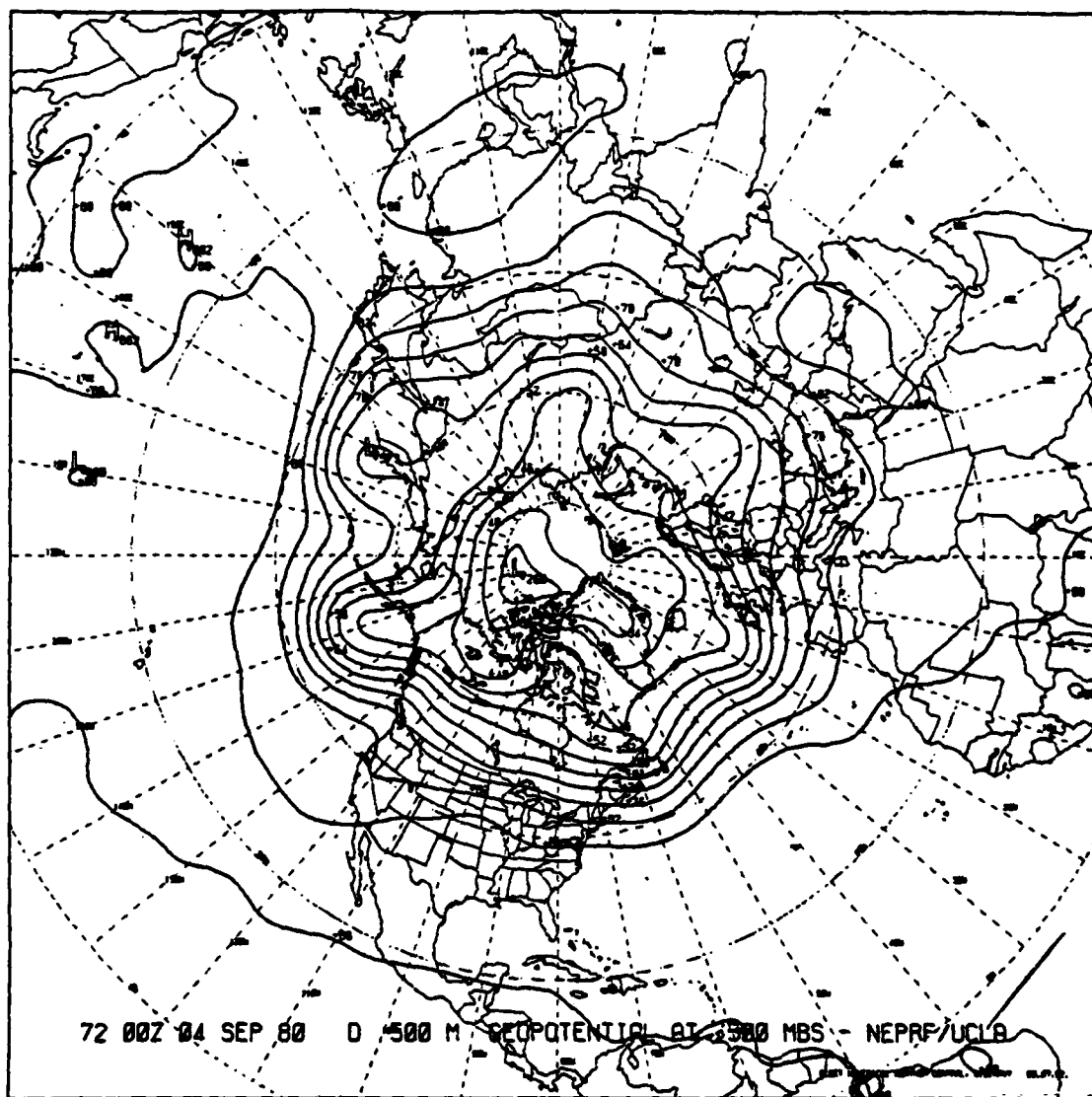


Fig. 3c — 72 hr. 500 mb geopotential (60 meter interval), Northern Hemisphere, no MSES

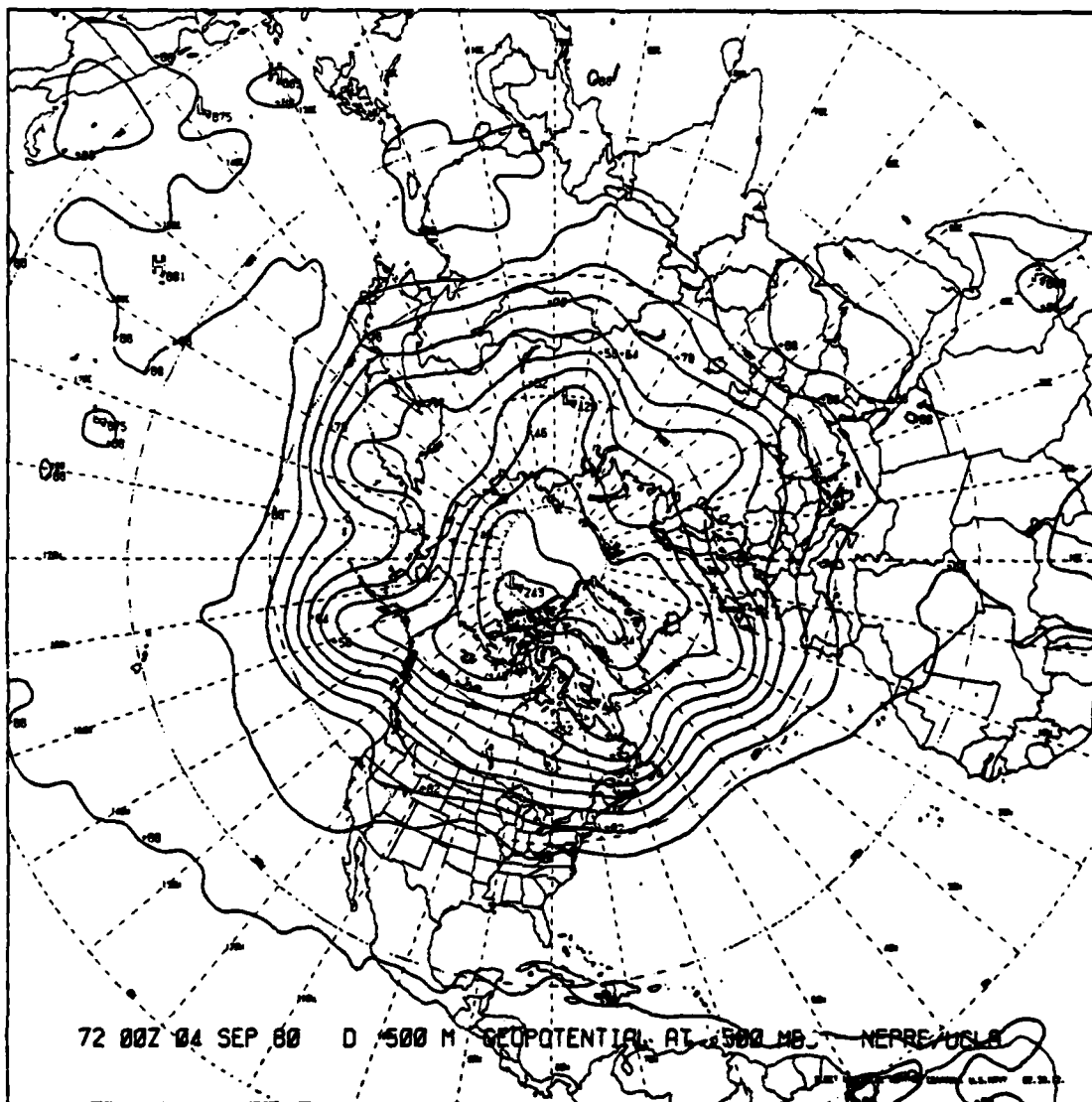


Fig. 3e — 72 hr. 500 mb geopotential (60 meter interval), Northern Hemisphere, with MSES

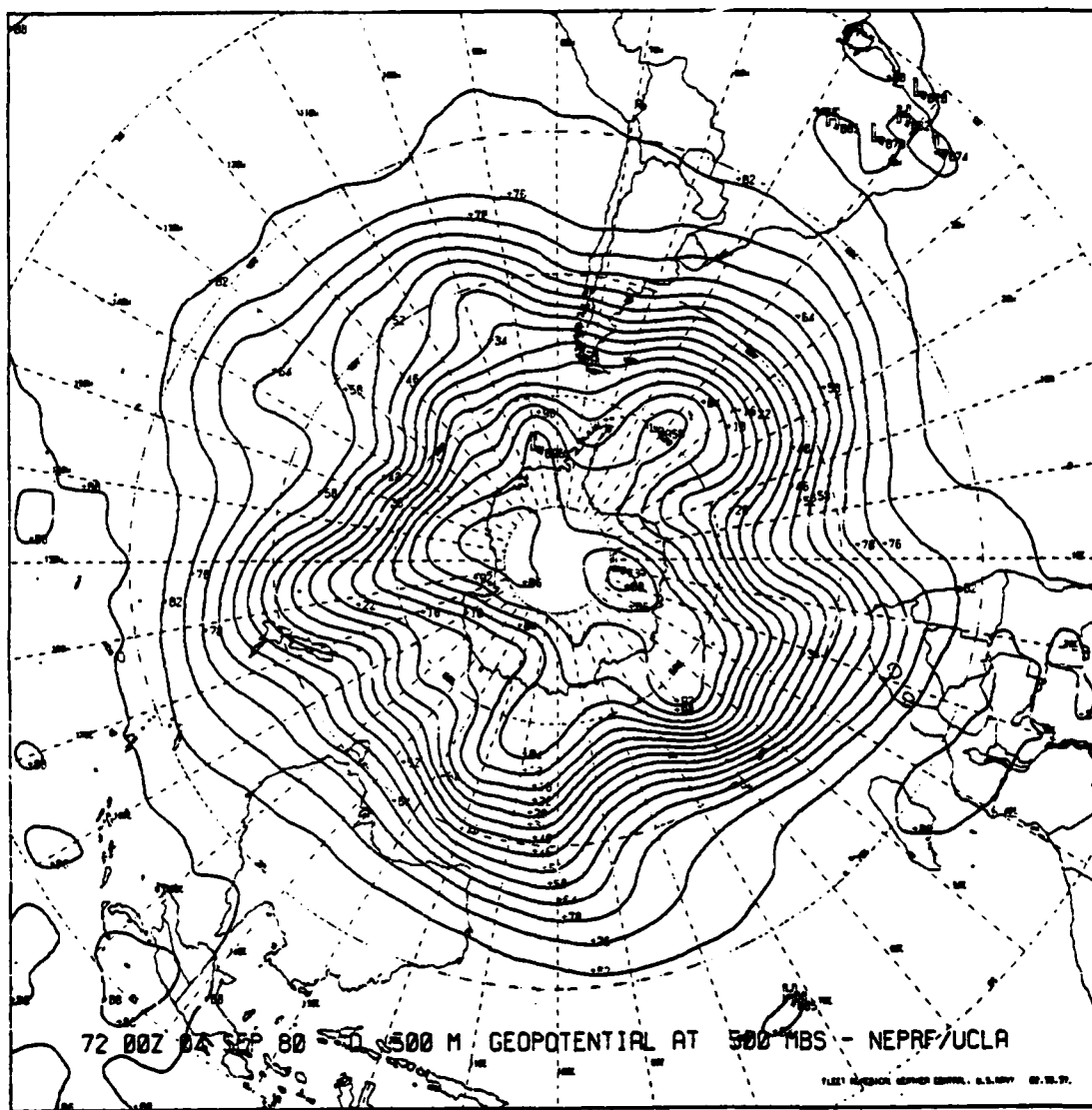


Fig. 3f — 72 hr. 500 mb geopotential (60 meter interval), Southern Hemisphere, with MSES

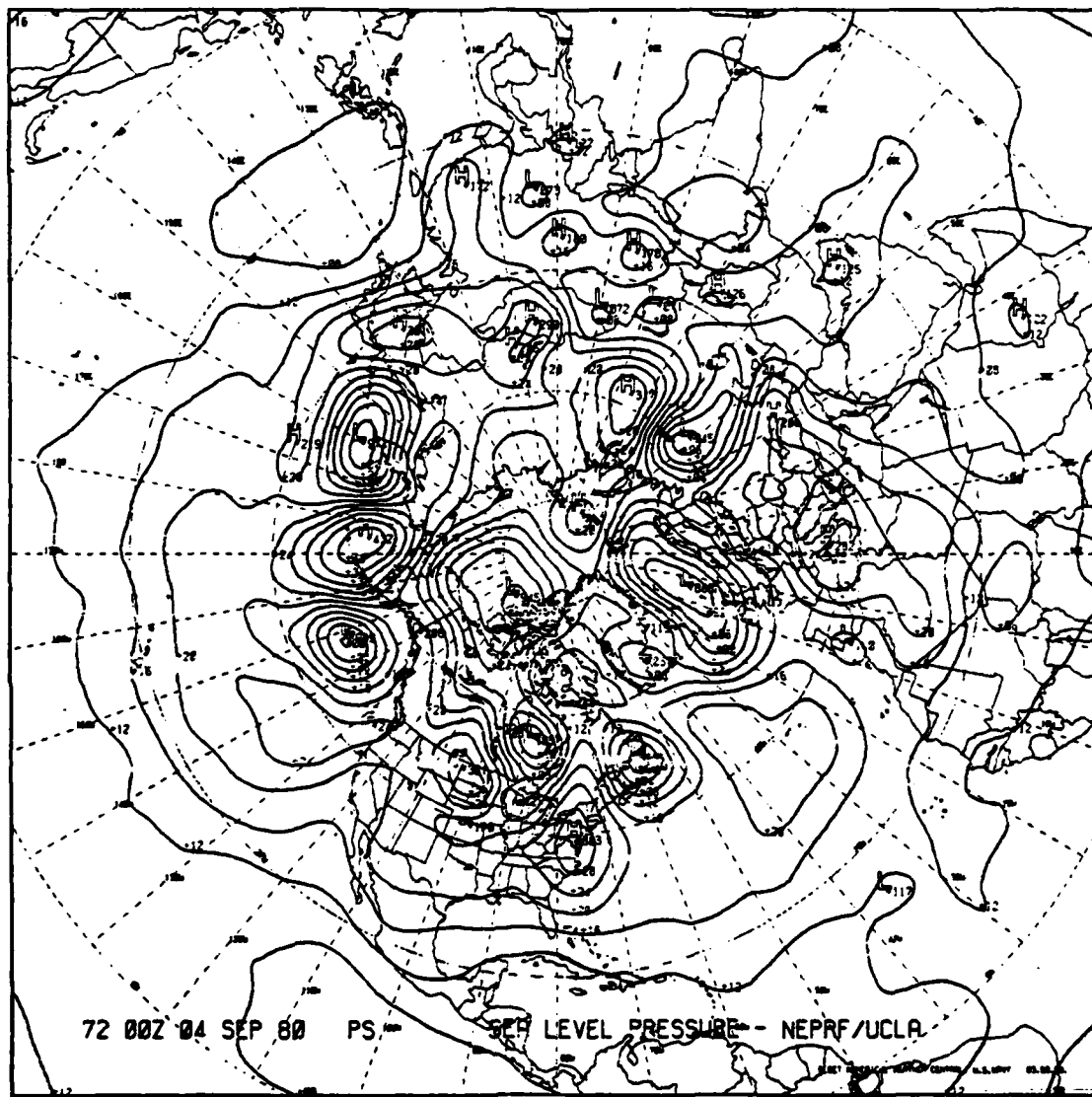


Fig. 4a - 72 hr. sea level pressure (mb), Northern Hemisphere, with MSES, dry model

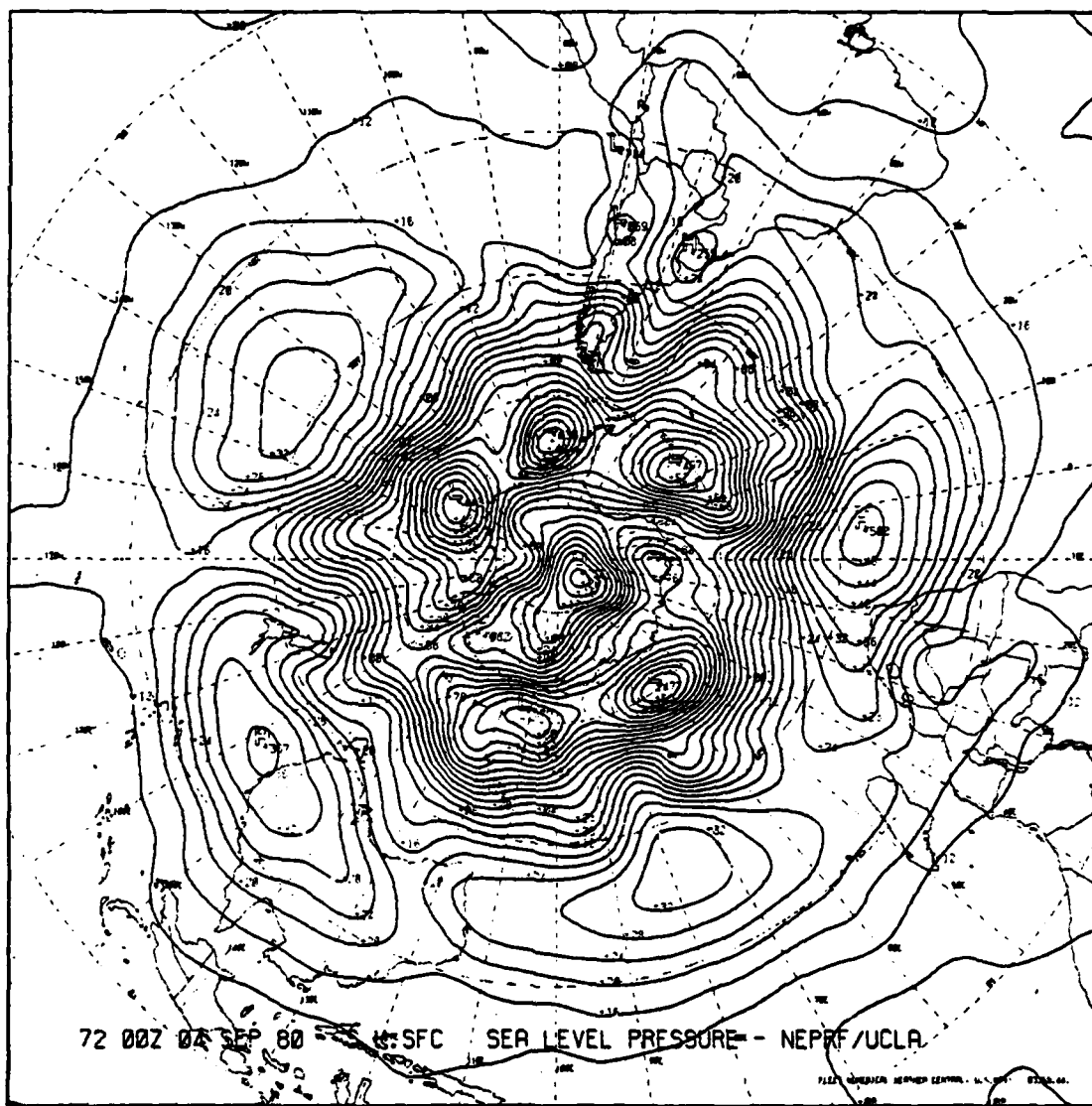


Fig. 4b — 72 hr. sea level pressure (mb), Southern Hemisphere, with MSES, dry model

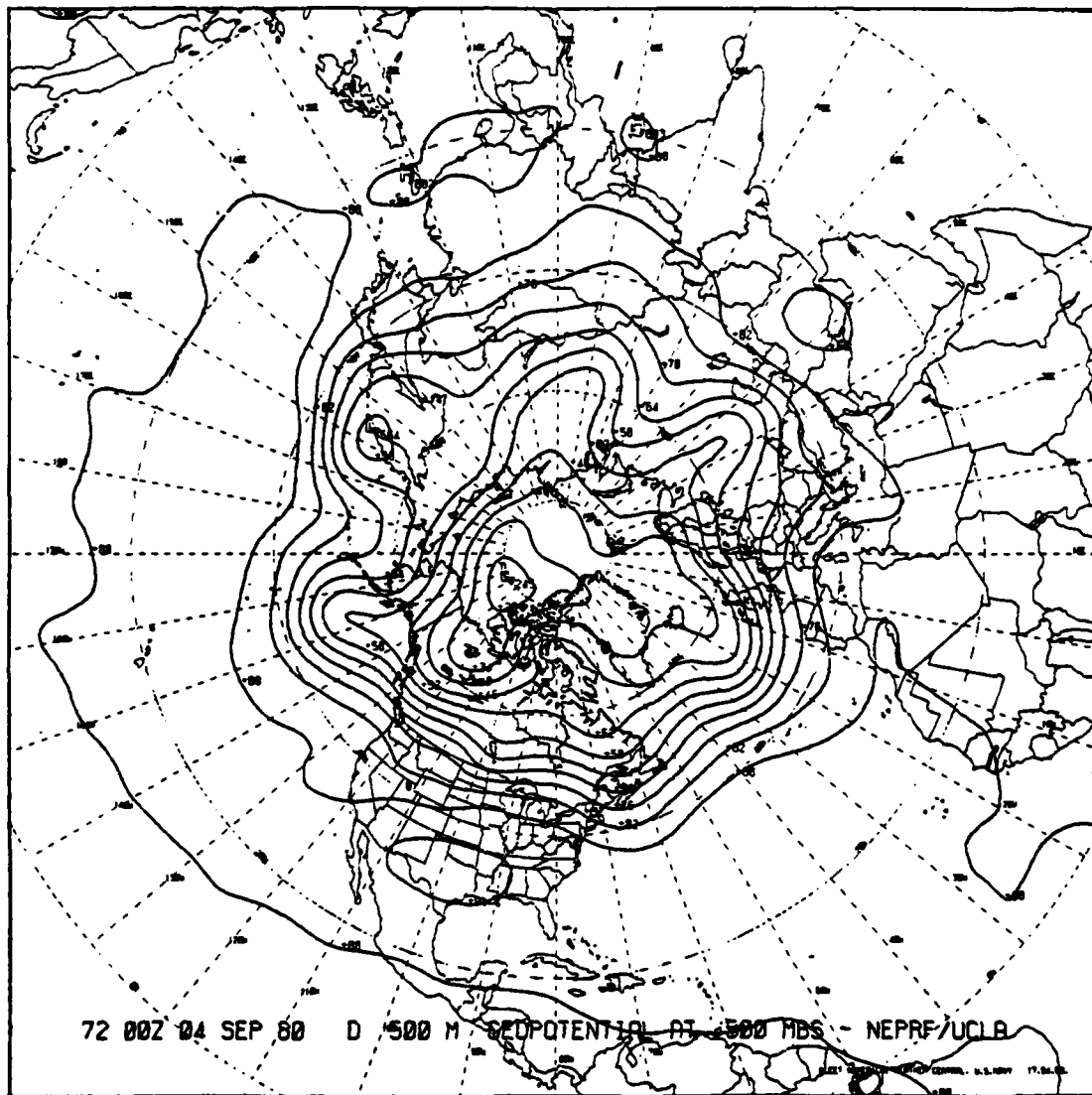


Fig. 4c — 72 hr. 500 mb geopotential (60 meter interval),
Northern Hemisphere, with MSES, dry model

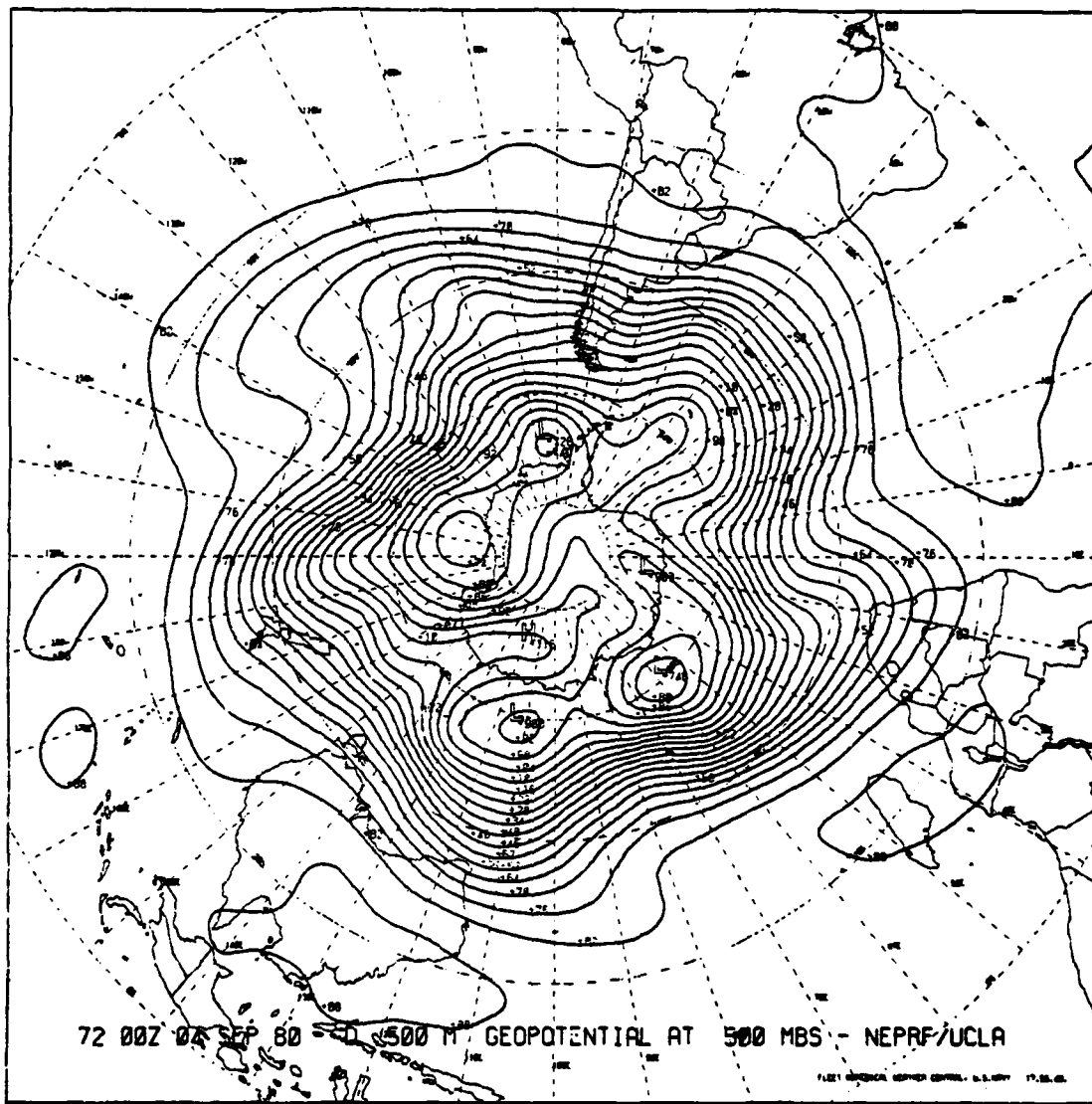


Fig. 4d - 72 hr. 500 mb geopotential (60 meter interval),
Southern Hemisphere, with MSES, dry model

APPENDIX

In a K-level σ coordinate model, where

$$\sigma = (P - P_T) / (P_S - P_T),$$

$$\langle N_2 \rangle^T = (\Delta\sigma_1, \Delta\sigma_2, \dots, \Delta\sigma_K),$$

The hydrostatic equation for ϕ_a (Arakawa, 1972, p. 25) is:

$$(\phi_a)_k - (\phi_a)_{k+1} = \frac{C_p}{2} \left[\left(\frac{\bar{P}}{\bar{P}_{k+1}} \right)^\kappa - \left(\frac{\bar{P}}{\bar{P}_k} \right)^\kappa \right]$$

$$\left(\frac{T_k}{\bar{P}_k^\kappa} + \frac{T_{k+1}}{\bar{P}_{k+1}^\kappa} \right) \quad (A-1)$$

where $\kappa = R/c_p$, and

$$(\phi_a)_K = \sum_{k=1}^K \bar{\pi}_\sigma \frac{R}{\bar{P}_k} \Delta\sigma_k - (\sigma_{k+1} \beta_k + \sigma_{k-1} \alpha_k) T_k, \quad (A-2)$$

$$\beta_k = \begin{cases} \frac{1}{2} \left[\left(\frac{\bar{P}_{k+1}}{\bar{P}_k} \right)^\kappa - 1 \right] & \text{for } k \leq K-1 \\ 0 & \text{for } k = K, \end{cases}$$

and

$$c_k = \begin{cases} 0 & \text{for } k = 1 \\ \frac{1}{2} \left[1 - \left(\frac{\bar{p}_{k-1}}{\bar{p}_k} \right)^K \right] & \text{for } k \geq 2 \end{cases}$$

The matrix M_1 can be constructed from the preceding equations, where Equations (A-1) and (A-2) give ϕ_k ($k = 1, \dots, K$) as a linear function of T_k ($k = 1, \dots, K$). The element $(M_1)_{i,j}$ equals the ϕ_i , computed using $T_j = 1$ and $T_k = 0$ for all $k \neq j$.

$$[N_1] = - \begin{pmatrix} \Delta\sigma_1 & 0 & \dots & 0 \\ \Delta\sigma_1 & \Delta\sigma_2 & \dots & 0 \\ \dots & \dots & \dots & \dots \\ \Delta\sigma_1 & \Delta\sigma_2 & \dots & \Delta\sigma_K \end{pmatrix} + \begin{pmatrix} \sigma_2^E \Delta\sigma_1 & \sigma_2^E \Delta\sigma_2 & \dots & \sigma_2^E \Delta\sigma_K \\ \sigma_3^E \Delta\sigma_1 & \sigma_3^E \Delta\sigma_2 & \dots & \sigma_3^E \Delta\sigma_K \\ \dots & \dots & \dots & \dots \\ \sigma_{K+1}^E \Delta\sigma_1 & \sigma_{K+1}^E \Delta\sigma_2 & \dots & \sigma_{K+1}^E \Delta\sigma_K \end{pmatrix} \quad (A-3)$$

σ^E denotes σ at an interface between two layers as shown in Fig. A-1. When $\langle \pi \dot{\sigma} \rangle = [N_1] \langle D \rangle$ is substituted in the thermodynamic equation M_2 and M_4 can easily be constructed.

The thermodynamic equation is

$$\begin{aligned} \frac{\partial}{\partial t} (\pi T_k) + \nabla \cdot (\pi v_k T_k) + \frac{1}{\Delta\sigma_k} (\kappa \dot{\sigma})_{k+\frac{1}{2}} p_k \hat{\theta}_{k+\frac{1}{2}} \\ - (\pi \dot{\sigma})_{k-\frac{1}{2}} p_k \hat{\theta}_{k-\frac{1}{2}} \end{aligned} \quad (A-4)$$

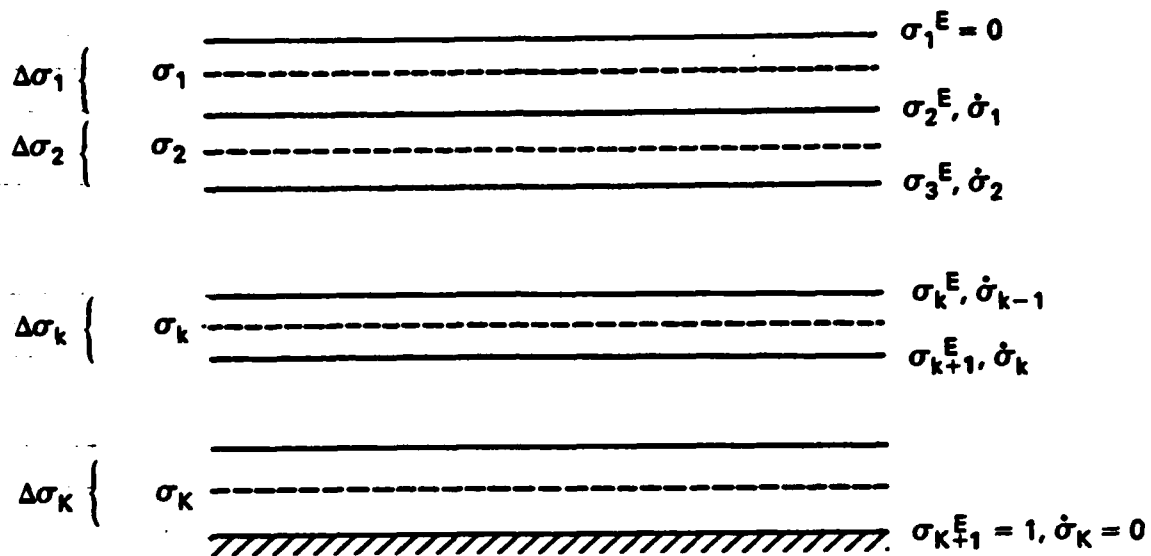


Fig. A1 — Schematic diagram indicating the definitions of σ , σ^E and $\Delta\sigma$

$$= \underbrace{\pi \frac{T_k}{p_k} \frac{\partial p_k}{\partial \pi} \left(\frac{\partial}{\partial t} + v_k \cdot \nabla \right) \pi + \pi Q_k / c_p}_{||} ,$$

$$\frac{1}{c_p} (\sigma \pi \alpha)_k$$

where $\hat{\theta}_{k+\frac{1}{2}} = \frac{\ln \theta_k - \ln \theta_{k+1}}{\frac{1}{\theta_{k+1}} - \frac{1}{\theta_k}}$,

Thus,

$$\frac{\partial}{\partial t} \langle \pi T \rangle + [T] \langle D \rangle + [M_4] \langle D \rangle = - \langle \frac{\sigma \pi \alpha}{c_p} \rangle \langle N_2 \rangle^T \langle D \rangle + \langle R \rangle_T ,$$

where

$$[T] = \begin{pmatrix} \bar{\bar{T}}_1 & 0 & \text{----} & 0 \\ 0 & \bar{\bar{T}}_2 & \text{----} & \\ \text{-----} & & & \\ 0 & \text{-----} & \bar{\bar{T}}_K & \end{pmatrix}$$

and

$$[M_4]_{k,j} = (v_{k,j} p_k \hat{\theta}_{k+\frac{1}{2}} - v_{k-1,j} p_k \hat{\theta}_{k-\frac{1}{2}}) / \Delta \sigma_k ,$$

where $V \equiv [N_1]$

and

$$[M_2] = [M_4] + [T] + \frac{1}{c_p} \begin{pmatrix} (\sigma\pi\alpha)_1 \langle N_2 \rangle^T \\ \vdots \\ \vdots \end{pmatrix}.$$

It should be emphasized here that all quantities in the matrices are computed using the globally averaged temperature and surface pressure.

REFERENCES

- Arakawa, A., 1972: Design of the UCLA general circulation model. Numerical Simulation of Weather and Climate, Dept. of Meteorology, Univ. of California, Los Angeles, Tech. Report. 7, 116 pp.
- Arakawa, A., and Lamb, V. R., 1977: Computational design of the UCLA General Circulation Model. Methods in Computational Physics, Vol. 17, Academic Press, 173-265.
- Arakawa, A., and Mintz, Y., 1974: The UCLA atmospherical general circulation model, Workshop notes, Dept. of Meteorology, UCLA.
- Brown, J. A., and Campana, K., 1978: An economical time-differencing system for numerical weather prediction, Mon. Wea. Rev. 106, 1125-1136.
- Burridge, D. M., 1975: A split semi-implicit reformulation of the Bushby-Timpson 10-level model, Quart. J. R. Met. Soc., 101, 777-792.
- Courant, R., Friedrichs, K., and Lewy, H., 1928. Über die partiellen Differenzengleichungen der mathematischen Physik. Math. Annalen, 100, 32-74.
- Gadd, A. J., 1978: A split explicit integration scheme for numerical weather prediction, Quart. J. R. Met. Soc., 104, 569-582.

- Kwizak, M., and Robert, A. J., 1971. A semi-implicit scheme for grid point atmospheric models of the primitive equations. Mon. Wea. Rev., 99, 32-36.
- Madala, R. V., 1981: Efficient time integration schemes for atmosphere and ocean models, Chap. 4, Finite-difference techniques for vectorized fluid dynamics calculations, Springer Series in Computational Physics.
- Marchuk, G. I., 1974: Numerical methods in weather prediction. Academic Press, 277 pp.
- Messinger, F., and Arakawa, A., 1976: Numerical methods used in atmospheric models. WMO-ICSU GARP Publication Series No. 17, 64 pp.
- Robert, A. J., 1969 : The integration of a spectral model of the atmosphere by the implicit method. Proc. WMO/IUGG Symposium on Numerical Weather Prediction in Tokyo, 1968. Meteor. Soc. Japan. VII-19-VII-24.
- Robert, A. J., Henderson, J., and Turnbull, C. A., 1972: An implicit time integration scheme for baroclinic models of the atmosphere. Mon. Wea. Rev., 100, 329-335.
- Shuman, F. G., 1971: Resuscitation of an integration procedure. NMC Office Note 54, 55 pp.

Appendix S

DIOCOTRON INSTABILITY OF A RELATIVISTIC
COAXIAL MULTI-RING HOLLOW ELECTRON BEAM

Diocotron instability of a relativistic coaxial multi-ring hollow electron beam

H. C. Chen

Science Applications, Inc., McLean, Virginia 22102

P. J. Palmadesso

Plasma Physics Division, Naval Research Laboratory, Washington, D.C. 20375

(Received 15 May 1980; accepted 27 October 1980)

The diocotron stability properties of a relativistic coaxial multi-ring hollow electron beam are investigated using a macroscopic cold fluid description based on moment-Maxwell equations. It is found that for a broad range of beam parameters and somewhat more general type beam profiles, the growth rate of instability has a sensitive dependence on fractional charge neutralization, relative position of the rings with conducting wall, and gap-length of the rings. In the case of a sharp boundary density profile, the beam can easily be stabilized by a small fractional charge neutralization with appropriate gap-length. The growth rate can be either enhanced or reduced depending on the position and gap-length of the rings.

I. INTRODUCTION

There has been considerable interest in recent years in the development of powerful relativistic electron beams.¹⁻³ Intense relativistic hollow electron beams have recently been used in the laboratory for high-power microwave generation,² in electron ring accelerators, and auto-accelerators,³ etc.

The auto-acceleration process is a collective acceleration mechanism for generating a high kinetic energy hollow electron beam. Such beams are often designed to have approximately uniform electron density within an annular space near the wall of a cylindrical drift tube with no electrons outside the annulus. Previous theoretical studies of the diocotron instability in hollow beams have assumed a beam profile of this type.

We have considered a somewhat more general type beam profile, namely, a hollow coaxial multi-ring electron beam. Using a macroscopic cold fluid model, the diocotron instability which characterizes a hollow multi-ring electron beam has been investigated for a broad range of beam parameters and different geometries. Significantly different results exist between the multi-ring and single-ring hollow beams. Description of these differences is the purpose of this paper.

The basic theory and assumptions are described and the equilibrium properties of the beam are examined in Sec. II. In Sec. III, we confine our study to systems exhibiting linear behavior from which an eigenvalue equation for the perturbed potential is derived. In the case of a square radial density profile a closed algebraic dispersion relation for the complex eigenfrequency is extracted. The dispersion relation is solved numerically in Sec. IV and the stability properties are investigated in detail. The conclusions are drawn in Sec. V.

II. BASIC THEORY

We start by considering a two-ring electron hollow beam with a smooth perfectly conducting wall as shown in Fig. 1. The analysis of dynamic properties is based on a macroscopic cold fluid model which is idealized in that the flow is laminar and there is no variation in the

axial direction.⁴ We assume a system infinite in the axial direction, and a strong uniform background magnetic field which prevents the beam from spreading. We consider a cylindrically symmetrical electron beam containing n electrons per unit volume moving along a strong axial magnetic field in a conducting drift tube at low pressure so that the beam is neither current nor charge neutralized. Two components are assumed, ions with charge q have no component of velocity along the beam and electrons move with velocity $\beta c \hat{z}$, which is assumed large compared with the transverse velocity. We allow partial neutralization by a fraction f of charges of opposite sign trapped in the beam. The neutralization fraction f denoting the ratio of neutralizing charge to beam charge is assumed uniform across the beam. By virtue of these assumptions the electrons are described in cylindrical geometry (r, θ, z) as a macroscopic cold fluid immersed in a uniform axial magnetic field $B_0 \hat{z}$, with both radial space-charge and azimuthal self-magnetic fields included. The continuity equation and the equation of motion for the electron fluid can be expressed in the relativistic form as

$$\frac{\partial n}{\partial t} + \nabla \cdot (n \mathbf{V}) = 0, \quad (1)$$

$$\left(\frac{\partial}{\partial t} + \mathbf{V} \cdot \nabla \right) \gamma m \mathbf{V} = q(\mathbf{E} + \mathbf{V} \times \mathbf{B}), \quad (2)$$

where $n(\mathbf{x}, t)$ and $\mathbf{V}(\mathbf{x}, t)$ are the density and mean velocity and $\mathbf{E}(\mathbf{x}, t)$ and $\mathbf{B}(\mathbf{x}, t)$ are the electric and magnetic

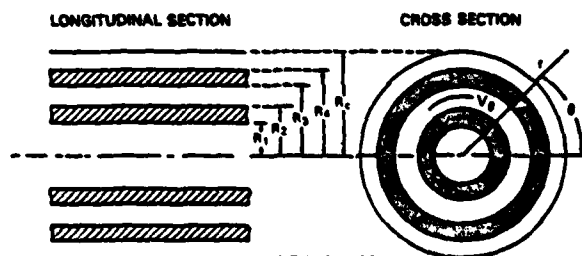


FIG. 1. Longitudinal and cross section of equilibrium configuration and coordinate system.

fields, respectively. q and m are the charge and rest mass of the electron and $\gamma = (1 - \beta^2)^{-1/2}$ and $\beta = v/c$ are the standard relativistic quantities, and c is the velocity of light in vacuum. The system can be closed by adding Poisson's equation and Ampere's law

$$\nabla \cdot \mathbf{E} = \epsilon_0^{-1}(1-f)qn, \quad (3)$$

$$\nabla \times \mathbf{B} = \mu_0 q \beta c n \hat{e}_z + \mu_0 \epsilon_0 \frac{\partial \mathbf{E}}{\partial t}, \quad (4)$$

where μ_0 and ϵ_0 are the permeability and permittivity of free space.

The equilibrium state ($\partial/\partial t = 0$) is azimuthally symmetric ($\partial/\partial \theta = 0$ and $\partial/\partial z = 0$) and is characterized by electron density $n(r)$ and azimuthal electron fluid velocity $V_\theta \hat{e}_\theta$. The deviation from charge neutrality produces a radial electric field that influences the azimuthal motion of the electron fluid. In the case of a sharp-boundary equilibrium in which the electrons have a double rectangular density profile as shown in Fig. 2, where $r = R_c$ is the radial location of a grounded conducting wall, the self-generated radial electric and azimuthal fields can be obtained by integrating Eqs. (3) and (4). Thus,

$$E_r(r) = (1-f)\beta^{-1}B_\theta(r),$$

$$E_r(r) = \frac{1}{2\epsilon_0}qn(1-f) \begin{cases} (r^2 - R_1^2)/r & R_1 < r < R_2, \\ (R_2^2 - R_1^2)/r & R_2 < r < R_3, \\ (R_2^2 - R_1^2 + r^2 - R_3^2)/r & R_3 < r < R_4, \\ (R_2^2 - R_1^2 + R_4^2 - R_3^2)/r & R_4 < r < R_c, \end{cases} \quad (5)$$

The radial electric field arising from the space charge has been reduced by a factor of $(1-f)$ because of the effect of partial neutralization by ions. It follows from Eq. (2) that equilibrium force balance in the radial direction can be expressed as

$$-\gamma m V_\theta^2/r = q(E_r + V_\theta B_\theta - \beta c B_\theta). \quad (6)$$

Equation (6) is simply a statement of the radial force balance of the centrifugal, magnetic, and electric forces on an electron fluid element. The self-magnetic field produces a force toward the axis which is weaker than the outward radial electrostatic force. The balance among electric, centrifugal, and magnetic forces gives the angular velocity $\omega_\theta(r)$ of an electron fluid element in slow rotational equilibrium

$$\omega_\theta(r) = \frac{V_\theta}{r} = \frac{\omega_{ce}}{2\gamma^2} \begin{cases} (r^2 - R_1^2)/r^2 & R_1 < r < R_2, \\ (R_2^2 - R_1^2 + r^2 - R_3^2)/r^2 & R_3 < r < R_4, \end{cases} \quad (7)$$

where ω_{ce} and ω_p are the electron cyclotron and plasma frequencies, respectively. ω_p can be permitted to depend on r , giving sheared cold fluid rotation rather than

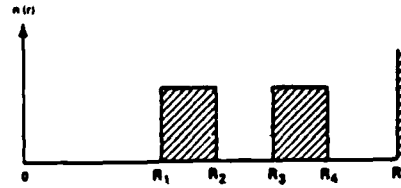


FIG. 2. Beam electron density profile for two-ring geometry.

rigid rotation. Laminar flow and the assumption of azimuthal symmetry together imply that individual charges move in helices of constant radius.

III. STABILITY ANALYSIS

We assume that all the perturbed quantities satisfy the conditions $\partial[\]/\partial z = 0$, $\partial[\]/\partial t = i\omega[\]$, and $\partial[\]/\partial \theta = -il[\]$ with $\text{Im}(\omega) < 0$, where l is the azimuthal harmonic number. After Fourier decomposing the fluid-Maxwell equations (1) to (4), it is straightforward to show that in the strong magnetic field regime $\omega_{ce} \gg \omega_p$, the eigenvalue equation for the perturbed field has the form

$$\left(\frac{1}{r} \frac{\partial}{\partial r} r \frac{\partial}{\partial r} - \frac{l^2}{r^2} \right) \delta \varphi(r) = \frac{-2l\delta \varphi(r) [\delta(r-R_1) - \delta(r-R_2) + \delta(r-R_3) - \delta(r-R_4)]}{r[(\omega/\omega_D) - (l\omega_p^2/\omega_D)]}, \quad (8)$$

where the perturbed potential $\delta \varphi(r) = \delta \phi(r) - \beta \delta A_\theta(r)$, ϕ and A are the scalar and vector potentials of the electromagnetic field, the diocotron frequency is defined by $\omega_D = \omega_{ce}^2/2\gamma^2\omega_{ce}$, and $\omega_p(r)$ was given in (7). The right-hand side of the eigenvalue Eq. (8) is equal to zero except at the surface of the beam. Moreover, the eigenfunction $\delta \varphi(r)$ satisfies the vacuum Poisson equation except at $r = R_1, R_2, R_3$, and R_4 ; therefore, the piecewise solution for the homogeneous equation can be expressed as

$$\delta \varphi(r) = \begin{cases} a r^l + b r^{-l}, & 0 < r < R_1, \\ c r^l + d r^{-l}, & R_1 < r < R_2, \\ e r^l + f r^{-l}, & R_2 < r < R_3, \\ g r^l + h r^{-l}, & R_3 < r < R_4, \\ i r^l + j r^{-l}, & R_4 < r < R_c. \end{cases} \quad (9)$$

The ten coefficients are functions of $R_1, R_2, R_3, \dots, R_c$ to be determined by the boundary conditions, the requirement implied by delta functions. The eigenfunction is continuous at each boundary and vanishes both at $r = 0$ and $r = R_c$. The effect of the delta function can be considered by multiplying both sides of r and integrating over the infinitesimal interval from $r(1-\epsilon)$ to $r(1+\epsilon)$ with $\epsilon \rightarrow 0$ in the vicinity of $r = R_1, R_2, R_3$, and R_4 , respectively. Therefore, we have the following dispersion relation given by ten equations with ten unknowns:

$$\begin{aligned}
b &= 0, \quad aR_1^{-1} + bR_1^{-1} = cR_1^{-1} + dR_1^{-1}, \quad cR_1^{-1} - dR_1^{-1} - aR_1^{-1} + bR_1^{-1} = -2(aR_1^{-1} + bR_1^{-1})(\omega/\omega_D)^{-1}, \\
cR_2^{-1} + dR_2^{-1} &= eR_2^{-1} + fR_2^{-1}, \quad eR_2^{-1} - fR_2^{-1} - cR_2^{-1} + dR_2^{-1} = 2(cR_2^{-1} + dR_2^{-1})[(\omega/\omega_D) - Y_1]^{-1}, \\
eR_3^{-1} + fR_3^{-1} &= gR_3^{-1} + hR_3^{-1}, \quad gR_3^{-1} - hR_3^{-1} - eR_3^{-1} + fR_3^{-1} = -2(eR_3^{-1} + fR_3^{-1})[(\omega/\omega_D) - Y_2]^{-1}, \\
gR_4^{-1} + hR_4^{-1} &= iR_4^{-1} + jR_4^{-1}, \quad iR_4^{-1} - jR_4^{-1} - gR_4^{-1} + hR_4^{-1} = 2(gR_4^{-1} + hR_4^{-1})[(\omega/\omega_D) - Y_3]^{-1}, \\
iR_5^{-1} + jR_5^{-1} &= 0,
\end{aligned} \tag{10}$$

where

$$Y_1 = (1 - \gamma^2 f)(R_2^2 - R_1^2)/R_2^2, \quad Y_2 = (1 - \gamma^2 f)(R_3^2 - R_1^2)/R_3^2, \quad Y_3 = (1 - \gamma^2 f)(R_4^2 - R_1^2 + R_2^2 - R_1^2)/R_4^2.$$

The determinant of the ten linear equations gives a dispersion relation of the form

$$\left(\frac{\omega}{\omega_D}\right)^4 + c_1\left(\frac{\omega}{\omega_D}\right)^3 + c_2\left(\frac{\omega}{\omega_D}\right)^2 + c_3\left(\frac{\omega}{\omega_D}\right) + c_4 = 0, \tag{11}$$

where

$$c_1 = R_{1c} - R_{2c} + R_{3c} - R_{4c} - Y_1 - Y_2 - Y_3,$$

$$\begin{aligned}
c_2 &= K_{12} - R_{13} + R_{14} + R_{23} - R_{24} + R_{34} + Y_1 - Y_2 + Y_3 - 2 + Y_1 Y_2 + Y_2 Y_3 + Y_1 Y_3 - R_{1c}(1 + Y_1 + Y_2 + Y_3) + K_{2c}(1 + Y_2 + Y_3) \\
&\quad - R_{3c}(1 + Y_1 + Y_3) + R_{4c}(1 + Y_1 + Y_2),
\end{aligned}$$

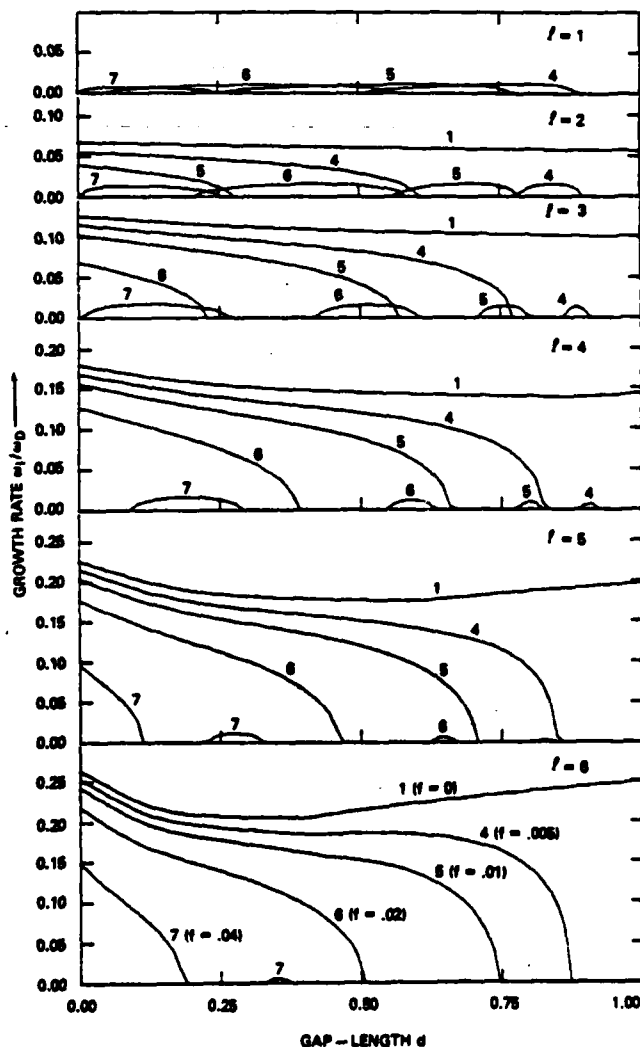


FIG. 3. Growth rate ω_i/ω_D vs gap-length $d = (R_3 - R_2)/(R_4 - R_1)$ for $R_1 = 0.84 R_c$, $R_4 = 0.92 R_c$ ($\omega_r < 0.6 \omega_D$).

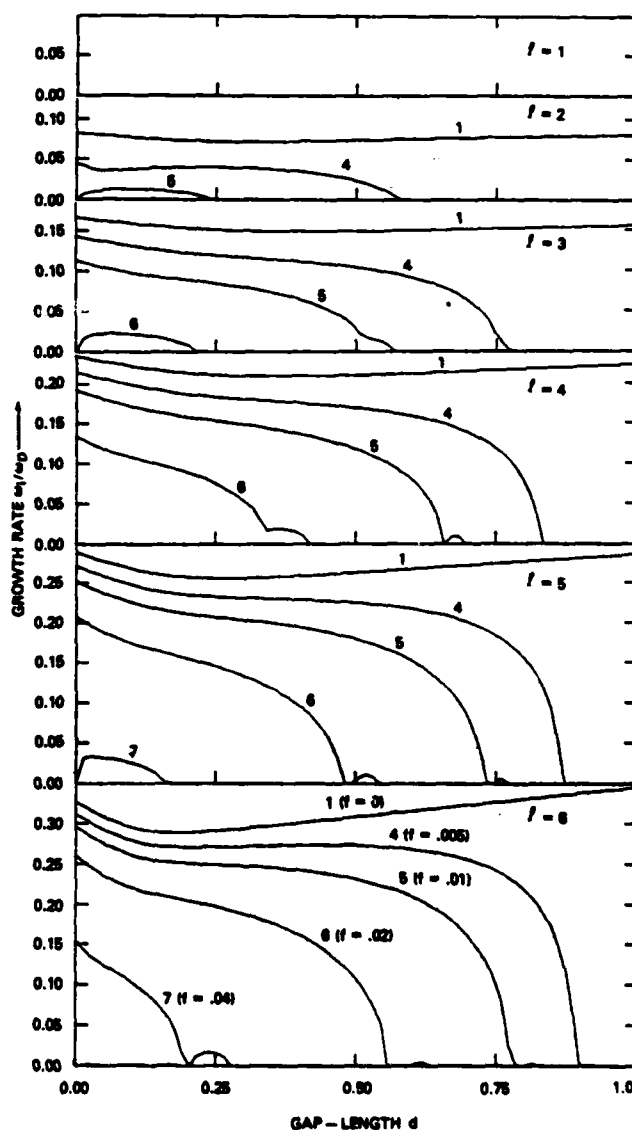


FIG. 4. Growth rate ω_i/ω_D vs gap-length $d = (R_3 - R_2)/(R_4 - R_1)$ for $R_1 = 0.64 R_c$, $R_4 = 0.72 R_c$.

$$\begin{aligned}
c_3 &= Y_1 + Y_2 + Y_3 - 2Y_1Y_3 - Y_1Y_2Y_3 - R_{12}(Y_2 + Y_3) + R_{13}(Y_1 + Y_3) - R_{14}(Y_1 + Y_2) - R_{23}Y_3 + R_{24}Y_2 - R_{34}Y_1 - R_{1c}(1 - 2Y_2 - Y_1Y_2 \\
&\quad - Y_1Y_3 - Y_2Y_3 - R_{4c}) + R_{2c}(1 - 2Y_2 - Y_2Y_3 - R_{4c}) - R_{3c}(1 - 2Y_1 - Y_1Y_3 - R_{12}) + R_{4c}(1 - 2Y_1 - Y_1Y_2 - R_{12}), \\
c_4 &= (Y_1 - 1)(Y_2 + 1)(Y_3 - 1) + R_{1c}[(1 + Y_1)(1 - Y_2)(1 + Y_3) - (1 + Y_1)R_{4c}] - R_{2c}[(1 - Y_2)(1 + Y_3) - R_{4c}] \\
&\quad - R_{3c}(1 + Y_3)(Y_1 - 1 + R_{12}) + R_{4c}(1 + Y_2)(Y_1 - 1 + R_{12}) - R_{12}[(Y_2 + 1)(Y_3 - 1) - R_{34}] + R_{12}(1 + Y_1)(1 - Y_3) \\
&\quad - R_{14}(1 - Y_2)(1 + Y_1) - R_{23}(1 - Y_3) + R_{24}(1 - Y_2) + R_{34}(Y_1 - 1),
\end{aligned}$$

where R_{ij} denotes the ratio of R_i^{2j} to R_j^{2i} . If we let $R_2 = R_3$, then Eq. (11) gives the results for the mono-ring hollow beam case as shown in Uhm and Siambis.⁶ By the methods analogous to those here, it is straightforward to extend the case to multi-ring beams.

IV. NUMERICAL RESULTS

It is concluded in Sec. III, that the dispersion relation has a quadratic form for the single-ring case and a quartic form for two rings, and so on; i.e., the order of the polynomial equation is twice the number of rings. The dispersion relation (11) is solved numerically⁷ for the complex eigenfrequency $\omega = \omega_r + i\omega_i$ with real oscillation frequency ω_r and growth rate ω_i for the unstable mode. One important feature of Eq. (11) is that the complex eigenfrequency is linearly proportional to the diocotron frequency. Consequently, the applied magnetic field strongly reduces the growth rate for fixed beam density. As a result, it is more instructive to keep the beam and plasma parameters fixed and study the growth rates for different geometries. Figure 3 shows the growth rate for a two-ring beam versus gap-length d of the rings for different mode numbers l and specified values of f . The gap-length d is defined as the distance between R_2 and R_3 while we fix the position R_1 and R_4 and keep the beamwidth of each ring identical. The total current of the beam has been held constant for various geometries so that the growth rates are evaluated at the same beam energy. As we can expect from Eq. (10), the growth rate has a strong dependence on $\gamma^2 f$. For simplicity, we specify $\gamma = 2$ and show the values of f on each curve. Note that the zero-gap case is equivalent to a single ring which is always stable for mode $l=1$ as observed by Uhm and Siambis.⁶ Therefore, beams with various gap lengths will destabilize the $l=1$ mode at least for $0.04 > f > 0.005$ as can easily be seen from Fig. 3. Note that there is no instability for the $l=1$ mode when $f=0$. The growth rate is higher for larger mode numbers. For $l \geq 2$, the growth rate remains almost constant for $f=0$ while it decreases rapidly as the fractional charge neutralization f is increased, i.e., the unstable modes can easily be stabilized by a small fractional charge neutralization with appropriate gap-length. The real frequency for the unstable modes shown in Fig. 3 is larger for higher l but does not exceed $0.6\omega_D$. It has been demonstrated that the growth rate of the instability exhibits a sensitive dependence on f . Neutralization is commonly produced from the residual gas in the apparatus. It is difficult to give a universal theory⁸ for f which depends very much on such factors as the energy of the beam and the composition and pressure of the residual gases, ionization cross section, the energy of the

secondary electrons, and whether the ion can escape from the end of the beam.

Another interesting feature is that for higher modes the double region in gap-length for instability disappears from Fig. 3 to Fig. 4. Generally, the unstable mode for a single ring can be stabilized by increasing the gap-length of a two-ring beam in this kind of geometry. Next, we want to demonstrate the effect of the total beamwidth ($R_4 - R_1$) on the diocotron instability which is illustrated in Figs. 5 and 6. The $l=1$ mode is unstable as before when the single-ring beam becomes a

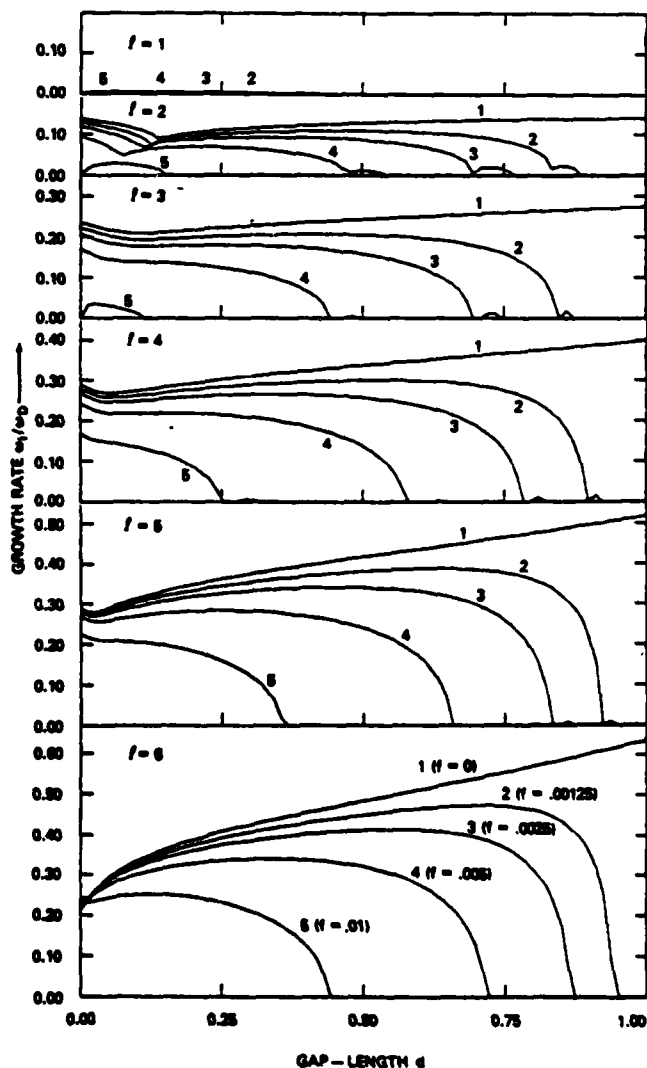


FIG. 5. Growth rate ω_i/ω_D vs gap-length $d = (R_3 - R_2)/(R_4 - R_1)$ for $R_1 = 0.64R_0$, $R_4 = 0.8R_0$.

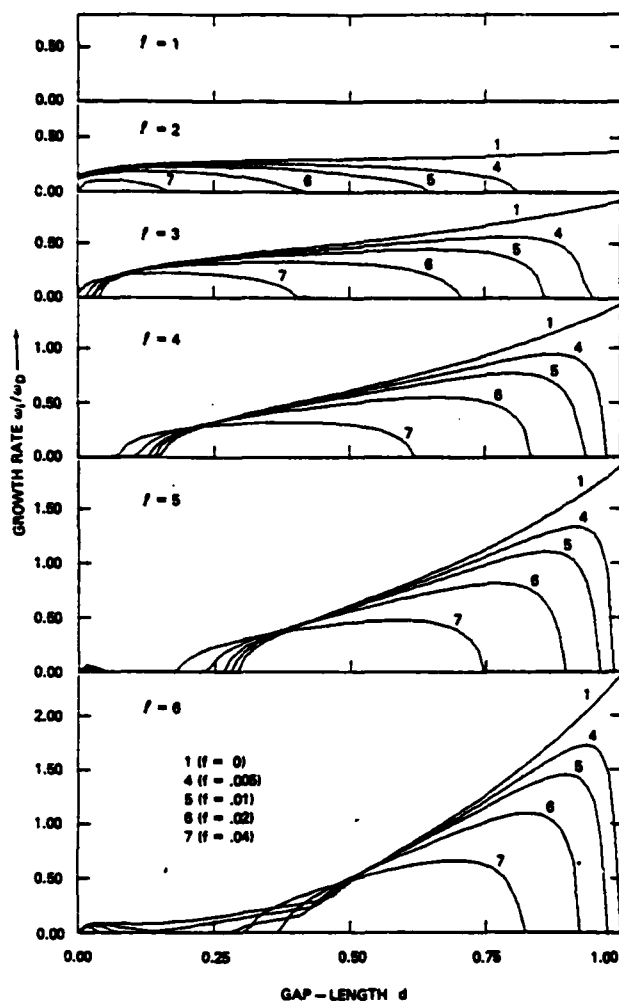


FIG. 6. Growth rate ω_i/ω_D vs gap length $d = (R_3 - R_2)/(R_4 - R_1)$ for $R_1 = 0.4R_c$, $R_4 = 0.8R_c$.

two-ring beam as shown in Fig. 5. However, the fundamental mode can no longer occur if the total beam width has expanded to the one shown in Fig. 6. Clearly, the $l=1$ mode can be destabilized by moving two rings together. For $l \geq 2$, the growth rate increases with respect to gap-length when $f=0$. Nevertheless, the growth rate for small f first increases with respect to gap-length and then decreases sharply.

Finally, it is straightforward to extend the analysis to a three-ring geometry as shown in Fig. 7. For easy comparison between the two-ring and three-ring cases,

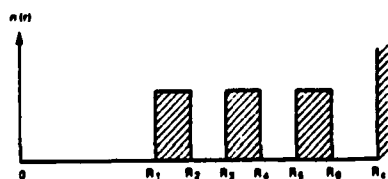


FIG. 7. Beam electron density profile for three-ring geometry.

we plot the growth rate versus gap-length $d = (R_3 - R_2)$ while fixing the positions R_1 and R_6 and keeping the beamwidth of each ring identical, the total current is also fixed. The effect of inserting the center ring can easily be seen while comparing Fig. 8 with Fig. 3. The unstable modes in two-ring geometry have been retained in the three-ring case, but also the growth rate has been enhanced by inserting the third ring in the middle, which may be caused by the strong coupling among the self-fields of the beams. For higher mode numbers, unstable modes can be found in three separate regions in the gap-length domain. If we move the outer edge of the beam away from the wall, Fig. 9 gives the geometry which can be compared to Fig. 6. It comes as no surprise that the $l=1$ mode again becomes unstable. For higher modes, the triple region for instability is obviously not seen. The conducting wall plays an important role in the diocotron instability.

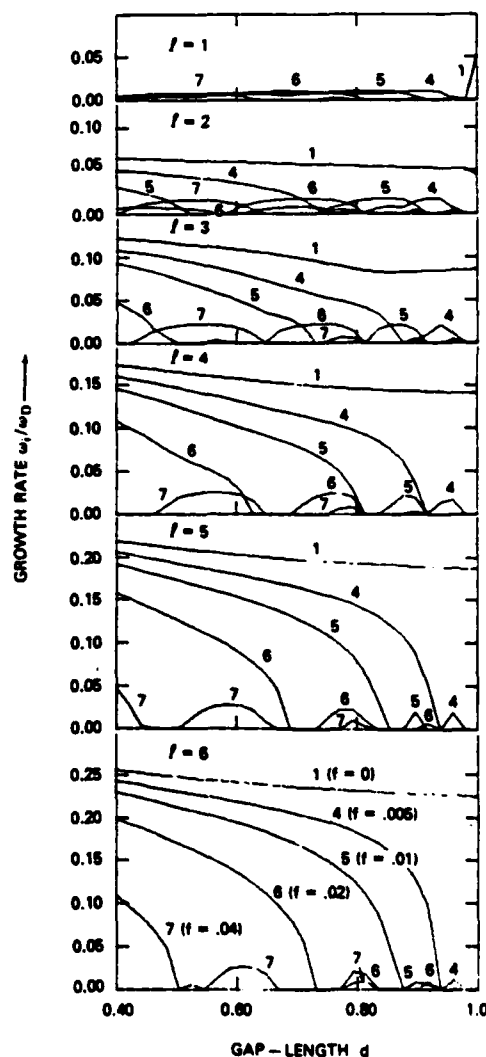


FIG. 8. Growth rate ω_i/ω_D vs gap-length $d = (R_3 - R_2)/(R_6 - R_1)$ for $R_1 = 0.84R_c$, $R_6 = 0.92R_c$.

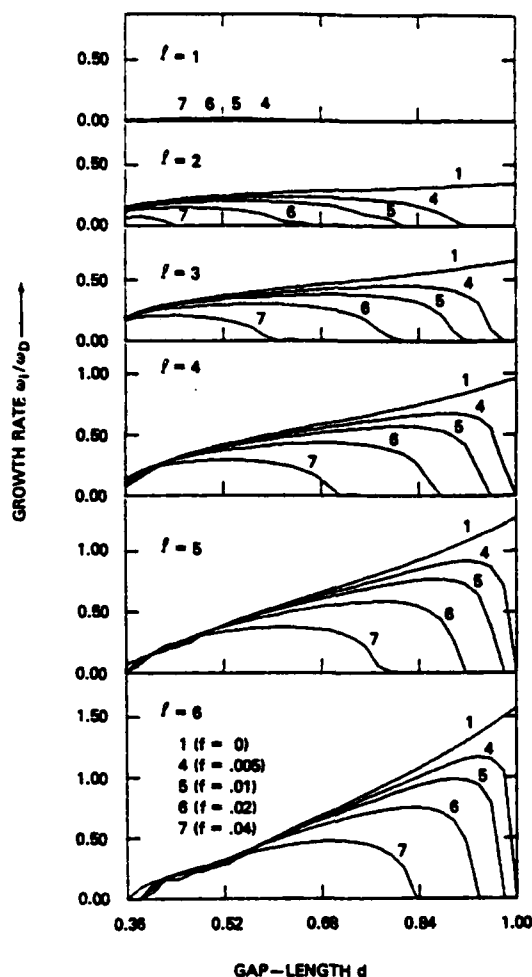


FIG. 9. Growth rate ω_i/ω_D vs gap-length $d = (R_2 - R_1)/(R_2 + R_1)$ for $R_1 = 0.4 R_2$, $R_2 = 0.8 R_1$.

V. CONCLUSION

We have formulated a fluid-Maxwell theory of the diocotron instability in an infinitely long relativistic electron beam propagating parallel to a uniform applied axial magnetic field. In beams with self-fields it fre-

quently permits simple models which illustrate many of the essential features of more realistic types of beam. The growth rate has been calculated with special emphasis on displaying results as a function of conducting wall geometry, i.e., conducting wall location relative to the position of the beam. The results show the strong influence of the neutralization fraction f , the relative position of the rings with conducting wall and gap-length of the rings on the diocotron instability. It seems that the instability has been enhanced by the multiring geometry in a rather complicated manner. In short, the $l=1$ mode which is always stable in the single-ring case can become unstable in multiring geometries. However, in the two-ring geometry, the $l=1$ mode diocotron instability can be avoided by either moving two hollow beams away from the wall or spreading two rings farther apart. For the $l \geq 2$ modes, the growth rate can be either enhanced (e.g., Figs. 5 and 6) or reduced (e.g., Figs. 3 and 4) depending on the position and gap-length of the rings. In the three-ring case, all the unstable modes occurring in the two-ring geometries have been retained and the growth rates have been enhanced at the same gap-length.

ACKNOWLEDGMENT

This work was supported by the Office of Naval Research.

- ¹D. L. Chapin, and J. J. Duderstadt, *Phys. Fluids* 18, 325 (1975); M. A. Greenspan, C. Ekdahl, J. D. Sethian, and C. B. Wharton, *Phys. Fluids* 23, 205 (1980).
- ²V. L. Granatstein, P. Sprangle, M. Herndon, R. K. Parker, and S. P. Schlesinger, *J. Appl. Phys.* 46, 3800 (1975).
- ³J. G. Slambis and M. Friedman, *Part. Accel.* 8, 217 (1978); T. R. Lockner and M. Friedman, *IEEE Trans. Nucl. Sci.* 26, 4238 (1979); J. G. Slambis, *Phys. Fluids* 19, 1784 (1976).
- ⁴J. D. Lawson, *The Physics of Charged-Particle Beams* (Clarendon Press, Oxford, 1977).
- ⁵R. H. Levy, *Phys. Fluids* 8, 1288 (1965); R. C. Davidson, *Theory of Non-Neutral Plasmas* (Benjamin, New York, 1974).
- ⁶H. S. Uhm, and J. G. Slambis, *Phys. Fluids* 22, 2377 (1979).
- ⁷S. D. Conte, and C. Boor, *Elementary Numerical Analysis* (McGraw-Hill, New York, 1965).
- ⁸A. V. Engel and M. Steenbeck, *Elektrische Gasentladungen* (Springer-Verlag, Berlin, 1932); M. J. Druryvesteyn and F. M. Penning, *Rev. Mod. Phys.* 12, 87 (1940).

END

DATE
FILMED

3-82

DTIC